Multiscale Modelling of Biological Rhythms and Systems

by

Stéphanie M. C. Abo

A thesis
presented to the University of Waterloo
in fulfillment of the
thesis requirement for the degree of
Doctor of Philosophy
in
Applied Mathematics

Waterloo, Ontario, Canada, 2024

Examining Committee Membership

The following served on the Examining Committee for this thesis. The decision of the Examining Committee is by majority vote.

External Examiner:	Karin Leiderman Associate Professor, Dept. of Mathematics University of North Carolina at Chapel Hill
Supervisor(s):	Anita Layton Professor, Dept. of Applied Mathematics University of Waterloo
Internal Member:	Sue Ann Campbell Professor, Dept. of Applied Mathematics University of Waterloo
Internal-External Member:	Brian Dixon Professor, Dept. of Biology University of Waterloo
Other Member(s):	N Sri Namachchivaya Professor, Dept. of Applied Mathematics University of Waterloo

Author's Declaration

This thesis consists of material all of which I authored or co-authored: see Statement of Contributions included in the thesis. This is a true copy of the thesis, including any required final revisions, as accepted by my examiners.

I understand that my thesis may be made electronically available to the public.

Statement of Contributions

- Chapter 4: The work in this chapter was performed by Stéphanie Abo (SA), under the supervision of Prof. Anita Layton (AL), resulting in a co-authored paper published in PLoS Computational Biology [1]. SA conceived of the study, developed the model and associated MATLAB code, performed analysis, and wrote the first draft. AL supervised the work. All authors revised the manuscript.

- Chapter 5: The work in this chapter was performed by SA, under the supervision of Prof. Anita Layton and Prof. Jose Carrillo (JC), resulting in a co-authored paper published in the SIAM Journal of Applied Dynamical Systems [2]. SA conceived of the study, developed the model and associated MATLAB code, performed analysis, and wrote the first draft. AL and JC supervised the work. All authors revised the manuscript.

- Chapter 6: The work in this chapter was performed by SA and Elisa Casella (a 3rd-year Computational Biology co-op student at the time of the study), under the supervision of AL, resulting in a co-authored paper published in the Bulletin of Mathematical Biology [3]. SA and EC conceived of the study, developed the model and associated MATLAB code, performed analysis, and wrote the first draft. AL supervised the work. SA and AL revised the manuscript.

- Chapter 7: This chapter is based on a manuscript to be submitted to PLoS Computational Biology. SA conceived of the study, developed the model and associated MATLAB code, performed analysis, and wrote the first draft. AL supervised the work, and all authors revised the manuscript.

Abstract

Living organisms possess the remarkable ability to both respond to rhythms and generate them. In some instances, unintended rhythms arise, leading to undesirable or even hazardous consequences, such as synchronized neuronal firing during epilepsy. However, in other cases, such biological rhythms are beneficial in regulating essential processes across all life forms. From bacteria to humans, rhythms permeate various aspects of life, influencing everything from biochemical reactions to lifestyle habits. Here, our focus is on understanding systems that actively generate rhythms, known as clocks. Clocks, in particular, are systems that not only generate rhythms but also respond to environmental signals. Examining rhythms in isolation, without considering their generation, alteration, or regulation, would provide limited insights into the complexities of biological systems.

We study the interaction between biological clocks and physiological processes: sleep, the immune system, metabolism, and environmental perturbations such as fluctuations in photoperiods. We develop mathematical and computational frameworks to investigate rhythms and their influence on biological processes at tissue and system levels. We specifically study cell-cell interactions at the level of the suprachiasmatic neuleus (SCN) in the hypothalamus of the brain, also called the master circadian clock. We investigate how noise at the level of the individual cells affect properties of the ensemble: period, oscillation amplitude, and bifurcation boundaries. Starting from individual dynamics, we derive macroscopic descriptions called *mean field limits* for interacting cells. Going up in scale, we also study the interactions between the peripheral circadian clock in the lung and the innate immune system during inflammation. At this organ scale, we investigate protein-protein interactions between clock proteins and immune agents, called cytokines. We are interested in the reciprocal modulation between these two systems, especially when the circadian rhythm is disrupted. Finally, we move from organ-level to the whole-body level. We develop multi-organ models of metabolism. These whole-body models integrate exercise and diet. Given the ubiquity of circadian rhythms at all levels of our physiology, these models are intended for the study of the role of external signals, beside neural signals emanating from the SCN, on (re-)synchronizing rhythms in the periphery. The interplay between such signals and metabolic processes plays a role in maintaining homeostasis, while also organizing and timing physiological processes in a proactive rather than reactive manner.

This thesis contributes to the development of novel frameworks aimed at understanding multiscale systems, analyzing the relationships between network structure and dynamics, and ultimately deriving candidate mechanisms that can be experimentally verified.

Acknowledgments

This thesis is the result of not only my work but also the support, encouragement, and contributions of many individuals who have walked this journey with me.

First and foremost, I wish to thank my advisor, Prof. Anita Layton, for her unwavering guidance, support, and trust throughout this journey. Prof. Layton, your mentorship and teachings have been instrumental to my progress. I am profoundly grateful for your encouragement and support, both academically and beyond. During the difficult times while writing this thesis, you provided me with the moral support and freedom I needed to move forward. I also extend my heartfelt thanks to my committee members: Prof. Sue Ann Campbell, Prof. N Sri Namachchivaya, Prof. Brian Dixon, and Prof. Karin Leiderman. Thank you for your availability to answer my questions, your support, your dedication to reading my thesis, and accompanying me on this path. Prof. Campbell, I am particularly grateful for your patience and mentorship, as well as for welcoming me into your research group. I would also like to thank my collaborator, Prof. Jose Carrillo, for his invaluable teachings and our insightful conversations, which have greatly influenced my research direction.

À ma chère famille, votre présence et votre soutien sans faille ont été ma force tout au long. Je suis profondément reconnaissante pour chaque moment partagé, chaque encouragement donné, et chaque obstacle surmonté ensemble. To my parents, Sonia Kafando and Alphonse Abo, and to my sisters, Ange et Alexandra, your unwavering faith in me has shaped the very foundation of my aspirations, and for that, I am forever thankful. Together, you have been my pillars of strength, providing solace in moments of doubt and celebrating every milestone with boundless enthusiasm.

Next, I would like to thank the members of the Layton group, both past and present, for their contributions to an intellectually stimulating research environment, as well as for the cherished moments of laughter and camaraderie.

I have crossed paths with many remarkable individuals in the Department of Applied Mathematics and through other activities on campus who have turned into cherished friends, colleagues, and even mentors over the years. My dear friends—Atiyeh Ahmadi, William Bell, Liang Chen, Marina Chugunova, Pritha Dutta, Aiden Huffman, Brittany Howell, Megha Manoj, Amrita Punnavajhala, Hassaan Qazi, Melissa Stadt, and my Stammtisch friends—thank you for the uncountable moments of joy, learning, and growth that I have experienced through our shared journey. Thank you also for the multitude of enriching discussions on various aspects of life, in addition to research conversations, which have certainly helped me broaden my scope of knowledge. To my beloved friends whom I

met during my time in Waterloo—Maliha Ahmed, Ala' Alalabi, Kiersten Burseze, Mariam Elsherbini, and Kimber Munford—I am grateful for your friendships, encouragement, and compassion. Thank you also for challenging me both at work and in life to grow and strive for what I desire. To the Hickey family, thank you for your kindness, support, and love throughout the years. We are now family, and I am immensely grateful to have met you.

I extend my deepest gratitude to my professors in the Department of Applied Mathematics. Your dedication to teaching and your unwavering support have been instrumental in my academic journey. I am thankful for your wisdom, patience, and the knowledge you have imparted to me. To my mentor, Somantika Datta, thank you for your guidance, consistency, and candor. As you once said to me, "good mentorship makes a huge difference, and I want myself to be that way to the next generation of scholars. I see that as a way to repay what I have so generously received." Ditto.

And thank you to God for endless love, mercy, and grace.

Dedication

This is dedicated to my beloved Yaaba.

Table of Contents

List of Figures

List of Tables

Chapter 1

Introduction

Sleep, diet, and exercise form the cornerstone of a healthy lifestyle, promoting critical biological functions to uphold physical and mental well-being. Yet, amidst the cadence of modern life, sleep disorders afflict millions, while the prevalence of type 2 diabetes steadily increases. According to the National Institutes of Health, 1 in 3 adults in the United States alone suffer from sleep deprivation, and 50 to 70 million Americans have chronic sleep disorders [19]. Aditionally, about 422 million people worldwide have diabetes, and 1.6 million deaths are directly attributed to diabetes each year [20]. Both the number of cases and the prevalence of diabetes have been steadily increasing over the past few decades. Type 2 diabetes accounts for about 90-95% of all adult diabetes cases [21]. Of particular concern for the steady increase in these disorders is the disruption of circadian rhythms—the endogenous rhythms in behavioral and physiological processes, which cycle with a period of approximately (*circa*) 24 hours. A master clock located in the suprachiasmatic nuclei (SCN) of the brain regulates the circadian rhythm of physiological and behavioral activities in mammals. Circadian disruption is a modern-day lifestyle hazard exacerbated by factors like shift work, inadequate diet, and physical inactivity [22–24]. Epidemiological evidence underscores the association between circadian disruptions and an elevated risk of type 2 diabetes, with shift work alone linked to a 10 to 40% increased risk [25].

Research on circadian biology is still in its nascent stages, while studies on metabolism and exercise have long been established. However, a significant gap persists in the scientific community, impacting research waves, both old and new: the lack of sex-specific research. For instance, concerning the escalating rates of sleep deprivation, emerging evidence suggests that women may be more susceptible to extended wakefulness and circadian misalignment, potentially amplifying their susceptibility to sleep and metabolic disorders compared to men [19]. This raises concerns regarding long-term health consequences. Sex-

specific research lags due to the underrepresentation of females in relevant studies [26, 27]. Historically, women were sidelined in biomedical investigations, with studies predominantly focusing on male subjects under the assumption of generalizability across sexes [26–28]. However, contemporary research underscores fundamental morphological and physiological distinctions between males and females [26–29]. This gap in research risks overlooking crucial insights into sex-based physiological variations, with far-reaching implications such as sex-specific adverse drug reactions [30, 31].

Key components of maintaining health, such as the sleep-wake cycle, exercise regimen, and dietary habits, are intricately regulated by circadian rhythms. Our internal clocks provide a way to anticipate external cues and hence to organize physiology and behavior in a proactive rather than a responsive manner [32]. For instance, the restriction of molecular and behavioural processes to specific day-times has the advantage of temporally separating incompatible metabolic processes [33]. Evidence suggests that disruptions in circadian rhythmicity are closely linked to metabolic disorders like type 2 diabetes. In turn, other biological systems, such as our immune, cardiovascular, and metabolic systems, can affect the circadian system and modulate the rhythms either in a supportive or pervasive manner [34]. Understanding how our biological clocks integrate with our whole-body machinery and how circadian disruptions contribute to diseases is paramount. Equally essential is addressing the disparity in research between sexes to investigate how sex and hormonal factors impact various physiological processes, including metabolic health, cardiovascular function, immune responses, and neurological conditions. As such, computational modelling has emerged as a valuable tool to investigate physiological mechanisms [29] *in silico*.

Several mathematical models have emerged to explore properties of the SCN in isolation, including synchrony, ensemble period, and entrainment ability [35–42]. Most of these models are deterministic and formulated as coupled ordinary differential equations. However, recent studies have delved into the impact of noise on the circadian clock using stochastic differential equations or experimental analyses of stochastic rhythms [43–45]. These models adopt a particle-like description of interacting neurons and are called individual-based models (IBMs). They are typically employed in animal swarming scenarios [46, 47]. Common coupling topologies include all-to-all coupling and small-world networks [35–37, 48, 49]. For systems with a large number of interacting agents, macroscopic descriptions based on the evolution of a density of individuals are utilized, leading to continuum models. The scaling limit of these models is referred to as the *mean field limit* [47, 50, 51]. Continuum models are valuable for simplifying IBMs into an effective one-body problem: the particle probability density [50].

There exists coupled mathematical models of the circadian clock and its interaction with various systems such as immunity and glucose metabolism. In the realm of immunity,

models can be categorized into two main groups. The first category explores the interplay between circadian rhythms and the immune system through neuroendocrine mediators like melatonin and cortisol [52–54]. These models utilize rhythmic hormones to drive circadian variations without explicitly modelling the core clock machinery. Conversely, the second category incorporates the core clock system but features unidirectional coupling from the clock to the immune system, as seen in models of the NF-κB network modulated by the circadian clock [55]. Recent insights suggest a reciprocal relationship between the immune system and the circadian clock [56, 57]. Mathematical models focusing on glucose metabolism can be classified into three groups. The first group explores the interplay between the SCN and glucose metabolism via rhythmic glucocorticoids like cortisol and melatonin [58, 59], often without incorporating peripheral clocks or disruptions due to feeding/fasting schedules. The second group models glucose-stimulated insulin secretion, incorporating circadian modulation via insulin granule trafficking but omitting the core clock circuitry [60, 61]. Finally, liver-specific models integrate feeding and fasting cycles with the clock while disregarding interactions with other organs [62, 63].

As for models of metabolism alone (with no circadian influence), various types of mathematical models have been developed. Early models extensively simulated glucose-insulin metabolism to analyze the effect of insulin secretion on glucose homeostasis [64, 65]. However, many of these early models used coarse-grained compartmental models that were not always based on molecular mechanisms, limiting their applicability to specific functions. In contrast, multi-scale, large-scale dynamic models have emerged to provide a more comprehensive understanding of metabolism [3, 66–77]. These biochemistry-based mechanistic models are better suited for identifying specific components that contribute to the metabolic interface at the whole-body level.

The current state of research in metabolic and immune health highlights the necessity for sex-specific, multi-organ, and multi-scale models that capture the reciprocal interactions between organs and systems. This thesis aims to address these gaps by integrating circadian biology with related systems, particularly immunity and metabolism. Utilizing new biology and new mathematics, this thesis intends to highlight: 1) how network properties of biological oscillators contribute to broadband synchronization and the emergence of robust circadian cycles; 2) how sex differences impact circadian regulation in humans, with a particular focus on immunity under circadian disruption; and 3) how sex differences modulate energy metabolism related to diet and exercise. Specifically, for the latter, our work lays down mathematical frameworks for future studies of feeding-fasting cycles, diet regimens, and their role in shaping the clock-metabolic interface. Ultimately, our research justifies factoring in sex differences when optimizing mathematical models geared towards personalized medicine. Our mathematical models serve as computational tools with broad

applicability across diverse problem domains, ultimately facilitating the generation of experimentally verifiable predictions.

The remainder of this manuscript is organized as follows.

Chapter 2. Mathematical background
Chapter 2 provides an introduction to the mathematical concepts necessary for the later work in this thesis. It covers dynamical systems theory, elements of bifurcation theory, and important results regarding the derivation of mean field limits for Vlasov and McKean-Vlasov systems.

Chapter 3. Biological background
Chapter 3 presents the biological foundations supporting the applications of our multiscale models. We delve into concepts such as circadian systems, ranging from the master synchronizer in the brain to peripheral clocks. Additionally, we cover innate and adaptive immunity, as well as metabolism, including energy homeostasis and substrate utilization patterns during feeding and fasting cycles. These concepts are important for informing our model constructions and shaping our modelling assumptions throughout the thesis.

Chapter 4. Modelling the circadian regulation of the immune system: sexually dimorphic effects of shift work
In Chapter 4, we develop a coupled mathematical model of the interplay between the circadian clock in the lung and the innate immune system, with a specific emphasis on how circadian disruption, such as shift work, affects immune responses. We construct both male and female versions of the model. This study marks the first attempt to model the circadian-immune interaction system, incorporating circadian disruption and sex-specific adjustments. This research was conducted in collaboration with Prof. Anita T. Layton, and the chapter has been published in PLoS Computational Biology [1].

Chapter 5. Can the clocks tick together despite the noise? Stochastic simulations and analysis
In Chapter 5, we derive a macroscopic description of the SCN network based on mean field PDEs for the evolution of a density of individuals. The biochemical dynamics of each neuron are modeled by a Goodwin-type oscillator. We conduct a numerical bifurcation analysis of the continuum limit and characterize the bifurcations resulting from noise-induced transitions. To the best of our knowledge, no study has discussed the influence of external noise on the circadian clock through mean-field equations. This research was performed with Prof. Anita T. Layton and Prof. José A. Carrillo, and the chapter has

been published in the SIAM Journal on Applied Dynamical Systems [2].

Chapter 6. Sexual dimorphism in substrate metabolism during exercise
In Chapter 6, we construct sex-specific whole-body models of energy metabolism during aerobic exercise. We develop and utilize these models to address a gap in the literature regarding the mechanism underlying the observation that women oxidize significantly more lipids and fewer carbohydrates than men. This sexual dimorphism in substrate metabolism has been attributed, in part, to observed differences in epinephrine and glucagon levels between men and women during exercise, as well as differences in body composition. We quantify the extent of sex differences in carbohydrate and lipid metabolism in various organs and tissues and identify a candidate physiological mechanism in the liver that drives the observed sex differences in substrate utilization. This research was performed with Prof. Anita T. Layton and Elisa Casella, and the chapter has been published in the Bulletin of Mathematical Biology [3].

Chapter 7. Modelling sex-specific whole-body metabolic responses to feeding and fasting
In Chapter 7, we further develop our whole-body models to establish connections between cellular metabolism in organs and systemic responses following different mixed meals. Our models investigate how men and women metabolize mixed meals, especially those high in carbohydrates and fats. We specifically address a gap in the experimental literature regarding women exhibiting lower hepatic glucose output compared to men, despite taking up and oxidizing more FFA. We quantify sex differences in carbohydrate and lipid metabolism at the whole-body level and propose a candidate physiological mechanism that drives sex differences in glucose production and fat oxidation patterns. This research was conducted in collaboration with Prof. Anita T. Layton, and the chapter is currently being prepared for submission.

Chapter 8. Conclusions and future directions
Chapter 8 summarizes the main findings of this thesis and proposes future research directions centered around the theme of "timed lifestyle interventions." We will discuss related approaches for modelling the influence of biological rhythms through both oscillatory signals, such as hormones and light, and non-oscillatory signals, such as diet and exercise.

Chapter 2

Mathematical background

In this chapter, we introduce some mathematical background necessary for understanding the mathematical concepts and modelling principles in this thesis. We begin with a brief overview of dynamical systems and bifurcations in the next section. Then, we discuss the special case of Hopf bifurcations in section 2.2. In section 2.3, we introduce the theory of mean field limits and propagation of chaos. Specific mathematical prerequisites pertinent to the biological systems of interest (diet, exercise, immunity, and circadian rhythms) are presented directly within the relevant chapters, where we explain how to translate biological information into mathematical formalisms.

The introduction to dynamical systems theory and bifurcations follows closely from the books of Kuznetsov [4], Wiggins [78], and Strogatz [79]. The section on mean field theory follows closely from the work of Carrillo et al. [47, 80] and Chaintron and Diez [81, 82].

2.1 A review of dynamical systems

A system is characterized by the set X of all its possible states, called an abstract state space or phase space. The transition of a state over time $t \in T$, where T is a number set, is called *evolution*. In this thesis we will study the evolution of systems in continuous time $T = \mathbb{R}$. The evolution of an initial state $x_0 \in X$ to a state $x_t \in X$, as time t changes, can be described by an evolution operator or flow of the system ϕ parametrized by t, i.e. a family of maps given by

$$\phi^t : X \to X, \quad x_t = \phi^t(x_0)$$

We proceed to define a dynamical system. We note that not any map is admissible as an evolution operator of a dynamical system. We make precise the conditions for admissible evolution operators below.

Definition 2.1.1 (Dynamical system)**.** A state space X, time set T, and evolution operator ϕ^t are said to uniquely define a dynamical system $\{T, X, \phi^t\}$ if

$$\phi^0(x) = x, \quad \forall x \in X, \tag{2.1}$$

$$\phi^{t+s}(x) = \phi^s(\phi^t(x)), \quad \forall x \in X, \quad t, s \in T. \tag{2.2}$$

Condition (2.1) is called the continuity condition, and (2.2) is the semi-group property. There are two main types of dynamical systems: differential equations and iterated maps (also known as difference equations). This thesis focuses solely on differential equations.

We next define some preliminary mathematical objects.

Definition 2.1.2 (Orbit)**.** An orbit or trajectory with initial condition x_0 is the ordered set defined by

$$\left\{x \in X : x = \phi^t(x_0),\ t \in T\right\} \subset X$$

Definition 2.1.3 (Phase portrait)**.** The phase portrait of a dynamical system is the partitioning of the state space into orbits.

Definition 2.1.4 (Smoothness)**.** A dynamical system $\{T, X, \phi^t\}$ is said to be smooth of index r, or C^r, if the first r derivatives of ϕ with respect to x exist and are continuous at every point $x \in X$.

Definition 2.1.5 (Invariant set)**.** A set of states $Y \subseteq X$ is called an invariant set if for all $x_0 \in Y$, $\phi^t(x_0) \in Y$, $\forall t \in T$.

Equilibria are an important special class of invariant sets.

Definition 2.1.6 (Equilibrium)**.** An equilibrium or fixed point $x^* \in X$ is such that $\phi^t(x^*) = x^*$, for all $t \in T$.

In this thesis we consider states $x \in X \subset \mathbb{R}^n$ of dynamical systems that evolve in continuous time $t \in T = \mathbb{R}$ and are described by a system of ordinary differential equations (ODEs)

$$\frac{\mathrm{d}x}{\mathrm{d}t} \equiv \dot{x} = F(x), \quad x \in \mathcal{D} \subset \mathbb{R}^n \tag{2.3}$$

where $\mathcal{D}$ is a domain and $F : \mathbb{R}^n \to \mathbb{R}^n$ is smooth in an open region $U \subset \mathbb{R}^n$. Then by classical theory (Peano, Picard, and Lindelöf), there is a function $x = x(t, x_0), x : \mathbb{R} \times \mathbb{R}^n \to \mathbb{R}^n$, which is smooth in (t, x) and, for each initial condition $x_0 \in U$, satisfies the conditions

1. $x(0, x_0) = x_0$, and
2. $\exists\ \mathcal{I} = (\delta_1, \delta_2)$, where $\delta_{1,2} > 0$ such that $\forall t \in \mathcal{I}$

$$y(t) = x(t, x_0) \in U, \quad \text{and} \quad \dot{y}(t) = F(y(t)).$$

Let $\mathcal{D} = X \subset \mathbb{R}^n$ then the ODE system given by (2.3) is a continuous dynamical system $\{T, X, \phi^t\}$ with evolution operator $\phi^t(x_0) := x(t, x_0)$. We will assume that F depends only on the states $x \in X$ explicitly and not on time $t \in T$. Then the dynamical system $\{T, X, \phi^t\}$ is called **autonomous**.

For our system of ODEs (2.3) the condition in definition 2.1.6 becomes

$$F(x^*) = 0.$$

Definition 2.1.7 (Periodic orbit)**.** A periodic orbit is a non-constant (non-equilibrium) orbit Γ such that each $x^* \in \Gamma$ satisfies

$$x(t + T^*, x^*) = x(t, x^*)$$

with some constant $T^* > 0$. We call the smallest T^* which satisfies this definition the *period* of Γ.

A periodic orbit Γ on a plane is a closed curve. We call **limit cycle** an isolated periodic orbit, i.e., if in the neighborhood of Γ, there are no other periodic orbits. A significant portion of this thesis is devoted to modelling systems that exhibit limit cycle behaviour. Such behaviours arise from a transition in the dynamics of a flow, such as a loss of stability or a change in the number of invariant sets—a *bifurcation*. Before we formalize this statement, we remind the reader that a *homeomorphism* is a continuous invertible function with a continuous inverse.

Definition 2.1.8 (Topological equivalence)**.** A dynamical system $\{T, \mathbb{R}^n, \phi^t\}$ is called topologically equivalent in a region $V \in \mathbb{R}^n$ to a dynamical system $\{T, \mathbb{R}^n, \psi^t\}$ in a region $W \in \mathbb{R}^n$ if there is a homeomorphism $h : \mathbb{R}^n \to \mathbb{R}^n$ mapping orbits of the first system in V to orbits of the second system in W, preserving the direction of time.

Definition 2.1.9 (Bifurcation)**.** A bifurcation occurs at $\mu = \mu^* \in \mathbb{R}^p$ if the phase portrait of the dynamical system is not topologically equivalent as μ is varied through the value $\mu = \mu^*$.

As part of the analysis conducted in this thesis, we explore local bifurcations, focusing specifically on the *Hopf bifurcation* type. For reference, local bifurcations arise when a change in a parameter leads to a shift in the stability of an equilibrium, or fixed point. In continuous systems, this corresponds to the real part of an eigenvalue of an equilibrium crossing through zero. The topological changes in the phase portrait of the system can be confined to arbitrarily small neighbourhoods of the bifurcating fixed points by moving the bifurcation parameter close to the bifurcation point, hence the term 'local'. There exist global bifurcations, which occur when larger invariant sets, like periodic orbits, collide with equilibria. This causes changes in the topology of the trajectories which cannot be confined to a small neighbourhood, as is the case with local bifurcations.

2.2 The case of Hopf bifurcations

2.2.1 Hopf bifurcation for flows

The *Hopf bifurcation*, also known as the *Poincaré-Andronov-Hopf bifurcation*, refers to a switch in the stability of a system accompanied by the emergence of a periodic solution. In differential equations, a Hopf bifurcation typically occurs when a pair of complex conjugate eigenvalues of the linearized flow at a fixed point become purely imaginary, indicating that the fixed point becomes a small-amplitude limit cycle as a parameter changes. This type of bifurcation can only occur in systems of dimension two or higher. The Hopf bifurcation is a local (as opposed to global) bifurcation. The following version of the Hopf bifurcation theorem [83] makes the above precise.

Theorem 2.2.1 (Hopf bifurcation)**.** *Consider the planar system*

$$\dot{x} = f_\mu(x, y), \quad \dot{y} = g_\mu(x, y), \tag{2.4}$$

where μ is a parameter. Suppose it has fixed point $(x, y) = (x_0, y_0)$, which may depend on μ. Let the eigenvalues of the linearized system about this fixed point be given by $\lambda(\mu)$, $\bar{\lambda}(\mu) = \alpha(\mu) \pm i\beta(\mu)$. Suppose further that for a certain value of μ, say $\mu = \mu_0$, the following conditions are satisfied:

1. *Non-hyperbolicity condition: conjugate pair of imaginary eigenvalues $\alpha(\mu_0) = 0$, $\beta(\mu_0) = \omega \neq 0$, where $\mathrm{sgn}(\omega) = \mathrm{sgn}[(\partial g_\mu/\partial x)\big|_{\mu=\mu_0}(x_0, y_0)]$*
2. *Transversality condition: eigenvalues cross the imaginary axis with non-zero speed $\dfrac{\mathrm{d}\alpha(\mu)}{\mathrm{d}\mu}\Big|_{\mu=\mu_0} = d \neq 0$*

3. *Genericity condition*
   $a \neq 0$, *where*
   $a = \frac{1}{16}(f_{xxx}+f_{xyy}+g_{xxy}+g_{yyy})+\frac{1}{16\omega}(f_{xy}(f_{xx}+f_{yy})-g_{xy}(g_{xx}+g_{yy})-f_{xx}g_{xx}+f_{yy}g_{yy})$,
   with $f_{xy} = (\partial^2 f_\mu/\partial x \partial y)\big|_{\mu=\mu_0}(x_0, y_0)$, *etc.*

Then a unique curve of periodic solutions bifurcates from the fixed point into the region $\mu > \mu_0$ *if* $ad < 0$ *or* $\mu < \mu_0$ *if* $ad > 0$. *The fixed point is stable for* $\mu > \mu_0$ *(resp.* $\mu < \mu_0$*) and unstable for* $\mu < \mu_0$ *(resp.* $\mu > \mu_0$*) if* $d < 0$ *(resp.* $d > 0$*) whilst the periodic solutions are stable (resp. unstable) if the fixed point is unstable (resp. stable) on the side of* $\mu = \mu_0$ *where the periodic solutions exist. The amplitude of the periodic orbits grows like* $\sqrt{|\mu - \mu_0|}$ *whilst their periods tend to* $2\pi/|\omega|$ *as* μ *tends to* μ_0. *The bifurcation is called supercritical if the bifurcating periodic solutions are stable, and subcritical if they are unstable.*

Figure 2.1 below shows the two possible Hopf bifurcations, as described by the theorem.

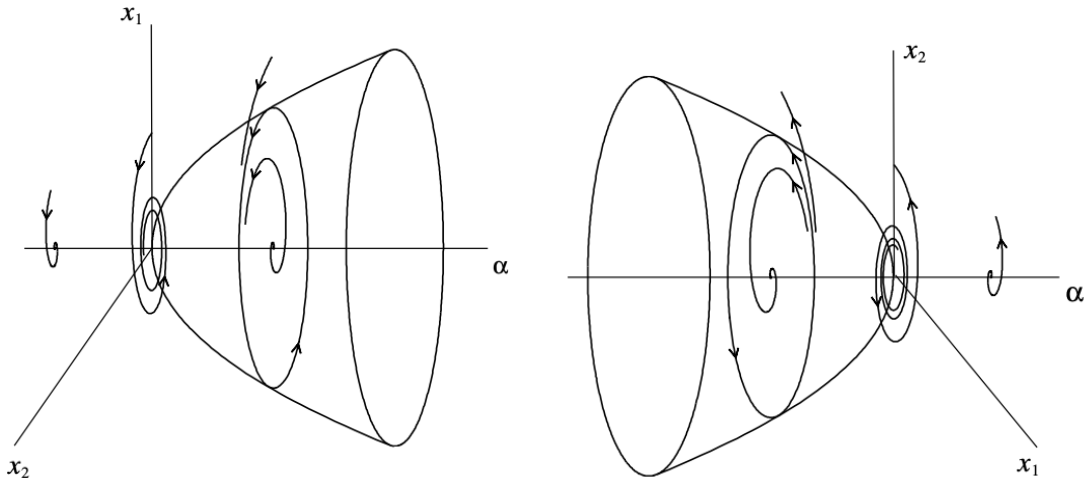

(a) Supercritical Hopf bifurcation (b) Subcritical Hopf bifurcation

Figure 2.1: In (a), the system undergoes a supercritical Hopf bifurcation, leading to the emergence of a stable limit cycle as the parameter α varies. The equilibrium point transitions from stable to unstable. In (b), a similar transition occurs where the equilibrium point shifts from stable to unstable, coinciding with the disappearance of an unstable limit cycle. Figure reproduced from Kuznetsov [4].

The 2D version of the Hopf bifurcation theorem has roots dating back to Poincaré in

the early 1890s [84], and to Andronov and colleagues in the 1930s [85]. Hopf, in 1942 [86], provided a proof for arbitrary (finite) dimensions. Using *center manifold reduction*, the higher-dimensional version essentially reduces to the planar one, provided that, aside from the two purely imaginary eigenvalues, no other eigenvalues possess zero real parts. The proof by Hopf, predating the center manifold theorem, assumes analyticity of the functions f_μ and g_μ, although C^5 differentiability suffices (a proof is available in [87]). Extensions exist to infinite-dimensional problems such as differential delay equations and certain classes of PDEs (including the Navier-Stokes equations) [87].

2.2.2 Degenerate Hopf bifurcations

If any of the specified conditions for a Hopf bifurcation are not met (e.g., due to symmetry), the emergence of a periodic orbit may still occur, but some conclusions of the theorem may no longer apply. In such cases, the bifurcation is termed a *degenerate Hopf bifurcation*. For example, if the transversality condition is unmet, the stability of the fixed point may remain unchanged, or multiple periodic solutions may bifurcate. A important case arises in Hamiltonian systems, where complex eigenvalues appear in symmetric quadruples, rendering the transversality condition unsatisfiable. Consequently, the analogous bifurcation in Hamiltonian systems, known as the *Hamiltonian-Hopf bifurcation* [88], is considerably more difficult, requiring a 4-dimensional phase space.

2.3 Mean field theory

Mean field theory is about analyzing the collective behavior of a dynamical system comprising many interacting particles. The approach allows to derive a continuous limit for the macroscopic behavior of the system, the 1-particle distribution, for a large number of interacting particles. Large systems of interacting particles have become ubiquitous. While their corresponding microscopic models are typically conceptually simple, they pose analytical and computational challenges due to the large number N of particles, especially in physical settings. The classical approach to reduce this complexity involves deriving a mesoscopic or macroscopic system, which provides a continuous description of the dynamics. The information is embedded in densities, typically solving nonlinear partial differential equations (PDEs). The concept of employing a kinetic description for large systems of particles dates back to the to the original derivation of statistical mechanics and the seminal works of Maxwell and Boltzmann [89].

We focus here on the stochastic case and refer to Refs. [90, 91] for a review of the mean field limit for deterministic systems. In the rest of this introduction, we present some of the classical theory that one typically considers. The material in this section follows closely from Refs. [81, 82, 89].

2.3.1 Basic concepts and main tools

Definition 2.3.1 (Polish space)**.** A topological space E is

(a) **Completely metrizable** if there is a metric d defining the topology of E such that (E, d) is complete,

(b) **Polish** if it is separable and completely metrizable.

Definition 2.3.2 (Exchangeability)**.** A family $(X^i)_{i\in I}$ of random variables is said to be *exchangeable* when the law of $(X^i)_{i\in I}$ is invariant under every permutation of a finite number of indeces $i \in I$.

Definition 2.3.3 (Wasserstein distances)**.** Let (E, d_E) be a Polish space. The space of probability measures with finite p-th moment is denoted by $\mathcal{P}_p(E)$. For $p \geq 1$, the Wasserstein-p distance between the probability measures μ and ν in $\mathcal{P}_p(E)$ is defined by

$$W_p(\mu, \nu) := \inf_{\pi\in\Pi(\mu,\nu)} \left(\int_{E\times E} d_E(x, y)^p \pi(\mathrm{d}x, \mathrm{d}y) \right)^{1/p},$$

where $\Pi(\mu, \nu)$ is the set of all couplings of μ and ν, that is to say, the set of probability measures on $E \times E$ with first and second marginals respectively equal to μ and ν.

Definition 2.3.4 (Kullback-Leibler (KL) divergence)**.** Let P and Q be two discrete probability distributions defined on the same sample space X. That is, both $P(x)$ and $Q(x)$ sum up to 1, and $P(x) > 0$ and $Q(x) > 0$ for any $x \in X$. The relative entropy from Q to P is defined to be

$$D_{\mathrm{KL}}(P||Q) = \sum_{x\in X} P(x) \log \left(\frac{P(x)}{Q(x)} \right)$$

Typically $P(x)$ represents the "true" distribution of data, observations, or a precisely calculated theoretical distribution. The measure $Q(x)$ typically represents a theory, model, description, or approximation of $P(x)$. The continuous version of the KL divergence is

$$D_{\mathrm{KL}}(P||Q) = \int_{-\infty}^{+\infty} P(x) \log \left(\frac{P(x)}{Q(x)} \mathrm{d}x \right)$$

The KL divergence is not a distance (metric) measure because it is not symmetric.

Itô's lemma

Given an Itô process $\mathrm{d}X_t = u_t\,\mathrm{d}t + v_t\,\mathrm{d}B_t$, where B_t is the standard Brownian motion. Let us introduce the notation $(\mathrm{d}X_t)^2$ which stands for $V_t^2\,\mathrm{d}t$. Equivalently, $(\mathrm{d}X_t)^2$ is $(\mathrm{d}X_t)\cdot(\mathrm{d}X_t)$ which is computed using the rules $\mathrm{d}t\cdot\mathrm{d}t = \mathrm{d}t\cdot\mathrm{d}B_t = \mathrm{d}B_t\cdot\mathrm{d}t = 0, \mathrm{d}B_t\cdot\mathrm{d}B_t = \mathrm{d}t$.

Definition 2.3.5 (Itô's lemma)**.** *Itô's lemma* is the chain rule for stochastic calculus. Let X_t be an Itô process $\mathrm{d}X_t = u_t\,\mathrm{d}t + v_t\,\mathrm{d}B_t$. Let $g(t,x) \in C^2([0,\infty)\times\mathbb{R})$, i.e. g is a twice continuously differentiable function. Then $Y_t = g(t, X_t)$ is again an Itô process and

$$\mathrm{d}Y_t = \frac{\partial g}{\partial t}(t,X_t)\,\mathrm{d}t + \frac{\partial g}{\partial x}(t,X_t)\,\mathrm{d}X_t + \frac{1}{2}\frac{\partial^2 g}{\partial x^2}(t,X_t)\big(\mathrm{d}X_t\big)^2$$

Using the notational convention for $\mathrm{d}X_t = u_t\,\mathrm{d}t + v_t\,\mathrm{d}B_t$ and $(\mathrm{d}X_t)^2$, we can rewrite Itô's formula as

$$\mathrm{d}Y_t = \left(\frac{\partial g}{\partial t}(t,X_t) + u_t\frac{\partial g}{\partial x}(t,X_t) + \frac{v_t^2}{2}\frac{\partial^2 g}{\partial x^2}(t,X_t)\right)\mathrm{d}t + v_t\frac{\partial g}{\partial x}(t,X_t)\,\mathrm{d}B_t.$$

Thus, the space of Itô processes is closed under twice-continuously differentiable transformations.

Convergence of probability measures

The following are classical theorems for studying the limits of sequences of probability measures. The first theorem links weak convergence and almost sure convergence of random variables.

Theorem 2.3.1 (Skorokhod's representation theorem)**.** *Let $(f_n)_{n\in\mathbb{N}}$ be a sequence of probability measures on a Polish space E which converges weakly towards $f \in \mathcal{P}(E)$ as $n \to +\infty$. Then there exists a probability space $(\Omega, \mathcal{F}, \mathbb{P})$ and some E-valued random variables X, X_n defined on this space for all $n \in \mathbb{N}$, such that*

$$\mathrm{Law}(X_n) = f_n, \qquad \mathrm{Law}(X) = f, \qquad X_n(\omega) \xrightarrow[n\to+\infty]{} X(\omega), \quad \mathbb{P}\text{-}a.s.$$

The second theorem is Prokhorov's theorem which gives a helpful characterization of compactness for the weak convergence topology. It relates tightness of measures to relative compactness. The notion of tightness is defined below.

Definition 2.3.6 (Tightness)**.** A family $(f_i)_{i\in I}$ of probability measures on a separable metric space E (endowed with its Borel σ-field) is said to be *tight* when for every $\varepsilon > 0$, there exists a compact set $K_\varepsilon \in E$ such that

$$\forall i \in I, \quad f_i(K_\varepsilon) > 1 - \varepsilon.$$

A sequence of random variables is said to be tight when the sequence of their laws is tight.

Theorem 2.3.2 (Prokhorov's theorem)**.** *A tight sequence $(f_n)_{n\in\mathbb{N}}$ of probability measures on E is weakly relatively compact. Conversely, if E is also complete, any weakly relatively compact family $(f_n)_{n\in\mathbb{N}}$ is tight.*

Skorokhod's topology and tightness in the Skorokhod space

In Chapter 5, the stochastic processes are assumed to belong (at least) to the Skorokhod space of càdlàg functions.

Definition 2.3.7 (Càdlàg)**.** Let T in $(0, +\infty]$. A function $x : [0, T] \to E$ is said to belong to the Skorokhod space $D([0, T], E)$ of càdlàg functions when x is right-continuous and has a left-limit at any time $t \in [0, T]$:

$$x(t^-) := \lim_{\substack{s\to t \\ s<t}} x(s) \text{ exists}, \quad x(t) = x(t^+).$$

A càdlàg function admits an at most countable number of discontinuities.

The law of a stochastic process is therefore an element of $\mathcal{P}(D([0, T], E))$. In order to characterize the compact sets of this space, it is first necessary to precise the topology on $D([0, T], E)$. For a much more detailed study of the Skorokhod space, we refer to [81] (Appendix A.2).

Definition 2.3.8 (Skorokhod J1 topology)**.** Let Λ denote the set of strictly increasing homeomorphisms from $[0, T]$ onto itself. The Skorokhod J1 metric on $D([0, T], E)$ is defined by

$$d(x, y) := \inf_{\lambda\in\Lambda} \left\{ \sup_{0\le t\le T} \rho\Big(x(t), y(\lambda(t))\Big) + \sup_{s<t} \left| \log \frac{\lambda(t) - \lambda(s)}{t - s} \right| \right\}.$$

Endowed with this metric, the Skorokhod space $D([0, T], E)$ is complete and seperable.

2.3.2 Particle systems, chaos, and propagation of chaos

We consider a system of N particles

$$\mathcal{X}_I^N \equiv (\mathcal{X}_t^N)_{t\in I} \equiv (X_t^{1,N}, \dots, X_t^{N,N})_{t\in I}, \tag{2.5}$$

where each particle $(X_t^{i,N})_{t\in I}$ is a stochastic process with values in the state space E which is at least Polish (i.e., separable and completely metrizable) and defined on a time interval $I = [0, T]$ with $T \in (0, +\infty]$. For ease of reading, we drop the N superscript and only write $X_t^i \equiv X_T^{i,N}$ for the i-th particle when no confusion is possible.

The particle particle system is understood as a Markov process $(\mathcal{X}_t^N)_{t\in I}$ with values in E^N. From the theory of Markov processes (see [81], Appendix A.4), the probbaility distribution of the particle system at time t denoted by $f_t^N \in \mathcal{P}(E^N)$ satistfies the (weak) *Liouville equation*

$$\forall \varphi_N \in \mathrm{Dom}(\mathcal{L}_N), \quad \frac{\mathrm{d}}{\mathrm{d}t}\langle f_t^N, \varphi_N\rangle = \langle f_t^N, \mathcal{L}_N\varphi_N\rangle \tag{2.6}$$

where $\mathcal{L}_N$ is the infinitesimal generator of a particle system acting on a (dense) subset of test functions $\mathrm{Dom}(\mathcal{L}_N) \subset C_b(E^N)$.

Remark 1. Equation (2.6) is also called the *master equation* in a probabilistic context and is better known as the *Liouville equation* in classical (deterministic) kinetic theory. In this thesis, we follow this latter terminology and (2.6) will be called the *(weak) Liouville equation*. The forward Kolmogorov equation, or (strong) Liouville equation, reads

$$\partial f_t^N = \mathcal{L}^N f_t^N,$$

where $\mathcal{L}^N \equiv \mathcal{L}_N^*$ is the dual operator of $\mathcal{L}^N$. In general, no explicit expression for $\mathcal{L}^N$ is available and it is thus easier to focus on the weak point of view.

In stochastic analysis, the pathwise law $f_{[0,T]}^N \in \mathcal{P}(D([0,T], E^N))$ is sometimes preferred and is characterised as a solution of the martingale problem. This means that $f_{[0,T]}^N$ is the unique probability distribution on the Skorokhod space of càdlàg functions such that for all test function $\varphi_N \in \mathrm{Dom}(\mathcal{L}_N)$, the process defined by

$$M_t^{\varphi_N} := \varphi_N(\mathbf{X}_t^N) - \varphi_N(\mathbf{X}_0^N) - \int_0^t \mathcal{L}_N\varphi_N(\mathbf{X}_s^N)\,\mathrm{d}s, \tag{2.7}$$

is a $f_{[0,T]}^N$-martingale. The particle system is assume to be *exchangeable* in the sense that f_t^N (resp. its pathwise version $f_{[0,T]}^N$) is a symmetric probability distribution on E^N (resp. on $D([0,T],E)^N \simeq D([0,T],E^N)$).

We define next the notions of chaos and propagation of chaos introduced by Kac [92].

Definition 2.3.9 (Kac's chaos)**.** Let $f \in \mathcal{P}(E)$. A sequence $(f^N)_{N\geq 1}$ of symmetric probability measures on E^N is said to be *f-chaotic* when for any $k \in \mathbb{N}$ and any function $\varphi_k \in C_b(E^k)$,

$$\lim_{N\to+\infty} \left\langle f^N, \varphi_k \otimes 1^{\otimes N-k} \right\rangle = \langle f^{\otimes k}, \varphi_k \rangle.$$

It means that for all $k \in \mathbb{N}$, the k-th marginal satisfies $f^{k,N} \to f^{\otimes k}$ for the weak topology.

From now on, the initial distribution $f_0^N \in \mathcal{P}(E^N)$ of the particle system is always assumed to be f_0-chaotic for a given $f_0 \in \mathcal{P}(E)$. The goal is to prove that this initial chaoticity assumption is propagated at later times as in the following definition.

Definition 2.3.10 (Pointwise and pathwise propagation of chaos)**.** Let $f_0^N \in \mathcal{P}(E^N)$ be the initial f_0-chaotic distribution of $\mathcal{X}_0^N$ at time $t = 0$.

- *Pointwise propagation of chaos* holds towards a flow of measures $(f_t)_t \in C(I, \mathcal{P}(E))$ when the law $f_t^N \in \mathcal{P}(E^N)$ of $\mathcal{X}_t^N$ is f_t-chaotic for every time $t \in I$. Note that the flow of measures is continuous in time as it is the solution of a PDE, but the (random) trajectories of the particle are càdlàg.
- *Pointwise propagation of chaos* holds towards a distrubtion $f_I \in \mathcal{P}(D(I, E))$ on the path space when the law $f_I^N \in \mathcal{P}(D(I, E)^N)$ of the process $\mathcal{X}_I^N$ (seen as a random element in $D(I, E)^N$) is f_I-chaotic.

The propagation of chaos property, whether considered pointwise or pathwise, describes the behavior of the particle system as the number of particles tends to infinity. It implies that any subsystem of a fixed size within the N-particle system eventually behaves as a system of independent and identically distributed (i.i.d.) processes, each following the same law f_t (note that the particles are always identically distributed by the exchangeability assumption). As the system size increases, only an averaged behavior can be observed instead of the detailed correlated trajectories of each particle. This notion of average behavior can be understood through the following characterization of the notion of chaos. We omit the proof, but it can be found in the classical course by Sznitman ([93], Proposition 2.2).

Lemma 2.3.3. *Each of the following assumptions is equivalent to Kac's chaos.*

(i) There exists $k \geq 2$ such that $f^{k,N}$ comverges weakly towards $f^{\otimes k}$.

(ii) The random empirical measure

$$\mu_{\mathcal{X}^N} := \frac{1}{N}\sum_{i=1}^{N} \delta_{X^i},$$

converges in law towards the deterministic measure f, where for any $N \in \mathbb{N}$, $\mathcal{X}^N = (X^1, \dots, X^N) \sim f^N$.

2.3.3 McKean-Vlasov Diffusion

When the particle system is the solution to the following system of SDEs

$$\forall i \in \{1, \dots, N\}, \quad \mathrm{d}X_t^{i,N} = b(X_t^{i,N}, \mu_{\mathcal{X}_t^N})\,\mathrm{d}t + \sigma(X_t^{i,N}, \mu_{\mathcal{X}_t^N})\,\mathrm{d}B_t^i, \tag{2.8}$$

for $i \in \{1, \dots, N\}$ where $(B_t^i)_t$ are N independent Brownian motions and the drift function b and diffusion matrix σ are of the form

$$b : \mathbb{R}^d \times \mathcal{P}(\mathbb{R}^d) \to \mathbb{R}^d, \quad \sigma : \mathbb{R}^d \times \mathcal{P}(\mathbb{R}^d) \to \mathcal{M}_d(\mathbb{R}), \tag{2.9}$$

where $\mathcal{M}_d(\mathbb{R})$ is the set of d-dimensional square real matrices.

Remark 2. Note that there are actually dN independent one-dimensional Brownian motions. This observation can be particularly useful in scenarios where the Brownian motions in the different directions are different.

The mean field limit $N \to +\infty$ is given by the (strong form) nonlinear Fokker-Planck equation

$$\partial_t f_t(x) = -\nabla_x \cdot \{b(x, f_t) f_t\} + \frac{1}{2}\sum_{i,j=1}^{d} \partial_{x_i}\partial_{x_j}\{a_{ij}(x, f_t) f_t\}, \tag{2.10}$$

where $a(x, \mu) := \sigma(x, \mu)\sigma(x, \mu)^{\mathrm{T}}$. This is the law of the *nonlinear McKean-Vlasov process* $(\overline{X}_t)_t$ which solves the following nonlinear SDE

$$\mathrm{d}\overline{X}_t = b(\overline{X}_t, f_t)\,\mathrm{d}t + \sigma(\overline{X}_t, f_t)\,\mathrm{d}B_t, \tag{2.11}$$

where B_t is a Brownian motion and $f_t = \mathrm{Law}(\overline{X}_t)$. The well-posedness of (2.11) is proved under Lipschitz assumptions on b and σ, which we discuss next.

Proposition 2.3.4. *Let us assume that the functions b and σ are globally Lipschitz: there exists $C > 0$ such that for all $x, y \in \mathbb{R}^d$ and for all $\mu, \nu \in \mathcal{P}_2(\mathbb{R}^d)$ it holds that*

$$|b(x,\mu) - b(y,\nu)| + |\sigma(x,\mu) - \sigma(y,\nu)| \leq C\big(|x-y| + W_2(\mu,\nu)\big),$$

where W_2 is the Wasserstein-2 distance (see Definition 2.3.3). Assume that $f_0 \in \mathcal{P}_2(\mathbb{R}^d)$. Then for any $T > 0$ the SDE (2.11) has a unique strong solution on $[0,T]$ and consequently, its law is the unique weak solution to the Fokker-Planck equation (2.10).

We omit the proof, which can be found in Ref. [81] (Proposition 1).

2.3.4 Proving propagation of Chaos

Since the seminal work of McKean [94], later extended by Sznitman [93], one of the most widely used techniques for establishing the propagation of chaos in mean field systems is the synchronous coupling method. In recent years, some alternative coupling methods have been proposed to handle either weaker regularity or to get uniform in time estimates under mild physically relevant assumptions [82]. In addition to these SDE techniques, convergence can be studied via a compactness argument [95, 96]. Compactness methods provide (non-quantitative) results applicable to mixed jump-diffusion models. For a review of synchronous coupling and compactness methods, see Ref. [82]. The methods are briefly outlined below. We use a compactness argument in Chapter 5 and Appendix B.2.

Synchronous coupling

When a SDE description of the particle system is available, the coupling method initiated by McKean [94] and Sznitman [93] consists in comparing the trajectories of the particle system with the trajectories of a system of N i.i.d processes with common law f_t.

Definition 2.3.11 (Chaos by coupling trajectories)**.** Let be given a final time $T \in (0, \infty]$, a distance d_E on E and $p \in \mathbb{N}$. Propagation of chaos holds by coupling the trajectories when for all $N \in \mathbb{N}$ there exist

- a system of particles $(\mathcal{X}_t^N)_t$ with law $f_t^N \in \mathcal{P}(E^N)$ at time $t \leq T$,
- a system of independent processes $(\overline{\mathcal{X}}_t^N)_t$ with law $f_t^{\otimes N} \in \mathcal{P}(E^N)$ at time $t \leq T$,
- a number $\varepsilon(N,T) > 0$ such that $\varepsilon(N,T) \underset{N\to+\infty}{\longrightarrow} 0$,

such that (pathwise)

$$\frac{1}{N}\sum_{i=1}^{N}\mathbb{E}\left[\sup_{t\leq T} d_E(X_t^i,\overline{X}_t^i)^p\right]\leq \varepsilon(N,T), \tag{2.12}$$

or (pointwise)

$$\frac{1}{N}\sum_{i=1}^{N}\sup_{t\leq T}\mathbb{E}\left[d_E(X_t^i,\overline{X}_t^i)^p\right]\leq \varepsilon(N,T). \tag{2.13}$$

Note that (2.12) implies (2.13). The bound (2.13) implies

$$\sup_{t\leq T} W_p(f_t^N, f_t^{\otimes N})\leq \varepsilon(N,T)\underset{N\to+\infty}{\longrightarrow} 0, \tag{2.14}$$

where W_p denotes the Wasserstein-p distance on $\mathcal{P}(E^N)$ (see Definition 2.3.3). It implies the propagation of chaos in the sense of Definition 2.3.10 since the topology induced by the Wasserstein distance is stronger than the topology of the weak convergence of probability measures.

2.3.5 Mckean's theorem

The following theorem is due to McKean and is the most important result of this section. For a function $K : E^2 \to \mathbb{R}$, we recall the notation $K \star \mu(x) := \int K(x,y)\mu(\mathrm{d}y)$.

Theorem 2.3.5 (McKean). *Let the drift and diffusion coefficients in (2.8) be defined by*

$$\forall x\in\mathbb{R}^d, \forall \mu\in\mathcal{P}(\mathbb{R}^d),\quad b(x,\mu) := \tilde{b}\big(x, K_1\star\mu(x)\big),\quad \sigma(x,\mu) := \tilde{\sigma}\big(x, K_2\star\mu(x)\big), \tag{2.15}$$

where $K_1 : \mathbb{R}^d\times\mathbb{R}^d\to\mathbb{R}^m$, $K_2 : \mathbb{R}^d\times\mathbb{R}^d\to\mathbb{R}^n$, $\tilde{b} : \mathbb{R}^d\times\mathbb{R}^m\to\mathbb{R}^d$, and $\tilde{\sigma} : \mathbb{R}^d\times\mathbb{R}^n\to\mathcal{M}_d(\mathbb{R})$ are globally Lipschitz and K_1, K_2 are bounded. Then pathwise chaos by coupling in the sense of Definition 2.3.11 holds for any $T>0$, $p=2$, with the synchronous coupling

$$X_t^{i,N} = X_0^i + \int_0^t \tilde{b}\big(X_s^{i,N}, K_1\star\mu_{\mathcal{X}_s^N}\big(X_s^{i,N}\big)\big)\,\mathrm{d}s + \int_0^t \tilde{\sigma}\big(X_s^{i,N}, K_2\star\mu_{\mathcal{X}_s^N}\big(X_s^{i,N}\big)\big)\,\mathrm{d}B_s^i, \tag{2.16}$$

and

$$\overline{X}_t^{i,N} = X_0^i + \int_0^t \tilde{b}\big(\overline{X}_s^{i,N}, K_1\star f_s\big(X_s^{i,N}\big)\big)\,\mathrm{d}s + \int_0^t \tilde{\sigma}\big(\overline{X}_s^{i,N}, K_2\star f_s\big(\overline{X}_s^{i,N}\big)\big)\,\mathrm{d}B_s^i. \tag{2.17}$$

It means that the trajectories satisfy

$$\frac{1}{N}\sum_{i=1}^{N}\mathbb{E}\left[\sup_{t\leq T}\left|X_t^i-\overline{X}_t^i\right|^2\right]\leq\varepsilon(N,T),$$

where the convergence rate is given by

$$\varepsilon(N,T)=\frac{c_1(b,\sigma,T)}{N}\mathrm{e}^{c_2(b,\sigma,T)T}, \tag{2.18}$$

for some absolute constants $C,\tilde{C},C_{\mathrm{BDG}}>0$ not depending on N,T,

$$c_1(b,\sigma,T):=CT\Big(T\|K_1\|_\infty^2\|\tilde{b}\|_{\mathrm{Lip}}^2+C_{\mathrm{BDG}}\|K_2\|_\infty^2\|\tilde{\sigma}\|_{\mathrm{Lip}}^2\Big), \tag{2.19}$$

and

$$c_2(b,\sigma,T):=\tilde{C}\Big(T\big(1+\|K_1\|_{\mathrm{Lip}}^2\big)\|\tilde{b}\|_{\mathrm{Lip}}^2+C_{\mathrm{BDG}}\big(1+\|K_2\|_{\mathrm{Lip}}^2\big)\|\tilde{\sigma}\|_{\mathrm{Lip}}^2\Big). \tag{2.20}$$

We omit McKean's original proof [94]. Sznitman's proof [93] offers a slightly shorter and more general version of McKean's argument. It is worth noting that McKean's proof is fundamentally an existence result, whereas Sznitman's proof relies on the well-posedness result outlined in Proposition 2.3.4. McKean's argument was initially published in Ref. [97] and subsequently republished in Ref. [94].

Compactness methods

Thanks to Lemma 2.3.3, the propagation of chaos property is equivalent to the convergence in law of the sequence of empirical measures. A common approach is to demonstrate the possibility of extracting a converging subsequence, while also proving the uniqueness of the accumulation point by applying tightness criteria, as outlined in Section 2.3.1. However, we note that there are three distinct and non-equivalent points of view on the empirical measure. These points of view are explained in great detailed in Ref. [81], and we provide a brief summary here.

- The strongest point of view, called *(strong) pathwise*, considers the empirical measure as the empirical measure associated to a sequence of N random processes defined in the Skorokhod space, that is the sequence $(\mu_{\mathcal{X}^N_{[0,T]}})_N$. For each N, the empirical measure is thus a random element $\mu_{\mathcal{X}^N_{[0,T]}}\in\mathcal{P}(D([0,T],E))$ and the goal is to prove the convergence of the laws in the space $\mathcal{P}(\mathcal{P}(D([0,T],E)))$.

- The second, weaker point of view, called *functional law of large numbers*, interprets the empirical measure as a measure-valued process, that is, for each N, a random process $t \in [0,T] \mapsto \mu_{\mathcal{X}_t^N} \in \mathcal{P}(E)$, i.e. a random variable in the space $D([0,T],\mathcal{P}(E))$. The goal is to prove the convergence of the sequence of pathwise laws in the space $\mathcal{P}(D([0,T],\mathcal{P}(E)))$.
- Finally, the weakest point of view, called *pointwise* point of view studies the flow of time marginals of the law of the empirical measure process, that is the mapping $t \in [0,T] \mapsto \text{Law}(\mu_{\mathcal{X}_t^N}) \in \mathcal{P}(\mathcal{P}(E))$. This defines a deterministic sequence in the functional space $C([0,T],\mathcal{P}(\mathcal{P}(E)))$. Our proof in Appendix B.2 is based on this perspective.

Chapter 3

Biological background

3.1 Architecture and molecular mechanisms of the mammalian circadian clock

3.1.1 The suprachiasmatic nucleus

In mammals, an endogenous clock regulates circadian rhythms, with the central component located in the suprachiasmatic nucleus (SCN) of the hypothalamus [98, 99]. The pacemaker within the SCN oscillates with a nearly 24-hour period and synchronizes with the daily light-dark cycle. Loss of SCN function leads to a complete lack of a regular sleep/wake rhythm [100]. Studies in rodents and non-human primates also indicate that the SCN serves as the brain's internal clock, allowing organisms to predict cyclic environmental changes [32].

The structure of SCN

The SCN comprises a distinctive cluster of neurons located in the basal region of the anterior hypothalamus, situated just dorsal to the optic chiasm on both sides of the third ventricle. With a volume of approximately 1 mm^3, each bilateral SCN houses nearly 100,000 neurons in total [101, 102]. Structurally, the SCN is a heterogeneous network that can be categorized into a dorsomedial portion, referred to as the shell, and a ventrolateral portion, known as the core. These two segments demonstrate both structural and functional distinctions, with the dorsomedial aspect exhibiting a faster pace than the ventrolateral

component [103]. Comprising approximately 25% of SCN neurons, the core region primarily processes light information, transmitting it to the shell, which consists of the remaining 75% of SCN neurons [104]. The core region receives both primary and secondary visual inputs and is primarily composed of neurons producing vasoactive intestinal polypeptide (VIP), gastrin-releasing peptide, neurotensin, neuropeptide-Y, substance-P, and calbindin. In contrast, the shell, enveloping the core, predominantly receives input from nonphotic sources and consists mainly of neurons containing arginine-vasopressin (AVP). Many neurons in both the core and shell contain γ-aminobutyric acid (GABA). Asymmetric coupling between the core and shell is observed, characterized by dense projections from the ventrolateral to the dorsomedial and sparse projections in the opposite direction [105]. Functional experiments support the existence of this asymmetry [103, 106, 107]. Figure 8.2 illustrates the structural layout of the SCN network.

Although the connectivity and topological properties of the SCN cellular network remain poorly understood, investigations into anatomical and functional connectivity in other brain regions, such as the cortex, have revealed small-world properties [5, 17].

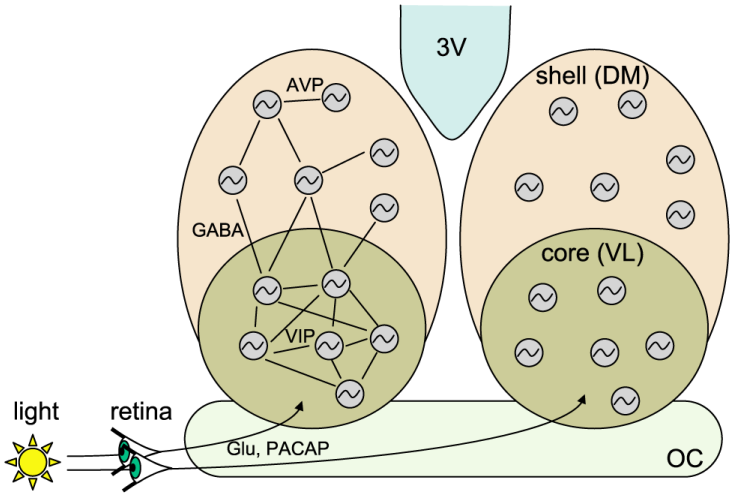

Figure 3.1: The SCN is divided in two identical hemispheres (left and right), each composed of two groups of neurons (core and shell, shown on the right hemisphere), distinguished by the type of neurotransmitters they release. In the ventrolateral part (VL), the neurons mainly express VIP (shown on the left hemisphere), whereas in the dorsomedial part (DM), AVP is expressed. The two parts also differ by their coupling properties. Moreover, only a subset of VL neurons are light-sensitive and are entrained by light cues originating from the optic chiasm. Reproduced from [5], with permission.

3.1.2 The molecular clock

Each SCN neuron expresses clock genes—a complex network of genes able to generate stable oscillations with a period of *circa* 24 hours [98]. The molecular clock network in mammals comprises at least two large interconnected autoregulatory feedback loops, which drive rhythms [108, 109]. At the center of this network is the CLOCK/BMAL1 heterodimer complex, which serves as the pivotal node and initiates transcription within the feedback loops. The CLOCK/BMAL1 complex arises from the products of the circadian locomotor output cycles kaput (*Clock*) and brain and muscle aryl hydrocarbon receptor nuclear translocator like–Arntl 1 (*Bmal1*) genes [98]. By binding to enhancer box (E-box) *cis*-elements in the promoter regions of various target genes such as *Period* homolog 1, 2, and 3 (*Per*1, *Per*2, *Per*3), *Cryptochrome* genes (*Cry*1, *Cry*2), retinoic acid-related orphan receptor (*Rora*, *Rorb*, *Rorc*), and *Rev-Erb* nuclear orphan receptors (*Rev-Erbα*, *Rev-Erbβ*), CLOCK/BMAL1 activates their transcription [32]. The time cues encoded by the dynamic molecular states of these intertwined feedback loops are relayed to the rest of the cell, orchestrating its activities. Next, we detail the mechanisms of these self-sustaining transcriptional–translational feedback loops (see Figure 3.2).

The PER/CRY loop

At circadian dawn (referred to as circadian time (CT) 0), the heterodimers of CLOCK and BMAL1 (also known as ARNTL), acting as positive regulators, initiate the transcription of Per and Cry genes. These genes produce the period (PER) and cryptochrome (CRY) proteins, which act as negative regulators, through E-box regulatory sequences [110]. By the end of the circadian day (CT12), PER–CRY complexes accumulate in the nucleus and begin to repress their own expression [110, 111]. Consequently, during the subsequent circadian night (CT12–CT24 (CT0)), the levels of Per and Cry mRNA decrease, and the existing PER–CRY complexes undergo degradation, releasing their inhibitory effect on CLOCK/BMAL1 and allowing for the initiation of a new transcriptional cycle [98]. This degradation enables the cycle to restart approximately 24 hours after the previous transcriptional initiation. The negative feedback loop involving PER/CRY is commonly recognized as the primary driver of circadian rhythms [32, 112, 113].

So far, research consistently highlights the remarkable sensitivity of the circadian period length in mammals to alterations in the phosphorylation status of the PER proteins and the stability of the CRY proteins. Casein kinases CKIδ and CKIε sequentially phosphorylate multiple residues on the PER proteins. These kinases control the rate at which the PER/CRY complexes degrade or enter the nucleus, thereby determining the intrinsic

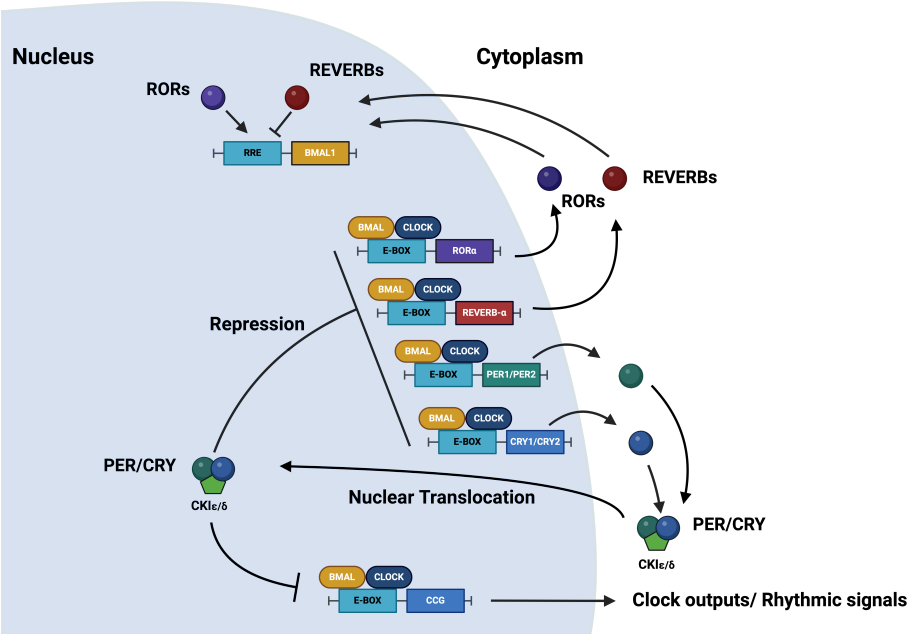

Figure 3.2: Schematic diagram of the transcription-translation feedback loop of the endogenous molecular circadian clock. Adapted from "BIOLOGICAL CLOCK", by E. Murgo (2024) BioRender. Retrieved from https://app.biorender.com/biorender-templates/figures/all/t-65bbb7c5e6423ca0a08e50d9-biological-clock

period of the clock. Phosphatases PP1 and PP5 counteract or regulate the activity of CKIδ and CKIε, respectively [114, 115]. Familial mutations, such as the loss of a single phospho-acceptor site on PER2 (S662G) [116] or a loss-of-function mutation in CKIδ (T44A) [117], lead to a shortened intrinsic period of the clock in mice and cause sleep phase disorders in humans. Phosphorylation also affects the stability of CRY1 and CRY2 [118]. However, unlike the PER proteins, CRY phosphorylation by AMP-activated protein kinase (AMPK) does not involve a complex multisite phosphorylation sequence. When genetically or pharmacologically manipulated, changes in CRY protein abundance closely correspond to alterations in the circadian period length [119].

The ROR/REV-ERB loop

The clock genes Rev-Erb and Ror are transcribed during the circadian day (CT0–CT12) and the messages are exported to the cytoplasm for translation. The newly translated

proteins, the nuclear receptors RORa, RORb, RORc, REV-ERBα (also known as NR1D1) and REV-ERBβ (also known as NR1D2), in turn act via REV response element (RRE) sequences to activate and suppress Bmal1 transcription, respectively. ROR and REV-ERB proteins compete for ROR regulatory element binding sites in the promoter region of *Bmal1* and respectively activate and repress its transcription [98]. REV-ERB proteins, which also repress *Cry1* transcription [120] in the PER/CRY loop, are essential for robust oscillations [98, 121, 122]. The cross connection with REV-ERB [123] reinforces the interaction of the two loops and allows fine-tuning of the regulation of *Cry*. Mutations in the genes of these nuclear receptors alter the amplitude and period of activity rhythms, and Rev-erb-double-knockout mice exhibit severely disrupted circadian behaviour [124]. Moreover, administration of a synthetic REV-ERB agonist can suppress the amplitude of the SCN rhythm and nocturnal behaviour in mice [125]. Thus, an output of the ROR/REV-ERB loop, circadian expression of REV-ERB proteins, is also an input to it. The ROR/REV-ERB feedback loop is usually seen as adding robustness to the system [111].

Beyond transcriptional mechanisms

The mammalian clock relies not only on transcriptional mechanisms but also on membrane depolarization, intracellular calcium flux, and activation of cyclic AMP (cAMP) signaling, which have emerged as significant regulators [126]. Intracellular calcium, for instance, plays a fundamental role in the rhythmic firing of neurons in SCN slices [127]. Moreover, rhythmic expression of core clock components in SCN neurons necessitates adequate membrane depolarization, periodic calcium influx, and daily activation of cAMP signaling [128–130]. Importantly, these effects stem from the phosphorylation-dependent activation of the calcium/cAMP response element-binding protein (CREB), which binds to calcium/cAMP regulatory elements (CREs) on DNA. Notably, CRE sequences have been identified in the promoters of several clock genes, including PER1 and PER2 [130, 131]. Given that membrane potential [132], calcium flux [127], and activation of cAMP signaling [128, 130] also exhibit rhythmicity in the SCN, they serve as both outputs and inputs to the transcriptional clock, potentially forming positive feedback loops that contribute to rhythm generation [126].

3.1.3 Peripheral circadian clocks

Identification of clock genes revealed that not only SCN neurons but also most peripheral cells engage in intracellular molecular processes of cellular circadian clocks [99]. As such,

our body hosts almost as many peripheral circadian clocks as there are cells. Both the SCN and peripheral clocks share identical molecular architecture [108] (Figure 3.2).

Peripheral clocks in organs such as the lung, liver, heart, kidney, and skin are involved in regulating local transcriptional activity and can be coordinated by systemic cues originating from the SCN, including neuronal connections and endocrine signals [32]. Additionally, peripheral clocks can be synchronized by external cues such as temperature, feeding schedules, exercise, and light [109]. This internal synchronization orchestrates the physiological functions of individual organs in a temporally coordinated manner to optimize overall organismal performance [133]. These peripheral clocks likely orchestrate the daily rhythms of local functions within individual tissues and organs. Research by Sinturel et al. [134] supports the concept of autonomous peripheral oscillators, which depend on the SCN only to establish synchrony among but not within peripheral body clocks [133]. Indeed, Sinturel et al. [134] demonstrate that peripheral circadian rhythms persist *in vivo* even in the absence of rhythmic input from the SCN. To achieve this, they employed their RT-Biolumicorder technology [135], an advanced method for monitoring peripheral circadian bioluminescence rhythms from clock gene reporters in real time in freely moving mice. These results differ from those reported by Koronowski et al. [136], where there was no rhythmic gene expression in mice under constant conditions. However, because this study obtained tissue samples from different animals at each time point, it is probable that low-amplitude peripheral rhythms were not detected due to desynchronization between animals rather than within tissue oscillators.

Nevertheless, the hierarchical concept cannot be entirely discarded. The significance of the SCN as the central clock remains solid, as it functions as the timekeeper and disseminates the standard time throughout the entire body according to the environmental day/night cycle, via neural, humoral, and other pathways to drive and/or entrain multiple peripheral clocks. Sinturel et al. [134] also demonstrate that in SCN-lesioned animals housed in constant conditions, the amplitude of whole-body bioluminescence rhythms is significantly reduced. This indicates that the SCN master clock plays a crucial role in maintaining synchrony among non-SCN body clocks. In this sense, our body comprises a multi-oscillator system. Therefore, disruption of such temporal coordination, i.e., internal desynchronization, due to jet lag, shift work, irregular lifestyle, and so on, could lead to various health problems [137].

3.1.4 Coupling among circadian clocks

Almost every cell in the body functions as a self-sustained and cell-autonomous circadian oscillator. Cellular populations display a typical distribution of periods and phases ranging

from approximately 20 to 28 hours [138]. If individual cells operated independently with their own periods, the phases of cellular oscillators would gradually drift apart, leading to desynchronized tissue rhythms over time. Thus, single-cell oscillators within central and peripheral tissue clocks, such as the SCN or the lung, must either synchronize with each other or align with external or systemic cues to maintain coherent network rhythms.

Since the central pacemaker in the SCN maintains synchrony among body clocks, the significance of systemic coupling may not be immediately evident. Nevertheless, there could be a reciprocal exchange of timing information among different body clocks, potentially offering synchronized feedback from the periphery to the SCN or regulating organismic responses to external entrainment signals [138]. Although various communication pathways among body clocks have been identified (see Figure 3.3), it is uncertain whether these pathways facilitate bidirectional coupling or merely unilateral clock entrainment or resetting. Feeding signals or energetic changes may constitute a systemic coupling pathway, as adjustments in the mammalian clock system to these signals are plausible. Feeding-fasting cycles serve as prominent Zeitgebers for peripheral clocks, while also influencing SCN activity, body temperature, and rest-activity cycles through the release of feeding-related hormones [119]. This, in turn, leads to feedback regulations of peripheral oscillators via neuronal pathways.

Coupling facilitates phase- and period-locking of individual oscillators, ensuring synchronized rhythms at the population level. Without coupling, generating consistent network oscillations necessitates additional external or internal forcing signals. Coupling within the circadian system can occur at various organizational levels (for a comprehensive review, see Refs [139]), and whether it operates at the systemic level remains an open question.

3.2 Immune system: innate and adaptive immunity

The immune system consists of cells, chemicals, and processes that defend the skin, respiratory passages, intestinal tract, and other areas against foreign antigens like microbes (such as bacteria, fungi, and parasites), viruses, cancer cells, and toxins. It comprises two primary lines of defense: innate immunity and adaptive immunity [140]. Innate immunity acts as the initial immunological defense against invading pathogens, initiating a rapid immune response within minutes or hours. The innate immune response lacks immunologic memory, meaning it cannot recognize or "remember" the same pathogen upon future exposure to it. In contrast, adaptive immunity is antigen-specific—it has the ability to

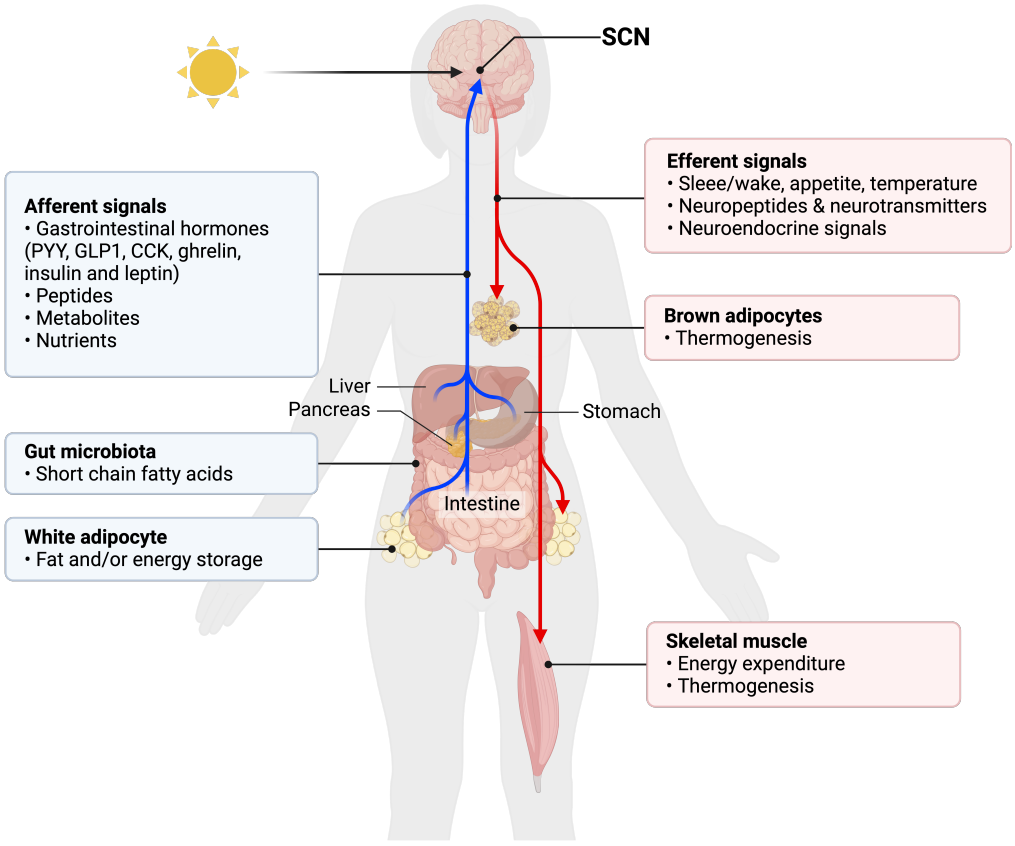

Figure 3.3: Coupling among body clocks: the central clock and selected peripheral clocks in humans. Adapted from "Key Metabolic Mechanisms on Body Weight Regulation", by E. Huang (2022) BioRender. Retrieved from https://app.biorender.com/biorender-templates/figures/all/t-62065ff195cacf009f2f7190-key-metabolic-mechanisms-on-body-weight-regulation

"form memory" that facilitates a faster and more efficient immune response upon subsequent encounters with the antigen [140]. Innate and adaptive immunity do not operate independently; rather, they complement each other. Defects in either system render the host susceptible to infections or elicit inappropriate responses [141–143].

3.2.1 Innate immunity

Innate immunity consists of four types of defensive barriers: anatomical (skin and mucous membranes), physiological (temperature, low pH, and chemical mediators), endocytic and phagocytic, and inflammatory. It relies on pattern recognition receptors (PRRs) that enable a limited range of immune cells to swiftly detect and respond to a broad spectrum of pathogens sharing common structures known as pathogen-associated molecular patterns (PAMPs). Examples of these patterns include bacterial cell wall components like lipopolysaccharides (LPS) released during bacterial infection and double-stranded ribonucleic acid (RNA) produced during viral infections [140].

Innate immunity plays a crucial role in rapidly recruiting immune cells to infection and inflammation sites by producing cytokines and chemokines, small proteins involved in cell–cell communication and recruitment. Cytokines are involved in cell signaling, while chemokines specifically mediate cell migration and recruitment to sites of infection or injury. Cytokine production mobilizes numerous defense mechanisms throughout the body during innate immunity, activating local cellular responses to infection or injury. The complement system, a biochemical cascade, identifies and opsonizes (coats) bacteria and other pathogens, rendering them susceptible to phagocytosis, the process in which immune cells engulf microbes. The phagocytic activity of the innate immune response also facilitates the clearance of dead cells or antibody complexes and eliminates foreign substances from organs, tissues, blood, and lymph. Furthermore, it can activate the adaptive immune response by mobilizing and activating antigen-presenting cells (discussed in section 3.2.2) [141, 143].

Various cells participate in the innate immune response, including phagocytes (macrophages and neutrophils), dendritic cells, mast cells, basophils, eosinophils, natural killer (NK) cells, and innate lymphoid cells. Figure 3.4 shows immune cells lineage. Phagocytes, categorized into neutrophils and macrophages, share the function of engulfing microbes and eliminating them through multiple bactericidal pathways. Neutrophils are short-lived and possess granules and enzyme pathways aiding in microbial elimination, whereas macrophages are long-lived cells involved not only in phagocytosis but also in antigen presentation to T cells. Cytokines are mainly produced by macrophages [140]. In this thesis, we focus on discussing the functions of cytokines released by macrophages, along with summarizing their release mechanisms. Interested readers may refer to Ref. [144] for a comprehensive review of immune cells.

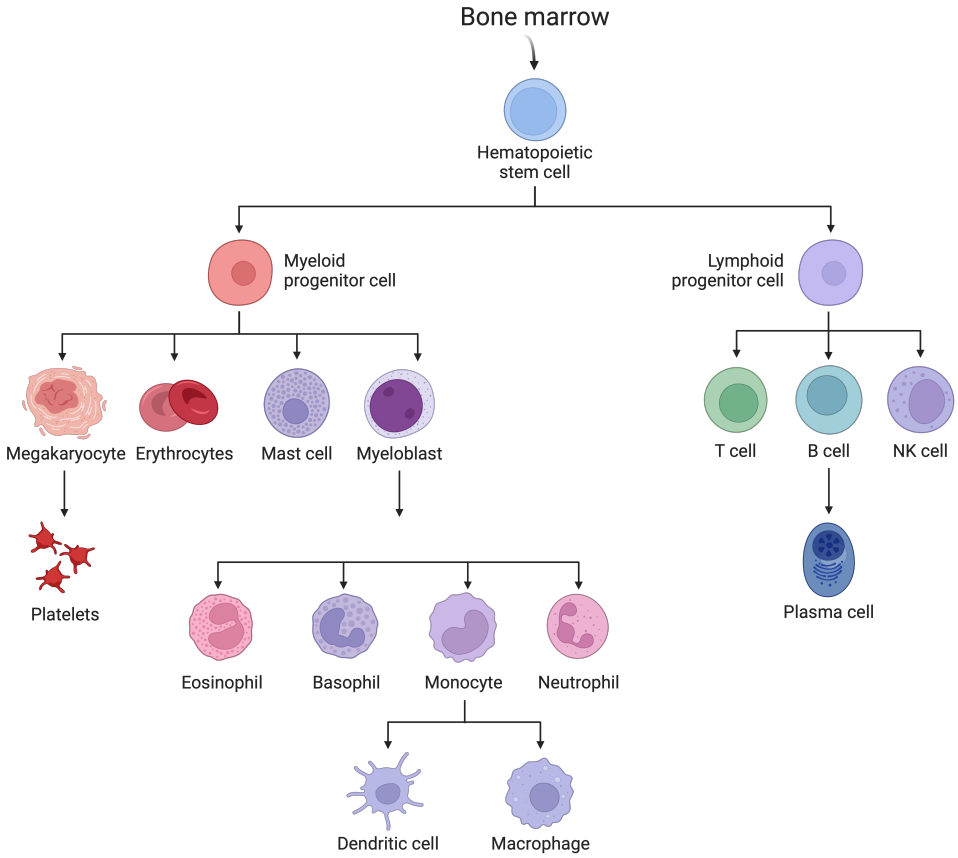

Figure 3.4: Cells of the immune system. The immune system comprises cells from two primary lineages: lymphoid cells, which originate from a lymphoid progenitor, and myeloid cells, which derive from a myeloid progenitor. Myeloid cells execute a diverse array of innate immune functions, whereas lymphoid cells are involved in adaptive immunity. Created with BioRender.com.

3.2.2 Adaptive immunity

Adaptive immunity serves several key functions: recognizing specific foreign antigens and distinguishing them from self-antigens, generating targeted immunological responses to eliminate particular pathogens or infected cells, and forming immunological memory to mount rapid responses upon re-exposure to specific pathogens [142]. Effective immunization against infectious diseases relies on adaptive immune responses. The cells of the

adaptive immune system include antigen-specific T cells, which undergo activation and proliferation upon interaction with antigen-presenting cells, and B cells that differentiate into plasma cells to produce antibodies [140] (see Figure 3.4).

T cells

T cells originate from hematopoietic stem cells in the bone marrow and undergo maturation in the thymus. They bear distinctive antigen-binding receptors on their membrane, referred to as the T-cell receptor (TCR). Each T cell expresses a unique type of TCR and possesses the ability to undergo rapid proliferation and differentiation upon receiving appropriate signals. As noted earlier, the recognition of a specific antigen by T cells necessitates the involvement of antigen-presenting cells (typically dendritic cells, although also macrophages, B cells, fibroblasts, and epithelial cells) [142, 143].

B cells

B cells, like T cells, originate from hematopoietic stem cells in the bone marrow. Upon maturation, they leave the marrow equipped with a unique antigen-binding receptor on their membrane. Unlike T cells, B cells can directly recognize antigens without depending on antigen-presenting cells, thanks to specific antibodies expressed on their cell surface. Upon activation by foreign antigens matching their specific antigen receptors, B cells undergo proliferation and differentiate into either antibody-secreting plasma cells or memory B cells. Memory B cells, considered as long-term survivors of prior infections, retain the expression of antigen-binding receptors. They are poised to mount rapid responses upon re-exposure by generating antibodies and eliminating the antigen. In contrast, plasma cells, relatively short-lived, often undergo apoptosis once the inciting agent triggering the immune response is eradicated [142, 143].

3.2.3 A summary of the macrophage cytokine repertoire

Proinflammatory cytokines

In the early stages of bacterial infection, key inflammatory cytokines released include tumor necrosis factor (TNF), interleukin 1 (IL-1), and interleukin 6 (IL-6). While mainly originating from monocytes and macrophages, these cytokines can also be produced by activated lymphocytes, endothelial cells, and fibroblasts. They collectively induce vascular permeability and attract inflammatory cells [144]. While the inflammatory response proves beneficial when cytokines are produced in appropriate amounts, their excessive production

can lead to toxicity. For example, overproduction of IL-1β and TNF can trigger an acute generalized inflammatory response characteristic of septic shock and multi-organ failure [145].

TNF

Tumor necrosis factor (formerly known as tumor necrosis factor alpha, TNF-α), a 185-amino acid glycoprotein, was initially identified for its capacity to induce necrosis in some tumors [146]. It acts as a potent pyrogenic cytokine and is among the first to be released upon pathogen exposure [145], thus playing a crucial role in septic shock. TNF promotes vasodilation and increased vascular permeability, which facilitates the infiltration of lymphocytes, neutrophils, and monocytes into the affected area. Additionally, it regulates the release of chemokines to recruit these cells to the site of inflammation. TNF, in conjunction with IL-17, stimulates the expression of neutrophil-attracting chemokines CXCL1, CXCL2, and CXCL5 [147], and can also enhance the expression of cell adhesion molecules involved in diapedesis [144, 148].

IL-1

Three forms of IL-1 have been identified: IL-1α, IL-1β, and IL-1Ra. Both IL-1α and IL-1β exhibit strong proinflammatory properties. Similar to TNF, IL-1β functions as an endogenous pyrogen. During inflammation, IL-1β promotes the production of acute phase proteins from liver and affects the central nervous system, inducing fever and stimulating prostaglandin secretion. In mast cells, IL-1β triggers the release of histamine, leading to vasodilation and localized inflammation. IL-1Ra competes for the same receptor as IL-1α and IL-1β, but the precise secretion mechanism remains unclear. Its binding to the IL-1R does not initiate the proinflammatory signaling cascade prompted by IL-1α and IL-1β [144].

IL-6

IL-6 is a multifunctional cytokine with both proinflammatory and anti-inflammatory properties. It stimulates the differentiation of B cells into plasma cells, activates cytotoxic T cells, and regulates bone homeostasis. Like TNF and IL-1β, IL-6 acts as an endogenous pyrogen, inducing fever and the synthesis of acute phase proteins in the liver [144]. Its proinflammatory effects are mediated by trans-signaling, wherein IL-6 binds to soluble IL-6 receptors, which then bind to $gp130$ receptors present in all cell types. On the other hand, its anti-inflammatory effects are mediated by classical signaling, involving interaction with IL-6 receptors expressed by only a subset of cells. The anti-inflammatory role of IL-6 is evident in IL-$6^{-/-}$ mice, which display hepatosteatosis, insulin resistance, and liver inflammation [149].

Anti-inflammatory cytokines

IL-10

IL-10 is synthesized by activated macrophages, B cells, and T cells. Its primary functions involve suppressing macrophage activation and the production of TNF, IL-1β, IL-6, IL-8, and IL-12 [144]. Macrophages, when exposed to IL-10, experience decreased microbicidal activity and a reduced ability to respond to IFN-γ [140]. Studies in murine models have demonstrated that blocking or neutralizing IL-10 results in elevated levels of TNF and IL-6, while administration of exogenous IL-10 enhances survival and decreases inflammatory cytokine levels [150]. Lower levels of IL-10 have been associated with an increased risk of gastrointestinal pathologies such as inflammatory bowel disease [150].

TGF-β

TGF-β is a potent anti-inflammatory cytokine that acts on various target cells to dampen the inflammatory effects of TNF, IL-1β, IL-2, IL-12, and others [151, 152]. Its significance in the immune system is highlighted by studies showing that mice deficient in the TGF-β1 isoform, which is prevalent in immune cells, develop severe multi-organ inflammation and succumb by week 4 [153]. Additionally, TGF-β plays a role in hematopoiesis and is crucial for embryogenesis, tissue regeneration, and cell proliferation and differentiation [144].

3.3 Energy metabolism

In this section, we discuss the integration of carbohydrate and fat metabolism across various tissues within the body, with a significant role played by the hormonal system. We note that this discussion involves approximations and should be viewed as illustrative only. For the sake of continuity with the work presented in chapters 6 and 7, we will assume a healthy individual weighing 58–70 kg for most purposes. The information presented here is summarized from Refs. [6] and [154].

3.3.1 Carbohydrate metabolism

Glucose maintains a relatively stable concentration in the blood, hovering around 5 mmol/l in humans. Among all circulating energy substrates, glucose exhibits the most constant levels. This stems from its role in providing a constant energy source to tissues, particularly those regulated by extracellular glucose levels. Glucose enters the bloodstream through

three primary mechanisms: absorption from the intestine, breakdown of liver glycogen (glycogenolysis), and liver gluconeogenesis (production of new glucose).

The postabsorptive state

The term *postabsorptive state* indicates that all the nutrients from the last meal have been absorbed from the intestines, but not enough time has passed for signs of starvation to appear. In humans, this state typically occurs after an overnight fast before breakfast is consumed. During the postabsorptive state, blood glucose concentration is usually just below 5 mmol/l, while plasma insulin levels vary widely among individuals, averaging around 60 pmol/l. The concentration of glucagon typically ranges from 20 to 25 pmol/l. However, determining typical glucagon concentrations presents challenges due to varying measurement methods in different laboratories. Moreover, since glucagon primarily affects metabolism in the liver, its relevant concentration in the hepatic portal vein is not easily measured in normal volunteers. During the postabsorptive state, glucose turnover predominantly arises from glycogen breakdown, which accounts for approximately half of the total glucose supply. This process is stimulated by a decreased insulin/glucagon ratio. The remaining glucose entry is attributed to gluconeogenesis. Substrates utilized for gluconeogenesis primarily consist of lactate, along with pyruvate, alanine (mainly sourced from muscle), and glycerol (derived from adipose tissue lipolysis, i.e., fat breakdown). On the utilization side, the brain consumes about 60% of the available glucose per day. The remainder is utilized by various tissues, including red blood cells, skeletal muscle, the renal medulla, and adipose tissue. The pattern of glucose metabolism after an overnight fast is illustrated in Figure 3.5.

Breakfast: the absorptive state

The postabsorptive state typically lasts only a few hours before being interrupted by the arrival of a meal, marking a dramatic shift from production to storage. Following a meal, there is a rapid increase in blood glucose concentration, detectable within approximately 15 minutes. This concentration peaks around 30–60 minutes after consuming a moderate breakfast—the exact timing varies based on factors like meal size and carbohydrate composition. As blood glucose concentration rises, the pancreas responds by stimulating insulin secretion, leading to an increase in plasma insulin concentration. Figure 3.6 summarizes glucose metabolism during the absorptive phase and key regulatory points.

The liver receives blood from the small intestine via the hepatic portal vein, and so it experiences the most significant change in blood glucose concentration. Glucose flows into

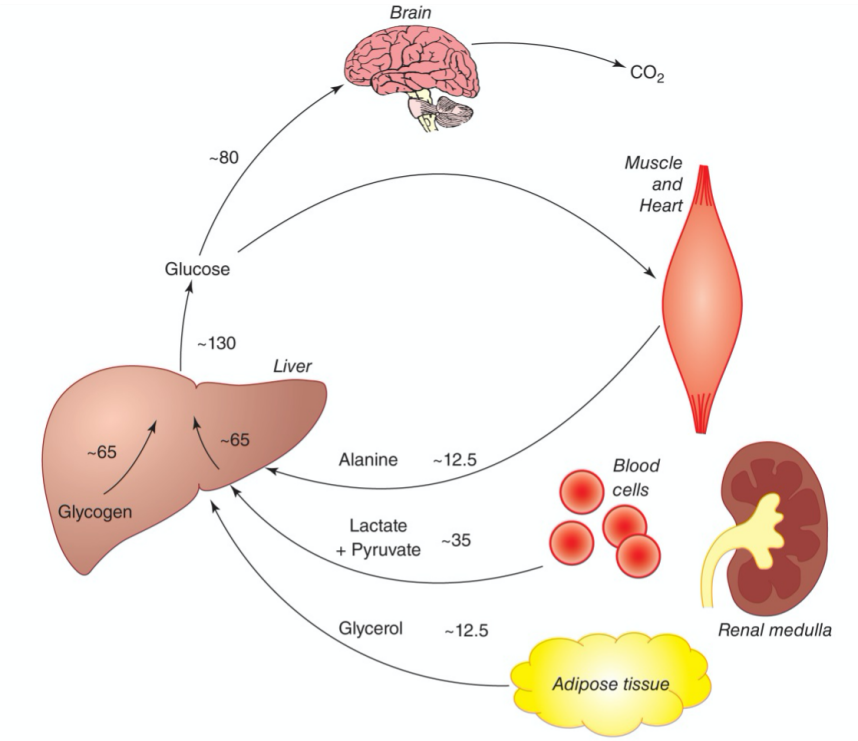

Figure 3.5: The pattern of glucose metabolism after an overnight fast. The numbers are approximations only, in mg per min, for a typical person of 65 kg body weight. Much of the glucose delivered to peripheral tissues (muscle, adipose tissue, blood cells, etc.) is "recycled" as lactate, which returns to the liver as a substrate for gluconeogenesis. However, a large proportion is oxidized, especially in the brain, and this constitutes an irreversible loss from the body's store of carbohydrate. Figure from Ref. [6]. Copyright © 2019 Keith N. Frayn and Rhys Evans. Reproduced with permission of John Wiley & Sons, Ltd.

hepatocytes via the transporter GLUT2. The rise in intracellular glucose concentration within hepatocytes, coupled with the altered insulin/glucagon ratio, results in the inhibition of glycogen phosphorylase and the activation of glycogen synthetase, shifting from glycogen breakdown to glycogen storage. While one might anticipate that the pathway of gluconeogenesis would be suppressed by this hormonal shift, empirical evidence suggests otherwise. Following carbohydrate ingestion, there is consistently an increase in blood lactate concentration. This lactate production sustains gluconeogenesis without causing glucose release into the bloodstream; instead, lactate is directed toward glycogen storage.

The redirection of lactate into glycogen in the liver reflects a strong drive to maximize glucose storage. Other tissues also respond to the increase in insulin levels. In skeletal muscle and adipose tissue, insulin prompts glucose uptake by increasing the presence of GLUT4 transporters on the cell membrane and enhancing glucose disposal within the cell. Concurrently, the plasma concentration of non-esterified fatty acids decreases due to the suppression of fat mobilization in adipose tissue, a topic we will delve into further later. Consequently, tissues like skeletal muscle, which can utilize either fatty acids or glucose for energy, switch to predominantly using glucose. However, insulin also activates muscle glycogen synthase, leading to glycogen storage in muscles. This metabolic shift towards glucose utilization and storage characterizes the postprandial period after carbohydrate-rich meals.

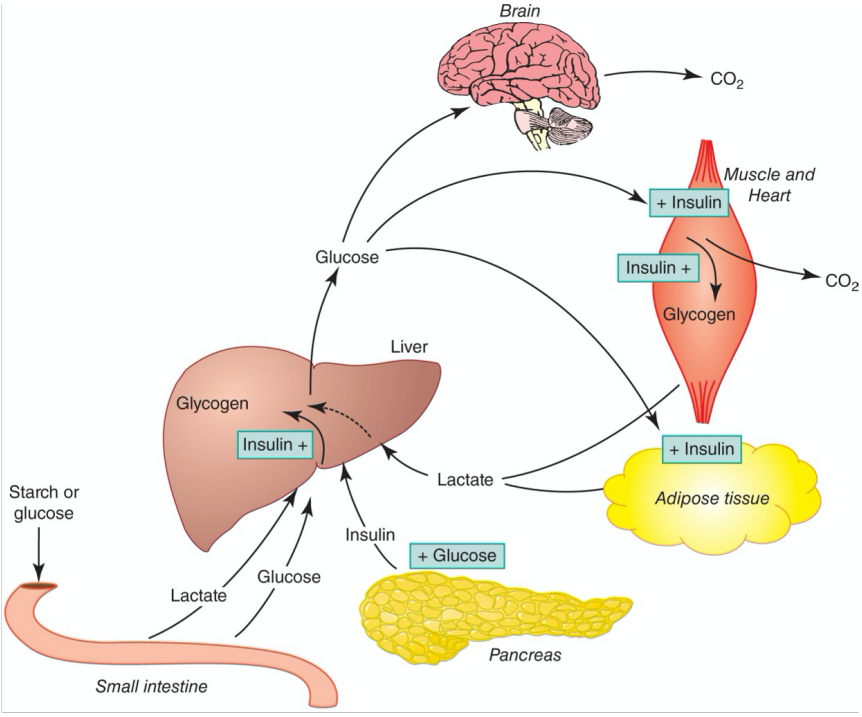

Figure 3.6: The pattern of glucose metabolism after a carbohydrate breakfast. The direct pathway of glycogen storage is shown (glucose from small intestine going to liver glycogen), as is the indirect pathway (glucose forming lactate in the small intestine or in peripheral tissues, lactate then being used for liver glycogen synthesis). Figure from Ref. [6]. Copyright © 2019 Keith N. Frayn and Rhys Evans. Reproduced with permission of John Wiley & Sons, Ltd.

3.3.2 Fat metabolism

There are different forms of fat and their concentrations may vary considerably throughout a normal day. In this section, we will consider the regulation of non-esterified fatty acid (also known as free fatty acid or FFA), as well as the fate of dietary fat consumed in the form of triglyceride (TG). TG exists in various forms, and the variant that enters the bloodstream after a meal is referred to as *chylomicron*. Chylomicrons are large triglyceride-rich lipoproteins. They transport dietary lipids from the intestines to other tissues in the body.

The postabsorptive state

In the postabsorptive state, FFA consitute an important energy source. Their turnover involves liberation from adipose tissue and uptake by tissues like skeletal muscle and liver. Lipolysis, the breakdown of TG, yields three fatty acids, providing energy equivalent to a concentration of 3 mmol/l of FFA. Utilization of FFA from plasma largely depends on their concentration: higher FFA concentration correlates with increased utilization. Plasma FFA concentration mirrors their release from adipose tissue, which in turn determines their utilization rate in other tissues. FFA are not water soluble, and they are transported in plasma bound to the protein albumin. The plasma FFA concentration during a normal day is an inverse reflection of the plasma glucose and insulin. When the body is relatively starved—for instance after overnight fast—the concentrations of glucose and insulin are at their lowest and the concentration of FFA is at its highest. Various factors such as exercise or illness may disrupt this relationship. Figure 3.7 shows the pattern of pattern of FFA metabolism after an overnight fast.

Breakfast: the absorptive state

After a meal, increased glucose levels stimulate insulin secretion, causing insulin concentration in the plasma to rise. This directly inhibits lipolysis in adipose tissue. However, elevated glucose and insulin levels also enhance glucose uptake and glycolysis in adipose tissue, leading to increased production of glycerol 3-phosphate and re-esterification of fatty acids into TG within the tissue. Consequently, the release of FFA from adipose tissue is nearly completely suppressed following a carbohydrate-rich meal, resulting in a significant decrease in plasma FFA concentration from its postabsorptive level of approximately 0.5 mmol/l to less than 0.1 mol/l. The decrease in plasma FFA concentration impacts the metabolism of tissues relying on fatty acids as an oxidative fuel post-overnight fast, such

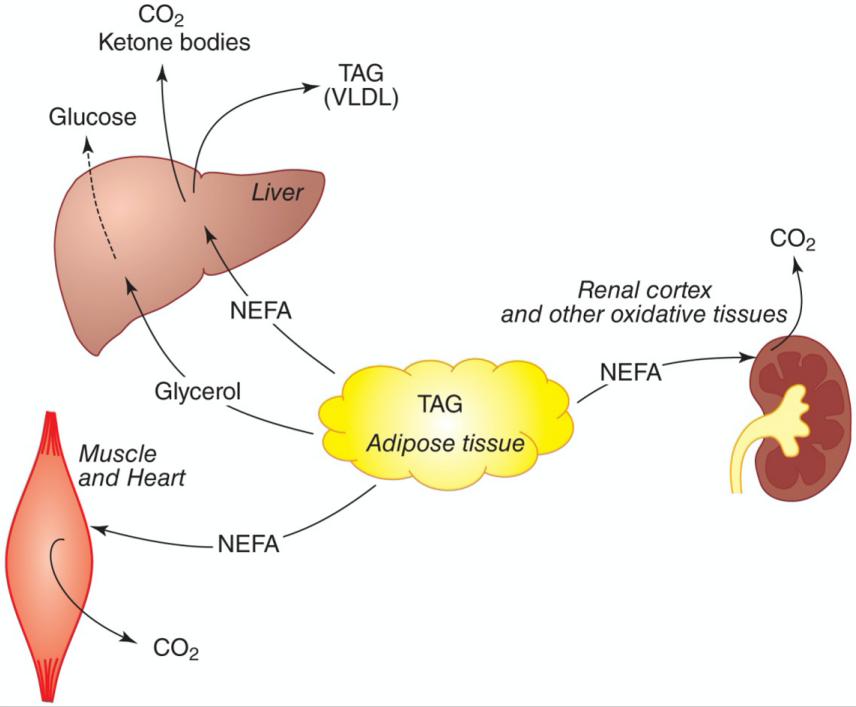

Figure 3.7: The pattern of FFA metabolism after an overnight fast. Fatty acids are released by lipolysis of the triacylglyceride stores in adipose tissue. VLDL: very-low-density lipoprotein. Figure from Ref. [6]. Copyright © 2019 Keith N. Frayn and Rhys Evans. Reproduced with permission of John Wiley & Sons, Ltd.

as skeletal muscle. The rate of FFA uptake by muscle primarily depends on fatty acid delivery—namely, plasma concentration and blood flow. However, with the availability of glucose in the plasma post-meal, insulin prompts glucose utilization over FFA. Skeletal muscle has no direct way of turning off fatty acid utilization, but the coordinated control of metabolism in the whole body leads instead to its supply being cut off.

If the meal includes a significant fat content, it elicits additional responses. However, the processing of dietary fat does not directly impact the coordinated responses of the glucose/FFA-insulin/glucagon system. Dietary fat is mostly in the form of TG, absorbed in the small intestine and processed into chylomicron particles. These particles are released into the bloodstream via the lymphatic system. This process is much slower than the absorption of glucose, so that the peak in plasma TG concentration after a fatty meal does not occur until 3-5 hours after the meal. Unlike other nutrients, dietary fat bypasses the liver upon entry into the circulation. Instead, most of TG are extracted from chylomicrons

in tissues outside the liver, especially adipose tissue, skeletal muscle, and the heart. Figure 3.8 shows the pattern of plasma TG metabolism after a breakfast containing both fat and carbohydrates.

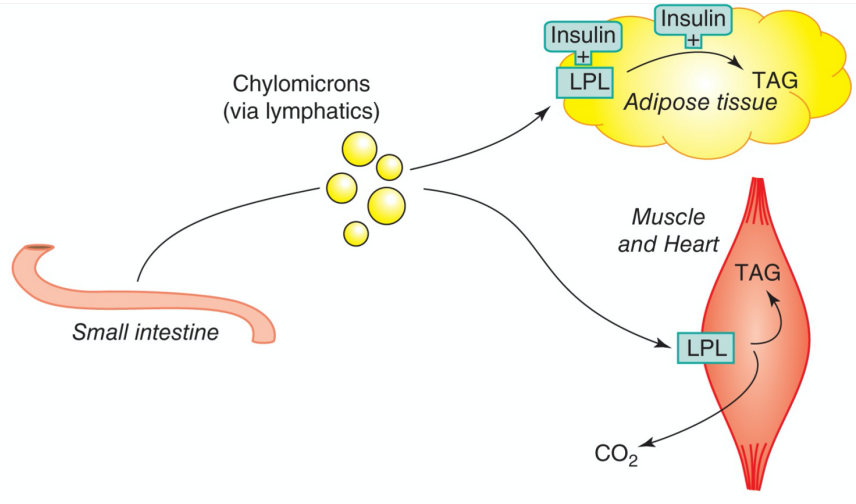

Figure 3.8: The pattern of plasma triacylglyceride metabolism after a breakfast containing both fat and carbohydrates. TG enters the circulation in the form of chylomicron particles and is hydrolyzed by the enzyme lipoprotein lipase (LPL) in the capillaries of tissues. Figure from Ref. [6]. Copyright © 2019 Keith N. Frayn and Rhys Evans. Reproduced with permission of John Wiley & Sons, Ltd.

Chapter 4

Modelling the circadian regulation of the immune system: sexually dimorphic effects of shift work

The content of this chapter is based on the paper: S. M. Abo and A. T. Layton, "Modeling the circadian regulation of the immune system: Sexually dimorphic effects of shift work," *PLoS Comput Biol*, vol. 17, no. 3, p. e1008514, 2021. URL: https://doi.org/10.1371/journal.pcbi.1008514. Reproduced with permission from PLOS Computational Biology.

Abstract

The circadian clock exerts significance influence on the immune system and disruption of circadian rhythms has been linked to inflammatory pathologies. Shift workers often experience circadian misalignment as their irregular work schedules disrupt the natural light-dark cycle, which in turn can cause serious health problems associated with alterations in genetic expressions of clock genes. In particular, shift work is associated with impairment in immune function, and those alterations are sex-specific. The goal of this study is to better understand the mechanisms that explain the weakened immune system in shift workers. To achieve that goal, we have constructed a mathematical model of the mammalian pulmonary circadian clock coupled to an acute inflammation model in male and female rats. Shift work was simulated by an 8h-phase advance of the circadian system with sex-specific modulation of clock genes. The model reproduces the clock gene expression in the lung and the immune response to various doses of lipopolysaccharide (LPS). Under normal conditions, our model predicts that a host is more sensitive to LPS at circadian time (CT) 12 versus CT0 due to alterations in Interleukin 10 (IL-10) dynamics. We identify REV-ERB as a key modulator of IL-10 activity throughout the circadian day. The model also predicts a reversal of the times of lowest and highest sensitivity to LPS, with males and females exhibiting an exaggerated response to LPS at CT0, which is countered by a blunted immune response at CT12.

4.1 Introduction

Most organisms from bacteria to humans are equipped with an internal biological clock, known as a circadian clock—a network of molecular interactions generating biochemical oscillations with a near 24-hour period [32]. In mammals, the circadian timing system consists of almost as many clocks as there are cells, as most cells house self-sustained and autonomous circadian oscillators [32]. This coordination of rhythms with the diurnal cycle is under the control of a central synchronizer, the suprachiasmatic nucleus (SCN), located in the ventral hypothalamus [155]. The SCN receives direct photic input from the retina, produces rhythmic outputs and orchestrates local clocks in the brain and peripheral clocks throughout the body [109].

Peripheral clocks can be coordinated by systemic cues emanating from the SCN [32], and they can be synchronized also by external cues such as temperature, feeding schedules and light [109]. In particular, the circadian circuitry in the lungs is exquisitely sensitive to environmental factors and exposomes [156], including air pollutants [157], cigarette

smoke [158, 159], shift work [160–162], jet lag [163, 164], pathogens [165, 166] and much more. Of particular interest is the impact of circadian disruption on immune cell function, host defense and inflammation. The emerging picture is that the strength of the immune response varies throughout the day and that dysregulation of clock genes can lead to inflammatory disease or immunodeficiency [57].

Over the past decades, our societies have experienced rapid growth in the need for work in recurring periods other than traditional daytime periods. Research shows that shift work disrupts the natural sleep-wake cycle and feeding patterns [167], which may in turn cause serious health problems [168]. Here, we use mathematical modelling to study the effects of shift work, also known as chronic jet lag (CJL), on the lung circadian clock and consequently the immune response to inflammation. We address important questions: How do interactions between clock genes affect the strength of the inflammatory response at CT0 compared to CT12? Does the disruptive effect of shift work manifest itself differently in males and females? If so, what are the clock genes responsible for the sex-specific responses? Existing mathematical models of the circadian clock that focus on immunity can be classified into two categories: 1) models of the interplay between circadian rhythms and the immune system via neuroendocrine players (e.g. melatonin, cortisol) [52–54]; 2) models for the NF-κB network modulated by the circadian clock [55]. The former do not model the core clock machinery, but rather use rhythmic hormones such as cortisol to drive the circadian variations in the system. The latter include the core clock system but with unidirectional coupling from the clock to the immune system. It is now known that the immune system can affect the circadian clock in a reciprocal manner [56, 57]. Given this observation, we have developed a model of the core circadian clock genes and proteins and their reciprocal interactions with the immune system under acute inflammation. Our mathematical model was extended to include the effect of shift work, represented as an 8h-advance[a] of the circadian phase with sex-specific alterations in the expression of clock genes and proteins (see Figure 4.1).

The immune system is under control of the circadian clock. A primary means of circadian control over the immune system is through direct interactions of clock proteins with components of key inflammatory pathways such as members of the NF-κB protein family [56]. This regulation is independent of transcription and allows the immune system to also reciprocally exert control over the function of the circadian clock [56]. Our model, which is composed of core clock genes (*Bmal1*, *Per*, *Cry*, *Rev-Erb* and *Ror*) and their related proteins as well as the regulatory mechanism of pro- and anti-inflammatory mediators (e.g.

[a]Based on the study by Hadden et al. [164], shift work or CJL consisted of serial 8h advances of light-dark cycle every two days for 4 week. Experiments were performed on 2- to 3-month old C57BL6J female and male mice.

IL-6, TNF-α and IL-10), predicts temporal profiles of clock gene expression and cytokine expression during inflammation. This allows us to study how immune parameters respond to shift work-mediated circadian disruption. Moreover, we compare how the disruptive effect of shift work manifests itself differently in males and females.

4.2 Methods

We present a mathematical model for simulating the circadian clock in the lung of a rat, the immune system under acute inflammation, and the interactions between the two systems. A schematic diagram that depicts the regulatory network is shown in Figure 4.1. Model equations and parameters can be found in Tables A.1-A.10 in Appendix A.

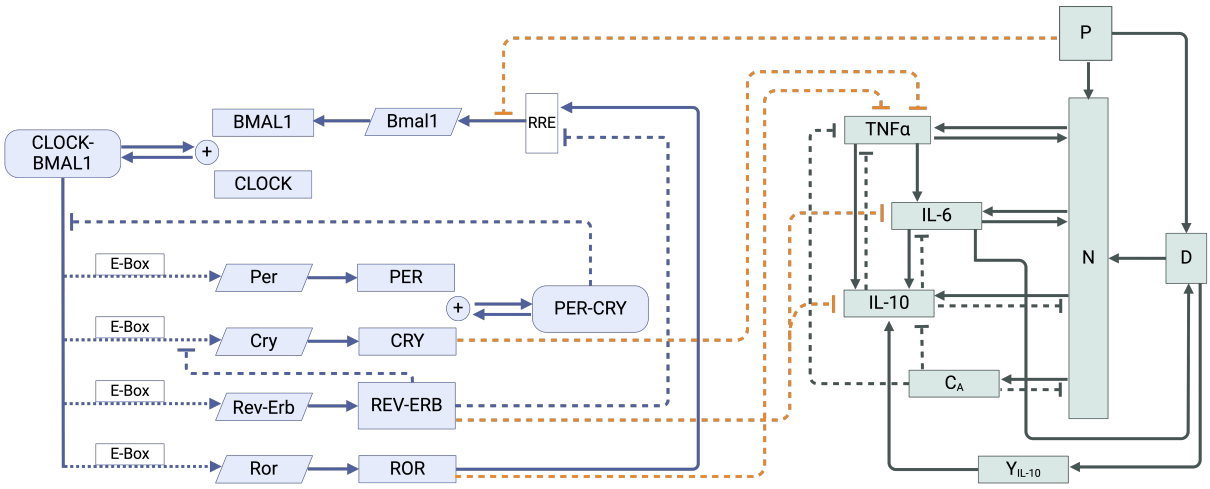

Figure 4.1: Regulatory network of the coupled immune system and circadian clock. Schematic diagram of the acute immune response model (green boxes) and the circadian clock (blue boxes) in the lung of a rat. In the circadian clock model, slanted boxes denote mRNAs; rectangles denote proteins; ovals denote protein complexes. Dotted arrows represent transactivation; solid arrow represent mRNA translation into proteins (or the process of two proteins forming a complex through heterodimerization, or vice versa); blunt dashed arrows represent inhibition. In the acute inflammation model, P denotes endotoxin; D, damage marker; N, activated phagocytic cells; C_A, slow-acting anti-inflammatory cytokines; IL-6 and TNFα are pro-inflammatory cytokines; IL-10 is an anti-inflammatory cytokine; $\mathrm{Y_{IL-10}}$ is a tissue-driven (non-accessible) IL-10 promoter.

4.2.1 Circadian clock in the lung

The mammalian clock consists of interlocked transcriptional-translational feedback loops that drive the circadian oscillations of core clock components [169]. Both the master and peripheral clocks share essentially the same molecular architecture [108]. The activators CLOCK and BMAL1 dimerize to induce the transcription of target genes, including the *Period* genes (*Per1, 2, 3*), *Cryptochrome* genes (*Cry1, 2*), retinoic acid-related orphan receptor (*Rora, Rorb, Rorc*) and *Rev-Erb* nuclear orphan receptor (*Rev-Erbα, Rev-Erbβ*) to activate their transcription [32]. PERs and CRYs then heterodimerize and enter the nucleus to inhibit their own transcription by acting on the CLOCK-BMAL1 protein complex, and thus form the main feedback loop [32, 112, 113]. In the secondary loop, the nuclear receptors REV-ERBα, β and RORa, b, c compete for ROR regulatory element (RRE) binding sites in the promoter region of *Bmal1* and respectively repress and activate its transcription. The REV-ERBs, which also repress *Cry1* transcription [120], are essential for robust oscillations [98, 121, 122]. See the clock network in Figure 4.1, and refer to Refs.[98, 109, 113] for a detailed overview of the molecular clock architecture.

The present lung circadian clock model, inspired by Ref.[170], describes the time evolution of mRNA and corresponding protein concentrations of *Per*, *Cry*, *Rev-Erb*, *Ror*, and *Bmal1*, and their modulation of proximal tubule epithelial transport [171]. In our model we refer to gene family groups, or gene entities: we grouped the three *Period* homologs (*Per1-3*) as a single *Per* gene and the two *cryptochromes* (*Cry1,2*) as a single *Cry* gene. Similarly, the two isoforms *Rev-Erbα* and *Rev-Erbβ* and three isoforms *Rora*, *Rorb* and *Rorc* are represented by single variables *Rev-Erb* and *Ror*, respectively. It was assumed that the CLOCK protein is constitutively expressed. We did not include post-translational protein modifications, considering that transport between the cytoplasm and the nucleus is fast on a circadian timescale [172]. The time evolution of the core clock genes and proteins is described by Eqs. (A.1)–(A.12) in Table A.2.

4.2.2 Acute immune response

The acute immune response model, inspired by Refs.[173] and [174] with some modifications, consists of eight variables: endotoxin concentration (P); the total number of activated phagocytic cells (N, which includes activated immune response cells such as neutrophils and monocytes); a non-accessible tissue damage marker (D); concentrations of pro- and anti-inflammatory cytokines, namely IL-6, TNF-α and IL-10; a tissue driven non-accessible IL-10 promoter (Y_{IL10}); and a state representing the level of slow acting anti-inflammatory

mediators (C_A), which comprises slow-acting anti-inflammatory agents such as cortisol and TGF-β1.

The introduction of bacterial insult in the system activates the phagocytic cells, N, and inflicts direct tissue damage, D [175]. This is different from the work of Roy et al. [173] in which endotoxin only activates phagocytic cells. The activated cells up-regulate the production of inflammatory agents (TNF-α, IL-6, IL-10, and C_A) [176]. The pro-inflammatory cytokines TNF-α and IL-6 exert a positive feedback on the system by further activating N, as well as up-regulating other cytokines [176, 177]. The anti-inflammatory cytokines IL-10 and C_A, on the other hand, have a negative feedback on the system. They inhibit the activation of N and other cytokines [178, 179]. The model also incorporates tissue damage, represented by a non-accessible damage marker, D. Tissue damage further up-regulates activation of N [180] and also contributes to up-regulation of *IL-10* [181, 182]. In our model, D is up-regulated by IL-6 because it has been shown that IL-6 is associated with the development of sepsis [183–185]. This differs from Ref.[173] in which damage is up-regulated by N. Note also that D should not be interpreted directly as a cell type in the model. The acute inflammatory response is described by Eqs. (A.13)–(A.20) in Table A.2; see also Figure 4.1.

4.2.3 Coupling between the circadian clock and the immune system

Most studies on circadian-immune interactions have focused on *Bmal1*, since inactivation of this gene is a convenient way to abrogate clock function [165, 186, 187]. Thus, care should be taken in distinguishing *Bmal1*-specific effects from downstream effects because other clock components act as intermediaries. The inhibitory effects that the circadian clock and the inflammatory response have on each other are shown in Figure 4.1. Specifically:

- **CRY proteins.** *Cry1*$^{-/-}$ *Cry2*$^{-/-}$ mice exhibit an elevated number of T cells in the spleen with increased TNF-α levels [56, 188]. Other studies showed that *Cry1* and *Cry2* double KO in fibroblasts and bone-marrow-derived macrophages (BMDMs) leads to increased *Il6* and *Tnf-α* mRNA and an hypersensitivity to lipopolysaccharide (LPS) infection [57, 189]. Furthermore, the NF-κB signaling pathway was shown to be constitutively activated in *Cry1*$^{-/-}$ *Cry2*$^{-/-}$ BMDMs [189]. Due to the ensuing higher constitutive inflammatory state, *Cry1*$^{-/-}$ *Cry2*$^{-/-}$ mice exhibit increased infiltration of leukocytes in lungs and kidneys [190]. Therefore, CRYs play an important anti-inflammatory role by downregulating inflammatory cytokines.

Because IL-6 is inducible with TNF-α, effects on IL-6 in CRY double KO experiments are primarily mediated by TNF-α [189]. In our model, CRY directly inhibits the production of TNF-α, hence indirectly inhibits the TNF-α-induced IL-6 production (see Eq. (A.17) in Table A.2).

- **ROR proteins.** Similarly to the CRY proteins, experiments have shown that Ror$a^{-/-}$ mice, also known as the staggerer mutant, exhibit higher levels of IL-6 in bronchoalveolar lavage fluid, which renders them more susceptible to LPS lethality [191]. Interestingly, staggerer mutant mice have an increased production of IL-6 and TNF-α in mast cells and macrophages after LPS stimulation [192, 193]. Furthermore, overexpression of RORa in human primary smooth muscle cells inhibits TNF-α-induced expression of IL-6 [194]. The present model assumes that ROR downregulates TNF-α, thus indirectly downregulates IL-6 (see Eq. (A.17) in Table A.2). We recall that the model does not distinguish between the three isoforms *Rora*, *Rorb* and *Rorc*.

- **REV-ERB proteins.** There is compelling evidence for a role for REV-ERBα in the control of the immune system. REV-ERBα is encoded by *Nr1d1* and *in vivo* challenge of *Nr1d1*$^{-/-}$ mice with LPS leads to IL-6 upregulation in serum in comparison to wildtype animals [195]. REV-ERBα represses *Il6* expression not only indirectly through an NF-κB binding motif but also directly through a REV-ERBα binding motif in the murine *Il6* promoter region [196]. A more recent study showed that the dual mutation of REV-ERBα and its paralog REV-ERBβ in bronchial epithelial cells further augmented inflammatory responses and chemokine activation [197]. REV-ERBα also negatively affects the expression of anti-inflammatory cytokine IL-10. *Rev-Erb*α mRNA binds to the IL-10 proximal promoter and represses expression in human macrophages [198]. Together, these studies reveal the role of REV-ERBα as an equilibrist. In our model, REV-ERB directly inhibits the production of IL-6 and IL-10 (Eqs. (A.16) and (A.18) in Table S2, respectively). We note that the two isoforms *Rev-Erb*α and *Rev-Erb*β are represented by a single model variable *Rev-Erb*.

- **Inflammation.** In a reciprocal manner, inflammation induced by agents such as LPS, TNF-α, and IFN-γ [199–203] or acute bacterial infection [204] can affect the circadian clock. In particular, rodent studies indicate that LPS transiently suppresses clock gene expression and oscillations in the SCN and peripheral tissues [172, 203, 205, 206]; notably, a number studies show significant suppression of *Bmal1* [57, 205, 207]. The inhibition of the circadian mechanism during endotoxemia lasts

for at least 24 h [203, 207]. To represent the sustained effect of a bacterial infection on the circadian clock, we introduced a filter function for LPS (Eq. (A.21) in Table A.2), which acts on the clock through its inhibition of *Bmal1* (Eq. (A.5) in Table A.2). The filter function decays linearly over 24h and causes circadian disruption for at least this amount of time. We assume that the effects of cytokines such as TNF-α are incorporated in the net effect of LPS on clock genes, and so we do not include direct links from cytokines to clock genes and proteins.

4.2.4 Model parameters

Most of the model parameters are not well characterized, and were estimated by fitting model dynamics to experimental data. Due to the transient nature of acute inflammation, this is done in a two-step process: we first fit the circadian clock model in isolation, in an infection-free state. In the absence of infection, the acute inflammation model is idle and therefore has no influence on the expression of clock genes. Likewise, clock genes have no effect on inflammation variables whose initial conditions are zero. The fitting of the clock model is done using data on the expression of circadian genes in the mouse lung (*CircaDB*: `http://circadb.hogeneschlab.org`). Animals were entrained to a 12h light:12h dark schedule for one week, then released into constant darkness. Clock gene expression was recorded starting at CT18 postrelease [208]. It is noteworthy that the present model is based on the rat, whereas the parameters for the circadian clock were based on mouse data. However, while species differences exist, core clock gene expressions of the mouse and rat lungs exhibit substantial similarities [209]. Our model inherits the period of the data which is 24 h.

In a second step, we fit the acute inflammation model together with the clock-inflammation coupling, without changing the circadian clock parameters. This is done by simultaneously fitting experimental measurements of the cytokines IL-6, TNF-α, and IL-10 in rat following the administration of endotoxin at 3 mg/Kg and also at 12 mg/Kg [173, 174]. In other words, we fit the time profiles for all variables (P, D, N, CA, IL-6, IL-10, TNF-α) using measured data on IL-6, IL-10 and TNF-α only. This fitting was conducted with the coupling with the clock model taken into account. Some parameters in the model were specified. The clearance rate of endotoxin, P, captured by the parameter d_P in Eq. (A.13) was obtained from the literature [210, 211]. Parameters s_{IL10} and s_{CA} from Eqs. (A.18) and (A.20) were extracted directly from the experimental data, respectively [173]. Model parameters are shown in Tables A.3–A.10.

Parameter estimation

Parameter estimation for the coupled system was carried out with a nonlinear least-squares method with a normalized residual, which minimizes the error between the computed model output and the experimental data. To this end, we defined:

$$\chi^2 = \sum_{i=1}^{Q} \left[\frac{y_i - y(t_i, \boldsymbol{\theta})}{\max(y_{i(i=1,\ldots,Q)})} \right]^2 \tag{4.1}$$

Here, y_i, is the measured data at time t_i. The model prediction is given by $y(t_i, \boldsymbol{\theta})$, where $\boldsymbol{\theta}$ represent model parameters. Q is the total number of data points. Experimental error bars, as shown in Figure 4.4, were not taken into account. The cost function that we minimize is given by:

$$\kappa(\boldsymbol{\theta}) = \chi^2_{IL6_3} + \chi^2_{IL6_{12}} + \chi^2_{TNF\alpha_3} + \chi^2_{TNF\alpha_{12}} + \chi^2_{IL10_3} + \chi^2_{IL10_{12}} \tag{4.2}$$

The subscripts 3 and 12 refer to the injected dose of endotoxin (mg/Kg). As proposed in Ref. [212], the cost function has been minimized by using an optimization function in MATLAB known as *fminsearch* to search for the parameter estimated values which give the best fit of the model to the experimental data. *fminsearch* is an unconstrained multidimensional minimizer that uses the Nelder-Mead algorithm. Nelder-Mead is a derivative-free algorithm that evaluates the cost function at the vertices of a parameter simplex, ranks the values of the function, replaces the worst value with a best one based on a set of rules, and repeats until a tolerance error or a number of function evaluations prescribed by the authorized user has been reached. A more detailed description of Nelder-Mead algorithm can be found elsewhere. Still, obtaining our final result required a series of educated guesses, manually correcting the most obvious differences before restarting the optimization. We have found that the parameter values are not uniquely determined, as different sets of parameters provide almost the same goodness of fit. In order to assess the relative influence of each parameter on the outcomes, we performed a global sensitivity analysis using the Sobol' method (Appendix A, Section A.2).

4.2.5 Sexual dimorphism in clock gene alterations under circadian disruption

In their 2012 study, Hadden et al. [164] reported sexual dimorphism in clock gene expression in the lungs of mice exposed to chronic jet lag. Male and female mice were assigned to either

remain in a light-dark (LD) LD12:12 regimen or to undergo experimental chronic jet lag (CJL). Under the CJL regimen, mice were subjected to serial 8-h advances of the light-dark cycle every 2 days for 4 weeks. Then using quantitative polymerase chain reaction (PCR) to measure the relative amount of clock gene mRNAs, Hadden et al. [164] observed that *Rev-Erbα* gene expression is upregulated in CJL males and downregulated in CJL females by 98% and 70% on average, respectively. *Bmal1* is downregulated in CJL females only by 43% on average, while *Clock*, which forms a heterodimer with *Bmal1* (CLOCK-BMAL1) [208], is downregulated in males only by 26%. The repressors *Per2* and *Cry2* are both upregulated when compared with same-sex control animals, although *Cry2* upregulation was not significant for CJL males. In particular, *Per2* and *Cry2* increased by 497% and 69%, respectively in CJL female mice, while *Per2* increased by 230% in CJL male mice. The authors did not test the effects of chronic jet lag on *Ror* gene expression. This could be explained by the fact that *Ror* is not directly related to the shift work phenotype. Indeed, the association between *Ror* and shift work disorder has been shown to be weak at best [213].

We used this information to create separate mathematical models of the lung circadian clock for males and females undergoing CJL. The decrease in *Clock* mRNA for CJL males is not taken into account because we do not model this gene explicitly and only constitutively represent the associated CLOCK protein. In addition, NPAS2, a paralog of CLOCK, has been shown to compensate for the loss of CLOCK in peripheral circadian oscillators [214, 215]. We note also that the baseline immune system likely differs between the sexes, but due to insufficient quantitative data, we were only able to construct one baseline model. Figure 4.2 shows the male-to-female relative abundance of mRNAs for controls and shifters, as reported by Hadden et al., normalized by control male-to-female ratios.

A method similar to that of the baseline system was used for the calibration of the CJL male and CJL female models. Hadden et al. did not measure clock gene expression over a 24-hour period, which would have allowed identification of rhythm differences, i.e. mesor, amplitude and phase expression of these genes, but rather reported the average expression level of clock genes. We have therefore modified the cost function, Eqs. 4.1–4.2, to minimize the error between the average gene concentration in our models and the experimental data. A comparison between the change in mean gene expression between our models and experimental data is available in Table A.12 in Appendix A.

Only a few parameters changed drastically from the nominal values in the baseline model. Thus, we fixed the parameters that had not changed much, and repeated the calibration with a reduced set of free parameters for the CJL models: 6 parameters for the male CJL model and 10 parameters for the female CJL model. CJL model parameters can be found in Table A.11 in Appendix A. This process resulted in a change in the average con-

centration of clock genes in CJL models to the levels specified by the data. Consequently, the amplitude of the oscillations increased or decreased depending on the direction of the change. A previous study using the same experimental protocol has recorded sustained alterations to the average gene concentration as well as the amplitude of clock genes in the SCN and peripheral tissues [216].

At the time of this study, Ref. [164] is the only work known to us that reports quantitative data on the sexual dimorphism of clock gene expression in the lungs of mice exposed to CJL. However, other studies involving only male rats or mice have recorded changes similar to CJL males [216, 217].

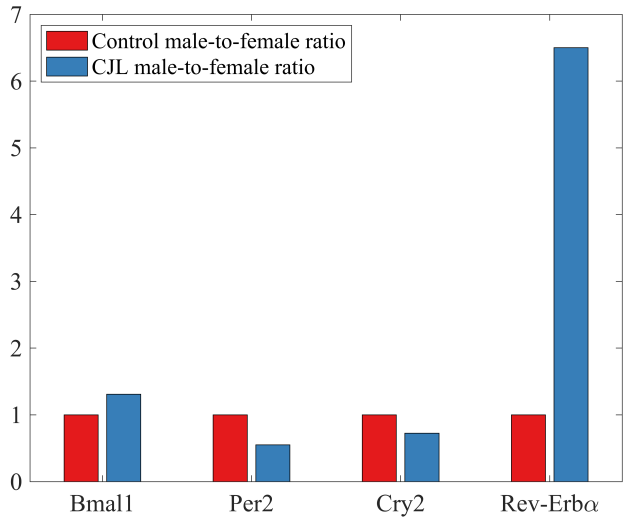

Figure 4.2: Male-to-female relative abundance of mRNAs for controls and shifters, normalized by control male-to-female ratios.

4.3 Results

4.3.1 Expression of clock genes in lungs is accurately reproduced by the model

Using the baseline model parameters (Tables A.3–A.10), the circadian clock model predicts limit-cycle oscillations in the expression levels of all clock components with a system period of 24 h. Figure 4.3 compares the predicted time profiles of *Bmal1*, *Per*, *Cry*, *Rev-Erb* and

Ror with experimental observations for *Bmal1*, *Per2*, *Cry1*, *Rev-Erbα* and *Rorc*. We refer to the onset of the rest phase of night-active organisms as CT0 and to the onset of activity as CT12 [218]. These two times correspond to the onset of the light and dark phases, respectively. Good agreement can be observed between the predicted and experimental temporal profiles. Note that the parameter estimation procedure above (4.1) concerns the baseline model and does not involve CJL. Thus, all CJL results are model predictions.

4.3.2 Cytokine dynamics during endotoxemia are accurately reproduced by the model

We estimated the parameter values for the acute inflammation model by simultaneously fitting experimental measurements of the cytokines IL-6, TNF-α, and IL-10 at endotoxin doses 3 mg/Kg and 12 mg/Kg. The predicted time profiles are shown in Figure 4.4, left and center columns. The model performs similarly well for all three cytokines, and is able to capture the second peak in IL-10 expression. We note that the predicted IL-10 concentrations at 1 h and after 10 h are slightly underestimated compared to the value recorded experimentally for the endotoxin dose 12 mg/Kg.

Model predictions were validated by comparing model simulations with available cytokine data at a 6 mg/Kg endotoxin challenge level. These data were not used in the parameter fitting. The results are shown in Figure 4.4, right column. In general, model predictions of the measured cytokines are in good agreement with the experimental data. We observe that TNF-α concentration is overestimated at 1 h. This discrepancy may be explained by the apparent inconsistency between the data collected at 1 h with samples collected at the same time point for endotoxin dose levels of 3 and 12 mg/Kg. A similar model behavior was observed in the initiating article [173]. We note also that the model over-predicts IL-10 concentration after 12 h.

4.3.3 Effect of infection timing on immune response

It is well established that the survival of rodents after endotoxemic shock varies with the time of administration of bacterial insult. Studies have shown an increased lethality towards the end of the resting phase in controlled light-dark experiments [195, 219, 220]. Since an organism's ability to fight off an infection depends in part on having a sufficiently large population of cytokines, we investigate how the timing of infection affects cytokine dynamics. Interestingly, a discrepancy can be discerned in post-infection IL-10 dynamics: some studies reported a single peak [221], whereas others reported two peaks [173].

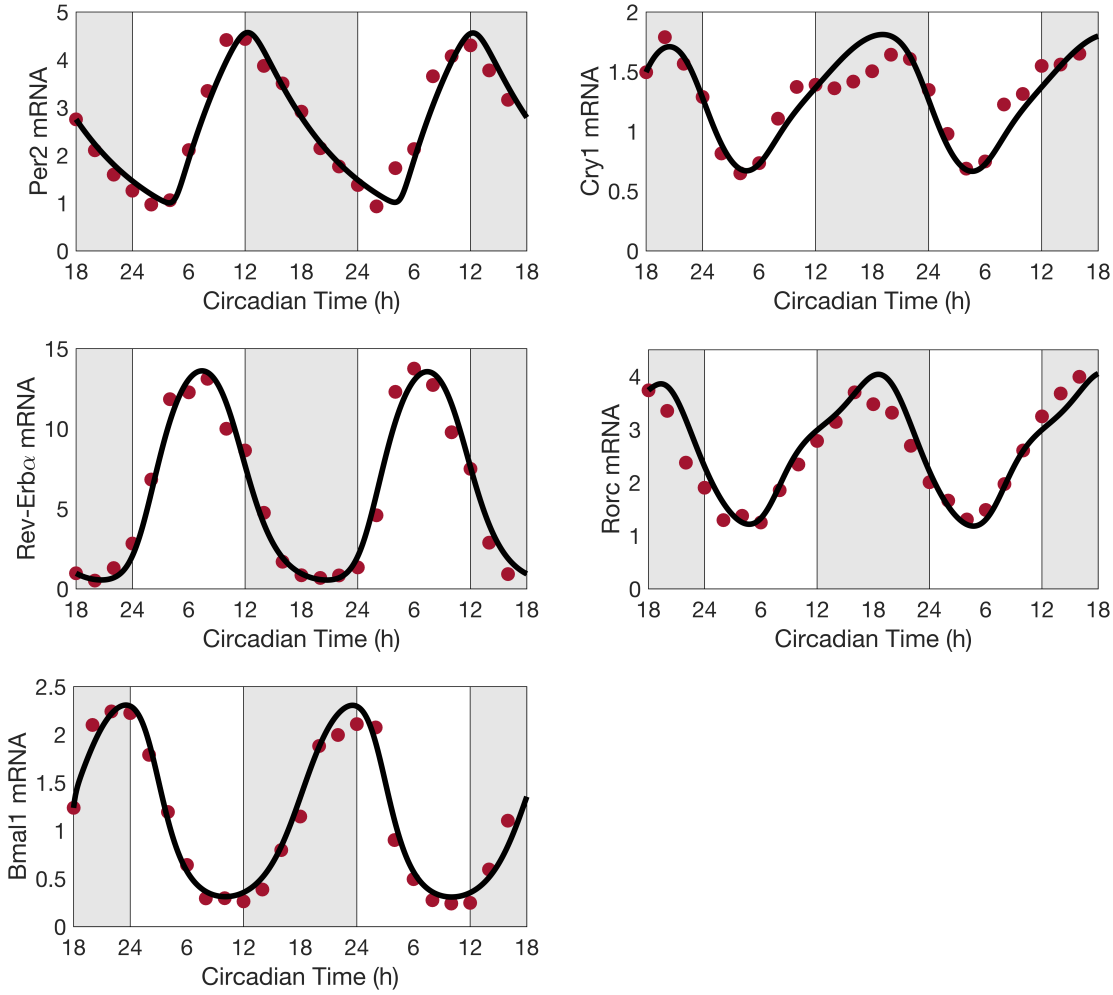

Figure 4.3: Predicted clock gene time profiles. Comparison of predicted time profiles (solid lines) for *Per*, *Cry*, *Rev-Erb*, *Ror* and *Bmal*1, with experimental data (circles) for *Per*2, *Cry*1, *Rev-Erbα*, *Rorc*, and *Bmal1* mRNA expression levels obtained in mouse lungs in constant darkness. Gray shading and white regions correspond to activity and restcycles, respectively.

We hypothesize that this discrepancy can be explained by the different infection timing (unfortunately infection timing was not reported in those studies).

We first seek to explain how the time of infection affects its lethality. Model simulations predict higher concentrations of inflammatory cytokines (IL-6 and TNF-α) and more tissue damage result from an infection administered at CT12 compared to CT0 (Figure 4.5a-

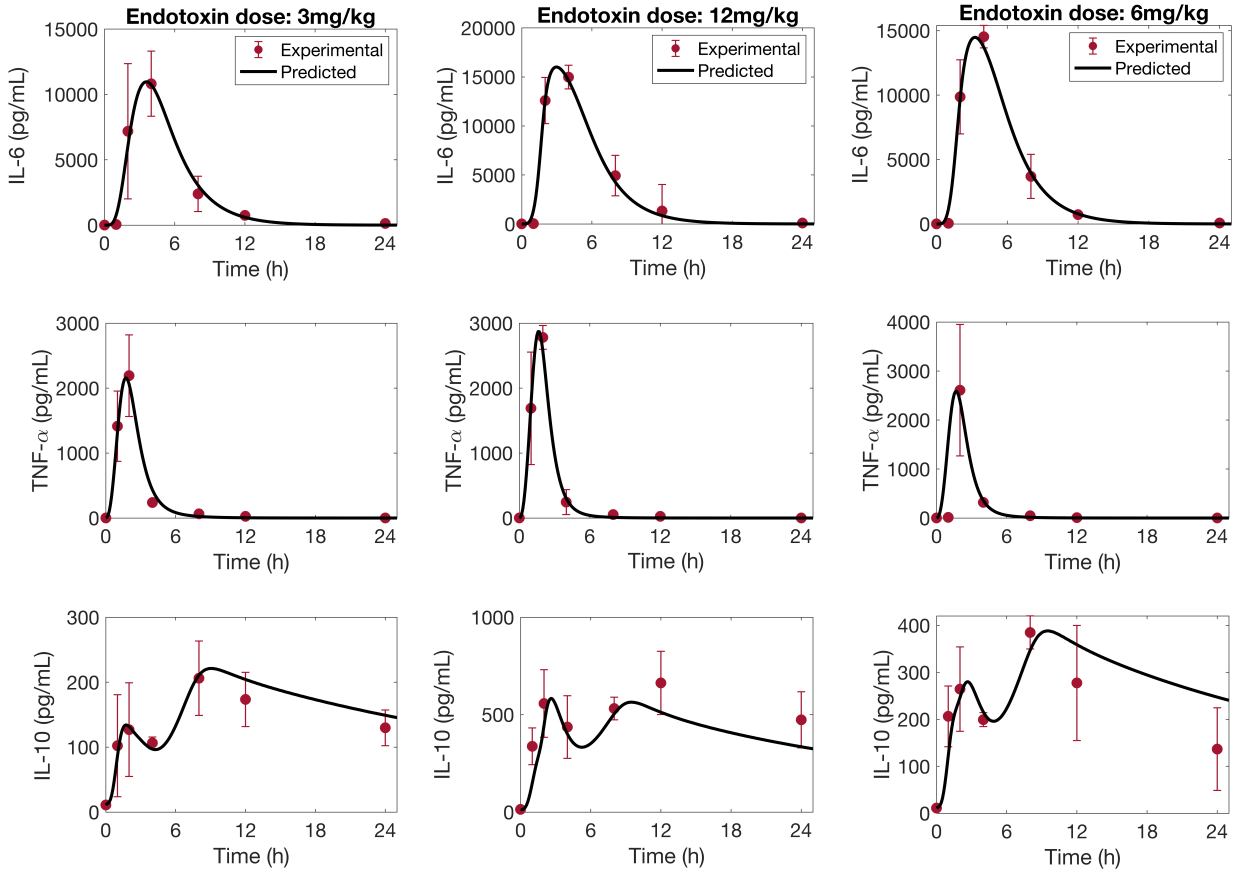

Figure 4.4: Predicted cytokine time profiles. Comparison of predicted time-courses of IL-6, TNF-α and IL-10 (solid line), against experimental data (circle) (mean $\pm$ SD), in response to endotoxin challenge at dosages of 3 mg/Kg, 12 mg/Kg and 6 mg/Kg.

b,d). This difference can be explained in terms of the organism's sensitivity to LPS, which is predicted to be highest at CT12, consistent with the observed phenotype of increased cytokine release [57, 195]. This increased sensitivity to LPS can be explained by a mismatch in the acrophases of REV-ERB and ROR in particular. Figure 4.6 shows the phase relations between CRY, REV-ERB and ROR. REV-ERB crests while ROR attains its minimum at CT12. Thus ROR inhibition of TNF-α and IL-6 is considerably reduced, hence allowing for a greater production of the cytokines. At the same time, the inhibition of IL-6 and IL-10 by REV-ERB is maximized, but since IL-10 also inihibits IL-6, its inhibition by REV-ERB repeals its action on IL-6, leading IL-6 to more than double (Figure 4.5a). We note that TNF-α increases less than IL-6 due to the inhibitory action of CRY which increases

as REV-ERB decreases (see Figure 4.1 and Figure 4.6). The larger increase in cytokine populations following a CT12 infection results in more tissue damage, compared to a CT0 infection (Figure 4.5).

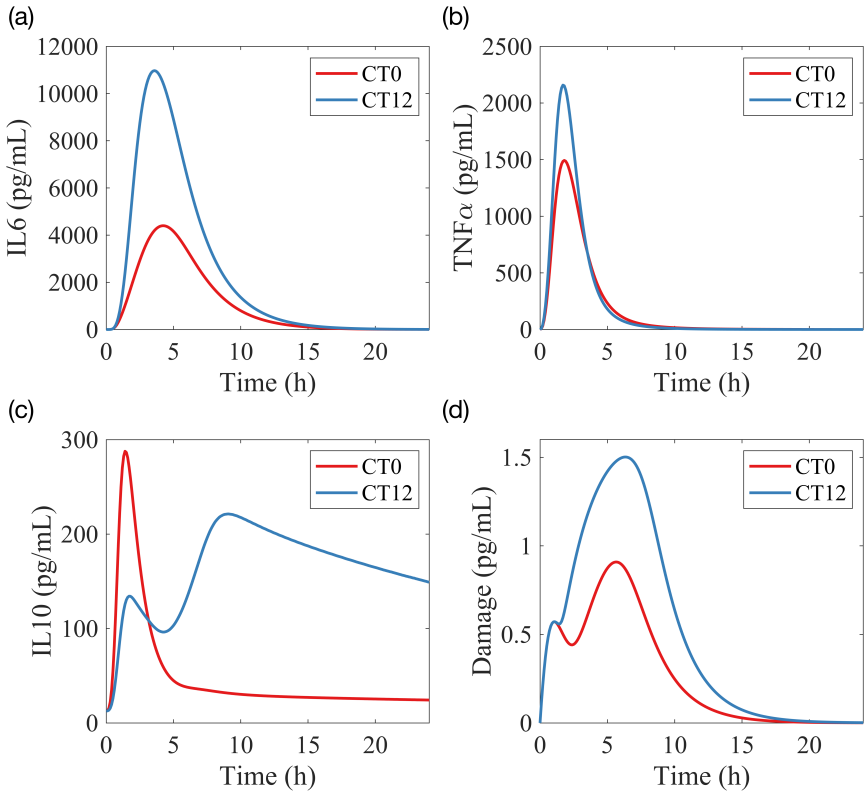

Figure 4.5: Inflammatory response after infection at CT0 and CT12. Model simulations of the time course of (a) *IL-6*, (b) *TNF-α*, (c) *IL-10* and (d) the damage marker for the control model in response to endotoxin dose 3 mg/Kg administered at CT0 and CT12

It is noteworthy that our model predicts a single peak in the expression of the anti-inflammatory cytokine IL-10 when the host is infected at CT0 versus two peaks when the infection occurs at CT12 (Figure 4.5c). This behavior persists across different doses of endotoxin (results not shown), which indicates that the immune response might be different at CT0 compared to CT12 regardless of the extent of the infection. We hypothesize that the different timing of infection may explain the single peak versus two peaks in IL-10 time profiles in previous studies [173, 221]

A closer look at the dynamics of REV-ERB revealed the following: at CT0 and without

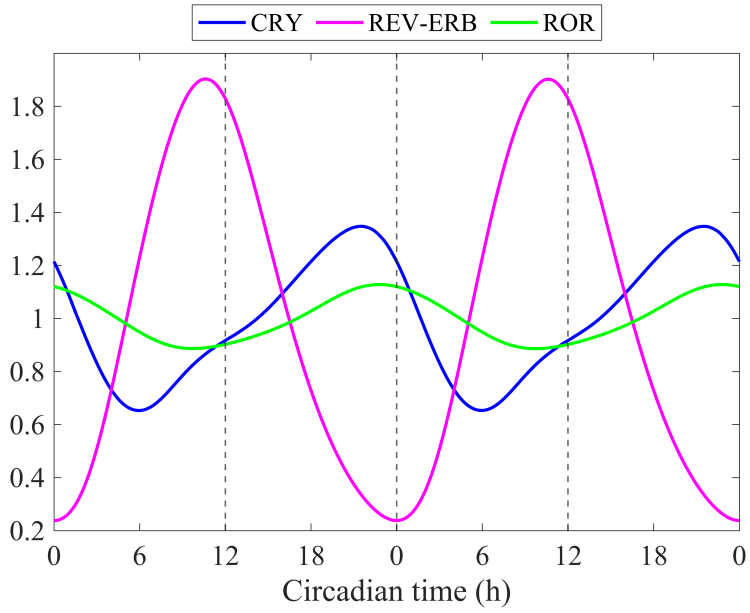

Figure 4.6: Phase relations between CRY, REV-ERB and ROR. Baseline model simulation of the main clock genes involved in the inflammatory response. Normalized temporal expression profiles of CRY, REV-ERB and ROR proteins, relative to their respective mean value.

infection, REV-ERB is close to its minimum. An attack by pathogens inhibits *Bmal1*, causing REV-ERB to drop below its nadir. This is followed by an almost complete loss of IL-10 inhibition by REV-ERB, and thus leads to a single IL-10 spike. The high levels of circulating IL-10 limit the production of proinflammatory cytokines (Figures 4.5a-b). On the contrary, REV-ERB is close to its maximum at CT12, and while an attack by pathogens inhibits its production, REV-ERB concentration remains sufficiently high for the first few hours. Therefore, REV-ERB still inhibits IL-10 during the early stages of inflammation and only a weak peak in IL-10 emerges. This inhibitory action is later counteracted by the accumulation of circulating IL-6 and TNF-α which upregulate IL-10 production, hence explaining the rise of a second peak in IL-10 when the infection occurs at CT12. About ten hours after the onset of inflammation, REV-ERB finally drops below its normal minimum levels. This is similar to the case at CT0, and leads to sustained elevated levels of IL-10 for a few hours after the elimination of IL-6 and TNF-α (see Figure 4.5, >10 h).

We hypothesize that the lower production of pro-inflammatory cytokines at CT0 is due to high levels of IL-10, which spikes earlier during endotoxemia due to the loss of REV-ERB. The second peak in IL-10 production can be an indicator of a stronger inflammatory

response as can be seen at CT12. To test our hypothesis, we simulate acute inflammation under three scenarios at CT12: *Rev-Erb* KO, *Cry* KO and *Ror* KO. Figure 4.7A shows that the loss of *Rev-Erb* leads to a loss of the second peak of IL-10, while the absence of *Cry* or *Ror* does not give rise to qualitatively different dynamics. As expected, a CT12 infection following *Rev-Erb* KO produces results similar to a CT0 infection (see Figure 4.5) because in both cases the concentration of the REV-ERB is at a minimum or even zero. Additionally, the damage marker is greatly reduced by the loss of *Rev-Erb* (Figure 4.7b). This is due to the inhibition of IL-6 following the sharp increase in the anti-inflammatory cytokine IL-10. Consequently, IL-6 induced activation of D is abrogated. In this case, the damage marker indicates an inadequate immune response because not enough inflammatory cytokines are produced to fight the infection. The different timing of infection may indeed explain the single peak versus two peaks in the IL-10 temporal profiles.

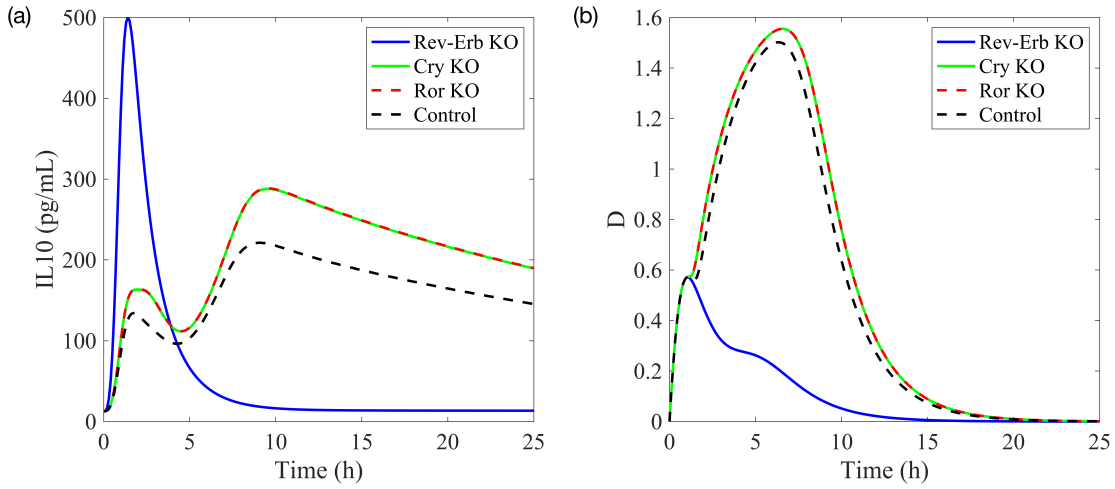

Figure 4.7: Knockout experiment at CT12. Model simulations of the time course of *IL-10* (a) and the damage marker (b) in response to endotoxin dose 3 mg/Kg administered CT12. Three scenarios are simulated: *Rev-Erb* KO, *Cry* KO and *Ror* KO.

4.3.4 Circadian disruption alters host immune response

It has been reported that a challenge of LPS in rodents with a disrupted circadian clock leads to a stronger inflammatory response and increased mortality [222, 223]. Particularly, Castanon-Cervantes et al. [223] observed a sustained reduction in *Bmal1* transcript following CJL. This is similar to findings by Hadden et al. [164] for female mice. Below

we conduct simulations to illustrate that *how* circadian disruption alters immune response depends on (i) the time of infection, and (ii) the sex of the organism.

When endotoxin is administered at the onset of the rest phase (CT0), our model predicts an increased production of IL-6 and TNF-α in CJL males compared to controls (Figure 4.8b-c). Similar results were shown in experiments on CJL male mice [224] and CJL male rats [225] where the animals were injected with LPS during the early rest period. This stronger response is due to the 8h-advance circadian disruption which resets their clock to the middle of the active phase. In contrary, CJL females remained relatively close to baseline compared to their male counterparts (Figure 4.8). Unlike males, the upregulation of CRY in CJL females decreases TNF-α and IL-6 production, while the downregulation of REV-ERB leads to increased levels of IL-10 and therefore more IL-10-induced IL-6 inhibition. In sum, CJL rats suffer more tissue damage from LPS administered at CT0, with CJL males more so than females (Figure 4.8a).

The trend is reversed at CT12. Figure 4.8 shows that CJL rats have blunted IL-6 and TNF-α responses. We recall that REV-ERB is upregulated in CJL males compared to CJL females and controls (Figure 4.2d). Higher levels of REV-ERB further inhibit the production of IL-10, which then releases its inhibitory action on pro-inflammatory cytokines. This explains why CJL males, while having a blunted immune response, still produce more cytokines than CJL females. The downregulation of IL-6 following CJL has also been observed in all-male mice experiments [226–228]. Moreover, the weaker immune response in both CJL males and females is explained by their internal circadian disruption (8-h phase advance) which puts them at a circadian phase similar to CT4 in control rats. The reduced production of cytokine is represented by a lower damage marker and could indicate an inadequate and disrupted immune response (Figure 4.8a), particularly for CJL females. We note that the damage marker for CJL females (Figure 4.8a) is similar to that of the *Rev-Erb* KO experiment (Figure 4.7a). This highlights the role of REV-ERB in promoting an adequate immune response. Our model predictions at CT12 are consistent with experimental reports that the immune system in females is detrimentally affected more than that of males during CJL [229].

4.3.5 Effect of infection timing on immune response: Beyond CT0 and CT12

Previous studies have shown, in the absence of CJL, increased lethality towards the end of the resting phase, approximately 2 h before the onset of activity [219, 220]. We tested our baseline (no CJL) model predictions for different time points of infection, and indeed

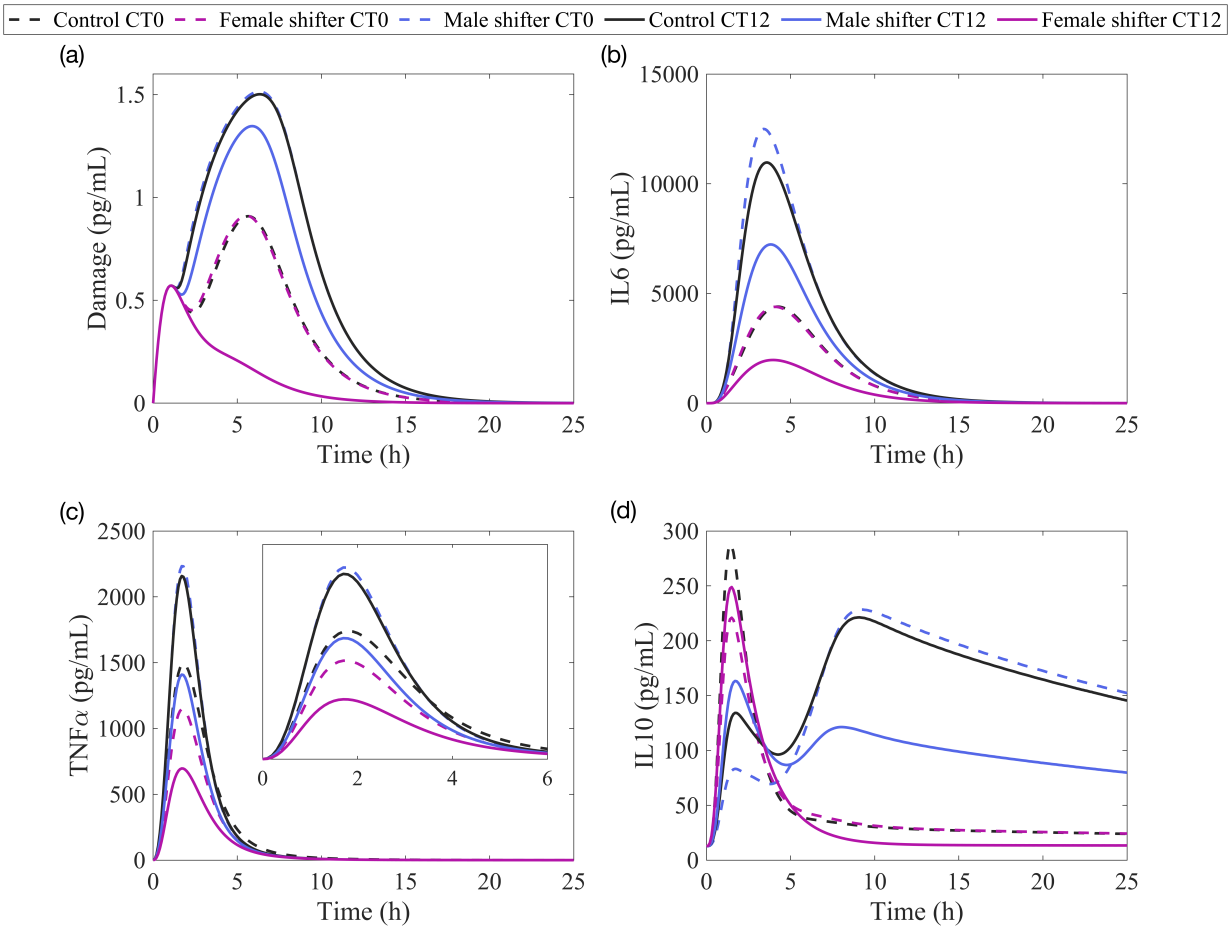

Figure 4.8: Sex-specific response to infection during CJL at CT0 and CT12. Model simulations of the time course of (a) *IL-6*, (b) *TNF-α*, (c) *IL-10* and (d) the damage marker for controls (black) against CJL males (blue) and CJL females (pink) in response to endotoxin challenge of 3 mg/Kg administered at CT0 and CT12.

our results show higher sensitivity to LPS infection at CT9, followed closely by CT12 (see Figure 4.9a-d: Control).

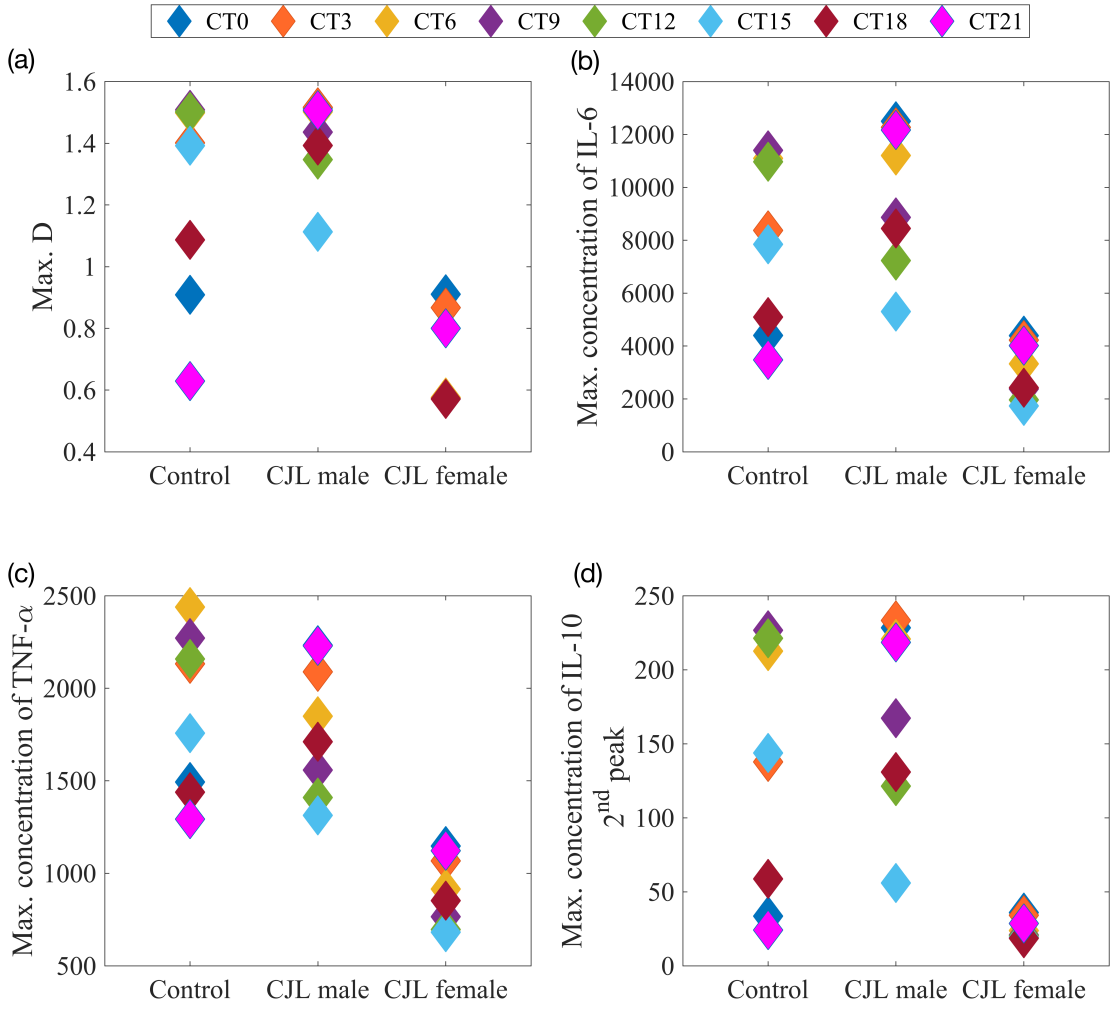

Figure 4.9: Simulated acute inflammation across different circadian times. *IL-6* (a), *TNF-α* (b), *IL-10* (c), *Damage marker* (d). The endotoxin dose is 3 mg/Kg. Left column, no CJL; middle column, CJL females; right column, CJL males.

We also conducted simulations under CJL. As shown in Figure 4.9a-d, CJL males and females are more sensitive to LPS than controls at CT0, and exhibit reduced induction of cytokines at CT12. This supports our hypothesis that the CJL induced by an 8-h phase advance of the lung circadian clock would reverse the times of lowest and highest sensitivity to LPS. Interestingly, CT18 appears to be a time of lesser sensitivity to LPS regardless of the experience of the host: CJL or normal lighting conditions (Figure 4.9).

In general, the extent of sequelae experienced by male and female rats varied across

the circadian day. Females had a more disrupted inflammatory response closer to CT12. Figure 4.9d shows that CJL females were not able to recover the second peak in IL-10 at any of the times tested. This means that CJL females did not produce as much pro-inflammatory cytokines (e.g. CT9, CT12) as controls. Compared to CJL males, CJL females produce less cytokines overall during acute inflammation. Males, however, lost their circadian gating of cytokines closer to CT0 (see Figure 4.9: CT21, CT0) and produced greater amounts of pro-inflammatory cytokines, making them more susceptible to sepsis at that time, as indicated by experiments [230, 231].

4.4 Discussion

The circadian clock is responsible for the daily rhythms in immune functions [232]. A growing body of research supports the role of clock genes in regulating cytokines before and during infection [233]. In a reciprocal fashion, immune agents can impact the clock [234]. To investigate the interplay between the immune system and the circadian clock, we developed a mathematical model incorporating the bidirectional coupling between the lung circadian clock and the acute inflammatory response. We adapted this model to study the sexual-dimorphic effects of shift work (also known as CJL) on both the clock mechanism and inflammation. It has been recognized that shift work has a negative impact on health [235] and a better understanding of the mechanisms by which disruption of circadian rhythms affects immunity, and how that effect differs between males and females, may help the development of chronotherapies for treating shift work-related disorders such as shift work sleep disorder (SWSD) and its related health-risks.

Given that sensitivity to LPS is highest at CT12 in rodents [57, 195], we showed circadian disruption induced by an 8-h phase advance reduces cytokine production at this time while exacerbating the response at CT0. Remarkably, our models predict a second peak in the production of the anti-inflammatory cytokine IL-10 when the immune system is poised for attack (e.g. CT12). At times when the immune system is undergoing regeneration and repair (e.g. CT18-CT6) [57], the model predicts a single peak in IL-10 because the inflammatory response is weaker. The recurrence of this pattern at different doses of LPS implies the existence of qualitative differences at CT0 compared to CT12.

Overall, our results show that the extent of sequelae experienced by male and female rats depends on the time of infection. Females suffered more severe sequelae than males when infected during the late rest or early active periods. Specifically, IL-6 and TNF-α production at CT12 was greatly lowered in females. This response is not potent enough to maintain long term control of the infection. Female rats produce less cytokines overall

during acute inflammation when compared to males. Nonetheless, males also suffer from circadian-induced immune disruption. Their higher levels of IL-6 and TNFα and damage could increase their susceptibility to sepsis.

The modulation of circadian activity by cytokines has been reported over the last years. For instance, TNFα-incubation has been shown to suppress *Per* gene expression *in vitro* and *in vivo* in mice [201] as well as *Cry1* [236]. Some recent work by Yoshida et al. [237] and Ertosun et al. [238] reveals that TNFα modulates the transcription of *Bmal1* through the up-regulation of *Ror*α. The present model does not include the direct links from cytokines to clock genes and proteins, but those links can be incorporated into future extensions of the model. It should be noted that different lengths of phase advances and phase delays in expression of clock genes could lead to different immune responses in males and females. Our current model focuses on 8h advance of the circadian phase, but if more data is available in the future, it could lead to an extension of this investigation to different lengths of phase shifts. Testing different shifts will help determine 1) if specific changes are better than others, 2) if the male/female difference is as crucial as the polymorphisms that alter circadian timing in specific individuals. These questions will be considered in future extensions of this model. The development of mathematical models that investigate the role of circadian rhythms in immunity and vice versa help our understanding of the dynamics involved in the interplay between these two systems. Extending the model to investigate the circadian control of other organ systems such as the liver [239] and kidney [240] would also be worthwhile.

In conclusion, our results suggest that circadian disruption due to shift work is primarily mediated by the circadian disruption of REV-ERB and CRY. REV-ERB in particular acts as an equilibrist by negatively affecting the expression of pro-inflammatory cytokine IL-6 and anti-inflammatory cytokine IL-10. We also showed the importance of sexual dimorphism in the magnitude of the inflammatory response during CJL. A functional and rhythmic clock confers immunoprotection and improves organismal fitness [241]. Thus, it is important to understand the molecular mechanisms that link the clock to immune functions, particularly during unrest caused by behavioral changes such as shift work.

Chapter 5

Can the clocks tick together despite the noise? Stochastic simulations and analysis

The content of this chapter is based on the paper: S. M. Abo, J. A. Carrillo, and A. T. Layton, "Can the clocks tick together despite the noise? stochastic simulations and analysis," *SIAM J Appl Dyn Syst*, vol. 22, no. 2, pp. 850–877, 2023. URL: https://doi.org/10.1137/22M147788X

Abstract

The suprachiasmatic nucleus (SCN), also known as the circadian master clock, consists of a large population of oscillator neurons. Together, these neurons produce a coherent signal that drives the body's circadian rhythms. What properties of the cell-to-cell communication allow the synchronization of these neurons, despite a wide range of environmental challenges such as fluctuations in photoperiods? To answer that question, we present a mean-field description of globally coupled neurons modeled as Goodwin oscillators with standard Gaussian noise. Provided that the initial conditions of all neurons are independent and identically distributed, any finite number of neurons becomes independent and has the same probability distribution in the mean-field limit, a phenomenon called propagation of chaos. This probability distribution is a solution to a Vlasov-Fokker-Planck type equation, which can be obtained from the stochastic particle model. We study, using the macroscopic description, how the interaction between external noise and intercellular coupling affects the dynamics of the collective rhythm, and we provide a numerical description of the bifurcations resulting from the noise-induced transitions. Our numerical simulations show a noise-induced rhythm generation at low noise intensities, while the SCN clock is arrhythmic in the high noise setting. Notably, coupling induces resonance-like behavior at low noise intensities, and varying coupling strength can cause period locking and variance dissipation even in the presence of noise.

5.1 Introduction

The suprachiasmatic nucleus (SCN) in the brain serves as the central clock in mammals and regulates most circadian rhythms in the body [110, 242]. The SCN is remarkable – it not only synchronizes the biological rhythms to the external light–dark cycle [243], but also generates robust rhythmic outputs with an endogenous period of around 24 h in constant darkness [44, 244].The specific mechanism responsible for this behaviour continues to be the subject of numerous experimental and theoretical studies. The rhythmic output emanates from a regulatory circuit with a negative feedback loop. We refer to the reviews [245, 246] for a description of the architecture of the SCN clock.

Although single neurons produce autonomous oscillations, the emergence of global and robust oscillations of the SCN activity requires the synchronization of neural cells [247]. Oscillations at the global level arise from the interaction, also called *coupling*, between SCN neurons. In this work, we study how a population of SCN neurons manages to synchronize and remain synchronized despite external perturbations. Our focus is on the effect of

coupling strength and external noise on synchronization dynamics. Experimental studies have shown that cell-to-cell coupling in the SCN is carried out in part by neurotransmitters [35, 246]. Vasoactive intestinal polypeptide (VIP), arginine vasopressin (AVP) and gamma-aminobutyric acid (GABA) are examples of neurotransmitters which play a role in the coupling [248]. The SCN is divided into two hemispheres, each of which contains two groups of neurons: a dorsomedial shell (DM) and a ventrolateral (VL) core. These two sets of neurons differ by their light sensitivity, the neurotransmitters they produce, hence their coupling properties. DM cells mainly express AVP, whereas VL neurons express VIP [5, 249]. Yet, all SCN neurons express the neurotransmitter GABA [250]. In addition to coupling, SCN function is influenced by stochastic noise, which includes exogenous and endogenous cellular noise [251]. Exogenous noise results from changes in the environment [44, 251], such as fluctuations in light signals, and has been shown to play an important role in the amplitudes of neural oscillators and the entrainment to a new environmental cycle [43, 252]. The endogenous noise is caused by low molecular counts of the mRNA and protein species involved [251].

A number of mathematical models of coupled oscillators have been developed to study the SCN properties such synchrony, the ensemble period and the entrainment ability of the SCN [35–42]. Most of these models are in the form of coupled ordinary differential equations, and are therefore deterministic. Some recent modeling and experimental studies, however, investigate the influence of noise [43–45] on the circadian clock by means of stochastic differential equations or experimental analysis of stochastic rhythms. All of these models based on the particle-like description of a set of interacting neurons are called individual-based models (IBM), and often used in animal swarming [46, 47]. The topologies often considered are all-to-all coupling between the neurons [35–37] and small world networks [48, 49]. For a large number of interacting agents, the collective motion in the system can be studied through macroscopic descriptions based on the evolution of a density of individuals. These models are known as continuum models, and the scaling limit is called the *mean-field limit* [47, 50, 51]. These continuum models are useful in reducing IBMs into an effective one-body problem: the particle probability density [50].

Naturally, noise at the level of the IBMs which represent the SCN network is essential since the neuronal activity is not totally deterministic. The randomness should be reflected in the macroscopic description. As pointed out in [253], stochastic IBMs lead to Fokker-Planck type equations in the mean-field limit for second order models. The proof of this stochastic mean-field limit relies on standard hypotheses: global Lipschitz continuity and linear growth condition of the drift and diffusion coefficients, and the Lipschitz continuity of the interaction function [93, 94, 254].

In the present article, we consider a stochastic system of interacting SCN neurons in

a diffusive scaling and study the effects of external noise, as the network size approaches infinity, on SCN properties: robust oscillation amplitude and period. We also investigate the effect of noise on bifurcation boundaries. SCN neurons are characterized by small size and high density [39], and all express GABA [250]. We assume, based on this information, that intercellular coupling is carried out by chemical signals released by each cell and that spatial transmission is fast in comparison to the time scale of the oscillations (24h). We derive the mean-field equation for a system of globally-coupled Goodwin-type neurons with noise. The Goodwin model is commonly employed for circadian oscillators because it describes a biological process with a negative feedback loop — one of the key circadian clock regulation mechanisms [37]. Many studies have considered the SCN as a network where neurons are globally connected [35, 36, 40, 41, 255], but other network topologies for coupling oscillators have also been studied: Newman-Watts (NW) small-world networks [5, 256], regular networks [39, 257], random networks [258] and scale-free networks [5, 258].

To the best of our knowledge, no study has discussed the influence of external noise on the circadian clock through mean-field equations. We present numerical results on the relation between amplitude of circadian oscillations and coupling strength. We also discuss the effect of noise on bifurcation boundaries. The question arises as to whether fluctuations in the noise level can influence bifurcation boundaries and therefore influence the robustness of circadian oscillations with respect to external noise. Moreover, synchronization will be understood to mean the dissipation of the empirical variance. This approach does not rely on the stability properties of individual neurons nor on the existence of limiting oscillatory behaviors [259].

The work is organized as follows: in Section 5.2, the mean-field model is introduced to describe a network of coupled SCN neurons with noise. Simulation results about the dependence of the rhythms on the coupling strength and noise intensity are discussed in Section 5.3. Then, we assess the accuracy of our numerical scheme in Section 5.4. The conclusions and discussion are presented in Section 5.5. We present the derivation of the continuum model in Appendix B.2, convergence results for stochastic and mean-field solutions in Appendix B.1, and a complete description of the numerical scheme in Appendix B.3.

5.2 A minimal SCN model and its mean-field description

5.2.1 Model description

In this paper, we propose a mathematical model for describing the collective activity of SCN neurons. The core architecture in mammals of the circadian clock consists of two feedback loops that interact to generate biochemical oscillations with a period of nearly 24 h [260]. The primary feedback loop is driven by clock proteins CLOCK and BMAL1. The proteins dimerize to create the CLOCK-BMAL1 complex which initiates the transcription of the target period (PER) and cryptochrome (CRY) genes. Negative feedback is achieved through PER-CRY heterodimers that repress their own transcription after delays due to cellular processes, such as transcription, translation, and nuclear transport [261]. In a secondary loop, CLOCK-BMAL1 proteins activate the transcription of Rev-Erbα. After being translated into proteins, Rev-Erbα downregulates *Bmal1* transcription, thus completing the loop [255, 260]. The Goodwin model, a negative feedback oscillator with variables X, Y and Z, can be used to represent these two regulatory loops; see Eqs.(5.1)-(5.2) and Figure 5.1. In general, the mechanism behind biological oscillators consists of delayed negative feedback loops. [262].

The Goodwin model has been widely studied theoretically [261, 263, 264] and applied to various biological systems, such as circadian clocks [35–37, 243] or enzymatic regulation [265]. The temporal evolution of a single Goodwin-type neuron is governed by the following equations:

$$\dot{X} = f(Z) - k_2 X, \quad \dot{Y} = k_3 X - k_4 Y, \quad \dot{Z} = k_5 Y - k_6 Z, \tag{5.1}$$

where

$$f(Z) = k_1 \frac{K_i^n}{K_i^n + Z^n}. \tag{5.2}$$

In this model, X denotes the mRNA concentration of a certain clock gene, Y is the matching protein, and Z is a transcriptional inhibitor in the nuclear form or the phosphorylated form of the protein. The inhibition term is described by a nonlinear and hyperbolic function (i.e. Hill function), $f(Z)$. All other terms are linear. The Hill function is parametrized by a Hill coefficient n characterizing the response steepness, and an inhibition threshold K_i that describes the concentration of inhibitor that halves the production rate, i.e., half-maximal repression occurs when $Z = K_i$. In many organisms, the Hill function has been employed to characterize transcriptional repression: Neurospora [266, 267],

Drosophila [124, 266, 268] and mammals [35, 36, 260, 269]. Hill functions are often employed to describe cooperative binding of repressors to the gene promotor in transcription [270] or repression based on multisite phosphorylation [264]. The latter is a more realistic mechanism, especially because a large Hill exponent is required for oscillations in the Goodwin model ($n > 8$). The recent work of Cao et al. [271], which builds upon [272, 273], provides some evidence for repression based on multisite phosphorylation in mammals. The authors show that removal of CLOCK–BMAL1 involves phosphorylation (hyperphosphorylation) of CLOCK, which is accomplished by CK1δ when CRY and PER deliver CK1δ to the CLOCK–BMAL1 complex in the nucleus of cells. A different transcriptional repression mechanism based on protein sequestration has been proposed to describe the negative feedback underlying circadian oscillators. See Refs. [274–277] for details. The various rate constants parametrize transcription (k_1, k_3), degradation (k_2, k_4, k_6), and nuclear import (k_5). Note that all reaction rates are positive. Concentrations X, Y, Z and K_i have units nM. Rate constants have units h^{-1}, except for k_1 which has units nM h^{-1}. Depending on parameter values, the model can produce limit cycle oscillations. Following the approach

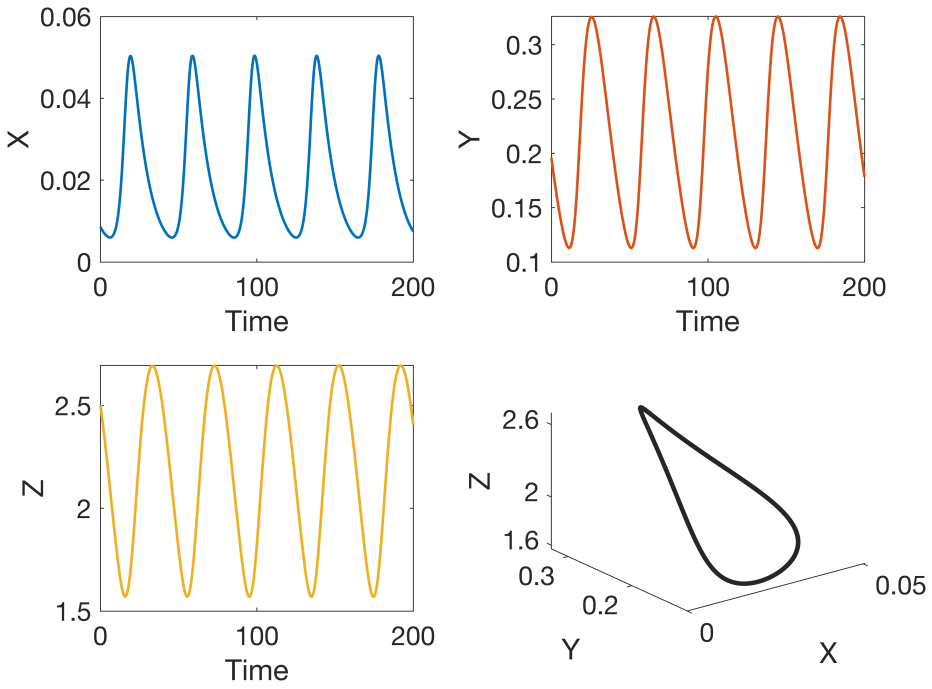

Figure 5.1: Limit cycle oscillations for the following parameter values: $k_1 = 1\mathrm{nM}\cdot\ \mathrm{h}^{-1}$, $k_3 = k_5 = 1\mathrm{h}^{-1}$, $k_2 = k_4 = k_6 = 0.1\mathrm{h}^{-1}$, $K_i = 1\mathrm{nM}$, and $n = 10$ in (5.1). The oscillation period is about 40h.

in [263], we reformulate the equations in (5.1) in dimensionless form. Assuming equal degradation rates ($k_2 = k_4 = k_6$), we introduce the new variables:

$$x = \frac{k_3 k_5}{k_2^2 K_i} X, \quad y = \frac{k_5}{k_2 K_i} Y, \quad z = \frac{Z}{K_i}, \quad t = \frac{k_2 T}{\tau},$$

with τ chosen to make the intrinsic period of the oscillator 23.5. We obtain,

$$\frac{\mathrm{d}x}{\mathrm{d}t} = \frac{\alpha}{1+z^n} - x, \quad \frac{\mathrm{d}y}{\mathrm{d}t} = x - y, \quad \frac{\mathrm{d}z}{\mathrm{d}t} = y - z, \tag{5.3}$$

where

$$\alpha \equiv \frac{k_1 k_3 k_5}{k_2^3 K_i} \tag{5.4}$$

is the only parameter for a given n. Figure 5.2 represents the bifurcation and stability diagrams for system (5.3). At the critical value α_H, the system transitions from a stable steady state to an unstable steady state (via a Hopf bifurcation), and a periodic solution arises (Figure 5.2a). The steady state is stable if $\alpha < \alpha_H$ and unstable otherwise. To obtain limit-cycle oscillations, the Hill coefficient must be larger than 8 (Figure 5.2b).

We now consider a population of N identical neurons. Let $x_i(t), y_i(t), z_i(t) \in \mathbb{R}$ denote the concentration of mRNA, protein and inhibitor protein of neuron i at time t, respectively. To produce a functional SCN network, there must be reciprocal signalling between neurons. We examine our network under *all-to-all* coupling conditions. Each neuron in the group adjusts its production of mRNA (x) by averaging with all the others. We obtain,

$$\begin{cases} \frac{\mathrm{d}x_i}{\mathrm{d}t} &= \frac{\alpha}{1+z_i^n} - x_i + K(\bar{x} - x_i) \\ \frac{\mathrm{d}y_i}{\mathrm{d}t} &= x_i - y_i \\ \frac{\mathrm{d}z_i}{\mathrm{d}t} &= y_i - z_i \end{cases} \tag{5.5}$$

Here, and throughout this paper, the coupling parameter K is assumed to be the same for all oscillators. $\bar{x}(t)$ is the average value of all individual variables $x_i(t)$ at time t:

$$\bar{x}(t) = \frac{1}{N} \sum_{i=1}^{N} x_i(t) \tag{5.6}$$

5.2.2 Stochastic extension and mean-field limit

Our goal is to analyze a system of the type (5.5) with Gaussian noise. Biological clocks, although noisy at the microscopic level due to both external noise (e.g., fluctuations in

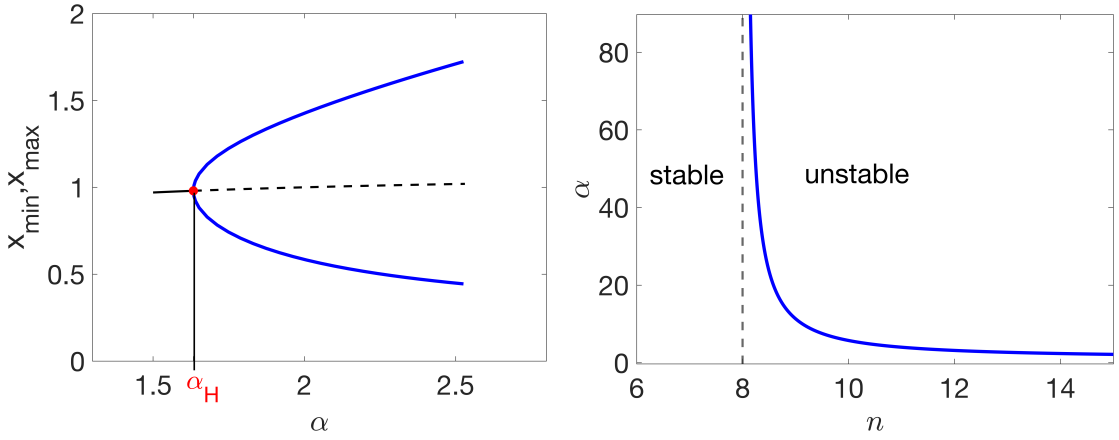

Figure 5.2: (a) Bifurcation diagram of the stable periodic solutions near the Hopf bifurcation point ($\alpha_H = 1.633$) when $n = 20$. At α_H, the system's stability switches from stable (solid black line) to unstable (dashed black line) and a periodic solution arises. The bifurcation is supercritical (solid blue curves). (b) Two-parameter bifurcation diagram in terms of α and n. Hill exponent $n > 8$ is required for oscillations. If $n < 8$, the steady state is a stable focus for all values of α.

photoperiods) and inherent stochasticity (e.g., coupling between cells), can be relatively precise at the macroscopic level [278, 279]. We represent stochasticity via additive white noise acting through the first variable x. Specifically, we will consider a large network of N interacting $\mathbb{R}^3$-valued processes $(x_i(t), y_i(t), z_i(t))_{t\geq 0}$ with $1 \leq i \leq N$ solution of

$$\begin{cases} dx_i(t) = \left[\left(\frac{\alpha}{1+z_i(t)^n} - x_i(t)\right) + \frac{K}{N}\sum_{j=1}^{N} H(x_i(t) - x_j(t))\right] dt + \sqrt{2D}\, dW_i(t) \\ dy_i(t) = \big(x_i(t) - y_i(t)\big)\, dt \\ dz_i(t) = \big(y_i(t) - z_i(t)\big)\, dt \end{cases} \tag{5.7}$$

where $H(\omega) := -\omega$ and with independent and identically distributed initial data (x_i^0, y_i^0, z_i^0), $1 \leq i \leq N$. The processes $(W_i(t))_{t\geq 0}$ with $1 \leq i \leq N$ are independent Brownian motions in $\mathbb{R}$ and the noise intensity is $\sqrt{2D}$, with $D > 0$. To our knowledge, the stochastic mean-field limit description of a system of coupled Goodwin-type neurons has not yet been considered.

All neurons have the same distribution on $\mathbb{R}^3$ at time t due to the symmetry of the initial configuration and of the evolution [50]. For any $t > 0$ the neurons become correlated

due to the coupling term $\frac{K}{N}\sum_{j=1}^{N} H(x_j - x_i)$ in the evolution, though they are independent at $t = 0$. However, given the order $1/N$ of the interaction term, it seems reasonable that any fixed number k of these interacting neurons become less correlated as N gets large. This property is called *propagation of chaos* [50]; see Definition 2.3.10 in Chapter 2.

The following assumptions hold for the stochastic model: 1) global Lipschitz continuity of the drift and diffusion terms; 2) linear growth condition of the drift and diffusion terms; 3) Lipschitz continuity of the coupling function. These assumptions imply that the system of stochastic differential equations (5.7) is well-posed.

It follows from the general theory of Sznitman [93] (see also the more recent [50, 280]) that our N interacting processes $(x_i(t), y_i(t), z_i(t))_{t\geq 0}$ respectively behave as $N \to \infty$ like the processes $(\tilde{x}_i(t), \tilde{y}_i(t), \tilde{z}_i(t))_{t\geq 0}$, solutions of the kinetic McKean-Vlasov type processes on $\mathbb{R}^3$:

$$\begin{cases} d\tilde{x}_i(t) = \psi(\rho)\, dt + \sqrt{2D}\, dW_i(t) \\ d\tilde{y}_i(t) = (\tilde{x}_i(t) - \tilde{y}_i(t))\, dt \\ d\tilde{z}_i(t) = (\tilde{y}_i(t) - \tilde{z}_i(t))\, dt \\ \big(\tilde{x}_i^0, \tilde{y}_i^0, \tilde{z}_i^0\big) = \big(x_i^0, y_i^0, z_i^0\big), \quad \rho = \mathrm{law}\big(\tilde{x}_i(t), \tilde{y}_i(t), \tilde{z}_i(t)\big) \\ \psi\big(\rho\big)\big(\tilde{x}_i, \tilde{y}_i, \tilde{z}_i, t\big) = \frac{\alpha}{1+\tilde{z}_i(t)^n} - \tilde{x}_i(t) + K\big(H \star \rho(\tilde{x}_i, \tilde{y}_i, \tilde{z}_i, t)\big) \end{cases} \tag{5.8}$$

The Brownian motions $(W_i(t))_{t\geq 0}$ in (5.8) are those governing the evolution of $(x_i(t), y_i(t), z_i(t))_{t\geq 0}$. The processes $(\tilde{x}_i(t), \tilde{y}_i(t), \tilde{z}_i(t))_{t\geq 0}$ with $i \geq 1$ are independent since the initial conditions and governing Brownian motions are independent. Notice that they are identically distributed and, by the Itô formula (see Definition 2.3.5), their common law ρ at time t should evolve according to the kinetic McKean-Vlasov equation

$$\frac{\partial \rho}{\partial t} = D\partial_x^2 \rho - \partial_x\big[\xi(\rho)\rho\big] - \partial_y\big[(x-y)\rho\big] - \partial_z\big[(y-z)\rho\big] \tag{5.9}$$

where

$$\xi\big(\rho\big)\big(x, y, z, t\big) = \frac{\alpha}{1+z^n} - x + K\big(H \star \rho\big) \tag{5.10}$$

with

$$H \star \rho(x, y, z, t) = \int_{\mathbb{R}^3} H(x-w)\rho(w, y, z, t)\, dw\, dy\, dz\,. \tag{5.11}$$

Since (5.8) models the evolution of concentrations $(\tilde{x}_i(t), \tilde{y}_i(t), \tilde{z}_i(t))_{t\geq 0}$ we constrained the solutions of the network when performing numerical simulations to ensure that they remained in a smooth positive domain in $\mathbb{R}^3_+$. In particular, we used the compact support

$[0,2] \times [0,2] \times [0,2]$. The boundaries of the domain are instantaneously reflecting in an oblique direction. See [281, 282] and the references therein for a detailed discussion of Euler schemes for reflected stochastic differential equations. In this case, the general theory of Snitzman [93, 283, 284] still applies, but we recover (5.9) with no-flux boundary conditions.

5.3 Numerical results

We focus on the dynamic evolution of solutions in the mean field scaling of the SCN network with noise. Our model (5.9) is a nonlocal nonlinear transport equation with no-flux boundary conditions. Such characteristics of the mean-field equation make it difficult to conduct a theoretical study using center manifold or bifurcation theory [285, 286]. Instead, we investigate the nature of the bifurcations numerically and compare the solution to the mean-field equation with that of the finite SCN network. We consider two main parameters in our analysis, namely the strength of the coupling K and the noise level D. In all our simulations, we refer to the marginal probability densities for x, y and z as ρ_1, ρ_2, and ρ_3, respectively.

A noise-free network analysis is outside the scope of this article, but we refer the reader to [263, 277] for details on the stability of the noise-free system and associated bifurcation diagrams. In the case of the noise-free network with identical Goodwin cells (5.5), the linear stability of steady states is tractable and bifurcation diagrams can be determined by solving for the steady states of the amplitude equations [287]. Moreover, for oscillators with weak coupling the phase-locked states could be studied using weakly coupled oscillator theory, where the network can be reduced to its phase model description [288–290]. The stability of the synchronous state for strong coupling can be studied using the master stability function, which allows to calculate the stability as determined by a particular choice of stability measure, like Lyapunov or Floquet exponents [291, 292].

5.3.1 Coupling strength and synchronization

The SCN coordinates physiological cycles throughout the body with incredible precision [293]. Nevertheless, local oscillations at the level of individual neurons can be substantially different from global network-wide oscillations [293, 294]. In fact, defining characteristics of circadian rhythms such as period, large amplitude, accuracy and synchrony arise due to coupling [294–296]. In this section, we investigate the effect of coupling in the overall dynamics of the SCN. We perform a numerical bifurcation analysis by varying the parameter

K, which quantifies the strength of the chemical signal that is transmitted to oscillator cells. A value of $K < 1$ signifies a decay of the chemical signal before it reaches the target cell, while $K = 1$ represents the perfect transduction of the chemical signal to the target cell. In particular, $K = 0$ implies an uncoupled network where oscillations are localized in individual neuronal cells. Following the approach done in [285, 297], a stationary solution of (5.9) characterises *asynchronous activity*, a state in which neurons exhibit out-of-phase oscillations. *Synchronized activity* refers to a state where the mean-field is periodic in time.

In Figure 5.3 we show a bifurcation diagram of the spatial averages in x, y, and z as a function of the coupling strength K. $E[x]$, $E[y]$ and $E[z]$ are calculated from the solution to the mean-field equation (5.9). We call $E[\cdot]$ the average over the values of a given variable across the space domain. We assume a low level of noise with $D = 0.01$. Figure 5.3a shows the transition from a stable regime without oscillations to a regime of sustained oscillations, which correspond to the progression of solutions toward a periodic orbit [298]. For values of K less than 0.3, the mean-field solution shows damped oscillations that eventually result in an invariant distribution. This indicates that the network of SCN neurons is out of sync. However, past the critical value $K_H \approx 0.3$, synchronized activity emerges within the network as shown by a periodic solution to (5.9). Figures 5.3a and 5.3b suggest the existence of a bifurcation of the asynchronous state. At this bifurcation emerges a limit cycle corresponding to a stable and robust sinusoidal oscillation. Mathematically, the expansion of amplitude as the periodic orbit moves away from the bifurcation boundary (Figure 5.3a) and the relatively constant period of the oscillations (Figure 5.3b) are characteristic of a supercritical Hopf bifurcation. Moreover, the amplitude grows as the coupling strength increases, and this phenomena is especially prominent near the bifurcation boundary (Figure 5.3a). Previous studies have shown that coupling can induce amplitude expansion near the Hopf bifurcation [243, 294, 299]. This so-called "resonance" may be enhanced by synchronizing factors, here represented by the coupling strength K.

Examining the temporal evolution of the empirical variance offers a complementary perspective on the role of coupling. Synchronization can be understood as the dissipation of the empirical variance for the spatial averages of x, y and z computed from the solution of (5.9) as time goes by. In Figure 5.4 and Figure 5.5 we show two extreme scenarios in this regard: absence of coupling where $K = 0$ and perfect coupling with $K = 1$. Figure 5.4 gives the time evolution of $E[x]$. The solution to the mean-field equation approaches a steady state when $K = 0$ as shown by damped oscillations in $E[x]$, but looses its stability to rapidly settle into a periodic orbit when $K = 1$. The other variables y and z, which are not shown here, are qualitatively similar with x. It should be noted that regardless of initial conditions, the system follows the same trajectories (data not presented). For each

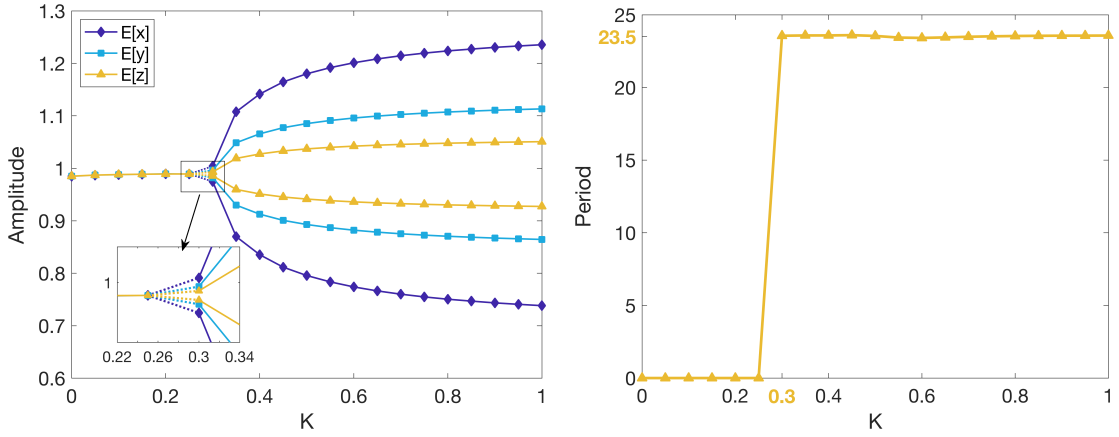

Figure 5.3: (a) Bifurcation diagram associated with the coupling strength K in the mean-field model. $E[x]$, $E[y]$ and $E[z]$ refer to spatial averages. Numerical simulations are run until a steady state is reached or until the oscillation amplitude becomes stable. For the latter, the graph shows the peaks and troughs of oscillations as a function of K. (b) Period of oscillations of $E[z]$. Noise level is constant at $D = 0.01$ in both (a) and (b). A Hopf bifurcation appears around the critical value $K_H \approx 0.3$.

scenario, the time evolution of the variance for all three variables is recorded in Figure 5.5. Assuming a low level of noise ($D = 0.01$), we observe when $K = 0$ an asynchronous state represented by an empirical variance of constant order in time and which is greater than the input noise level. However, for perfect coupling $K = 1$, the empirical variance dissipates to a minimum equal to the magnitude of the external noise, and the global output is rhythmic (see Figure 5.4B and Figure 5.5B). In the ideal case of perfect coupling, the variance in y and z decreases to about zero, whereas the variance in x decreases to about 0.01 (the level of input noise D).

Our numerical experiment suggests the following about the qualitative behavior of the coupled SCN network in terms of D: for $D > 0$ the neuron trajectories are enclosed in a band whose width rises with D, whereas a noise-free network will ultimately reach perfect synchronisation where the empirical variance decreases to zero. The direct consequence of these observations is that the threshold K_H is itself a function of D. To see this, consider Figure 5.6 which shows the joint probability distribution between x and z at $t = 600h$, $\rho(t = 600, x, z)$, for different values of K. We choose a long integration time in order to not be influenced by the initial conditions. As the coupling parameter increases, variance decreases and the distribution $\rho(t = 600, x, z)$ tends to concentrate on a delta function in

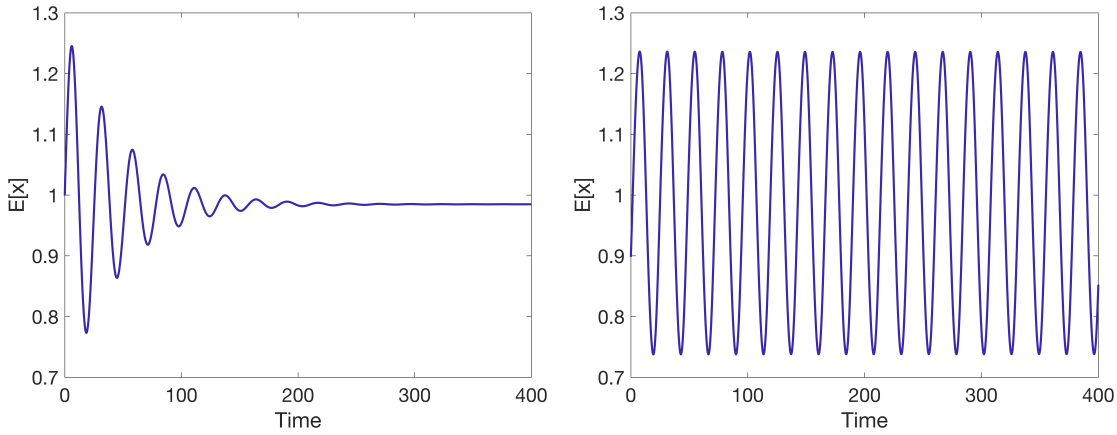

Figure 5.4: Evolution of the average in x for two limiting scenarios: (a) no coupling with $K = 0$ and (b) perfect coupling with $K = 1$. $E[x]$ is computed from the solution to the mean-field equation (5.9).

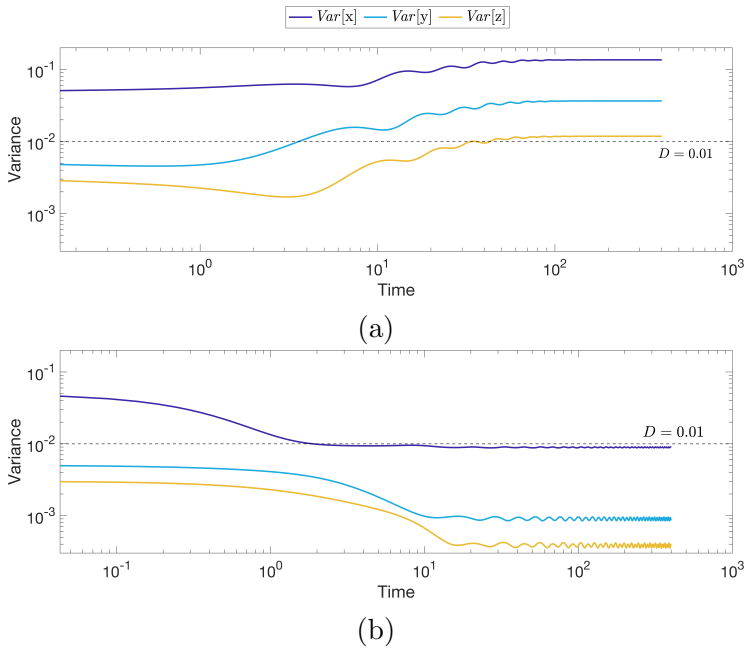

Figure 5.5: Time evolution of the empirical variance in two limiting scenarios: (a) no coupling with $K = 0$ and (b) perfect coupling with $K = 1$. $D = 0.01$ in all simulations.

the z dimension and to be distributed only along the spatial dimension x due to noise. Overall, studying the effects of coupling on the solution to the mean-field limit gave the following numerical predictions: increasing coupling strength can lead to period locking, variance dissipation, and larger amplitudes due to resonance effects.

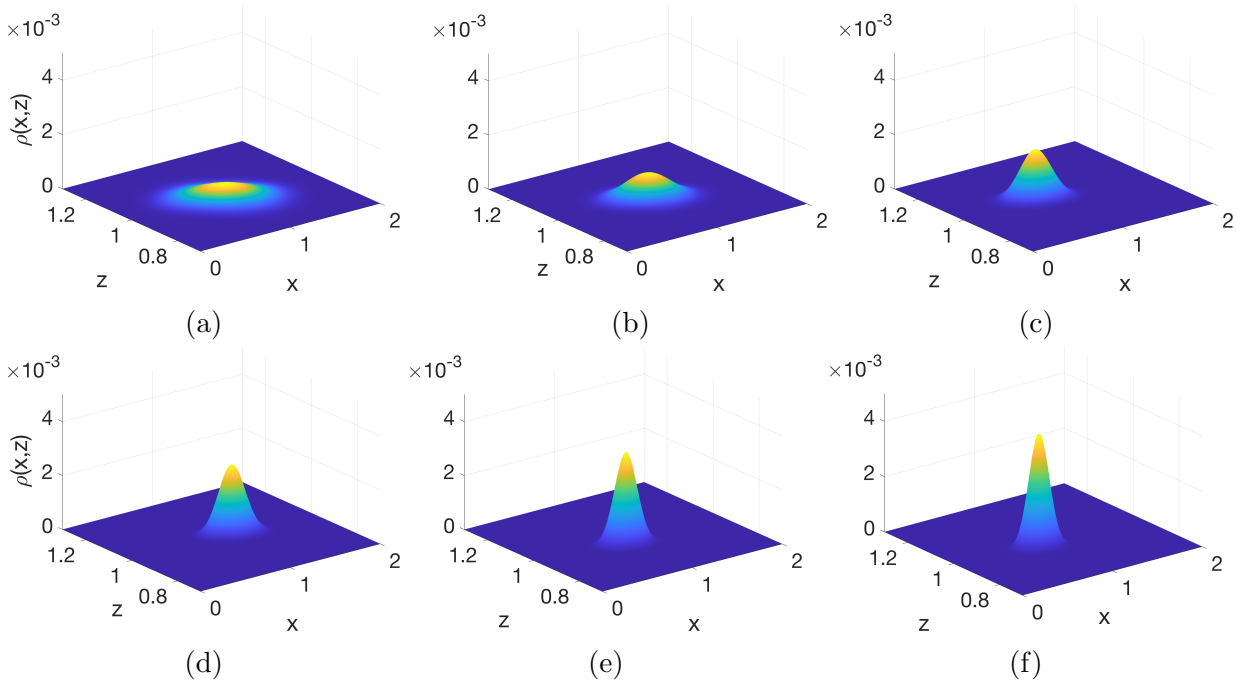

Figure 5.6: Joint probability distribution between x and z at $t = 600$. (A) K=0.1, (B) K=0.2, (C) K=0.4, (D) K=0.6, (E) K=0.8 and (F) K=1. Noise level $D = 0.01$.

5.3.2 Effect of noise on bifurcation boundaries

Using our stochastic mean-field model, we examine how the robustness of the SCN clock is affected by noise. This refers to how the noise intensity in the system affects the distance to a bifurcation point. We proceed by varying the parameter α in (5.9) for different noise levels, and we look for synchronized activity within the network. Robustness is used here to denote the persistence of a certain type of dynamic behavior over a significant range of parameter values. The term "robustness" refers to the persistence of a specific dynamic behavior over a wide range of parameter values.

Consider $D = 0.01$ as an example of low noise setting. As shown in Figure 5.7, there is in the low noise setting a critical value α_H at which the system's stability appears to change from a stable stationary distribution to an oscillatory solution. This result shows that the development and maintenance of a global rhythmic output requires the synchronization of single-cell rhythms [247]. The existence of such invariant distributions characterizes a state of incoherence within the SCN network (see Figure 5.7a). Noting that $\alpha = k_1 k_3 k_5 / k_2^3 K_i$, Figure 5.7 suggests that the circadian system is more favorable to lower degradation rates in the presence of noise.

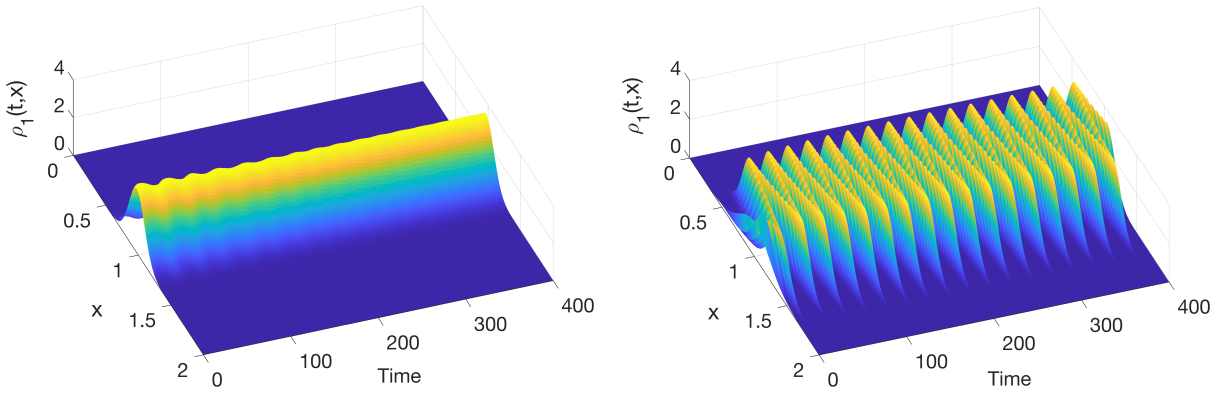

(a) steady state regime (b) oscillatory regime

Figure 5.7: Evolution of the marginal density of x in the presence of noise. (a) steady state regime with $\alpha = 1.5$, (b) oscillatory regime with $\alpha = 2$. Other parameters: $n = 20$, $K = 0.6$, $D = 0.01$.

To formally investigate the bifurcation in Figure 5.7, we use the same parameters and initial conditions as in Figure 5.7, with the exception of the parameter α which now varies from 1.5 to 3. Results are displayed in Figure 5.8a. When $\alpha < 1.73$, the network is not synchronised and evolves towards a steady state. Above the critical value $\alpha_H \approx 1.73$, the network is synchronised and the solution to the mean-field equation (5.9) is periodic in time. As characteristic of a local Hopf bifurcation, the cycle that is born is nearly elliptical with a small amplitude; see Figure 5.8b.

We investigate further how increasing the level of noise affects bifurcation boundaries. Figure 5.9 shows a high-low plot for the peaks and troughs of oscillations of the means in x, y and z as a function of the parameter α for different noise levels. Since it is difficult to numerically estimate exact bifurcation values, we use dotted lines to represent intervals containing exact bifurcation points, which we call α_H. We estimate $\alpha_H \in (1.72, 1.73]$,

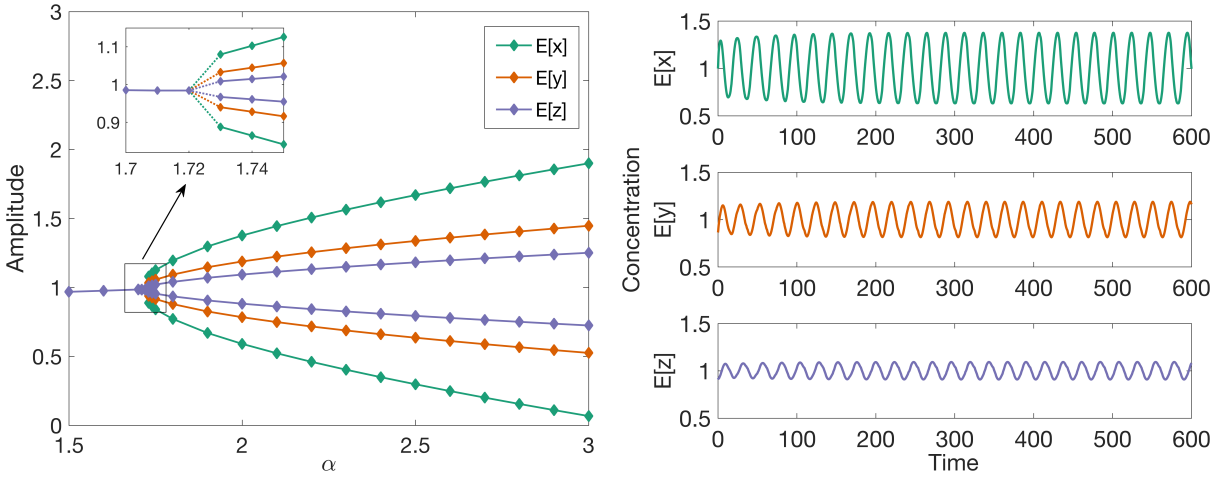

Figure 5.8: (a) Bifurcation diagram associated with the parameter α. Details of the diagram are the same as those of Figure 5.3. (b) Example of a periodic orbit when $\alpha = 2$. Other parameters: $n = 20$, $K = 0.6$, $D = 0.01$.

$(1.8, 1.9]$ or $(2.0, 2.1]$ when the noise intensity is low, moderate or high, respectively. As the noise level increases, the value of α_H necessary to obtain sustained circadian oscillations also increases. From Figure 5.9d, the amplitude of these oscillations gradually decreases as noise intensity increases, and the oscillations disappear through a supercritical Hopf bifurcation, thus resulting in trivial behavior with a single fixed point.

These findings indicate that higher noise levels render synchronisation more difficult to achieve. That is because a new and larger value α_H becomes the *sine qua non* condition for oscillations. Given the biological meaning of α in (5.3), its value could increase to recover oscillations if: 1) activation rate k_1, k_3, or k_5 increases for x, y or z, respectively; 2) degradation rates decrease for all three clock components (k_2, k_4, k_6 where $k_2 = k_4 = k_6$); 3) inhibition of x by z is attenuated (i.e., lower K_i).

We argue that noise can affect synchrony-dependent rhythmicity. The noise can affect ensemble properties of oscillators including their coupling and their period of oscillations. In Figure 5.10, we present solutions to (5.9) which are qualitatively different from the solutions shown in Figure 5.6: as the intensity of the noise increases, the variance increases and the distribution tends to widen and shorten in all directions, indicating that a wider spread of values is possible and that external noise impairs the synchrony of the system. Although we showed that uniformly coupled networks can robustly synchronize (Figure 5.6), it can

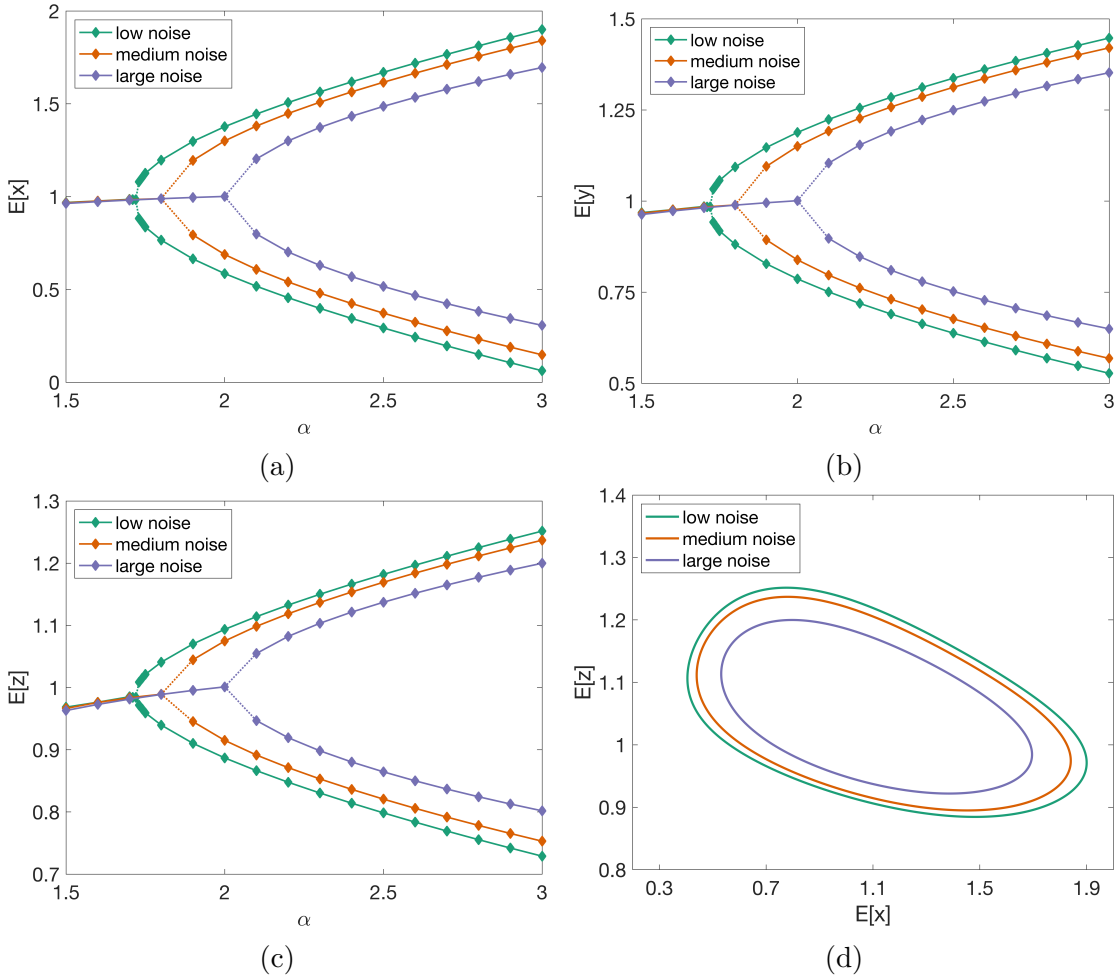

Figure 5.9: Bifurcation diagrams associated with the parameter α for the spatial averages (a) $E[x]$, (b) $E[y]$ and (c) $E[z]$. (d) Stable limit cycles in the $E[x]$–$E[z]$ plane when $\alpha = 3$. We model low noise ($D = 0.01$), medium noise($D = 0.025$) and high noise ($D = 0.05$). Dotted lines represent intervals containing exact bifurcation values α_H. Details of the figures are the same as those of Figure 5.3.

also be concluded that noise weakens synchronization degree and affects the robustness of the system. Figure 5.11 illustrates that the SCN is able to withstand higher noise levels with increasing coupling strength. However, noise eventually abrogate the oscillation in the SCN (Figure 5.11b). For instance, when $K = 0.6$, a noise intensity superior to 0.08 is sufficient to desynchronize the neurons as indicated by the null period in Figure 5.11a.

When $D < 0.08$, the system remains in synchrony with an ensemble period between 24.5 and 22.

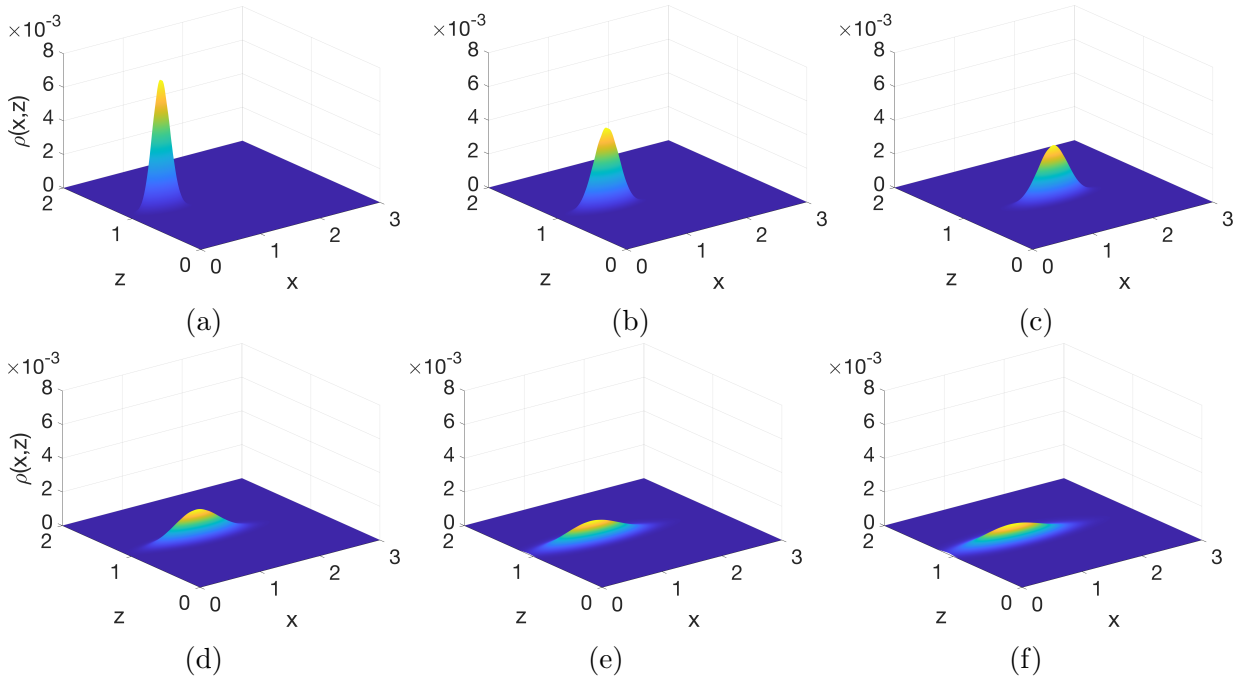

Figure 5.10: Joint probability distribution between x and z at $t = 600$. (a) $D = 0.01$, (b) $D = 0.02$, (c) $D = 0.04$, (d) $D = 0.08$, (e) $D = 0.12$ and (f) $D = 0.15$. Coupling strength $K = 0.6$.

5.4 Convergence studies

In this section, we report numerical results relating to the spatial accuracy of the numerical method. Our discussion focuses on a mesh convergence study to validate the order of convergence of the scheme in space. If the solution ρ is sufficiently smooth, then the spatial discretization is expected to be second-order accurate (see Appendix B.3).

In default of an analytical solution to our problem, we instead compute relative errors using different grid sizes. More precisely, we compute deviations from the estimated solution on a 3D fine mesh made of 384^3 cells. Figure 5.12 illustrates the results in L_1 and L_∞ norms. The time step Δt is determined by the CFL condition derived in equation (B.12)

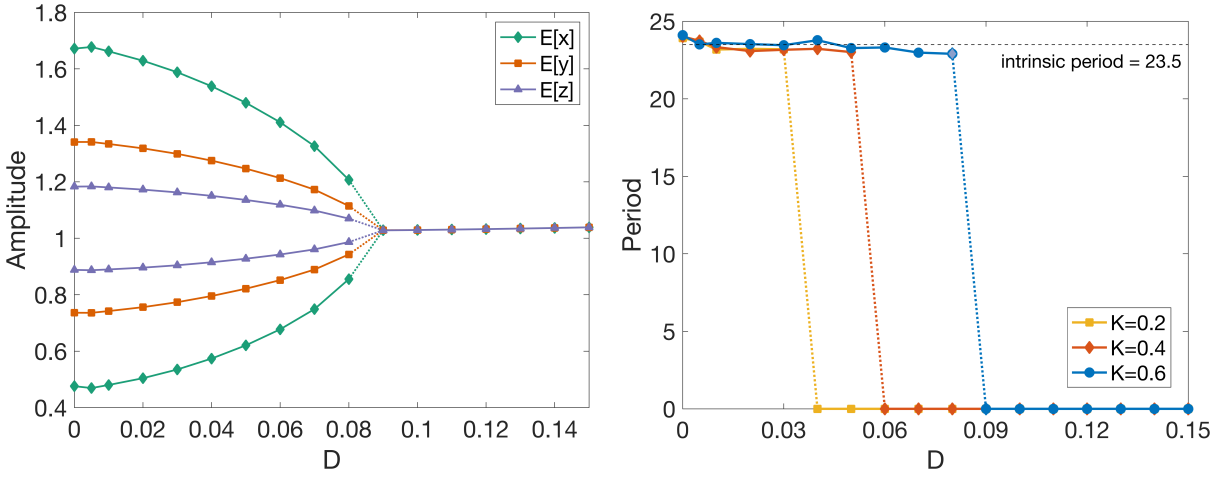

(a) (b)

Figure 5.11: (a) Bifurcation diagram associated with the noise intensity (D). A Hopf bifurcation appears around the critical value $D_H \approx 0.8$ for K fixed at 0.6. Details of the figure are the same as those of Figure 5.3. (b) Period of oscillations of $E[z]$ as a function of noise for different coupling strengths.

and the spatial step size is uniform in all directions ($\Delta x = \Delta y = \Delta z$). We used zero-flux boundary conditions. The initial probability density function $\rho(x, y, z, 0)$ is Gaussian,

$$\rho(x, y, z, 0) = \frac{1}{(2\pi)^{3/2}\sigma_{x_0}\sigma_{y_0}\sigma_{z_0}} e^{-(x-\mu_{x_0})^2/(2\sigma_{x_0}^2)-(y-\mu_{y_0})^2/(2\sigma_{y_0}^2)-(z-\mu_{z_0})^2/(2\sigma_{z_0}^2)}. \tag{5.12}$$

It appears from Figure 5.12 that the numerical scheme is at least second-order accurate, as anticipated. Figure 5.13 shows a qualitative similarity between solutions to the network equations and those obtained by solving the mean-field equation. In particular, we expect that the network and mean-field equation solutions will condense their mass around the periodic orbit [300]. This is shown in Figure 5.13a where the dynamics evolve to sustained oscillations. Table 5.1 summarizes all of the parameters involved in the aforementioned simulations.

5.5 Discussion

To summarize, we have conducted an analysis of the Goodwin model using the mean-field limit approach from kinetic theory. We developed a minimal yet effective macroscopic

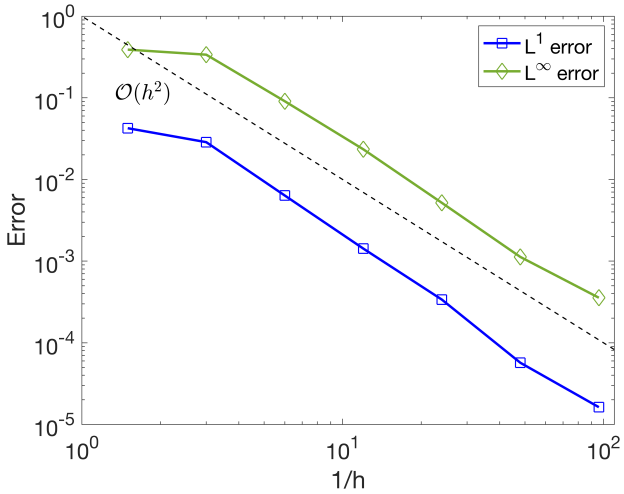

Figure 5.12: Convergence of error for the solution to the mean-field equation (5.9) in L^1 and L^∞ norms. Grid cells are uniform in size across all three variables, $h = \Delta x = \Delta y = \Delta z$. The final time is $\mathrm{t}_{final} = 1$.

Initial conditions	Domain	Goodwin neuron
$\mu_{x_0} = 1$	$x_{min} = 0$	$\alpha = 1.8$
$\mu_{y_0} = 0.9$	$x_{max} = 2$	$n = 20$
$\mu_{z_0} = 0.9$	$y_{min} = 0$	$K = 0.5$
$\sigma^2_{x_0} = 0.05$	$y_{max} = 2$	$D = 0.005$
$\sigma^2_{y_0} = 0.02$	$z_{min} = 0$	$\tau = 6.4885$
$\sigma_{z_0} = 0.01$	$z_{max} = 2$	
	$\Delta x = 0.002$	
	$\Delta y = 0.002$	
	$\Delta z = 0.002$	

Table 5.1: Model parameters. These parameters apply to the validation results presented in Section 5.4.

model of the SCN circuit level dynamics and investigated the impact of noise on the emerging properties of the SCN — rhythmicity (i.e., synchronisation), amplitude expansion, and ensemble period. We applied a positivity-preserving finite volume scheme developed in [301] for our numerical simulations.

We presented simulation results indicating that coupling is important in maintaining the synchronization and amplitude expansion characteristics of the SCN, at least in the

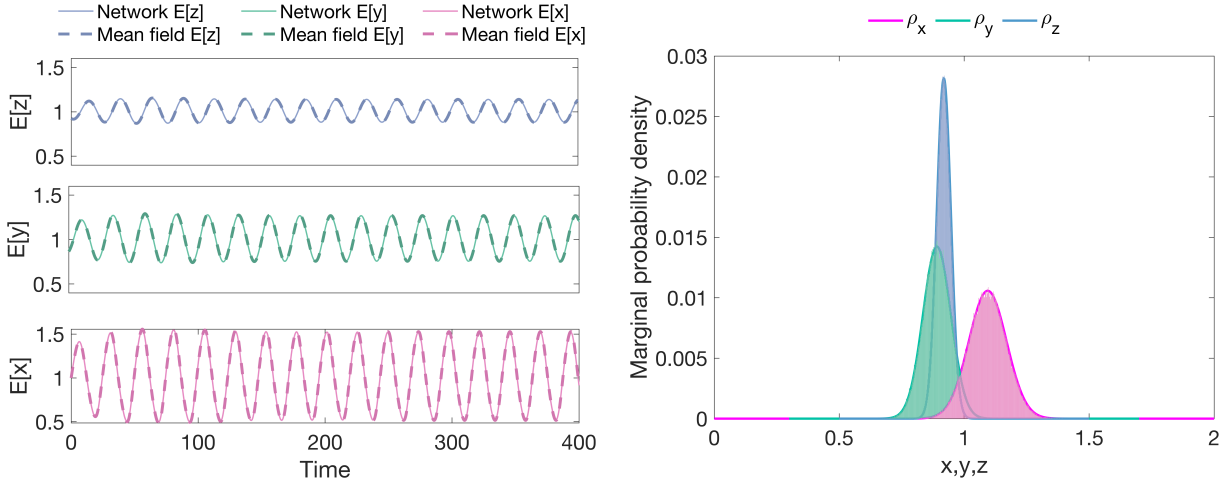

(a) (b)

Figure 5.13: (a) Time evolution of the averages in x, y, and z obtained by simulating the network equations (solid curves) and the mean-field equation (dashed curves). We ran 100 Monte Carlo simulations of the network with network size N=100 up to time t_{final} = 400. (b) Comparison between marginal probability densities $\rho_1(t,x)$, $\rho_2(t,y)$, $\rho_3(t,z)$ derived from the network and mean-field equation solutions. We conducted 10,000 Monte Carlo simulations with a network size N=10,000 up to time t_{final} = 1.

mean-field limit. Notably, increasing the coupling strength leads to phase transitions. We provided numerical evidences for the existence of Hopf bifurcations, with respect to the coupling parameter, which is synonymous with synchronized activity (Figures 5.3 and 5.6). On the one hand, low coupling strengths result in a decrease of the amplitude of the SCN rhythm. In particular, if the coupling strength is less than a certain threshold (K_H), the oscillation amplitude becomes null, meaning that the circadian rhythm is lost due to neuronal oscillators being out of phase with each other. Our findings, on the other hand, show that significant coupling causes resonance effects. This leads to amplitude expansion and the rapid establishment of a coherent evolution implying the dissipation of variance in the system.

Moreover, we provided a numerical description of the bifurcations that govern the instabilities caused by noise-induced transitions, i.e., Hopf bifurcations. Our approach allows us to identify where the system of coupled SCN neurons exhibit a stable stationary state (incoherence within the SCN network) or limit cycle oscillations (synchronized activity). We suggest that noise weakens synchrony-dependent rhythmicity and affects the robustness of the system (Figure 5.10). Robustness to external noise decreases in proportion

to the noise level: bifurcation boundaries are pushed forward as the noise level increases, making it more difficult to reach the oscillatory regime (Figure 5.9). However, in a biological context, rhythmicity could be recovered with higher activation rates (k_1, k_3), lower degradation rates (k_2, k_4, k_6) or slower inhibition of the mRNA by its inhibitor protein (K_i) in equation (5.4).

The repression mechanism used in modelling the negative feedback loop in circadian clocks can affect significantly properties of models, including robustness to perturbations. We use a Hill-type repression function to explain how transcriptional activity decreases as repressor concentration rises (see equation 5.2). Recently, a new mechanism of transcriptional repression based on protein sequestration has been proposed: repressors tightly bind activators to form an inactive 1:1 stoichiometric complex (see [274] for details). In Hill-type (HT) and protein-sequestration (PS) models, Kim and Forger investigated the qualitative differences based on the repression mechanisms [274, 276]. According to their analyses, the HT and PS models have different prerequisites for generating rhythms: a large Hill exponent and a 1:1 molar ratio between repressor and activator, respectively. Kim and colleagues [275] also showed that the coupled periods are near the mean period of the SCN when transcriptional repression occurs via protein sequestration, whereas the collective period is farther from the mean if modeled with Hill-type regulation. Apart from the repression mechanism, the models mentioned above are IBMs and differ from ours in that the coupling function is different, cells are heterogeneous in terms of period, and noise is not taken into account. In our mean-field model that uses Hill-type repression, we observe that the collective period is close to the intrinsic period of the cells in the presence of low to moderate noise. This could be explained by our use of a homogeneous network (see Figure 5.3b and Figure 5.11b). Moreover, according to Chen et al. [277], there exist coupling strengths c in both HT and PS models such that the collective frequency equals the average frequency of individual cells. For the HT model, such strength c is larger.

Despite these differences between HT and PS models, many intercellular coupling properties are shared between the two and some general trends are similar. For instance, the logarithmic sensitivity of the repression function should be greater than 8 at steady state for both models to generate oscillations [276], and increasing coupling strength causes amplitude expansion in both models [276, 277]. Our results can be extended when the protein sequestration function is used instead of the Hill function up to a constant in the bifurcation values for homogeneous networks of cells. Further study is needed when heterogeneous oscillators with different periods are coupled.

In addition to nonlinearity in the repression function, oscillations require sufficiently long delays in feedback loops. This can be achieved by adding intermediate steps in the ODE formulation or by introducing explicit delays representing the durations of post-

translational regulations. Our numerical scheme, first developed in [301], applies when time-independent delays are modeled with noise, white or colored additive and multiplicative. However, numerical challenges may arise from adding explicit time delays. First, a delay may further constrain the stability condition on the time step so that the solver's time step is smaller than its value. Second, delays require storing a history of the function, which can be memory-prohibitive. Not the least is the noise effect, as noise causes the stochastic solution to disperse around the deterministic solution and the empirical variance stabilizes but for large time, with a limit value which increases as spatial regularity decreases and noise intensity increases. Importantly, the major numerical challenges would be due neither to noise nor to delay, but rather to the nature of the equation whose type degenerates at certain points of the domain of definition or at the boundary of this domain. The proposed scheme is able to cope with non-smooth stationary states, different time scales including metastability, as well as concentrations and self-similar behavior induced by singular nonlocal kernels [301].

Lastly, our model has limitations, which should be acknowledged. It has been shown that the SCN is a heterogeneous network, consisting of two groups of neurons that are structurally and functionally different. Namely, the ventralateral part (VL) which receives light information and transmits it to the dorsalmedial part (DM). This second group is only indirectly sensitive to light [302]. Within these regions different neurotransmitters are used for communication between the cells [43]. Network topology, in addition to network heterogeneity, has a substantial influence on the SCN's collective behaviour. In this article, we tested an all-to-all linear coupling between neurons, which may not be a realistic architecture for the SCN network. Extensions of our work could include a dual-network representation of the VL-DM architecture, as well as an emphasis on nonlinear cross-regional coupling. Future research could also look at the molecular details of the repression pathway, which could include both phosphorylation and protein sequestration.

Chapter 6

Sexual dimorphism in substrate metabolism during exercise

The content of this chapter is based on the paper: S. M. Abo, E. Casella, and A. T. Layton, "Sexual dimorphism in substrate metabolism during exercise," *Bull Math Biol*, vol. 86, no. 2, p. 17, 2024. URL: https://doi.org/10.1007/s11538-023-01242-4. Reproduced with permission from Springer Nature.

Abstract

During aerobic exercise, women oxidize significantly more lipids and less carbohydrates than men. This sexual dimorphism in substrate metabolism has been attributed, in part, to the observed differences in epinephrine and glucagon levels between men and women during exercise. To identify the underpinning candidate physiological mechanisms for these sex differences, we developed a sex-specific multi-scale mathematical model that relates cellular metabolism in the organs to whole-body responses during exercise. We conducted simulations to test the hypothesis that sex differences in the exercise-induced changes to epinephrine and glucagon would result in the sexual dimorphism of hepatic metabolic flux rates via the glucagon-to-insulin ratio (GIR). Indeed, model simulations indicate that the shift towards lipid metabolism in the female model is primarily driven by the liver. The female model liver exhibits resistance to GIR-mediated glycogenolysis, which helps maintain hepatic glycogen levels. This decreases arterial glucose levels and promotes the oxidation of free fatty acids. Furthermore, in the female model, skeletal muscle relies on plasma free fatty acids as the primary fuel source, rather than intramyocellular lipids, whereas the opposite holds true for the male model.

6.1 Introduction

Men and women exhibit physiological differences beyond their reproductive system and reproductive organs. Indeed, significant sexual dimorphism has been observed in anatomy, cardiovascular activity, and metabolic functions [29, 303]. Despite this, many studies focus on the male sex and their results are then generalized to the entire population. The choice of males as the dominant research subject is often justified by the idea that females experience fluctuations in sex hormones throughout the menstrual cycle, potentially leading to variability in results [304]. For the sake of time and costs, it is often cheaper for researchers to study only the male sex. However, thousands of genes exhibit differences in expression between the sexes in all organs. These differences are most prevalent in the liver, muscle, and adipose tissue [305–307]. In fact, the liver has been regarded as "the best example of a sexually dimorphic non-reproductive organ" [308]. Sex differences in liver metabolism can be attributed to gene regulation by sex hormones. By binding to estrogen receptors (ERs) and estrogen response elements (EREs), estrogens exercise their effects on the liver through estrogen signalling [34]. For instance, cellular 17β-estradiol (E2) signaling is mediated primarily via nuclear ERs, ER-α, and ER-β [309]. In carbohydrate metabolism, estrogens are known to reduce glucose production in the liver via gluconeogenesis and glycogenolysis,

and lower blood glucose levels [309–311]. In fat metabolism, endogenous estrogens regulate many aspects of hepatic free fatty acid (FFA), triglyceride, and cholesterol metabolism, but the physiologic control of these effects is distributed across different tissues, primarily adipose and liver. Lipids are primarily transported between tissues as free fatty acids released by adipose tissue or as lipoprotein carriers produced primarily by the liver and gut [312]. Gaps in sex-specific research threaten the validity and applicability of findings, since biological differences between men and women can alter how the body responds to medication or metabolic disturbances. One such disturbance is exercise. Specifically, in the context of endurance exercise, sex differences in performance are known to exist when metrics are expressed relative to body mass and composition. Females have a metabolic advantage over males when training at the same submaximal intensity [313]. This is due to lower muscle fatigability and greater activation of fatigue resistant muscle fibers [314]. There are also sex differences in the relative utilization of carbohydrates and lipids as fuel sources at rest or in response to exercise [14, 315, 316]. Notably, at the whole-body level, females have a lower respiratory exchange ratio (RER) during endurance exercise than males, indicating a greater contribution of lipids to oxidative metabolism during exercise [8, 14, 317–320]. In addition, studies have shown that females rely less on liver and muscle glycogen stores during endurance exercise [319, 321, 322]. It is not yet clear whether the mechanisms behind this difference involve the fact that women have a higher overall body fat percentage, making lipids an available resource to meet the fuel demands of exercise, or the fact that women have a greater deposition of intramyocellular lipids (IMCL) in contact with mitochondria, possibly leading to a greater ability to utilize IMCL [321]. Researchers have also reported sex differences epinephrine and glucagon levels during exercise [14], and some studies suggest that such hormones may play a role in the sexual dimorphism of carbohydrate and lipid metabolism [8, 323, 324].

In a well-controlled study [325], females had higher adipose tissue triglyceride lipolysis and plasma FFA availability than males who were matched for percent body fat and aerobic fitness. However, due to a reciprocal decrease in the oxidation rate of non-plasma-derived FFA, both sexes showed similar total fat oxidation. Such findings draw our attention to some inconsistencies in the literature on this subject. Indeed, some studies have found no statistically significant differences in substrate utilization between sexes during exercise [16, 326, 327]. In Ref. [16], a sample of 7 men is compared to 7 eumenorrheic women (mid-follicular phase) during a submaximal cycling test. Participants were controlled in terms of nutrient composition as well as energy content for eight days preceding the experiment. The results indicated that no sex difference existed in the relative contribution from carbohydrate and lipids to the oxidative metabolism across the leg during submaximal exercise at the same relative workload. We should note, however, that all subjects in this study were

endurance trained, and the lack of a sex difference may be due to their history of endurance training, as opposed to sedentary individuals. In Ref. [326], 6 age- and fitness-matched men and women (follicular phase of their menstrual cycle) were studied. Both groups had comparable exercise responses in terms of systemic and leg FFA release. This study did not control for body composition, specifically whole-body fat and lean body mass. The study in Ref. [327] included 28 people of similar weight and fitness status, 12 women and 16 men, with the goal of determining whether there exist differences in glucoregulatory responses to exercise. Glucose production, after stepwise multiple regression and covariance analysis, showed no effect of sex, body weight or free fat mass. Although the study verified that all participants were non-smokers and not taking any medications, no monitoring of menstrual cycle phase, except for a negative pregnancy test, was implemented.

It is reasonable to hypothesize that body composition influences the extent of substrate oxidation during exercise, because a higher basal body fat percentage in females would result in greater regional lipolysis [320, 328], assuming similar substrate oxidation efficiencies. Inadequate control of this parameter may be to blame for the controversies surrounding reported differences in lipid oxidation rates. Importantly, hormonal and enzymatics aspects, in addition to histological factors, contribute to sex differences in performance, fatigability, and substrate handling and may have confounding effects [329]. This becomes particularly important when studying fuel sources and utilization, given differences in body composition, endogenous sex hormones, and pathway-preferential signalling of said hormones. This could explain why contrasting findings regarding the type of substrate used to sustain submaximal endurance exercise can be found in the available sex-comparative literature. There are also methodological differences that come into play [330]. Inconsistencies in results may be attributed to poor control of training and nutritional status, the various methods used to assess metabolic rates, and the characteristics of populations studied (e.g., age, ethnicity, diet, drinking and smoking habits). Furthermore, overlooking menstrual cycle phases and hormonal profiles can result in a highly heterogenous female population. Not to mention that insufficient sample sizes can have a significant impact on the precision and accuracy of estimates reported in individual studies. We refer interested readers to a meta-analysis [329] and reviews [312, 322] for more details.

Computational modelling has played an increasingly important role in medicine. By simulating biological processes, revealing their underlying mechanisms, and predicting physiological responses, the incorporation of mathematics in medicine can lead to more refined methods for disease diagnosis, prevention, and treatment. That said, major benefits can only be achieved if model predictions are valid for both halves of the population, given the ubiquitous sex differences. Thus, there is an opportunity to harness the power of mathematical modelling in investigating sexual dimorphism in cellular and whole-body

metabolism. The human body utilizes carbohydrates and lipids as its primary fuel sources. For medical conditions related to glucose and lipid metabolism, such as diabetes and obesity, understanding the regulatory mechanisms behind the body's response to perturbations in fuel homeostasis can guide exercise and nutritional recommendations. Although exercise perturbs metabolism on a whole-body level, individual changes occur in cellular signalling pathways within different organs. Integrating these multi-scale processes allows for the understanding of how cellular reactions affect whole-body responses [68]. Since experimental observations of cellular processes on an organ-specific level during exercise are scarce and difficult to obtain, mathematical modelling can provide supplementation to these studies.

This study aims to develop a sex-specific multi-scale mathematical model that relates cellular metabolism in the organs to whole-body responses during exercise. We hypothesized that sex differences in the exercise-induced changes to epinephrine and glucagon would result in the sexual dimorphism of hepatic metabolic flux rates via the glucagon-to-insulin ratio (GIR = glucagon/insulin). Additionally, we hypothesized that the female model would predict a relatively larger contribution from lipids vs. carbohydrates to oxidative metabolism due to the sex-specific alterations in the hormones and liver portion of the model. To investigate these questions, we extended a whole-body metabolism model described in Ref. [68], which models a young adult man, to incorporate sex-specific experimental observations and to test hypotheses of mechanisms that seem to explain experimental observations in the sexual dimorphism of carbohydrate and lipid oxidation during exercise. We (1) quantified the extent of sex differences in carbohydrate and lipid metabolism in different organs and tissues; (2) identified a candidate physiological mechanism in the liver that drives sex differences in glucose production; and (3) assessed the subsequent metabolic responses in skeletal muscle and adipose tissue and their role in potentiating differences in substrate utilization.

6.2 Methods

We describe a multi-scale computational model of energy balance during exercise. Whole-body responses are influenced by cellular metabolism in organ-level systems connected via the circulation. The model predicts glucose homeostasis during a moderate-intensity exercise (150 W power output at 60% of peak oxygen consumption, $\dot{V}O_{2max}$), separately for a healthy young adult man and a healthy young adult woman. It comprises seven tissue compartments: brain, heart, liver, gastrointestinal (GI) tract, skeletal muscle, adipose tissue, and "other tissues" (Figure 6.1). This last compartment includes kidneys, upper extremity muscles, and the rest of tissues. Each compartment is connected to the others

via blood circulation and is described by dynamic mass balance equations for 25 cellular metabolic reactions involving 22 substrates (see Table 6.1). The basic assumption of the model regarding the effect of physical activity is that during moderate-intensity exercise, circulating blood levels of epinephrine directly affect heart and skeletal muscle metabolism, and indirectly other tissues by affecting the release of pancreatic insulin and glucagon.

Table 6.1: List of substrates and metabolic reactions

Substrates	**Reactions**
1. GLC: Glucose	1. Glycolysis I, $\phi_{\mathrm{GLC}\rightarrow\mathrm{G6P}}$
2. PYR: Pyruvate	2. Glycolysis II, $\phi_{\mathrm{G6P}\rightarrow\mathrm{GAP}}$
3. LAC: Lactate	3. Glycolysis III, $\phi_{\mathrm{GAP}\rightarrow\mathrm{PYR}}$
4. ALA: Alanine	4. Gluconeogenesis I, $\phi_{\mathrm{PYR}\rightarrow\mathrm{GAP}}$
5. GLR: Glycerol	5. Gluconeogenesis II, $\phi_{\mathrm{GAP}\rightarrow\mathrm{G6P}}$
6. FFA: Free fatty acids	6. Gluconeogenesis III, $\phi_{\mathrm{G6P}\rightarrow\mathrm{GLC}}$
7. TG: Triglycerides	7. Glycogenesis, $\phi_{\mathrm{G6P}\rightarrow\mathrm{GLY}}$
8. O_2: Oxygen	8. Glycogenolysis, $\phi_{\mathrm{GLY}\rightarrow\mathrm{G6P}}$
9. CO_2: Carbon dioxide	9. Pyruvate reduction, $\phi_{\mathrm{PYR}\rightarrow\mathrm{LAC}}$
10. G6P: Glucose-6-phosphate	10. Lactate oxidation, $\phi_{\mathrm{LAC}\rightarrow\mathrm{PYR}}$
11. GLY: Glycogen	11. Glycerol phosphorylation, $\phi_{\mathrm{GLR}\rightarrow\mathrm{GRP}}$
12. GAP: Glyceraldehyde-3-phosphate	12. GAP reduction, $\phi_{\mathrm{GAP}\rightarrow\mathrm{GRP}}$
13. GRP: Glycerol-3-phosphate	13. GRP oxidation, $\phi_{\mathrm{GRP}\rightarrow\mathrm{GAP}}$
14. ACoA: Acetyl coenzyme A	14. Alanine formation, $\phi_{\mathrm{PYR}\rightarrow\mathrm{ALA}}$
15. CoA: Coenzyme A	15. Alanine utilization, $\phi_{\mathrm{ALA}\rightarrow\mathrm{PYR}}$
16. NAD^+: Nicotinamide adenine dinucleotide[a]	16. Pyruvate oxidation, $\phi_{\mathrm{PYR}\rightarrow\mathrm{ACoA}}$
17. NADH: Nicotinamide adenine dinucleotide[b]	17. Fatty acids oxidation, $\phi_{\mathrm{FFA}\rightarrow\mathrm{ACoA}}$
18. ATP: Adenosine triphosphate	18. Fatty acids synthesis, $\phi_{\mathrm{ACoA}\rightarrow\mathrm{FFA}}$
19. ADP: Adenosine diphosphate	19. Lipolysis, $\phi_{\mathrm{TG}\rightarrow\mathrm{FFA\text{–}GLR}}$
20. Pi: Phosphate	20. Triglycerides synthesis, $\phi_{\mathrm{FFA\text{–}GRP}\rightarrow\mathrm{TG}}$
21. PCR: Phosphocreatine	21. TCA cycle, $\phi_{\mathrm{ACoA}\rightarrow\mathrm{CO_2}}$
22. CR: Creatine	22. Oxidative phosphorylation, $\phi_{\mathrm{O_2}\rightarrow\mathrm{H_2O}}$
	23. Phosphocreatine breakdown, $\phi_{\mathrm{PCR}\rightarrow\mathrm{CR}}$
	24. Phosphocreatine synthesis, $\phi_{\mathrm{CR}\rightarrow\mathrm{PCR}}$
	25. ATP hydrolysis, $\phi_{\mathrm{ATP}\rightarrow\mathrm{ADP}}$

[a] Oxidized
[b] Reduced

The goal of this work is to provide mechanistic models with known sex differences

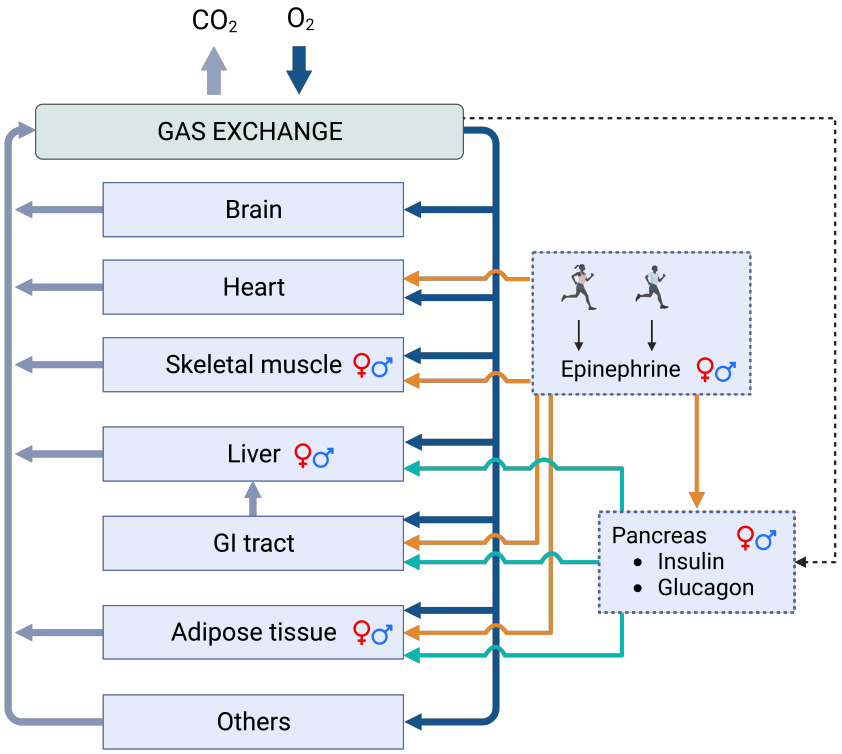

Figure 6.1: Whole-body system diagram. The systemic circulation connects all tissues/organs by transporting substrates in arterial oxygenated blood to the organs/tissues (solid dark blue arrows). Venous blood (solid light blue arrows) leaving these tissues/organs eliminates by-products and becomes arterial blood to restart circulation after releasing carbon dioxide and absorbing oxygen in the lungs (gas exchange). Blood supply to the liver comes from both the hepatic artery and venous blood from the GI tract. Exercise promotes epinephrine release, which modulates the secretion of insulin and glucagon and acts as a neuroendocrine signal for the heart, skeletal muscle, GI tract, and adipose tissue (solid orange arrows). Changes in glucagon and insulin production thereby influence metabolic fluxes in the liver, GI tract, and adipose tissue via the glucagon–to-insulin ratio signal (solid green arrows). Finally, arterial glucose concentration (dashed arrow) signals the pancreas to regulate insulin and glucagon levels, thus completing the feedback regulatory mechanism. Male and female sex symbols represent compartments where sex-differences, besides differences in tissue/organ weights, are implemented.

to quantify the energy expenditure of organs according to sex. Dynamic mass balance equations are developed for key metabolites in the biochemical pathways of organs and tissues. Our approach allows for quantitative analysis of metabolic fluxes after an overnight fast and following an exercise bout. Key organs/tissues such as the liver, skeletal muscle, and adipose tissue provide metabolic fuels needed for energy balance and lead adaptive responses during exercise. The model also represents a modified pancreas-like controller which models the actions of insulin, glucagon, and the stress hormone epinephrine. Sex differences are represented mainly in the liver, skeletal muscle, and adipose tissue. Sex-specific modifications include also the descriptions of epinephrine production, insulin and glucagon, hepatic blood flow, lipolysis, gluconeogenesis, and glycogenolysis. Appendix C contains a full description of the modelling approach, parameter values, and experimental data used. In addition, the present work improves on the published model [68] (i) by modeling the general circulation as a dynamic rather than instantaneous compartment because blood volume is sufficiently large that the rate of change in concentrations is comparable to that of tissues, (ii) and by representing the modulation of the effect of epinephrine on insulin secretion by glucose levels, allowing glucose to remain the primary driver of insulin secretion even during exercise. Details are described below.

Subjects' characteristics and exercise parameters

Female: a lean healthy adult female of childbearing age weighing 58 Kg. We assumed that the female subject's peak oxygen consumption ($\dot{V}O_{2max}$) is 2.7 l/min [8]. The exercise intensity is set to 60% $\dot{V}O_{2max}$, which corresponds to moderate-intensity exercise with a power output of 150W. We assumed that 60% of the subject's $\dot{V}O_{2max}$ is below the lactate threshold. The subject is overnight-fasted (8–12h) and has a cardiac output of 5 l/min and a resting Respiratory Quotient (RQ) of 0.8.

Male: a lean healthy adult male with 70 Kg body weight. We assumed that the male subject has a peak oxygen consumption ($\dot{V}O_{2max}$) of 3.4 l/min [7]. The exercise intensity is set to 60% $\dot{V}O_{2max}$, which corresponds to moderate-intensity exercise with a power output of 150W. We assumed that 60% of the subject's $\dot{V}O_{2max}$ is below the lactate threshold. The subject is overnight-fasted (8–12h) and has a cardiac output of 5.5 l/min and a resting Respiratory Quotient (RQ) of 0.8.

6.2.1 Compartmental modelling

We present a dynamic description of the different compartments based on the net rate of substrate uptake or release by tissues. The following substrates are transported between blood and tissue: glucose, pyruvate, lactate, alanine, glycerol, free fatty acids, triglyceride, oxygen, and carbon dioxide. With the exception of "other tissues", and under the assumption of a perfectly mixed tissue-capillary compartment, the concentration dynamics of substrate i in tissue x are described as follows:

$$V_x \frac{\mathrm{d}C_{x,i}}{\mathrm{d}t} = P_{x,i} - U_{x,i} + Q_x(C_{a,i} - \sigma_{x,i}C_{x,i}), \tag{6.1}$$

where V_x is a constant parameter and represents the volume of tissue x, $P_{x,i}$ and $U_{x,i}$ are respectively the production and utilization rates of substrate i, Q_x is the blood flow to tissue x, $C_{a,i}$ is the arterial concentration of substrate i, $C_{x,i}$ is the respective concentration of substrate i in tissue x, and $\sigma_{x,i}$ is the partition coefficient of substrate i. These partition coefficients are fixed and represent the relative distribution of metabolites between blood and tissues at rest. The first two terms on the right side of Eq (6.1) represent the net metabolic reaction rate of substrate i in tissue x. The third term, $Q_x(C_{a,i} - \sigma_{x,i}C_{x,i})$ represents the net rate of absorption or release of substrate i in tissue x. The net metabolic rate for substrates that are present only within tissues is

$$V_x \frac{\mathrm{d}C_{x,i}}{\mathrm{d}t} = P_{x,i} - U_{x,i}. \tag{6.2}$$

Production and utilization rates must account for all major metabolic processes, which can be expressed as

$$P_{x,i} - U_{x,i} = \sum_{k=1}^{m} \gamma_{s_k \to s_i} \phi_{x,s_k \to s_i} - \sum_{k=1}^{n} \gamma_{s_i \to s_k} \phi_{x,s_i \to s_k}, \tag{6.3}$$

where $\phi_{x,s_k \to s_i}$ is the rate of utilization of substrate s_k for the formation of substrate s_i in tissue x and similarly for $\phi_{x,s_i \to s_k}$. The constants $\gamma_{(\cdot)}$ are the corresponding stoichiometric coefficients, m is the number of processes forming substrate i, and n is the number of processes consuming substrate i. Figure 6.2 shows a union map of all the metabolic pathways represented in our models, and Table 6.2 highlights tissue-specific metabolic pathways.

Our model includes a central blood compartment that is connected to all other compartments. The rate of change in the concentration of a substrate in the circulation is

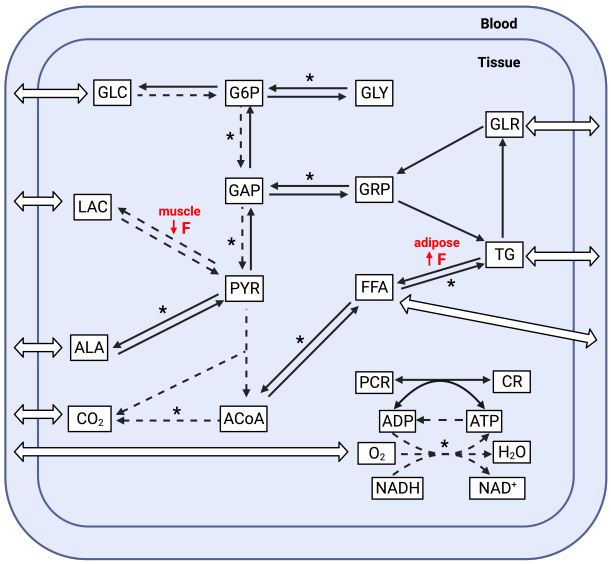

Figure 6.2: Union map of all-organ metabolic pathways. 9 substrates are transported between blood and tissues (open arrows). Black arrows are tissue-specific pathways, whereas dashed arrows represent common pathways found in all tissues. Pathways marked with an asterisk (*) are composed of multiple reaction steps but grouped together as a single step in this model. Reaction rates in females that are significantly different from males at rest are marked by an arrow indicating the direction of change and the symbol F. Substrate abbreviations are listed in Table 6.1.

determined by the net sum of transport fluxes between all organs and the circulation. As a result, the arterial concentration of the substrate i is updated according to

$$V_{\text{blood}} \frac{\mathrm{d}C_{a,i}}{\mathrm{d}t} = -\sum_{x} Q_x (C_{a,i} - \sigma_{x,i} C_{x,i}), \tag{6.4}$$

where V_{blood} is the whole-body blood volume. Table 6.3 outlines sex differences in physical characteristics such as tissue weights and basal blood flows to specific compartments.

6.2.2 Metabolic rates and rate coefficients

Rates of utilization ($\phi_{x,s_i \to s_k}$) of any substrate s_i in tissue x are functions of the substrate concentration $C_{x,i}$, except when stated otherwise, and of the phosphorylation state ($C_{\text{ATP}}/C_{\text{ADP}}$), and the redox state ($C_{\text{NADH}}/C_{\text{NAD+}}$). The dependence of these rates on the

Table 6.2: Map of tissue-specific metabolic pathways. A filled box means the existence of the corresponding pathway. In addition to the common pathways depicted in Figure 6.2, each tissue has its own different set of metabolic pathways.

Pathways	Brain	Heart	Skeletal muscle	GI tract	Liver	Adipose tissue
Gluconeogenesis I, II, III (PYR→GAP,GAP→G6P,G6P→GLC)					■	
Glycogen synthesis (GLY→G6P)	■	■	■		■	
Glycogenolysis (G6P→GLY)	■	■	■		■	
Fatty acid synthesis (ACoA→FFA)					■	
Fatty acid oxidation (FFA→ACoA)		■	■		■	■
Lipolysis (TG→FFA+GLR)		■	■	■	■	■
TG synthesis (FFA+GRP→TG)		■	■	■	■	■
Glycerol phosphorylation (GLR→GRP)		■	■		■	
GAP reduction (GAP→GRP)						■
GRP oxidation (GRP→GAP)					■	
Alanine breakdown (ALA→PYR)					■	
Alanine synthesis (PYR→ALA)			■			
PCR breakdown (PCR→CR)	■	■	■	■		
PCR synthesis (CR→PCR)	■	■	■	■		

concentration of the substrate $C_{x,i}$ provides mass action-based regulation, while the reliance on metabolic modulators ATP, ADP, NADH and NAD^+ provides feedback mechanisms to control the rates of reaction processes. Each reaction rate is expressed as an irreversible uni-uni (or bi-bi when two reactants are involved) substrate to product enzymatic reaction coupled with metabolic modulator pairs. As a general reaction, we consider reactants X

Table 6.3: Sex differences in physical characteristics

	Male		Female		References
Tissue/Organ	Weight (Kg)	Volume (L)†	Weight (Kg)	Volume (L)†	
Brain	1.40	1.35	1.20	1.15	[70, 331, 332]
Heart	0.331	0.315	0.253	0.241	[70, 331, 333]
Skeletal muscle	22.4[a]	21.33	13.6[a]	12.95	[70, 331, 333]
GI tract	2.0	1.89	2.0	1.89	[68, 70, 333]
Liver	1.80	1.67	1.40	1.30	[70, 331, 334]
Adipose tissue	11.0[b]	11.9	17.1[c]	18.5	[68, 70, 331, 333]
Others[d]	31.069	29.59	22.447	21.38	[335]
Whole-body	70.0	68.045	58.0	57.411	[70, 331]
Blood flow (l/min)[e]					
Brain	0.75		0.75		
Heart	0.25		0.25		
Skeletal muscle	0.9		0.9		
GI tract	1.1		1.1		
Liver	1.50		1.35		[336]
Adipose tissue	0.36		0.36		
Others[d]	1.74		1.39		
Whole-body	5.5		5.0		[70, 337]

[a] Skeletal muscles, excluding upper extremities which account for 18-20% of total weight. Male total: 28 Kg; female total: 17 Kg.
[b] Based on 16% body fat content.
[c] Based on 29.5% body fat content.
[d] Values for "Others" are chosen to balance whole-body values.
[e] Unless otherwise noted, regional blood flows are assumed to be the same between sexes. Values are reproduced from Ref. [68]. †Organ volumes are calculated by dividing each tissue weight by its density: brain (1.04 Kg/L)[332], heart and skeletal muscle (1.05 Kg/L)[333], GI tract (1.06 Kg/L)[333], liver (1.08 Kg/L)[334], adipose tissue (0.923 Kg/L)[333]. Assuming that *others* include only nonfat tissues, a tissue density of 1.05 Kg/L is used [335]. The total volume of the body is calculated by adding the volumes of all compartments.

and Y and products Z and W. The corresponding reaction rate equation in tissue x is

$$\phi_{x,X\text{–}Y\to Z\text{–}W} = V_{\max,x,X\text{–}Y\to Z\text{–}W}\left(\frac{\frac{C_X}{K_X}\cdot\frac{C_Y}{K_Y}}{1+\frac{C_X}{K_X}+\frac{C_Y}{K_Y}+\frac{C_X}{K_X}\cdot\frac{C_Y}{K_Y}}\right) \times\left(\frac{\mathrm{PS}^{\pm}}{\mu^{\pm}+\mathrm{PS}^{\pm}}\right)\left(\frac{\mathrm{RS}^{\pm}}{\nu^{\pm}+\mathrm{RS}^{\pm}}\right) \tag{6.5}$$

where $V_{\max,x,X\text{–}Y\to Z\text{–}W}$, K_X, and K_Y are Michaelis-Menten parameters specific to the reaction process, C_X and C_Y are concentrations of substrate X and Y in tissue x. Phosphorylation states are $\mathrm{PS}^+ = C_{\mathrm{ATP}}/C_{\mathrm{ADP}}$ in the forward direction and $\mathrm{PS}^- = C_{\mathrm{ADP}}/C_{\mathrm{ATP}}$ in the opposite direction. Redox states are analogous, i.e., $\mathrm{RS}^+ = C_{\mathrm{NADH}}/C_{\mathrm{NAD^+}}$ and $\mathrm{RS}^- = C_{\mathrm{NAD^+}}/C_{\mathrm{NADH}}$. Parameters $\mu^\pm$ and $\nu^\pm$ are related to the metabolic modulator pairs. It is worth noting that AMP is a key allosteric regulator of glycogen phosphorylase for glycogenolysis (GLY→G6P) and phosphofructokinase-1 (PFK-1) for glycolysis II (G6P→GAP). As AMP is not included in this model, AMP/ATP is approximated by $[\mathrm{ADP/ATP}]^2$ in these reactions (see Table C.13 in Appendix C). Micahelis-Menten parameters and substrate concentrations are obtained from Ref. [68] and references therein. Parameters $\mu^\pm$ and $\nu^\pm$ are estimated from data as discussed later in section 6.2.5. As an example of a bi-bi irreversible mechanism, consider the metabolic process of pyruvate oxidation

$$\mathrm{PYR} + \mathrm{CoA} + \mathrm{NAD^+} \longrightarrow \mathrm{ACoA} + \mathrm{NADH} + \mathrm{CO_2}$$

which mathematically corresponds to

$$\phi_{\mathrm{PYR\text{–}CoA\to ACoA\text{–}CO_2}} = V_{\max,\mathrm{PYR\text{–}CoA\to ACoA\text{–}CO_2}} \left(\frac{\frac{C_{\mathrm{PYR}}}{K_{\mathrm{PYR}}} \cdot \frac{C_{\mathrm{CoA}}}{K_{\mathrm{CoA}}}}{1 + \frac{C_{\mathrm{PYR}}}{K_{\mathrm{PYR}}} + \frac{C_{\mathrm{CoA}}}{K_{\mathrm{CoA}}} + \frac{C_{\mathrm{PYR}}}{K_{\mathrm{PYR}}} \cdot \frac{C_{\mathrm{CoA}}}{K_{\mathrm{CoA}}}} \right) \times \left(\frac{\mathrm{RS}^-}{\mu^- + \mathrm{RS}^-} \right) \tag{6.6}$$

6.2.3 Regulation of glucose by glucagon and insulin

Pancreatic α- and β-cells in the islets of Langerhans secrete glucagon and insulin, respectively. A healthy pancreas secretes both insulin and glucagon at rest; after a meal or during exercise, both are released, but at different rates [338]. During exercise in particular, the concentration of glucagon increases and that of insulin decreases to maintain normoglycemia. These hormonal changes are also influenced by the parasympathetic nervous system and the sympathetic nervous system (SNS). Although insulin production by pancreatic β-cells is primarily mediated by circulating glucose levels, the release of epinephrine from sympathetic neurons during exercise inhibits insulin secretion and thus increases the release of glucagon [339]. In this study, we model the effect of exercise via epinephrine, which directly modulates insulin secretion and indirectly glucagon secretion.

Many adaptations, both at rest and during exercise, are mediated by stress hormones epinephrine and norepinephrine. In fact, epinephrine and norepinephrine are the primary

hormones whose concentrations rise significantly during exercise. Experimentalists reported increases ranging from 1.5 to more than 20 times basal concentrations [330]. The magnitude of these changes is a function of exercise characteristics (e.g., exercise duration, exercise type, training status, and sex). Horton et al. [8] showed a significantly lower mean epinephrine concentration at rest, during exercise, and after exercise in women compared with men. Some studies observed similar results [14, 340]. In another study, Horton and colleagues investigated the effects of exercise during different phases of the menstrual cycle and found no effect of the menstrual cycle on resting and exercise epinephrine concentrations [341], as others have too [342, 343]. Given these findings, we can reasonably assume that physical activity causes an increase in circulating epinephrine, which is significantly lower in women than in men. Yet, these changes do not depend on the phase of the menstrual cycle. In both male and female models, blood epinephrine level changes with a step increase in work rate:

$$C_E(t) = C_E(0) + \omega(\mathrm{WR}) \cdot (1 - \exp(t/\tau_E)), \tag{6.7}$$

where $C_E(0)$ is the initial concentration of epinephrine at rest, WR is the work rate fixed at 150W or 60% of $\dot{\mathrm{V}}\mathrm{O}_{2\mathrm{max}}$, and $\omega(\mathrm{WR})$ is a parameter determining the gain with respect to a step change in work rate applied during exercise; τ_E is a time constant for epinephrine dynamics.

The hormones insulin and glucagon are modeled as an *integral rein* controller, which is a modelling concept developed by Saunders et al. to maintain blood glucose homeostasis [338]. Under most conditions both glucagon and insulin are produced and control is achieved by altering the balance between the two hormones [338]. An important feature of the model is that the set point of blood glucose is determined by the dynamics of the two hormones and specifically by the intersection of two chemical response curves, making the model resilient to perturbations in either direction. In our model, the action of epinephrine on insulin dynamics is included in the formulation of the integral rein control. This modelling choice was motivated by the fact that pancreatic hormone production in low glucose settings, such as during exercise, depends on glucose levels and SNS activity (e.g., epinephrine level) [344]. This approach was also implemented in Ref. [69], but it differs from Ref. [68] in which epinephrine's action on insulin is independent of blood glucose levels. The set of equations shown below still adhere to the formalism proposed by Saunders et al. Insulin dynamics are described by:

$$\begin{aligned}\frac{\mathrm{d}C_I}{\mathrm{d}t} = C_I(t)\Big(\psi(C_{a,\mathrm{GLC}}) \cdot \big(h - k_3(C_G(t) - C_G(0)) - k_4(C_I(t) - C_I(0)) \\ - k_5(C_E(t) - C_E(0))\big) - D\Big),\end{aligned} \tag{6.8}$$

and glucagon dynamics by:

$$\frac{\mathrm{d}C_G}{\mathrm{d}t} = C_G(t)\Big(\theta(C_{a,\mathrm{GLC}}) \cdot \big(h - k_1(C_G(t) - C_G(0)) - k_2(C_I(t) - C_I(0))\big) - D\Big), \tag{6.9}$$

where $\psi(C_{a,\mathrm{GLC}})$ is an increasing function of $C_{a,\mathrm{GLC}}$, $\theta(C_{a,\mathrm{GLC}})$ is a decreasing function of $C_{a,\mathrm{GLC}}$, and h, D, k_1, k_2, k_3, k_4 and k_5 are estimated parameters. $\theta(C_{a,\mathrm{GLC}})$ and $\psi(C_{a,\mathrm{GLC}})$ are formulated to result in a steady-state arterial glucose concentration of 5 mM [345].

$$\psi(C_{a,\mathrm{GLC}}) = \begin{cases} 0 & C_{a,\mathrm{GLC}} < 2.5 \\ 1 - (C_{a,\mathrm{GLC}} - 7.5)^2/25 & 2.5 \leq C_{a,\mathrm{GLC}} \leq 7.5 \\ 1 & 7.5 < C_{a,\mathrm{GLC}} \end{cases} \tag{6.10}$$

$$\theta(C_{a,\mathrm{GLC}}) = \begin{cases} 1 & C_{a,\mathrm{GLC}} < 2.5 \\ 1 - (C_{a,\mathrm{GLC}} - 2.5)^2/25 & 2.5 \leq C_{a,\mathrm{GLC}} \leq 7.5 \\ 0 & 7.5 < C_{a,\mathrm{GLC}} \end{cases} \tag{6.11}$$

Bi-hormonal pancreatic responses exhibit some sex differences. Glucagon concentration is higher in women than in men at rest and during submaximal exercise, but the increment in glucagon from rest to exercise is lower in women [8]. However, neither insulin response nor insulin concentrations differ significantly between men and women during exercise [8]. These findings apply to young, healthy individuals. The implication of these differences is that, while the glucagon-to-insulin ratio (GIR) is higher in women during exercise, it may increase at a slower rate than in men.

6.2.4 Parallel activation during exercise

Hormonal control of metabolic reaction rates. Blood glucose levels tend to rise during intense exercise, but gradually fall during moderate-intensity exercise. Yet, exercise is typically characterized by euglycemia. This implies, in general, that the increase in hepatic glucose production during exercise matches roughly with the increase in glucose uptake. This tight regulation is made possible by hormonal signals, specifically insulin and glucagon, which provide an important feedback mechanism between the pancreas and tissues that interact via blood circulation. The ratio of glucagon to insulin, which strongly correlates with changes in hepatic glucose, characterizes the effect of signalling [346]. As a result, we hypothesize that the glucagon-to-insulin ratio influences glycogenolysis and all gluconeogenesis steps in the liver, including the conversion of glucogenic amino acids such

as *alanine*. Namely, these correspond to reactions 4,5,6,8, and 15 in Table 6.1. For these reactions, maximum rate coefficients $V_{\max,x,i}$, characterizing the metabolic flux i in tissue x (liver), are modulated as follows:

$$V_{\max,x,i} = V^0_{\max,x,i} \left(1.0 + \lambda^G_{x,i} \frac{(\mathrm{GIR}(t) - \mathrm{GIR}(0))^2}{\alpha^G_{x,i} + (\mathrm{GIR}(t) - \mathrm{GIR}(0))^2}\right), \tag{6.12}$$

where GIR is the ratio of glucagon (C_G) to insulin (C_I) arterial concentrations (i.e., GIR = C_G/C_I), $\lambda^G_{x,i}$ and $\alpha^G_{x,i}$ are the associated hormonal control parameters.

Skeletal muscle cells lack glucagon receptors [347], and although glucagon receptors are found in the heart, improving cardiac contractility is not the primary function of glucagon in this organ [348]. Thus, we hypothesized that the heart and skeletal muscle primarily respond to an epinephrine signal during exercise. In particular, we assume that the rates of glycolysis, glycogenolysis, oxidative phosphorylation, the tricarboxylic acid (TCA) cycle, fatty acid oxidation, and lipolysis are modulated by epinephrine. For metabolic rate i (reactions 1,8,14,17, and 19 in Table 6.1) in tissue x (heart or skeletal muscle), the maximum rate coefficient $V_{\max,x,i}$ is:

$$V_{\max,x,i} = V^0_{\max,x,i} \left(1.0 + \lambda^E_{x,i} \frac{(C_E(t) - C_E(0))^2}{\alpha^E_{x,i} + (C_E(t) - C_E(0))^2}\right), \tag{6.13}$$

where C_E is the arterial concentration of epinephrine, $\lambda^E_{x,i}$ and $\alpha^E_{x,i}$ are the hormonal regulatory parameters for epinephrine.

Lipolysis in adipose and GI tissues is influenced by epinephrine and insulin levels. Hence, this reaction rate is controlled by a combination of GIR and epinephrine factors:

$$V_{\max,x,i} = V^0_{\max,x,i} \left(1.0 + \lambda^G_{x,i} \frac{(\mathrm{GIR}(t) - \mathrm{GIR}(0))^2}{\alpha^G_{x,i} + (\mathrm{GIR}(t) - \mathrm{GIR}(0))^2} + \lambda^E_{x,i} \frac{(C_E(t) - C_E(0))^2}{\alpha^E_{x,i} + (C_E(t) - C_E(0))^2}\right). \tag{6.14}$$

In Eqs (6.12),(6.13), and (6.14), $C_E(0)$ and $GIR(0)$ are the initial values for epinephrine and GIR, respectively, $V^0_{\max,x,i}$ are the maximum rate coefficients at rest, and $V_{\max,x,i}$ are the corresponding maximum rate coefficients modulated by hormones during exercise. The latter interact with the rest of the model through Eq (6.5). $V^0_{\max,x,i}$ are constant parameters and $V_{\max,x,i}$ are dynamic parameters. Our choice to model the hormonal activation

using sigmoidal functions is motivated as follows: 1) the change in hormone concentrations relative to the initial conditions serves as a proxy measure of metabolic demand induced by exercise; 2) the use of the second power steepens the response curves and helps to represent the rapid increase in metabolic rates from baseline at the beginning of exercise. We note that the differences $(C_E(t) - C_E(0))$ and $(\mathrm{GIR}(t) - \mathrm{GIR}(0))$ are nonnegative during exercise as both epinephrine and GIR increase during exercise, and thus the exponent only potentiates the response in the positive direction; 3) gains in the middle region of the response curve are better than gains in bilateral regions, implying that maximum rate coefficients eventually reach saturation when hormone concentrations are high enough. This is typical of real-world systems, where unlimited activation is not possible.

Neural control of metabolic reaction rates. Neural activation prompted by exercise causes an increase in intracellular calcium concentration, which helps the heart and skeletal muscles contract. Calcium ions are the major signaling ions in the cells, and are an important activator for metabolic process rates such as glycolysis, glycogenolysis, TCA cycle, and oxidative phosphorylation. Changes in calcium concentrations are much faster (<100 ms) than hormonal or allosteric activators (>1 min), and cause instantaneous changes in metabolic rates [68]. As a result, we assume that the maximum reaction rates for glycolysis II and III, glycogenolysis, pyruvate oxidation, TCA cycle, oxidative phosphorylation, and ATP hydrolysis undergo a step change at the start of exercise (see reactions 2,3,8,16,21,22, and 25 in Table 6.1). The work rate determines the level of activation as follows:

$$V_{\max,x,i} = V^0_{\max,x,i} \cdot \frac{\phi_{x,ATP\to ADP(\mathrm{WR})}}{\phi^0_{x,ATP\to ADP}}. \tag{6.15}$$

$V^0_{\max,x,i}$ represent basal maximum rate coefficients, whereas $V_{\max,x,i}$ are dynamic maximum rate coefficients modulated by exercise that influence metabolic rates via Eq (6.5). According to Cabrera et al. [349], the rate of ATP hydrolysis in skeletal muscle is directly proportional to work rate (WR):

$$\phi_{x,ATP\to ADP}(\mathrm{WR}) = \phi^0_{x,ATP\to ADP} + \gamma_x \cdot \mathrm{WR}, \tag{6.16}$$

where $\phi^0_{x,ATP\to ADP}$ is the basal rate of ATP hydrolysis, and γ_x is a conversion factor in skeletal muscle. In the heart, the force and frequency of myocyte contraction increase during exercise, pushing more blood out of the heart and thus increasing stroke volume. In healthy people, acute increases in heart rate and stroke volume during exercise can cause cardiac output to increase four to eightfold [350, 351]. Because the heart has a very high energy demand and must continuously produce large amounts of ATP to sustain contractile function [352], we model exercise-induced increases in cardiac ATP energy demand

similarly to skeletal muscle. Therefore the rate of ATP hydrolysis in the heart is also modulated by work rate and x ={heart, skeletal muscle} in Eq (6.16). ATP hydrolysis rates are kept constant in other tissues.

Blood flow regulation. In response to exercise, blood flow is markedly increased in contracting cardiac and skeletal muscles, while perfusion in other organs (brain and bone) is only slightly increased or even reduced (visceral organs) [353]. In this model, a step increase in work rate causes an increase in blood flow to the heart and skeletal muscle, a decrease in blood flow to the GI tract and liver, and no change in blood flow to other organs (brain, adipose, and *other tissues*). The blood flow for affected tissue x changes according to:

$$Q_x(t) = Q_x(0) + \delta_x(1 - e^{-t/\tau_Q}), \tag{6.17}$$

where δ_x is a parameter or step gain that represents the change in blood flow in tissue x, and τ_Q is a time constant. Notably, the blood flow to the liver is different between the sexes in absolute terms. In adults, typical steady state hepatic blood flow is 1.35 L/min in women and 1.5 L/min in men [336]. Cardiac output (CO) determines regional blood flows. Since CO is related to body size, it is best to normalize it based on surface area. When normalized in this manner, men and women have similar average cardiac indices of 3.5 L/min/m^2 [354]. As a result, this variation in hepatic blood flow may reflect anatomical differences in liver size between the sexes. In our model, total blood flow to the liver includes inflow from the hepatic artery as well as venous blood from the GI tract. To account for sexual dimorphism, basal blood flow ($Q_x(0)$) from the GI tract was kept constant at 1.1 L/min for both sexes, while basal blood flow from the hepatic artery is 0.4 L/min for the male model and 0.25 L/min for the female model. It is also worth noting that absolute resting blood flows to adipose tissue and skeletal muscle are the same in both male and female models. Thus, when expressed per unit tissue weight, blood flows to adipose tissue (greater in women) and skeletal muscle (greater in men) differ between the sexes. Sex differences in parameters related to blood flow regulation are listed in Table 6.3.

6.2.5 Parameter estimation

Parameter values for simulating the metabolism of a healthy adult (either male or female) in an overnight fasted condition are available in the literature and are described in Appendix C. Parameters that represent metabolic changes in response to exercise, which are listed in Table 6.4, are estimated by a least-squares method. In particular, we used *fminsearch*, a nonlinear least-squares algorithm with a normalized residual, to minimize the

difference between model-predicted substrate concentrations and concentration data for at least 60 minutes of exercise. Call p_0 the set of initial guesses for model parameters. For parameters related to the glucagon-insulin controller and blood flow regulation, the initial guess is set to 1, except for δ_{GI}, which is set to -1 because blood flow to the viscera decreases during exercise [354]. GIR and neural regulatory factors, $\lambda^G_{x,i}$ and $\lambda^E_{x,i}$, are set to 1, while $\alpha^G_{x,i}$ and $\alpha^E_{x,i}$ are set to $[\mathrm{GIR}(t=60)-\mathrm{GIR}(t=0)]^2$ and $[C_E(t=60)-C_E(t=0)]^2$, respectively, where values at $t=0$ and $t=60$ are obtained from experimental data. Other neural regulatory factors, γ_x are set to 1. In the case of epinephrine, the initial guess for τ_E is set to 30 and that for $\omega(\mathrm{WR})$ is set to $C_E(t=60)$ (experimental datum). The maximum rate coefficients of pyruvate oxidation in muscle ($V_{x,\mathrm{PYR}\to\mathrm{LAC}}$) and lipolysis in adipose tissue ($V_{x,\mathrm{TG}\to\mathrm{FFA–GLR}}$) are estimated only in the female model, and initial estimates are set to male values from Ref. [68]. We noted that the parameter estimates are not determined uniquely, as different sets of parameters provide nearly the same goodness of fit. As a result, we extended the calibration step to include the use of *fmincon*, a gradient-based constrained optimization algorithm. Once we obtained a preliminary set of suitable parameters (say, p_1) using *fminsearch*, we ran *fmincon* with p_1 as the starting point and upper and lower bounds that were an order of magnitude larger ($p_1 \times 10$) and lower ($p_1/10$), respectively, until the algorithm converged. Final fitted parameter values are available in Tables S9 and S10 in Appendix C. Parameters for the male and female models are fitted separately to their respective set of experimental data. Differential equations are solved using *ode15s* (MATLAB 2020a), a variable-step, variable-order solver of orders 1 to 5. It is an implicit integration algorithm for stiff systems.

For a given substrate s, consider the weighted residuals:

$$\epsilon_s^2 = \sum_{i=1}^{N_s} \frac{\left(y_{s,i} - \hat{y}_{s,i}(\boldsymbol{\theta})\right)^2}{\sigma_{s,i}^2}, \tag{6.18}$$

where $y_{s,i}$, is the measured data point i for substrate s, $\sigma_{s,i}$ is the corresponding experimental standard error, N_s is the total number of data points for substrate s, and $\hat{y}_{s,i}(\boldsymbol{\theta})$ is the predicted value over the set of parameters $\boldsymbol{\theta}$. Therefore, the cost to minimize is given by:

$$\xi(\boldsymbol{\theta}) = \sum_{s\in S} \epsilon_s^2. \tag{6.19}$$

Set $S = \{\text{insulin, glucagon, GLC, LAC, GLR, FFA, TG, } \mathrm{R}_a, \mathrm{R}_d\}$ for male and female models. R_a is the rate of glucose appearance, also known as hepatic glucose production, and R_d is the rate of glucose disappearance, also known as tissue glucose disposal. In both models, epinephrine parameters are fitted independently, and the cost function simplifies

Table 6.4: Estimated parameters

Parameter description	Symbols	Compartment(s)	Equation(s)
Epinephrine parameters	$\tau_E, \omega(\text{WR})$	blood	(6.7)
Glucagon-Insulin controller[a]	$h, D, k_1, k_2, k_3, k_4, k_5$	pancreas	(6.8),(6.9)
GIR regulatory factors	$\lambda^G_{x,i}, \alpha^G_{x,i}$	liver, GI tract, adipose tissue	(6.12),(6.13)
Neural regulatory factors	$\lambda^E_{x,i}, \alpha^E_{x,i}, \gamma_x$	heart, muscle, GI tract, adipose tissue	(6.13),(6.14),(6.16)
Blood flow regulation	δ_x, τ_Q	heart, muscle, GI tract	(6.17)
Maximum rate coefficients[b]	$V_{x,\text{PYR}\rightarrow\text{LAC}}$, $V_{x,\text{TG}\rightarrow\text{FFA–GLR}}$	muscle, adipose tissue	(6.5)

[a] Decay rate D is set to 0.1, then h is calculated assuming steady state conditions with a blood glucose level of 5 mM [338].
[b] These maximum rate coefficients are estimated only for the female model. The direction of the change relative to the male values is described in Figure 6.2. Values for the male model are obtained from Ref. [68].

to Eq (6.18). Data represent plasma concentrations of hormones and substrates and are reported in Table C.11 in Appendix C. We used time series data that reflect dynamic concentrations throughout a cycling session. In particular, male model parameters were fitted to eight data points for each of epinephrine, insulin, glucagon, GLC, FFA, R_a and R_d, five data points for LAC and four data points for each of TG and GLR. Female model parameters were fitted to nine epinephrine data points, six LAC data points, five data points for each of R_a and R_d, and three data points for each of GLC and GLU. Male data for INS, FFA, and GLR were used to calibrate the female model since neither substrate concentrations nor substrate dynamics differ between the sexes [8, 16]. Each data set includes a data point for the initial resting concentration of the substrate. The data for both male and female models cover 60 minutes of exercise. Except for epinephrine, all datasets were used simultaneously for calibration. A list of estimated parameters is presented in Table 6.4.

When it comes to model calibration, the initial parameter guesses can have an impact on the resulting estimates and, more importantly, the mechanistic insight. We ran *fmincon*, as described above, with different initial parameter sets, namely $S_p = \{p_1 \cdot [0.1, 0.2, 0.5, 2, 5, 10]\}$,

to test the dependence of estimates on initial parameters. We found only minor differences in final estimates. Most importantly, the mechanistic insight, as discussed in the 'Results' section below, remained unchanged. This gives us confidence in the robustness of parameter estimates. Sensitivity analysis results are available in Appendix C.

6.3 Results

6.3.1 What are the regional hubs of sex-based differences in energy substrate utilization?

In this study, the respiratory quotient (RQ) is used to calculate the proportion of carbohydrates and lipids to whole-body ATP generation during exercise. RQ is the metabolic exchange of gas ratio at the cellular level that equals the ratio of CO_2 eliminated to oxygen consumed. According to the Fick principle, oxygen consumption = blood flow $\times$ arteriovenous oxygen difference, and similarly for CO_2 production. *In vivo*, it is a direct measurement obtained from the blood; *in silico*, we use the ratio between the CO_2 release rate into the blood compartment and the oxygen uptake rate for all tissues/organs. This offers a calorimetry measure of the amount of heat produced by metabolism or energy expenditure. In other words, RQ indicates which fuel source (e.g., carbohydrate or fat) is being metabolized to supply the body with energy [355]. Physiological values for whole-body RQ typically range between 0.7 and 1.0, and vary with substrate oxidation. The RQ of glucose is 1.0, whereas that of fat is 0.7 [356]. Our sex-specific dynamic models predict that the whole-body RQ increases from 0.80 at rest in both male and female models to 0.9 for the male model and 0.87 for the female model at the end of 60 minutes of moderate exercise. On average, during low-intensity exercise, RQ normally ranges between 0.80 and 0.88, when fatty acids are the primary fuel. The RQ increases to between 0.9 and 1.0 as exercise intensity increases and carbohydrates play a predominant role as fuel [321]. Based on this information, model results for moderate intensity exercise indicate that, while both male and female models rely primarily on carbohydrates for fuel, the relative contribution of fat is lower in the male model ($\overline{RQ}$ = 0.9, whole-body average value over 60 minutes) than in the female model ($\overline{RQ}$= 0.88, whole-body average value over 60 minutes), where a larger FFA fraction is used as fuel (see Table 6.5). This difference could initially be attributed to tissue weight differences (body fat content of 16% and 29.5% for male and female models, respectively), allowing females to burn more fat for fuel. However, when the adiposity in the male model is matched to that of the female model, our simulations show that RQ values do not change during exercise (Table 6.5), nor does the time-average

whole-body value ($\overline{\mathrm{RQ}} = 0.9$). This implies that, while the difference in RQ is small, it is a matter of sex. Females have higher lipolytic efficiency [314], meaning that they are better able to use their fat stores as fuel under stress conditions such as moderate-intensity exercise.

Table 6.5: Whole-body sex-specific RQ during exercise at 60% $\dot{\mathrm{V}}\mathrm{O}_{2\mathrm{max}}$.

Time (min)	rest	15	30	45	60
Male model	0.80	0.93	0.91	0.91	0.90
Male (F-matched) model[a]	0.80	0.93	0.91	0.91	0.91
Male (exp.)[b]	0.79 ± 0.02	0.92 ± 0.01	0.92 ± 0.02	0.90 ± 0.01	0.91 ± 0.01
Female model	0.80	0.90	0.89	0.88	0.87
Female (exp.)[b]	0.79 ± 0.02	0.89 ± 0.02	0.90 ± 0.02	0.89 ± 0.02	0.89 ± 0.02

[a] Male model with female-matched adiposity. The weight of adipose tissue represents 29.5% of the total body weight, as is the case for the female model.
[b] Data from [16] on the assumption that the respiratory exchange ratio (RER) reflected the systemic nonprotein RQ. Females and males completed a bicycle exercise test at a workload averaging $58 \pm 1\%$ of $\mathrm{V}_{\mathrm{O_2max}}$.

Figure 6.3 illustrates the relative contribution of carbohydrates and lipids to fuel utilization in response to a 60-minute exercise session. First, we note that whole-body RQ was computed as $\dot{\mathrm{V}}\mathrm{CO}_2/\dot{\mathrm{V}}\mathrm{O}_2$, where $\dot{\mathrm{V}}\mathrm{CO}_2$ and $\dot{\mathrm{V}}\mathrm{O}_2$ are the sums of CO_2 elimination and oxygen consumption rates in all tissues, respectively. Using indirect calorimetry methods as outlined by Roepstorff et al. [16], the relative contribution of fuel sources was determined:

$$\begin{aligned} \mathrm{RQ} = \frac{\dot{\mathrm{V}}\mathrm{CO}_2}{\dot{\mathrm{V}}\mathrm{O}_2} &= \frac{\sum_x Q_x (C_{a,\mathrm{CO}_2} - \sigma_{x,\mathrm{CO}_2} C_{x,\mathrm{CO}_2})}{\sum_x Q_x (C_{a,\mathrm{O}_2} - \sigma_{x,\mathrm{O}_2} C_{x,\mathrm{O}_2})}, \\ \%\ \text{carbohydrate in } \dot{\mathrm{V}}\mathrm{O}_2 &= \frac{\mathrm{RQ} - 0.7}{0.3} \cdot 100\%, \\ \%\ \text{lipid in } \dot{\mathrm{V}}\mathrm{O}_2 &= 100 - \%\ \text{carbohydrate in } \dot{\mathrm{V}}\mathrm{O}_2. \end{aligned} \tag{6.20}$$

Since lipids require more oxygen than carbohydrates in order to be oxidized, the increased oxygen consumption from lipids will indicate a lower RQ. The female model predicted a lower RQ during exercise compared with the male model, which is consistent with

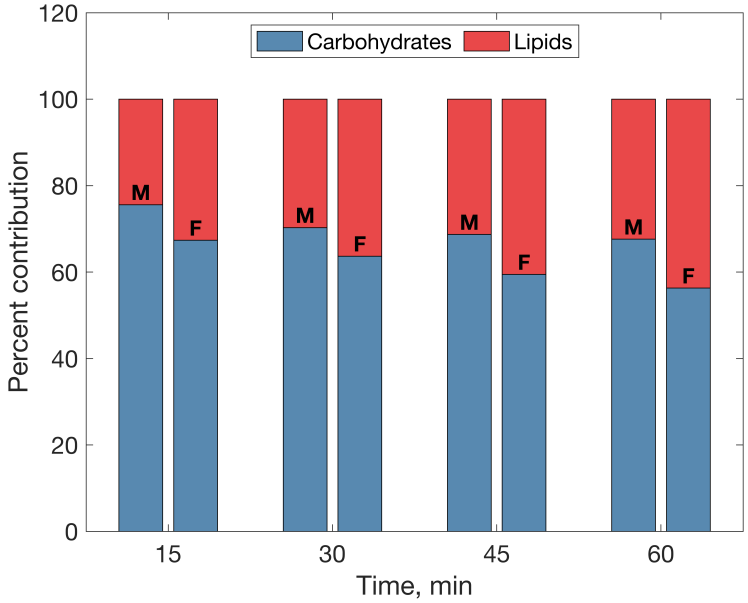

Figure 6.3: Relative contribution of fuel sources to whole-body ATP production. Percent contribution values are instantaneous values at 15, 30, 45 and 60 min, respectively. Moderate intensity exercise at 60% $\dot{V}O_{2max}$ (150W). **M**: male model; **F**: female model.

the experimental data and implies that females are oxidizing more lipids than males [16]. Specifically, the male model predicts 76% of energy from carbohydrates and 24% from lipids after 15 minutes, decreasing to 68% from carbohydrates and 32% from lipids after 60 minutes. The female model predicts 67% of energy from carbohydrates and 33% from lipids soon after the onset of exercise (15 minutes), decreasing to 56% from carbohydrates and 44% from lipids after 60 minutes. Percentage values are consistent with the literature that suggests higher lipid oxidation in females [14, 16, 321, 329]. Our mechanistic models make it possible to determine the RQ of each tissue. Table 6.6 shows organ/tissue specific RQ values during 60 minutes of moderate-intensity exercise. Carbohydrates are the principal fuel source for skeletal muscle in both males and females, as evidenced by high tissue RQ values (0.91 vs. 0.89). These results, however, suggest that carbohydrate oxidation and glycogen utilization are higher in men than in women. Besides skeletal muscle, our results show that adipose tissue is also a site of sex-based differences in fuel utilization. For both sexes, the RQ values are less than 0.8, indicating significant fat burning, with females being more so dependent on lipids than males (adipose tissue RQ of 0.71 vs 0.76 for female and male, respectively). Surprisingly, our models predict a marginal sex difference in liver RQ (0.73 for male vs 0.72 for female). Since the liver is the primary gluconeogenic organ,

we postulate that sex-specific compensatory mechanisms exist at the gluconeogenic and glycogenogenic steps in response to differences in substrate metabolism in skeletal muscle and adipose tissue across sexes. The benefit of such a mechanism would be better plasma glucose maintenance to avoid hyperglycemia when other fuel sources, such as lipids, are employed alongside glucose. Building on our observations of whole-body and tissue-specific RQ values for males and females, we now aim to identify underlying candidate physiological mechanisms in the liver that potentiate the role of skeletal muscle and adipose tissue as hubs of sex differences in substrate manipulation during exercise. Since our models do not represent direct effects of sex hormones, but rather indirect actions through sex differences in circulating levels of epinephrine and GIR, we will thus investigate the role of these specific hormones in the liver.

Table 6.6: Organ/tissue specific RQ over 60 min of exercise at 60% $\dot{V}O_{2max}$.

Organ/Tissue	Respiratory quotient (RQ)	
	Male	Female
Brain	1.0	1.0
Heart	0.87	0.87
Skeletal muscle	0.91	0.89
GI tract	1.0	1.0
Liver	0.73	0.72
Adipose tissue	0.76	0.71
Others	0.73	0.73
Whole-body	0.90	0.88

6.3.2 Is there a compensatory mechanism in the liver that drives sex differences in glucose production?

In order to understand the liver's response to the metabolic demand of exercise, it is important to first understand the role of sex differences in the hormones that drive hepatic responses: insulin, glucagon, and epinephrine. In particular, we recall that insulin and glucagon inhibit the production of each other and that epinephrine inhibits the production of insulin during exercise; see Eqs (6.8) and (6.9). Figure 6.4 illustrates the dynamic responses of plasma insulin, glucagon and epinephrine to an increase in work rate from a resting state. In comparison to males, females have lower levels of circulating epinephrine

at rest and during exercise. The magnitude of sex differences in epinephrine levels is exacerbated during exercise. At rest, our models predict that males have 67% higher epinephrine levels than females and up to 175% higher levels after 60 minutes of exercise. This time course effect for epinephrine is also seen in experimental studies [8, 14]. In Ref. [8], the authors reported epinephrine concentrations 200% higher in men than in women after 90 minutes of moderate exercise. When it comes to pancreatic hormones, there is no sex difference in insulin concentration during exercise, except at rest where women have higher insulin levels than men [8]. Given the large gap in epinephrine concentration between the sexes, insulin sensitivity to epinephrine would have to be higher in women to justify maintaining similar insulin levels to men during exercise (see k_5 in Table C.9 in Appendix C). Glucagon levels rise in both models during exercise, but female glucagon levels are higher than male values throughout exercise. Higher absolute levels of glucagon in females are consistent with experimental findings from Refs. [8, 14]. Consequently, the female model has a higher GIR both at rest and during exercise; see Figure 6.5a.

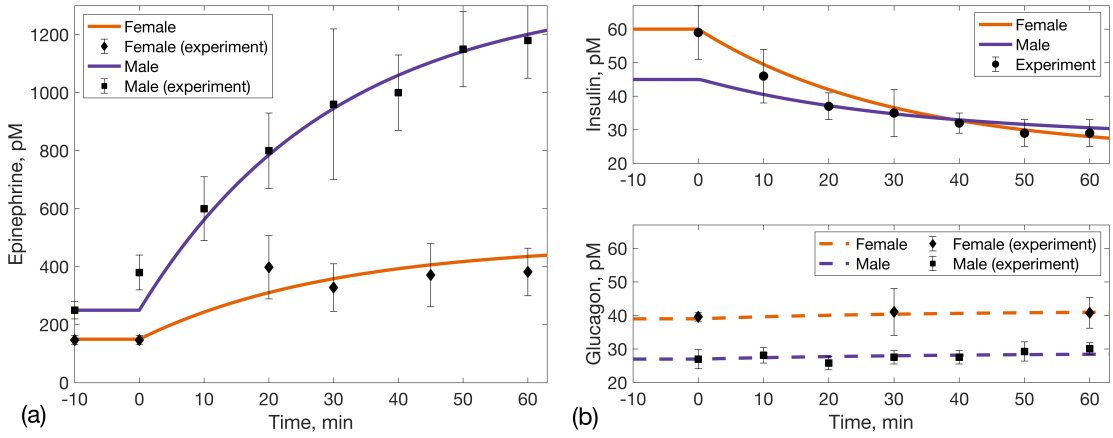

Figure 6.4: Dynamic responses of (a) epinephrine, (b) insulin and glucagon to a step increase in work rate (150W) during 60 min exercise. Data from [7, 8]. Only one dataset [7] is used for insulin concentration as there are no significant sex differences between the sexes.

Exercise induces hormonal changes through the GIR, which modulates metabolic reaction rates in the liver. As a result, whole-body glucose production increased about 2 fold for the female model and about 3 fold for the male model by the end of exercise (Figure 6.6). The liver produces glucose at rest from glycogenolysis and gluconeogenesis equally [7]. During exercise net hepatic glycogen breakdown increased from 0.38 to 1.4 mmol/min in the male model and from 0.38 to 0.83 mmol/min in the female model. Net

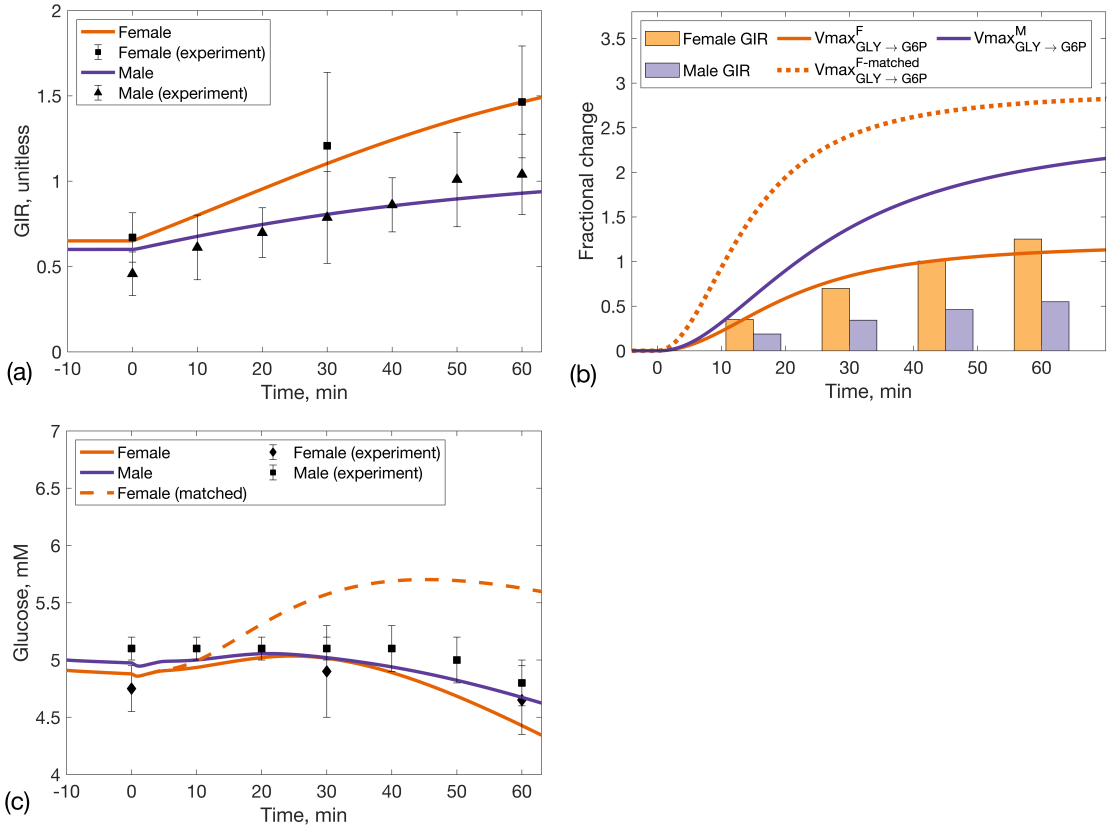

Figure 6.5: (a) Glucagon-insulin ratio (GIR) response to an increase in work rate (150W) from rest at 0 min. The simulations ranging from -10 to 0 min show steady-state responses; (b) fractional change in GIR and in maximal rate of glycogenolysis ($\mathrm{Vmax}_{\mathrm{GLY}\rightarrow\mathrm{G6P}}$) in the liver in response to a step increase in work rate (150W) from resting state at 0 min. Fractional change refers to the ratio of the change in the quantity to its original value. Bars represent instantaneous values and lines represent dynamic responses. (c) Whole-body glucose homeostasis during exercise. Data from exercise experiments in humans [7, 8].

hepatic gluconeogenesis increased from 0.35 to 0.51 mmol/min in the male model and from 0.35 to 0.40 mmol/min in the female model. Effectively, this suggests that most of glucose production during exercise results from glycogenolysis. These results support experimental reports that men rely more on stored glucose during exercise compared with women [14, 321, 329]. Since glycogenolysis and gluconeogenesis are facilitated by the GIR, the rise in glucagon during exercise is thought to be the driver of these reaction rates [8].

However, this may not be the full explanation, as the simulations below suggest. GIR is higher throughout exercise in females than males, so we would normally expect higher rates of glucose production by the female liver. However, this is not true. Figure 6.5 shows fractional changes in GIR and in maximal rates of glycogenolysis ($\text{Vmax}_{\text{GLY}\rightarrow\text{G6P}}$) in response to exercise. Despite the male GIR's slower increase over time, the rate of glycogenolysis after 60 minutes of exercise is three times higher than its rest value. The rate of glycogenolysis in the female liver, on the other hand, is about two times the rest value. As represented in the parameters of our models, we have assumed that females are less sensitive to the glycolytic effects of pancreatic hormones than males (see Table C.10 in Appendix C). Thus, differences in carbohydrate utilization during moderate exercise may be primarily related to sex-based differences in tissue sensitivity rather than circulating levels of hormones such as glucagon, insulin, and epinephrine.

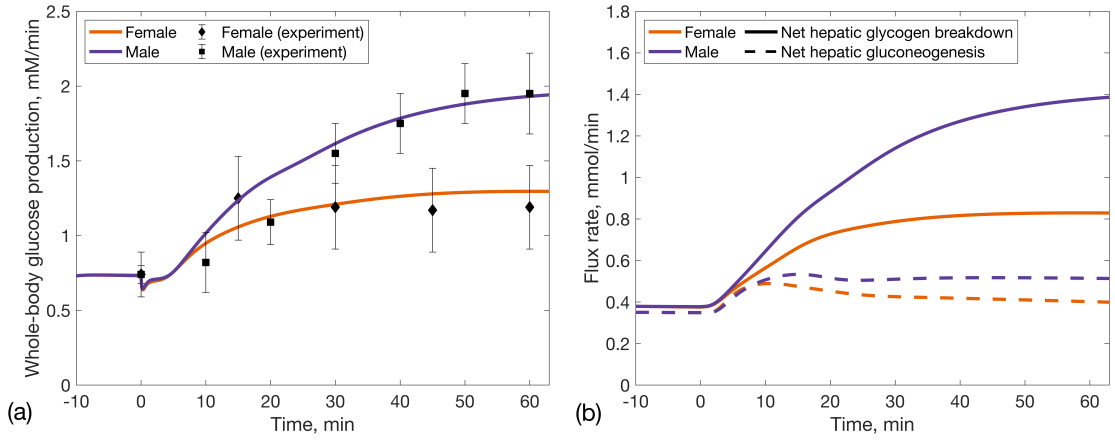

Figure 6.6: Dynamic responses of (a) whole-body glucose production, (b) net hepatic glycogen breakdown, and net hepatic gluconeogenesis to an increase in work rate (150W) during 60 min exercise. Net hepatic glycogen breakdown is defined as the difference in metabolic rates between glycogenolysis (breakdown of glycogen) and glycogenesis (production of glycogen) in the liver. Net hepatic gluconeogenesis is defined as the difference between gluconeogenesis II (production of glucose-6-phosphate) and glycolysis II (utilization of glucose-6-phosphate) in the liver.

To investigate this question further, we matched female liver hormonal control parameters for glycogenolysis ($\lambda^G_{x,GLY\rightarrow G6P}, \alpha^G_{x,GLY\rightarrow G6P}$, with $x :=$ liver) to male values. These control parameters represent tissue sensitivities to changes in the GIR; see Eq (6.12). Results are shown in Figure 6.5b. Assuming identical hepatic sensitivity to GIR in males and females, higher GIR levels for females translate to higher maximal rates of glycogenoly-

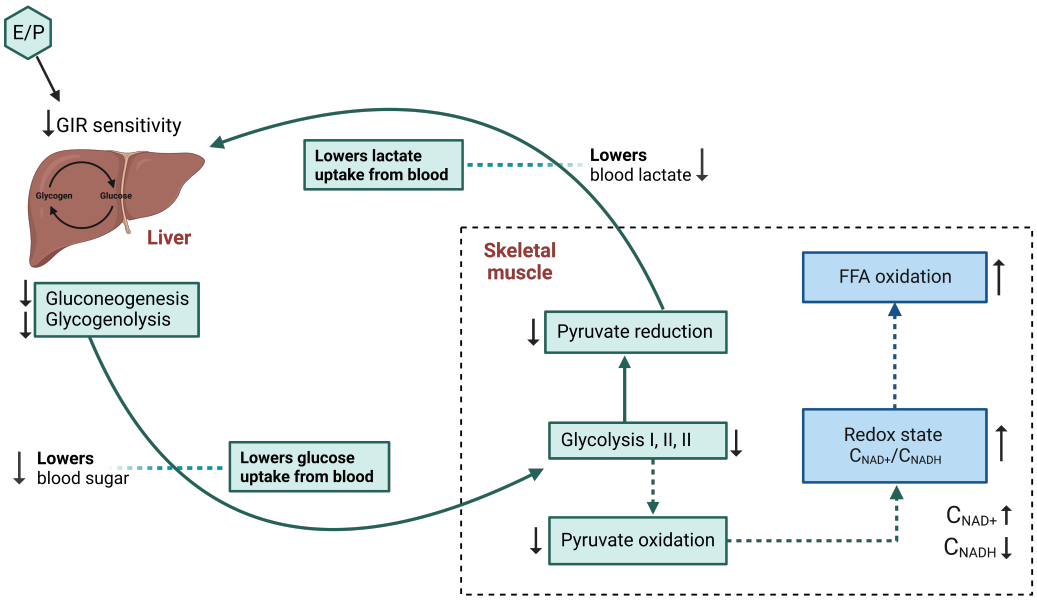

Figure 6.7: Hypothetical compensatory mechanism between the liver and skeletal muscle in females. The figure illustrates the direct (green boxes) and indirect (blue boxes) effects of female sex hormones (E, estrogens; P, progesterone) on metabolic processes during exercise. Solid arrows indicate the Cori Cycle, while dotted arrows represent the compensatory mechanism for fat oxidation.

sis than males, meaning higher glucose production. In this case, blood sugar rises above euglycemic levels for the female model, as shown in Figure 6.5c. Our *in silico* matching experiment supports the hypothesis that sex differences in hepatic glucose production are driven by tissue sensitivity to hormones rather than absolute hormone concentrations.

Another factor that contributes to females lower glucose production during exercise may be the engagement of the female liver in a liver-muscle crosstalk. That crosstalk may act as a compensatory mechanism for glycogen sparing, thereby preventing the higher GIR in females from over-activating glucose-producing pathways and instead promoting fat oxidation in working muscles. Our proposed mechanism is shown in Figure 6.7. Reduced glycogenolysis during exercise reduces gluconeogenesis and thus blood glucose concentration. As the arteriovenous difference in glucose decreases, so does the net exchange of glucose with other tissues. Skeletal muscle consumes the most glucose during exercise and is the most affected by decreased hepatic glycogenolysis. When less glucose enters the muscles, all stages of glycolysis (glycolysis I, II, and III) slow down. As a result, both pyruvate reduction (PYR→LAC) and pyruvate oxidation (PYR→ACoA) decrease. The latter is

an important step in the utilization of NADH and the production of NAD^+. NADH and NAD^+ concentrations decrease and increase, respectively, as pyruvate oxidation decreases. The increase in NAD^+ concentration stimulates fatty acid oxidation. Furthermore, decreasing pyruvate reduction, a critical step in the cori cycle, reduces lactate delivery from muscles to the liver. The liver uses lactate as a gluconeogenic precursor, and a decrease in blood lactate directly affects glucose production, further lowering blood sugar. This creates a positive feedback loop for fatty acid oxidation. In fact, fatty acid oxidation is also increased in the heart, GI tract, and adipose tissue following the decrease in pyruvate reduction, but changes are most significant in skeletal muscle.

We further suggest that female sex hormones may regulate liver sensitivity, which would explain why glycogenolysis and gluconeogenesis are less engaged during exercise in females than in males. Consistent with our observations, it was observed that female sex hormones cause a decrease in glycogenolysis, and that estrogen specifically decreases gluconeogenesis [341]. Additionally, the combination of estrogen and progesterone can decrease glucose production in response to glucagon [341]. The added value of our results lies in identifying a potential candidate compensatory mechanism to explain how sex hormones affect glucose production and utilization during exercise. With this mechanism in place in the female model, both models are able to maintain normoglycemia during exercise (see Figure 6.5). It is thus possible that the sex difference in exercise-related glucose production (and utilization) is only apparent in the setting of low hepatic glycogen stores, which occurs here because the model is initialized using overnight-fasted conditions for all tissues, and that differences in glucose kinetics become apparent only when hepatic stores are further depleted with moderate exercise [8]. Athough sex difference in carbohydrate use have been linked to differences in gluconeogenesis and glycogenolysis in the liver, it is still debated whether the significant increase in lipid metabolism in women during exercise is due to a preference for oxidation of plasma FFAs or intramyocellular lipids [321, 329]. We explore this question next.

6.3.3 Is increased lipid metabolism in females owing to the breakdown of intramyocellular lipids or plasma FFA oxidation?

Tissue-specific RQ values indicated that adipose tissue and skeletal muscle show marked sex differences in substrate utilization. In addition, our study of hepatic glucose production has shown that the female liver, due to a lower sensitivity to GIR, saves more hepatic glycogen than the male liver in order to promote the use of lipids by the other organs. Here, we are interested in the consequent dynamics of carbohydrate and lipid utilization in skeletal muscle and adipose tissue.

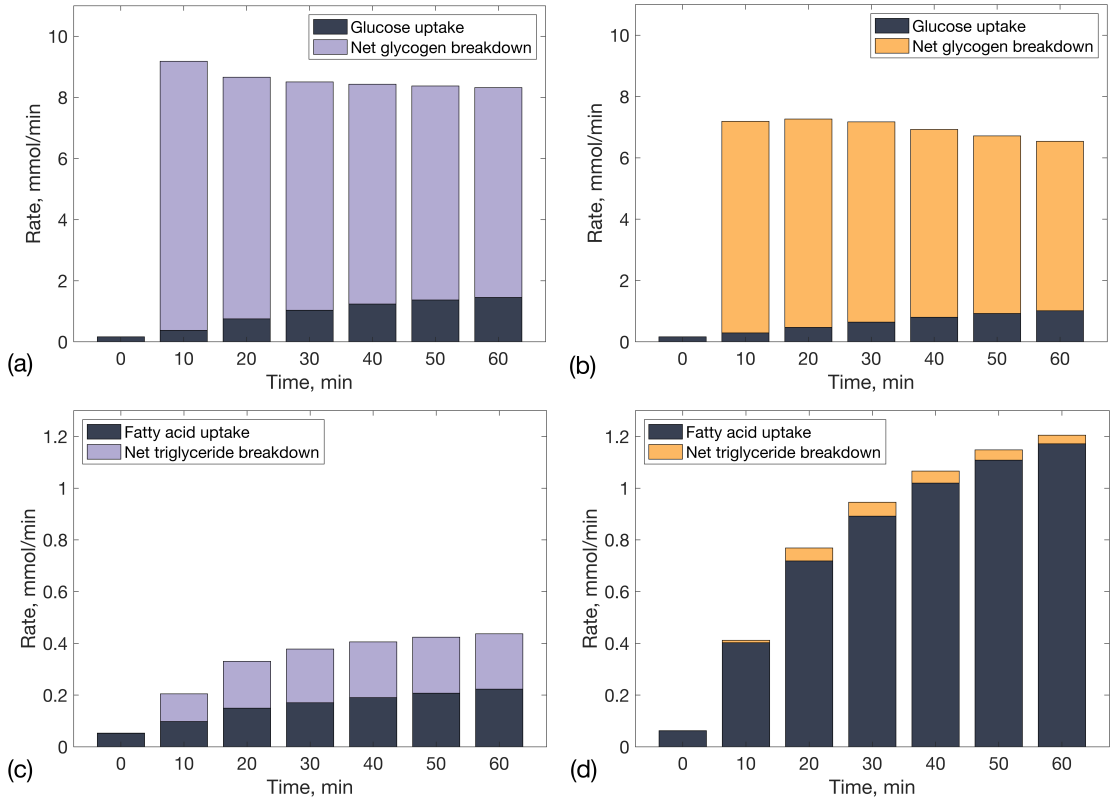

Figure 6.8: Dynamic response of intramuscular glucose uptake, net glycogen breakdown, FFA uptake and net triglyceride breakdown to an increase in work rate (150W) during 60 min exercise. (a) Male, carbohydrate utilization; (b) Female, carbohydrate utilization; (c) Male, fat utilization; (d) Female, fat utilization. Glucose uptake is defined as the uptake rate of glucose in the muscle. Net glycogen breakdown is defined as the difference in metabolic rates between glycogenolysis (breakdown of glycogen) and glycogenesis (production of glycogen) in the muscle. Net triglyceride breakdown is defined as the difference in metabolic rates between the utilization of triglycerides and the production of triglycerides in the muscle.

Starting with glucose turnover in skeletal muscle, Figs. 6.8a and 6.8b show that glucose uptake and net glycogen breakdown are both lower in the female model compared to the male model. On the one hand, the rate of glucose uptake into the muscles in the male model increases from 0.16 mmol/min at rest to 1.4 mmol/min after 60 minutes, while in the female model it goes from 0.16 mmol/min to a maximum of 1.0 mmol/min. Net glycogen breakdown, on the other hand, is highest in the male model shortly after the start

of exercise (9 mmol/min), then falls to 6.8 mmol/min after 60 minutes. Comparatively, net glycogen breakdown goes from 7 mmol/min to 5.5. mmol/min in the female model. Specific to skeletal muscle is the fact that glycogenolysis is promoted by epinephrine. Thus, the quantitative difference in net glycogen breakdown is a direct result of the fact that epinephrine is lower in females. Intramuscular FFA uptake is higher during exercise in females than males, while net TG breakdown is lower in females (Figs. 6.8c and 6.8d). Notably, FFA uptake in the female model increases from 0.06 mmol/min at rest to 0.9 mmol/min after 30 minutes of exercise. In contrast, after 30 minutes, the male model's FFA uptake rate increases from 0.05 mmol/min to 0.17 mmol/min. On average over 60 minutes, plasma FFAs contribute 45% and 89% of total fat oxidation for male and female models, respectively, with the balance owing to other fat sources. The male average is consistent with data from Refs. [357–359], in which plasma FFAs count for 40% to 60% of total fat oxidation in men; data specific for women is scarce. Throughout exercise, males have a higher rate of TG breakdown than females; however, the sex difference is not as pronounced as it is for FFA. Since each TG contains three fatty acids, it significantly reduces the dependence on plasma FFAs for males. There is evidence of differing amounts fat oxidation between the sexes, with females oxidizing more fats, but researchers are unclear whether the source is intramyocellular lipids (IMCL) or plasma FFAs [324, 360]. Our results suggest that the mechanism for increased fat oxidation is increased FFA uptake in the muscle.

Adipose tissue is the primary source of plasma FFAs. In the female model, the whole-body lipolysis rate increases from 0.29 mmol/min at rest to 0.86 mmol/min during the exercise session. In the male model, the total rate of lipolysis increases from 0.27 mmol/min to 0.64 mmol/min. Women have a higher rate of lipolysis in adipose tissue at rest and during exercise than men (see Figure 6.2). As a result, females have increased lipid availability and oxidation of FFAs by tissues such as skeletal muscle. Figure 6.9 shows the contribution of organs and tissues to the total rate of lipolysis during exercise. In the female model, adipose tissue lipolysis predominates, whereas muscle lipolysis prevails in the male model. This implies that women rely more on FFA from adipose tissue, whereas men rely more on IMCL stores. Muscle, splanchnic region, and adipose tissue contribute 26%, 20%, and 54%, respectively, to whole-body lipolysis in the female model. In the male model, muscle, splanchnic region, and adipose tissue contribute 59%, 15%, and 26%, respectively. These values are averages over 60 minutes of exercise. The splanchnic region includes the liver and GI tract; the muscle region contains the heart and skeletal muscle. We note that the heart's contribution to whole-body lipolysis is minor (data not shown).

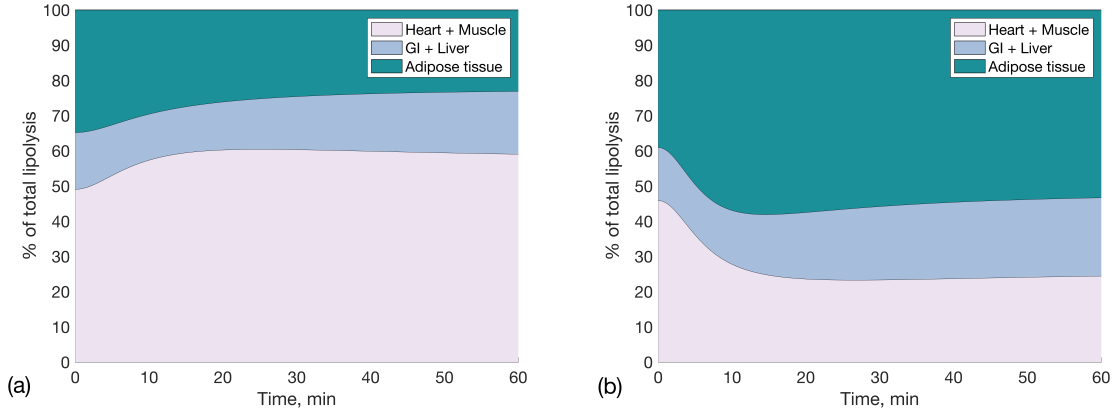

Figure 6.9: Fractional contribution of different organs and tissues to whole-body lipolysis rate for (a) Male, (b) Female. Total lipolysis = $\sum_x \phi_{x,\mathrm{TG}\rightarrow\mathrm{FFA+GLR}}$ where x is heart, skeletal muscle, liver, GI tract, and adipose tissue.

6.4 Discussion

We developed sex-specific whole-body models of energy metabolism to (1) investigate sex-based disparities in substrate utilization during moderate-intensity exercise and (2) identify candidate underlying physiological mechanisms. Our main results are summarized as follows.

- Compared to the female model, the male model oxidizes less lipids during exercise. Averaged over 60 minutes of exercise, the female model predicted a 10% higher contribution of lipids to whole-body ATP production.
- The shift in the female model towards lipid metabolism originates in the liver. The female liver is resistant to GIR-mediated glycogenolysis, thus leading to the preservation of hepatic glycogen. The resulting decrease in arterial glucose promotes FFA oxidation by working muscles via NAD^+ and NADH.
- The primary fuel source for skeletal muscle in the female model is the predominant oxidation of plasma FFAs and not intramyocellular lipids. The reverse is true for the male model.

In experimental studies, when compared to women, men rely significantly more on whole-body carbohydrate oxidation to sustain low- to moderate-intensity exercise [14, 321]. Recent meta-analyses by Cano and colleagues [329] assessed substrate use during moderate

aerobic activity in healthy men and women of reproductive age. Their findings support sex differences in substrate utilization: in sedentary populations, men are more carbohydrate-dependent while women are more fat-dependent, and the greater oxidation of carbohydrates in men persists in athletic populations. Our results for moderate intensity exercise indicate that the relative contribution of fats, primarily FFAs, is indeed higher in women. Whole-body RQ values over 60 minutes are 0.88 for the female model and 0.9 for the male model (see Table 6.5). A closer look at tissue-specific RQ values (Table 6.6) shows that skeletal muscle and adipose tissue are major sites of sex differences: male skeletal muscle burns more glucose for energy than female skeletal (RQ of 0.91 for male vs. 0.89 for female). In particular, FFAs released from adipose tissue lipolysis are mobilized by working muscles in the female model for energy.

While sex differences in carbohydrate and lipid metabolism during exercise have been widely studied, fewer studies have investigated the role of sex differences in tissue-specific substrate utilization. Sex hormones are thought to be significant biological contributors to sex-based variations in substrate use. Women, in particular, have lower muscle fatigability and a metabolic advantage when exercising at the same intensity as men. Both estrogen and progesterone have been shown to influence metabolic responses, ostensibly in different ways [329]. In animal models, estrogen stimulates lipolysis and increases fatty acid availability [361–364], while lowering the rate of gluconeogenesis and sparing musculoskeletal and hepatic glycogen [364, 365]. Controversially, data collected during the luteal phase (when progesterone predominates) demonstrate reduced muscle glycogen utilization during exercise compared to the follicular phase (when estrogen predominates) [321]. Progesterone has also been shown to counteract the lipolytic actions of estrogen and decrease the availability of fatty acids [364, 366]. Although a large amount of evidence suggests that progesterone has an anti-estrogenic effect [360, 364, 367], further research on progesterone is needed to understand its effects on substrate use at different phases of the menstrual cycle. The physiological processes through which sex hormones regulate substrate metabolism are attributed to both direct and indirect actions. The former are mentioned above, and the latter are those ascribed to their role as facilitators for other hormones (e.g., epinephrine, glucagon) that enhance lipolysis as well as glycogenesis at rest and attenuate glycogenolysis during exercise. For instance, women have lower epinephrine concentrations than men, which is thought to be due to estrogens. In females 17β-estradiol is associated with a reduction in plasma epinephrine concentrations during exercise [14, 323]. In addition, women have higher absolute glucagon levels when compared to men [8]. Greater glucagon levels have been found in the luteal phase of the menstrual cycle compared to the follicular phase [341], and progesterone receptors are present on pancreatic α-cells [368], implying that progesterone may augment tonic glucagon secretion [8].

Given the lack of an insulin sex difference during exercise (Figure 6.4), our models suggest that glucagon is the hormone responsible for driving sex differences in liver metabolism via the GIR. Since glycogenolysis and gluconeogenesis are regulated by the GIR, the rise in glucagon during exercise is thought to be the driver of these reaction rates [8]. Yet, despite a higher GIR throughout exercise in females than males, the female liver produces less glucose per unit of time (Figure 6.6). We hypothesized that the female liver initiates a compensatory mechanism for glycogen sparing, thus causing a shift to lipid utilization by other organs. As seen on the flow chart (Figure 6.7), reduced glycogenolysis leads to reduced arterial glucose availability and lower uptake by other organs. Glucose concentration in tissues leads the glycolysis cascade to produce pyruvate. So the lower uptake of glucose by tissues causes a slow down of pyruvate production and downstream pyruvate oxidation. This explains why the female model oxidizes less carbohydrates than the male model. The shift to FFA oxidation, however, is an indirect consequence of this. The rate of pyruvate oxidation, i.e., $\phi_{x,\mathrm{PYR}\rightarrow\mathrm{ACoA}}$, contributes to the production of NADH and the utilization of NAD^+. Hence, the redox ratio $\mathrm{RS}^- = C_{\mathrm{NAD}^+}/C_{\mathrm{NADH}}$ is higher in the female model compared to the male model since $\phi_{x,\mathrm{PYR}\rightarrow\mathrm{ACoA}}$ is lower in females. The redox state RS^- activates FFA oxidation in the heart, skeletal muscle, liver and adipose tissue. Therefore, the lower rate of glycogenolysis in the liver directly affects hepatic glucose production and glycolysis everywhere else, but also indirectly activates fat mobilization and oxidation in several other tissues, skeletal muscle in particular. This chain of events is independent from the exercise-induced lipolysis in adipose tissue and GI tract. We call this mechanism compensatory because the reduction in glucose-producing pathways leads to an increase in lipid-utilizing pathways. Female sex hormones, possibly estrogens, may be the starting point of the compensatory mechanism marked by hepatic GIR resistance, which would explain why certain processes are less engaged during exercise in women than in men.

An important consideration is that the relative contribution and source of carbohydrates and lipids utilized to fuel exercise are determined by the intensity and duration of the exercise bout [321]. Fat oxidation contributes the most during moderate-intensity exercise (40-65% $\dot{\mathrm{V}}\mathrm{O}_{2\mathrm{max}}$), accounting for 40-60% of total energy expenditure [358, 359]. In this study, fat oxidation accounted for an average of 30% of whole-body energy expenditure in the male model and 40% in the female model. This quantitative difference is mediated by sex differences in skeletal muscle substrate origin and utilization. Figure 6.9 shows that in the male model, skeletal muscle is the primary site of lipolysis, whereas in the female model, adipose tissue serves as a lipolysis hub. As a result, skeletal muscle in the female model relies heavily on plasma FFAs for fuel during exercise. The work of Devries et al. [321] has shown that women have a higher area density of IMCL than men. Our female model represents this sex difference with 28% more muscle TG density (mmol/l) than the

male model [321]. Despite this IMCL density advantage, our results suggest that women may be less efficient in utilizing these IMCL stores because they are clearly dependent on plasma FFAs. Adipose tissue is the primary source of plasma FFAs, and the female model has a higher rate of lipolysis in adipose tissue at rest and during exercise than the male model (Figure 6.2). Therefore, the female model has increased lipid availability and oxidation of FFAs by tissues such as skeletal muscle. We recall that lipolysis in adipose tissue is influenced by both epinephrine and GIR levels. Therefore, in addition to the sex difference in basal lipolysis rates, the higher GIR in females further stimulates adipose tissue lipolysis. However, in skeletal muscle, lipolysis is modulated by epinephrine alone. This may be the reason why men use IMCL more. Indeed, our male model represents both the higher muscle mass in males (Table 6.3) and the significantly higher epinephrine concentrations. It follows that the *in situ* breakdown of TGs into FFAs would be higher in males than in females as the drastic increase in epinephrine during exercise would potentiate the activation of lipolysis in working muscles in males.

A number of sex comparison studies in human subjects [316–318, 360, 369] found that women oxidize proportionately more lipids and fewer carbohydrates during submaximal endurance exercise per relation to men. Importantly, these studies controlled for menstrual cycle timing and length, workout duration, pairing between sexes for oxygen consumption relative to lean body mass, and measurement and provision of isoenergetic diets. It is unclear whether these sex differences were driven by differences in sex hormones or by known sex differences in fat mass and energy intake [370], even when the latter two are expressed relative to lean body mass [317, 318, 360, 369]. Consistent with the earlier claim that female sex hormones promote lipolysis, lipid availability, and lipid oxidation, we hypothesize that female sex hormones increase lipolysis rates in response to epinephrine and GIR to increase uptake of FFA into skeletal muscle in women (Figure 6.8). It is this increased intramyocellular uptake of FFAs, and subsequent oxidation, that leads to greater lipid utilization during submaximal endurance exercise in women than in men. We note, however, that carbohydrates fuel the first phase of exercise in both models, while fat oxidation becomes a more important source of energy after 30 minutes (see Table 6.5). These results suggest that women may be more sensitive to the lipolytic effects of pancreatic hormones and catecholamines like epinephrine, whereas men may be more sensitive to the glycolytic effects of hormones. Different patterns of adrenergic receptor activation in men and women may be responsible for the disparities in lipolysis regulation. Moderate-intensity exercise, in particular, stimulates both β_1 (lipolysis-activating) and α_2 (lipolysis-inhibiting) receptors in men, but only β_1 receptors in women [317, 328, 371, 372]. We conclude that during exercise, men have increased carbohydrate oxidation responses, but women have increased lipolytic responses. Women may compensate for decreased

autonomic nervous system activity (i.e., epinephrine) during exercise through increased lipolytic responses.

In this sex-specific model of whole-body metabolism during exercise, each tissue is treated as a perfectly mixed tissue-capillary compartment with no separate mitochondrial region. The metabolic modulators ATP, ADP, NADH, and NAD+ are essential regulators of cellular respiration, with distinctly different concentrations in the mitochondrial domain [72]. This consideration becomes particularly important in working muscles. As a result, the model may not be suitable for predicting heavy high intensity exercise or modeling metabolic adaptations during prolonged endurance exercise. Another limitation of our models is that the pancreas is abstracted to two hormones, insulin and glucagon, and is modelled as a rein controller. Alternative formalisms can be based on Michaelis-Menten type expressions that apply to the relationship between blood glucose concentrations and pancreatic hormone secretion [154]. A circumstantial limitation is the scarcity of data on exercise in women. There are few studies that control for menstrual cycle timing and length, workout duration, sex pairing for oxygen consumption relative to lean body mass, and provision of isoenergetic diets. This reduces the amount of data available for determining sex differences in substrate metabolism and informing model development and parameter estimation for kinetic reactions. Future research should focus on the regional kinetics of substrate to better understand sex-based differences in substrate use. Although the emphasis is frequently on patterns of substrate utilization throughout the body, future research should include organ and histological data. Moreover, up-to-date information on the basal metabolic state of women is required for model development. In other words, a sophisticated *in vivo* body composition analysis (BCA) that will improve on the *1975 Reference Man*, which was last updated in 2002 by the International Commission on Radiological Protection (ICRP) [373], is required. Such an analysis should provide for new estimates of average body weight, organ weight, fat mass, lean mass, and skeletal muscle mass in men and women, taking into account age and ethnicity. A BCA should also include data on substrate concentrations in resting tissues. Importantly for experimental research, it is necessary to standardize how data is normalized by weight, height, or height^2 [374]. The normalization is necessary to understand how the size of individual body components relates to metabolism [375]. With regard to endurance exercise, female-specific experimental data on the rate of utilization and production of key substrates such as FFA, TG, glycerol, and lactate at the organ level, as well as the rate of oxidation of non-plasma and plasma-derived FFA, would be beneficial for model calibration. Furthermore, data on changes in substrate concentrations (glycogen in the liver and skeletal muscle, TG in adipose tissue and skeletal muscle) would allow validation of model predictions at the tissue level. Most importantly, these studies will need to control for pre-test dietary conditions,

menstrual phase, training duration and intensity relative to peak O2 consumption, exercise modalities (e.g. walking, cycling, etc.), and outcome measures (i.e., raw, percentage normalized, or normalized to body composition).

6.5 Conclusions

With the use of sex-specific metabolic modifications that link sex differences to cellular metabolism in the organs, we were able to successfully extend a previously developed model of whole-body metabolism during exercise. We obtained good agreement with experimental data for moderate intensity exercise. Our models predict that women oxidize significantly more lipids and significantly less carbohydrates than men, and we identified candidate underlying physiological mechanisms for this sexual dimorphism in substrate utilization. The female liver, in particular, is resistant to GIR-mediated glycogenolysis, resulting in hepatic glycogen preservation. The resulting decrease in arterial glucose promotes FFA oxidation by working muscles via NAD+ and NADH. Moreover, in contrast to the male model, where intramyocellular lipids serve as the principal fuel source for skeletal muscle, the female model relies mostly on plasma free fatty acids for this purpose.

Chapter 7

Modelling sex-specific whole-body metabolic responses to feeding and fasting

Abstract

Men exhibit a preference for carbohydrate metabolism, whereas women tend to favor lipid metabolism. Significant sex-based differences in energy oxidation are evident across various metabolic states, including fasting and feeding. While some of these differences can be attributed to variations in body composition—such as increased fat mass in women and higher muscle mass in men—there are also inherent disparities in metabolic fluxes. For instance, women exhibit increased rates of lipolysis independent of body composition. However, there remain gaps in our understanding of how sex influences the metabolism of specific organs and how these differences manifest at the systemic level. To address some of these gaps, we developed a sex-specific, whole-body, multi-scale model of metabolism during feeding and fasting. Our model represents healthy young adults (male and female) and integrates cellular metabolism in organs with whole-body responses following various mixed meals, particularly high-carbohydrate and high-fat meals. We explored sex-related variations in metabolic responses during both the absorptive and postabsorptive phases following meals. Our model predicted that sex-related metabolic differences observed at the systemic level are driven by variations in nutrient storage and oxidation patterns in the liver, skeletal muscle, and adipose tissue. We hypothesized that sex differences in hepatic glucose output during short-term fasts are partly influenced by variations in free fatty acids, glycerol, and glycogen handling. We also identified a candidate mechanism, possibly more prevalent in the female liver, where lipids are redirected toward carbohydrate metabolism to support hepatic glucose production. Integrating sex-specific data and parameters into multi-scale frameworks holds promise for enhancing our understanding of human metabolism and its modulation by sex.

7.1 Introduction

Obesity and related metabolic disorders, such as type 2 diabetes, have emerged as worldwide epidemics [376, 377]. Nutrition has been identified as the primary modifiable factor that can be addressed to mitigate the escalating prevalence of obesity and metabolic diseases. Nutritional consumption of humans composes largely of carbohydrates, fat, and proteins. A key factor in determining the ideal nutritional intake is the relative efficiency of substrate oxidation and conversion. Carbohydrates are preferentially oxidized over fats, which helps stabilize blood glucose levels. While carbohydrate consumption acutely boosts carbohydrate oxidation, it usually only minimally increases *de novo* lipogenesis. In humans, the storage capacity for carbohydrates is limited, but that for adipose tissue is much more

extensive; as a result, fat storage is favored when there is excessive caloric intake. The high energy density of fats, providing more than twice the energy per gram compared to carbohydrates or protein, may further contribute to weight gain if not offset by increased energy expenditure.

One significant aspect influencing whole-body metabolism is the role of sex. The impact of sex on metabolic processes is a burgeoning field of research, and recent experimental evidence underscores its importance [321, 378–380]. Sexual dimorphism is observed not only in body composition but also in metabolic rates, substrate utilization, and hormonal regulation [303, 378, 381–386]. Sex differences in metabolism manifest across various physiological conditions: fasting [70, 387], feeding [14, 381, 388], hypoglycemia [328, 380, 389], exercise [3, 69, 321], and more [309–311, 313]. While both sexes exhibit general responses such as hepatic glycogenolysis, gluconeogenesis, and adipose tissue lipolysis, quantitative distinctions in substrate utilization are notable [309–311]. Studies have revealed a propensity for carbohydrate metabolism in men and lipid metabolism in women, highlighting significant sex-based differences in fuel oxidation during different metabolic states [14, 317, 318, 320]. The distribution of adipose storage exhibits distinct sexual dimorphism, with men tending to accumulate more fat in the android region and women favoring the gynoid region [378]. Apart from adipose tissue, lipid storage occurs in various tissues, including the liver and skeletal muscle, exhibiting sex-specific patterns. Women tend to demonstrate greater lipid storage in muscle [321, 381], while men display more pronounced storage in the liver [388]. These sex-based disparities influence resting, postprandial, fasting, and exercise metabolism, contributing to differences in substrate utilization and the risk of metabolic diseases [3, 378]. Understanding the role of sex in mediating metabolic responses can inform tailored nutritional guidelines and therapeutic strategies, potentially enhancing glycemic control and mitigating the risk of metabolic disorders in both sexes. However, despite the acknowledged significance of sex-specific differences, integrating these nuances into comprehensive models has been a challenging yet necessary endeavor.

Many mathematical models address metabolism, spanning various scales and facets crucial for studying energy metabolism and whole-body homeostatic balance [3, 66–77]. For instance, there exist well developed compartment models of glucose homeostasis. Cobelli et al. [390] developed the artificial pancreas for type 1 diabetes mellitus—a simulator model of the glucose-insulin system. Approved by the Food and Drug Administration in 2013, this model can be used as a substitute for preclinical trials for select insulin treatments. An improved iteration, transitioning from simulating a single meal to a full day, was introduced in 2018 by Visentin et al. [391]. There are also computational models of glucose homeostasis that are liver-centric: linking the liver to other organ compartments [392, 393] with the goal of investigating how food composition influences hepatic lipid synthesis and could

lead to the development of different types of diabetes [394, 395]. Despite their instrumental role, these compartment models often adopted a coarse-grained approach. In recent years, stoichiometry-based mechanistic models have become popular, employing a rate equation for each metabolic reaction within a cell or organ [66, 68, 71–75]. For instance, Kurata [66] proposed a comprehensive whole-body model, incorporating enzyme and transporter reactions alongside hormonal regulation in postprandial and postabsorptive states. Panunzi et al. [396] extended a whole-body model initially proposed by Sorensen [397] by incorporating food intake. Sluka et al. [76] proposed a liver model for acetaminophen pharmacology, integrating three-scale modules of enzyme reactions within a cell, physiologically based pharmacokinetics of acetaminophen at organs, and its distribution at the whole-body level. Ashworth et al. [77] developed a spatial kinetic model of hepatic glucose and lipid metabolism, treating sinusoidal tissue units instead of single hepatocytes. Carstensen et al. [67] introduced a formalism for developing whole-body multi-scale models, based on constraint-based modelling approaches described by Yasemi and Jolicoeur [398]. Per their formalism, the metabolism inside the organs is explained by the stoichiometry of enzymatic reactions, and Michaelis-Menten kinetics are used to describe enzymatic reactions. Some other models have focused on the metabolism of energy expenditure, with Dash et al. [72] developing a computational model of skeletal muscle metabolism linking cellular adaptations induced by altered loading states to metabolic responses during exercise, and Kim et al. [68] developing a whole-body model of fuel homeostasis during exercise using hormonal control over cellular metabolic processes.

While many models provide valuable insights into metabolic processes, few adequately address the nuanced differences between male and female physiology. Palmisano et al. [310] and Abo et al. [3] developped sex-specific models of exercise with the aim of achieving greater generalization. Thiele et al. [70] introduced the virtual humans: Harvey and Harvetta, which are network stoichiometric reconstructions based on omics data that simulate steady-state metabolic fluxes. There is also *LiverSex*, a sex based multi-tissue and multi-level liver metabolic model [308]. Swapnasrita et al. [399] developed sex-specific models to compare kidney function in male and female patients with different stages of diabetes. This overview of the multi-compartment modelling literature is not an exhaustive tabulation of the diverse range of published metabolic models.

In this work, we introduce a sex-specific, multi-organ, and multi-scale whole-body model of metabolism, which accurately simulates key metabolite dynamics following various mixed meals. Six major organs—brain, heart, skeletal muscle, gastrointestinal (GI) tract, liver, and adipose tissue—are modeled, along with an *other tissues* compartment representing the rest of tissues. Metabolism within organs is modeled by stoichiometric enzymatic reactions. We used mass-action kinetics to describe these reactions. This model

extends our previously published sex-specific model of energy metabolism during aerobic exercise [3]. Here, our goal is to connect cellular metabolism in organs with whole-body responses following different mixed meals, particularly high-carbohydrate and high-fat meals. We investigated sex-related differences in metabolic responses during both the absorptive and postabsorptive phases following a meal. We hypothesized that the female model will exhibit a greater reliance on lipid metabolism during both phases. Moreover, we hypothesized that whole-body sex differences will stem from organ-level variations, particularly in the liver, skeletal muscle, and adipose tissue, given the inherent differences in body composition between the sexes. Our objectives are to: (1) quantify sex differences in carbohydrate and lipid metabolism at the whole-body level, (2) assess sex differences in carbohydrate and lipid metabolism across various organs and tissues, identifying key organs driving whole-body responses, and (3) propose a candidate physiological mechanism driving sex differences in glucose production and fat oxidation patterns. Notably, point (3) addresses a gap in the experimental literature: while experiments demonstrate that increased hepatic free fatty acids (FFA) uptake and subsequent FFA oxidation enhance glucose production [400–402], women exhibit lower hepatic glucose output compared to men despite taking up and oxidizing more FFA [378, 384, 388, 403].

Novel contributions of our work to the existing literature involve developing a comprehensive, sex-specific model encompassing whole-body dynamics during feeding and fasting. Extending from our prior work on exercise metabolism, this computational model proves versatile, offering insights into various functions such as exercise, diet, and sex modulation.

The remainder of this chapter is structured as follows: simulation results are presented in Section 7.2. In particular, Sections 7.2.1-7.2.2 provide an overview of model construction and results for model calibration and validation. Our main results are presented in Sections 7.2.3 and 7.2.4, covering whole-body and organ-specific metabolic responses, respectively. In Section 7.3, we analyze our key findings and relate them to model assumptions. Section 7.4 summarizes our results. Appendix D.1 presents a detailed explanation of our mathematical model and modelling approach, while Appendix D.2 outlines the parameter estimation process. A comprehensive list of all parameter values and model equations is available in Appendix D.3.

7.2 Results

7.2.1 Model construction

We present a whole-body model of food intake comprising seven compartments: brain, heart, liver, GI tract, skeletal muscle, adipose tissue, and "other tissues", 22 metabolites and 25 reactions including the hormonal effect from pancreatic hormones, insulin and glucagon. *Other tissues* include kidneys, upper extremity muscles, and the rest of tissues. We specifically model the metabolic response to the intake of a mixed meal (carbohydrates and fat) from immediately after the meal (postprandial phase) to the postabsorptive phase (short-term fast). Figure 7.1 illustrates the multi-scale whole-body model. A fundamental assumption of the model concerning feeding and fasting states is that circulating levels of insulin and glucagon directly influence the carbohydrate and fat metabolism of organs and tissues, including the heart, skeletal muscle, GI tract, liver, and adipose tissue. Our model is tailored to sex, representing the metabolic states of healthy young adult man and woman. A complete mathematical description of the model is available in Appendix D.1.

7.2.2 Model calibration and validation

In this section, we show the time profiles of key metabolites following diverse single meals. Model simulations are presented alongside experimental data utilized for model calibration and validation. The results discussed here pertain to four experiments in which participants consumed a mixed meal after an overnight fast lasting 12 to 14 hours: (Experiment 1) 96 g carbohydrate and 33 g fat [9, 13], (Experiment 2) 139 g carbohydrate and 17 g fat [10], (Experiment 3) 58 g carbohydrate and 27.7 g fat [11], and (Experiment 4) 289 g carbohydrate and 45 g fat [12]. Specifically, selected sets of data from experiments 1, 2, and 4 were employed for model calibration, while data from experiments 2 (not used in calibration) and 3 were utilized to validate model predictions. We explored two metabolic states: (i) the absorptive or postprandial state, also known as the fed state, is defined as the period (0–6h) following meal ingestion, encompassing the processes of nutrient digestion and absorption; (ii) the postabsorptive state (6–12h), a fasting period that involves the utilization and storage of nutrients in specific tissues [154].

To formulate the male model, we first identified parameter values (see Table 7.1) using data from experiments 1, 2, and 4 [9, 10, 12, 13]. To formulate the female model, we extended our previously published model that simulates a woman's metabolism during aerobic exercise to simulate a meal [3]. The meal-related model components and parameters

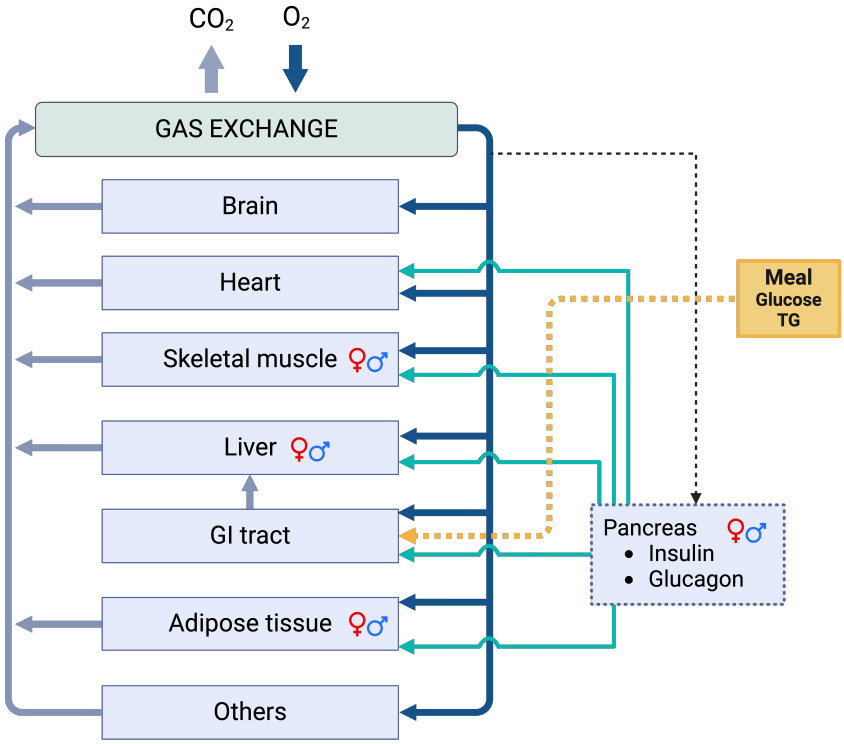

Figure 7.1: Whole-body system diagram. The systemic circulation connects all tissues/organs by transporting substrates in arterial oxygenated blood to the organs/tissues (solid dark blue arrows). Venous blood (solid light blue arrows) leaving these tissues/organs eliminates by-products and becomes arterial blood to restart circulation after releasing carbon dioxide and absorbing oxygen in the lungs (gas exchange). Blood supply to the liver comes from both the hepatic artery and venous blood from the GI tract. Nutrients are assimilated in the GI tract and subsequently enter the bloodstream. The nutrient-rich blood flows to all other organs and tissues. The pancreas responds to variations in arterial glucose concentration (indicated by the dashed arrow), regulating the levels of insulin and glucagon. Alterations in the concentrations of insulin and glucagon impact metabolic fluxes in the heart, skeletal muscle, liver, gastrointestinal tract, and adipose tissue (depicted by solid green arrows), thereby concluding the feedback regulatory mechanism. Male and female sex symbols represent compartments where sex-differences, besides differences in tissue/organ weights, are implemented.

were taken to be the same as in the male model. We then validated both models by comparing their predictions with additional data from experiments 2 and 3 [10, 11]. We emphasize that all simulations for the female model are predictions.

Table 7.1: General description of estimated model parameters

	Parameters	Description	Equations
Insulin	k_I^0	basal secretion rate	(D.7)
	$\mathrm{V}_{\mathrm{max}_I}$	maximum rate coefficient	(D.7)
Glucagon	k_G^0	basal secretion rate	(D.8)
	$\mathrm{V}_{\mathrm{max}_G}$	maximum rate coefficient	(D.8)
	n_2, n_3	hill coefficients	(D.8)
Dietary input	K_G	half-emptying glucose threshold	(D.5)
	K_T	half-emptying fat threshold	(D.6)
(Post)absorptive regulation	$\mathrm{V}^x_{\mathrm{max}_\beta}$, $\mathrm{V}^x_{\mathrm{max}_\gamma}$ $\mathrm{V}^x_{\mathrm{max}_\beta,\mathrm{fat}}$, $\mathrm{V}^x_{\mathrm{max}_\gamma,\mathrm{fat}}$	maximum rate coefficients for enzyme activity factors (B_x, Γ_x, B_x^{fat}, Γ_x^{fat})	(D.18-D.25)
	$\mathrm{K}^x_{\mathrm{max}_\beta}$, $\mathrm{K}^x_{\mathrm{max}_\gamma}$ $\mathrm{K}^x_{\mathrm{max}_\beta,\mathrm{fat}}$, $\mathrm{K}^x_{\mathrm{max}_\gamma,\mathrm{fat}}$	Michaelis constants for enzyme activity factors (B_x, Γ_x, B_x^{fat}, Γ_x^{fat})	(D.18-D.25)
	n, k, m, q	hill coefficients for enzyme activity factors (B_x, Γ_x, B_x^{fat}, Γ_x^{fat})	(D.18-D.25)

Postprandial dynamics of insulin and glucose

To calibrate the model, model parameters were chosen such that the model adequately simulates the temporal evolution of key metabolites after an overnight fast and following a single meal. Figure 7.2 shows the time course of plasma insulin and plasma glucose for the male model. Similar profiles are observed for the female model (data not shown). Following a meal, glucose enters the bloodstream by absorption from the intestine. In general, a rise in blood glucose concentration becomes apparent within approximately 15 minutes and reaches its peak around 30–60 minutes after a meal, subsequently returning to the baseline

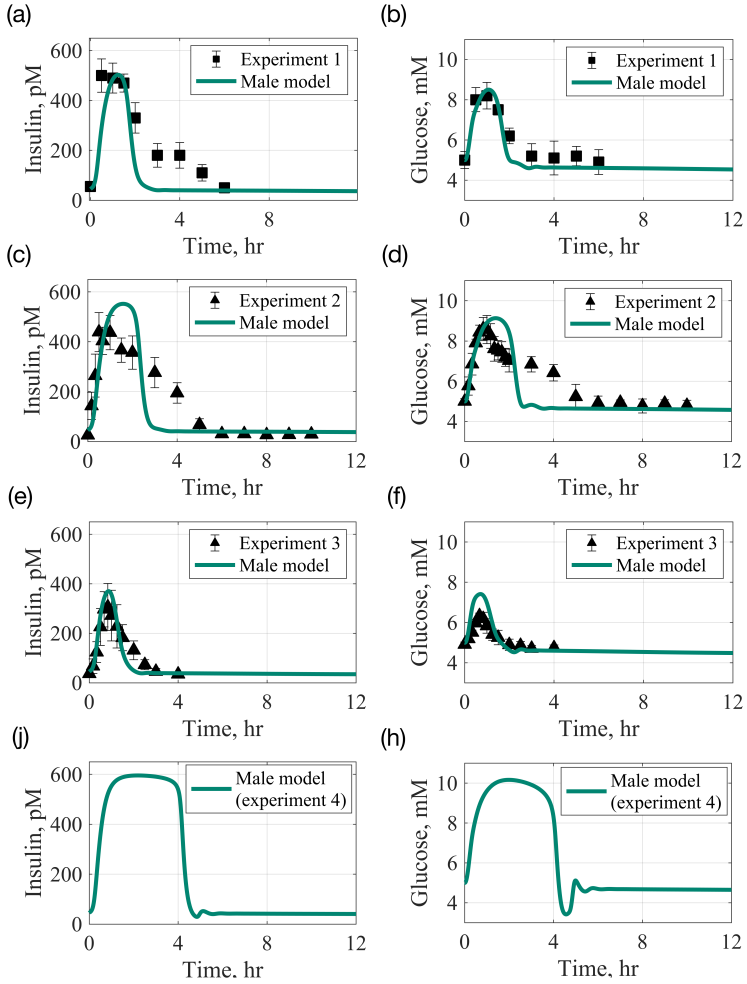

Figure 7.2: Time profile of plasma insulin and glucose concentrations after an overnight fast and following a single meal. Experiment 1: 96 g carbohydrate and 33 g fat [9]; Experiment 2: 139 g carbohydrate and 17 g fat [10]; Experiment 3: 58 g carbohydrate and 27.7 g fat [11]; Experiment 4: 289 g carbohydrate and 45 g fat [12]. Square markers (■) with lines represent calibration data with standard errors [9]; Triangular markers (▲) with lines represent validation data with standard errors [10, 11]. Lines represent model simulations. (a), (c), (e), (g): plasma insulin; (b), (d), (f), (h): plasma glucose. Absorptive phase, 0–6h; postabsorptive phase, 6–12h.

level of approximately 5 mM roughly two hours post-meal. Similar timescales of exogenous glucose appearance into the bloodstream have been reported in the literature [9, 13, 66,

154]. Our results indicate no sexual dimorphism in the glucose and insulin responses to a mixed meal (data not shown) during the absorptive (0–6h) and early postabsorptive phases (6–12h). The absence of sexual dimorphism was also reported in a study involving young and healthy individuals during the absorptive phase [387]. Regarding the postabsorptive phase, some studies have shown no significant sex difference between women and men for fasts of up to 22 hours, where individuals were either matched on percent body fat [388] or not [384].

Using the parameters identified above, we conducted a comparison between model predictions and data from experiments 2 and 3 that were not used in the model calibration [10, 11]. In Figs 7.2c-7.2f, the time profiles of insulin and glucose are presented after a single meal containing 139 g of carbohydrates and 17 g of fat (experiment 2, data from Ref. [10]), as well as after a single meal with 58 g of carbohydrates and 27.7 g of fat (experiment 3, data from Ref. [11]). Our simulations exhibit good qualitative agreement with the experimental data; however, certain discrepancies are noted. Specifically, our model tends to overestimate the insulin peak in Figure 7.2c and the glucose peak in Figure 7.2f. For the former (Figure 7.2c), the rise in glucose is similar to that observed in our calibration dataset, resulting in insulin reaching a level comparable to what was observed in the calibration dataset (Figure 7.2a). The type and composition of a meal influence insulin secretion. Meals with higher carbohydrate content (Figure 7.2c-d, 139g of carbohydrates) are expected to yield higher insulin excursions compared to meals with lower carbohydrate content (Figure 7.2a-b, 96g of carbohydrates). However, it is important to note that the glycemic index of a meal, contributing to different insulin responses, could introduce variability into the observations [404]. In the case of the glucose peak in Figure 7.2f, as the dataset does not explicitly specify the proportion of carbohydrate represented by glucose, we assumed that the entire 58g corresponds to glucose. This assumption may account for the discrepancy observed in our simulations, where the glucose peak is approximately 7.5 mM compared to the dataset's peak of around 6.5 mM. It is worth noting that the nature and composition of a meal can influence the elevation of glucose levels [404].

Post-meal hyperglycemia and glucose clearance depend on three factors: gut-emptying times, peak times, and the time-to-return to baseline concentrations for glucose and insulin. We provide a detailed explanation of how we model gut-emptying times in Appendix D.1, Eqs D.3-D.6. These factors are largely influenced by the size and composition of the meal. Figure 7.2 illustrates that meals with carbohydrate quantities of 58g (experiment 3), 96g (experiment 1), 139g (experiment 2), and 289g (experiment 4) have gut-emptying times for glucose of 39, 50, 61, and 79 minutes, respectively. Trends for peak times and times-to-return to baseline are similar: larger carbohydrate loads lead to delayed glucose peaks, with substantial meals causing postprandial hyperglycemia for over 3 hours. Notably, in

the case of experiment 4 (289 g of carbohydrates), glucose peaks after 1 hour and remains elevated for over 3 hours after the meal. Such an occurrence characterizes postprandial hyperglycemia, formally defined as plasma glucose levels exceeding 7.8 mmol/L 1-2 hours after food intake, and can lead to vascular complications, particularly in diabetic patients [405]. For larger meals, like those in experiments 2 and 4 shown in Figure 7.2, an undershoot occurs as glucose concentration returns to baseline. This happens because insulin usually peaks and returns to its baseline levels 10-30 minutes after glucose. Therefore, a large carbohydrate meal prolongs elevated circulating insulin levels, causing a delay in the time organs stay sensitive to insulin and, in turn, uptake glucose. This delay manifests as an initial undershoot in glucose levels before eventually stabilizing at basal levels.

Overall, we observe no sexual dimorphism in insulin and glucose responses following different mixed meals, and the simulated results are consistent with experimental data from several healthy subjects [9–11, 154].

Postprandial dynamics of glycogen storage

In the postprandial phase, glucose is stored as glycogen through a process called glycogenesis, primarily occurring in the liver and skeletal muscle [154]. Figure 7.3 shows the change in glycogen, relative to its initial concentration, in liver (left column) and skeletal muscle (right column). The female model tends to accumulate more glycogen than the male model in both organs, particularly after a carbohydrate-rich meal (>100 g carbohydrate, liver: Figs 7.3c and 7.3g; skeletal muscle: Figs 7.3d and 7.3h). We note that basal glycogen concentrations are the same for both organs in both models, as indicated in the literature [406, 407]. In these organs, glycogen concentrations increase due to insulin action following a meal (i.e., insulin activates glycogenesis), as confirmed by experimental data [10, 12]. The relative change in hepatic glycogen stores and the duration until the initiation of glycogen breakdown for energy needs depend on the size of the carbohydrate load. Specifically, for meals comprising 58g, 96g, 139g, and 289g of carbohydrates, glycogen concentrations in the male model increase by 15%, 21%, 33%, and 80%, respectively, peaking at 1.5, 2, 3, and 4.5 hours, respectively. In the female model, glycogen concentrations rise by 15%, 27%, 42%, and 100%, respectively, with similar peak times as the male model. Although the peak times in skeletal muscle align with those in the liver, the extent of glycogen accumulation is lower in skeletal muscle for both sexes. We observed increases of 3%, 5%, 7%, and 14% in the male model and increases of 5%, 8%, 12%, and 21% in the female model following carbohydrate loads of 58g, 96g, 139g, and 289g, respectively. These results imply a preferential replenishment of hepatic glycogen stores over intramuscular stores.

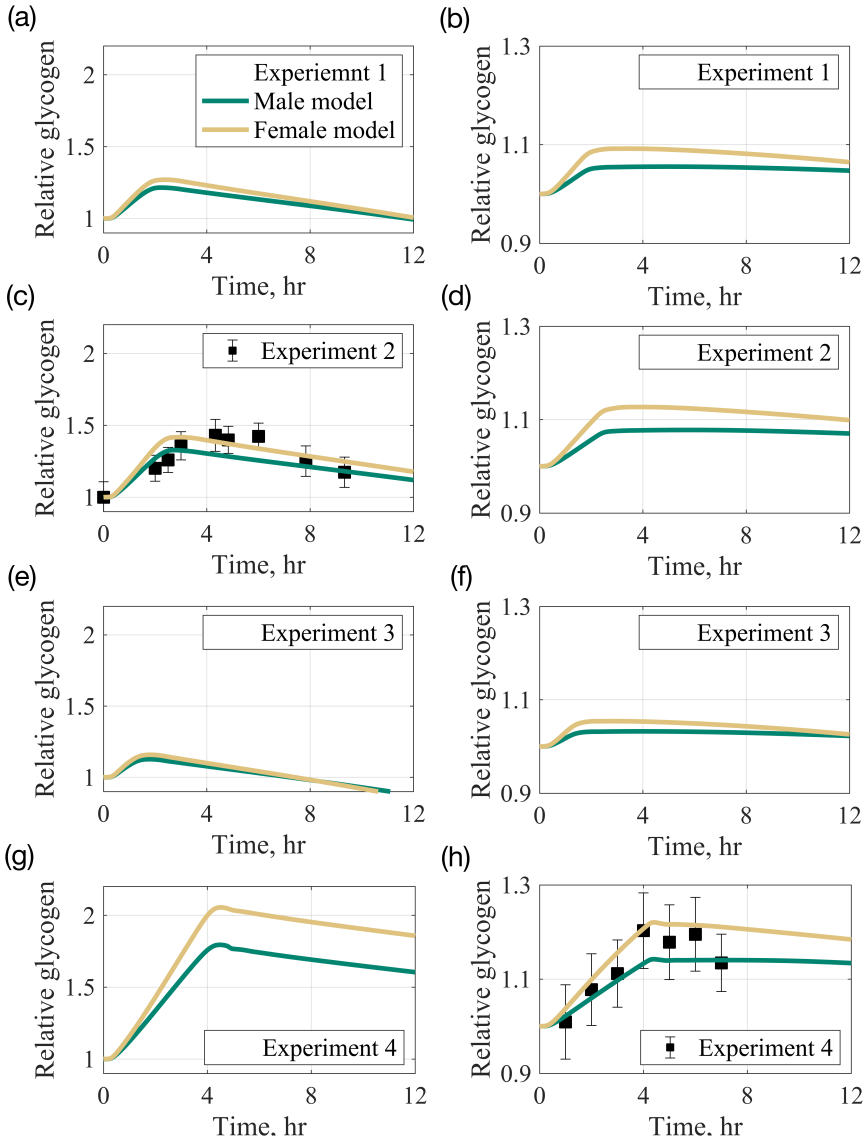

Figure 7.3: Time profile of glycogen concentration in liver (left column) and skeletal muscle (right column), relative to its initial value, after an overnight fast and following a single meal. Experiment 1: 96 g carbohydrate and 33 g fat [9]; Experiment 2: 139 g carbohydrate and 17 g fat [10]; Experiment 3: 58 g carbohydrate and 27.7 g fat [11]; Experiment 4: 289 g carbohydrate and 45 g fat [12]. Square markers (■) with lines represent calibration data with standard errors [10, 12]. Lines represent model simulations.

A few hours after the meal, liver glycogen undergoes degradation into glucose (glycogenolysis), which is then released into the bloodstream. Our model simulations demonstrate relatively constant blood glucose levels during the postabsorptive phase (beyond 6 hours; see Figure 7.2, right column), attributed to liver glycogen being degraded into glucose via glycogenolysis and subsequently released into the bloodstream. Skeletal muscle glycogen remains relatively constant during the postabsorptive phase, as indicated by Ref. [408]. This observation holds true irrespective of the meal composition and sex, as shown in the right column of Figure 7.3. Skeletal muscle lacks the essential enzyme glucose 6-phosphatase for glycogenolysis and therefore cannot release glucose. Muscle glycogen primarily serves as a local energy substrate for exercise rather than as an energy source to maintain blood glucose concentration during fasting [408]. The body's major fuel store is TG in adipose tissue, while liver and muscle glycogen serve as short-term carbohydrate stores [154].

Postprandial dynamics of other key metabolites

Figure 7.4 shows the time evolution of plasma lactate, TG, FFA, and glycerol concentrations after an overnight fast and following a single meal of 96g carbohydrate and 33g of fat (Experiment 1). Model predictions show consistent trends across various meal compositions for both female and male models (data not shown). Beside glucose, there is also an elevation of the plasma lactate concentration after ingestion of carbohydrates (Figure 7.4a), as indicated in [9]. There is qualitative agreement between simulations and experimental data for plasma lactate, although the peak in the simulations occurs approximately two hours after the experimentally observed peak. While the increase in blood glucose and lactate production can be correlated, they may not peak at the exact same time. Lactate levels are influenced by various factors, including tissue-specific metabolic activities, oxygen availability, and the overall metabolic state of the body [409–411]. For instance, Ref. [410] showed that following the uptake of carbohydrates, plasma lactate, glucose, and insulin increased within 15-30 min, reaching peak levels at 180, 90, and 90 min, respectively. Numerical simulations show no sex-related differences in lactate response following a mixed meal.

Dietary fat is absorbed at a much slower rate than glucose, so the peak in plasma TG concentration occurs 4 hours after the meal (Figure 7.4b). Following the initial post-meal peak, plasma TG gradually decreases, in line with experimental data [379]. Directly after the meal, plasma FFA and glycerol drop, then gradually increase to pre-meal levels after approximately 4 hours (Figure 7.4c and Figure 7.4d). This decrease may be caused by the reduced release of FFA (and glycerol) from adipose tissue into the bloodstream. The increase in insulin directly suppresses lipolysis in adipose tissue, causing a postprandial

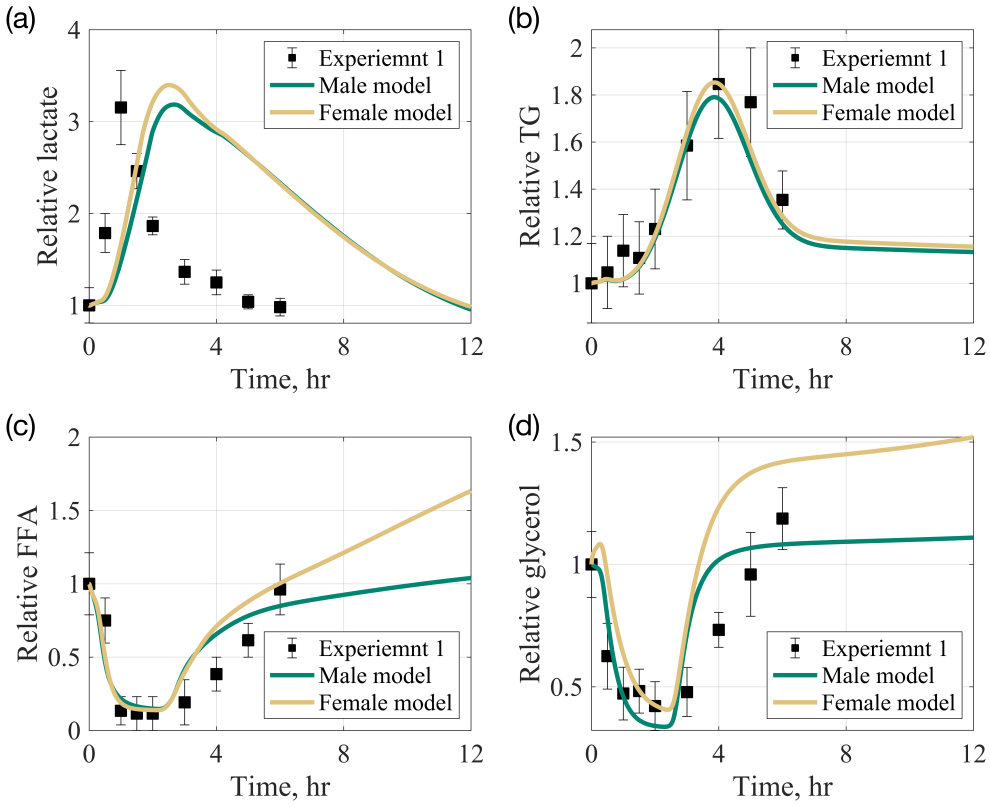

Figure 7.4: Time profile of plasma metabolite concentrations after an overnight fast and following a single meal. Experiment 1: 96 g carbohydrate and 33 g fat. Square markers with lines represent experimental data with standard errors [9, 13]; Lines correspond to the male and female model simulations. (a)-(d) concentrations, relative to initial values, of plasma lactate, plasma free fatty acids (FFA), plasma triglycerides (TG), and plasma glycerol, respectively. Basal concentrations of the following substrates differ significantly between the sexes: glucose (5 vs. 4.91 mM) [14], FFA (0.66 vs. 0.76 mM) [14], and TG (0.99 vs. 0.93 mM) [15] in males and females, respectively. The initial concentrations of other substrates are taken to be the same in both male and female models. Absorptive phase, 0–6h; postabsorptive phase, 6–12h.

reduction in plasma FFA and glycerol concentrations, as evidenced in the literature [154]. General lipid responses (TG, FFA, glycerol) to a mixed meal are sex-neutral in the postprandial phase. However, sexual dimorphism becomes evident as soon as 4 hours after the meal, particularly for FFA and TG. The surge in FFA and glycerol, the products of lipolysis, is greater in the female model than in the male model. Similar sex differences in lipid metabolism, but not glucose metabolism, have also been reported in the literature [388, 403].

7.2.3 Whole-body sexual dimorphism emerge in lipid metabolism

The respiratory quotient (RQ) reflects the relative oxidation levels of macronutrients to meet metabolic demands. Precisely, RQ is the metabolic exchange of gas ratio at the cellular level that equals the ratio of CO_2 eliminated to oxygen consumed. *In vivo*, it is directly measured from blood, while *in silico*, we use the ratio between CO_2 release rate into the blood compartment and oxygen uptake rate across all tissues/organs [3]. This method provides an indirect calorimetry measure indicating the primary fuel source (e.g., carbohydrate or fat) supporting the body's energy needs [355]. Physiological RQ values typically range between 0.7 and 1.0, varying with substrate oxidation; glucose has a RQ of 1.0, while fat has a RQ of 0.7 [356]. RQ inversely correlates with lipid oxidation, where a high RQ signifies low lipid oxidation and high carbohydrate oxidation.

Figure 7.5 illustrates the dynamics of whole-body RQ during both the absorptive (0-6h) and postabsorptive (>6h) phases for two meal compositions: high-carbohydrate and high-fat meals (refer to Table 7.2). Irrespective of sex and meal composition, there is a significant increase in RQ during the absorptive phase (RQ$\geq$0.88), indicating a predominant utilization of carbohydrates for energy metabolism. In the absorptive phase, female RQ shows a higher increase than male RQ, suggesting a slightly higher reliance on carbohydrate oxidation in the female model. As the absorptive phase transitions to the postabsorptive phase, a general decrease in RQ is observed. In the postabsorptive phase, RQ values remain elevated (RQ$>$ 0.8), but no discernible differences in RQ between sexes become apparent. These RQ values indicate sustained carbohydrate oxidation during the early postabsorptive phase.

In both male and female models, RQ reaches its peak 2 hours after a high-fat meal and 3 hours after a high-carbohydrate meal. This observation, where RQ peaks earlier for a high-fat meal compared to a high-carbohydrate meal, is not trivial and may be linked to a differential modulation of metabolic pathways by these macronutrients. Figure 7.6 shows the fractions of carbohydrate and fat utilized for energy production, specifically

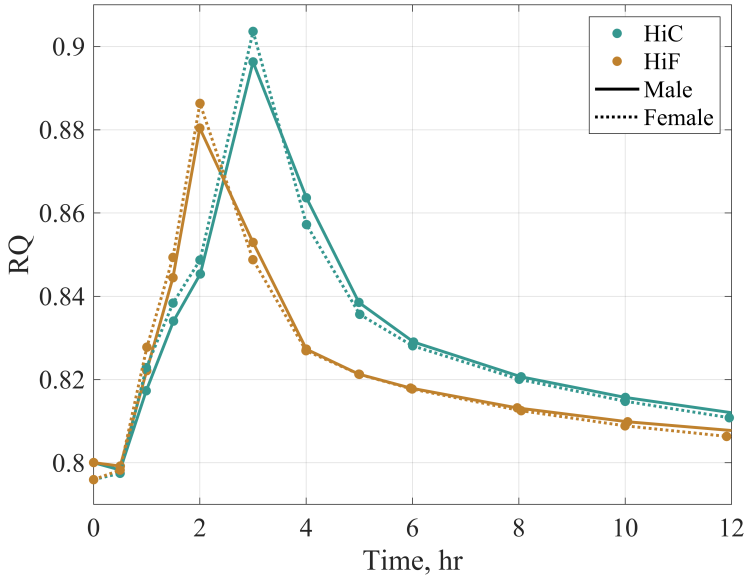

Figure 7.5: Time profile of whole-body respiratory quotient (RQ) in response to a single 800 kcal meal. Two distinct meal types were investigated: high-carbohydrate (HiC) and high-fat (HiF) meals. The whole-body RQ was calculated as the ratio of $\dot{V}CO_2/\dot{V}O_2$, where $\dot{V}CO_2$ and $\dot{V}O_2$ represent the sums of CO_2 production and O_2 consumption rates across all organs and tissues, respectively. We assumed that the respiratory exchange ratio (RER) reflects systemic nonprotein RQ, as suggested in Ref. [16]. Absorptive phase, 0–6h; postabsorptive phase, 6–12h.

Table 7.2: Meal compositions

Meal type	% CHO	% Fat	CHO (g)	Fat (g)	CHO (cal)	Fat (cal)
High-carbohydrate (HiC)	90	10	180	8.9	720	80
High-fat (HiC)	50	50	100	44.4	400	400

We consider isocaloric meals consisting of 800 calories (kcal). Fat (lipids) provides 9 kcal/g, whereas carbohydrates offer approximately 4 kcal/g [154].

for ATP hydrolysis ($\phi_{\mathrm{ATP}\to\mathrm{ADP}}$). There is no noticeable difference between the sexes in the oxidation fractions. However, once again, the peak in carbohydrate oxidation occurs earlier for the high-fat meal compared to the high-carbohydrate meal (Figure 7.6a). For the high-fat meal, carbohydrate oxidation peaks after 2 hours and remains elevated until hour 4. In contrast, for the high-carbohydrate meal, carbohydrate oxidation peaks after 3

hours and remains elevated until hour 6. Fat oxidation, significantly reduced during the absorptive phase, also exhibits a similar difference in trough time between the different meal compositions (Figure 7.6b). During the postabsorptive phase, the contribution of fat to energy production increases to exceed the contribution of carbohydrates. This transition from carbohydrate to fat metabolism results in an eventual decline in RQ, as shown in Figure 7.5.

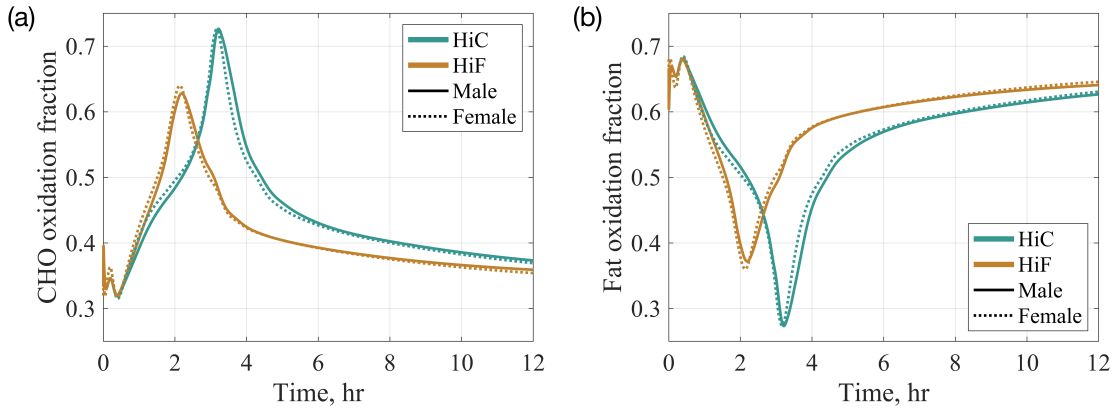

Figure 7.6: Carbohydrates and fat oxidation fractions in response to a single 800 kcal meal. HiC, high-carbohydrate meal; HiF, high-fat meal; CHO, carbohydrate. The oxidation fractions (unitless) establish a relationship between RQ values and the actual proportion of carbohydrates and fat utilized for ATP hydrolysis ($\phi_{\mathrm{ATP}\rightarrow\mathrm{ADP}}$). Indirect calorimetry methods, as outlined by Roepstorff et al. [16], were employed: CHO oxidation fraction = (RQ - 0.7)/0.3; fat oxidation fraction = 1 - CHO oxidation fraction. Absorptive phase, 0–6h; postabsorptive phase, 6–12h.

A closer examination of whole-body metabolic fluxes (Table 7.3) reveals sexual dimorphism during both the absorptive and postabsorptive phases. We introduced a quantity called the percent relative difference between the sexes ($\Delta_{F/M}$). For each flux, it is calculated as (female flux/male flux $-$ 1) $\times$ 100. During the absorptive phase and for both diet types, the female model exhibits greater rates of glycogen storage ($> 5\%$) compared to the male model, along with similarly higher rates of *de novo* lipogenesis ($> 5\%$)—the conversion of excess carbohydrate into fatty acids that are then esterified and stored as TG. Given that blood glucose levels are similar between the sexes during the absorptive phase (Figure 7.2), this result suggests that the higher rate of net glycogenolysis may not directly contribute to raising blood glucose. Instead, a higher amount of carbohydrates may be redirected for storage as fat in the female model rather than being utilized for direct oxidation. Moreover, the female model exhibits lower rates of TG breakdown ($< -20\%$)

compared to the male model. Overall, the sex-related difference is more prominent in fat metabolism than glucose metabolism immediately after a meal. Thus, metabolic changes at the whole-body level in the absorptive phase could involve sexual dimorphism in lipid but not glucose metabolism, as indicated in Ref. [387].

Interestingly, the trend in the female model for fat preservation is reversed during the postabsorptive phase for both high-fat and high-carbohydrate meals, where the female model shows an approximately 8% higher net rate of TG breakdown compared to the male model. Overall, sexual dimorphism is more prominent in the postabsorptive phase following a high-carbohydrate meal. For instance, the net rate of glycogen breakdown is 10% higher, and the net rate of gluconeogenesis is 15% lower in the female model. Since glucose output in the postabsorptive phase is a combination of glycogen breakdown and gluconeogenesis, with these processes contributing almost equally to glucose production (see net rates in Table 7.3; postabsorptive), there is a net decrease of about 5% in the rate of glucose output in the female model compared to the male model. Consequently, the observed increase in systemic fat oxidation (>8%) for the female model may compensate, in part, for the decrease in glucose availability.

It is worth noting that the net rate of systemic gluconeogenesis is negative in both the absorptive and postabsorptive phases. This is intuitive during the absorptive phase: all organs and tissues are utilizing glucose (*glycolysis*) at a faster rate than the liver performs gluconeogenesis (marginal during this phase). However, during the postabsorptive phase, this suggests that the rate of glucose synthesis (hepatic gluconeogenesis) is lower than the rate of glycolysis by other organs. As a result, blood glucose levels decrease during the postabsorptive phase (refer to Figure 7.4). This aligns with our model assumption that blood glucose decreases at rest at a rate of 0.03 mmol/min.

7.2.4 Sexual dimorphism is tissue-specific and differences start appearing even during short-term fasting

Tissue-specific sex differences in the absorptive phase

In the absorptive phase, ingested carbohydrates elevate blood glucose levels. Insulin is released, promoting glucose uptake by cells for energy or storage as glycogen. Simultaneously, dietary fats are broken down into FFA, absorbed into the bloodstream, re-esterified, and stored as TG within cells. These processes ensure energy balance and nutrient storage after a meal, contributing to maintaining blood glucose homeostasis and regulating lipid storage in the body. In this section, our focus is on exploring potential sex-related vari-

Table 7.3: Whole-body metabolic fluxes

	HiC			HiF		
Metabolic flux (mmol/min)[a]	Male	Female	$\Delta_{F/M}$	Male	Female	$\Delta_{F/M}$
			Absorptive phase			
Net glycogen breakdown[b]	-1.05	-1.11	5.25%	-0.708	-0.753	6.32%
Net gluconeogenesis [c]	-1.01	-1.05	4.06%	-0.791	-0.814	2.90%
Net TG breakdown[d]	0.041	0.0321	**-21.7%**	0.0427	0.0314	**-26.5%**
De novo lipogenesis[e]	0.0193	0.0204	5.47%	0.0177	0.0186	5.37%
			Postabsorptive phase			
Net glycogen breakdown	0.335	0.372	**10.8%**	0.347	0.366	5.42%
Net gluconeogenesis	-0.380	-0.320	**-15.8%**	-0.309	-0.311	0.902%
Net TG breakdown	0.0936	0.101	**8.31%**	0.0954	0.103	**7.64%**
De novo lipogenesis	0.0125	0.0127	1.71%	0.0127	0.0132	3.40%

[a] Values are averages over the specified phase and following a single 800 kcal meal. HiC, high-carbohydrate meal; HiF, high-fat meal. Percent change in the female model relative to the male model ($\Delta_{F/M}$) for each flux is calculated as (female flux/male flux -1) $\times$ 100.
[b] Net glycogen breakdown is defined as the difference in metabolic rates between glycogenolysis (breakdown of glycogen) and glycogenesis (production of glycogen).
[c] Net gluconeogenesis is defined as the difference between gluconeogenesis II (production of glucose-6-phosphate), specifically in the liver, and glycolysis II (utilization of glucose-6-phosphate).
[d] Net TG breakdown is defined as the difference between lipolysis (TG breakdown) and TG synthesis.
[e] *De novo* lipogenesis refers to the conversion of glyceraldehyde-3-phosphate to glycerol-3-phosphate.
All fluxes, except for *De novo* lipogenesis, are net fluxes for which a positive value indicates breakdown (or release) of the associated substrate, and a negative value indicates storage (or utilization). Absorptive phase, 0–6h; postabsorptive phase, 6–12h.

ations in substrate storage and utilization, as well as the potential implications of these differences for metabolic cross-talk among organs and tissues.

Glycogen, the storage form of glucose, is primarily stored in the liver and skeletal muscle. While other organs, such as the heart and small intestine, contain glycogen in smaller amounts, the liver and skeletal muscle are the main reservoirs. Figure 7.7 shows the change in glycogen concentration in the liver (Figure 7.7a) and skeletal muscle (Figure 7.7b) after a single meal, comparing high-carbohydrate and high-fat content meals.

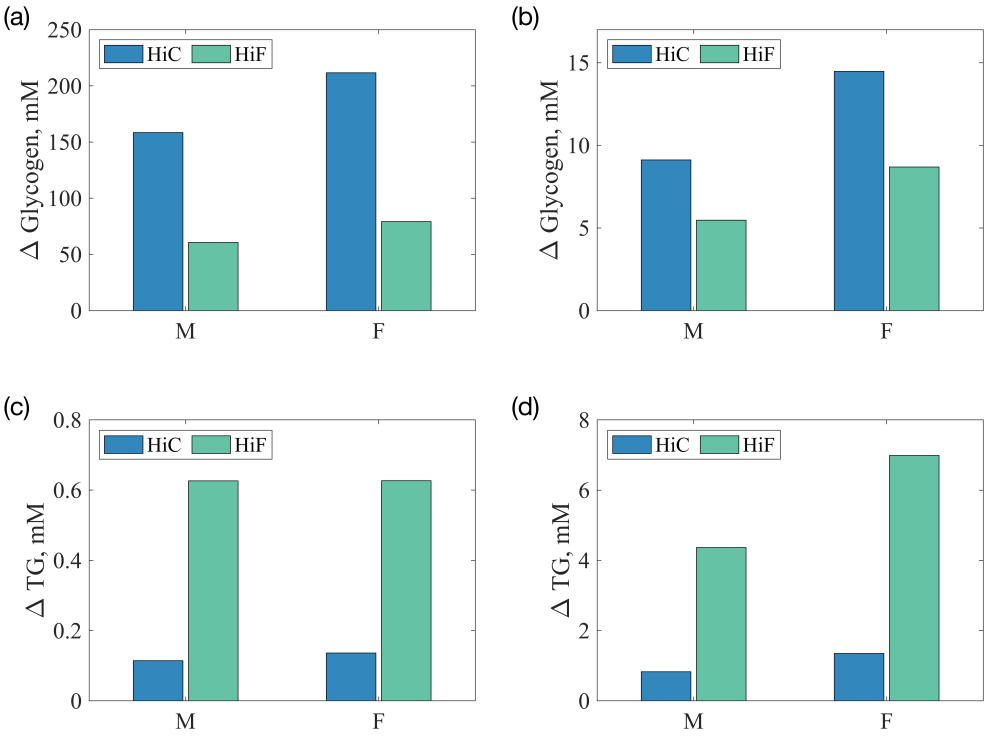

Figure 7.7: Carbohydrates (glycogen) and fat (TG) storage during the absorptive phase (0–6h). A single meal of 800 kcal is simulated at t=0. (a) liver glycogen; (b) skeletal muscle glycogen; (c) liver TG; (d) skeletal muscle TG. HiC, high-carbohydrate meal; HiF, high-fat meal. Δ refers to the absolute change in a given substrate, $C_{x,i}(T) - C_{x,i}(0)$, where $C_{x,i}$ is the concentration of substrate i in tissue x, and $T = 6$h.

Irrespective of sex, the liver accumulates more glycogen compared to skeletal muscle during the absorptive phase. In particular, the liver stores about 15 times more glycogen following a high-carbohydrate meal and about 9 times more glycogen following a high-fat meal than skeletal muscle. A comparison between sexes shows that the female model

stores more glycogen in both the liver and skeletal muscle compared to the male model, a trend consistent across diet types. Specifically, the female model stores approximately 30% more hepatic glycogen and 58% more intramuscular glycogen than the male model, following either meals. Unlike glycogen, which is a short-term energy storage molecule in the liver and muscles, TG are primarily stored in adipose tissue, providing a concentrated and long-lasting reservoir of energy. However, TG are also stored in small amounts in other tissues, including the liver and skeletal muscle. Regarding hepatic TG, our model shows marginal differences in TG concentration between the sexes during the absorptive phase (Figure 7.7c). However, the female model stores approximately 60% more intramuscular TG, termed intramyocellular lipids (IMCL), than the male model following either meals (Figure 7.7d). Experimental studies have shown that women store more IMCL than men [321, 381]. Women were found to have 84% higher lipid density than men [381]. Our predictions agree well with quantitative experimental findings, as shown in Figure 7.7d.

Tissue-specific sex differences in the postabsorptive phase

In our models, sex-specific differences become evident during short-term fasting, also referred to as short-term calorie restriction. We thus investigated sex-related differences in carbohydrate and fat metabolism during a short-term fast of 24 hours following a single 800 kcal meal (see Figure 7.8).

Figure 7.8a shows the uptake and release rates of FFA by organs and tissues during the last 12 hours of a 24-hour fast. FFA flux is nil for the brain compartment as the blood-brain barrier restricts the passage of large, hydrophobic molecules like FFA. Instead, the brain predominantly relies on other energy sources, primarily glucose. For both sexes, adipose tissue and the GI tract release the most FFA, while the liver uptakes the most FFA. Although no significant sex difference appears for the GI tract, skeletal muscle, liver, and adipose tissue exhibit sex-related differences. For both high-carbohydrate and high-fat meals, the release (and uptake) rates of FFA are higher in the female model compared to the male model. In particular, female skeletal muscle releases 6 times more FFA during the fast period following the high-carbohydrate meal and 5 times more FFA following the high-fat meal. Female adipose tissue releases 17% and 21% more FFA during the fast period following the high-carbohydrate and high-fat meals, respectively. Consequently, the female liver uptakes FFA at rates 32% and 28% higher than the male model for high-carbohydrate and high-fat meals, respectively. Overall, more FFA is being released into the circulation during the fast than is being taken up by tissues in the female model, thus explaining the higher increase in plasma FFA in the postabsorptive phase in the female model compared to the male model (refer to Figure 7.4c), as observed in experiments [384, 388].

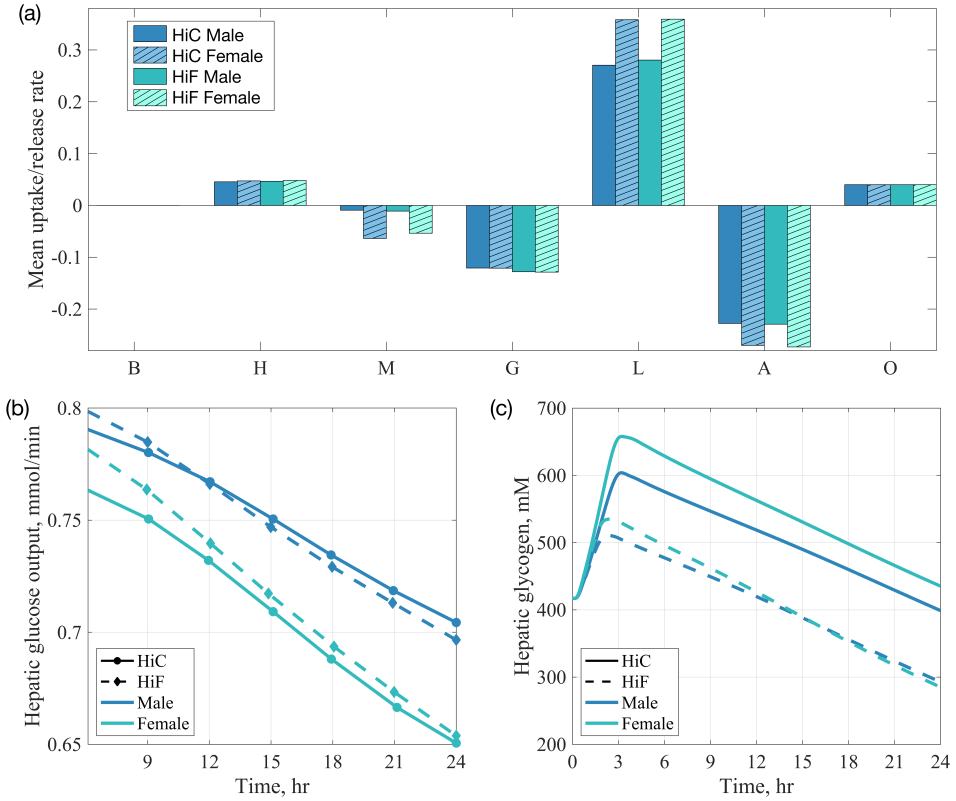

Figure 7.8: Metabolism of carbohydrates during a short-term fast (24h) following a single 800 kcal meal. HiC, high-carbohydrate meal; HiF, high-fat meal. (a) average uptake (or release) rate (mmol/min) of FFA per organ during the last 12 hours of the fasting window following HiC and HiF meals; (b) rate of hepatic glucose output (mmol/min) into the blood; (c) concentration of hepatic glycogen; mM, mmol/L. B, brain; H, heart; M, muscle; G, GI tract; L, liver, A, adipose tissue; O, other tissues.

The increased reliance of the female liver on circulating FFA may be attributed to intracellular sex differences in substrate handling. For instance, as illustrated in Figure 7.8b, hepatic glucose production is lower in the female model compared to the male model during a short-term fast. Moreover, the difference in glucose release between the sexes becomes larger over time. This result applies to both high-carbohydrate and high-fat meals. Furthermore, Figure 7.8c shows that, alongside storing more glycogen during the absorptive phase, the female liver tends to maintain higher concentrations of glycogen during short-term fasting compared to the male model, specifically following a high-carbohydrate meal. There is no sex-related difference in hepatic glycogen content after a high-fat meal, yet

the difference in hepatic glucose production persists. The tendency of the female liver to retain more glycogen throughout both absorptive and postabsorptive phases could explain the reduced glucose output, and thus the stronger reliance on FFA, potentially as a buffer to meet energy demands, especially during fasting periods.

We focus next on the following gap in knowledge in sex differences in metabolism: experiments have shown that increasing hepatic FFA uptake and subsequent FFA oxidation increases gluconeogenesis [400–402]. Yet, women are known to have lower hepatic glucose output than men despite uptaking and oxidizing more FFA [378, 384, 388, 403]. We postulate that sex differences in hepatic glucose output during short-term fasts are influenced, at least in part, by differences in both FFA *and* glycerol, as well as glycogen handling. More precisely, we hypothesize that in the female liver, more lipids are redirected towards carbohydrate metabolism to contribute to glucose production. However, the tendency of the female liver to conserve glycogen hinders a net increase in glucose output.

To test the aforementioned hypothesis, we began by analyzing the upstream fluxes responsible for hepatic glucose output. We note first that in addition to uptaking more FFA, the female liver also uptakes more glycerol than the male liver: 25% and 14% more glycerol uptake in the last 12 hours of a 24-hour fast following high-carbohydrate and high-fat meals, respectively. In a short-term fast, the liver produces glucose through both glycogenolysis and gluconeogenesis. The major substrates of gluconeogenesis are pyruvate (a carbohydrate precursor), glycerol (a fat precursor), and amino acids [154]. Figure 7.9 shows a comparison between the sexes of the hepatic fluxes involved in glucose production. There is a marginal difference between the sexes in the gluconeogenic flux from pyruvate ($\phi_{\text{PYR—GAP}}$). However, for a high-carbohydrate meal, the gluconeogenic flux from glycerol ($\phi_{\text{GRP—GAP}}$) is 11% higher in the female model, and glycogenolysis is 7% lower in the female model than in the male model. In the case of a high-fat meal, the gluconeogenic flux from glycerol ($\phi_{\text{GRP—GAP}}$) is 9.5% higher in the female model, with glycogenolysis 7% lower compared to the male model. These results suggest that although females take up more FFA during fasting, FFA may be oxidized for energy or re-esterified to TG in the liver. At the same time, glycerol, the other product of lipolysis, is uptaken at higher rates in the female liver and stimulates gluconeogenesis via glycerol oxidation ($\phi_{\text{GRP—GAP}}$). But the concurrent decrease in glycogenolysis in females may explain why the net glucose output is lower during fasting. We summarized in Figure 7.10 the sex-related differences in hepatic metabolic fluxes contributing to the sexual dimorphism in hepatic glucose output during short-term fasts.

Turning to fat metabolism in adipose tissue, our results show that the male model stores more fat as TG in adipose tissue than the female model following a high-fat meal. However, this sex difference in TG accumulation is small and subsides for the case of

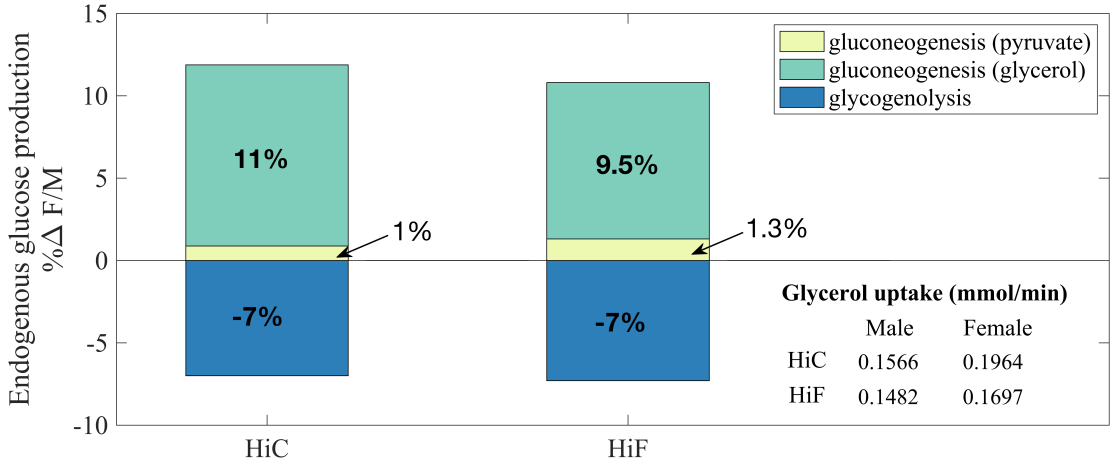

Figure 7.9: Change in hepatic energy metabolism with fasting. Values represent averages over the last 12 hours of a 24-hour fast following a single 800 kcal meal. HiC, high-carbohydrate meal; HiF, high-fat meal. %Δ F/M refers to the percent relative difference between the sexes. It calculated as (female flux/male flux -1)×100.

a high-carbohydrate meal (see Figure 7.11a). The rate of fat breakdown (lipolysis) in adipose tissue is 22% higher in the female model compared to the male model during the postabsorptive phase (>6h; see Figure 7.11b), despite the two sexes having similar levels of TG accumulation in adipose tissue. This result is consistent with our modelling assumption that body composition influences the extent of regional substrate oxidation: a higher basal body fat percentage in females (29% in the female model vs. 16% in the male model) would result in greater regional lipolysis [320, 328], assuming similar substrate oxidation efficiencies. Notably, Figure 7.11c shows that greater amounts of TG are released into the circulation by the female liver during the short-term fast irrespective of meal composition. Hepatic fat is mainly delivered to adipose tissue for the purpose of lipolysis. During this time and following a high-carbohydrate meal, skeletal muscle and the GI tract in the female model also uptake more fat than the male model, albeit to a smaller extent than adipose tissue. Following a high-fat meal, skeletal muscle in both models switches from uptake to release of TG, and the male model more so than the female model—an observation consistent with our earlier result that skeletal muscle in females tends to store more IMCL (refer to Figure 7.7).

The exchange of fat, either as TG or FFA, between organs and tissues highlights a metabolic exchange between the liver and adipose tissue. This inter-organ metabolic pathway is more prominent in the female model (Figs 7.8,7.9, and 7.11). Overall the female

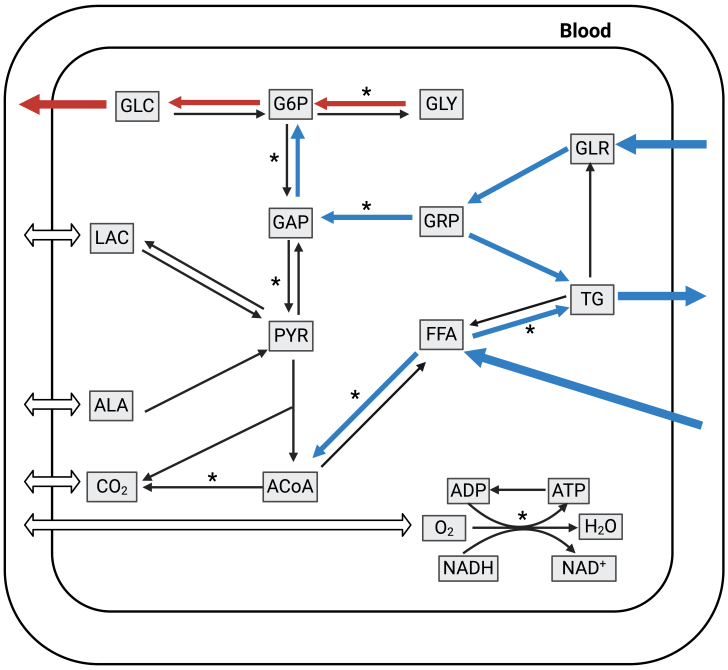

Figure 7.10: Sex-related differences in liver metabolic pathways during the postabsorptive phase (>12 h). Rates higher (lower) in the female model compared to the male model are shown in blue (red). 9 substrates are transported between blood and tissues (open double-sided arrows). Single-sided arrows indicate the direction of transport flux, which varies between the sexes. However, we note that these arrows would be more accurately depicted as double-sided arrows since substrates can be either taken up or released. Pathways marked with an asterisk (*) are composed of multiple reaction steps but grouped together as a single step in this model. Substrate abbreviations are listed in Table D.1

model has a greater capacity to remove fat from the liver through TG secretion, which is exported to adipose tissue for either storage as TG (e.g., following a high-fat meal) or to be broken down into FFA. For the later, our results show that FFA is then returned to the liver during a short-term fast. This cycle may be the result of a trade-off of efficiencies: adipose tissue is reasonably efficient at extracting FFA from chylomicrons (large triglyceride-rich lipoproteins) while the liver is efficient at converting different gluconeogenic precurssors (e.g., pyruvate, glycerol) into glucose to meet systemic energy needs. Importantly, we note that the hepatic TG pool is not a major energy store for the rest of the body (that function is performed by the TG stored in adipose tissue) but appears to be a local store for

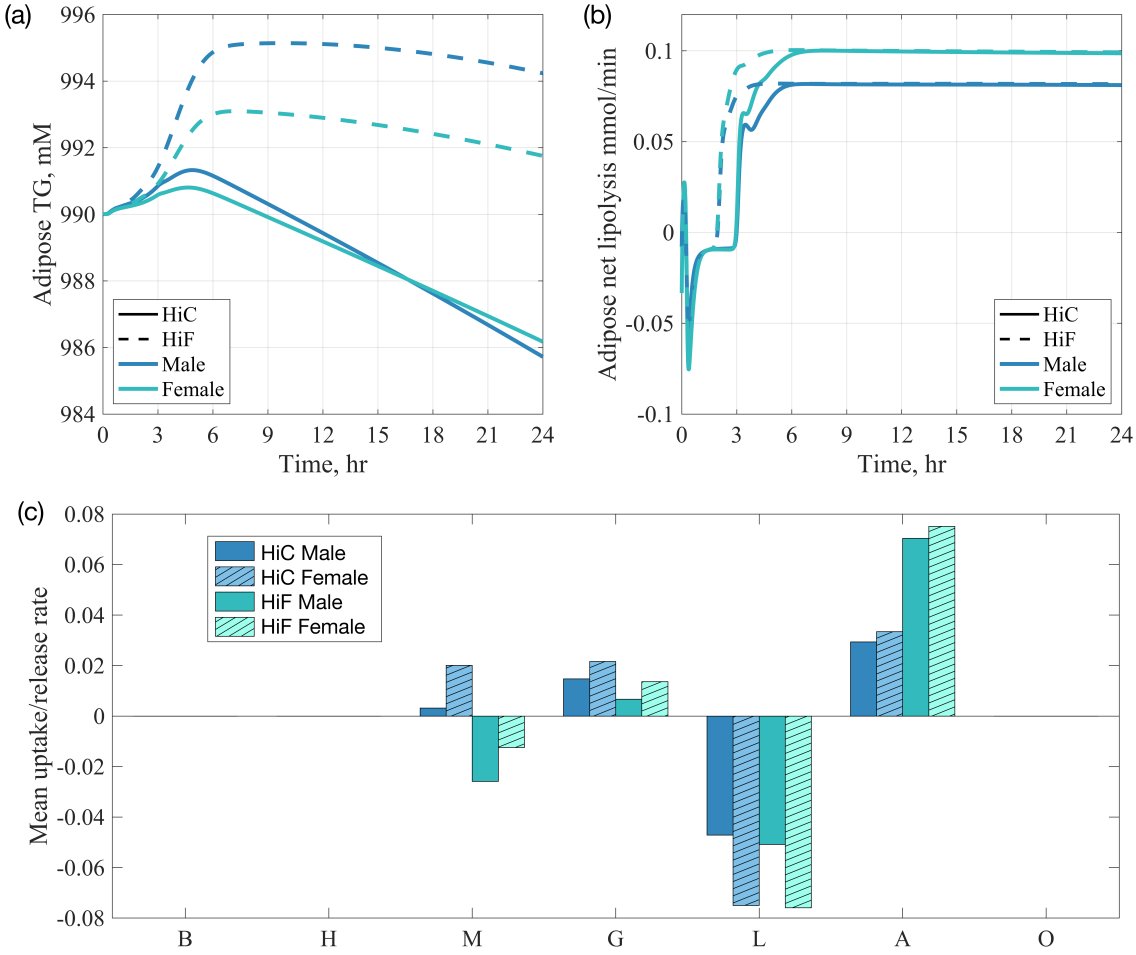

Figure 7.11: Fat metabolism during a short-term fast (24h) following a single 800 kcal meal. HiC, high-carbohydrate meal; HiF, high-fat meal. (a) Adipose tissue TG concentration; (b) Net lipolysis rate (the difference between TG breakdown and TG synthesis) in adipose tissue ; (c) average uptake (or release) rate (mmol/min) of TG per organ during the last 12 hours of the fasting period following the HiC and HiF meals, respectively; mM, mmol/L. B, brain; H, heart; M, skeletal muscle; G, GI tract; L, liver, A, adipose tissue; O, other tissues.

hepatic needs, and the stored TG also acts as a substrate for hepatic secretion of fat into the bloodstream (see Figure 7.10).

Metabolic flux sensitivity to body composition

Our model predicted that sex-related differences in metabolic responses are small during the absorptive phase but become more pronounced during fasting. We argued that the majority of these differences are attributable to differences between sexes in liver and adipose tissue function. Considering the significance of body composition in metabolism, we sought to examine the robustness of our findings in response to variations in body composition. Specifically, we aimed to assess how changes in fat mass and muscle mass impact key metabolic fluxes, such as glycolysis, gluconeogenesis, glycogenesis, glycogenolysis in the liver, and lipolysis in adipose tissue. These fluxes are key in driving whole-body sex differences, as outlined in Table 7.3. Figures 7.12 and 7.13 present the results of a local sensitivity analysis of the mentioned fluxes when fat mass or skeletal muscle mass is varied by either a 5% increase or decrease in both male and female models. Our focus was on the postabsorptive phase, where key sex differences become apparent.

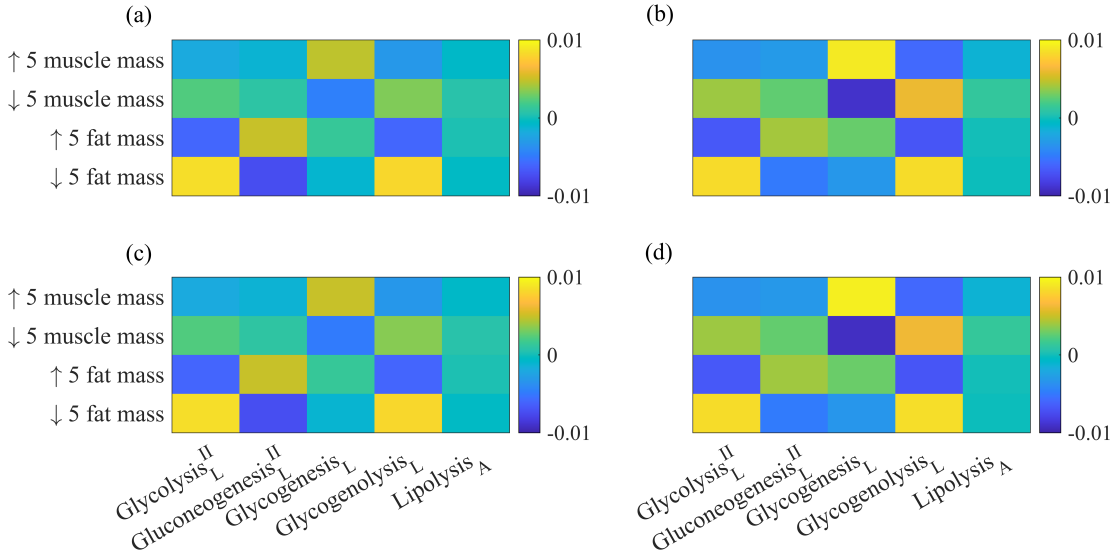

Figure 7.12: Results of local sensitivity analysis at 9 hours post-meal. (a) Male model and HiC; (b) female model and HiC; (c) male model and HiF; (d) Female model and HiF. HiC, high-carbohydrate meal; HiF, high-fat meal. Glycolysis II, $\phi_{\text{G6P}\rightarrow\text{GAP}}$; gluconeogenesis II, $\phi_{\text{GAP}\rightarrow\text{G6P}}$; glycogenesis, $\phi_{\text{G6P}\rightarrow\text{GLY}}$; glycogenolysis, $\phi_{\text{GLY}\rightarrow\text{G6P}}$, lipolysis, $\phi_{\text{TG}\rightarrow\text{FFA–GLR}}$.

Figure 7.12 shows sensitivity results 9 hours after a meal, while Figure 7.13 shows the results 24 hours after a meal. In general, at 9 hours post-meal (Figure 7.12), the male

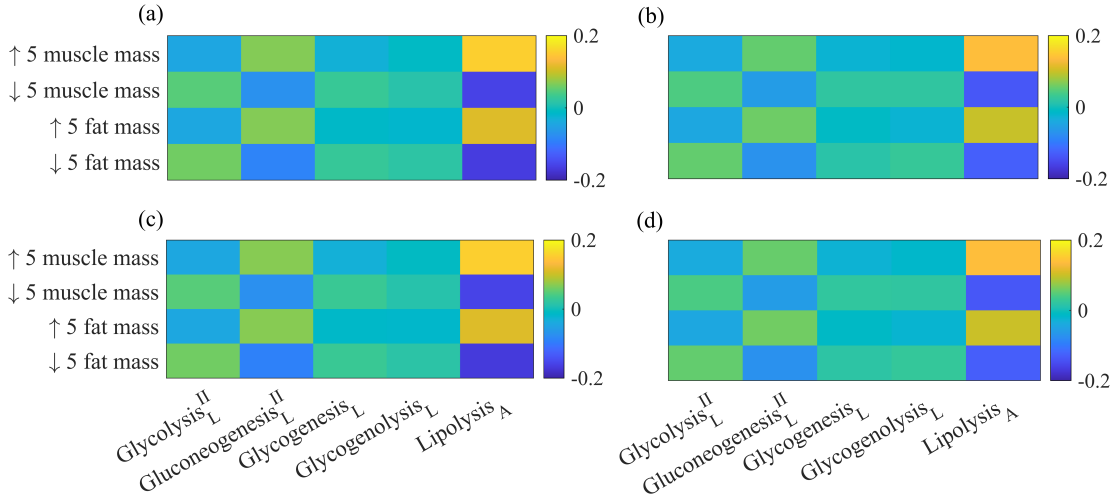

Figure 7.13: Results of local sensitivity analysis at 24 hours post-meal. (a) Male model and HiC; (b) female model and HiC; (c) male model and HiF; (d) Female model and HiF. HiC, high-carbohydrate meal; HiF, high-fat meal. Glycolysis II, $\phi_{\text{G6P}\rightarrow\text{GAP}}$; gluconeogenesis II, $\phi_{\text{GAP}\rightarrow\text{G6P}}$; glycogenesis, $\phi_{\text{G6P}\rightarrow\text{GLY}}$; glycogenolysis, $\phi_{\text{GLY}\rightarrow\text{G6P}}$, lipolysis, $\phi_{\text{TG}\rightarrow\text{FFA–GLR}}$.

model shows that a 5% increase or decrease in fat mass induces larger changes compared to the same variation in muscle mass in either direction. Across meal types, an increase in fat mass augments gluconeogenesis but diminishes glycolysis and glycogenolysis. The opposite holds for a decrease in fat mass. In the female model, greater variations are observed for changes in muscle mass. A 5% increase in muscle mass results in increased hepatic glycogenesis and reduced hepatic glycogenolysis, with the reverse occurring for a decrease in muscle mass. As the fasting period extends to 24 hours (Figure 7.13), lipolysis in adipose tissue exhibits more substantial variations than hepatic fluxes, particularly in the male model compared to the female model. During this stage of fasting, changes in fat mass or muscle mass lead to similar sensitivity indices in magnitude, but the direction of change varies. For example, both a decrease in muscle mass and fat mass reduce the lipolysis flux, while the opposite leads to an increase in lipolysis. These results apply to both high-carbohydrate and high-fat diets. Comparing Figure 7.12 and Figure 7.13 reveals that hepatic fluxes are most sensitive to body composition during the early postabsorptive period, whereas lipolysis in adipose tissue is most sensitive during the late postabsorptive phase.

Overall, the magnitudes of the sensitivity indices remain small, with $-0.2 < S_i < 0.2$

and where i represents either fat mass or muscle mass. This observation applies to both models and across both meal types. Such findings provide increased confidence that the model predictions reflect genuine sex-related metabolic differences, regardless of variations in body composition. We also point out that the sensitivity indices at 24 hours post-meal are higher than those at 9 hours post-meal by an order of magnitude. This suggests that the model is more sensitive to changes in body compositions during the latter stages of the postabsorptive period, indicating that sex differences associated with body composition may become more pronounced during longer fasts. This aligns well with our findings that sex differences become more apparent during the late postabsorptive phase. More detail about our sensitivity analysis method and actual values of sensitivity indices are available in Appendix D.4.

7.3 Discussion

Variations in whole-body metabolism resulting from dietary factors. Throughout the absorptive phase (0-6h), both sexes experience a marked increase in RQ ($\geq$ 0.88), indicative of a preference for carbohydrate oxidation. Figure 7.5 shows the whole-body RQ results for male and female models. During the transition to the postabsorptive phase, RQ values, although decreasing, remain $>$ 0.8, suggesting sustained carbohydrate oxidation in the early postabsorptive period (6-12h). This trend is consistent across sexes, showing no significant differences in RQ values. A 2021 experimental study [412] also shows no sex-related difference in RQ in lean, healthy young males and females in the short term following a high-fat diet.

Importantly, meal composition, rather than sex, exerts the most significant influence on the evolution of whole-body RQ after a single mixed meal. Our results indicate that RQ peaks over an hour earlier for a high-fat meal compared to a high-carbohydrate meal (Figure 7.6). In line with this observation, the oxidation fractions of carbohydrates, reflecting the extent to which carbohydrates contribute to ATP energy production, peak earlier and remain elevated for 2.5 hours following a high-fat meal compared to a high-carbohydrate meal. Yet, the increased availability of carbohydrate following a high-carbohydrate meal leads to a swift increase in carbohydrate oxidation, surpassing that induced by a high-fat meal after 3 hours.

This seemingly counterintuitive result, considering that a high-carbohydrate meal has 40% more carbohydrate content than a high-fat meal in our simulations, raises questions about the underlying metabolic pathways and energy utilization during the digestion of carbohydrates and fats. Mechanistically for a high-fat meal, the initial spike in RQ can be

attributed to the body's preference for utilizing carbohydrates for quick energy. However, as the digestion and absorption of dietary fat progress, the body gradually shifts to using fatty acids for energy. This transition from carbohydrate to fat metabolism contributes to the eventual decline in RQ. Conversely, with a high-carbohydrate meal, the body promptly responds by prioritizing the export of carbohydrates from the systemic circulation. This is followed by the breakdown and storage of excess carbohydrates as glycogen, primarily in organs like skeletal muscle and the liver. This rapid uptake into organs prevents postprandial hyperglycemia, characterized by elevated blood glucose levels persisting for more than 1-2 hours after food ingestion [405].

The delayed increase in RQ following a high-carbohydrate meal can be attributed to this differential metabolic response: aggressively storing glucose to restore normal glycemia, thus continuing to burn fat to some extent during the initial phase following a high-carbohydrate meal. Then, the body eventually transitions to using carbohydrate as fuel. In summary, the sequence of RQ peaks reflects the dynamic interplay between carbohydrate and fat metabolism during the absorptive phase, illustrating the body's adaptive mechanisms to efficiently extract energy from different macronutrients over time.

Variations in whole-body metabolism resulting from sex differences. We observed sex-related differences in whole-body metabolic fluxes that persist across meal types, with more pronounced effects following a high-carbohydrate meal (Table 7.3). In the absorptive phase, our findings indicate that the female model tends to preserve significantly more fat than the male model. This is evident in the net rate of TG synthesis, which is 21% and 26% higher in the female model for high-carbohydrate and high-fat meals, respectively. Additionally, *de novo* lipogenesis, the process synthesizing FFA from substrates such as glucose and amino acids, is higher in the female model (Table 7.3). This implies that more glucose is stored as fat in the female model than in the male model during the absorptive phase. Sex differences in glucose metabolism during the absorptive phase are also apparent and suggest a preference in the female model to utilize more carbohydrates to meet energy needs (Table 7.3). Notably, rates of glycogen breakdown and gluconeogenesis are higher in the female model during this period. Experimental data indicate a complex role of sex hormones, with sexual dimorphisms depending on the individual's metabolic status. For example, women in the prandial and postprandial states utilize more carbohydrates than men to meet energy needs, while during fasting or exercise, women rely more on fat oxidation than men [303, 380, 383, 386, 406]. Our results align with the former during the absorptive phase, and we will revisit the latter below for the postabsorptive phase.

In the postabsorptive phase, sex differences become more evident in both fat and glucose metabolism and following a high-carbohydrate meal. The female model produces less

glucose but oxidizes more fat. Specifically, our female model exhibits a 10% higher *net rate* of glycogenolysis and a 15% lower *net rate* of gluconeogenesis compared to the male model. The female model shows lower rates of glucose production as the decrease in gluconeogenesis dominates. Experimental studies have also demonstrated this sexual dimorphism in glucose production [303, 380]. Additionally, lipolysis is 8% higher in the female model, suggesting a higher reliance on FFA by other organs and tissues during the postabsorptive phase. Following mass action principles, higher glycogen levels may lead to increased rates of glycogen breakdown, and higher fat levels may lead to increased rates of fat hydrolysis. As expected, these rates are higher for the female model, given that the female liver stores more glycogen during the absorptive phase, and the female model has a higher initial body fat percentage (and mass). Mechanistically, the reduced rate of gluconeogenesis in the female model is a consequence of increased systemic lipolysis. Since the rate of glucose output from the liver to the circulation depends on the rate of glucose uptake by other organs, the inherent net rate of gluconeogenesis is reduced in the female model as other organs and tissues supplement their energy needs by uptaking and oxidizing FFAs during the postabsorptive phase. Our predictions aligns with experimental observations indicating that women rely more on fat oxidation than men during fasting [303, 380, 383, 406]. After a high-fat meal, the female model continued to show elevated rates of lipolysis. In general, disparities related to sex are more noticeable in the postabsorptive phase compared to the absorptive phase, particularly following a high-carbohydrate meal compared to a high-fat meal.

Sex-differences at the organ and tissue levels drive systemic differences. Our analysis revealed sex-related differences during both the absorptive and postabsorptive phases, which persisted for both high-carbohydrate and high-fat meals. Notably, these differences tended to be more pronounced following a high-carbohydrate meal. In the absorptive period, two substrates, namely glycogen and TG, exhibited a significant difference between the sexes (Figure 7.7). The male model tended to store less glycogen in the liver and skeletal muscle than the female model, consequently producing and oxidizing more glucose for energy. Regarding TG, our models showed similar amounts stored in the liver, while the male model stored significantly less TG in skeletal muscle fibers (approximately 60% less). This aligns with the findings of Devries et al. [321] and Tarnopolsky et al. [381], indicating that men have lower IMCL density compared to women (28%–84% less).

Sex-related differences became more evident during the postabsorptive period (more than 6 hours after a meal). The female liver's inclination to preserve more glycogen than the male model extended into the postabsorptive phase (Figure 7.8c). Consequently, the female liver released less glucose into the circulation during that time (Figure 7.8c). To

offset the reduced glucose output, the liver and other organs increased their reliance on FFA oxidation for energy. For example, the female liver took up significantly more FFA to meet its energy needs, and some of that FFA was also re-esterified and released into the bloodstream as TG (Figure 7.11c). The rate of FFA uptake is directly linked to the substrate's availability in the circulation [154]. The increased FFA availability is attributed to lipolysis in adipose tissue, the GI tract, and skeletal muscle (Figure 7.8a). We note that the basal rate of lipolysis in adipose tissue is higher in our female model by 20%, in line with findings from experimental studies [320, 328]. Overall, FFA release is higher from adipose tissue and skeletal muscle in the female model. For the latter, the greater amount of IMCL in the female model explains the higher rate of muscle lipolysis. We identified a candidate mechanism, driven by adipose tissue and the liver, which could mechanistically explain the observed sex differences in hepatic glucose output and FFA availability/oxidation between the sexes. We discuss it next.

Liver and adipose tissue emerge as hubs of sex-related metabolic differences. Especially during the late postabsorptive phase (more than 12 hours after a meal), our models have highlighted a metabolic exchange between the liver and adipose tissue that enables the body to meet energy requirements when glycogen stores are low or depleted (Fog 7.10). For instance, we observed that in addition to FFA, the female liver also takes up more glycerol, the other product of lipolysis. On the one hand, when FFA enters hepatic cells, some of it is oxidized for energy, and some is re-esterified to TG. Our models show that these processes occur at higher rates in the female model compared to the male model. On the other hand, the glycerol entering hepatic cells is diverted to promote gluconeogenesis. We observed no sex difference in the rate of gluconeogenesis from pyruvate. In net, the rate of gluconeogenesis is higher in the female model than the male model. Simultaneously, the rate of glycogenolysis is reduced in the female liver to the extent that the net rate of glucose production and subsequent glucose output is lower in the female model compared to the male model. We recall that glycogenolysis and gluconeogenesis contribute almost equally during the postabsorptive phase to glucose production. As such, other organs compensate for glucose by taking up and oxidizing FFA (except the brain).

The TG released by the liver is then taken up by adipose tissue, broken down into FFA, and released into the circulation for re-uptake by liver. This cycle implies that females both synthesize and burn more fat than males during a short-term fast. A result supported by the higher levels of plasma FFA and glycerol during the postabsorptive period and regardless of meal composition (Figs 7.4c and d7.4). The greater glycerol rate of appearance is an index of the whole-body lipolytic rate [380]. This metabolic exchange between the liver and adipose tissue is independent of sex, but the difference in body

composition and reaction rates between the sexes causes the female model to rely more heavily on it.

Our candidate mechanism could partly explain a current gap in the literature. Increased uptake of FFA is known to increase gluconeogenesis [400–402], but females, who significantly uptake more FFA than males, also produce less glucose [378, 384, 388, 403]. This suggests that an alternate mechanism hinders the increase in gluconeogenesis from leading to increased glucose output. In summary, we posit that gluconeogenesis is increased in females due to the concurrent uptake of FFA *and* glycerol. Glycerol specifically increases gluconeogenesis in the liver, but the reduction in the rate of glycogenolysis is such that the net contribution to glucose output is negative in females. At the core of these sex differences are the liver, which preserves more glycogen in females, and adipose tissue, which provides FFA and glycerol to meet the body's energy needs. The latter is accentuated in females, who have a higher basal rate of lipolysis regardless of the fact that they have a higher percentage of body fat [320, 328]. Our candidate mechanism is summarized in Figure 7.10.

7.4 Conclusion

We developed a whole-body, multi-scale, and sex-specific model of energy metabolism. We incorporated metabolic adjustments that connect cellular metabolism in organs to systemic responses following different mixed meals. Our model aligns well with experimental data. According to our predictions, sex-related metabolic differences are more noticeable following a high-carbohydrate meal compared to a high-fat meal, with differences becoming more pronounced during a short-term fast. In summary, women tend to preserve more fat than men during the absorptive period but oxidize significantly more fat during the postabsorptive period. We hypothesized that the increased reliance on fat metabolism in females is influenced by sex differences in the liver and adipose tissue, and we have outlined a candidate underlying mechanism for this sexual dimorphism. Specifically, the female liver conserves more glycogen, leading to reduced glucose output. This decrease in arterial glucose promotes FFA oxidation by other organs and tissues, except the brain. Computational biology offer promising avenues for refining whole-body metabolic models. Integrating sex-specific data and parameters into multi-scale frameworks holds the potential to enhance our understanding of human metabolism and its modulation by sex. By accounting for the intricate interplay between organs, hormones, and metabolic pathways, these models can provide valuable insights into the underlying mechanisms driving sex-specific metabolic responses.

Chapter 8

Conclusions and future directions

In this chapter, I provide a summary of the key findings from this thesis and discuss avenues for future research aligned with my overarching theme of "timed lifestyle interventions." This may involve mechanistic modeling of multi-scale biological systems (sections 8.2 and 8.4), as well as mean field analysis of networks of oscillators (section 8.3). In section 8.2, I discuss future directions for our model of circadian-immune interactions. Then, in section 8.3, I outline methods for introducing heterogeneity in continuum models of interacting circadian neurons. Similarly, in section 8.4, I discuss related approached for modeling the influence of rhythms through both oscillatory signals such as hormones and non-oscillatory signals such as diet and exercise.

8.1 Summary of work

My work in this thesis entailed building and analyzing mathematical models for biological systems, as well as developing computational tools for the numerical investigation of these systems. I was particularly interested in addressing problems with practical impact, and my projects focused on applications in systems biology ranging from the single cell to the network or system level. The approaches were: (1) develop multiscale mathematical models to address fundamental questions in metabolism, immunity, and circadian rhythms, including their intricate interactions; and (2) derive macroscopic descriptions for interacting neurons, which describe the system's behavior as the number of particles approaches infinity, to investigate the neurophysiological mechanisms underlying the emergence of an ensemble rhythm.

We developed sex-specific whole-body models representing healthy young adults. Our models explore how men and women metabolize mixed meals, especially high-carbohydrate and high-fat meals, as well as how energy utilization varies between the sexes during exercise. From modelling exercise, we were able to (i) quantify the extent of sex differences in carbohydrate and lipid metabolism in different organs and tissues; (ii) identify a candidate physiological mechanism in the liver that drives sex differences in glucose production; and (iii) assess the subsequent metabolic responses in skeletal muscle and adipose tissue and their role in potentiating differences in substrate utilization. From modelling feeding and fasting, we were able to (iv) quantify sex differences in carbohydrate and lipid metabolism at the whole-body level, (v) assess sex differences in carbohydrate and lipid metabolism across various organs and tissues, identifying key organs driving whole-body responses, and (vi) propose a candidate physiological mechanism driving sex differences in glucose production and fat oxidation patterns. We particularly addressed a gap in the experimental literature: while experiments demonstrate that increased hepatic free fatty acids (FFA) uptake and subsequent FFA oxidation enhance glucose production [400–402], women exhibit lower hepatic glucose output compared to men despite taking up and oxidizing more FFA [378, 384, 388, 403]. We showed that the female liver conserves more glycogen, leading to reduced glucose output. This decrease in arterial glucose promotes FFA oxidation by other organs and tissues, except the brain. We also proposed candidate mechanisms suggesting cross-talk between the liver and skeletal muscle during exercise, and between the liver and adipose tissue during feeding and fasting.

We further developed a model of the circadian clock within the lung, which we coupled with an acute inflammation model to investigate how the disruptive effects of shift work manifest differently between males and females during inflammation. Drawing from experimental data, we incorporated sex-specific differences in gene expression into our model and tested how these variations translate into immune responses. Notably, we (vii) identified REV-ERB as a key regulator influencing the expression of pro-inflammatory cytokine IL-6 and anti-inflammatory cytokine IL-10. Additionally, our findings (viii) highlighted the significance of sexual dimorphism in shaping the magnitude of inflammatory responses during shift work: females exhibited a weakened immune response attributed to the significant downregulation of Rev-Erbα, whereas males displayed heightened responses due to the overexpression of Rev-Erbα.

Starting from individual dynamics, we also derived macroscopic descriptions of neural networks based on mean field PDEs for the evolution of a density of individuals. These continuum models allow us to explore the influence of factors such as noise and interactions on emergent macroscopic properties in the scaling limit ($N \to \infty$). We provided (ix) a numerical description of the bifurcations resulting from the noise-induced transitions: Hopf

bifurcations with respect to the coupling and noise parameters, which are synonymous with synchronized activity. Our numerical simulations show a noise-induced rhythm at low noise intensities, while the SCN clock is arrhythmic in the high noise setting. Notably, we showed that (x) coupling induces amplitude expansion at low noise intensities, and varying coupling strength can cause period locking and variance dissipation even in the presence of noise.

A recurring theme in this thesis is the incorporation of sex differences into modelling. Computational modelling is increasingly crucial in medicine, offering refined methods for disease diagnosis, prevention, and treatment by simulating biological processes and uncovering their underlying mechanisms. Given the ubiquitous sex differences, substantial benefits can only be realized if model predictions apply to both sexes. In the next few years, I aim to pursue several questions stemming from (1) how neural networks in the brain develop topologies that are efficient and robust, and (2) how molecular networks at the tissue level interact with neural signals in healthy and pathological states. It is my hope that these model predictions and hypotheses serve to guide future experimental endeavors.

8.2 Conclusions and future directions for the clock-immune interaction model

We have successfully developed a model of the bi-directional interactions between innate immune responses and the circadian clock within the lung. Model parameters have been estimated from experimental data concerning key immune agents (cytokines) as well as clock genes and proteins. Furthermore, we simulated scenarios of shift work or chronic jet lag by inducing an 8-hour phase advance in the circadian system and incorporated sex differences in gene expression levels. This coupled system enabled us to explore the intricate interactions between immune agents and the lung clock. Through our investigations, we have identified a key circadian regulator in the modulation of inflammatory response: REV-ERB. Acting as an equilibrist, REV-ERB exerts a negative influence on the expression of pro-inflammatory cytokine IL-6 and anti-inflammatory cytokine IL-10. Additionally, our research highlights the significance of sexual dimorphism in the magnitude of the inflammatory response during chronic jet lag. Specifically, the female model exhibited a reduced production of pro-inflammatory cytokines compared to the male model, whereas the male model displayed exacerbated responses. We hypothesize that males may be more susceptible to sepsis due to their heightened inflammatory response, while females may endure longer-term effects of infection.

8.2.1 Modelling active infection with pathogen replication and death

In our model of acute inflammation, the immune response is initiated by a bolus injection of LPS. LPS, or lipopolysaccharide, is a molecule present in the outer membrane of Gram-negative bacteria. It serves as a potent stimulator of the immune system, triggering inflammatory responses throughout the body. However, it is important to note that LPS itself does not undergo replication. Instead, it is a constituent of the bacterial cell wall, and as bacteria multiply, they produce more LPS as part of their outer membrane.

An intuitive extension of our model is to replace LPS with an active, dynamic compartment representing bacterial agents. Unlike adaptive immune responses, which are specific to particular pathogens, innate immune responses, as depicted in our model, depend on a set of proteins (cytokines) and phagocytic cells capable of recognizing conserved features of pathogens and rapidly activating to combat invading microorganisms. As such, a generalization of the pathogen compartment can be based on the assumptions that:

(i) Bacteria reproduce asexually through binary fission, where a parent cell divides into two equal-sized daughter cells, leading to exponential growth;
(ii) Cells in the bacterial population are well mixed, with replication and dwelling times following exponential distributions.

Relevant modifications to the model include:

(i) Bacteria grow at a rate k, which corresponds to the reciprocal of the doubling time;
(ii) Bacteria can be eliminated by host immune defenses (phagocytic cells) at a rate μ;
(iii) Bacteria can undergo bursting or death at a rate ζ.

These modifications are particularly interesting because they allow for direct specification of the parameter k based on the known doubling time of the bacteria being modeled. Alternatively, exploring a range of k values and simulating different scenarios can provide insights into how the severity of acute inflammation correlates with bacterial growth rates and whether the responses of the circadian clock are influenced by varying growth rates. Incorporating mechanisms for bacterial replication within mathematical models describing bacterial infections in a host would enhance the adaptability and applicability of our model. A schematic diagram illustrating the structure of the proposed new model is presented in Figure 8.1.

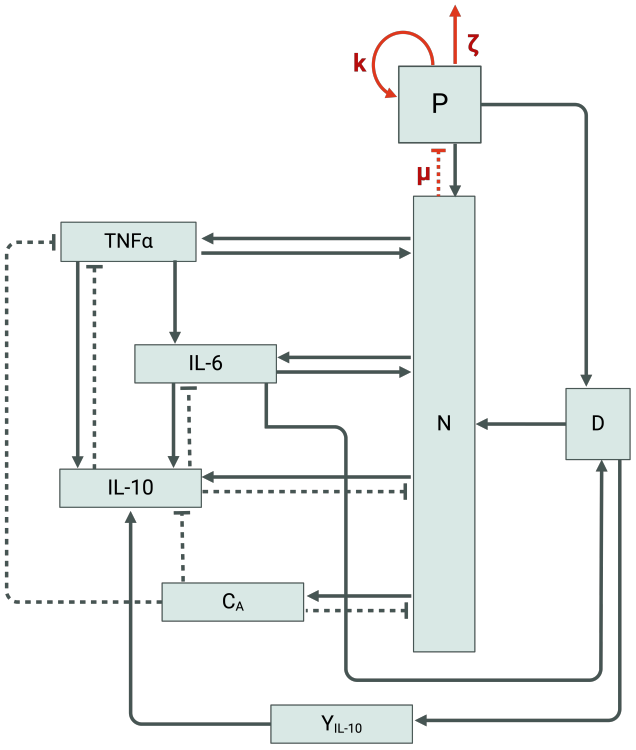

Figure 8.1: Dotted arrows represent activation; blunt dashed arrows represent inhibition. In the acute inflammation model, P denotes an active replicating bacterial agent; D, damage marker; N, activated phagocytic cells; C_A, slow-acting anti-inflammatory cytokines; IL-6 and TNFα are pro-inflammatory cytokines; IL-10 is an anti-inflammatory cytokine; $\mathrm{Y}_{\mathrm{IL}-10}$ is a tissue-driven (non-accessible) IL-10 promoter.

8.2.2 Integrating cytokine-clock interactions

The circadian clock regulates immune processes through precise molecular mechanisms, with clock proteins such as BMAL1 and REV-ERBα exerting significant control over innate immune responses. This interplay between the circadian clock and inflammation operates in a bidirectional manner, whereby inflammation can disrupt the clock mechanism.

For example, active inflammation accelerates the degradation of REV-ERBα [197]. Within our model, we represent active inflammation using a damage marker. This damage marker can serve as the link between inflammation and the rate of REV-ERBα degradation. Moreover, studies have shown that TNFα incubation suppresses the expression of *Per*

genes both *in vitro* and *in vivo* in mice [201], as well as *Cry1* [236]. Yoshida et al. [237] and Ertosun et al. [238] have demonstrated that TNFα modulates the transcription of *Bmal1* through the up-regulation of *Ror*α. While our current model does not incorporate direct connections from cytokines to clock genes and proteins, these associations could be integrated into future expansions of the model.

8.3 Understanding the role of heterogeneity in macroscopic dynamics

In Chapter 5, we developed a model of coupled oscillators to study synchronization dynamics in the presence of noise (Gaussian). Naturally, noise at the level of the SCN network is essential since the neuronal activity is not totally deterministic. Our focus was on the macroscopic picture that approximates the microscopic dynamics as the number of particles goes to infinity, with the goal to characterize the bifurcations resulting from noise-induced transitions in a SCN network. We considered an all-to-all coupling topology with Goodwin-type neurons and derived the scaling limit, called the *mean field limit* [47, 50, 51]. Our results showed that increasing the coupling strength leads to phase transitions through Hopf bifurcations. The same type of bifurcation governs the instabilities caused by noise. This approach allowed to identify where the system of coupled SCN neurons exhibit a stable stationary state (incoherence within the SCN network) or limit cycle oscillations (synchronized activity). Overall, coupling induced resonance-like behavior at low noise intensities, and varying coupling strength caused period locking even in the presence of noise. We also confirmed numerically the convergence of error between solutions to the stochastic system and the mean field equation when the number of neurons tends to infinity. This prior work lends itself to two areas of improvement: investigating (1) how the type of interaction or connectivity between cells leads to system-level synchronization, and (2) how cellular heterogeneity influences ensemble characteristics and potentially influences the transition to complete network synchrony.

We recall that a circadian rhythm is a natural oscillation that repeats roughly every 24 hours. A master clock located in the suprachiasmatic nuclei (SCN) of the brain regulates the circadian rhythm of physiological and behavioral activities in mammals. What we are learning now is that the SCN is not a homogeneous cellular centre but a complex heterogeneous network with two distinct groups of neurons (Figure 8.2)—the light-receptive ventralateral (VL) region (containing 25% of neurons) and the light-insensitive dorsalmedial (DM) region (containing 75% of neurons). It is not possible to fully infer the network

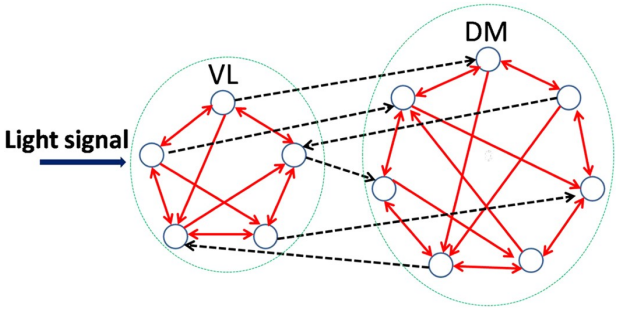

Figure 8.2: Scheme of the SCN network. Reproduced from [17] with permission.

structure of the SCN from experimental data, and the causality between network topology/heterogeneity and SCN function remains unclear. While awaiting advancements in experimental techniques, mathematical models can be employed to investigate the role of heterogeneity in the SCN. Thus, a *long-term goal* of my research is to investigate how heterogeneity in the SCN leads to efficient and robust circadian rhythms. Remarkably, almost every cell in the body has a circadian rhythm [32]. I will apply mean field theory to connect the individual properties of neurons to the overall population dynamics. Besides the previously mentioned differences between the VL and DM regions, neurons of the same cell type can also exhibit significant variations in their response properties [413]. Therefore, a more suitable model for the diversity of cell types in the SCN should account for both genuinely distinct cell types and variations among cells within a specific type. We refer to the latter as *within-type* heterogeneity and the former as *between-type* heterogeneity. An important consideration is the choice of topology for the connections between neurons. It would be reasonable to begin this analysis with all-to-all coupled neurons. However, recent work [17] has shown that robust rhythms with large amplitudes, a high synchronization degree, and a large entrainment ability exist mainly in small-world and scale-free type networks (Figure 8.3), and therefore investigating these topologies will be part of my future work.

8.3.1 How does within-type heterogeneity affect synchronization and SCN function?

The goal is to investigate the specific contributions of within-type heterogeneity to SCN properties by making use of a recently developed mean field theory for networks of coupled neurons with distributed parameters [414, 415]. My proposed approach is as follows: (i) identify a suitable oscillator model such as coupled phase-amplitude models or mechanistic negative-feedback oscillator as we did in Chapter 5; (ii) derive the mean field limit that

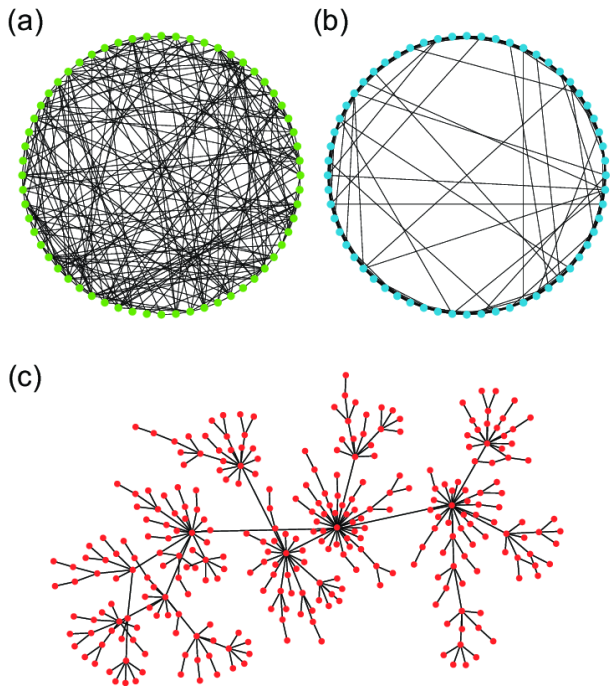

Figure 8.3: Different kinds of network topology. (a) Random network (erdos-renyi model); (b) small-world network (watts and strogatz model); (c) scale free network (barabasi-albert model). Reproduced from [18]. Copyright © 2014, IEEE.

governs the network dynamics in the scaling limit $N \to \infty$; (iii) identify relevant sources of heterogeneity and treat relevant model parameters as distributed values across the population. For example, one can assume that the membrane potential or the recovery time at any $t > 0$ is fully captured by a Lorentzian probability distribution. Importantly, point (ii) involves proving that some limit exists in a suitable topology, identifying the limit as the solution of a nonlinear problem, and proving that the nonlinear problem is well-posed, i.e., limit is uniquely defined. This can be a challenge if the interaction kernel is not as "nice" or regular. Classical mean field limit results require that the interaction kernel be essentially Lipschitz.

8.3.2 How does between-type heterogeneity affect synchronization and SCN function?

Extending on the idea above, heterogeneity can be represented via two interacting neuron populations (VL and DM). Between-type heterogeneity can be represented by asymetric coupling strengths between the two populations, as suggested in Ref. [17]. In addition, I will differentiate between the two populations by applying the Lorentzian ansatz with different centers and half-width-at-half-maximum values. If the models have explicit stationary solutions, I can also investigate heterogeneity via a linear stability analysis that links to the model parameters. I hypothesize that synchronization arises from bifurcations of the stationary solutions. In particular, the degree of heterogeneity could act as a bifurcation parameter and be inversely related to the strength of the connectivity. A majority of work in this direction aims at obtaining limiting ODEs for the proportions of different compartments of the population [414–416], and the scaling limits presented are by design approximate. This proposed approach introduces heterogeneity and aims to provide macroscopic descriptions of neural networks using mean field PDEs for the evolution of a density of individuals.

8.4 Conclusions and future directions for the metabolism models

A significant part of this thesis was devoted to the development of whole-body mechanistic models of metabolism. We first developed a sex-specific multi-scale model that relates cellular metabolism in the organs to whole-body responses during exercise. We then developed a new module for this model that represents the metabolism of food intake and fasting. Our current model proves versatile, offering insights into various functions such as exercise, diet, and sex modulation. These were constructed with the future goal of investigating the effect of timed lifestyle interventions such as exercise and diet on metabolic efficiency. These are important considerations for pathologies such as diabetes, in particular type 2 diabetes (T2D). The alternation of eating and fasting, in conjunction with exercise, could be manipulated to balance blood sugar levels.

Besides the light-dark cycle, other environmental and behavioral cues can fine-tune our circadian rhythm. Our bodies have a peripheral clock system that is primarily composed of muscle, adipose tissue, liver, and gut, and which also participates in the regulation of the circadian rhythm. Exercise, and food in particular, have the ability to reset the clocks

of all of our peripheral tissues. Although the 'brain clock' continues to synchronize with the light signal, peripherical clocks are more responsive to the timing of food and exercise. Exercise is a strong Zeitgeber of the muscle clock, and it has the ability to effectively reset circadian rhythms. In addition, physical ability is known to fluctuate throughout the day. Physical strength and skeletal muscle function, for example, peak in the late afternoon.

In recent years, evidence has emerged that the circadian clock can interact with the nutrients we consume to influence how our bodies work. The term "chrononutrition" refers to this relatively new field. Throughout the day, our blood glucose follows a circadian rhythm. The body is better able to manage blood glucose earlier in the day, when food is typically consumed, but less so at night, when fasting is typically observed. Hormones involved in glucose metabolism, such as insulin and cortisol, also exhibit circadian rhythms. Eating when the body expects insulin to rise improves insulin response and glucose removal from the bloodstream, allowing us to maintain normal blood sugar levels. This ultimately results in lower insulin levels during fasting hours, which is a good thing.

Three primary sources contribute to the entrainment of peripheral clocks: (a) direct entrainment by the SCN via neural and hormonal signals; (b) entrainment through feeding-fasting rhythms; and (c) entrainment via body temperature fluctuations. We will now explore how we can integrate sources (a) and (b) into our existing models.

8.4.1 Entrainment through neural and hormonal signals

In 1943, Pincus [417] initially observed that the concentration of specific adrenal hormones in urine displayed oscillations following a day-night pattern. Nearly twenty years later, it was discovered that isolated adrenal glands exhibited inherent metabolic rhythmicity in culture, indicating the presence of an autonomous, internal clock [418]. Subsequent research suggested the SCN as a potential regulator of circadian adrenal function, as evidenced by the loss of circadian oscillations in adrenal corticosterone content following SCN lesioning [419]. Furthermore, consistent with these findings, studies in humans showed low circulating catecholamine levels during nighttime hours and elevated levels during the daytime [420, 421]. Specifically, epinephrine was observed to display distinct, self-sustained rhythmicity [421]. Our models incorporate the dynamics of epinephrine, which govern the production of insulin and thus indirectly influence blood glucose balance. Moreover, epinephrine serves as a direct neuroendocrine signal for various tissues, including the heart, skeletal muscle, gastrointestinal tract, and adipose tissue (refer to Chapter 6, Figure 6.1). The current models consider epinephrine to be constant at rest, but to go through a step

increase during exercise. We recall that

$$C_E(t) = C_E(0) + \omega(\mathrm{WR}) \cdot (1 - \exp(t/\tau_E)), \tag{8.1}$$

where $C_E(0)$ is the initial concentration of epinephrine at rest, WR is the work rate fixed at 150W or 60% of $\dot{\mathrm{V}}\mathrm{O}_{2\mathrm{max}}$, and $\omega(\mathrm{WR})$ is a parameter determining the gain with respect to a step change in work rate applied during exercise; τ_E is a time constant for epinephrine dynamics.

We propose replacing $C_E(0)$ with an oscillatory signal at rest denoted as $C_E^0(t)$. It is worth mentioning that if epinephrine oscillates, so will insulin, glucagon and consequently glucose in our models. Basal epinephrine can be depicted either as a sinusoidal wave or a square wave. For the sinusoidal form:

$$C_E^0(t) = \frac{A}{2} + \frac{A}{2}\sin(\omega t + \varphi), \tag{8.2}$$

where $\omega = 2\pi/24$ and $C_E^0(t)$ varies between 0 and A with a period of 24 hours. Here, φ represents a phase shift. Alternatively, for the square wave form:

$$C_E^0(t) = \frac{A}{2} + \frac{A}{2}\mathrm{sgn}\Big(\sin(\omega t + \varphi)\Big), \tag{8.3}$$

where $\omega = 2\pi/24$ and $C_E^0(t)$ also varies between 0 and A with a period of 24 hours. Again, φ denotes a phase shift, and sgn represents the sign function of a sinusoid, taking the value of 1 when the sinusoid is positive, -1 when negative, and 0 at discontinuities.

While a sinusoidal signal may be more realistic, the square wave offers greater control for investigation. With a square wave, we can easily manipulate, in silico, the duration of the light period in the light-dark cycle. This allows for simulations of various light exposure schedules to examine how the duration of the dark phase, possibly corresponding to sleep duration, influences the metabolic response to exercise.

8.4.2 Entrainment through feeding-fasting rhythms

Modelling the bidirectional relationship between the circadian clock and metabolism can be approached in a tissue-specific manner, as peripheral clocks in organs respond to signals beyond light cues. Particularly in the context of feeding-fasting cycles, the liver clock exhibits heightened responsiveness to these signals [422]. I suggest that future research prioritize investigating the molecular mechanisms underlying hepatic circadian gene regulation and

exploring the connections between hepatic circadian clock systems and metabolism. Below, I provide a concise literature review outlining the current understanding of the bidirectional interactions between the liver clock and metabolites, including hormones and substrates. This review is not exhaustive.

Hepatic clock regulation (→). The expression levels of numerous hepatic genes, including both clock-related and liver-specific genes, exhibit circadian periodicity [422, 423]. Mice deficient in Bmal1 lose rhythmic behavior in both the brain and liver, while those lacking Clock exhibit impaired hepatic circadian rhythms but retain central periodicity [424]. However, hepatic periodicity demonstrates relative autonomy from central regulation, partly attributed to food intake. Even when the central brain clock functions correctly, more than 80% of the hepatic transcriptome is influenced by meal intake [425].

Bmal1. Mice lacking Bmal1 in the liver exhibit severe hypoglycemia during the inactive period [424]. Another study has demonstrated that the loss of daily BMAL1 fluctuations leads to a decrease in the expression of GLUT2 (Glucose transporter 2) and several other genes involved in hepatic glucose storage, transport, and export [424]. BMAL1 has also been shown to promote gluconeogenic gene expression through the HDAC5 pathway [426]. Overall, these findings suggest defective liver gluconeogenesis following Bmal1 knockout. Additionally, liver-specific Bmal1$^{-/-}$ causes dyslipidemia, characterized by elevated circulating FFA and high hepatic TGs [427].

Clock. Hepatic glycogen content exhibits strong circadian fluctuations, peaking at the end of the active phase in mammals. Circadian rhythms are also observed in the activities of key enzymes responsible for both glycogenesis and glycogenolysis. Transient reporter assays have revealed that CLOCK drives the transcriptional activation of Gys2 (glycogen synthase 2). Thus, CLOCK regulates the circadian patterns of hepatic glycogen synthesis by promoting the transcriptional activation of Gys2 [428]. Furthermore, Clock$^{-/-}$ mice demonstrate decreased hepatic triglyceride accumulation when subjected to high-fat diets [427].

Per. Mice lacking Per1/2 experience severe hypoglycemia [422, 424]. Similar results have been confirmed in humans, where Per2 was found to regulate glucose homeostasis [429]. In particular, loss of PER causes hyperinsulinemia [430, 431].

Cry. Cry1 and Cry2, core components of the clock, are rhythmically expressed in the liver. Hepatic overexpression of Cry lowers blood glucose concentrations and improves insulin sensitivity [125]. The activity of cAMP response element–binding protein (Creb) during fasting is modulated by Cry1 and Cry2, which are rhythmically expressed in the liver. Cry1 expression is elevated during the night-day

transition, when it inhibits gluconeogenic gene expression [125, 422].

Rev-Erb. In human hepatoma cells, Rev-erbα specifically inhibits the expression of genes encoding gluconeogenic enzymes G6Pase and PEPCK in metabolic gene regulation [432]. Both liver Rev-Erbα and Rev-Erbβ deficient mice exhibit remarkable hepatic steatosis (intrahepatic fat accumulation) [427].

Hormonal regulation ($\leftarrow$). Insulin secretion is tightly regulated by the circadian clock. Deficiencies in both CLOCK and BMAL1 lead to hypoinsulinemia [433, 434], while the absence of PER and CRY results in hyperinsulinemia [430, 431]. In turn, insulin and glucose also influence the clock. In a model using rat hepatocytes and primary mouse hepatocytes, insulin resynchronized the liver clock [435, 436]. Specifically, the expressions of liver Per2 and Rev-erbα genes were advanced in phase within one day of refeeding after a fast. Moreover, within two hours, insulin injection in intact mice not only influenced gene expression through food intake but also upregulated Per2 and downregulated Rev-erbα. Additionally, glucose was found to downregulate Per1 and Per2 expression in cultured rat fibroblasts [437].

Future extensions of this research should explore the concept of time-restricted eating (TRE), a behavioral intervention approach driven by the emerging understanding of circadian rhythms in physiology and metabolism. In TRE, all caloric intake is confined to a regular interval of less than 12 hours, without any deliberate reduction in calorie intake. The objective of modeling will be to integrate our model of the circadian gene regulatory network with the liver compartment in our whole-body model. It is worth noting that the circadian clock model operates as an autonomous oscillator, and when linked to substrates in the liver, it will induce oscillations, particularly in the rate of glucose production. Interactions will be modelled as either upregulation or inhibition of maximum rate coefficients, as we did for the diet and exercise models. The clock model can be adapted to the liver through parameter estimation using clock gene data specific to hepatocytes. For example, clock gene expression data can be obtained from various circadian databases, including CircaDB [438] for 24-hour periodicity profiles in mouse and human, RhythmicDB [439] providing re-analyzed gene expression datasets from 48 publicly available experiments, and CGDB [440], a comprehensive resource for circadian genes containing information on both validated and predicted genes. Subsequently, we will simulate various TRE schedules, incorporating meals with varying fat and carbohydrate content. Manipulating the alternation of eating and fasting intervals could help regulate blood sugar levels. There may be favorable effects on lipid metabolism, including reduced triglyceride levels and enhanced lipolytic efficiency, especially given the observed communication between the liver and adipose tissue during fasting (see Chapter 7).

In this context, our research will address the following questions: (i) Which clock genes play a significant role in maintaining glucose homeostasis, and which metabolic pathways in the liver drive systemic circadian-induced changes? (ii) How does food intake, mediated through insulin and glucose signaling, influence clock resetting? (iii) Are high-carbohydrate or high-fat diets more effective in entraining the liver clock? The interplay between the core clock and metabolism carries significant implications for the management of metabolic disorders such as diabetes. When peripheral clocks become desynchronized from the central clock, it leads to chronodisruption [441], which is associated with various health conditions including cancer, cardiovascular diseases, depression, obesity, and metabolic syndrome [442]. For instance, in the treatment of obesity, a fundamental dietary intervention involves reducing energy intake [443]. The circadian clock plays a crucial role in energy balance and metabolic processes [444]. Therefore, evaluating factors such as shift work, irregular sleep patterns, and dietary habits that may disrupt circadian rhythms in individuals with metabolic disorders like obesity, and planning exercise and meal timings according to normal biological rhythms, can enhance the effectiveness of treatment strategies.

8.5 Closing remarks

A unique aspect of this research involves the integration of both new mathematics and new biology. For the latter, we used data and mechanistic modeling to learn new models of the interaction between circadian rhythms and biological systems. We targeted specific open questions in the literature about sex-differences in metabolism and immunity and identified potential candidate mechanisms for the observed differences. For the former, we applied mean field theory to biochemical models of oscillators to connect the individual properties of circadian neurons to the overall population dynamics. We also developed new models of the transition between feeding and fasting cycles, with the goal of using diet as a synchronizing cue for peripheral circadian clocks. Mathematically, this research contributes to the development of frameworks designed to understand multiscale systems, analyze the relationships between network structure and dynamics, and explore the dynamics of entrainment by rhythms. The mathematical models we developed can be used as computational tools to explore applications in different problem domains. Ultimately, the goal is to make predictions that can be verified experimentally.

References

[1] S. M. Abo and A. T. Layton, "Modeling the circadian regulation of the immune system: Sexually dimorphic effects of shift work," *PLoS Comput Biol*, vol. 17, no. 3, p. e1008514, 2021. URL: https://doi.org/10.1371/journal.pcbi.1008514

[2] S. M. Abo, J. A. Carrillo, and A. T. Layton, "Can the clocks tick together despite the noise? stochastic simulations and analysis," *SIAM J Appl Dyn Syst*, vol. 22, no. 2, pp. 850–877, 2023. URL: https://doi.org/10.1137/22M147788X

[3] S. M. Abo, E. Casella, and A. T. Layton, "Sexual dimorphism in substrate metabolism during exercise," *Bull Math Biol*, vol. 86, no. 2, p. 17, 2024. URL: https://doi.org/10.1007/s11538-023-01242-4

[4] Y. A. Kuznetsov, *Elements of applied bifurcation theory*, 2nd ed., ser. Applied Mathematical Sciences. Springer-Verlag, New York, 1998, vol. 112.

[5] M. Hafner, H. Koeppl, and D. Gonze, "Effect of network architecture on synchronization and entrainment properties of the circadian oscillations in the suprachiasmatic nucleus," *PLoS Comput Biol*, vol. 8, no. 3, p. e1002419, 2012. URL: https://doi.org/10.1371/journal.pcbi.1002419

[6] K. N. Frayn and R. Evans, *Human metabolism: A regulatory perspective*. John Wiley & Sons, 2019.

[7] I. Hirsch, J. C. Marker, L. J. Smith, R. J. Spina, C. Parvin, J. Holloszy, and P. Cryer, "Insulin and glucagon in prevention of hypoglycemia during exercise in humans," *Am J Physiol Endocrinol Metab*, vol. 260, no. 5, pp. E695–E704, 1991. URL: https://doi.org/10.1152/ajpendo.1991.260.5.E695

[8] T. J. Horton, G. K. Grunwald, J. Lavely, and W. T. Donahoo, "Glucose kinetics differ between women and men, during and after exercise," *J Appl Physiol*, vol. 100, no. 6, pp. 1883–1894, 2006. URL: https://doi.org/10.1152/japplphysiol.01431.2005

[9] K. N. Frayn, S. W. Coppack, S. M. Humphreys, M. L. Clark, and R. D. Evans, "Periprandial regulation of lipid metabolism in insulin-treated diabetes mellitus," *Metabolism*, vol. 42, no. 4, pp. 504–510, 1993. URL: https://doi.org/10.1016/0026-0495(93)90110-A

[10] R. Taylor, I. Magnusson, D. L. Rothman, G. W. Cline, A. Caumo, C. Cobelli, G. I. Shulman *et al.*, "Direct assessment of liver glycogen storage by 13c nuclear magnetic resonance spectroscopy and regulation of glucose homeostasis after a mixed meal in normal subjects." *J Clin Invest*, vol. 97, no. 1, pp. 126–132, 1996. URL: https://doi.org/10.1172/JCI118379

[11] K. B. Hansen, T. Vilsbøll, J. I. Bagger, J. J. Holst, and F. K. Knop, "Increased postprandial gip and glucagon responses, but unaltered glp-1 response after intervention with steroid hormone, relative physical inactivity, and high-calorie diet in healthy subjects," *J Clin Endocrinol Metab*, vol. 96, no. 2, pp. 447–453, 2011. URL: https://doi.org/10.1210/jc.2010-1605

[12] R. Taylor, T. B. Price, L. Katz, R. G. Shulman, and G. I. Shulman, "Direct measurement of change in muscle glycogen concentration after a mixed meal in normal subjects," *Am J Physiol Endocrinol Metab*, vol. 265, no. 2, pp. E224–E229, 1993. URL: https://doi.org/10.1152/ajpendo.1993.265.2.E224

[13] S. Coppack, R. Fisher, G. Gibbons, S. Humphreys, M. McDonough, J. Potts, and K. Frayn, "Postprandial substrate deposition in human forearm and adipose tissues in vivo," *Clin Sci*, vol. 79, no. 4, pp. 339–348, 1990. URL: https://doi.org/10.1042/cs0790339

[14] S. Carter, C. Rennie, and M. Tarnopolsky, "Substrate utilization during endurance exercise in men and women after endurance training," *Am J Physiol Endocrinol Metab*, 2001. URL: https://doi.org/10.1152/ajpendo.2001.280.6.E898

[15] M. D. Carroll, D. A. Lacher, P. D. Sorlie, J. I. Cleeman, D. J. Gordon, M. Wolz, S. M. Grundy, and C. L. Johnson, "Trends in serum lipids and lipoproteins of adults, 1960-2002," *JAMA*, vol. 294, no. 14, pp. 1773–1781, 2005. URL: https://doi.org/10.1001/jama.294.14.1773

[16] C. Roepstorff, C. H. Steffensen, M. Madsen, B. Stallknecht, I.-L. Kanstrup, E. A. Richter, and B. Kiens, "Gender differences in substrate utilization during submaximal exercise in endurance-trained subjects," *Am J Physiol Endocrinol Metab*, vol. 282, no. 2, pp. E435–E447, 2002. URL: https://doi.org/10.1152/ajpendo.00266.2001

[17] C. Gu, J. Li, J. Zhou, H. Yang, and J. Rohling, "Network structure of the master clock is important for its primary function," *Front Physiol*, vol. 12, p. 678391, 2021. URL: https://doi.org/10.3389/fphys.2021.678391

[18] T. Onaga and S. Shinomoto, "Bursting activity spreading through asymmetric interactions," in *2014 Tenth International Conference on Signal-Image Technology and Internet-Based Systems*, 2014, pp. 388–395. URL: https://doi.org/10.1109/SITIS.2014.66

[19] R. Lok, J. Qian, and S. L. Chellappa, "Sex differences in sleep, circadian rhythms, and metabolism: Implications for precision medicine," *Sleep Med Rev*, p. 101926, 2024. URL: https://doi.org/10.1016/j.smrv.2024.101926

[20] WHO, "Diabetes," Jun 2020. URL: https://www.who.int/news-room/fact-sheets/detail/diabetes

[21] N. I. of Health, "What is diabetes?" Dec 2016. URL: https://www.niddk.nih.gov/health-information/diabetes/overview/what-is-diabetes

[22] N. C. for Health Statistics, "Public-use data files and documentation," Jun 2018. URL: https://www.cdc.gov/nchs/data_access/ftp_data.htm

[23] C. M. Sheehan, S. E. Frochen, K. M. Walsemann, and J. A. Ailshire, "Are us adults reporting less sleep?: Findings from sleep duration trends in the national health interview survey, 2004–2017," *Sleep*, vol. 42, no. 2, 2019. URL: https://doi.org/10.1093/sleep/zsy221

[24] T. Roenneberg, K. V. Allebrandt, M. Merrow, and C. Vetter, "Social jetlag and obesity," *Curr Biol*, vol. 22, no. 10, pp. 939–943, 2012. URL: https://doi.org/10.1016/j.cub.2012.03.038

[25] C. Vetter, H. S. Dashti, J. M. Lane, S. G. Anderson, E. S. Schernhammer, M. K. Rutter, R. Saxena, and F. A. Scheer, "Night shift work, genetic risk, and type 2 diabetes in the uk biobank," *Diabetes Care*, vol. 41, no. 4, pp. 762–769, 2018. URL: https://doi.org/10.2337/dc17-1933

[26] A. K. Beery and I. Zucker, "Sex bias in neuroscience and biomedical research," *Neurosci Biobehav Rev*, vol. 35, no. 3, pp. 565–572, 2011. URL: https://doi.org/10.1016/j.neubiorev.2010.07.002

[27] F. Mauvais-Jarvis, N. Bairey Merz, P. J. Barnes, R. D. Brinton, J.-J. Carrero, D. L. DeMeo, G. J. De Vries, C. N. Epperson, R. Govindan, S. L. Klein, A. Lonardo, P. M. Maki, L. D. McCullough, V. Regitz-Zagrosek, J. G. Regensteiner, J. B. Rubin, K. Sandberg, and A. Suzuki, "Sex and gender: modifiers of health, disease, and medicine," *Lancet*, vol. 396, no. 10250, pp. 565–582, Aug. 2020. URL: https://www.sciencedirect.com/science/article/pii/S0140673620315610

[28] P. S. Sizer and C. R. James, "Considerations of Sex Differences in Musculoskeletal Anatomy," in *The Active Female: Health Issues Throughout the Lifespan*, J. J. Robert-McComb, R. L. Norman, and M. Zumwalt, Eds. New York, NY: Springer, 2014, pp. 33–60. URL: https://doi.org/10.1007/978-1-4614-8884-2_3

[29] A. T. Layton, "His and her mathematical models of physiological systems," *Math Biosci*, vol. 338, p. 108642, 2021. URL: https://doi.org/10.1016/j.mbs.2021.108642

[30] O. P. Soldin and D. R. Mattison, "Sex Differences in Pharmacokinetics and Pharmacodynamics," *Clin Pharmacokinet*, vol. 48, no. 3, pp. 143–157, Mar. 2009. URL: https://doi.org/10.2165/00003088-200948030-00001

[31] J. Heinrich, "Drug safety: Most drugs withdrawn in recent years had greater health risks for women," Feb. 2001. URL: https://www.gao.gov/products/gao-01-286r

[32] C. Dibner, U. Schibler, and U. Albrecht, "The mammalian circadian timing system: organization and coordination of central and peripheral clocks," *Annu Rev Physiol*, vol. 72, pp. 517–549, 2010. URL: https://doi.org/10.1146/annurev-physiol-021909-135821

[33] G. Asher and U. Schibler, "Crosstalk between components of circadian and metabolic cycles in mammals," *Cell Metab*, vol. 13, no. 2, pp. 125–137, 2011. URL: https://doi.org/10.1016/j.cmet.2011.01.006

[34] S. Abo, D. Smith, M. Stadt, and A. Layton, "Modelling female physiology from head to toe: Impact of sex hormones, menstrual cycle, and pregnancy," *J Theor Biol*, vol. 540, p. 111074, 2022. URL: https://www.sciencedirect.com/science/article/pii/S0022519322000728

[35] N. Komin, A. C. Murza, E. Hernández-García, and R. Toral, "Synchronization and entrainment of coupled circadian oscillators," *Interface Focus*, vol. 1, no. 1, pp. 167–176, 2011. URL: https://doi.org/10.1098/rsfs.2010.0327

[36] D. Gonze, S. Bernard, C. Waltermann, A. Kramer, and H. Herzel, "Spontaneous synchronization of coupled circadian oscillators," *Biophys J*, vol. 89, no. 1, pp. 120–129, 2005. URL: https://doi.org/10.1529/biophysj.104.058388

[37] D. H. Nguyen and S. Hara, "Synchronization behaviors in goodwin oscillator networks driven by external periodic signals," in *2013 European Control Conference (ECC)*, 2013, pp. 4275–4280. URL: https://doi.org/10.23919/ECC.2013.6669437

[38] C. Pittendrigh and S. Daan, "A functional analysis of circadian pacemakers in nocturnal rodents - i. the stability and lability of spontaneous frequency," *J Comp Physiol*, vol. 106, no. 3, pp. 223–252, 1976. URL: https://doi.org/10.1007/BF01417856

[39] S. Bernard, D. Gonze, B. Čajavec, H. Herzel, and A. Kramer, "Synchronization-induced rhythmicity of circadian oscillators in the suprachiasmatic nucleus," *PLoS Comput Biol*, vol. 3, no. 4, pp. 667–679, 2007. URL: https://doi.org/10.1371/journal.pcbi.0030068

[40] C. Gu, J. Wang, and Z. Liu, "Free-running period of neurons in the suprachiasmatic nucleus: Its dependence on the distribution of neuronal coupling strengths," *Phys Rev E Stat Nonlinear Soft Matter Phys*, vol. 80, no. 3, 2009. URL: https://doi.org/10.1103/PhysRevE.80.030904

[41] J. Locke, P. Westermark, A. Kramer, and H. Herzel, "Global parameter search reveals design principles of the mammalian circadian clock," *BMC Syst Biol*, vol. 2, 2008. URL: https://doi.org/10.1186/1752-0509-2-16

[42] C. Gu, J. Wang, J. Wang, and Z. Liu, "Mechanism of phase splitting in two coupled groups of suprachiasmatic- nucleus neurons," *Phys Rev E Stat Nonlinear Soft Matter Phys*, vol. 83, no. 4, 2011. URL: https://doi.org/10.1103/PhysRevE.83.046224

[43] C. Gu, J. Xu, J. Rohling, H. Yang, and Z. Liu, "Noise induces oscillation and synchronization of the circadian neurons," *PLoS ONE*, vol. 10, no. 12, 2015. URL: https://doi.org/10.1371/journal.pone.0145360

[44] J. Li, C. Gu, and H. Yang, "Noise induces oscillation in the two weakly coupled subgroups of the suprachiasmatic nucleus," *Nonlinear Dyn*, vol. 102, no. 4, pp. 2759–2766, 2020. URL: https://doi.org/10.1007/s11071-020-06034-2

[45] C. H. Ko, Y. R. Yamada, D. K. Welsh, E. D. Buhr, A. C. Liu, E. E. Zhang, M. R. Ralph, S. A. Kay, D. B. Forger, and J. S. Takahashi, "Emergence of noise-induced

oscillations in the central circadian pacemaker," *PLoS Biol*, vol. 8, no. 10, p. e1000513, 2010. URL: https://doi.org/10.1371/journal.pbio.1000513

[46] A. Mogilner and L. Edelstein-Keshet, "A non-local model for a swarm," *J Math Biol*, vol. 38, no. 6, pp. 534–570, 1999. URL: https://doi.org/10.1007/s002850050158

[47] J. A. Carrillo, M. Fornasier, G. Toscani, and F. Vecil, "Particle, kinetic, and hydrodynamic models of swarming," in *Mathematical modeling of collective behavior in socio-economic and life sciences*, ser. Model Simul Sci Eng Technol. Birkhäuser Boston, Boston, MA, 2010, pp. 297–336. URL: https://doi.org/10.1007/978-0-8176-4946-3_12

[48] A. Webb, S. Taylor, K. Thoroughman, F. Doyle III, and E. Herzog, "Weakly circadian cells improve resynchrony," *PLoS Comput Biol*, vol. 8, no. 11, 2012. URL: https://doi.org/10.1371/journal.pcbi.1002787

[49] V. Šimonka, M. Fras, and M. Gosak, "Stochastic simulation of the circadian rhythmicity in the scn neuronal network," *Phys A*, vol. 424, pp. 1–10, 2015. URL: https://doi.org/10.1016/j.physa.2014.12.034

[50] F. Bolley, J. A. Cañizo, and J. A. Carrillo, "Stochastic mean-field limit: non-Lipschitz forces and swarming," *Math Models Methods Appl Sci*, vol. 21, no. 11, pp. 2179–2210, 2011. URL: https://doi.org/10.1142/S0218202511005702

[51] P.-E. Jabin, "A review of the mean field limits for Vlasov equations," *Kinet Relat Models*, vol. 7, no. 4, pp. 661–711, 2014. URL: https://doi.org/10.3934/krm.2014.7.661

[52] M. Meyer-Hermann, M. T. Figge, and R. H. Straub, "Mathematical modeling of the circadian rhythm of key neuroendocrine–immune system players in rheumatoid arthritis: A systems biology approach," *Arthritis Rheum*, vol. 60, no. 9, pp. 2585–2594, 2009. URL: https://doi.org/10.1002/art.24797

[53] J. D. Scheff, S. E. Calvano, S. F. Lowry, and I. P. Androulakis, "Modeling the influence of circadian rhythms on the acute inflammatory response," *J Theor Biol*, vol. 264, no. 3, pp. 1068–1076, 2010. URL: https://doi.org/10.1016/j.jtbi.2010.03.026

[54] E. O. Bangsgaard, "Mathematical modelling of the dynamic role of the HPA axis in the immune system," mthesis, Technical University of Denmark, Department of Applied Mathematics and Computer Science, Richard Petersens Plads, Building 324,

DK-2800 Kgs. Lyngby, Denmark, computecompute.dtu.dk, 2016, supervisor: Poul G. Hjorth, pghjdtu.dk, DTU Compute.

[55] X. Wang, W. Yu, and L. Zheng, "The dynamics of nf-κb pathway regulated by circadian clock," *Math Biosci*, vol. 260, pp. 47–53, 2015. URL: https://doi.org/10.1016/j.mbs.2014.07.012

[56] S. Hergenhan, S. Holtkamp, and C. Scheiermann, "Molecular interactions between components of the circadian clock and the immune system," *J Mol Biol*, pp. 3700–3713, 2020. URL: https://doi.org/10.1016/j.jmb.2019.12.044

[57] A. M. Curtis, M. M. Bellet, P. Sassone-Corsi, and L. A. O'Neill, "Circadian clock proteins and immunity," *Immunity*, vol. 40, no. 2, pp. 178–186, 2014. URL: https://doi.org/10.1016/j.immuni.2014.02.002

[58] E. Zavala, C. A. Gil-Gómez, K. C. A. Wedgwood, R. Burgess, K. Tsaneva-Atanasova, and M. A. Herrera-Valdez, "Dynamic modulation of glucose utilisation by glucocorticoid rhythms in health and disease," *bioRxiv*, 2020. URL: https://doi.org/10.1101/2020.02.27.968354

[59] E. Mühlbauer, E. Gross, K. Labucay, S. Wolgast, and E. Peschke, "Loss of melatonin signalling and its impact on circadian rhythms in mouse organs regulating blood glucose," *Eur J Pharmacol*, vol. 606, no. 1-3, pp. 61–71, 2009. URL: https://doi.org/10.1016/j.ejphar.2009.01.029

[60] A. Bertuzzi, S. Salinari, and G. Mingrone, "Insulin granule trafficking in β-cells: mathematical model of glucose-induced insulin secretion," *Am J Physiol Endocrinol Metab*, vol. 293, no. 1, pp. E396–E409, 2007. URL: https://doi.org/10.1152/ajpendo.00647.2006

[61] S.-A. Bae and I. P. Androulakis, "Mathematical modeling informs the impact of changes in circadian rhythms and meal patterns on insulin secretion," *Am J Physiol Regul Integr Comp Physiol*, vol. 317, no. 1, pp. R98–R107, 2019. URL: https://doi.org/10.1152/ajpregu.00230.2018

[62] A. Woller, H. Duez, B. Staels, and M. Lefranc, "A mathematical model of the liver circadian clock linking feeding and fasting cycles to clock function," *Cell Rep*, vol. 17, no. 4, pp. 1087–1097, 2016. URL: https://doi.org/10.1016/j.celrep.2016.09.060

[63] K. B. Koronowski and P. Sassone-Corsi, "Communicating clocks shape circadian homeostasis," *Science*, vol. 371, no. 6530, 2021. URL: https://doi.org/10.1126/science.abd0951

[64] C. Cobelli, G. Toffolo, and E. Ferrannini, "A model of glucose kinetics and their control by insulin, compartmental and noncompartmental approaches," *Math Biosci*, vol. 72, no. 2, pp. 291–315, 1984. URL: https://doi.org/10.1016/0025-5564(84)90114-7

[65] M. Berger and D. Rodbard, "Computer simulation of plasma insulin and glucose dynamics after subcutaneous insulin injection," *Diabetes Care*, vol. 12, no. 10, pp. 725–736, 1989. URL: https://doi.org/10.2337/diacare.12.10.725

[66] H. Kurata, "Virtual metabolic human dynamic model for pathological analysis and therapy design for diabetes," *iScience*, vol. 24, no. 2, 2021. URL: https://doi.org/10.1016/j.isci.2021.102101

[67] P. E. Carstensen, J. Bendsen, A. T. Reenberg, T. K. Ritschel, and J. B. Jørgensen, "A whole-body multi-scale mathematical model for dynamic simulation of the metabolism in man," *IFAC Pap OnLine*, vol. 55, no. 23, pp. 58–63, 2022. URL: https://doi.org/10.1016/j.ifacol.2023.01.015

[68] J. Kim, G. M. Saidel, and M. E. Cabrera, "Multi-scale computational model of fuel homeostasis during exercise: Effect of hormonal control," *Ann Biomed Eng*, 2006. URL: https://doi.org/10.1007/s10439-006-9201-x

[69] M. C. Palumbo, M. Morettini, P. Tieri, F. Diele, M. Sacchetti, and F. Castiglione, "Personalizing physical exercise in a computational model of fuel homeostasis," *PLoS Comput Biol*, vol. 14, no. 4, p. e1006073, 2018. URL: https://doi.org/10.1371/journal.pcbi.1006073

[70] I. Thiele, S. Sahoo, A. Heinken, J. Hertel, L. Heirendt, M. K. Aurich, and R. M. Fleming, "Personalized whole-body models integrate metabolism, physiology, and the gut microbiome," *Mol Syst Biol*, vol. 16, no. 5, p. e8982, 2020. URL: https://doi.org/10.15252/msb.20198982

[71] M. König, S. Bulik, and H.-G. Holzhütter, "Quantifying the contribution of the liver to glucose homeostasis: A detailed kinetic model of human hepatic glucose metabolism," *PLOS Comput Biol*, vol. 8, no. 6, pp. 1–17, 06 2012. URL: https://doi.org/10.1371/journal.pcbi.1002577

[72] R. K. Dash, J. A. DiBella, and M. E. Cabrera, "A computational model of skeletal muscle metabolism linking cellular adaptations induced by altered loading states to metabolic responses during exercise," *Biomed Eng Online*, vol. 6, no. 1, pp. 1–28, 2007. URL: https://doi.org/10.1186/1475-925X-6-14

[73] N. Berndt and H.-G. Holzhütter, "Dynamic metabolic zonation of the hepatic glucose metabolism is accomplished by sinusoidal plasma gradients of nutrients and hormones," *Front Physiol*, vol. 9, p. 1786, 2018. URL: https://doi.org/10.3389/fphys.2018.01786

[74] N. Berndt, S. Bulik, I. Wallach, T. Wünsch, M. König, M. Stockmann, D. Meierhofer, and H.-G. Holzhütter, "Hepatokin1 is a biochemistry-based model of liver metabolism for applications in medicine and pharmacology," *Nat Commun*, vol. 9, no. 1, p. 2386, 2018. URL: https://doi.org/10.1038/s41467-018-04720-9

[75] Y. Li, T. P. Solomon, J. M. Haus, G. M. Saidel, M. E. Cabrera, and J. P. Kirwan, "Computational model of cellular metabolic dynamics: effect of insulin on glucose disposal in human skeletal muscle," *Am J Physiol Endocrinol Metab*, vol. 298, no. 6, pp. E1198–E1209, 2010. URL: https://doi.org/10.1152/ajpendo.00713.2009

[76] J. P. Sluka, X. Fu, M. Swat, J. M. Belmonte, A. Cosmanescu, S. G. Clendenon, J. F. Wambaugh, and J. A. Glazier, "A liver-centric multiscale modeling framework for xenobiotics," *PLoS One*, vol. 11, no. 9, p. e0162428, 2016. URL: https://doi.org/10.1371/journal.pone.0162428

[77] W. B. Ashworth, N. A. Davies, and I. D. L. Bogle, "A computational model of hepatic energy metabolism: understanding zonated damage and steatosis in nafld," *PLoS Comput Biol*, vol. 12, no. 9, p. e1005105, 2016. URL: https://doi.org/10.1371/journal.pcbi.1005105

[78] S. Wiggins, *Introduction to applied nonlinear dynamical systems and chaos*, 2nd ed., ser. Texts in Applied Mathematics. Springer-Verlag, New York, 2003, vol. 2.

[79] S. H. Strogatz, *Nonlinear dynamics and chaos*, 2nd ed. Westview Press, Boulder, CO, 2015, with applications to physics, biology, chemistry, and engineering.

[80] J. A. Cañizo, J. A. Carrillo, and J. Rosado, "A well-posedness theory in measures for some kinetic models of collective motion," *Math Models Methods Appl Sci*, vol. 21, no. 3, pp. 515–539, 2011. URL: https://doi.org/10.1142/S0218202511005131

[81] L.-P. Chaintron and A. Diez, "Propagation of chaos: a review of models, methods and applications. i. models and methods," *arXiv preprint arXiv:2203.00446*, 2022. URL: https://hal.science/hal-03585065v3

[82] ——, "Propagation of chaos: a review of models, methods and applications. ii. applications," *arXiv preprint arXiv:2106.14812*, 2022. URL: https://hal.science/hal-03585067v3

[83] G. van der Heijden, "Hopf bifurcation," https://www.ucl.ac.uk/~ucesgvd/hopf.pdf.

[84] H. Poincaré, *Les méthodes nouvelles de la mécanique céleste. Tome II*, ser. Les Grands Classiques Gauthier-Villars. [Gauthier-Villars Great Classics]. Librairie Scientifique et Technique Albert Blanchard, Paris, 1987.

[85] A. A. Andronov, A. A. Vitt, and S. E. Khaikin, *Theory of oscillators*. Pergamon Press, Oxford-New York-Toronto, 1966, translated from the Russian by F. Immirzi; translation edited and abridged by W. Fishwick.

[86] E. Hopf, "Abzweigung einer periodischen Lösung von einer stationären eines Differentialsystems," *Ber. Verh. Sächs. Akad. Wiss. Leipzig Math.-Nat. Kl.*, vol. 95, no. 1, pp. 3–22, 1943, an English translation, with comments, is included as Section 5 in [87].

[87] J. E. Marsden and M. McCracken, *The Hopf bifurcation and its applications*, ser. Applied Mathematical Sciences, Vol. 19. Springer-Verlag, New York, 1976, with contributions by P. Chernoff, G. Childs, S. Chow, J. R. Dorroh, J. Guckenheimer, L. Howard, N. Kopell, O. Lanford, J. Mallet-Paret, G. Oster, O. Ruiz, S. Schecter, D. Schmidt and S. Smale.

[88] J.-C. van der Meer, *The Hamiltonian Hopf bifurcation*, ser. Lecture Notes in Mathematics. Springer-Verlag, Berlin, 1985, vol. 1160. URL: https://doi.org/10.1007/BFb0080357

[89] P.-E. Jabin and Z. Wang, "Mean field limit for stochastic particle systems," in *Active particles. Vol. 1. Advances in theory, models, and applications*, ser. Model Simul Sci Eng Technol. Birkhäuser/Springer, Cham, 2017, pp. 379–402.

[90] F. Golse, "On the dynamics of large particle systems in the mean field limit," in *Macroscopic and large scale phenomena: coarse graining, mean field limits and ergodicity*, ser. Lect. Notes Appl. Math. Mech. Springer, [Cham], 2016, vol. 3, pp. 1–144. URL: https://doi.org/10.1007/978-3-319-26883-5_1

[91] P.-E. Jabin, "A review of the mean field limits for Vlasov equations," *Kinet Relat Models*, vol. 7, no. 4, pp. 661–711, 2014. URL: https://doi.org/10.3934/krm.2014.7.661

[92] M. Kac, "Foundations of kinetic theory," in *Proceedings of the Third Berkeley Symposium on Mathematical Statistics and Probability, 1954–1955, vol. III.* Univ. California Press, Berkeley-Los Angeles, Calif., 1956, pp. 171–197.

[93] A.-S. Sznitman, "Topics in propagation of chaos," in *École d'Été de Probabilités de Saint-Flour XIX—1989*, ser. Lecture Notes in Math. Springer, Berlin, 1991, vol. 1464, pp. 165–251. URL: https://doi.org/10.1007/BFb0085169

[94] H. P. McKean, Jr., "Propagation of chaos for a class of non-linear parabolic equations," in *Stochastic Differential Equations (Lecture Series in Differential Equations, Session 7, Catholic Univ., 1967).* Air Force Office Sci. Res., Arlington, Va., 1967, pp. 41–57.

[95] C. Graham and S. Méléard, "Stochastic particle approximations for generalized Boltzmann models and convergence estimates," *Ann Probab*, vol. 25, no. 1, pp. 115–132, 1997. URL: https://doi.org/10.1214/aop/1024404281

[96] A.-S. Sznitman, "Nonlinear reflecting diffusion process, and the propagation of chaos and fluctuations associated," *J Funct Anal*, vol. 56, no. 3, pp. 311–336, 1984. URL: https://doi.org/10.1016/0022-1236(84)90080-6

[97] H. P. McKean, Jr., "Propagation of chaos for a class of non-linear parabolic equations," in *Stochastic Differential Equations (Lecture Series in Differential Equations, Session 7, Catholic Univ., 1967)*, ser. Lecture Series in Differential Equations, Session 7. Air Force Office of Scientific Research, Office of Aerospace Research, United States Air Force, Arlington, VA, 1967, pp. 41–57.

[98] A. Relógio, P. O. Westermark, T. Wallach, K. Schellenberg, A. Kramer, and H. Herzel, "Tuning the mammalian circadian clock: robust synergy of two loops," *PLoS Comput Biol*, vol. 7, no. 12, p. e1002309, 2011. URL: https://doi.org/10.1371/journal.pcbi.1002309

[99] M. Mieda, "The central circadian clock of the suprachiasmatic nucleus as an ensemble of multiple oscillatory neurons," *Neurosci Res*, vol. 156, pp. 24–31, 2020, oscillology: Nonlinear Neural Oscillations. URL: https://doi.org/10.1016/j.neures.2019.08.003

[100] M. A. Hofman, *Human Circadian Timing System*. Berlin, Heidelberg: Springer Berlin Heidelberg, 2009, pp. 1869–1873. URL: https://doi.org/10.1007/978-3-540-29678-2_2264

[101] M. A. Hofman and D. F. Swaab, "Living by the clock: The circadian pacemaker in older people," *Ageing Res Rev*, vol. 5, no. 1, pp. 33–51, 2006. URL: https://doi.org/10.1016/j.arr.2005.07.001

[102] D. Swaab, *The Human Hypothalamus. Basic and Clinical Aspects: part I: Nuclei of the human hypothalamus.*, ser. Handbook of Clinical Neurology. Elsevier, 2003, vol. 79, series Editors: M.J. Aminoff, F. Boller, D.F. Swaab.

[103] T. Noguchi, K. Watanabe, A. Ogura, and S. Yamaoka, "The clock in the dorsal suprachiasmatic nucleus runs faster than that in the ventral," *Eur J Neurosci*, vol. 20, no. 11, pp. 3199–3202, 2004. URL: https://doi.org/10.1111/j.1460-9568.2004.03784.x

[104] H. S. Lee, J. L. Nelms, M. Nguyen, R. Silver, and M. N. Lehman, "The eye is necessary for a circadian rhythm in the suprachiasmatic nucleus," *Nat Neurosci*, vol. 6, no. 2, pp. 111–112, 2003. URL: https://doi.org/10.1038/nn1006

[105] D. K. Welsh, J. S. Takahashi, and S. A. Kay, "Suprachiasmatic nucleus: cell autonomy and network properties," *Annu Rev Physiol*, vol. 72, pp. 551–577, 2010. URL: https://doi.org/10.1146/annurev-physiol-021909-135919

[106] J. H. Rohling, H. Tjebbe vanderLeest, S. Michel, M. J. Vansteensel, and J. H. Meijer, "Phase resetting of the mammalian circadian clock relies on a rapid shift of a small population of pacemaker neurons," *PLoS One*, vol. 6, no. 9, p. e25437, 2011. URL: https://doi.org/10.1371/journal.pone.0025437

[107] C. Gu, M. Tang, and H. Yang, "The synchronization of neuronal oscillators determined by the directed network structure of the suprachiasmatic nucleus under different photoperiods," *Sci Rep*, vol. 6, no. 1, pp. 1–8, 2016. URL: https://doi.org/10.1038/srep28878

[108] C. H. Ko and J. S. Takahashi, "Molecular components of the mammalian circadian clock," *Hum Mol Genet*, vol. 15, no. suppl_2, pp. R271–R277, 2006. URL: https://doi.org/10.1093/hmg/ddl207

[109] J. A. Mohawk, C. B. Green, and J. S. Takahashi, "Central and peripheral circadian clocks in mammals," *Annu Rev Neurosci*, vol. 35, pp. 445–462, 2012. URL: https://doi.org/10.1146/annurev-neuro-060909-153128

[110] M. Hastings, E. Maywood, and M. Brancaccio, "Generation of circadian rhythms in the suprachiasmatic nucleus," *Nat Rev Neurosci*, vol. 19, no. 8, pp. 453–469, 2018. URL: https://doi.org/10.1038/s41583-018-0026-z

[111] E. E. Zhang and S. A. Kay, "Clocks not winding down: unravelling circadian networks," *Nat Rev Mol Cell Biol*, vol. 11, no. 11, pp. 764–776, 2010. URL: https://doi.org/10.1038/nrm2995

[112] H. A. Duong, M. S. Robles, D. Knutti, and C. J. Weitz, "A molecular mechanism for circadian clock negative feedback," *Science*, vol. 332, no. 6036, pp. 1436–1439, 2011. URL: https://doi.org/10.1126/science.1196766

[113] J. S. Takahashi, "Transcriptional architecture of the mammalian circadian clock," *Nat Rev Genet*, vol. 18, no. 3, p. 164, 2017. URL: https://doi.org/10.1038/nrg.2016.150

[114] H.-m. Lee, R. Chen, H. Kim, J.-P. Etchegaray, D. R. Weaver, and C. Lee, "The period of the circadian oscillator is primarily determined by the balance between casein kinase 1 and protein phosphatase 1," *PNAS*, vol. 108, no. 39, pp. 16 451–16 456, 2011. URL: https://doi.org/10.1073/pnas.1107178108

[115] C. L. Partch, K. F. Shields, C. L. Thompson, C. P. Selby, and A. Sancar, "Posttranslational regulation of the mammalian circadian clock by cryptochrome and protein phosphatase 5," *PNAS*, vol. 103, no. 27, pp. 10 467–10 472, 2006. URL: https://doi.org/10.1073/pnas.0604138103

[116] K. L. Toh, C. R. Jones, Y. He, E. J. Eide, W. A. Hinz, D. M. Virshup, L. J. Ptácek, and Y.-H. Fu, "An h per2 phosphorylation site mutation in familial advanced sleep phase syndrome," *Science*, vol. 291, no. 5506, pp. 1040–1043, 2001. URL: https://doi.org/10.1126/science.1057499

[117] Y. Xu, Q. S. Padiath, R. E. Shapiro, C. R. Jones, S. C. Wu, N. Saigoh, K. Saigoh, L. J. Ptáček, and Y.-H. Fu, "Functional consequences of a ckiδ mutation causing familial advanced sleep phase syndrome," *Nature*, vol. 434, no. 7033, pp. 640–644, 2005. URL: https://doi.org/10.1038/nature03453

[118] K. A. Lamia, U. M. Sachdeva, L. DiTacchio, E. C. Williams, J. G. Alvarez, D. F. Egan, D. S. Vasquez, H. Juguilon, S. Panda, R. J. Shaw *et al.*, "Ampk regulates the circadian clock by cryptochrome phosphorylation and degradation," *Science*, vol. 326, no. 5951, pp. 437–440, 2009. URL: https://doi.org/10.1126/science.1172156

[119] A. Patke, M. W. Young, and S. Axelrod, "Molecular mechanisms and physiological importance of circadian rhythms," *Nat Rev Mol Cell Biol*, vol. 21, no. 2, pp. 67–84, 2020. URL: https://doi.org/10.1038/s41580-019-0179-2

[120] A. C. Liu, H. G. Tran, E. E. Zhang, A. A. Priest, D. K. Welsh, and S. A. Kay, "Redundant function of rev-erbα and β and non-essential role for bmal1 cycling in transcriptional regulation of intracellular circadian rhythms," *PLoS Genet*, vol. 4, no. 2, p. e1000023, 2008. URL: https://doi.org/10.1371/journal.pgen.1000023

[121] H. Cho, X. Zhao, M. Hatori, T. Y. Ruth, G. D. Barish, M. T. Lam, L.-W. Chong, L. DiTacchio, A. R. Atkins, C. K. Glass *et al.*, "Regulation of circadian behaviour and metabolism by rev-erb-α and rev-erb-β," *Nature*, vol. 485, no. 7396, pp. 123–127, 2012. URL: https://doi.org/10.1038/nature11048

[122] A. Bugge, D. Feng, L. J. Everett, E. R. Briggs, S. E. Mullican, F. Wang, J. Jager, and M. A. Lazar, "Rev-erbα and rev-erbβ coordinately protect the circadian clock and normal metabolic function," *Genes Dev*, vol. 26, no. 7, pp. 657–667, 2012. URL: https://doi.org/10.1101/gad.186858.112

[123] T. K. Sato, R. G. Yamada, H. Ukai, J. E. Baggs, L. J. Miraglia, T. J. Kobayashi, D. K. Welsh, S. A. Kay, H. R. Ueda, and J. B. Hogenesch, "Feedback repression is required for mammalian circadian clock function," *Nature Genet*, vol. 38, no. 3, pp. 312–319, 2006. URL: https://doi.org/10.1038/ng1745

[124] H. Ueda, M. Hagiwara, and H. Kitano, "Robust oscillations within the interlocked feedback model of drosophila circadian rhythm," *J Theor Biol*, vol. 210, no. 4, pp. 401–406, 2001. URL: https://doi.org/10.1006/jtbi.2000.2226

[125] E. E. Zhang, Y. Liu, R. Dentin, P. Y. Pongsawakul, A. C. Liu, T. Hirota, D. A. Nusinow, X. Sun, S. Landais, Y. Kodama *et al.*, "Cryptochrome mediates circadian regulation of camp signaling and hepatic gluconeogenesis," *Nat Med*, vol. 16, no. 10, pp. 1152–1156, 2010. URL: https://doi.org/10.1038/nm.2214

[126] F. Fagiani, D. Di Marino, A. Romagnoli, C. Travelli, D. Voltan, L. Di Cesare Mannelli, M. Racchi, S. Govoni, and C. Lanni, "Molecular regulations of circadian rhythm and implications for physiology and diseases," *Sig Transduct Target Ther*, vol. 7, no. 1, p. 41, 2022. URL: https://doi.org/10.1038/s41392-022-00899-y

[127] M. Ikeda, T. Sugiyama, C. S. Wallace, H. S. Gompf, T. Yoshioka, A. Miyawaki, and C. N. Allen, "Circadian dynamics of cytosolic and nuclear ca2+ in single

suprachiasmatic nucleus neurons," *Neuron*, vol. 38, no. 2, pp. 253–263, 2003. URL: https://doi.org/10.1016/S0896-6273(03)00164-8

[128] G. B. Lundkvist, Y. Kwak, E. K. Davis, H. Tei, and G. D. Block, "A calcium flux is required for circadian rhythm generation in mammalian pacemaker neurons," *J Neurosci*, vol. 25, no. 33, pp. 7682–7686, 2005. URL: https://doi.org/10.1523/JNEUROSCI.2211-05.2005

[129] S.-S. Nahm, Y. Z. Farnell, W. Griffith, and D. J. Earnest, "Circadian regulation and function of voltage-dependent calcium channels in the suprachiasmatic nucleus," *J Neurosci*, vol. 25, no. 40, pp. 9304–9308, 2005. URL: https://doi.org/10.1523/JNEUROSCI.2733-05.2005

[130] J. S. O'Neill, E. S. Maywood, J. E. Chesham, J. S. Takahashi, and M. H. Hastings, "camp-dependent signaling as a core component of the mammalian circadian pacemaker," *Science*, vol. 320, no. 5878, pp. 949–953, 2008. URL: https://doi.org/10.1126/science.1152506

[131] Z. Travnickova-Bendova, N. Cermakian, S. M. Reppert, and P. Sassone-Corsi, "Bimodal regulation of mperiod promoters by creb-dependent signaling and clock/bmal1 activity," *PNAS*, vol. 99, no. 11, pp. 7728–7733, 2002. URL: https://doi.org/10.1073/pnas.102075599

[132] M. de Jeu, M. Hermes, and C. Pennartz, "Circadian modulation of membrane properties in slices of rat suprachiasmatic nucleus," *NeuroReport*, vol. 9, no. 16, pp. 3725–3729, 1998. URL: https://doi.org/10.1097/00001756-199811160-00028

[133] A.-M. Finger and A. Kramer, "Peripheral clocks tick independently of their master," *Genes Dev*, vol. 35, no. 5-6, pp. 304–306, 2021. URL: https://doi.org/10.1101/gad.348305.121

[134] F. Sinturel, P. Gos, V. Petrenko, C. Hagedorn, F. Kreppel, K.-F. Storch, D. Knutti, A. Liani, C. Weitz, Y. Emmenegger *et al.*, "Circadian hepatocyte clocks keep synchrony in the absence of a master pacemaker in the suprachiasmatic nucleus or other extrahepatic clocks," *Genes Dev*, vol. 35, no. 5-6, pp. 329–334, 2021. URL: https://doi.org/10.1101/gad.346460.120

[135] C. Saini, A. Liani, T. Curie, P. Gos, F. Kreppel, Y. Emmenegger, L. Bonacina, J.-P. Wolf, Y.-A. Poget, P. Franken *et al.*, "Real-time recording of circadian liver gene expression in freely moving mice reveals the phase-setting behavior

of hepatocyte clocks," *Genes Dev*, vol. 27, no. 13, pp. 1526–1536, 2013. URL: https://doi.org/10.1101/gad.221374.113

[136] K. B. Koronowski, K. Kinouchi, P.-S. Welz, J. G. Smith, V. M. Zinna, J. Shi, M. Samad, S. Chen, C. N. Magnan, J. M. Kinchen *et al.*, "Defining the independence of the liver circadian clock," *Cell*, vol. 177, no. 6, pp. 1448–1462, 2019. URL: https://doi.org/10.1016/j.cell.2019.04.025

[137] J. Bass and M. A. Lazar, "Circadian time signatures of fitness and disease," *Science*, vol. 354, no. 6315, pp. 994–999, 2016. URL: https://doi.org/10.1126/science.aah4965

[138] A.-M. Finger, C. Dibner, and A. Kramer, "Coupled network of the circadian clocks: a driving force of rhythmic physiology," *FEBS Lett*, vol. 594, no. 17, pp. 2734–2769, 2020. URL: https://doi.org/10.1002/1873-3468.13898

[139] V. Pilorz, M. Astiz, K. O. Heinen, O. Rawashdeh, and H. Oster, "The concept of coupling in the mammalian circadian clock network," *J Mol Biol*, vol. 432, no. 12, pp. 3618–3638, 2020. URL: https://doi.org/10.1016/j.jmb.2019.12.037

[140] J. S. Marshall, R. Warrington, W. Watson, and H. L. Kim, "An introduction to immunology and immunopathology," *Allergy Asthma Clin Immunol*, vol. 14, pp. 1–10, 2018. URL: https://doi.org/10.1186/s13223-018-0278-1

[141] S. E. Turvey and D. H. Broide, "Innate immunity," *J Allergy Clin Immunol*, vol. 125, no. 2, pp. S24–S32, 2010. URL: https://doi.org/10.1016/j.jaci.2009.07.016

[142] F. A. Bonilla and H. C. Oettgen, "Adaptive immunity," *J Allergy Clin Immunol*, vol. 125, no. 2, pp. S33–S40, 2010. URL: https://doi.org/10.1016/j.jaci.2009.09.017

[143] K. Murphy and C. Weaver, *Janeway's immunobiology*. Garland science, 2016.

[144] G. Arango Duque and A. Descoteaux, "Macrophage cytokines: involvement in immunity and infectious diseases," *Front Immunol*, vol. 5, p. 117833, 2014. URL: https://doi.org/10.3389/fimmu.2014.00491

[145] B. A. Beutler, "The role of tumor necrosis factor in health and disease," *J Rheumatol Suppl*, vol. 57, pp. 16–21, 1999.

[146] E. Carswell, L. J. Old, R. Kassel, S. Green, N. Fiore, and B. Williamson, "An endotoxin-induced serum factor that causes necrosis of tumors," *PNAS*, vol. 72, no. 9, pp. 3666–3670, 1975. URL: https://doi.org/10.1073/pnas.72.9.3666

[147] G. K. Griffin, G. Newton, M. L. Tarrio, D.-x. Bu, E. Maganto-Garcia, V. Azcutia, P. Alcaide, N. Grabie, F. W. Luscinskas, K. J. Croce *et al.*, "Il-17 and tnf-α sustain neutrophil recruitment during inflammation through synergistic effects on endothelial activation," *J Immunol*, vol. 188, no. 12, pp. 6287–6299, 2012. URL: https://doi.org/10.4049/jimmunol.1200385

[148] S. Vieira, H. Lemos, R. Grespan, M. H. Napimoga, D. Dal-Secco, A. Freitas, T. Cunha, W. Verri Jr, D. Souza-Junior, M. C. Jamur *et al.*, "A crucial role for tnf-α in mediating neutrophil influx induced by endogenously generated or exogenous chemokines, kc/cxcl1 and lix/cxcl5," *Br J Pharmacol*, vol. 158, no. 3, pp. 779–789, 2009. URL: https://doi.org/10.1111/j.1476-5381.2009.00367.x

[149] V. B. Matthews, T. Allen, S. Risis, M. Chan, D. C. Henstridge, N. Watson, L. Zaffino, J. R. Babb, J. Boon, P. J. Meikle *et al.*, "Interleukin-6-deficient mice develop hepatic inflammation and systemic insulin resistance," *Diabetologia*, vol. 53, pp. 2431–2441, 2010. URL: https://doi.org/10.1007/s00125-010-1865-y

[150] F. N. Varzaneh, B. Keller, S. Unger, A. Aghamohammadi, K. Warnatz, and N. Rezaei, "Cytokines in common variable immunodeficiency as signs of immune dysregulation and potential therapeutic targets–a review of the current knowledge," *J Clin Immunol*, vol. 34, pp. 524–543, 2014. URL: https://doi.org/10.1007/s10875-014-0053-0

[151] M. A. Travis and D. Sheppard, "Tgf-β activation and function in immunity," *Annu Rev Immunol*, vol. 32, pp. 51–82, 2014. URL: https://doi.org/10.1146/annurev-immunol-032713-120257

[152] C. Becker, M. C. Fantini, C. Schramm, H. A. Lehr, S. Wirtz, A. Nikolaev, J. Burg, S. Strand, R. Kiesslich, S. Huber *et al.*, "Tgf-β suppresses tumor progression in colon cancer by inhibition of il-6 trans-signaling," *Immunity*, vol. 21, no. 4, pp. 491–501, 2004. URL: https://doi.org/10.1016/j.immuni.2004.07.020

[153] P.-E. Gleizes, J. S. Munger, I. Nunes, J. G. Harpel, R. Mazzieri, I. Noguera, and D. B. Rifkin, "Tgf-β latency: biological significance and mechanisms of activation," *Stem Cells*, vol. 15, no. 3, pp. 190–197, 1997. URL: https://doi.org/10.1002/stem.150190

[154] K. N. Frayn, *Metabolic regulation: A Human Perspective*, 3rd ed. Oxford, United Kingdom: John Wiley & Sons, 2009, ch. 2, pp. 33–37.

[155] U. Albrecht and G. Eichele, "The mammalian circadian clock," *Curr Opin Genet Dev*, vol. 13, no. 3, pp. 271–277, 2003. URL: https://doi.org/10.1016/s0959-437x(03)00055-8

[156] I. K. Sundar, H. Yao, M. T. Sellix, and I. Rahman, "Circadian molecular clock in lung pathophysiology," *Am J Physiol Lung Cell Mol Physiol*, vol. 309, no. 10, pp. L1056–L1075, 2015. URL: https://doi.org/10.1152/ajplung.00152.2015

[157] V. Pilorz, P. S. Cunningham, A. Jackson, A. C. West, T. T. Wager, A. S. Loudon, and D. A. Bechtold, "A novel mechanism controlling resetting speed of the circadian clock to environmental stimuli," *Curr Biol*, vol. 24, no. 7, pp. 766–773, 2014. URL: https://doi.org/10.1016/j.cub.2014.02.027

[158] V. T. Vasu, C. E. Cross, and K. Gohil, "Nr1d1, an important circadian pathway regulatory gene, is suppressed by cigarette smoke in murine lungs," *Integr Cancer Ther*, vol. 8, no. 4, pp. 321–328, 2009. URL: https://doi.org/10.1177/1534735409352027

[159] S. Gebel, B. Gerstmayer, P. Kuhl, J. Borlak, K. Meurrens, and T. Müller, "The kinetics of transcriptomic changes induced by cigarette smoke in rat lungs reveals a specific program of defense, inflammation, and circadian clock gene expression," *Toxicol Sci*, vol. 93, no. 2, pp. 422–431, 2006. URL: https://doi.org/10.1093/toxsci/kfl071

[160] S. Sukumaran, W. J. Jusko, D. C. DuBois, and R. R. Almon, "Light-dark oscillations in the lung transcriptome: implications for lung homeostasis, repair, metabolism, disease, and drug action," *J Appl Physiol*, vol. 110, no. 6, pp. 1732–1747, 2011. URL: https://doi.org/10.1152/japplphysiol.00079.2011

[161] R. W. Logan, C. Zhang, S. Murugan, S. O'Connell, D. Levitt, A. M. Rosenwasser, and D. K. Sarkar, "Chronic shift-lag alters the circadian clock of nk cells and promotes lung cancer growth in rats," *J Neuroimmunol*, vol. 188, no. 6, pp. 2583–2591, 2012. URL: https://doi.org/10.4049/jimmunol.1102715

[162] G. Wolff, M. J. Duncan, and K. A. Esser, "Chronic phase advance alters circadian physiological rhythms and peripheral molecular clocks," *J Appl Physiol*, vol. 115, no. 3, pp. 373–382, 2013. URL: https://doi.org/10.1152/japplphysiol.01139.2012

[163] A. J. Davidson, O. Castanon-Cervantes, T. L. Leise, P. C. Molyneux, and M. E. Harrington, "Visualizing jet lag in the mouse suprachiasmatic nucleus and

peripheral circadian timing system," *Eur J Neurosci*, vol. 29, no. 1, pp. 171–180, 2009. URL: https://doi.org/10.1111/j.1460-9568.2008.06534.x

[164] H. Hadden, S. J. Soldin, and D. Massaro, "Circadian disruption alters mouse lung clock gene expression and lung mechanics," *J Appl Physiol*, vol. 113, no. 3, pp. 385–392, 2012. URL: https://doi.org/10.1152/japplphysiol.00244.2012

[165] J. Gibbs, L. Ince, L. Matthews, J. Mei, T. Bell, N. Yang, B. Saer, N. Begley, T. Poolman, M. Pariollaud *et al.*, "An epithelial circadian clock controls pulmonary inflammation and glucocorticoid action," *Nat Med*, vol. 20, no. 8, pp. 919–926, 2014. URL: https://doi.org/10.1038/nm.3599

[166] I. K. Sundar, T. Ahmad, H. Yao, J.-w. Hwang, J. Gerloff, B. P. Lawrence, M. T. Sellix, and I. Rahman, "Influenza a virus-dependent remodeling of pulmonary clock function in a mouse model of copd," *Sci Rep*, vol. 5, no. 1, pp. 1–14, 2015. URL: https://doi.org/10.1038/srep09927

[167] E. L. Haus and M. H. Smolensky, "Shift work and cancer risk: potential mechanistic roles of circadian disruption, light at night, and sleep deprivation," *Sleep Med Rev*, vol. 17, no. 4, pp. 273–284, 2013. URL: https://doi.org/10.1016/j.smrv.2012.08.003

[168] S. Khan, P. Duan, L. Yao, and H. Hou, "Shiftwork-mediated disruptions of circadian rhythms and sleep homeostasis cause serious health problems," *Int J Genomics*, vol. 2018, 2018. URL: https://doi.org/10.1155/2018/8576890

[169] S. M. Reppert and D. R. Weaver, "Coordination of circadian timing in mammals," *Nature*, vol. 418, no. 6901, pp. 935–941, 2002. URL: https://doi.org/10.1038/nature00965

[170] N. Wei, M. L. Gumz, and A. T. Layton, "Predicted effect of circadian clock modulation of nhe3 of a proximal tubule cell on sodium transport," *Am J Physiol Renal Physiol*, vol. 315, no. 3, pp. F665–F676, 2018. URL: https://doi.org/10.1152/ajprenal.00008.2018

[171] Q. Li, A. McDonough, H. Layton, and A. Layton, "Functional implications of sexual dimorphism of transporter patterns along the rat proximal tubule: modeling and analysis," *Am J Physiol Renal Physiol*, vol. 315, pp. F692–F700, 2018. URL: https://doi.org/10.1152/ajprenal.00171.2018

[172] E. Lee and E. Y. Kim, "A role for timely nuclear translocation of clock repressor proteins in setting circadian clock speed," *Exp neurobiol*, vol. 23, no. 3, pp. 191–199, 2014. URL: https://doi.org/10.5607/en.2014.23.3.191

[173] A. Roy, G. Clermont, S. Daun, and R. S. Parker, "A mathematical model of acute inflammatory response to endotoxin challenge," in *AIChE Annual Meeting, Salt Lake City, UT, 538pp*, 2007.

[174] S. Daun, J. Rubin, Y. Vodovotz, A. Roy, R. Parker, and G. Clermont, "An ensemble of models of the acute inflammatory response to bacterial lipopolysaccharide in rats: results from parameter space reduction," *J Theor Biol*, vol. 253, no. 4, pp. 843–853, 2008. URL: https://doi.org/10.1016/j.jtbi.2008.04.033

[175] A. A. Nash, R. G. Dalziel, and J. R. Fitzgerald, "Mechanisms of cell and tissue damage," *Mims' Pathogenesis of Infectious Disease*, p. 171, 2015. URL: https://doi.org/10.1016/B978-0-323-35775-3.00001-1

[176] B. D. Freeman and C. Natanson, "Anti-inflammatory therapies in sepsis and septic shock," *Expert Opin Investig Drugs*, vol. 9, no. 7, pp. 1651–1663, 2000. URL: https://doi.org/10.1517/13543784.9.7.1651

[177] G. Bellingan, "Inflammatory cell activation in sepsis," *Br Med Bull*, vol. 55, no. 1, pp. 12–29, 1999. URL: https://doi.org/10.1111/imr.12499

[178] M. Pretolani, "Interleukin-10: an anti-inflammatory cytokine with therapeutic potential," *Clin Exp Allergy*, vol. 29, no. 9, pp. 1164–1171, 1999. URL: https://doi.org/10.3389/fimmu.2021.677008

[179] M. R. Pinsky, "Sepsis: a pro-and anti-inflammatory disequilibrium syndrome," *Contrib Nephrol*, vol. 132, pp. 354–366, 2001. URL: https://doi.org/10.1159/000060100

[180] P. Matzinger, "The danger model: a renewed sense of self," *science*, vol. 296, no. 5566, pp. 301–305, 2002. URL: https://doi.org/10.1126/science.1071059

[181] P. Giannoudis, R. Smith, S. Perry, A. Windsor, R. Dickson, and M. Bellamy, "Immediate il-10 expression following major orthopaedic trauma: relationship to anti-inflammatory response and subsequent development of sepsis," *Intensive Care Med*, vol. 26, pp. 1076–1081, 2000. URL: https://doi.org/10.1007/s001340051320

[182] K. Kamm, W. VanderKolk, C. Lawrence, M. Jonker, and A. T. Davis, "The effect of traumatic brain injury upon the concentration and expression of interleukin-1β and interleukin-10 in the rat," *J Trauma Acute Care Surg*, vol. 60, no. 1, pp. 152–157, 2006. URL: https://doi.org/10.1097/01.ta.0000196345.81169.a1

[183] A. Gouel-Chéron, B. Allaouchiche, C. Guignant, F. Davin, B. Floccard, G. Monneret, A. Group *et al.*, "Early interleukin-6 and slope of monocyte human leukocyte antigen-dr: a powerful association to predict the development of sepsis after major trauma," *PloS one*, vol. 7, no. 3, p. e33095, 2012. URL: https://doi.org/10.1371/journal.pone.0033095

[184] S. Mera, D. Tatulescu, C. Cismaru, C. Bondor, A. Slavcovici, V. Zanc, D. Carstina, and M. Oltean, "Multiplex cytokine profiling in patients with sepsis," *Apmis*, vol. 119, no. 2, pp. 155–163, 2011. URL: https://doi.org/10.1111/j.1600-0463.2010.02705.x

[185] H. Chaudhry, J. Zhou, Y. Zhong, M. M. Ali, F. McGuire, P. S. Nagarkatti, and M. Nagarkatti, "Role of cytokines as a double-edged sword in sepsis," *In Vivo*, vol. 27, no. 6, pp. 669–684, 2013.

[186] K. D. Nguyen, S. J. Fentress, Y. Qiu, K. Yun, J. S. Cox, and A. Chawla, "Circadian gene bmal1 regulates diurnal oscillations of ly6chi inflammatory monocytes," *Science*, vol. 341, no. 6153, pp. 1483–1488, 2013. URL: https://doi.org/10.1126/science.1240636

[187] A. M. Curtis, C. T. Fagundes, G. Yang, E. M. Palsson-McDermott, P. Wochal, A. F. McGettrick, N. H. Foley, J. O. Early, L. Chen, H. Zhang *et al.*, "Circadian control of innate immunity in macrophages by mir-155 targeting bmal1," *PNAS*, vol. 112, no. 23, pp. 7231–7236, 2015. URL: https://doi.org/10.1073/pnas.1501327112

[188] A. Hashiramoto, T. Yamane, K. Tsumiyama, K. Yoshida, K. Komai, H. Yamada, F. Yamazaki, M. Doi, H. Okamura, and S. Shiozawa, "Mammalian clock gene cryptochrome regulates arthritis via proinflammatory cytokine tnf-α," *J Neuroimmunol*, vol. 184, no. 3, pp. 1560–1565, 2010. URL: https://doi.org/10.4049/jimmunol.0903284

[189] R. Narasimamurthy, M. Hatori, S. K. Nayak, F. Liu, S. Panda, and I. M. Verma, "Circadian clock protein cryptochrome regulates the expression of proinflammatory cytokines," *PNAS*, vol. 109, no. 31, pp. 12 662–12 667, 2012. URL: https://doi.org/10.1073/pnas.1209965109

[190] Q. Cao, X. Zhao, J. Bai, S. Gery, H. Sun, D.-C. Lin, Q. Chen, Z. Chen, L. Mack, H. Yang *et al.*, "Circadian clock cryptochrome proteins regulate autoimmunity," *PNAS*, vol. 114, no. 47, pp. 12 548–12 553, 2017. URL: https://doi.org/10.1073/pnas.1619119114

[191] C. M. Stapleton, M. Jaradat, D. Dixon, H. S. Kang, S.-C. Kim, G. Liao, M. A. Carey, J. Cristiano, M. P. Moorman, and A. M. Jetten, "Enhanced susceptibility of staggerer (rorαsg/sg) mice to lipopolysaccharide-induced lung inflammation," *Am J Physiol Lung Cell Mol Physiol*, vol. 289, no. 1, pp. L144–L152, 2005. URL: https://doi.org/10.1152/ajplung.00348.2004

[192] I. Dzhagalov, V. Giguère, and Y.-W. He, "Lymphocyte development and function in the absence of retinoic acid-related orphan receptor α," *J Neuroimmunol*, vol. 173, no. 5, pp. 2952–2959, 2004. URL: https://doi.org/10.4049/jimmunol.173.5.2952

[193] N. Nejati Moharrami, E. Bjørkøy Tande, L. Ryan, T. Espevik, and V. Boyartchuk, "Rorα controls inflammatory state of human macrophages," *PloS one*, vol. 13, no. 11, p. e0207374, 2018. URL: https://doi.org/10.1371/journal.pone.0207374

[194] P. Delerive, D. Monté, G. Dubois, F. Trottein, J. Fruchart-Najib, J. Mariani, J.-C. Fruchart, and B. Staels, "The orphan nuclear receptor rorα is a negative regulator of the inflammatory response," *EMBO reports*, vol. 2, no. 1, pp. 42–48, 2001. URL: https://doi.org/10.1093/embo-reports/kve007

[195] J. E. Gibbs, J. Blaikley, S. Beesley, L. Matthews, K. D. Simpson, S. H. Boyce, S. N. Farrow, K. J. Else, D. Singh, D. W. Ray *et al.*, "The nuclear receptor rev-erbα mediates circadian regulation of innate immunity through selective regulation of inflammatory cytokines," *PNAS*, vol. 109, no. 2, pp. 582–587, 2012. URL: https://doi.org/10.1073/pnas.1106750109

[196] S. Sato, T. Sakurai, J. Ogasawara, K. Shirato, Y. Ishibashi, S. Oh-ishi, K. Imaizumi, S. Haga, Y. Hitomi, T. Izawa *et al.*, "Direct and indirect suppression of interleukin-6 gene expression in murine macrophages by nuclear orphan receptor rev-erbα," *ScientificWorldJournal*, vol. 2014, 2014. URL: https://doi.org/10.1155/2014/685854

[197] M. Pariollaud, J. E. Gibbs, T. W. Hopwood, S. Brown, N. Begley, R. Vonslow, T. Poolman, B. Guo, B. Saer, D. H. Jones *et al.*, "Circadian clock component rev-erbα controls homeostatic regulation of pulmonary inflammation," *J Clin Invest*, vol. 128, no. 6, pp. 2281–2296, 2018. URL: https://doi.org/10.1172/JCI93910

[198] V. Chandra, S. Mahajan, A. Saini, H. K. Dkhar, R. Nanduri, E. B. Raj, A. Kumar, and P. Gupta, "Human il10 gene repression by rev-erbα ameliorates mycobacterium tuberculosis clearance," *J Biol Chem*, vol. 288, no. 15, pp. 10 692–10 702, 2013. URL: https://doi.org/10.1074/jbc.M113.455915

[199] G. Lundkvist, R. Hill, and K. Kristensson, "Disruption of circadian rhythms in synaptic activity of the suprachiasmatic nuclei by african trypanosomes and cytokines," *Neurobiol Dis*, vol. 11, no. 1, pp. 20–27, 2002. URL: https://doi.org/10.1006/nbdi.2002.0536

[200] L. Marpegán, T. A. Bekinschtein, M. A. Costas, and D. A. Golombek, "Circadian responses to endotoxin treatment in mice," *J Neuroimmunol*, vol. 160, no. 1-2, pp. 102–109, 2005. URL: https://doi.org/10.1016/j.jneuroim.2004.11.003

[201] G. Cavadini, S. Petrzilka, P. Kohler, C. Jud, I. Tobler, T. Birchler, and A. Fontana, "Tnf-α suppresses the expression of clock genes by interfering with e-box-mediated transcription," *PNAS*, vol. 104, no. 31, pp. 12 843–12 848, 2007. URL: https://doi.org/10.1073/pnas.0701466104

[202] Y. Kwak, G. B. Lundkvist, J. Brask, A. Davidson, M. Menaker, K. Kristensson, and G. D. Block, "Interferon-γ alters electrical activity and clock gene expression in suprachiasmatic nucleus neurons," *J Biol Rhythms*, vol. 23, no. 2, pp. 150–159, 2008. URL: https://doi.org/10.1177/0748730407313355

[203] K. Okada, M. Yano, Y. Doki, T. Azama, H. Iwanaga, H. Miki, M. Nakayama, H. Miyata, S. Takiguchi, Y. Fujiwara *et al.*, "Injection of lps causes transient suppression of biological clock genes in rats," *J Surg Res*, vol. 145, no. 1, pp. 5–12, 2008. URL: https://doi.org/10.1016/j.jss.2007.01.010

[204] M. M. Bellet, E. Deriu, J. Z. Liu, B. Grimaldi, C. Blaschitz, M. Zeller, R. A. Edwards, S. Sahar, S. Dandekar, P. Baldi *et al.*, "Circadian clock regulates the host response to salmonella," *PNAS*, vol. 110, no. 24, pp. 9897–9902, 2013. URL: https://doi.org/10.1073/pnas.1120636110

[205] T. Shimizu, K. Watanabe, N. Anayama, and K. Miyazaki, "Effect of lipopolysaccharide on circadian clock genes per2 and bmal1 in mouse ovary," *J Physiol Sci*, vol. 67, no. 5, pp. 623–628, 2017. URL: https://doi.org/10.1007/s12576-017-0532-1

[206] B. Haimovich, J. Calvano, A. D. Haimovich, S. E. Calvano, S. M. Coyle, and S. F. Lowry, "In vivo endotoxin synchronizes and suppresses clock gene expression in

human peripheral blood leukocytes," *J Crit Care Med*, vol. 38, no. 3, p. 751, 2010. URL: https://doi.org/10.1097/CCM.0b013e3181cd131c

[207] Y. Wang, P. Pati, Y. Xu, F. Chen, D. W. Stepp, Y. Huo, R. D. Rudic, and D. J. Fulton, "Endotoxin disrupts circadian rhythms in macrophages via reactive oxygen species," *PloS one*, vol. 11, no. 5, p. e0155075, 2016. URL: https://doi.org/10.1371/journal.pone.0155075

[208] R. Zhang, N. F. Lahens, H. I. Ballance, M. E. Hughes, and J. B. Hogenesch, "A circadian gene expression atlas in mammals: implications for biology and medicine," *PNAS*, vol. 111, no. 45, pp. 16 219–16 224, 2014. URL: https://doi.org/10.1073/pnas.1408886111

[209] P. D. Mavroudis, D. C. DuBois, R. R. Almon, and W. J. Jusko, "Daily variation of gene expression in diverse rat tissues," *PloS one*, vol. 13, no. 5, p. e0197258, 2018. URL: https://doi.org/10.1371/journal.pone.0197258

[210] M. Iversen and R. Hahn, "Acute effects of vitamin a on the kinetics of endotoxin in conscious rabbits," *Intensive Care Med*, vol. 25, pp. 1160–1164, 1999. URL: https://doi.org/10.1007/s001340051029

[211] A. Warner, M. DeCamp Jr, R. Molina, and J. Brain, "Pulmonary removal of circulating endotoxin results in acute lung injury in sheep." *Lab Invest*, vol. 59, no. 2, pp. 219–230, 1988. URL: https://doi.org/10.1007/s001340051320

[212] H. T. Banks and H. T. Tran, *Mathematical and experimental modeling of physical and biological processes*. Chapman & Hall/CRC Press, 2009.

[213] E. Thun, S. Le Hellard, T. Osland, B. Bjorvatn, B. Moen, N. Magerøy, V. Steen, S. Giddaluru, H.-R. Brattbakk, and S. Pallesen, "Circadian clock gene variants and insomnia, sleepiness, and shift work disorder," *Sleep Biol Rhythms*, vol. 14, no. 1, pp. 55–62, 2016. URL: https://doi.org/10.1007/s41105-015-0023-9

[214] D. Landgraf, L. L. Wang, T. Diemer, and D. K. Welsh, "Npas2 compensates for loss of clock in peripheral circadian oscillators," *PLoS genetics*, vol. 12, no. 2, p. e1005882, 2016. URL: https://doi.org/10.1371/journal.pgen.1005882

[215] J. P. DeBruyne, D. R. Weaver, and S. M. Reppert, "Clock and npas2 have overlapping roles in the suprachiasmatic circadian clock," *Nat Neurosci*, vol. 10, no. 5, pp. 543–545, 2007. URL: https://doi.org/10.1038/nn1884

[216] M. Wu, J. Zeng, Y. Chen, Z. Zeng, J. Zhang, Y. Cai, Y. Ye, L. Fu, L. Xian, and Z. Chen, "Experimental chronic jet lag promotes growth and lung metastasis of lewis lung carcinoma in c57bl/6 mice," *Oncol Rep*, vol. 27, no. 5, pp. 1417–1428, 2012. URL: https://doi.org/10.3892/or.2012.1688

[217] A. Iwamoto, M. Kawai, M. Furuse, and S. Yasuo, "Effects of chronic jet lag on the central and peripheral circadian clocks in cba/n mice," *Chronobiol Int*, vol. 31, no. 2, pp. 189–198, 2014. URL: https://doi.org/10.3109/07420528.2013.837478

[218] I. Karatsoreos and R. Silver, "Body clocks in health and disease," in *Conn's Translational Neuroscience*. Elsevier, 2017, pp. 599–615. URL: https://doi.org/10.1016/B978-0-12-802381-5.00043-9

[219] F. Halberg, "Temporal coordination of physiologic function," in *Cold Spring Harbor symposia on quantitative biology*, vol. 25. Cold Spring Harbor Laboratory Press, 1960, pp. 289–310. URL: https://doi.org/10.1101/sqb.1960.025.01.031

[220] P. G. Shackelford and R. D. Feigin, "Periodicity of susceptibility to pneumococcal infection: influence of light and adrenocortical secretions," *Science*, vol. 182, no. 4109, pp. 285–287, 1973. URL: https://doi.org/10.1126/science.182.4109.285

[221] C. C. Chow, G. Clermont, R. Kumar, C. Lagoa, Z. Tawadrous, D. Gallo, B. Betten, J. Bartels, G. Constantine, M. P. Fink *et al.*, "The acute inflammatory response in diverse shock states," *Shock*, vol. 24, no. 1, pp. 74–84, 2005. URL: https://doi.org/10.1097/01.shk.0000168526.97716.f3

[222] L. Marpegan, M. J. Leone, M. E. Katz, P. M. Sobrero, T. A. Bekinstein, and D. A. Golombek, "Diurnal variation in endotoxin-induced mortality in mice: correlation with proinflammatory factors," *Chronobiol Int*, vol. 26, no. 7, pp. 1430–1442, 2009. URL: https://doi.org/10.3109/07420520903408358

[223] O. Castanon-Cervantes, M. Wu, J. C. Ehlen, K. Paul, K. L. Gamble, R. L. Johnson, R. C. Besing, M. Menaker, A. T. Gewirtz, and A. J. Davidson, "Dysregulation of inflammatory responses by chronic circadian disruption," *J Neuroimmunol*, vol. 185, no. 10, pp. 5796–5805, 2010. URL: https://doi.org/10.4049/jimmunol.1001026

[224] K. L. Adams, O. Castanon-Cervantes, J. A. Evans, and A. J. Davidson, "Environmental circadian disruption elevates the il-6 response to lipopolysaccharide in blood," *J Biol Rhythms*, vol. 28, no. 4, pp. 272–277, 2013. URL: https://doi.org/10.1177/0748730413494561

[225] N. N. Guerrero-Vargas, M. Guzmán-Ruiz, R. Fuentes, J. García, R. Salgado-Delgado, M. d. C. Basualdo, C. Escobar, R. P. Markus, and R. M. Buijs, "Shift work in rats results in increased inflammatory response after lipopolysaccharide administration: a role for food consumption," *J Biol Rhythms*, vol. 30, no. 4, pp. 318–330, 2015. URL: https://doi.org/10.1177/0748730415586482

[226] D. J. Phillips, M. I. Savenkova, and I. N. Karatsoreos, "Environmental disruption of the circadian clock leads to altered sleep and immune responses in mouse," *Brain Behav Immun*, vol. 47, pp. 14–23, 2015. URL: https://doi.org/10.1016/j.bbi.2014.12.008

[227] G. L. Pearson, M. Savenkova, J. J. Barnwell, and I. N. Karatsoreos, "Circadian desynchronization alters metabolic and immune responses following lipopolysaccharide inoculation in male mice," *Brain Behav Immun*, pp. 220–229, 2020. URL: https://doi.org/10.1016/j.bbi.2020.05.033

[228] A. Stowie, I. Ellis, K. Adams, O. Castanon-Cervantes, and A. J. Davidson, "A reductionist, in vitro model of environmental circadian disruption demonstrates scn-independent and tissue-specific dysregulation of inflammatory responses," *Plos one*, vol. 14, no. 5, p. e0217368, 2019. URL: https://doi.org/10.1371/journal.pone.0217368

[229] T. Tiwari, P. Basu, and M. Singaravel, "Differences in post-chronic jet lag parameters in male and female mice," *Biol Rhythm Res*, pp. 1–11, 2019. URL: https://doi.org/10.1080/09291016.2019.1586099

[230] M. K. Angele, S. Pratschke, W. J. Hubbard, and I. H. Chaudry, "Gender differences in sepsis: cardiovascular and immunological aspects," *Virulence*, vol. 5, no. 1, pp. 12–19, 2014. URL: https://doi.org/10.4161/viru.26982

[231] N. Nasir, B. Jamil, S. Siddiqui, N. Talat, F. A. Khan, and R. Hussain, "Mortality in sepsis and its relationship with gender," *Pak J Med Sci*, vol. 31, no. 5, p. 1201, 2015. URL: https://doi.org/10.12669/pjms.315.6925

[232] R. Orozco-Solis and L. Aguilar-Arnal, "Circadian regulation of immunity through epigenetic mechanisms," *Front Cell Infect Microbiol*, vol. 10, p. 96, 2020. URL: https://doi.org/10.3389/fcimb.2020.00096

[233] J. A. Haspel, R. Anafi, M. K. Brown, N. Cermakian, C. Depner, P. Desplats, A. E. Gelman, M. Haack, S. Jelic, B. S. Kim *et al.*, "Perfect timing: circadian rhythms, sleep, and immunity—an nih workshop summary," *JCI insight*, vol. 5, no. 1, 2020. URL: https://doi.org/10.1172/jci.insight.131487

[234] S. Barik, "Molecular interactions between pathogens and the circadian clock," *Int J Mol Sci*, vol. 20, no. 23, p. 5824, 2019. URL: https://doi.org/10.3390/ijms20235824

[235] S. M. James, K. A. Honn, S. Gaddameedhi, and H. P. Van Dongen, "Shift work: disrupted circadian rhythms and sleep—implications for health and well-being," *Curr Sleep Med Rep*, vol. 3, no. 2, pp. 104–112, 2017. URL: https://doi.org/10.1007/s40675-017-0071-6

[236] M. Perez-Aso, J. L. Feig, M. Aránzazu, and B. N. Cronstein, "Adenosine a 2a receptor and tnf-α regulate the circadian machinery of the human monocytic thp-1 cells," *Inflammation*, vol. 36, no. 1, pp. 152–162, 2013. URL: https://doi.org/10.1007/s10753-012-9530-x

[237] K. Yoshida, A. Nakai, K. Kaneshiro, N. Hashimoto, K. Suzuki, K. Uchida, T. Hashimoto, Y. Kawasaki, K. Tateishi, N. Nakagawa *et al.*, "Tnf-a induces expression of the circadian clock gene bmal1 via dual calcium-dependent pathways in rheumatoid synovial cells," *Biochem Biophys Res Commun*, vol. 30, p. 1e6, 2017. URL: https://doi.org/10.1016/j.bbrc.2017.12.015

[238] M. G. Ertosun, G. Kocak, and O. N. Ozes, "The regulation of circadian clock by tumor necrosis factor alpha," *Cytokine Growth Factor Rev*, pp. 10–16, 2019. URL: https://doi.org/10.1016/j.cytogfr.2019.04.001

[239] M. Sadria and A. T. Layton, "Interactions among mtorc, ampk and sirt: a computational model for cell energy balance and metabolism," *Cell Commun Signal*, vol. 19, no. 1, p. 57, 2021. URL: https://doi.org/10.1186/s12964-021-00706-1

[240] A. T. Layton, K. Laghmani, V. Vallon, and A. Edwards, "Solute transport and oxygen consumption along the nephrons: effects of na+ transport inhibitors," *Am J Physiol Renal Physiol*, vol. 311, no. 6, pp. F1217–F1229, 2016. URL: https://doi.org/10.1152/ajprenal.00294.2016

[241] K. Man, A. Loudon, and A. Chawla, "Immunity around the clock," *Science*, vol. 354, no. 6315, pp. 999–1003, 2016. URL: https://doi.org/10.1126/science.aah4966

[242] R. Refinetti, *Circadian physiology*. CRC press, 2019.

[243] U. Abraham, A. Granada, P. Westermark, M. Heine, A. Kramer, and H. Herzel, "Coupling governs entrainment range of circadian clocks," *Mol Syst Biol*, vol. 6, 2010. URL: https://doi.org/10.1038/msb.2010.92

[244] H. Daido, "Why circadian rhythms are circadian: Competitive population dynamics of biological oscillators," *Phys Rev Lett*, vol. 87, no. 4, pp. 48 101–1–48 101–4, 2001. URL: https://doi.org/10.1103/PhysRevLett.87.048101

[245] C. L. Partch, C. B. Green, and J. S. Takahashi, "Molecular architecture of the mammalian circadian clock," *Trends Cell Biol*, vol. 24, no. 2, pp. 90–99, 2014. URL: https://doi.org/10.1016/j.tcb.2013.07.002

[246] S. Honma, "The mammalian circadian system: a hierarchical multi-oscillator structure for generating circadian rhythm," *J Physiol Sci*, vol. 68, no. 3, pp. 207–219, 2018. URL: https://doi.org/10.1007/s12576-018-0597-5

[247] D. Gonze and A. Goldbeter, "Circadian rhythms and molecular noise," *Chaos*, vol. 16, no. 2, 2006. URL: https://doi.org/10.1063/1.2211767

[248] C. Gu, M. Tang, and H. Yang, "The synchronization of neuronal oscillators determined by the directed network structure of the suprachiasmatic nucleus under different photoperiods," *Sci Rep*, vol. 6, 2016. URL: https://doi.org/10.1038/srep28878

[249] H. Albus, M. Vansteensel, S. Michel, G. Block, and J. Meijer, "A gabaergic mechanism is necessary for coupling dissociable ventral and dorsal regional oscillators within the circadian clock," *Curr Biol*, vol. 15, no. 10, pp. 886–893, 2005. URL: https://doi.org/10.1016/j.cub.2005.03.051

[250] R. Y. Moore, J. C. Speh, and R. K. Leak, "Suprachiasmatic nucleus organization," *Cell Tissue Res*, vol. 309, no. 1, pp. 89–98, 2002. URL: https://doi.org/10.1007/s00441-002-0575-2

[251] P. St. John and I. Doyle, F.J., "Quantifying stochastic noise in cultured circadian reporter cells," *PLoS Comput Biol*, vol. 11, no. 11, 2015. URL: https://doi.org/10.1371/journal.pcbi.1004451

[252] L. Fonken, T. Aubrecht, O. Meléndez-Fernández, Z. Weil, and R. Nelson, "Dim light at night disrupts molecular circadian rhythms and increases body weight," *J Biol Rhythms*, vol. 28, no. 4, pp. 262–271, 2013. URL: https://doi.org/10.1177/0748730413493862

[253] J. A. Carrillo, M. R. D'Orsogna, and V. Panferov, "Double milling in self-propelled swarms from kinetic theory," *Kinet Relat Models*, vol. 2, no. 2, pp. 363–378, 2009. URL: https://doi.org/10.3934/krm.2009.2.363

[254] S. Méléard, "Asymptotic behaviour of some interacting particle systems; McKean-Vlasov and Boltzmann models," in *Probabilistic models for nonlinear partial differential equations (Montecatini Terme, 1995)*, ser. Lecture Notes in Math. Springer, Berlin, 1996, vol. 1627, pp. 42–95. URL: https://doi.org/10.1007/BFb0093177

[255] C. Ko and J. Takahashi, "Molecular components of the mammalian circadian clock," *Hum Mol Genet*, vol. 15, no. SUPPL. 2, pp. R271–R277, 2006. URL: https://doi.org/10.1093/hmg/ddl207

[256] C. Vasalou, E. D. Herzog, and M. A. Henson, "Small-world network models of intercellular coupling predict enhanced synchronization in the suprachiasmatic nucleus," *J Biol Rhythms*, vol. 24, no. 3, pp. 243–254, 2009. URL: https://doi.org/10.1177/0748730409333220

[257] H. Kunz and P. Achermann, "Simulation of circadian rhythm generation in the suprachiasmatic nucleus with locally coupled self-sustained oscillators," *J Theor Biol*, vol. 224, no. 1, pp. 63–78, 2003. URL: https://doi.org/10.1016/S0022-5193(03)00141-3

[258] C. Gu and H. Yang, "The circadian rhythm induced by the heterogeneous network structure of the suprachiasmatic nucleus," *Chaos*, vol. 26, no. 5, p. 053112, 2016. URL: https://doi.org/10.1063/1.4949012

[259] M. Bossy, J. Fontbona, and H. Olivero, "Synchronization of stochastic mean field networks of Hodgkin-Huxley neurons with noisy channels," *J Math Biol*, vol. 78, no. 6, pp. 1771–1820, 2019. URL: https://doi.org/10.1007/s00285-019-01326-7

[260] A. Relógio, P. Westermark, T. Wallach, K. Schellenberg, A. Kramer, and H. Herzel, "Tuning the mammalian circadian clock: Robust synergy of two loops," *PLoS Comput Biol*, vol. 7, no. 12, 2011. URL: https://doi.org/10.1371/journal.pcbi.1002309

[261] B. Ananthasubramaniam, C. Schmal, and H. Herzel, "Amplitude effects allow short jet lags and large seasonal phase shifts in minimal clock models," *J Mol Biol*, vol. 432, no. 12, pp. 3722–3737, 2020. URL: https://doi.org/10.1016/j.jmb.2020.01.014

[262] G. Tiana, S. Krishna, S. Pigolotti, M. Jensen, and K. Sneppen, "Oscillations and temporal signalling in cells," *Phys Biol*, vol. 4, no. 2, pp. R1–R17, 2007. URL: https://doi.org/10.1088/1478-3975/4/2/R01

[263] A. Woller, D. Gonze, and T. Erneux, "The goodwin model revisited: Hopf bifurcation, limit-cycle, and periodic entrainment," *Phys Biol*, vol. 11, no. 4, 2014. URL: https://doi.org/10.1088/1478-3975/11/4/045002

[264] D. Gonze and W. Abou-Jaoudé, "The goodwin model: Behind the hill function," *PLoS ONE*, vol. 8, no. 8, 2013. URL: https://doi.org/10.1371/journal.pone.0069573

[265] B. Goodwin, "Oscillatory behavior in enzymatic control processes," *Adv Enzyme Regul*, vol. 3, no. C, pp. 425–428,IN1–IN2,429–430,IN3–IN6,431–437, 1965. URL: https://doi.org/10.1016/0065-2571(65)90067-1

[266] P. Ruoff and L. Rensing, "The temperature-compensated goodwin model simulates many circadian clock properties," *J Theor Biol*, vol. 179, no. 4, pp. 275–285, 1996. URL: https://doi.org/10.1006/jtbi.1996.0067

[267] J.-C. Leloup, D. Gonze, and A. Goldbeter, "Limit cycle models for circadian rhythms based on transcriptional regulation in drosophila and neurospora," *J Biol Rhythms*, vol. 14, no. 6, pp. 433–448, 1999. URL: https://doi.org/10.1177/074873099129000948

[268] J.-C. Leloup and A. Goldbeter, "A model for circadian rhythms in drosophila incorporating the formation of a complex between the per and tim proteins," *J Biol Rhythms*, vol. 13, no. 1, pp. 70–87, 1998. URL: https://doi.org/10.1177/074873098128999934

[269] ——, "Modeling the mammalian circadian clock: sensitivity analysis and multiplicity of oscillatory mechanisms," *J Theoret Biol*, vol. 230, no. 4, pp. 541–562, 2004. URL: https://doi.org/10.1016/j.jtbi.2004.04.040

[270] A. Goldbeter, "A model for circadian oscillations in the drosophila period protein (per)," *Proc R Soc B Biol Sci*, vol. 261, no. 1362, pp. 319–324, 1995. URL: https://doi.org/10.1098/rspb.1995.0153

[271] X. Cao, Y. Yang, C. P. Selby, Z. Liu, and A. Sancar, "Molecular mechanism of the repressive phase of the mammalian circadian clock," *PNAS*, vol. 118, no. 2, 2021. URL: https://doi.org/10.1073/pnas.2021174118

[272] M. S. Robles, S. J. Humphrey, and M. Mann, "Phosphorylation is a central mechanism for circadian control of metabolism and physiology," *Cell Metab*, vol. 25, no. 1, pp. 118–127, 2017. URL: https://doi.org/10.1016/j.cmet.2016.10.004

[273] R. Narasimamurthy, S. R. Hunt, Y. Lu, J.-M. Fustin, H. Okamura, C. L. Partch, D. B. Forger, J. K. Kim, and D. M. Virshup, "Ck1δ/ε protein kinase primes the per2 circadian phosphoswitch," *PNAS*, vol. 115, no. 23, pp. 5986–5991, 2018. URL: https://doi.org/10.1073/pnas.1721076115

[274] J. K. Kim and D. B. Forger, "A mechanism for robust circadian timekeeping via stoichiometric balance," *Mol Syst Biol*, vol. 8, no. 1, p. 630, 2012. URL: https://doi.org/10.1038/msb.2012.62

[275] J. K. Kim, Z. P. Kilpatrick, M. R. Bennett, and K. Josić, "Molecular mechanisms that regulate the coupled period of the mammalian circadian clock," *Biophys J*, vol. 106, no. 9, pp. 2071–2081, 2014. URL: https://doi.org/10.1016/j.bpj.2014.02.039

[276] J. K. Kim, "Protein sequestration versus hill-type repression in circadian clock models," *IET Syst Biol*, vol. 10, no. 4, pp. 125–135, 2016. URL: https://doi.org/10.1049/iet-syb.2015.0090

[277] K.-W. Chen and C.-W. Shih, "Collective oscillations in coupled-cell systems," *Bull Math Biol*, vol. 83, no. 6, pp. Paper No. 62, 60, 2021. URL: https://doi.org/10.1007/s11538-021-00883-7

[278] A. Asgari-Targhi and E. Klerman, "Mathematical modeling of circadian rhythms," *Wiley Interdiscip Rev Syst Biol Med*, vol. 11, no. 2, 2019. URL: https://doi.org/10.1002/wsbm.1439

[279] E. Herzog, S. Aton, R. Numano, Y. Sakaki, and H. Tei, "Temporal precision in the mammalian circadian system: A reliable clock from less reliable neurons," *J Biol Rhythms*, vol. 19, no. 1, pp. 35–46, 2004. URL: https://doi.org/10.1177/0748730403260776

[280] F. Malrieu, "Convergence to equilibrium for granular media equations and their Euler schemes," *Ann Appl Probab*, vol. 13, no. 2, pp. 540–560, 2003. URL: https://doi.org/10.1214/aoap/1050689593

[281] E. Gobet, "Euler schemes and half-space approximation for the simulation of diffusion in a domain," *ESAIM Probab Statist*, vol. 5, pp. 261–297, 2001. URL: https://doi.org/10.1051/ps:2001112

[282] E. M. Hanks, D. S. Johnson, and M. B. Hooten, "Reflected stochastic differential equation models for constrained animal movement," *J Agric Biol Environ Stat*, vol. 22, no. 3, pp. 353–372, 2017. URL: https://doi.org/10.1007/s13253-017-0291-8

[283] A.-S. Sznitman, "Nonlinear reflecting diffusion process, and the propagation of chaos and fluctuations associated," *J Funct Anal*, vol. 56, no. 3, pp. 311–336, 1984. URL: https://doi.org/10.1016/0022-1236(84)90080-6

[284] P.-L. Lions and A.-S. Sznitman, "Stochastic differential equations with reflecting boundary conditions," *Comm Pure Appl Math*, vol. 37, no. 4, pp. 511–537, 1984. URL: https://doi.org/10.1002/cpa.3160370408

[285] A. Drogoul and R. Veltz, "Hopf bifurcation in a nonlocal nonlinear transport equation stemming from stochastic neural dynamics," *Chaos*, vol. 27, no. 2, pp. 021 101, 6, 2017. URL: https://doi.org/10.1063/1.4976510

[286] ——, "Exponential stability of the stationary distribution of a mean field of spiking neural network," *J Differ Equ*, vol. 270, pp. 809–842, 2021. URL: https://doi.org/10.1016/j.jde.2020.08.001

[287] Y. Zhang and M. Golubitsky, "Periodically forced Hopf bifurcation," *SIAM J Appl Dyn Syst*, vol. 10, no. 4, pp. 1272–1306, 2011. URL: https://doi.org/10.1137/10078637X

[288] G. B. Ermentrout and N. Kopell, "Frequency plateaus in a chain of weakly coupled oscillators. I," *SIAM J Math Anal*, vol. 15, no. 2, pp. 215–237, 1984. URL: https://doi.org/10.1137/0515019

[289] Y. Kuramoto, *Chemical oscillations, waves, and turbulence*, ser. Springer Series in Synergetics. Springer-Verlag, Berlin, 1984, vol. 19. URL: https://doi.org/10.1007/978-3-642-69689-3

[290] J. C. Neu, "Coupled chemical oscillators," *SIAM J Appl Math*, vol. 37, no. 2, pp. 307–315, 1979. URL: https://doi.org/10.1137/0137022

[291] L. M. Pecora and T. L. Carroll, "Master stability functions for synchronized coupled systems," *Phys Rev Lett*, vol. 80, no. 10, p. 2109, 1998. URL: https://doi.org/10.1103/PhysRevLett.80.2109

[292] J. Sun, E. M. Bollt, and T. Nishikawa, "Master stability functions for coupled nearly identical dynamical systems," *EPL*, vol. 85, no. 6, p. 60011, 2009. URL: https://doi.org/10.1209/0295-5075/85/60011

[293] E. Herzog, T. Hermanstyne, N. Smyllie, and M. Hastings, "Regulating the suprachiasmatic nucleus (scn) circadian clockwork: Interplay between cell-

autonomous and circuit-level mechanisms," *Cold Spring Harb Perspect Biol*, vol. 9, no. 1, 2017. URL: https://doi.org/10.1101/cshperspect.a027706

[294] C. Schmal, E. Herzog, and H. Herzel, "Measuring relative coupling strength in circadian systems," *J Biol Rhythms*, vol. 33, no. 1, pp. 84–98, 2018. URL: https://doi.org/10.1177/0748730417740467

[295] D. Welsh, J. Takahashi, and S. Kay, "Suprachiasmatic nucleus: Cell autonomy and network properties," *Annu Rev Physiol*, vol. 72, pp. 551–577, 2009. URL: https://doi.org/10.1146/annurev-physiol-021909-135919

[296] J. Mohawk and J. Takahashi, "Cell autonomy and synchrony of suprachiasmatic nucleus circadian oscillators," *Trends Neurosci*, vol. 34, no. 7, pp. 349–358, 2011. URL: https://doi.org/10.1016/j.tins.2011.05.003

[297] B. Aymard, F. Campillo, and R. Veltz, "Mean-field limit of interacting 2d nonlinear stochastic spiking neurons," 2019.

[298] D. Gonze, J. Halloy, and A. Goldbeter, "Robustness of circadian rhythms with respect to molecular noise," *PNAS*, vol. 99, no. 2, pp. 673–678, 2002. URL: https://doi.org/10.1073/pnas.022628299

[299] P. Ashwin, S. Coombes, and R. Nicks, "Mathematical frameworks for oscillatory network dynamics in neuroscience," *J Math Neurosci*, vol. 6, pp. Art. 2, 92, 2016. URL: https://doi.org/10.1186/s13408-015-0033-6

[300] J. Baladron, D. Fasoli, O. Faugeras, and J. Touboul, "Mean-field description and propagation of chaos in networks of Hodgkin-Huxley and FitzHugh-Nagumo neurons," *J Math Neurosci*, vol. 2, pp. Art. 10, 50, 2012. URL: https://doi.org/10.1186/2190-8567-2-10

[301] J. A. Carrillo, A. Chertock, and Y. Huang, "A finite-volume method for nonlinear nonlocal equations with a gradient flow structure," *Commun Comput Phys*, vol. 17, no. 1, pp. 233–258, 2015. URL: https://doi.org/10.4208/cicp.160214.010814a

[302] T. Noguchi, K. Watanabe, A. Ogura, and S. Yamaoka, "The clock in the dorsal suprachiasmatic nucleus runs faster than that in the ventral," *Eur J Neurosci*, vol. 20, no. 11, pp. 3199–3202, 2004. URL: https://doi.org/10.1111/j.1460-9568.2004.03784.x

[303] O. Varlamov, C. L. Bethea, and C. T. Roberts Jr, "Sex-specific differences in lipid and glucose metabolism," *Front Endocrinol*, vol. 5, p. 241, 2015. URL: https://doi.org/10.3389/fendo.2014.00241

[304] A. J. McGregor, M. Hasnain, K. Sandberg, M. F. Morrison, M. Berlin, and J. Trott, "How to study the impact of sex and gender in medical research: a review of resources," *Biol Sex Differ*, vol. 7, pp. 61–72, 2016. URL: https://doi.org/10.1186/s13293-016-0099-1

[305] J.-A. Gustafsson, A. Mode, G. Norstedt, and P. Skett, "Sex steroid induced changes in hepatic enzymes," *Annu Rev Physiol*, vol. 45, no. 1, pp. 51–60, 1983. URL: https://doi.org/10.1146/annurev.ph.45.030183.000411

[306] S. Welle, R. Tawil, and C. A. Thornton, "Sex-related differences in gene expression in human skeletal muscle," *PloS one*, vol. 3, no. 1, p. e1385, 2008. URL: https://doi.org/10.1371/journal.pone.0001385

[307] K. Karastergiou, S. R. Smith, A. S. Greenberg, and S. K. Fried, "Sex differences in human adipose tissues–the biology of pear shape," *Biol Sex Differ*, vol. 3, no. 1, pp. 1–12, 2012. URL: https://doi.org/10.1186/2042-6410-3-13

[308] T. Cvitanović Tomaš, Ž. Urlep, M. Moškon, M. Mraz, and D. Rozman, "Liversex computational model: sexual aspects in hepatic metabolism and abnormalities," *Front Physiol*, vol. 9, p. 360, 2018. URL: https://doi.org/10.3389/fphys.2018.00360

[309] S. Qiu, J. T. Vazquez, E. Boulger, H. Liu, P. Xue, M. A. Hussain, and A. Wolfe, "Hepatic estrogen receptor α is critical for regulation of gluconeogenesis and lipid metabolism in males," *Sci Rep*, vol. 7, no. 1, p. 1661, 2017. URL: https://doi.org/10.1038/s41598-017-01937-4

[310] B. T. Palmisano, L. Zhu, and J. M. Stafford, *Role of Estrogens in the Regulation of Liver Lipid Metabolism*. Cham: Springer International Publishing, 2017, pp. 227–256.

[311] M. Shen, H. Shi *et al.*, "Sex hormones and their receptors regulate liver energy homeostasis," *Int J Endocrinol*, vol. 2015, 2015. URL: https://doi.org/10.1155/2015/294278

[312] B. T. Palmisano, L. Zhu, R. H. Eckel, and J. M. Stafford, "Sex differences in lipid and lipoprotein metabolism," *Mol Metab*, vol. 15, pp. 45–55, 2018. URL: https://doi.org/10.1016/j.molmet.2018.05.008

[313] S. K. Hunter, "Sex differences in human fatigability: mechanisms and insight to physiological responses," *Acta Physiol (oxf)*, vol. 210, no. 4, pp. 768–789, 2014. URL: https://doi.org/10.1111/apha.12234

[314] J. Bergström and E. Hultman, "Muscle glycogen synthesis after exercise: an enhancing factor localized to the muscle cells in man," *Nature*, vol. 210, no. 5033, pp. 309–310, 1966. URL: https://doi.org/10.1038/210309a0

[315] A. L. Friedlander, G. A. Casazza, M. A. Horning, M. J. Huie, M. F. Piacentini, J. K. Trimmer, and G. A. Brooks, "Training-induced alterations of carbohydrate metabolism in women: women respond differently from men," *J Appl Physiol*, vol. 85, no. 3, pp. 1175–1186, 1998. URL: https://doi.org/10.1152/jappl.1998.85.3.1175

[316] T. J. Horton, M. J. Pagliassotti, K. Hobbs, and J. O. Hill, "Fuel metabolism in men and women during and after long-duration exercise," *J Appl Physiol*, vol. 85, no. 5, pp. 1823–1832, 1998. URL: https://doi.org/10.1152/jappl.1998.85.5.1823

[317] L. Tarnopolsky, J. MacDougall, S. Atkinson, M. Tarnopolsky, and J. Sutton, "Gender differences in substrate for endurance exercise," *J Appl Physiol*, vol. 68, no. 1, pp. 302–308, 1990. URL: https://doi.org/10.1152/jappl.1990.68.1.302

[318] M. Tarnopolsky, S. Atkinson, S. Phillips, and J. MacDougall, "Carbohydrate loading and metabolism during exercise in men and women," *J Appl Physiol*, vol. 78, no. 4, pp. 1360–1368, 1995. URL: https://doi.org/10.1152/jappl.1995.78.4.1360

[319] M. C. Devries, M. J. Hamadeh, S. M. Phillips, and M. A. Tarnopolsky, "Menstrual cycle phase and sex influence muscle glycogen utilization and glucose turnover during moderate-intensity endurance exercise," *Am J Physiol Regul Integr Comp Physiol*, 2006. URL: https://doi.org/10.1152/ajpregu.00700.2005

[320] X. Cheneviere, F. Borrani, D. Sangsue, B. Gojanovic, and D. Malatesta, "Gender differences in whole-body fat oxidation kinetics during exercise," *Appl Physiol Nutr Metab*, vol. 36, no. 1, pp. 88–95, 2011. URL: https://doi.org/10.1139/H10-086

[321] M. C. Devries, S. A. Lowther, A. W. Glover, M. J. Hamadeh, and M. A. Tarnopolsky, "Imcl area density, but not imcl utilization, is higher in women during moderate-intensity endurance exercise, compared with men," *Am J Physiol Regul Integr Comp Physiol*, vol. 293, no. 6, pp. R2336–R2342, 2007. URL: https://doi.org/10.1152/ajpregu.00510.2007

[322] M. C. Devries, "Sex-based differences in endurance exercise muscle metabolism: impact on exercise and nutritional strategies to optimize health and performance in women," *Exp Physiol*, vol. 101, no. 2, pp. 243–249, 2016. URL: https://doi.org/10.1113/EP085369

[323] B. C. Ruby, R. A. Robergs, D. L. Waters, M. Burge, C. Mermier, and L. Stolarczyk, "Effects of estradiol on substrate turnover during exercise in amenorrheic females." *Med Sci Sports Exerc*, vol. 29, no. 9, pp. 1160–1169, 1997. URL: https://doi.org/10.1097/00005768-199709000-00007

[324] S. Carter, S. McKenzie, M. Mourtzakis, D. Mahoney, and M. Tarnopolsky, "Short-term 17β-estradiol decreases glucose ra but not whole body metabolism during endurance exercise," *J Appl Physiol*, vol. 90, no. 1, pp. 139–146, 2001. URL: https://doi.org/10.1152/jappl.2001.90.1.139

[325] B. Mittendorfer, J. F. Horowitz, and S. Klein, "Effect of gender on lipid kinetics during endurance exercise of moderate intensity in untrained subjects," *Am J Physiol Endocrinol Metab*, vol. 283, no. 1, pp. E58–E65, 2002. URL: https://doi.org/10.1152/ajpendo.00504.2001

[326] B. Burguera, D. Proctor, N. Dietz, Z. Guo, M. Joyner, and M. D. Jensen, "Leg free fatty acid kinetics during exercise in men and women," *Am J Physiol Endocrinol Metab*, vol. 278, no. 1, pp. E113–E117, 2000. URL: https://doi.org/10.1152/ajpendo.2000.278.1.E113

[327] E. B. Marliss, S. H. Kreisman, A. Manzon, J. B. Halter, M. Vranic, and S. J. Nessim, "Gender differences in glucoregulatory responses to intense exercise," *J Appl Physiol*, vol. 88, no. 2, pp. 457–466, 2000. URL: https://doi.org/10.1152/jappl.2000.88.2.457

[328] S. N. Davis, P. Galassetti, D. H. Wasserman, and D. Tate, "Effects of gender on neuroendocrine and metabolic counterregulatory responses to exercise in normal man," *J Clin Endocrinol Metab*, vol. 85, no. 1, pp. 224–230, 01 2000. URL: https://doi.org/10.1210/jcem.85.1.6328

[329] A. Cano, L. Ventura, G. Martinez, L. Cugusi, M. Caria, F. Deriu, and A. Manca, "Analysis of sex-based differences in energy substrate utilization during moderate-intensity aerobic exercise," *Eur J Appl Physiol*, pp. 1–42, 2022. URL: https://doi.org/10.1007/s00421-021-04802-5

[330] H. Zouhal, C. Jacob, P. Delamarche, and A. Gratas-Delamarche, "Catecholamines and the effects of exercise, training and gender," *Sports Med*, vol. 38, pp. 401–423, 2008. URL: https://doi.org/10.2165/00007256-200838050-00004

[331] W. S. Snyder, M. Cook, E. Nasset, L. Karhausen, and I. H. Tipton, "Report of the task group on reference man," 1975.

[332] K.-C. Ho, U. Roessmann, J. Straumfjord, and G. Monroe, "Analysis of brain weight. i. adult brain weight in relation to sex, race, and age." *Arch Pathol Lab Med*, vol. 104, no. 12, pp. 635–639, 1980.

[333] B. Chowdhury, L. Sjöström, M. Alpsten, J. Kostanty, H. Kvist, and R. Löfgren, "A multicompartment body composition technique based on computerized tomography," *Int J Obes Relat Metab Disord*, vol. 18, no. 4, pp. 219–234, 1994.

[334] A. Heinemann, F. Wischhusen, K. Püschel, and X. Rogiers, "Standard liver volume in the caucasian population," *Liver Transpl Surg*, vol. 5, no. 5, pp. 366–368, 1999. URL: https://doi.org/10.1002/lt.500050516

[335] P. S. Price, R. B. Conolly, C. F. Chaisson, E. A. Gross, J. S. Young, E. T. Mathis, and D. R. Tedder, "Modeling interindividual variation in physiological factors used in pbpk models of humans," *Crit Rev Toxicol*, vol. 33, no. 5, pp. 469–503, 2003. URL: https://doi.org/10.1080/10408440390242324

[336] E. Krekels, J. Rower, J. Constance, C. Knibbe, and C. Sherwin, "Chapter 8 - hepatic drug metabolism in pediatric patients," in *Drug Metabolism in Diseases*, W. Xie, Ed. Boston: Academic Press, 2017, pp. 181–206.

[337] T. Brundin and J. Wahren, "Whole body and splanchnic oxygen consumption and blood flow after oral ingestion of fructose or glucose," *Am J Physiol Endocrinol Metab*, vol. 264, no. 4, pp. E504–E513, 1993. URL: https://doi.org/10.1152/ajpendo.1993.264.4.E504

[338] P. T. Saunders, J. H. Koeslag, and J. A. Wessels, "Integral rein control in physiology," *J Theor Biol*, vol. 194, no. 2, pp. 163–173, 1998. URL: https://doi.org/10.1006/jtbi.1998.0746

[339] B. Ahrén, "Autonomic regulation of islet hormone secretion–implications for health and disease," *Diabetologia*, vol. 43, pp. 393–410, 2000. URL: https://doi.org/10.1007/s001250051322

[340] S. N. Davis, P. Galassetti, D. H. Wasserman, and D. Tate, "Effects of gender on neuroendocrine and metabolic counterregulatory responses to exercise in normal man," *J Clin Endocrinol Metab*, vol. 85, no. 1, pp. 224–230, 01 2000. URL: https://doi.org/10.1210/jcem.85.1.6328

[341] T. J. Horton, E. K. Miller, D. Glueck, and K. Tench, "No effect of menstrual cycle phase on glucose kinetics and fuel oxidation during moderate-intensity exercise,"

Am J Physiol Endocrinol Metab, vol. 282, no. 4, pp. E752–E762, 2002. URL: https://doi.org/10.1152/ajpendo.00238.2001

[342] J.-M. Lavoie, N. Dionne, R. Helie, and G. Brisson, "Menstrual cycle phase dissociation of blood glucose homeostasis during exercise," *J Appl Physiol*, vol. 62, no. 3, pp. 1084–1089, 1987. URL: https://doi.org/10.1152/jappl.1987.62.3.1084

[343] S. P. Bailey, C. M. Zacher, and K. D. Mittleman, "Effect of menstrual cycle phase on carbohydrate supplementation during prolonged exercise to fatigue," *J Appl Physiol*, vol. 88, no. 2, pp. 690–697, 2000. URL: https://doi.org/10.1152/jappl.2000.88.2.690

[344] L. S. Marie and R. D. Palmiter, "Norepinephrine and epinephrine-deficient mice are hyperinsulinemic and have lower blood glucose," *Endocrinology*, vol. 144, no. 10, pp. 4427–4432, 10 2003. URL: https://doi.org/10.1210/en.2003-0561

[345] M. E. Cabrera, G. M. Saidel, and S. C. Kalhan, "Role of o2 in regulation of lactate dynamics during hypoxia: mathematical model and analysis," *Ann Biomed Eng*, vol. 26, no. 1, pp. 1–27, 1998. URL: https://doi.org/10.1114/1.28

[346] D. H. Wasserman and M. Vranic, "Interaction between insulin and counterregulatory hormones in control of substrate utilization in health and diabetes during exercise," *Diabetes Metab Rev*, vol. 1, no. 4, pp. 359–384, 1986. URL: https://doi.org/10.1002/dmr.5610010403

[347] L. Janah, S. Kjeldsen, K. D. Galsgaard, M. Winther-Sørensen, E. Stojanovska, J. Pedersen, F. K. Knop, J. J. Holst, and N. J. Wewer Albrechtsen, "Glucagon receptor signaling and glucagon resistance," *Int J Mol Sci*, vol. 20, no. 13, p. 3314, 2019. URL: https://doi.org/10.3390/ijms20133314

[348] J. Hernández-Cascales, "Does glucagon have a positive inotropic effect in the human heart?" *Cardiovasc Diabetol*, vol. 17, no. 1, p. 148, 2018. URL: https://doi.org/10.1186/s12933-018-0791-z

[349] M. E. Cabrera, G. M. Saidel, and S. C. Kalhan, "Lactate metabolism during exercise: analysis by an integrative systems model," *Am J Physiol Regul Integr Comp Physiol*, vol. 277, no. 5, pp. R1522–R1536, 1999. URL: https://doi.org/10.1152/ajpregu.1999.277.5.R15223

[350] M. J. Joyner and D. P. Casey, "Regulation of increased blood flow (hyperemia) to muscles during exercise: a hierarchy of competing physiological needs," *Physiol Rev*, 2015. URL: https://doi.org/10.1152/physrev.00035.2013

[351] I. L. Piña, C. S. Apstein, G. J. Balady, R. Belardinelli, B. R. Chaitman, B. D. Duscha, B. J. Fletcher, J. L. Fleg, J. N. Myers, and M. J. Sullivan, "Exercise and heart failure: a statement from the american heart association committee on exercise, rehabilitation, and prevention," *Circulation*, vol. 107, no. 8, pp. 1210–1225, 2003. URL: https://doi.org/10.1161/01.CIR.0000055013.92097.40

[352] G. D. Lopaschuk, J. R. Ussher, C. D. Folmes, J. S. Jaswal, and W. C. Stanley, "Myocardial fatty acid metabolism in health and disease," *Physiol Rev*, vol. 90, no. 1, pp. 207–258, 2010. URL: https://doi.org/10.1152/physrev.00015.2009

[353] I. Heinonen, K. K. Kalliokoski, J. C. Hannukainen, D. J. Duncker, P. Nuutila, and J. Knuuti, "Organ-specific physiological responses to acute physical exercise and long-term training in humans," *Physiology*, 2014. URL: https://doi.org/10.1152/physiol.00067.2013

[354] O. P. Soldin and D. R. Mattison, "Sex differences in pharmacokinetics and pharmacodynamics," *Clin Pharmacokinet*, vol. 48, no. 3, pp. 143–157, 2009. URL: https://doi.org/10.2165/00003088-200948030-00001

[355] A. Ramos-Jiménez, R. P. Hernández-Torres, P. V. Torres-Durán, J. Romero-Gonzalez, D. Mascher, C. Posadas-Romero, and M. A. Juárez-Oropeza, "The respiratory exchange ratio is associated with fitness indicators both in trained and untrained men: a possible application for people with reduced exercise tolerance," *Clin Med Circ Respirat Pulm Med*, vol. 2, pp. CCRPM–S449, 2008. URL: https://doi.org/10.4137/ccrpm.s449

[356] P. A. Deuster and Y. Heled, "Chapter 41 - testing for maximal aerobic power," in *The Sports Medicine Resource Manual*, P. H. Seidenberg and A. I. Beutler, Eds. Philadelphia: W.B. Saunders, 2008, pp. 520–528.

[357] J. A. Romijn, E. Coyle, L. Sidossis, A. Gastaldelli, J. Horowitz, E. Endert, and R. Wolfe, "Regulation of endogenous fat and carbohydrate metabolism in relation to exercise intensity and duration," *Am J Physiol Endocrinol Metab*, vol. 265, no. 3, pp. E380–E391, 1993. URL: https://doi.org/10.1152/ajpendo.1993.265.3.E380

[358] L. J. van Loon, P. L. Greenhaff, D. Constantin-Teodosiu, W. H. Saris, and A. J. Wagenmakers, "The effects of increasing exercise intensity on muscle fuel utilisation in humans," *J Physiol*, vol. 536, no. 1, pp. 295–304, 2001. URL: https://doi.org/10.1111/j.1469-7793.2001.00295.x

[359] L. J. Van Loon, R. Koopman, J. H. Stegen, A. J. Wagenmakers, H. A. Keizer, and W. H. Saris, "Intramyocellular lipids form an important substrate source during moderate intensity exercise in endurance-trained males in a fasted state," *J Physiol*, vol. 553, no. 2, pp. 611–625, 2003. URL: https://doi.org/10.1113/jphysiol.2003.052431

[360] S. Campbell, D. Angus, and M. Febbraio, "Glucose kinetics and exercise performance during phases of the menstrual cycle: effect of glucose ingestion," *Am J Physiol Endocrinol Metab*, 2001. URL: https://doi.org/10.1152/ajpendo.2001.281.4.E817

[361] T. M. D'Eon, C. Sharoff, S. R. Chipkin, D. Grow, B. C. Ruby, and B. Braun, "Regulation of exercise carbohydrate metabolism by estrogen and progesterone in women," *Am J Physiol Endocrinol Metab*, vol. 283, no. 5, pp. E1046–E1055, 2002. URL: https://doi.org/10.1152/ajpendo.00271.2002

[362] V. Benoit, A. Valette, L. Mercier, J. Meignen, and J. Boyer, "Potentiation of epinephrine-induced lipolysis in fat cells from estrogen-treated rats," *Biochem Biophys Res Commun*, vol. 109, no. 4, pp. 1186–1191, 1982. URL: https://doi.org/10.1016/0006-291X(82)91902-7

[363] F. M. Hansen, N. Fahmy, and J. H. Nielsen, "The influence of sexual hormones on lipogenesis and lipolysis in rat fat cells," *Eur J Endocrinol*, vol. 95, no. 4, pp. 566–570, 1980. URL: https://doi.org/10.1530/acta.0.0950566

[364] H. Hatta, Y. Atomi, S. Shinohara, Y. Yamamoto, and S. Yamada, "The effects of ovarian hormones on glucose and fatty acid oxidation during exercise in female ovariectomized rats," *Horm Metab Res*, vol. 20, no. 10, pp. 609–611, 1988. URL: https://doi.org/10.1055/s-2007-1010897

[365] T. Oosthuyse and A. N. Bosch, "Oestrogen's regulation of fat metabolism during exercise and gender specific effects," *Curr Opin Pharmacol*, vol. 12, no. 3, pp. 363–371, 2012. URL: https://doi.org/10.1016/j.coph.2012.02.008

[366] R. K. Kalkhoff, "Metabolic effects of progesterone," *Am J Obstet Gynecol*, vol. 142, no. 6, pp. 735–738, 1982. URL: https://doi.org/10.1016/S0002-9378(16)32480-2

[367] S. Campbell and M. Febbraio, "Effect of the ovarian hormones on glut4 expression and contraction-stimulated glucose uptake," *Am J Physiol Endocrinol Metab*, vol. 282, no. 5, pp. E1139–E1146, 2002. URL: https://doi.org/10.1152/ajpendo.00184.2001

[368] C. Doglioni, M. Gambacorta, G. Zamboni, G. Coggi, and G. Viale, "Immunocytochemical localization of progesterone receptors in endocrine cells of the human pancreas," *Am J Pathol*, vol. 137, no. 5, p. 999, 1990.

[369] M. Tarnopolsky, M. Bosman, J. Macdonald, D. Vandeputte, J. Martin, and B. Roy, "Postexercise protein-carbohydrate and carbohydrate supplements increase muscle glycogen in men and women," *J Appl Physiol*, vol. 83, no. 6, pp. 1877–1883, 1997. URL: https://doi.org/10.1152/jappl.1997.83.6.1877

[370] R. Pate, R. Sargent, C. Baldwin, and M. Burgess, "Dietary intake of women runners," *Int J Sports Med*, vol. 11, no. 06, pp. 461–466, 1990. URL: https://doi.org/10.1055/s-2007-1024838

[371] P. Arner, E. Kriegholm, P. Engfeldt, J. Bolinder *et al.*, "Adrenergic regulation of lipolysis in situ at rest and during exercise." *J Clin Invest*, vol. 85, no. 3, pp. 893–898, 1990. URL: https://doi.org/10.1172/JCI114516

[372] F. K. Blatchford, R. G. Knowlton, and D. A. Schneider, "Plasma ffa responses to prolonged walking in untrained men and women," *Eur J Appl Physiol Occup Physiol*, vol. 53, no. 4, pp. 343–347, 1985. URL: https://doi.org/10.1007/BF00422851

[373] ICRP, "Annual report of the international commission on radiological protection 2002," 2003, iCPR Publication No. 89.

[374] M. J. Müller, D. Langemann, I. Gehrke, W. Later, M. Heller, C. C. Glüer, S. B. Heymsfield, and A. Bosy-Westphal, "Effect of constitution on mass of individual organs and their association with metabolic rate in humans—a detailed view on allometric scaling," *PloS one*, vol. 6, no. 7, p. e22732, 2011. URL: https://doi.org/10.1371/journal.pone.0022732

[375] M. J. Müller, A. Bosy-Westphal, W. Braun, M. C. Wong, J. A. Shepherd, and S. B. Heymsfield, "What is a 2021 reference body?" *Nutrients*, vol. 14, no. 7, p. 1526, 2022. URL: https://doi.org/10.3390/nu14071526

[376] NCD Risk Factor Collaboration (NCD-RisC), "Trends in adult body-mass index in 200 countries from 1975 to 2014: a pooled analysis of 1698 population-based measurement studies with 19· 2 million participants," *Lancet*, vol. 10026, no. 387, pp. 1377–1396, 2016. URL: https://doi.org/10.1016/S0140-6736(16)30054-X

[377] N. H. Cho, J. Shaw, S. Karuranga, Y. Huang, J. da Rocha Fernandes, A. Ohlrogge, and B. Malanda, "Idf diabetes atlas: Global estimates of diabetes prevalence for

2017 and projections for 2045," *Diabetes Res Clin Pract*, vol. 138, pp. 271–281, 2018. URL: https://doi.org/10.1016/j.diabres.2018.02.023

[378] K. M. Beaudry and M. C. Devries, "Sex-based differences in hepatic and skeletal muscle triglyceride storage and metabolism," *Appl Physiol Nutr Metab*, vol. 44, no. 8, pp. 805–813, 2019. URL: https://doi.org/10.1139/apnm-2018-0635

[379] A. Bickerton, R. Roberts, B. Fielding, H. Tornqvist, E. Blaak, A. Wagenmakers, M. Gilbert, S. Humphreys, F. Karpe, and K. Frayn, "Adipose tissue fatty acid metabolism in insulin-resistant men," *Diabetologia*, vol. 51, pp. 1466–1474, 2008. URL: https://doi.org/10.1007/s00125-008-1040-x

[380] M. S. Hedrington and S. N. Davis, "Sexual dimorphism in glucose and lipid metabolism during fasting, hypoglycemia, and exercise," *Front Endocrinol*, vol. 6, p. 61, 2015. URL: https://doi.org/10.3389/fendo.2015.00061

[381] M. A. Tarnopolsky, C. D. Rennie, H. A. Robertshaw, S. N. Fedak-Tarnopolsky, M. C. Devries, and M. J. Hamadeh, "Influence of endurance exercise training and sex on intramyocellular lipid and mitochondrial ultrastructure, substrate use, and mitochondrial enzyme activity," *Am J Physiol Regul Integr Comp Physiol*, vol. 292, no. 3, pp. R1271–R1278, 2007. URL: https://doi.org/10.1152/ajpregu.00472.2006

[382] J. Oraha, R. F. Enriquez, H. Herzog, and N. J. Lee, "Sex-specific changes in metabolism during the transition from chow to high-fat diet feeding are abolished in response to dieting in c57bl/6j mice," *Int J Obes*, vol. 46, no. 10, pp. 1749–1758, 2022. URL: https://doi.org/10.1038/s41366-022-01174-4

[383] S. Santosa and M. D. Jensen, "The sexual dimorphism of lipid kinetics in humans," *Front Endocrinol*, vol. 6, p. 103, 2015. URL: https://doi.org/10.3389/fendo.2015.00103

[384] E. Corssmit, J. Stouthard, J. Romijn, E. Endert, and H. Sauerwein, "Sex differences in the adaptation of glucose metabolism to short-term fasting: effects of oral contraceptives," *Metabolism*, vol. 43, no. 12, pp. 1503–1508, 1994. URL: https://doi.org/10.1016/0026-0495(94)90008-6

[385] C. Pramfalk, M. Pavlides, R. Banerjee, C. A. McNeil, S. Neubauer, F. Karpe, and L. Hodson, "Sex-specific differences in hepatic fat oxidation and synthesis may explain the higher propensity for nafld in men," *J Clin Endocrinol Metab.*, vol. 100, no. 12, pp. 4425–4433, 2015. URL: https://doi.org/10.1210/jc.2015-2649

[386] J. Lebeck, "Sexual dimorphism in glucose and lipid metabolism," p. 166, 2016. URL: https://doi.org/10.3389/fendo.2016.00166

[387] A. Leone, R. De Amicis, S. Bertoli, A. Spadafranca, G. De Carlo, and A. Battezzati, "Absence of a sexual dimorphism in postprandial glucose metabolism after administration of a balanced mixed meal in healthy young volunteers," *Nutr Diabetes*, vol. 12, no. 1, p. 6, 2022. URL: https://doi.org/10.1038/s41387-022-00184-5

[388] B. Mittendorfer, J. F. Horowitz, and S. Klein, "Gender differences in lipid and glucose kinetics during short-term fasting," *Am J Physiol Endocrinol Metab*, vol. 281, no. 6, pp. E1333–E1339, 2001. URL: https://doi.org/10.1152/ajpendo.2001.281.6.E1333

[389] D. A. Sandoval and D. A. D'Alessio, "Physiology of proglucagon peptides: role of glucagon and glp-1 in health and disease," *Physiol Rev*, vol. 95, no. 2, pp. 513–548, 2015. URL: https://doi.org/10.1152/physrev.00013.2014

[390] C. Cobelli, E. Renard, and B. Kovatchev, "Artificial pancreas: past, present, future," *Diabetes*, vol. 60, no. 11, pp. 2672–2682, 2011. URL: https://doi.org/10.2337/db11-0654

[391] R. Visentin, E. Campos-Náñez, M. Schiavon, D. Lv, M. Vettoretti, M. Breton, B. P. Kovatchev, C. Dalla Man, and C. Cobelli, "The uva/padova type 1 diabetes simulator goes from single meal to single day," *J Diabetes Sci Technol*, vol. 12, no. 2, pp. 273–281, 2018. URL: https://doi.org/10.1177/1932296818757747

[392] T. Pearson, J. A. Wattis, J. King, I. A. MacDonald, and D. Mazzatti, "A mathematical model of the human metabolic system and metabolic flexibility," *Bull Math Biol*, vol. 76, pp. 2091–2121, 2014. URL: https://doi.org/10.1007/s11538-014-0001-4

[393] J. Hetherington, T. Sumner, R. Seymour, L. Li, M. V. Rey, S. Yamaji, P. Saffrey, O. Margoninski, I. Bogle, A. Finkelstein *et al.*, "A composite computational model of liver glucose homeostasis. i. building the composite model," *J R Soc Interf*, vol. 9, no. 69, pp. 689–700, 2012. URL: https://doi.org/10.1098/rsif.2011.0141

[394] A. C. Pratt, J. A. Wattis, and A. M. Salter, "Mathematical modelling of hepatic lipid metabolism," *Math Biosci*, vol. 262, pp. 167–181, 2015. URL: https://doi.org/10.1016/j.mbs.2014.12.012

[395] C. Z. H. Sweatman, "Mathematical model of diabetes and lipid metabolism linked to diet, leptin sensitivity, insulin sensitivity and vldltg clearance predicts paths

to health and type ii diabetes," *J Theor Biol*, vol. 486, p. 110037, 2020. URL: https://doi.org/10.1016/j.jtbi.2019.110037

[396] S. Panunzi, M. Pompa, A. Borri, V. Piemonte, and A. De Gaetano, "A revised sorensen model: Simulating glycemic and insulinemic response to oral and intra-venous glucose load," *PLoS One*, vol. 15, no. 8, p. e0237215, 2020. URL: https://doi.org/10.1371/journal.pone.0237215

[397] J. T. Sorensen, "A physiologic model of glucose metabolism in man and its use to design and assess improved insulin therapies for diabetes," Ph.D. dissertation, Massachusetts Institute of Technology, 1985.

[398] M. Yasemi and M. Jolicoeur, "Modelling cell metabolism: a review on constraint-based steady-state and kinetic approaches," *Processes*, vol. 9, no. 2, p. 322, 2021. URL: https://doi.org/10.3390/pr9020322

[399] S. Swapnasrita, A. Carlier, and A. T. Layton, "Sex-specific computational models of kidney function in patients with diabetes," *Front Physiol*, vol. 13, p. 14, 2022. URL: https://doi.org/10.3389/fphys.2022.741121

[400] H. Sekizkardes, S. T. Chung, S. Chacko, M. W. Haymond, M. Startzell, M. Walter, P. J. Walter, M. Lightbourne, R. J. Brown *et al.*, "Free fatty acid processing diverges in human pathologic insulin resistance conditions," *J Clin Invest*, vol. 130, no. 7, pp. 3592–3602, 2020. URL: https://doi.org/10.1172/JCI135431

[401] P. Staehr, O. Hother-Nielsen, B. R. Landau, V. Chandramouli, J. J. Holst, and H. Beck-Nielsen, "Effects of free fatty acids per se on glucose production, gluconeogenesis, and glycogenolysis," *Diabetes*, vol. 52, no. 2, pp. 260–267, 2003. URL: https://doi.org/10.2337/diabetes.52.2.260

[402] X. Chen, N. Iqbal, G. Boden *et al.*, "The effects of free fatty acids on gluconeogenesis and glycogenolysis in normal subjects," *J Clin Invest*, vol. 103, no. 3, pp. 365–372, 1999. URL: https://doi.org/10.1172/JCI5479

[403] J. D. Browning, J. Baxter, S. Satapati, and S. C. Burgess, "The effect of short-term fasting on liver and skeletal muscle lipid, glucose, and energy metabolism in healthy women and men," *J Lipid Res*, vol. 53, no. 3, pp. 577–586, 2012. URL: https://doi.org/10.1194/jlr.P020867

[404] D. S. Ludwig, "The glycemic index: physiological mechanisms relating to obesity, diabetes, and cardiovascular disease," *Jama*, vol. 287, no. 18, pp. 2414–2423, 2002. URL: https://doi.org/10.1001/jama.287.18.2414

[405] T. Hiyoshi, M. Fujiwara, and Z. Yao, "Postprandial hyperglycemia and postprandial hypertriglyceridemia in type 2 diabetes," *J Biomed Res*, vol. 33, no. 1, p. 1, 2019. URL: https://doi.org/10.7555/JBR.31.20160164

[406] A.-M. Lundsgaard and B. Kiens, "Gender differences in skeletal muscle substrate metabolism–molecular mechanisms and insulin sensitivity," *Front Endocrinol*, vol. 5, p. 195, 2014. URL: https://doi.org/10.3389/fendo.2014.00195

[407] P. A. Ivey and G. A. Gaesser, "Postexercise muscle and liver glycogen metabolism in male and female rats," *J Appl Physiol*, vol. 62, no. 3, pp. 1250–1254, 1987. URL: https://doi.org/10.1152/jappl.1987.62.3.1250

[408] J. Jensen, P. I. Rustad, A. J. Kolnes, and Y.-C. Lai, "The role of skeletal muscle glycogen breakdown for regulation of insulin sensitivity by exercise," *Front Physiol*, vol. 2, p. 112, 2011. URL: https://doi.org/10.3389/fphys.2011.00112

[409] C.-A. W. Emhoff and L. A. Messonnier, "Concepts of lactate metabolic clearance rate and lactate clamp for metabolic inquiry: a mini-review," *Nutrients*, vol. 15, no. 14, p. 3213, 2023. URL: https://doi.org/10.3390/nu15143213

[410] D. Hugi, V. Bracher, L. Tappy, and J. Blum, "Postprandial hydrogen breath excretion, plasma lactate concentration, glucose metabolism and insulin levels in veal calves," *J Anim Physiol Anim Nutr*, vol. 78, no. 1-5, pp. 42–48, 1997. URL: https://doi.org/10.1111/j.1439-0396.1997.tb00854.x

[411] R. Jackson, J. Hamling, B. Sim, M. Hawa, P. Blix, and J. Nabarro, "Peripheral lactate and oxygen metabolism in man: the influence of oral glucose loading," *Metabolism*, vol. 36, no. 2, pp. 144–150, 1987. URL: https://doi.org/10.1016/0026-0495(87)90008-4

[412] K. L. Whytock, S. O. Shepherd, M. Cocks, A. J. Wagenmakers, and J. A. Strauss, "Young, healthy males and females present cardiometabolic protection against the detrimental effects of a 7-day high-fat high-calorie diet," *Eur J Nutr*, vol. 60, pp. 1605–1617, 2021. URL: https://doi.org/10.1007/s00394-020-02357-3

[413] G. Marsat and L. Maler, "Neural heterogeneity and efficient population codes for communication signals," *J Neurophysiol*, vol. 104, no. 5, pp. 2543–2555, 2010. URL: https://doi.org/10.1152/jn.00256.2010

[414] T. B. Luke, E. Barreto, and P. So, "Complete classification of the macroscopic behavior of a heterogeneous network of theta neurons," *Neural Comput*, vol. 25, no. 12, pp. 3207–3234, 2013. URL: https://doi.org/10.1162/NECO_a_00525

[415] E. Montbrió, D. Pazó, and A. Roxin, "Macroscopic description for networks of spiking neurons," *Phys Rev X*, vol. 5, no. 2, p. 021028, 2015. URL: https://doi.org/10.1103/PhysRevX.5.021028

[416] R. Gast, S. A. Solla, and A. Kennedy, "Macroscopic dynamics of neural networks with heterogeneous spiking thresholds," *Phys Rev E*, vol. 107, p. 024306, 2023. URL: https://doi.org/10.1103/PhysRevE.107.024306

[417] G. Pincus, "A diurnal rhythm in the excretion of urinary ketosteroids by young men," *J Clin Endocrinol*, vol. 3, no. 4, pp. 195–199, 1943. URL: https://doi.org/10.1210/jcem-3-4-195

[418] R. V. Andrews, *Circadian metabolic patterns in cultured hamster adrenal glands*. The University of Iowa, 1964.

[419] R. Y. Moore and V. B. Eichler, "Loss of a circadian adrenal corticosterone rhythm following suprachiasmatic lesions in the rat." *Brain Res*, 1972. URL: https://doi.org/10.1016/0006-8993(72)90054-6

[420] C. Linsell, S. Lightman, P. Mullen, M. Brown, and R. Causon, "Circadian rhythms of epinephrine and norepinephrine in man," *J Clin Endocrinol Metab*, vol. 60, no. 6, pp. 1210–1215, 1985. URL: https://doi.org/10.1210/jcem-60-6-1210

[421] S. Leach and K. Suzuki, "Adrenergic signaling in circadian control of immunity," *Front Immunol*, vol. 11, p. 549312, 2020. URL: https://doi.org/10.3389/fimmu.2020.01235

[422] D. Gnocchi and G. Bruscalupi, "Circadian rhythms and hormonal homeostasis: pathophysiological implications," *Biology*, vol. 6, no. 1, p. 10, 2017. URL: https://doi.org/10.3390/biology6010010

[423] B. Kornmann, O. Schaad, H. Bujard, J. S. Takahashi, and U. Schibler, "System-driven and oscillator-dependent circadian transcription in mice with a

conditionally active liver clock," *PLoS Biol*, vol. 5, no. 2, p. e34, 2007. URL: https://doi.org/10.1371/journal.pbio.0050034

[424] K. A. Lamia, K.-F. Storch, and C. J. Weitz, "Physiological significance of a peripheral tissue circadian clock," *PNAS*, vol. 105, no. 39, pp. 15 172–15 177, 2008. URL: https://doi.org/10.1073/pnas.0909591106

[425] C. Vollmers, S. Gill, L. DiTacchio, S. R. Pulivarthy, H. D. Le, and S. Panda, "Time of feeding and the intrinsic circadian clock drive rhythms in hepatic gene expression," *PNAS*, vol. 106, no. 50, pp. 21 453–21 458, 2009. URL: https://doi.org/10.1073/pnas.0909591106

[426] J. Li, S. Lv, X. Qiu, J. Yu, J. Jiang, Y. Jin, W. Guo, R. Zhao, Z.-N. Zhang, C. Zhang *et al.*, "Bmal1 functions as a camp-responsive coactivator of hdac5 to regulate hepatic gluconeogenesis," *Protein Cell*, vol. 9, no. 11, pp. 976–980, 2018. URL: https://doi.org/10.1007/s13238-018-0514-y

[427] D. Shi, J. Chen, J. Wang, J. Yao, Y. Huang, G. Zhang, and Z. Bao, "Circadian clock genes in the metabolism of non-alcoholic fatty liver disease," *Front Physiol*, vol. 10, p. 447813, 2019. URL: https://doi.org/10.3389/fphys.2019.00423

[428] R. Doi, K. Oishi, and N. Ishida, "Clock regulates circadian rhythms of hepatic glycogen synthesis through transcriptional activation of gys2," *J Biol Chem*, vol. 285, no. 29, pp. 22 114–22 121, 2010. URL: https://doi.org/10.1074/jbc.M110.110361

[429] A. Englund, L. Kovanen, S. T. Saarikoski, J. Haukka, A. Reunanen, A. Aromaa, J. Lönnqvist, and T. Partonen, "Npas2 and per2 are linked to risk factors of the metabolic syndrome," *J Circadian Rhythms*, vol. 7, pp. 1–9, 2009. URL: https://doi.org/10.1186/1740-3391-7-5

[430] J. L. Barclay, A. Shostak, A. Leliavski, A. H. Tsang, O. Jöhren, H. Müller-Fielitz, D. Landgraf, N. Naujokat, G. T. van der Horst, and H. Oster, "High-fat diet-induced hyperinsulinemia and tissue-specific insulin resistance in cry-deficient mice," *Am J Physiol Endocrinol Metab*, vol. 304, no. 10, pp. E1053–E1063, 2013. URL: https://doi.org/10.1152/ajpendo.00512.2012

[431] Y. Zhao, Y. Zhang, M. Zhou, S. Wang, Z. Hua, and J. Zhang, "Loss of mper2 increases plasma insulin levels by enhanced glucose-stimulated insulin secretion and impaired insulin clearance in mice," *FEBS Lett*, vol. 586, no. 9, pp. 1306–1311, 2012. URL: https://doi.org/10.1016/j.febslet.2012.03.034

[432] L. Yin, N. Wu, J. C. Curtin, M. Qatanani, N. R. Szwergold, R. A. Reid, G. M. Waitt, D. J. Parks, K. H. Pearce, G. B. Wisely *et al.*, "Rev-erbα, a heme sensor that coordinates metabolic and circadian pathways," *Science*, vol. 318, no. 5857, pp. 1786–1789, 2007. URL: https://doi.org/10.1126/science.1150179

[433] B. Marcheva, K. M. Ramsey, E. D. Buhr, Y. Kobayashi, H. Su, C. H. Ko, G. Ivanova, C. Omura, S. Mo, M. H. Vitaterna *et al.*, "Disruption of the clock components clock and bmal1 leads to hypoinsulinaemia and diabetes," *Nature*, vol. 466, no. 7306, pp. 627–631, 2010. URL: https://doi.org/10.1038/nature09253

[434] L. A. Sadacca, K. A. Lamia, A. S. Delemos, B. Blum, and C. Weitz, "An intrinsic circadian clock of the pancreas is required for normal insulin release and glucose homeostasis in mice," *Diabetologia*, vol. 54, pp. 120–124, 2011. URL: https://doi.org/10.1007/s00125-010-1920-8

[435] Y. Tahara, M. Otsuka, Y. Fuse, A. Hirao, and S. Shibata, "Refeeding after fasting elicits insulin-dependent regulation of per2 and rev-erbα with shifts in the liver clock," *J Biol Rhythms*, vol. 26, no. 3, pp. 230–240, 2011. URL: https://doi.org/10.1177/0748730411405958

[436] D. Yamajuku, T. Inagaki, T. Haruma, S. Okubo, Y. Kataoka, S. Kobayashi, K. Ikegami, T. Laurent, T. Kojima, K. Noutomi *et al.*, "Real-time monitoring in three-dimensional hepatocytes reveals that insulin acts as a synchronizer for liver clock," *Sci Rep*, vol. 2, no. 1, p. 439, 2012. URL: https://doi.org/10.1038/srep00439

[437] T. Hirota, T. Okano, K. Kokame, H. Shirotani-Ikejima, T. Miyata, and Y. Fukada, "Glucose down-regulates per1 and per2mrna levels and induces circadian gene expression in cultured rat-1 fibroblasts* 210," *J Biol Chem*, vol. 277, no. 46, pp. 44 244–44 251, 2002. URL: https://doi.org/10.1074/jbc.M206233200

[438] A. Pizarro, K. Hayer, N. F. Lahens, and J. B. Hogenesch, "Circadb: a database of mammalian circadian gene expression profiles," *Nucleic Acids Res*, vol. 41, no. D1, pp. D1009–D1013, 2012. URL: https://doi.org/10.1093/nar/gks1161

[439] S. Castellana, T. Biagini, F. Petrizzelli, A. Cabibbo, G. Mazzoccoli, and T. Mazza, "Rhythmicdb: A database of predicted multi-frequency rhythmic transcripts," *Front Genet*, vol. 13, 2022. URL: https://doi.org/10.3389/fgene.2022.882044

[440] S. Li, K. Shui, Y. Zhang, Y. Lv, W. Deng, S. Ullah, L. Zhang, and Y. Xue, "Cgdb: a database of circadian genes in eukaryotes," *Nucleic Acids Res*, p. gkw1028, 2016. URL: https://doi.org/10.1093/nar/gkw1028

[441] M. Garaulet, J. Ordovas, and J. Madrid, "The chronobiology, etiology and pathophysiology of obesity," *Int J Obes*, vol. 34, no. 12, pp. 1667–1683, 2010. URL: https://doi.org/10.1038/ijo.2010.118

[442] M. Garaulet and P. Gómez-Abellán, "Timing of food intake and obesity: a novel association," *Physiol Behav*, vol. 134, pp. 44–50, 2014. URL: https://doi.org/10.1016/j.physbeh.2014.01.001

[443] O. Froy, "Circadian rhythms and obesity in mammals," *Int Sch Res Notices*, vol. 2012, 2012. URL: https://doi.org/10.5402/2012/437198

[444] Y. Serin and N. Acar Tek, "Effect of circadian rhythm on metabolic processes and the regulation of energy balance," *Ann Nutr Metab*, vol. 74, no. 4, pp. 322–330, 2019. URL: https://doi.org/10.1159/000500071

[445] I. M. Sobol', "On sensitivity estimation for nonlinear mathematical models," *Matematicheskoe modelirovanie*, vol. 2, no. 1, pp. 112–118, 1990.

[446] J. Nossent, P. Elsen, and W. Bauwens, "Sobol'sensitivity analysis of a complex environmental model," *Environ Model Softw*, vol. 26, no. 12, pp. 1515–1525, 2011. URL: https://doi.org/10.1016/j.envsoft.2011.08.010

[447] M. Bayram, T. Partal, and G. Orucova Buyukoz, "Numerical methods for simulation of stochastic differential equations," *Adv Difference Equ*, pp. Paper No. 17, 10, 2018. URL: https://doi.org/10.1186/s13662-018-1466-5

[448] J. A. Carrillo, Y.-P. Choi, and L. Pareschi, "Structure preserving schemes for the continuum Kuramoto model: phase transitions," *J Comput Phys*, vol. 376, pp. 365–389, 2019. URL: https://doi.org/10.1016/j.jcp.2018.09.049

[449] N. Kruk, J. A. Carrillo, and H. Koeppl, "A finite volume method for continuum limit equations of nonlocally interacting active chiral particles," *J Comput Phys*, vol. 440, pp. Paper No. 110 275, 26, 2021. URL: https://doi.org/10.1016/j.jcp.2021.110275

[450] K.-A. Lie and S. Noelle, "On the artificial compression method for second-order nonoscillatory central difference schemes for systems of conservation laws," *SIAM J Sci Comput*, vol. 24, no. 4, pp. 1157–1174, 2003. URL: https://doi.org/10.1137/S1064827501392880

[451] H. Nessyahu and E. Tadmor, "Nonoscillatory central differencing for hyperbolic conservation laws," *J Comput Phys*, vol. 87, no. 2, pp. 408–463, 1990. URL: https://doi.org/10.1016/0021-9991(90)90260-8

[452] P. K. Sweby, "High resolution schemes using flux limiters for hyperbolic conservation laws," *SIAM J Numer Anal*, vol. 21, no. 5, pp. 995–1011, 1984. URL: https://doi.org/10.1137/0721062

[453] B. van Leer, "Towards the ultimate conservative difference scheme. v. a second-order sequel to godunov's method," *J Comput Phys*, vol. 32, no. 1, pp. 101–136, 1979. URL: https://doi.org/10.1016/0021-9991(79)90145-1

[454] S. Gottlieb, C.-W. Shu, and E. Tadmor, "Strong stability-preserving high-order time discretization methods," *SIAM Rev*, vol. 43, no. 1, pp. 89–112, 2001. URL: https://doi.org/10.1137/S003614450036757X

[455] J. Cruz, "Expensive cerebral blood flow measurements alone are useless and misinformative in comatose patients: a comprehensive alternative," *Arq Neuropsiquiatr*, vol. 61, pp. 309–312, 2003. URL: https://doi.org/10.1590/S0004-282X2003000200031

[456] C. Putman, N. Jones, E. Hultman, M. Hollidge-Horvat, A. Bonen, D. McConachie, and G. Heigenhauser, "Effects of short-term submaximal training in humans on muscle metabolism in exercise," *Am J Physiol Endocrinol Metab*, vol. 275, no. 1, pp. E132–E139, 1998. URL: https://doi.org/10.1152/ajpendo.1998.275.1.E132

[457] J. Wahren, P. Felig, G. Ahlborg, L. Jorfeldt *et al.*, "Glucose metabolism during leg exercise in man," *J Clin Invest*, vol. 50, no. 12, pp. 2715–2725, 1971. URL: https://doi.org/10.1172/JCI106772

[458] F. Karpe, B. A. Fielding, J.-L. Ardilouze, V. Ilic, I. A. Macdonald, and K. N. Frayn, "Effects of insulin on adipose tissue blood flow in man," *J Physiol*, vol. 540, no. 3, pp. 1087–1093, 2002. URL: https://doi.org/10.1113/jphysiol.2001.013358

[459] A. Ronowska, A. Szutowicz, H. Bielarczyk, S. Gul-Hinc, J. Klimaszewska-Lata, A. Dyś, M. Zyśk, and A. Jankowska-Kulawy, "The regulatory effects of acetyl-coa distribution in the healthy and diseased brain," *Front cell Neurosci*, vol. 12, p. 169, 2018. URL: https://doi.org/10.3389/fncel.2018.00169

[460] G. Van Hall, J. Bülow, M. Sacchetti, N. A. Mulla, D. Lyngsø, and L. Simonsen, "Regional fat metabolism in human splanchnic and adipose tissues; the effect of exercise," *J Physiol*, vol. 543, no. 3, pp. 1033–1046, 2002. URL: https://doi.org/10.1113/jphysiol.2002.022392

[461] B. C. Bergman and G. A. Brooks, "Respiratory gas-exchange ratios during graded exercise in fed and fasted trained and untrained men," *J Appl Physiol*, vol. 86, no. 2, pp. 479–487, 1999. URL: https://doi.org/10.1152/jappl.1999.86.2.479

[462] T. G. Trucano, L. P. Swiler, T. Igusa, W. L. Oberkampf, and M. Pilch, "Calibration, validation, and sensitivity analysis: What's what," *Reliab Eng Syst Saf*, vol. 91, no. 10-11, pp. 1331–1357, 2006. URL: https://doi.org/10.1016/j.ress.2005.11.031

[463] G. A. Brooks, C. C. Curl, R. G. Leija, A. D. Osmond, J. J. Duong, and J. A. Arevalo, "Tracing the lactate shuttle to the mitochondrial reticulum," *Exp Mol Med*, vol. 54, no. 9, pp. 1332–1347, 2022. URL: https://doi.org/10.1038/s12276-022-00802-3

[464] D. Legouis, A. Faivre, P. E. Cippà, and S. de Seigneux, "Renal gluconeogenesis: an underestimated role of the kidney in systemic glucose metabolism," *Nephrol Dial Transplant*, vol. 37, no. 8, pp. 1417–1425, 2022. URL: https://doi.org/10.1093/ndt/gfaa302

[465] M. A. Puskarich, B. M. Illich, and A. E. Jones, "Prognosis of emergency department patients with suspected infection and intermediate lactate levels: a systematic review," *J Crit Care*, vol. 29, no. 3, pp. 334–339, 2014. URL: https://doi.org/10.1016/j.jcrc.2013.12.017

[466] J. L. Nelson, M. E. Harmon, and R. A. Robergs, "Identifying plasma glycerol concentration associated with urinary glycerol excretion in trained humans," *J Anal Toxicol*, vol. 35, no. 9, pp. 617–623, 2011. URL: https://doi.org/10.1093/anatox/35.9.617

[467] P. V. Röder, B. Wu, Y. Liu, and W. Han, "Pancreatic regulation of glucose homeostasis," *Exp Mol Med*, vol. 48, no. 3, pp. e219–e219, 2016. URL: https://doi.org/10.1038/emm.2016.6

[468] C. Berger and D. Zdzieblo, "Glucose transporters in pancreatic islets," *Pflugers Arch*, vol. 472, no. 9, pp. 1249–1272, 2020. URL: https://doi.org/10.1007/s00424-020-02383-4

[469] E. Vieira, A. Salehi, and E. Gylfe, "Glucose inhibits glucagon secretion by a direct effect on mouse pancreatic alpha cells," *Diabetologia*, vol. 50, pp. 370–379, 2007. URL: https://doi.org/10.1007/s00125-006-0511-1

[470] E. Vergari, J. G. Knudsen, R. Ramracheya, A. Salehi, Q. Zhang, J. Adam, I. W. Asterholm, A. Benrick, L. J. Briant, M. V. Chibalina *et al.*, "Insulin inhibits glucagon

release by sglt2-induced stimulation of somatostatin secretion," *Nat Commun*, vol. 10, no. 1, p. 139, 2019. URL: https://doi.org/10.1038/s41467-018-08193-8

[471] T. W. van Haeften, E. Boonstra, T. F. Veneman, J. E. Gerich, and E. A. van der Veen, "Dose-response characteristics for glucose-stimulated insulin release in man and assessment of influence of glucose on arginine-stimulated insulin release," *Metabolism*, vol. 39, no. 12, pp. 1292–1299, 1990. URL: https://doi.org/10.1016/0026-0495(90)90186-G

[472] G. Turco, C. Brossa, M. D'alberto, G. Regis, G. Segre, E. Bianchi, B. Bruni, and S. Gamba, "Kinetic analysis of the response of plasma glucose, insulin, and c-peptide to glucagon injection in normal and diabetic subjects," *Diabetes*, vol. 30, no. 8, pp. 685–693, 1981. URL: https://doi.org/10.2337/diab.30.8.685

[473] J. Tu and B. E. Tuch, "Glucose regulates the maximal velocities of glucokinase and glucose utilization in the immature fetal rat pancreatic islet," *Diabetes*, vol. 45, no. 8, pp. 1068–1075, 1996. URL: https://doi.org/10.2337/diab.45.8.1068

[474] L. J. Mandarino, R. C. Bonadonna, O. P. Mcguinness, A. E. Halseth, and D. H. Wasserman, "Regulation of muscle glucose uptake in vivo," *Compr Physiol*, pp. 803–845, 2010. URL: https://doi.org/10.1002/cphy.cp070227

[475] G. D. Dimitriadis, E. Maratou, A. Kountouri, M. Board, and V. Lambadiari, "Regulation of postabsorptive and postprandial glucose metabolism by insulin-dependent and insulin-independent mechanisms: an integrative approach," *Nutrients*, vol. 13, no. 1, p. 159, 2021. URL: https://doi.org/10.3390/nu13010159

[476] C. Geser, R. Müller-Hess, and J. Felber, "The insulin: glucagon ratio and the secretion of growth hormone after intravenous administration of amino acids and carbohydrates in healthy subjects," *Transfus Med Hemother*, vol. 1, no. 6, pp. 483–489, 1973. URL: https://doi.org/10.1159/000219092

[477] N. Geary, "Postprandial Suppression of Glucagon Secretion: A Puzzlement," *Diabetes*, vol. 66, no. 5, pp. 1123–1125, 04 2017. URL: https://doi.org/10.2337/dbi16-0075

[478] L. Sylow, V. L. Tokarz, E. A. Richter, and A. Klip, "The many actions of insulin in skeletal muscle, the paramount tissue determining glycemia," *Cell Metab*, vol. 33, no. 4, pp. 758–780, 2021. URL: https://doi.org/10.1016/j.cmet.2021.03.020

[479] Z.-X. Meng, J. Gong, Z. Chen, J. Sun, Y. Xiao, L. Wang, Y. Li, J. Liu, X. S. Xu, and J. D. Lin, "Glucose sensing by skeletal myocytes couples nutrient signaling to systemic homeostasis," *Mol Cell*, vol. 66, no. 3, pp. 332–344, 2017. URL: https://doi.org/10.1016/j.molcel.2017.04.007

[480] M. M. Adeva-Andany, R. Funcasta-Calderón, C. Fernández-Fernández, E. Castro-Quintela, and N. Carneiro-Freire, "Metabolic effects of glucagon in humans," *J Clin Transl Endocrinol*, vol. 15, pp. 45–53, 2019. URL: https://doi.org/10.1016/j.jcte.2018.12.005

[481] H. Prinz, "Hill coefficients, dose–response curves and allosteric mechanisms," *J Chem Biol*, vol. 3, pp. 37–44, 2010. URL: https://doi.org/10.1007/s12154-009-0029-3

[482] H. Kolb, M. Stumvoll, W. Kramer, K. Kempf, and S. Martin, "Insulin translates unfavourable lifestyle into obesity," *BMC Med*, vol. 16, pp. 1–10, 2018. URL: https://doi.org/10.1186/s12916-018-1225-1

[483] H. Kolb, K. Kempf, M. Röhling, and S. Martin, "Insulin: too much of a good thing is bad," *BMC Med*, vol. 18, pp. 1–12, 2020. URL: https://doi.org/10.1186/s12916-020-01688-6

[484] C. Li, E. S. Ford, L. C. McGuire, A. H. Mokdad, R. R. Little, and G. M. Reaven, "Trends in hyperinsulinemia among nondiabetic adults in the us," *Diabetes Care*, vol. 29, no. 11, pp. 2396–2402, 2006. URL: https://doi.org/10.2337/dc06-0289

APPENDICES

Appendix A

Appendix to Chapter 4

A.1 Model equations

Table A.1: List of variables. We adopt the notation where names with a mix of upper and lower case letters (e.g., Per) denote mRNAs, and names in all caps (e.g., PER) denote proteins.

Variable name	Description
Per	Concentration of *Per* mRNA
Cry	Concentration of *Cry* mRNA
Rev-Erb	Concentration of *Rev-Erb* mRNA
Ror	Concentration of *Ror* mRNA
Bmal1	Concentration of *Bmal1* mRNA
PER	Concentration of *PER* protein
CRY	Concentration of *CRY* protein
REV-ERB	Concentration of *REV-ERB* protein
ROR	Concentration of *ROR* protein
BMAL1	Concentration of *BMAL1* protein
PER-CRY	Concentration of *PER-CRY* protein
CLOCK-BMAL1	Concentration of *CLOCK-BMAL1* protein
P	Concentration of LPS
N	Total number of activated phagocytic cells
D	Tissue damage marker

TNF	Concentration of *tumor necrosis factor-α*
IL6	Concentration of *interleukin-6*
IL10	Concentration of *interleukin-10*
Y_{IL10}	Tissue damage driven non-accessible *interleukin-10* promoter
CA	Concentration of slow-acting anti-inflammatory mediators

Table A.2: Differential equations defining the mathematical model

Circadian genes and proteins (Eqs.1-12)

$$\frac{\mathrm{d}Per(t)}{\mathrm{d}t} = -dm\_per \cdot Per(t) + \frac{vmax\_per \cdot \left(1 + fold\_per \cdot \left(\frac{CLOCK\text{-}BMAL1(t)}{ka\_per\_cb}\right)^{hill\_per\_cb}\right)}{1 + \left(\frac{CLOCK\text{-}BMAL1(t)}{ka\_per\_cb}\right)^{hill\_per\_cb} \cdot \left(1 + \left(\frac{PER\text{-}CRY(t)}{ki\_per\_pc}\right)^{hill\_per\_pc}\right)}, \tag{A.1}$$

$$\frac{\mathrm{d}Cry(t)}{\mathrm{d}t} = -dm\_cry \cdot Cry(t) + \frac{1}{\left(1 + \left(\frac{REV\text{-}ERB(t)}{ki\_cry\_rev}\right)^{hill\_cry\_rev}\right)} \cdot \frac{vmax\_cry \cdot \left(1 + fold\_cry \cdot \left(\frac{CLOCK\text{-}BMAL1(t)}{ka\_cry\_cb}\right)^{hill\_cry\_cb}\right)}{1 + \left(\frac{CLOCK\text{-}BMAL1(t)}{ka\_cry\_cb}\right)^{hill\_cry\_cb} \cdot \left(1 + \left(\frac{PER\text{-}CRY(t)}{ki\_cry\_pc}\right)^{hill\_cry\_pc}\right)}, \tag{A.2}$$

$$\frac{\mathrm{d}Rev\text{-}Erb(t)}{\mathrm{d}t} = -dm\_rev \cdot Rev\text{-}Erb(t) + \frac{vmax\_rev \cdot \left(1 + fold\_rev \cdot \left(\frac{CLOCK\text{-}BMAL1(t)}{ka\_rev\_cb}\right)^{hill\_rev\_cb}\right)}{1 + \left(\frac{CLOCK\text{-}BMAL1(t)}{ka\_rev\_cb}\right)^{hill\_rev\_cb} \cdot \left(1 + \left(\frac{PER\text{-}CRY(t)}{ki\_rev\_pc}\right)^{hill\_rev\_pc}\right)}, \tag{A.3}$$

$$\frac{\mathrm{d}Ror(t)}{\mathrm{d}t} = -dm\_ror \cdot Ror(t) + \frac{vmax\_ror \cdot \left(1 + fold\_ror \cdot \left(\frac{CLOCK\text{-}BMAL1(t)}{ka\_ror\_cb}\right)^{hill\_ror\_cb}\right.}{1 + \left(\frac{CLOCK\text{-}BMAL1(t)}{ka\_ror\_cb}\right)^{hill\_ror\_cb} \cdot \left(1 + \left(\frac{PER\text{-}CRY(t)}{ki\_ror\_pc}\right)^{hill\_ror\_pc}\right)}, \tag{A.4}$$

$$\frac{\mathrm{d}Bmal1(t)}{\mathrm{d}t} = -dm\_bmal \cdot Bmal1(t) + \frac{x_P}{x_P + F_P(t)} \cdot \frac{vmax\_bmal \cdot \left(1 + fold\_bmal \cdot \left(\frac{ROR(t)}{ka\_bmal\_ror}\right)^{hill\_bmal\_ror}\right.}{1 + \left(\frac{REV\text{-}ERB(t)}{ka\_bmal\_rev}\right)^{hill\_bmal\_rev} + \left(\frac{ROR(t)}{ka\_bmal\_ror}\right)^{hill\_bmal\_ror}}, \tag{A.5}$$

$$\frac{\mathrm{d}PER(t)}{\mathrm{d}t} = -\,dp\_per \cdot PER(t) + kp\_per \cdot Per(t) - \big[kass\_pc \cdot PER(t) \cdot CRY(t) - kdiss\_pc \cdot PER\text{-}CRY(t)\big], \tag{A.6}$$

$$\frac{\mathrm{d}CRY(t)}{\mathrm{d}t} = -\,dp\_cry \cdot CRY(t) + kp\_cry \cdot Cry(t) - \big[kass\_pc \cdot PER(t) \cdot CRY(t) - kdiss\_pc \cdot PER\text{-}CRY(t)\big], \tag{A.7}$$

$$\frac{\mathrm{d}REV\text{-}ERB(t)}{\mathrm{d}t} = -dp\_rev \cdot REV\text{-}ERB(t) + kp\_rev \cdot Rev\text{-}Erb(t), \tag{A.8}$$

$$\frac{\mathrm{d}ROR(t)}{\mathrm{d}t} = -dp\_ror \cdot ROR(t) + kp\_ror \cdot Ror(t), \tag{A.9}$$

$$\frac{\mathrm{d}BMAL1(t)}{\mathrm{d}t} = -\,dp\_bmal \cdot BMAL1(t) + kp\_bmal \cdot Bmal1(t) - kass\_cb \cdot BMAL1(t) + kdiss\_cb \cdot CLOCK\text{-}BMAL1(t), \tag{A.10}$$

$$\frac{\mathrm{d}PER\text{-}CRY(t)}{\mathrm{d}t} = kass\_pc \cdot PER(t) \cdot CRY(t) - kdiss\_pc \cdot PER\text{-}CRY(t) - d\_pc \cdot PER\text{-}CRY(t), \tag{A.11}$$

$$\frac{\mathrm{d}CLOCK\text{-}BMAL1(t)}{\mathrm{d}t} = \big[kass\_cb \cdot BMAL1(t) - kdiss\_cb \cdot CLOCK\text{-}BMAL1(t)\big] - d\_cb \cdot CLOCK\text{-}BMAL1(t), \tag{A.12}$$

Immune system agents (Eqs.13-20)

Endotoxin concentration

$$\frac{\mathrm{d}P(t)}{\mathrm{d}t} = -d_p \cdot P(t), \tag{A.13}$$

The endotoxin insult injected intraperitoneally in the rats is a bolus administration, which initiates the inflammatory cascade. The initial conditions for P are either 3, 6, or 12 mg/Kg depending on the endotoxin dose level.

Total number of activated phagocytic cells

$$\frac{\mathrm{d}N(t)}{\mathrm{d}t} = k_N \cdot \Big(\frac{R(t)}{x_N + R(t)}\Big) - d_N \cdot N(t), \tag{A.14}$$

$$\begin{aligned} R(t) &= \big[k_{NP} \cdot P(t) + k_{ND} \cdot D(t)\big] \cdot fDN_{NCA}(t) \cdot fDN_{NIL10}(t) \\ &\quad \cdot (1 + k_{NTNF} \cdot fUP_{NTNF}(t)) \cdot (1 + k_{NIL6} \cdot fUP_{NIL6}(t)) \\ fUP_{NTNF}(t) &= \frac{TNF(t)}{x_{NTNF} + TNF(t)} \\ fUP_{NIL6}(t) &= \frac{IL6(t)}{x_{NIL6} + IL6(t)} \\ fDN_{NCA}(t) &= \frac{xNCA}{x_{NCA} + CA(t)} \\ fDN_{NIL10}(t) &= \frac{xNIL10}{x_{NIL10} + IL10(t)} \end{aligned}$$

The initial condition is $N(0) = 0$.

Tissue damage marker

$$\frac{\mathrm{d}D(t)}{\mathrm{d}t} = k_D \cdot \frac{IL6(t)^4}{x_D^4 + IL6(t)^4} + k_P \frac{P(t)}{x_P + P(t)} - d_D \cdot D(t), \tag{A.15}$$

The initial condition is $D(0) = 0$.

Concentration of interleukin-6

$$\begin{aligned}\frac{\mathrm{d}IL\text{-}6(t)}{\mathrm{d}t} &= k_{IL6} \cdot \frac{N(t)^4}{x_{IL6}^4 + N(t)^4} \cdot fDN_{IL6IL10}(t) \cdot fDN_{IL6CA}(t) \cdot fDN_{IL6REV}(t) \\ &\quad \cdot \left[1 + k_{IL6TNF} \cdot fUP_{IL6TNF}(t) + k_{IL6IL6} \cdot fUP_{IL6IL6}(t)\right] - d_{IL6} \cdot IL6(t),\end{aligned} \tag{A.16}$$

$$\begin{aligned} fUP_{IL6TNF}(t) &= \frac{TNF(t)}{x_{IL6TNF} + TNF(t)} \\ fUP_{IL6IL6}(t) &= \frac{IL6(t)}{x_{IL6IL6} + IL6(t)} \\ fDN_{IL6IL10}(t) &= \frac{x_{IL6IL10}}{x_{IL6IL10} + IL10(t)} \\ fDN_{IL6CA}(t) &= \frac{x_{IL6CA}}{x_{IL6CA} + CA(t)} \\ fDN_{IL6REV}(t) &= \frac{x_{IL6REV}}{x_{IL6REV} + REV(t)} \end{aligned}$$

The initial condition is *IL-6(0)=0*.

Concentration of tumor necrosis factor α

$$\begin{aligned}\frac{\mathrm{d}TNF\text{-}\alpha(t)}{\mathrm{d}t} &= k_{TNF} \cdot N(t)^{1.5} \cdot \left[1 + k_{TNFTNF} \cdot fUP_{TNFTNF}(t)\right] \cdot fDN_{TNFCA}(t) \cdot fDN_{TNFIL10}(t) \\ &\quad \cdot fDN_{TNFIL6}(t) \cdot fDN_{TNFCRY}(t) \cdot fDN_{TNFROR}(t) - d_{TNF} \cdot TNF(t),\end{aligned} \tag{A.17}$$

$$
\begin{aligned}
fUP_{TNFTNF}(t) &= \frac{TNF(t)}{x_{TNFTNF} + TNF(t)} \\
fDN_{TNFCA}(t) &= \frac{x_{TNFCA}^6}{x_{TNFCA}^6 + CA(t)^6} \\
fDN_{TNFIL10}(t) &= \frac{x_{TNFIL10}}{x_{TNFIL10} + IL10(t)} \\
fDN_{TNFIL6}(t) &= \frac{x_{TNFIL6}}{x_{TNFIL6} + IL6(t)} \\
fDN_{TNFCRY}(t) &= \frac{x_{TNFCRY}}{x_{TNFCRY} + CRY(t)} \\
fDN_{TNFROR}(t) &= \frac{x_{TNFROR}}{x_{TNFROR} + ROR(t)}
\end{aligned}
$$

The initial condition is $TNF\text{-}\alpha(0) = 0$.

Concentration of interleukin-10

$$
\begin{aligned}
\frac{\mathrm{d}IL10(t)}{\mathrm{d}t} = k_{IL10} \cdot \frac{N(t)^3}{x_{IL10}^3 + N(t)^3} \cdot \left[1 + k_{IL10IL6} \cdot fUP_{IL10IL6}(t) + k_{IL10TNF} \cdot fUP_{IL10TNF}(t)\right] \\
\cdot fDN_{IL6REV}(t) - d_{IL10} \cdot fDN_{IL10d}(t) + Y_{IL10}(t) + s_{IL10}, \qquad \text{(A.18)}
\end{aligned}
$$

$$
\begin{aligned}
fUP_{IL10IL6}(t) &= \frac{IL6(t)^4}{x_{IL10IL6}^4 + IL6(t)^4} \\
fUP_{IL10TNF}(t) &= \frac{TNF(t)}{x_{IL10TNF} + TNF(t)} \\
fDN_{IL10d}(t) &= \frac{x_{IL10d}}{x_{IL10d} + IL10(t)} \\
fDN_{IL10REV}(t) &= \frac{x_{IL10REV}}{x_{IL10REV} + REV(t)}
\end{aligned}
$$

The production of *IL-10* in the basal state is represented by the constant $sIL10$. With $N(0) = 0$, the initial condition is $IL\text{-}10(0) = \frac{s_{IL10} \cdot x_{IL10d}}{d_{IL10} \cdot x_{IL10d} - s_{IL10}}$.

Tissue damage driven non-accessible interleukin-10 promoter

$$
\frac{\mathrm{d}Y_{IL10}(t)}{\mathrm{d}t} = k_{IL102} \cdot \frac{D(t)^4}{x_{IL102}^4 + D(t)^4} - d_{IL102} \cdot Y_{IL10}(t), \qquad \text{(A.19)}
$$

The initial condition is $Y_{IL10}(0) = 0$.

Anti-inflammatory moderator

$$\frac{\mathrm{d}CA(t)}{\mathrm{d}t} = k_{CA} \cdot N(t) - d_{CA} \cdot CA(t) + s_{CA}, \tag{A.20}$$

At basal conditions, the system is assumed to be slightly anti-inflammatory. This was achieved by introducing a constant, sCA, into the ODE. Hence, with $N(0) = 0$, we obtain $CA(0) = \frac{sCA}{dCA}$.

LPS filter

$$F_P(t) = P_0 - \frac{P_0}{24}t. \tag{A.21}$$

where $P_0 = P(t = 0)$. $F_P(0)$ is either 3, 6, or 12 mg/Kg depending on the endotoxin dose level.

Table A.3: mRNA and protein degradation rate constants (in h^{-1})

Parameter	Value	Description
dm_per	0.10576	*Per* mRNA degradation rate constant
dm_cry	0.50633	*Cry* mRNA degradation rate constant
dm_rev	0.47914	*Rev-Erb* mRNA degradation rate constant
dm_ror	0.26786	*Ror* mRNA degradation rate constant
dm_bmal	4.6995	*Bmal1* mRNA degradation rate constant
dp_per	0.14989	*PER* protein degradation rate constant
dp_cry	1.9105	*CRY* protein degradation rate constant
dp_rev	0.28899	*REV-ERB* protein degradation rate constant
dp_ror	0.063637	*ROR* protein degradation rate constant
dp_bmal	0.22534	*BMAL1* protein degradation rate constant
d_pc	0.22571	*PER-CRY* protein complex degradation rate constant
d_cb	0.1709	*CLOCK-BMAL1* protein complex degradation rate constant

Table A.4: Maximal transcription rates (in $nmol \cdot l^{-1} \cdot h^{-1}$)

Parameter	Value	Description
vmax_per	0.83525	*Per* mRNA maximal transcription rate
vmax_cry	1.0418	*Cry* mRNA maximal transcription rate
vmax_rev	0.065746	*Rev-Erb* mRNA maximal transcription rate
vmax_ror	7.2287	*Ror* mRNA maximal transcription rate
vmax_bmal	0.29055	*Bmal1* mRNA maximal transcription rate

Table A.5: Activation ratios (dimensionless)

Parameter	Value	Description
fold_per	0.12156	Activation ratio of *Per* by *CLOCK-BMAL1*
fold_cry	13.828	Activation ratio of *Cry* by *CLOCK-BMAL1*
fold_rev	130.78	Activation ratio of *Rev-Erb* by *CLOCK-BMAL1*
fold_ror	0.078569	Activation ratio of *Ror* by *CLOCK-BMAL1*
fold_bmal	43.306	Activation ratio of *Bmal1* by *ROR*

Table A.6: Regulation thresholds (in *nmol/l*)

Parameter	Value	Description
Ka_per_cb	3.3679	Regulation threshold of *Per* by *CLOCK-BMAL1*
Ki_per_pc	0.14178	Regulation threshold of *Per* by *PER-CRY*
Ka_cry_cb	1.5508	Regulation threshold of *Cry* by *CLOCK-BMAL1*
Ki_cry_pc	0.0027556	Regulation threshold of *Cry* by *PER-CRY*
Ki_cry_rev	0.64066	Regulation threshold of *Cry* by *REV-ERB*
Ka_rev_cb	0.18454	Regulation threshold of *Rev-Erb* by *CLOCK-BMAL1*
Ki_rev_pc	550.46	Regulation threshold of *Rev-Erb* by *PER-CRY*
Ka_ror_cb	0.56517	Regulation threshold of *Ror* by *CLOCK-BMAL1*
Ki_ror_pc	0.072928	Regulation threshold of *Ror* by *PER-CRY*
Ka_bmal_ror	0.076498	Regulation threshold of *Bmal1* by *ROR*
Ki_bmal_rev	0.0002375	Regulation threshold of *Bmal1* by *REV-ERB*

Table A.7: Hill coefficients (dimensionless)

Parameter	Value	Description
hill_per_cb	17.025	hill coefficient, regulation of *Per* by *CLOCK-BMAL1*
hill_per_pc	22.829	hill coefficient, regulation of *Per* by *PER-CRY*
hill_cry_cb	7.4632	hill coefficient, regulation of *Cry* by *CLOCK-BMAL1*
hill_cry_pc	2.583	hill coefficient, regulation of *Cry* by *PER-CRY*
hill_cry_rev	58.733	hill coefficient, regulation of *Cry* by *REV-ERB*
hill_rev_cb	9.3373	hill coefficient, regulation of *Rev-Erb* by *CLOCK-BMAL1*
hill_rev_pc	0.95847	hill coefficient, regulation of *Rev-Erb* by *PER-CRY*
hill_ror_cb	6.0371	hill coefficient, regulation of *Ror* by *CLOCK-BMAL1*
hill_ror_pc	3.2993	hill coefficient, regulation of *Ror* by *PER-CRY*
hill_bmal_ror	2.8187	hill coefficient, regulation of *Bmal1* by *ROR*
hill_bmal_rev	1.5678	hill coefficient, regulation of *Bmal1* by *REV-ERB*

Table A.8: Translation rates (in molecules per hour per mRNA)

Parameter	Value	Description
kp_per	0.77741	*Per* translation rate
kp_cry	0.9308	*Cry* translation rate
kp_rev	0.0004355	*Rev-Erb* translation rate
kp_ror	0.010866	*Ror* translation rate
kp_bmal	0.97306	*Bmal1* translation rate

Table A.9: Complexation kinetic rates

Parameter	Value	Unit	Description
kass_cb	0.0057803	h^{-1}	*CLOCK-BMAL* association rate
kass_pc	0.15187	$nmol{\cdot}l^{-1} \cdot h^{-1}$	*PER-CRY* association rate
kdiss_cb	0.00022191	h^{-1}	*CLOCK-BMAL* disassociation rate
kdiss_pc	0.23509	h^{-1}	*PER-CRY* disassociation rate

Table A.10: Parameters of the inflammation model

Parameter	Value	Unit
	Endotoxin	
d_p	3	h^{-1}
	Phagocytes	
k_N	5.239009955e+07	h^{-1}
x_N	11.5345	N-unit
d_N	0.195335	h^{-1}
k_{NP}	46.8879	N-unit × Kg/mg
k_{ND}	0.01297224	N-unit/D-unit
x_{NTNF}	1530.0904	pg/ml
x_{NIL6}	52121.3480	pg/ml
x_{NCA}	0.0819918	pg/ml
x_{NIL10}	138.3830	pg/ml
k_{NTNF}	15.7694	
k_{NIL6}	2.916366	
	Damage	
k_D	0.747386	D-unit/h
d_D	0.434761	h^{-1}
x_D	3572.1137	pg/ml
k_P	1.385458	D-unit/h
x_P	0.5746	mg/Kg
	Slow-acting cytokines	
k_{CA}	1.381866e-09	pg/(ml × h × N-unit)
d_{CA}	3.1777e-2	h^{-1}
s_{CA}	0.004	pg/(ml × h)
	IL-6	
k_{IL6TNF}	23.15473	
x_{IL6TNF}	1072.9657	pg/ml
k_{IL6}	4.2094572e+07	pg/(ml × h)
d_{IL6}	0.410396	h^{-1}
x_{IL6}	2.012412e+08	N-unit
$x_{IL6IL10}$	1.32377	pg/ml
k_{IL6IL6}	101.1321	

x_{IL6IL6}	14308.8692	pg/ml
x_{IL6CA}	1.104116	pg/ml
	TNF-α	
k_{TNF}	9.326669e-08	pg/(ml $\times$ N-unit$^{1.5}$)
d_{TNF}	1.99835	h^{-1}
$x_{TNFIL10}$	6177.1302	pg/ml
x_{TNFCA}	0.223434	pg/ml
k_{TNFTNF}	0.198227	
x_{TNFTNF}	8520.5658	pg/ml
x_{TNFIL6}	40998.1848	pg/ml
	IL-10	
$k_{IL10TNF}$	0.212173	
$x_{IL10TNF}$	8905.7477	pg/ml
$k_{IL10IL6}$	3.27267	
$x_{IL10IL6}$	22345.6179	pg/ml
k_{IL10}	1.9301e+05	pg/(ml $\times$ h)
d_{IL10}	95.465	h^{-1}
x_{IL10}	5.938865e+07	N-unit
s_{IL10}	1187.2	pg/(ml $\times$ h)
x_{IL10d}	713.8094	pg/ml
	Y_{IL10}	
k_{IL102}	3.804797e+06	Y_{IL10}-unit/h
d_{IL102}	0.0224238	h^{-1}
x_{IL102}	8.470849	D-unit
	coupling parameters	
x_{IL6REV}	0.009	*nmol/l*
$x_{IL10REV}$	0.004	*nmol/l*
x_{TNFROR}	0.4534	*nmol/l*
x_{TNFCRY}	0.4315	*nmol/l*

Table A.11: List of parameters modified in CJL models

Parameter	Control	CJL male	CJL female
vmax_per	0.83525	2.1717	2.9568
vmax_cry	1.0418	unchanged	1.6669
vmax_rev	0.065746	0.1249	0.0164
vmax_bmal	0.29055	unchanged	0.1511
kdiss_pc	0.23509	0.6112	1.3315
kdiss_cb	2.2191e-4	unchanged	1.1539e-4
kass_pc	0.15187	0.0584	0.0268
kass_cb	0.0057803	unchanged	0.0111
Ki_bmal_rev	2.375e-4	4.5125e-4	5.9375e-5
Ki_cry_rev	0.64066	1.2173	0.1602

Table A.12: Percentage change in mean gene expression level due to CJL

Gene	CJL male	Experimental data [164]	CJL female	Experimental data [164]
Bmal1	+3%	Not significant	−44%	$-43\% \pm 38\%$
Per2	+236%	$+230\% \pm 201\%$	+510%	$+497\% \pm 234\%$
Cry2	+2%	Not significant	+69%	$+69\% \pm 18\%$
Rev-Erbα	+103%	$+98\% \pm 96.5\%$	−72%	$-70\% \pm 23\%$
Ror	+8%	Not recorded	+19%	Not recorded

A.2 The Sobol' sensitivity analysis

The method of Sobol' [445] is a global and model independent sensitivity analysis method that is based on variance decomposition. Variance-based measures of sensitivity are attractive because they measure sensitivity across the whole input space, they can handle non-linear and non-monotonic functions and models. They can also measure the effect of interactions in such systems.

A first order index, S_i, is a measure for the variance contribution of the individual parameter to the total model variance, whereas a total order index, S_{Ti} is the result of

the main effect of a given parameter and all its interactions with the other parameters. Note that for non-additive models as ours, interactions exist: S_{Ti} is greater than S_i and the sum of all S_i is less than 1. On the other hand, the sum of all S_{Ti} is greater than 1. By analyzing the difference between S_{Ti} and S_i, one can determine the impact of the interactions between a parameter of interest and the other parameters [446]. In this work, we will not discuss how to implement the Sobol' method, we refer to [445, 446] and the references therein.

A.2.1 The parameters considered for the sensitivity analysis

Based on our CJL male and CJL female models, 10 parameters are selected for the initial Sobol' sensitivity analysis. The set includes all parameters which took new values after fitting the CJL models. Lower and upper bounds to the parameter input space are obtained by halving and doubling nominal values, respectively (see Table A.13). Our outputs of interest are IL-6, TNF-α, IL-10 and D because they convey the most information about the state inflammation, and are also directly affected by the circadian clock model. For each output, we report first and total order effects. We performed 5000×(2+ number of input parameters) simulations to derive the Sobol' indices.

Table A.13: Parameters studied for the Sobol' sensitivity analysis

Parameter	nominal value	lower bound	upper bound
v_{max}^{per}	0.83525	0.4176	1.6705
v_{max}^{cry}	1.0418	0.5209	2.0836
v_{max}^{rev}	0.065746	0.0329	0.1315
v_{max}^{bmal}	0.29055	0.1453	0.5811
kdiss_pc	0.23509	0.1175	0.4702
kdiss_cb	2.2191e-4	1.110e-4	4.438e-4
kass_pc	0.15187	0.0759	0.3037
kass_cb	0.0057803	0.0029	0.0116
Ki_bmal_rev	2.375e-4	1.188e-4	4.750e-5
Ki_cry_rev	0.64066	0.3203	1.2813

A.2.2 Results of the Sobol' sensitivity analysis

We calculated Sobol' indices in order to assess the relative influence of each parameter. These values measure the relative sensitivity of the outcome to each parameter (first-order) and to all the interactions with the other parameters (total-order). Figure A.1 shows that total output uncertainty is primarily induced by the parameters *kass_pc*, PER-CRY association rate, and *vmax_cry*, *Cry* mRNA maximal transcription rate, and how they interact with the other parameters. The high sensitivity of D, IL-6, TNF-α and IL-10

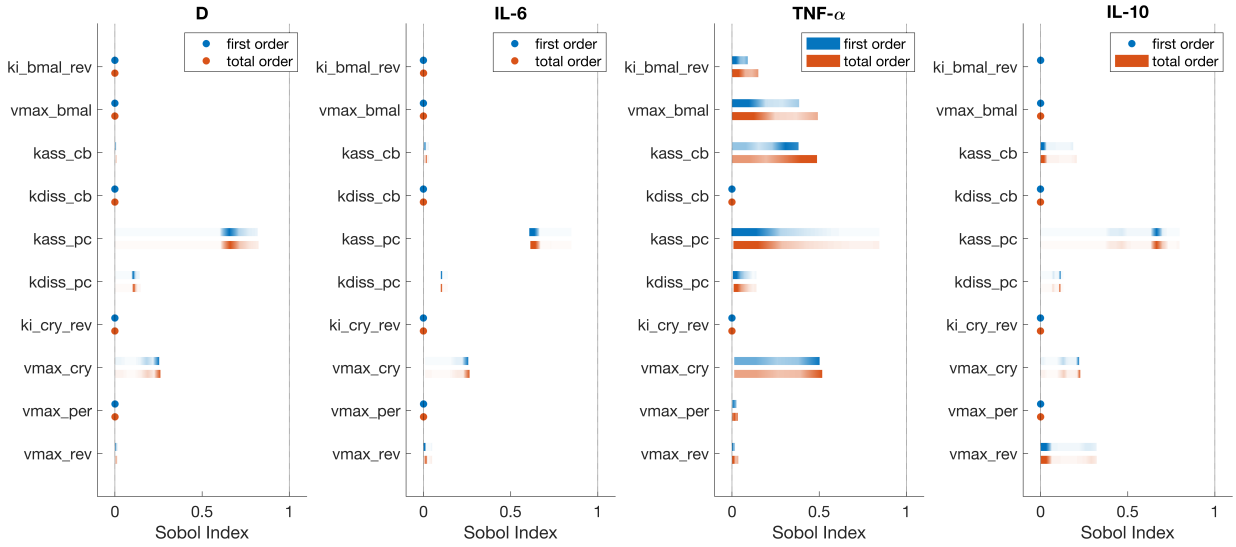

Figure A.1: Sobol' indices for parameters modified by CJL. Simulation of the baseline coupled model under acute inflammation with endotoxin dose 3 mg/Kg. Circles imply no sensitivity to a parameter. A darker area on an index bar indicates sensitivity levels that persisted for most of the simulation time, while faded areas represent sensitivity levels that lasted for shorter periods of time. Infection occurs at CT12.

to *kass_pc* (Sobol index > 0.5), is due to the consequential role of the complex PER-CRY in the circadian circuitry. Inhibitor proteins PER and CRY dimerize to inhibit their own transcription as well as that of REV-ERB and ROR by acting on CLOCK-BMAL1 protein complex [32]. Overall, D, IL-6 and IL-10 are less sensitive with respect to the parameter set tested (see Table A.13), whereas TNF-α is more sensitive to parameters affecting CRY and its related complex, PER-CRY.

Figure A.2 shows the time course of the total-order Sobol' indices for *vmax_cry*, *kass_pc*

and *kass_cb*, the three most influtential parameters as shown in Figure A.1. D, IL-6 and IL-10 are sensitive *kass_pc* and *vmax_cry* throughout the inflammation, but the sensitivity of TNF-α to these parameters decreases over time. Moreover, the times of lower sensitivity of IL-10 to *kass_pc*, correspond to the times of higher sensitivity of the cytokine to *kass_cb*. To assess the robustness of the outcomes to uncertainty in the input parameters in Table A.13, we plotted the computed simulation results showing the 90% quantile region for D, IL-6, TNF-α and IL-10 (see Figure A.3). Our results show that the inflammation output variables are qualitatively robust to uncertainty in the parameters that are modified by CJL.

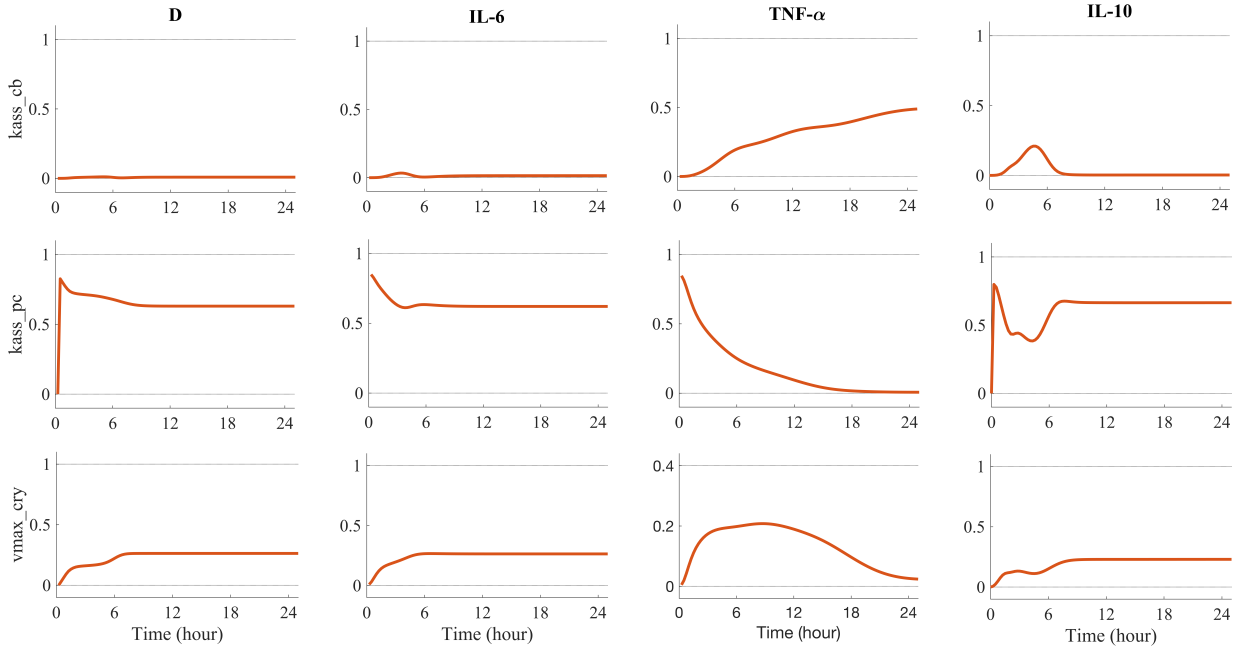

Figure A.2: Time course of total-order Sobol' indices for vmax_cry, kass_pc and kass_cb. Simulation of the baseline coupled model under acute inflammation with endotoxin dose 3 mg/Kg. Infection occurs at CT12.

A.2.3 Assessing sensitivities relative to coupling parameters

We extended our parameter input space to include all the clock model parameters and the coupling parameters. A sensitivity analysis of this larger parameter space allows us to

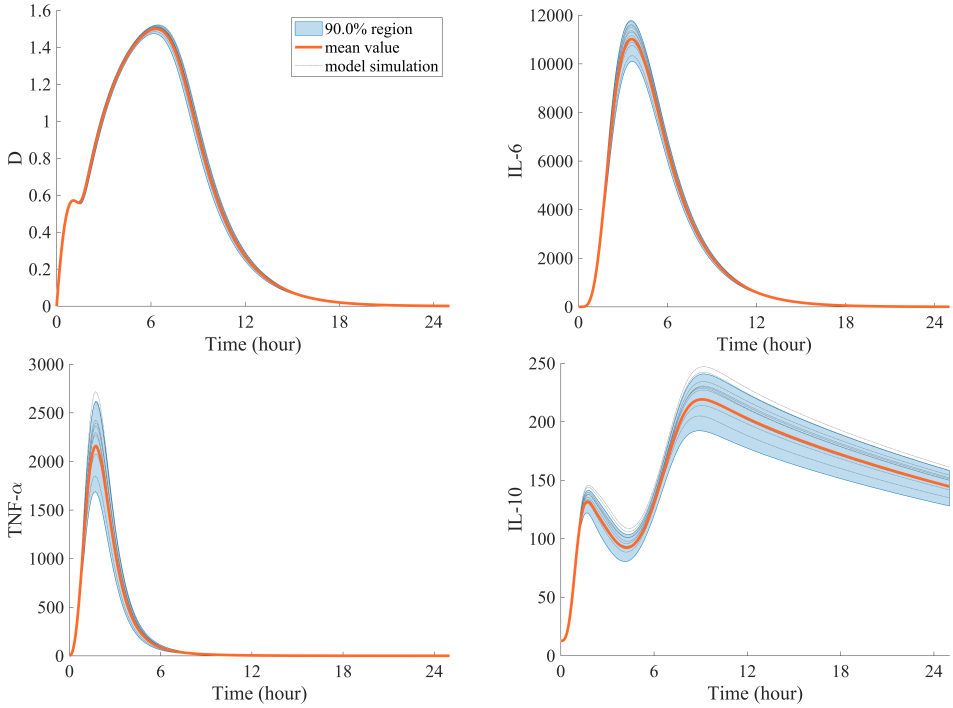

Figure A.3: Computed simulation results for *D*, *IL-6*, *TNF-α* and *IL-10*. Simulation of the baseline coupled model under acute inflammation with endotoxin dose 3 mg/Kg. Infection occurs at CT12. Parameters used in the sensitivity analysis are shown in Table A.13.

assess how perturbations to the clock parameters can affect the output of the acute inflammation model, regardless of CJL. We performed 5000×(2+ number of input parameters) simulations to derive the Sobol' indices.

Our results indicate that D, IL-6, TNF-α and IL-10 are most sensitive to the coupling parameters, as should be expected. Figure A.4 shows the Sobol' indices for the coupling parameters. These parameters directly link clock proteins to cytokines, and thus inferences about the effect of parameters on inflammation can be extended to inferences about the associated clock protein on inflammation. TNF-α is more sensitive to $xTNFCRY$ and $xTNFROR$ as CRY and ROR directly inhibit the production of the cytokine. IL-6 and IL-10 are sensitive to $xIL6REV$ and $xIL10REV$, respectively. This is naturally explained by the direct inhibition of IL-6 and IL-10 by REV-ERB. We note that the damage marker, D, is sensitive to the same parameters as IL-6. This is to be expected because D is upregulated by IL-6. Moreover, Figure A.5 shows the time course of the total-order Sobol'

indices for the coupling parameters. The results are summarized below for each cytokine:

- **IL-6 and Damage.** Both outcomes are sensitive to $xIL6REV$ and $xIL10REV$ throughout the duration of inflammation, but are also sensitive to $xTNFCRY$ and $xTNFROR$ at the beginning of inflammation. This indicates that most of the effect of the clock on the damage marker is induced by REV-ERB, but there exists an initial joint effect of REV-ERB, CRY and ROR on IL-6 and D. CRY and ROR act indirectly through their modulation of TNF-α.

- **TNF-α.** The cytokine is particularly sensitive to $xTNFCRY$ and $xTNFROR$. The sensitivity of TNF-α to $xTNFCRY$ decreases as its sensitivity to $xTNFROR$ increases during inflammation. Overall, ROR has a stronger influence on TNF-α compared to CRY. We note also the increased sensitivity of TNF-α to $xIL10REV$ a few hours after the onset of inflammation. This is due to the inhibitory action of IL-10 on TNF-α.

- **IL-10.** Throughout the period of inflammation, IL-10 is most sensitive to $xIL6REV$ and $xIL10REV$. The Sobol' index for $xIL10REV$ decreases shortly after the onset of inflammation, before rising again five hours post-infection. This suggests a role for REV-ERB in the formation of the first peak in IL-10 as well as the second peak that occurs 5h after the beginning of inflammation (see Figure 4.5 in the main text). IL-10 is also sensitive to $xTNFCRY$ and $xTNFROR$ at the start of inflammation. Since ROR and CRY inhibit TNF-α, the sensitivity of IL-10 to those parameters is because TNF-α peaks early during inflammation and activates its production.

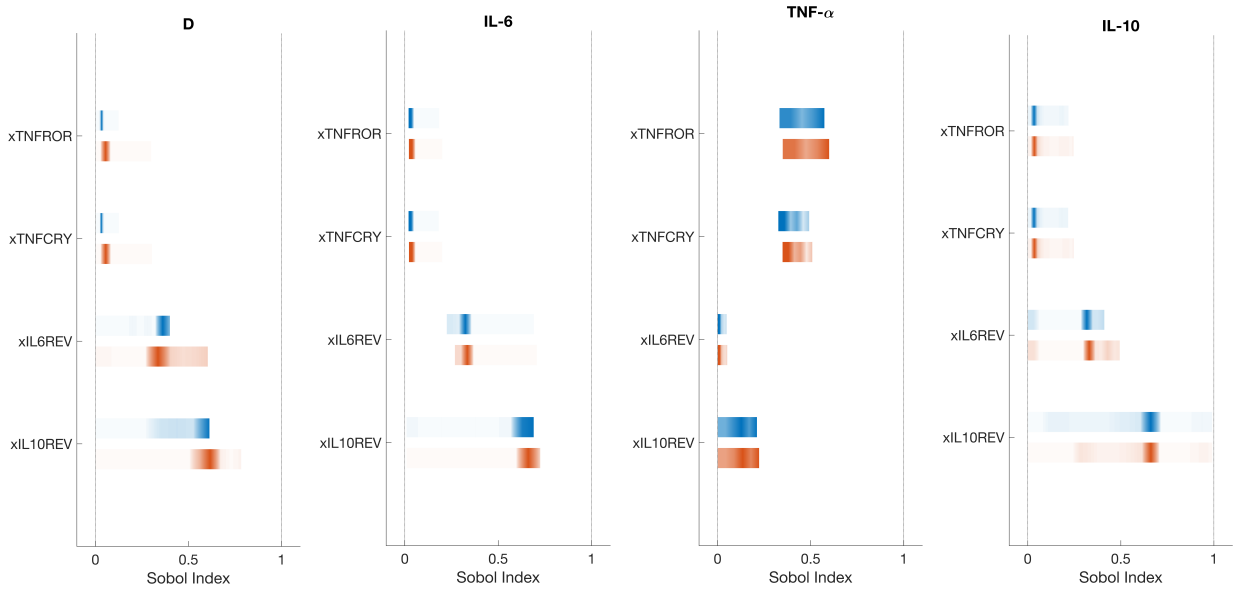

Figure A.4: Sobol' indices for the coupling parameters. Simulation of the baseline coupled model under acute inflammation with endotoxin dose 3 mg/Kg. Circles imply no sensitivity to a parameter. A darker area on an index bar indicates sensitivity levels that persisted for most of the simulation time, while faded areas represent sensitivity levels that lasted for shorter periods of time. Infection occurs at CT12.

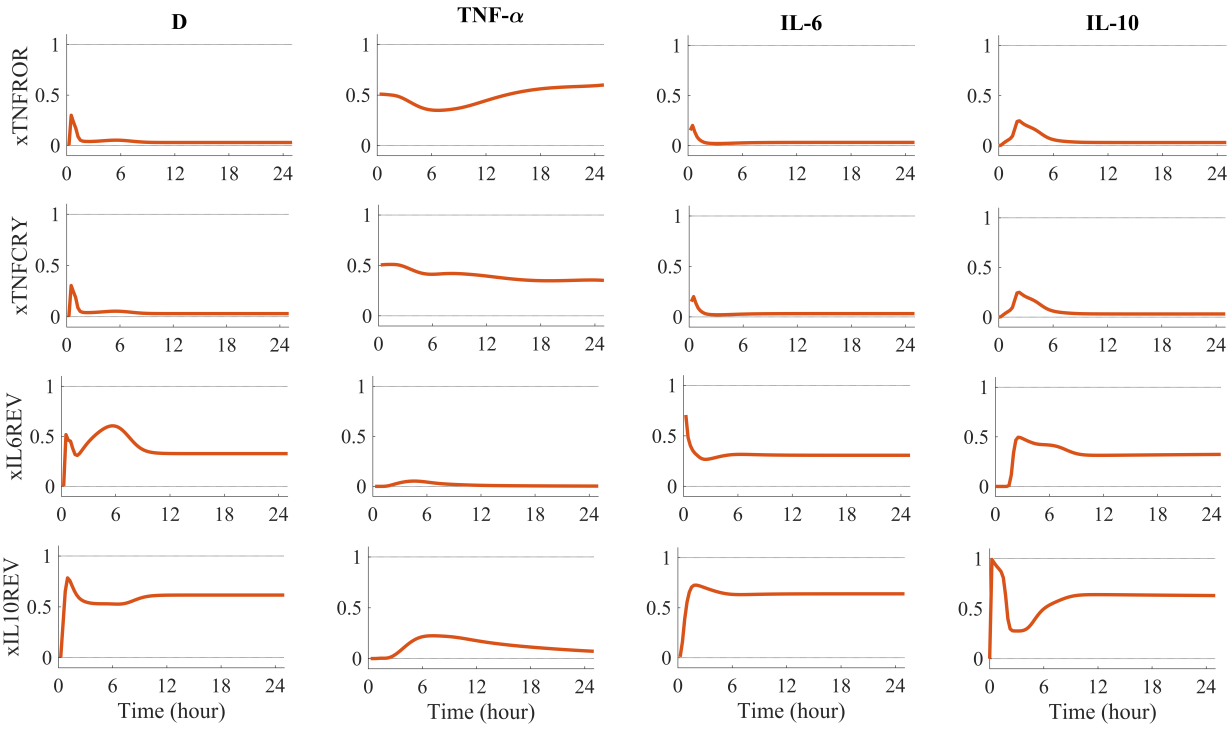

Figure A.5: Time course of total-order Sobol' indices for the coupling parameters. Simulation of the baseline coupled model under acute inflammation with endotoxin dose 3mg/Kg. Infection occurs at CT12.

Appendix B

Appendix to Chapter 5

B.1 Convergence of the particle-like and mean field solutions

We present, in this section, supplementary convergence results: the convergence of error between solutions to the stochastic system (5.8) and the mean-field equation (5.9) when the number of neurons tends to infinity. We have used a population of 10,000 Goodwin-type neurons and ran 10,000 Monte Carlo simulations of the network model using the Euler-Maruyama method [447]. Solutions of the network are constrained to remain in a smooth positive domain D. Namely, we simulate the case where the boundary ∂D is instantaneously reflecting in an oblique direction. See [281, 282] and the references therein.

The most classical way to show convergence is to reason in terms of trajectories and to show that, when the number of agents tends to infinity, the behavior of the stochastic system converges to the mean-field approximation almost surely or in probability. Thus, we present the Kullback-Leibler (KL) divergence $D_{KL}\big(\rho_{x,y,z}^{Network}||\rho_{x,y,z}^{Mean-field}\big)$ between marginal distributions; see Definition 2.3.4.

For increasing values of network size N, we ran 10,000 Monte Carlo simulations of the network equations until $t_{final} = 1$. As seen in Figure B.1a, the Kullback-Leibler divergence decreases as N increases, validating the efficiency of the mean-field model even for relatively small values of N. We conclude that the solution to the mean-field equation (5.9) accurately represents the network's average behaviour. These results highlight the accuracy of the

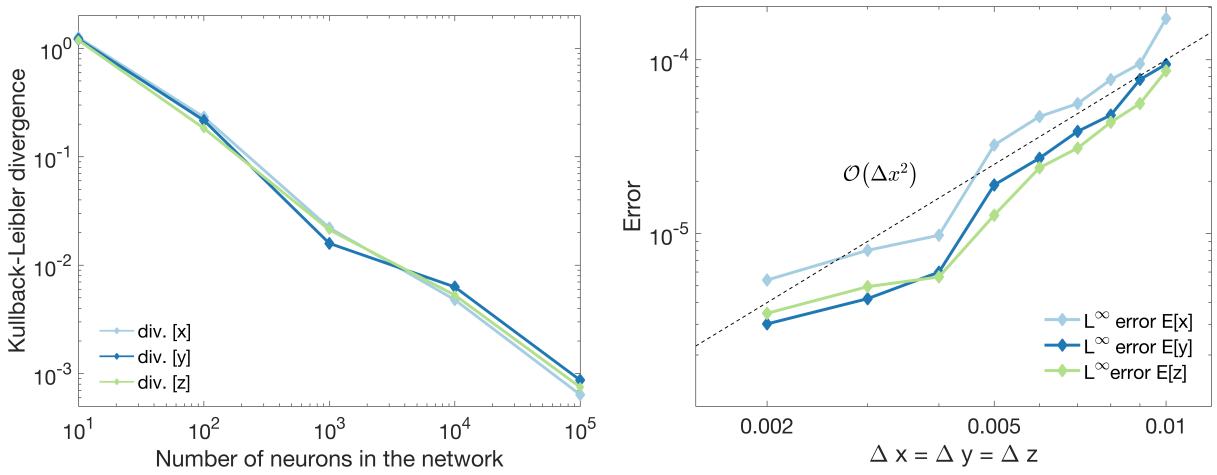

(a) (b)

Figure B.1: (a) Kullback-Leibler divergence between the marginal probability densities $\rho_1(t,x)$, $\rho_2(t,y)$, $\rho_3(t,z)$ calculated from the network and mean-field equation solutions as network size N increases. (b) Convergence of error between solutions to the stochastic system (5.8) and the mean-field equation (5.9) for the averages in x, y, and z in L_1 and L_∞ norms. Grid cells are assumed to be of uniform size in all three variables, $\Delta x = \Delta y = \Delta z$. We conducted 10,000 Monte Carlo simulations with a network size N=10,000 up to time $t_{final} = 1$.

numerical method in preserving long time behavior of the solutions. Solution remain strictly positive for all $t > 0$, thus the problem is not degenerate (see Remark 4 below).

Next, consider the spatial averages of x, y, and z separately, *i.e.* $E[x]$, $E[y]$ and $E[z]$. An estimation of the relative error in L_∞ norm at time T is given by:

$$e^{\infty}_{\Delta x} = \frac{\left\|\mu^{MF}_{\Delta x}(T) - \mu^{MC}_{\Delta x}(T)\right\|_{L_\infty(\Omega)}}{\left\|\mu^{MC}_{\Delta x}(T)\right\|_{L_\infty(\Omega)}}, \tag{B.1}$$

where $\mu^{MF}_{\Delta x}$ represents the average in x of the probability density computed on a uniform mesh of size Δx, and $\mu^{MC}_{\Delta x}$ represents the average in x from the Monte Carlo simulations of the network equations using a similar mesh size. Relative errors $e^{\infty}_{\Delta y}$ and $e^{\infty}_{\Delta z}$ are computed similarly. Results are shown in Figure B.1b. For reference, a dashed black line of slope two is added. We see that the slope of the dashed line appears to match well that of the error curves, suggesting that numerical scheme is indeed second-order in space, and that the continuum equation accurately describes the network for large N.

B.2 Derivation of the continuum model (5.9)

The equations in (5.9–5.11) can be derived via the *mean-field limit*. Here we present a formal description of this procedure. Starting from the deterministic model, define the empirical distribution density associated to a solution $(x(t), y(t), z(t))$ of (5.5) and given by

$$\rho^N(x, y, z, t) = \frac{1}{N} \sum_{i=1}^{N} \delta(x - x_i(t))\delta(y - y_i(t))\delta(v - z_i(t)), \quad t > 0,$$

where δ is the Dirac delta probability measure. Let us denote by $\mathcal{P}\big(\mathbb{R}^k\big)$ the space of probability measures on $\mathbb{R}^k$.

Let us assume that the particles remain in a fixed compact domain $(x_i(t), y_i(t), z_i(t)) \in \bar{\Omega} \subset \mathbb{R} \times \mathbb{R} \times \mathbb{R}$ for all N in the time interval $t \in [0, T]$. Our model (5.5) satisfies this assumption if for instance the initial configuration is obtained as an approximation of an initial compactly supported probability measure ρ_0 [47]. Since for each t the measure $\rho^N(t) := \rho^N(\cdot, \cdot, \cdot, t)$ is a probability measure in $\mathcal{P}\big(\mathbb{R}^3\big)$ with the uniform support in N, then Prokhorov's theorem implies that the sequence is weakly-$*$-relatively compact. Assume there exists a subsequence $\big(\rho^{N_k}\big)_k$ and $\rho : [0, T] \to \mathcal{P}\big(\mathbb{R}^3\big)$ such that $\rho^{N_k} \to \rho \quad (k \to \infty)$ in the w^*–convergence sense in $\mathcal{P}\big(\mathbb{R}^3\big)$, pointwise in time. Following the approach in [47], let us consider the test function $\varphi \in C_0^1\big(\mathbb{R}^3\big)$. To simplify the notation we will write φ for

$\varphi\big(x_i(t), y_i(t), z_i(t)\big)$, and x_i, y_i, and z_i for $x_i(t)$, $y_i(t)$, and $z_i(t)$, respectively. We compute

$$\begin{aligned}
\frac{\mathrm{d}}{\mathrm{d}t}\Big\langle \rho^N(t), \varphi \Big\rangle &= \frac{1}{N}\sum_{i=1}^{N} \frac{\mathrm{d}}{\mathrm{d}t}\varphi\big(x_i(t), y_i(t), z_i(t)\big) \\
&= \frac{1}{N}\sum_{i=1}^{N} \partial_x\varphi\left(\frac{\alpha}{1+z_i^n} - x_i + \frac{K}{N}\sum_{j=1}^{N} H(x_i - x_j)\right) + \frac{1}{N}\sum_{i=1}^{N}\partial_y\varphi\left(x_i - y_i\right) \\
&\quad + \frac{1}{N}\sum_{i=1}^{N}\partial_z\varphi\left(y_i - z_i\right) \\
&= \big\langle \rho^N(t), \partial_y\varphi\left(x-y\right)\big\rangle + \big\langle \rho^N(t), \partial_z\varphi\left(y-z\right)\big\rangle \\
&\qquad + \left(\frac{1}{N}\sum_{i=1}^{N}\partial_x\varphi\left(\frac{\alpha}{1+z_i^n} - x_i\right)\right) + \left(\frac{1}{N}\sum_{i=1}^{N}\left[\frac{K}{N}\sum_{j=1}^{N} H(x_i - x_j)\right]\partial_x\varphi\right) \\
&= \big\langle \rho^N(t), \partial_y\varphi\left(x-y\right)\big\rangle + \big\langle \rho^N(t), \partial_z\varphi\left(y-z\right)\big\rangle \\
&\qquad + \left\langle \rho^N(t), \left(\frac{\alpha}{1+z^n} - x\right)\partial_x\varphi\right\rangle + \left\langle \rho^N(t), \left(\frac{K}{N}\sum_{j=1}^{N} H(x - x_j)\right)\partial_x\varphi\right\rangle.
\end{aligned}$$

We can rewrite

$$\frac{1}{N}\sum_{j=1}^{N} H(x - x_j) = \frac{1}{N}\sum_{j=1}^{N}\big\langle H(x-\omega), \delta(\omega - x_j)\big\rangle_x = H \star m_{\rho^N}(y,z,t),$$

where

$$m_{\rho^N}(y,z,t) = \int_{\mathbb{R}} \rho^N(x,y,z,t)dx = \left\langle 1, \frac{1}{N}\sum_{j=1}^{N}\delta(\omega - x_j)\delta(y-y_j)\delta(z-z_j)\right\rangle_x;$$

Collecting all the terms we obtain

$$\frac{\mathrm{d}}{\mathrm{d}t}\Big\langle \rho^N(t), \varphi\Big\rangle = \Big\langle \rho^N(t), \partial_x\varphi\left(\frac{\alpha}{1+z^n} - x + K\big(H\star m_{\rho^N}\big)\right) + \partial_y\varphi\left(x-y\right) + \partial_z\varphi\left(y-z\right)\Big\rangle.$$

After integration by part in x, y, and z, we obtain

$$\left\langle \frac{\partial f}{\partial t} + \partial_x\Big[\xi\big(\rho^N\big)\rho^N\Big] + \partial_y\Big[(x-y)\rho^N\Big] + \partial_z\Big[(y-z)\rho^N\Big], \varphi\right\rangle = 0$$

or, in the strong form,

$$\frac{\partial f}{\partial t} + \partial_x \Big[\xi\big(\rho^N\big)\rho^N\Big] + \partial_y \Big[(x-y)\rho^N\Big] + \partial_z \Big[(y-z)\rho^N\Big] = 0,$$

where ξ is defined by

$$\xi\big(\rho\big)\big(x,y,z,t\big) = \frac{\alpha}{1+z^n} - x + K\big(H \star \rho\big),$$

with

$$H \star \rho(x,y,z,t) = \int_{\mathbb{R}^3} H(x-w)\rho(w,y,z,t)\,dw\,dy\,dz\,.$$

Letting $k \to \infty$ in the subsequence ρ^{N_k} leads formally to

$$\frac{\partial \rho}{\partial t} - \partial_x \big[\xi(\rho)\rho\big] - \partial_y \big[(x-y)\rho\big] - \partial_z \big[(y-z)\rho\big] = 0.$$

The case with noise in (5.9) follows a similar approach using the so-called coupling method introduced by Sznitman [93] together with [283, 284] to deal with boundary conditions. Defining a system of uncoupled copies of McKean-Vlasov particles and comparing the error with respect to the coupled system of particles is a common approach in many areas of applications of interacting particle systems in mathematical biology, see [47] for instance. By taking the difference between the two particle systems, one can develop direct Gronwall inequalities for the 2-Wasserstein distance among the marginals of the joint probability distributions. We refer the reader for the details to [50] for instance.

B.3 Presentation of the numerical scheme

In this section, we present our finite volume scheme for (5.9) preserving the structure of the gradient flow in the case of identical oscillators. We also prove the positivity preserving property for this scheme.

Inspired by [301, 448, 449], we construct a discrete numerical scheme in the variables x, y and z in (5.9) as follows. We introduce a Cartesian mesh consisting of the cells $C_{i,j,k} := \big[x_{i-\frac{1}{2}}, x_{i+\frac{1}{2}}\big] \times \big[y_{j-\frac{1}{2}}, y_{j+\frac{1}{2}}\big] \times \big[z_{k-\frac{1}{2}}, z_{k+\frac{1}{2}}\big]$, which for the sake of simplicity are assumed to be of uniform size $\Delta x \Delta y \Delta z$, that is, $x_{i+\frac{1}{2}} - x_{i-\frac{1}{2}} \equiv \Delta x$, $\forall\, i$, $y_{j+\frac{1}{2}} - y_{j-\frac{1}{2}} \equiv \Delta y$, $\forall\, j$, and $z_{k+\frac{1}{2}} - z_{k-\frac{1}{2}} \equiv \Delta z$, $\forall\, k$.

Here, we denote by

$$\bar{\rho}_{i,j,k}(t)=\frac{1}{\Delta x\Delta y\Delta z}\iiint_{C_{i,j,k}}\rho(x,y,z,t)\,dx\,dy\,dz \tag{B.2}$$

the computed cell averages of the solution ρ, which we assume to be known or approximated at time $t\geq 0$. A discrete finite volume scheme is obtained by integrating (5.9) over each cell $C_{i,j,k}$ and is given by the following system of ODEs for $\bar{\rho}_{i,j,k}$:

$$\begin{aligned}\frac{\mathrm{d}\bar{\rho}_{i,j,k}(t)}{\mathrm{d}t}=&-\frac{F^x_{i+\frac12,j,k}(t)-F^x_{i-\frac12,j,k}(t)}{\Delta x}-\frac{F^y_{i,j+\frac12,k}(t)-F^y_{i,j-\frac12,k}(t)}{\Delta y}\\&-\frac{F^z_{i,j,k+\frac12}(t)-F^z_{i,j,k-\frac12}(t)}{\Delta z},\end{aligned} \tag{B.3}$$

where $F^x_{i+\frac12,j,k}$, $F^y_{i,j+\frac12,k}$ and $F^z_{i,j,k+\frac12}$ are upwind numerical fluxes and approximate the continuous fluxes in the x, y and z directions, respectively. For simplicity, we will omit the dependence of the computed quantities on $t\geq 0$. In order to construct the upwind fluxes, we first construct piecewise linear polynomials in each cell $C_{i,j,k}$,

$$\begin{aligned}\tilde{\rho}_{i,j,k}(x,y,z)=\bar{\rho}_{i,j,k}&+(\rho_x)_{i,j,k}(x-x_i)+(\rho_y)_{i,j,k}(y-y_j)\\&+(\rho_z)_{i,j,k}(z-z_k),\quad (x,y,z)\in C_{i,j,k}\end{aligned} \tag{B.4}$$

and compute the right ("east"), $\rho^E_{i,j,k}$, and left ("west"), $\rho^W_{i,j,k}$, point values at the corresponding cell interfaces $(x_{i+\frac12},y_j,z_k)$, $(x_{i-\frac12},y_j,z_k)$, $(x_i,y_{j+\frac12},z_k)$, $(x_i,y_{j-\frac12},z_k)$, $(x_i,y_j,z_{k+\frac12})$ and $(x_i,y_j,z_{k+\frac12})$. Namely,

$$\begin{aligned}\rho^{E_x}_{i,j,k}&=\tilde{\rho}_{i,j,k}(x_{i+\frac12}-0,y_j,z_k)=\bar{\rho}_{i,j,k}+\frac{\Delta x}{2}(\rho_x)_{i,j,k},\\ \rho^{W_x}_{i,j,k}&=\tilde{\rho}_{i,j,k}(x_{i-\frac12}+0,y_j,z_k)=\bar{\rho}_{i,j,k}-\frac{\Delta x}{2}(\rho_x)_{i,j,k}.\end{aligned} \tag{B.5}$$

and analogously for the other two variables.

These values will be second-order accurate provided the numerical derivatives $(\rho_x)_{i,j,k}$, $(\rho_y)_{i,j,k}$ and $(\rho_z)_{i,j,k}$ are at least first-order accurate approximations. To ensure the point values in (B.5) are both second-order and nonnegative, the slopes $(\rho_x)_{i,j,k}$, $(\rho_y)_{i,j,k}$, $(\rho_z)_{i,j,k}$ are calculated according to the following adaptive procedure. First, the centered-difference

approximations

$$(\rho_x)_{i,j,k}=\frac{\rho_{i+1,j,k}-\rho_{i-1,j,k}}{2\Delta x},\quad (\rho_y)_{i,j,k}=\frac{\rho_{i,j+1,k}-\rho_{i,j-1,k}}{2\Delta y}$$
$$\text{and}\quad (\rho_z)_{i,j,k}=\frac{\rho_{i,j,k+1}-\rho_{i,j,k-1}}{2\Delta z} \tag{B.6}$$

are used for all i,j,k. Then, if the reconstructed point values in some cell $C_{i,j,k}$ become negative (i.e., either $\rho^E_{i,j,k}<0$ or $\rho^W_{i,j,k}<0$), we recalculate the corresponding slopes $(\rho_x)_{i,j,k}$, $(\rho_y)_{i,j,k}$ or $(\rho_z)_{i,j,k}$ using a monotone nonlinear slope limiter, which guarantees that the reconstructed point values are nonnegative as long as the cell averages $\bar\rho_{i,j,k}$ are nonnegative for all i,j,k. In our numerical experiments, we have used the one-parameter family of the generalized minmod limiter [301, 450–453]:

$$(\rho_x)_{i,j,k}=\text{minmod}\Big(\theta\frac{\bar\rho_{i+1,j,k}-\bar\rho_{i,j,k}}{\Delta x},\frac{\bar\rho_{i+1,j,k}-\bar\rho_{i-1,j,k}}{2\Delta x},\theta\frac{\bar\rho_{i,j,k}-\bar\rho_{i-1,j,k}}{\Delta x}\Big) \tag{B.7}$$

and analogously for the other two variables, where the minmod function and its parameters are chosen as in [301].

Given the polynomial reconstruction (B.4) and its point values (B.5), the upwind numerical fluxes in (B.3) are defined as

$$\begin{aligned}
F^x_{i+\frac12,j,k}&=\xi^+_{i+\frac12,j,k}\rho^{E_x}_{i,j,k}+\xi^-_{i+\frac12,j,k}\rho^{W_x}_{i+1,j,k}\\
F^y_{i,j+\frac12,k}&=u^+_{i,j+\frac12,k}\rho^{E_y}_{i,j,k}+u^-_{i,j+\frac12,k}\rho^{W_y}_{i,j+1,k}\\
F^z_{i,j,k+\frac12}&=v^+_{i,j,k+\frac12}\rho^{E_z}_{i,j,k}+v^-_{i,j,k+\frac12}\rho^{W_z}_{i,j,k+1},
\end{aligned} \tag{B.8}$$

where the discrete values $\xi_{i+\frac12,j,k}$, $u_{i,j+\frac12,k}$ and $v_{i,j,k+\frac12}$ of the velocities at midpoints are obtained as follows,

$$\begin{aligned}
\xi_{i+\frac12,j,k}&=-\left(\frac{D}{\Delta x}\log\frac{\bar\rho_{i+1,j,k}}{\bar\rho_{i,j,k}}-\frac{f^x_{i,j,k}+f^x_{i+1,j,k}}{2}-K\Big(\Delta x\Delta y\Delta z\sum_{i,j,k}\mathbf{x}\bar\rho_{i,j,k}-x_{i+\frac12}\Big)\right)\\
u_{i,j+\frac12,k}&=\frac{f^y_{i,j,k}+f^y_{i,j+1,k}}{2},\quad v_{i,j,k+\frac12}=\frac{f^z_{i,j,k}+f^z_{i,j,k+1}}{2},
\end{aligned} \tag{B.9}$$

and the positive and negative parts are denoted by

$$\xi^+_{i+\frac12,j,k}=\max\big(\xi_{i+\frac12,j,k},0\big),\quad \xi^-_{i+\frac12,j,k}=\min\big(\xi_{i+\frac12,j,k},0\big) \tag{B.10}$$

and analogously for the other two variables. We note that $\mathbf{x} = [x_{\frac{1}{2}}, x_{1+\frac{1}{2}}, \ldots, x_{N+\frac{1}{2}}]$ in (B.9) is a row vector of (inter)face values of the cells in the x-direction, and the values $f^x_{i,j,k}$, $f^y_{i,j,k}$, $f^z_{i,j,k}$ are calculated by discretizing (B.11):

$$f^x(x,y,z) := \frac{\alpha}{1+z^n} - x, \quad f^y(x,y,z) := x - y, \quad f^z(x,y,z) := y - z. \tag{B.11}$$

Finally, the semi-discrete scheme (B.3) is integrated using a stable and accurate ODE solver. In all our numerical examples, the third-order strong preserving Runge-Kutta (SSP-RK) ODE solver [454] is used.

Remark 3. The second-order finite volume scheme (B.3),(B.8)–(B.10), reduces to the first-order scheme if the piecewise constant reconstruction is used instead of (B.4), in which case we have $\tilde{\rho}_{i,j,k}(x,y,z) = \bar{\rho}_{i,j,k}$ and therefore

$$\rho^{E_x}_{i,j,k} = \rho^{W_x}_{i,j,k} = \rho^{E_y}_{i,j,k} = \rho^{W_y}_{i,j,k} = \rho^{E_z}_{i,j,k} = \rho^{W_z}_{i,j,k} = \bar{\rho}_{i,j,k}, \quad \forall i,j,k.$$

Remark 4. Given initial data $\rho_0(x) \geq 0$ for system (5.9), the semi-discrete finite-volume scheme (B.3),(B.8)–(B.10) preserves positivity for all $t > 0$. A CFL condition can be computed explicitly using equation (B.3) which is discretized by the forward Euler method. Specifically, the computed cell averages $\bar{\rho}_{i,j,k} \geq 0$, $\forall\, i,j,k$ provided that the following CFL condition is satisfied:

$$\Delta t \leq \min\left\{\frac{\Delta x}{6a}, \frac{\Delta y}{6b}, \frac{\Delta z}{6c}\right\}, \quad \text{where} \quad a = \max_{i,j,k}\left\{\xi^+_{i+\frac{1}{2},j,k}, -\xi^-_{i-\frac{1}{2},j,k}\right\},$$
$$b = \max_{i,j,k}\left\{u^+_{i,j+\frac{1}{2},k}, -u^-_{i,j-\frac{1}{2},k}\right\}, \quad c = \max_{i,j,k}\left\{v^+_{i,j,k+\frac{1}{2}}, -v^-_{i,j,k-\frac{1}{2}}\right\}, \tag{B.12}$$

with $\xi^\pm_{i+\frac{1}{2},j,k}$, $u^\pm_{i,j+\frac{1}{2},k}$ and $v^\pm_{i,j,k+\frac{1}{2}}$ defined in (B.10).

Remark 5. Numerical simulations with GPUs.- The finite volume algorithm for solving the mean-field equation described in Appendix B.3 is computationally very expensive. In fact, when the discretization steps Δx, Δy, and Δz are small, we must also maintain Δt small enough to ensure the algorithm's stability (see 4). The simulations will undoubtedly slow down as a result of this. We were able to mitigate this issue by employing more powerful hardware, specifically graphical processing units (GPUs). Through GPU computing we were able to adopt a more accurate and stable ODE solver, namely the strong stability-preserving Runge-Kutta (SSP-RK) solver of order three [454], thus allowing for three calls per time step at a lower computational cost.

Appendix C

Appendix to Chapter 6

C.1 Parameter estimation

Most parameters for healthy young male and female subjects at rest were obtained from the literature. Physiological parameters that represent physical characteristics, namely blood flow, tissue weights, and arterial substrate concentrations of substrates involved in blood-tissue transport are given in Tables C.1 and C.2. Information on tissue-specific metabolism in a male subject at rest after an overnight fast (8–12h) was gathered from Ref. [68] and references therein: substrate concentrations in each tissue/organ (Table C.3), which are assumed similar between the sexes, with the exception of intramyocellular TG concentration, which is higher in females [321]; rates of O_2 consumption and CO_2 production (Table C.4), which we assumed are similar at rest in females as evidenced in Ref. [16]; intracellular metabolic fluxes and reaction maximal velocities at rest (Table C.5), which we assumed similar between the sexes except for pyruvate reduction (PYR→LAC) and lipolysis (TG→FFA—GLR) which exhibit known sex differences even at rest. The maximal velocities for these reactions were estimated from experimental data and the corresponding fluxes at rest were then calculated using the intracellular substrate concentrations at rest and the corresponding Michaelis-Menten parameters, K_{m}. These K_{m} values are fixed at the initial tissue concentration of the corresponding substrate, unless otherwise indicated in the literature (Table C.6). Blood-tissue transport rates, $Q_x(C_{a,i} - \sigma_{x,i}C_{x,i})$ for each tissue are listed in Table C.7 [68]. Partition coefficients (Table C.8) are calculated from resting transport rates (Tables C.4 and C.7), blood flow, and arterial and tissue concentrations. Under typical physiological conditions, which are far from equilibrium, no whole body steady-state exists. In our models, it is also true that no steady-state exists for all

substrate concentrations in all compartments. In particular, after an overnight fast which corresponds to the resting state in our models, lipolysis in adipose tissue, glycogen degradation in the liver, pyruvate oxidation and FFA oxidation in the other tissues/organs are ongoing to maintain basal metabolism. As a result, TG in adipose tissue and glycogen in the liver continuously decrease at rest.

Parameters pertaining to moderate-intensity (150W or 60% $\dot{V}O_{2max}$) exercise (Tables C.9 and C.10) were then estimated based on experimental studies in humans. The set of experimental data used for parameter estimation is listed in Table C.11. Our calibration approach, as well as the cost function to minimize, are described in the main article (see the Parameter Estimation section). In total, 50 parameters for the female model and 48 for the male model were estimated. 14 of the 49 estimated parameters for the female model were close to male values, so we manually adjusted them to male values, leaving us with 35 distinct estimated parameters for the female model. Without sufficient physiological constraints, the calibration process would produce non-unique estimates due to the large number of unknown parameters. Acknowledging this limitation, we conducted a sensitivity analysis on our models. Result are presented in Section C.4.

Our models consist of systems of nonlinear ordinary differential equations (ODEs) and algebraic equations, which are solved numerically as initial value problems with a stiff solver, *ode15s* in MATLAB2020a. Each model has 154 ODEs (22 substrate ODEs per dynamic compartment, i.e., brain, heart, skeletal muscle, GI tract, liver, and adipose tissue) and 2 additional ODEs for the dynamics of insulin and glucagon. Model equations are described in Table C.13 and Table C.14.

The following subscripts serve as abbreviations for different tissues: brain, $x = B$; heart, $x = H$; skeletal muscle, $x = M$; GI tract, $x = GI$; liver, $x = L$; adipose tissue, $x = A$; others, $x = O$.

C.2 Supplementary results

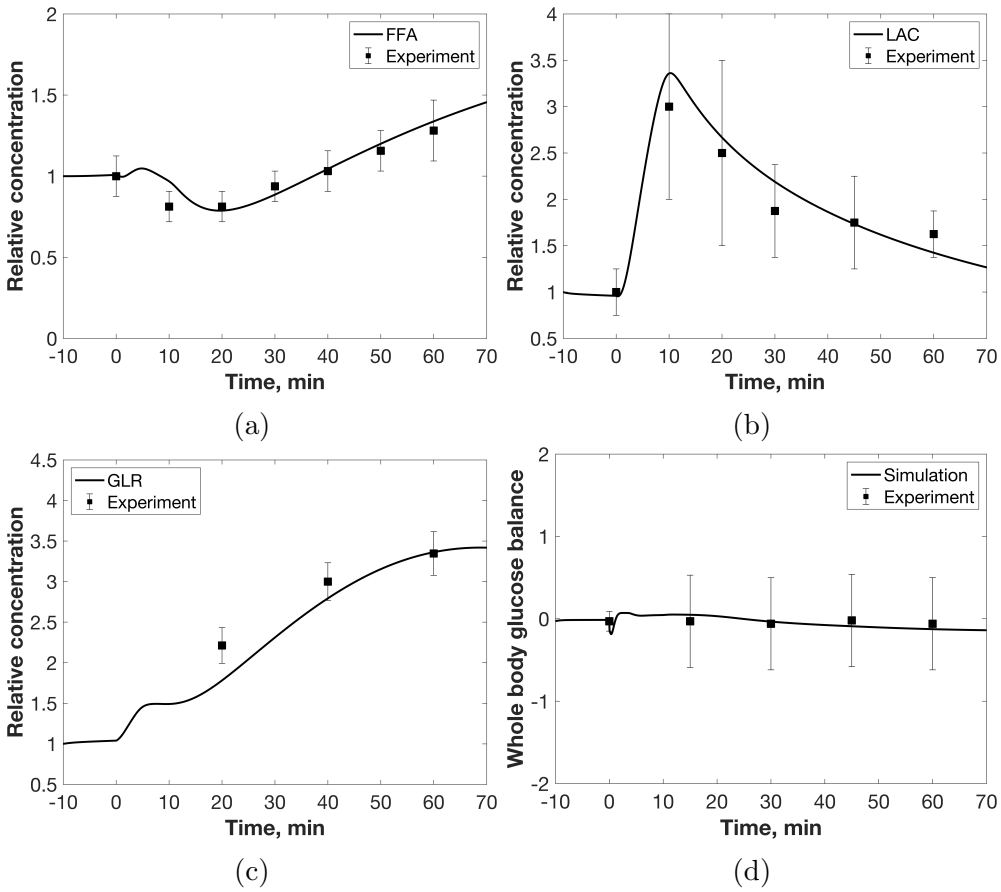

Figure C.1: Female model predictions. Dynamic responses of relative concentrations of arterial (a) FFA, (b) lactate, and (c) glycerol to a step increase in work rate (150W) during 60 min exercise. Relative concentration (unitless) refers to the ratio of the time-dependent arterial concentration of a substrate and its initial condition, $C_a(t)/C_a(0)$. (d) Whole-body glucose balance. Glucose balance refers to the difference between glucose production (R_a) and glucose utilization (R_d).

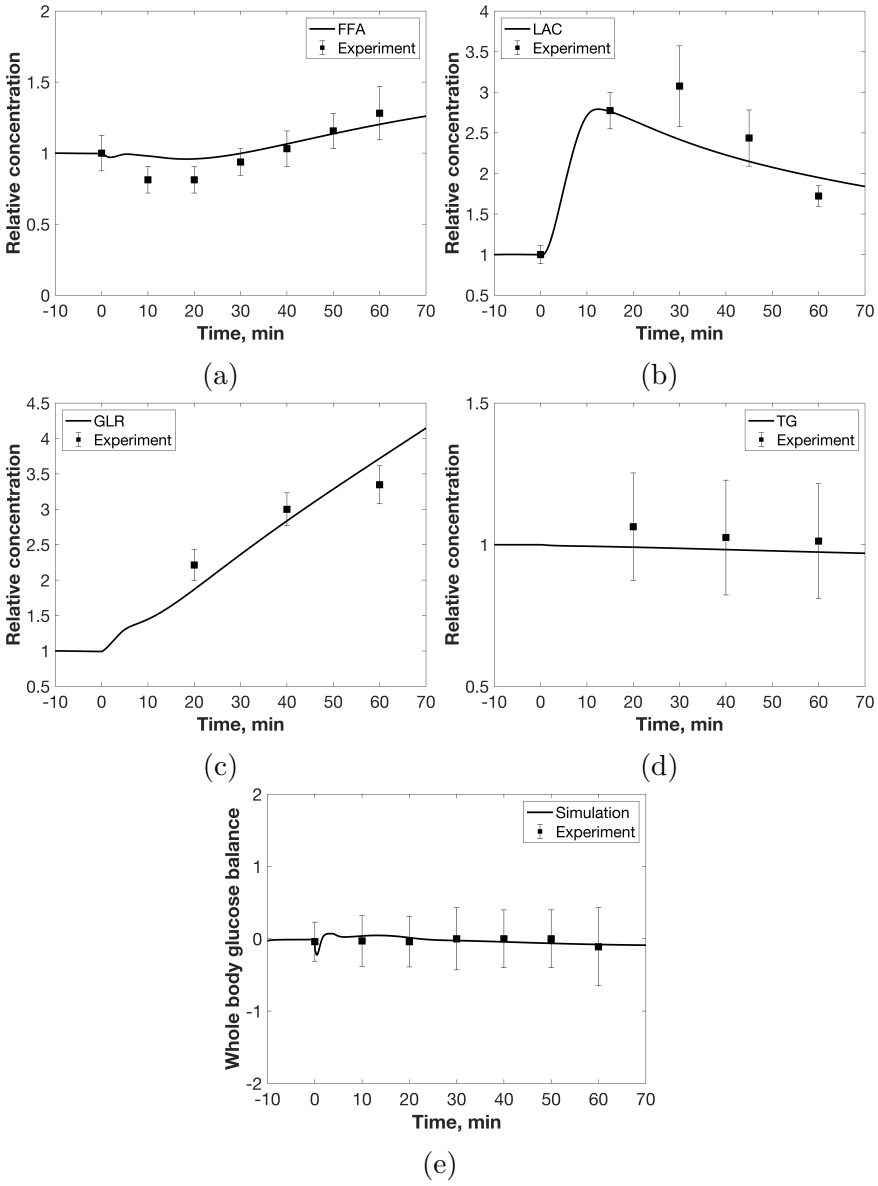

Figure C.2: Male model predictions. Dynamic responses of relative concentrations of arterial (a) FFA, (b) lactate, (c) glycerol, and (d) TG to a step increase in work rate (150W) during 60 min exercise. Relative concentration (unitless) refers to the ratio of the time-dependent arterial concentration of a substrate and its initial condition, $C_a(t)/C_a(0)$. (e) Whole-body glucose balance. Glucose balance refers to the difference between glucose production (R_a) and glucose utilization (R_d).

C.3 Model parameters

Table C.1: Physical characteristics

	Male		Female	
Organ/Tissue	Blood flow (l/min)	Weight (Kg)	Blood flow (l/min)	Weight (Kg)
Brain	0.75[455]	1.4[70, 331]	0.75	1.2[70, 331]
Heart	0.25	0.331[70, 331]	0.25	0.253[70, 331]
Skeletal muscle	0.9[456, 457]	22.4†[70, 331]	0.9	13.6†[70, 331]
GI tract	1.1	2.0[68, 70]	1.1	2.0[68, 70]
Liver	0.4[70, 331]	1.8[70, 331]	0.25[70, 331]	1.4[70, 331]
Adipose tissue	0.36[458]	11*[68, 70, 331]	0.36	17.1**[70, 331]
Others	1.74	31.069	1.39	22.447
Whole body	5.5[337]	70[68, 70, 331]	5.0[70]	58[70, 331]

Subjects are in overnight fasted conditions. Values for "Others" are chosen to balance whole-body values. † Skeletal muscles, excluding upper extremities which account for 18-20% of total weight. Male total: 28 kg; female total: 17 kg. $*$ Based on 16% body fat content. $**$ Based on 29% body fat content. References are given in brackets. Where experimental data is lacking, female values are assumed to be the same as male values.

Organ volumes are calculated by dividing each tissue weight by its density: brain (1.04 Kg/L)[332], heart and skeletal muscle (1.05 Kg/L)[333], GI tract (1.06 Kg/L)[333], liver (1.08 Kg/L)[334], adipose tissue (0.923 Kg/L)[333]. Assuming that *others* include only nonfat tissues, a tissue density of 1.05 Kg/L is used [335]. The total volume of the body is calculated by adding the volumes of all compartments. Tissue volumes are reported in the main article text.

Table C.2: Substrate and hormone concentrations in blood

	Male	Female
Substrate	Arterial concentration (mM)	Arterial concentration (mM)
GLC	5.0	4.91[14]
PYR	0.068	—
LAC	0.7	—
ALA	0.192	—
GLR	0.07	—
FFA	0.66	0.76[14]
TG	0.99	0.93[15]
O_2	8.0	—
CO_2	21.7	—
Hormone	Plasma concentration (pM)	Plasma concentration (pM)
C_E	250	150[8]
C_I	45	60
C_G	27	39 [8]

Values at rest for healthy subjects after an overnight fast. Male values are taken from Ref. [68] and references therein. C_E, C_I, and C_G denote concentrations of epinephrine, insulin, and glucagon, respectively. (—) Same values for male and female models. In brackets are references for significantly different values in females compared to males.

Table C.3: Substrate concentrations in each organ/tissue (mM)

Substrate	Brain	Heart	Skeletal muscle	GI tract	Liver	Adipose Tissue
GLC	1.12	1.0	0.48	1.0	8.0	2.54
PYR	0.15	0.2	0.048	0.2	0.37	0.37
LAC	1.45	3.88	1.44	3.88	0.82	0.82
ALA	0	0	1.3	0	0.23	0
GLR	0	0.015	0.064	0.015	0.07	0.22
FFA	0	0.021	0.53	0.021	0.57	0.57
TG	0	3.12	**14.8/18.94**†	450	2.93	**990***
O_2	0.027	0.96	0.49	0.49	0.027	0.027
CO_2	15.43	20.0	15.43	15.43	15.43	15.43
G6P	0.16	0.17	0.24	0.17	0.2	0.2
GLY	2.0	33.0	**95.0***	33.0	**417***	0
GAP	0.15	0.01	0.08	0.01	0.11	0.11
GRP	0	0.29	0.15	0.29	0.24	0.24
ACoA	0.0068**	0.0012	0.0022	0.0012	0.035	0.035
CoA	0.06	0.012	0.018	0.012	0.14	0.14
NAD^{+}	0.064	0.40	0.45	0.4	0.45	0.45
NADH	0.026	0.045	0.05	0.045	0.05	0.05
ATP	2.45	3.4	6.15	3.4	2.74	2.74
ADP	0.54	0.02	0.02	0.02	1.22	1.22
Pi	2.4	1.66	2.70	1.66	4.6	4.6
PCR	4.6	8.3	20.1	8.3	0	0
CR	5.6	3.5	10.45	3.5	0	0

Values at rest after an overnight fast taken from Ref. [68] and references therein. When two values are listed, they correspond to male/female, otherwise there is no sex difference in substrate concentrations. $*$ For most substrates (excluding null concentrations), sex differences in tissue weights, hence tissue volumes, lead to sex differences in substrate content in each tissue. For example, absolute GLY content is higher in male liver and skeletal muscle, and absolute TG content is higher in female adipose tissue. In addition, women have a higher concentration of intramyocellular lipid (IMCL), despite having a smaller tissue volume. † Women have a 28% higher area density compared to men. IMCL area density (%)= # IMCL/area×mean IMCL size×100% [321]. This result is directly proportional to the lipid concentration per unit volume (mM). $**$ Data from Ref. [459].

Table C.4: Resting values of O_2 consumption and CO_2 production

Organ/Tissue	$\dot{V}O_2$ (ml/min)	$\dot{V}CO_2$ (ml/min)
Brain	51.07	51.07
Heart	26.80	20.61
Skeletal muscle	41.04	32.01
GI tract	10.21	10.21
Liver	62.72	43.72
Adipose tissue	10.08	7.17
Others	48.08	35.21
Whole body	250	200

Subjects are at rest after an overnight fast. Whole-body respiratory quotient (RQ) at rest is 0.8 in female and male models. RQ= $\dot{V}CO_2/\dot{V}O_2$, where $\dot{V}O_2$ and $\dot{V}CO_2$ are oxygen consumption and carbon dioxide production rates. Values for "Others" are chosen to balance whole-body values. Data are taken from Ref. [68] for male. We assumed RQ values are the same at rest in females and males according to Ref. [16].

Table C.5: Organ/tissue metabolic fluxes, $\phi_{X\to Y}$(mmol/min) and reaction maximal velocities, $V_{X\to Y}$ (mmol/min)

	Brain		Heart		Skeletal muscle		GI tract		Liver		Adipose tissue	
Fluxes	$\phi_{X\to Y}$	$V^0_{X\to Y}$	$\phi_{X\to Y}$	$V^0_{X\to Y}$	$\phi_{X\to Y}$	$V^0_{X\to Y}$	$\phi_{X\to Y}$	$V^0_{X\to Y}$	$\phi_{X\to Y}$	$V^0_{X\to Y}$	$\phi_{X\to Y}$	$V^0_{X\to Y}$
$\phi_{GLC\to G6P}$	0.38	0.79	0.04	0.088	0.165	0.398	0.076	0.167	0.17	0.765	0.038	0.079
$\phi_{G6P\to GAP}$	0.38	1.52	0.04	0.16	0.165	0.66	0.076	0.304	0.17	0.68	0.038	0.152
$\phi_{GAP\to PYR}$	0.76	12.16	0.08	1.28	0.33	5.28	0.152	2.432	0.34	5.44	0.056	0.896
$\phi_{PYR\to GAP}$	0	0	0	0	0	0	0	0	0.93	7.44	0	0
$\phi_{GAP\to G6P}$	0	0	0	0	0	0	0	0	1.04	2.08	0	0
$\phi_{G6P\to GLC}$	0	0	0	0	0	0	0	0	0.9	1.8	0	0
$\phi_{G6P\to GLY}$	0.003	0.012	0.04	0.16	0.125	0.5	0	0	0.1	0.4	0	0
$\phi_{GLY\to G6P}$	0.003	0.024	0.04	0.32	0.125	1.0	0	0	0.48	3.84	0	0
$\phi_{PYR\to LAC}$	0.7	2.8	0.088	0.352	1.0/**0.85**†	14.85/**12.62**†	0.2	0.8	0.21	0.84	0.036	0.144
$\phi_{LAC\to PYR}$	0.7	2.8	0.128	0.512	0.488*	12.51	0.2	0.8	0.48	1.92	0.01	0.04
$\phi_{GLR\to GRP}$	0	0	0.004	0.016	0.127	0.508	0	0	0.144	0.576	0	0
$\phi_{GAP\to GRP}$	0	0	0	0	0	0	0	0	0	0	0.02	0.08
$\phi_{GRP\to GAP}$	0	0	0	0	0	0	0	0	0.111	0.444	0	0
$\phi_{PYR\to ALA}$	0	0	0	0	0.04	0.08	0	0	0	0	0	0
$\phi_{ALA\to PYR}$	0	0	0	0	0	0	0	0	0.32	0.64	0	0
$\phi_{PYR\to ACoA}$	0.76	6.08	0.12	0.96	0.292*	2.745	0.152	1.216	0.0013*	0.01*	0.03	0.24
$\phi_{FFA\to ACoA}$	0	0	0.035	0.28	0.088*	0.701	0	0	0.136	1.088	0.02*	0.16
$\phi_{ACoA\to FFA}$	0	0	0	0	0	0	0	0	0.112	0.896	0	0
$\phi_{TG\to FFA—GLR}$	0	0	0.004	0.008	0.13	0.26	0.04	0.08	0.004	0.008	0.095*/**0.114**†	0.19/**0.228**†
$\phi_{FFA—GRP\to TG}$	0	0	0.012	0.096	0.381	3.048	0	0	0.1	0.8	0.06	0.48
$\phi_{ACoA\to CO_2}$	0.76	12.16	0.4	6.4	0.623	9.968	0.152	2.432	0.976	15.62	0.08	1.28
$\phi_{O_2\to H_2O}$	2.28	18.71	1.165	9.327	1.832	14.68	0.456	3.653	2.702	22.18	0.25	2.05
$\phi_{PCR\to CR}$	1.86	7.44	2.0	8.0	20.0	80.0	2.0	8.0	0	0	0	0
$\phi_{CR\to PCR}$	1.86	7.44	2.0	8.0	20.0	80.0	2.0	8.0	0	0	0	0
$\phi_{ATP\to ADP}$	15.20	30.4	7.33	14.66	10.82	21.64	3.04	6.08	13.92	27.84	2.74	5.47

Values at rest after an overnight fast taken from Ref. [68]. When two values are listed, they correspond to male/female, otherwise we assumed no sex difference. $*$ Assumed fluxes under resting conditions. † Estimated female values based on experimental data;

Table C.6: Distinctive Michaelis-Menten parameters

Fluxes	K_M	Brain	Heart	Skeletal muscle	GI tract	Liver	Adipose tissue
$\phi_{GLC\to G6P}$	K_{GLC}	0.05	0.1	0.1	0.1	10.0	0.1
$\phi_{PYR\to LAC}$†	K_{PYR}			0.6			
$\phi_{LAC\to PYR}$	K_{LAC}			17.0			
$\phi_{PYR\to ACoA}$	K_{PYR}			0.065			
$\phi_{O_2\to H_2O}$	K_{O_2}	0.7	0.7	0.7	0.7	0.7	0.7

Values taken from Ref. [68] and references therein. All values are in mM, except for K_{O_2} values which are in μM. † Specifically for this flux, ν^+ or $K_{\frac{NADH}{NAD^+}} = 0.011$ mM. We assumed no sex difference.

Table C.7: Blood-tissue transport rates (mmol/min) in each tissue/organ

Organ/Tissue	GLC	PYR	LAC	ALA	GLR	FFA	TG
Brain	0.380	0	0	0	0	0	0
Heart	0.040	0	0.040	0	0	0.035	0
Skeletal muscle	0.165	0.005/0.003	-0.112/-0.095	-0.040	-0.003	0.046	0.003
GI tract	0.076	0	0	0	-0.040	-0.120	0.006
Liver	-0.731	0	0.270	0.320	0.140	0.210	-0.029
Adipose tissue	0.038	0	0.056	0	-0.097	-0.211	0.02
Others	0.062	-0.005/-0.003	-0.142/-0.271	-0.280	0	0.040	0
Sum	0.03	0	0	0	0	0	0

Values at rest after an overnight fast taken from Ref. [68] and references therein. These values correspond to the term $Q_x\big(C_a - \sigma_{x,i}C_{x,i}\big)$ in Eq (1) in the main article text. Positive values represent substrate uptake into tissue/organs, while negative values represent substrate release into the circulation. Values in "others" are chosen to yield a zero balance at rest. The net sum of 0.03 for glucose indicates that organs consume glucose for energy even when at rest, i.e., blood glucose levels gradually decrease following an overnight fast. When two values are listed, they correspond to male/female, otherwise we assumed no sex difference.

Table C.8: Blood-tissue transport partition coefficients (dimensionless)

Substrate	Brain	Heart	Skeletal muscle	GI tract	Liver	Adipose tissue
Male						
GLC	4.0119	4.84	10.0347	4.931	0.6796	1.9269
PYR	0.4533	0.34	1.3009	0.34	0.1838	0.1838
LAC	0.4828	0.1392	0.5725	0.1804	0.6341	1.0434
ALA	0	0	0.1819	0	-0.10	0
GLR	0	4.6667	1.1458	7.0909	0.0481	1.5429
FFA	0	24.762	1.1488	36.623	1.0526	2.1861
TG	0	0.3173	0.06667	2.187e-3	0.3430	
O_2	183.704	3.3483	12.1723	15.481	215.90	249.976
CO_2	1.6034	1.269	1.5092	1.4332	1.5104	1.4640
Female						
GLC	3.9315	4.75	9.8472	4.841	0.6744	1.8915
PYR	—	—	1.3530	—	—	—
LAC	—	—	0.5596	—	0.6098	—
ALA	0	0	—	0	-0.1958	0
GLR	0	—	—	—	-0.015	—
FFA	0	29.524	1.3375	41.385	1.2164	2.3616
TG	0	0.2981	0.0489	2.0545e-3	0.3232	8.8328e-4
O_2	—	—	—	—	206.97	—
CO_2	—	—	—	—	1.5219	1.4560

A value of zero indicates no substrate uptake or release. (—) Same values for male and female models.

Table C.9: Estimated hormonal control parameters I

Parameter	Male	Female	Unit
A. Epinephrine			
ω(WR)	1100	330	pM
τ_E	30	—	min
B. Insulin and glucagon			
$h^\dagger$	0.1333	—	min^{-1}
k_1	0.2757	0.3360	$\text{pM}^{-1}\text{min}^{-1}$
k_2	0.0270	0.020	$\text{pM}^{-1}\text{min}^{-1}$
k_3	0.20	0.0070	$\text{pM}^{-1}\text{min}^{-1}$
k_4	0.10	2.6740	$\text{pM}^{-1}\text{min}^{-1}$
k_5	0.0012	0.30	$\text{pM}^{-1}\text{min}^{-1}$
$D^\dagger$	0.10	—	min^{-1}
C. Blood flow regulation			
γ_M	2.930	2.850	$\text{mmol} \cdot \text{min}^{-1}\text{W}^{-1}$
γ_H	0.1	—	$\text{mmol} \cdot \text{min}^{-1}\text{W}^{-1}$
δ_{H}	0.75	—	$l \cdot \text{min}^{-1}$
δ_{M}	7.6210	7.6590	$l \cdot \text{min}^{-1}$
δ_{GI}	-0.2231	-0.2144	$l \cdot \text{min}^{-1}$
τ_Q	0.1	—	min
τ_{Q_M}	2.0	—	min

† Decay rate D is set to 0.1, then h is calculated assuming steady state conditions with a blood glucose level of 5 mM [338]. (—) Same values for male and female models. The subscripts H, M, and GI stand for heart, skeletal muscle, and GI tract, respectively.

Table C.10: Estimated hormonal control parameters II: λ_i (dimensionless) and α_i (pM)

Flux	Parameter	Heart	Skeletal muscle	GI tract	Liver	Adipose tissue
D. Epinephrine-regulated						
$\phi_{\text{GLC}\to\text{G6P}}$	$\lambda_{\text{GLC}\to\text{G6P}}$	4.0 / 12.3	23.3 / 93.15			
	$\alpha_{\text{GLC}\to\text{G6P}}$	1100^2 / 1200^2	1200^2 / 1100^2			
$\phi_{\text{GLY}\to\text{G6P}}$	$\lambda_{\text{GLY}\to\text{G6P}}$		0.014			
	$\alpha_{\text{GLY}\to\text{G6P}}$		1705			
$\phi_{\text{PYR}\to\text{ALA}}$	$\lambda_{\text{PYR}\to\text{ALA}}$		2.2			
	$\alpha_{\text{PYR}\to\text{ALA}}$		1000^2			
$\phi_{\text{FFA}\to\text{ACoA}}$	$\lambda_{\text{FFA}\to\text{ACoA}}$	1.2 / 6.06	5.0 / 8.0			
	$\alpha_{\text{FFA}\to\text{ACoA}}$	1100^2	912			
$\phi_{\text{TG}\to\text{FFA—GLR}}$	$\lambda_{\text{TG}\to\text{FFA—GLR}}$	0.66 / 0.53	2.3 / 2.0	2.0		0.58 / 1.0
	$\alpha_{\text{TG}\to\text{FFA—GLR}}$	1200^2 / 1000^2	$198e3$	1470^2 / 1200^2		1100^2 / 900^2
E. GIR-regulated						
$\phi_{\text{PYR}\to\text{GAP}}$	$\lambda_{\text{PYR}\to\text{GAP}}$				2.0 / 0.2	
	$\alpha_{\text{PYR}\to\text{GAP}}$				0.06 / 0.4	
$\phi_{\text{GAP}\to\text{G6P}}$	$\lambda_{\text{GAP}\to\text{G6P}}$				0.6 / 0.014	
	$\alpha_{\text{GAP}\to\text{G6P}}$				0.1 / 0.4	
$\phi_{\text{G6P}\to\text{GLC}}$	$\lambda_{\text{G6P}\to\text{GLC}}$				1.0 / 0.04	
	$\alpha_{\text{G6P}\to\text{GLC}}$				0.02 /0.2	
$\phi_{\text{GLY}\to\text{G6P}}$	$\lambda_{\text{GLY}\to\text{G6P}}$				3.0 / 1.285	
	$\alpha_{\text{GLY}\to\text{G6P}}$				0.05 / 0.11	
$\phi_{\text{ALA}\to\text{PYR}}$	$\lambda_{\text{ALA}\to\text{PYR}}$				1.45	
	$\alpha_{\text{ALA}\to\text{PYR}}$				0.01 / 0.06	
$\phi_{\text{TG}\to\text{FFA—GLR}}$	$\lambda_{\text{TG}\to\text{FFA—GLR}}$			2.0 / 4.0		0.28 / 3.0
	$\alpha_{\text{TG}\to\text{FFA—GLR}}$			0.08		0.8 / 0.01

When two values are listed, they correspond to male/female, otherwise there is no sex difference.

Table C.11: Experimental data used for parameter estimation and model validation

Study	Subjects' characteristics			Exercise parameters		Observables		
	Sex	Age	BW	Duration	$\%VO_{2max}$	Hormones	Substrates	Others
Hirsch et al. [7]	13M	22–28	66–85	60	60	EPI GLU INS†	GLC FFA†	R_a R_d
Van Hall et al. [460]	6M	22–28	73–86	60	60		GLR† TG	
Bergamn et al. [461]	7M	21–23	69–82	120	59		LAC	
Roepstorff et al. [16]	7M	25–27	73–77	90	58			RER
	7F	24–26	63–69	90	58			RER
Horton et al. [8]	10F	28–40	49–65	90	51	EPI GLU	LAC GLC	R_a R_d
Horton et al. [341]	13F	24–34	53–67	90	50	EPI		
Campbell et al. [360]	8F	22–26	59–63	120	70		GLC	

Sex is male (M) or female (F); Age is in years; Body Weight (BW) is in Kg; Duration is the exercise duration in minutes. ‡ refers to plasma concentration; † Data used to calibrate female model since substrate concentrations and dynamics do not differ between the sexes during exercise [8, 16]. EPI: epinephrine; GLC: glucose, GLU: glucagon, GLR: glycerol; INS: insulin, LAC: lactate, TG: triglyceride, FFA: free fatty acids; RER: respiratory exchange ratio; R_a: rate of appearance of glucose; R_d: rate of disappearance of glucose.

C.4 Sensitivity analysis

In the following, we present results of a local sensitivity analysis of the male and female models. We considered all 50 estimated parameters for the female model, and all 48 estimated parameters for the male model. Local analysis is based on calculating the influence of small perturbations around a nominal parameter value on model output. Often, the perturbation is applied to one parameter at a time, resulting in an approximation of the first-order partial derivative of the model output with respect to the perturbed parameter [462]. Aside from being numerically efficient, sensitivity coefficients obtained from local deterministic sensitivity analysis have the advantage of being intuitive in their interpretation, regardless of the method used.

For each parameter p_j, we calculated relative sensitivities using a forward difference approximation:

$$S_{ij}(t) \approx \frac{p_j}{y_i(p_j, t)} \cdot \frac{y_i(p_j + \Delta p_j, t) - y_i(p_j, t)}{\Delta p_j}, \tag{C.1}$$

where S_{ij} is the first-order local sensitivity coefficient of parameter p_j on model output y_i at time t. We used Δp_j of 10% either up or down, and $t = 60$ minutes, which corresponded to the end of the exercise session. We decided to focus our analysis on the ten model outputs most relevant to our main text results. Specifically, arterial concentrations of glucose, lactate, glycerol, and FFA, GIR, gluconeogenesis and glycogenolysis in the liver, glycogenolysis and TG breakdown in the muscle, and whole-body lipolysis. Results are shown in Figures C.3 and C.4. The ten most influential parameters in the female model, whether perturbed up or down, are parameters 2,5,10,11,19,20,27,39,43, and 49 (see Table C.12). For the male model, the most influential parameters are 2,5,7,8,10,11,19,20,27, and 39 (see Table C.12). These results imply that parameters related to blood flow, glycolysis, and lipolysis in skeletal muscle, glycogenolysis in the liver, and lipolysis in adipose tissue have the greatest influence on model outputs. This is to be expected, as these parameters help to tightly regulate glucose homeostasis during exercise. Most other parameters have little effect on the outputs of interest, with sensitivities ranging between -0.25 and $+0.25$ (Figures C.3 and C.4). Overall, the results of this sensitivity analysis, when combined with our calibration approach, show that model output variables are robust to uncertainty in most parameters related to exercise.

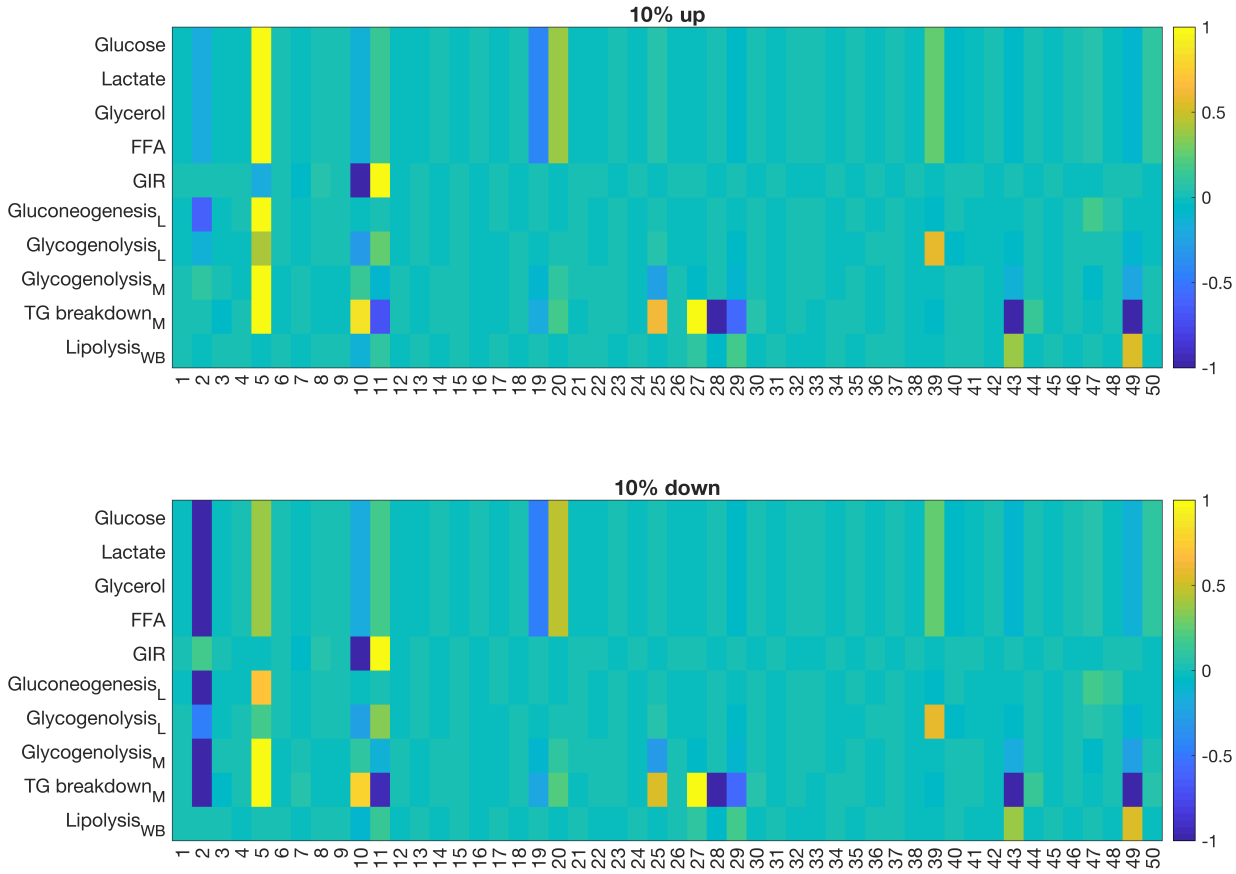

Figure C.3: Local sensitivity results for the female model. Sensitivity coefficients are scaled to between -1 and 1. The subscripts L, M, and WB indicate the liver, skeletal muscle, and whole-body, respectively. Each index $j = \{1, 2, 3, \ldots, 50\}$ represents one of the 50 perturbed parameters. Table C.12 shows a one-to-one correspondence between indices and parameters.

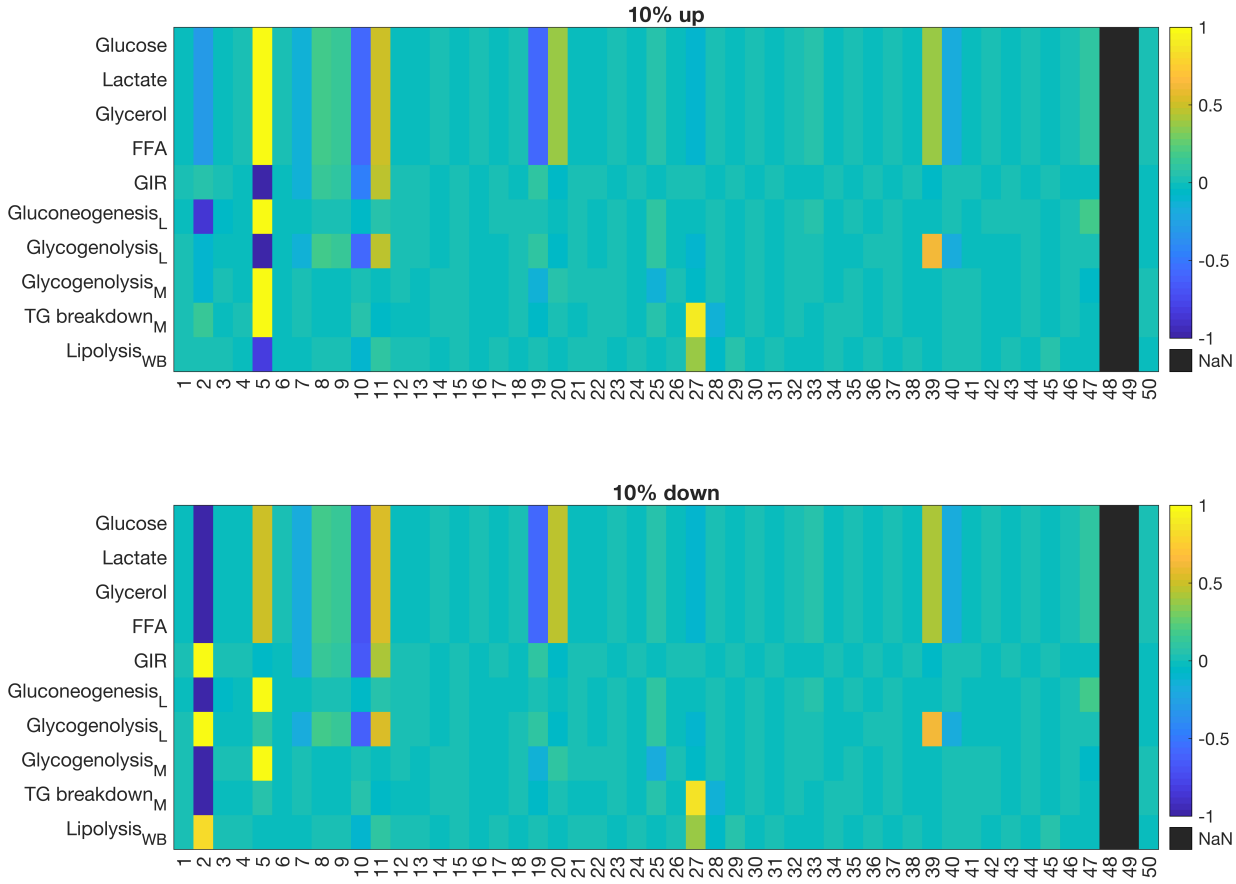

Figure C.4: Local sensitivity results for the male model. Sensitivity coefficients are scaled to between -1 and 1. The subscripts L, M, and WB indicate the liver, skeletal muscle, and whole-body, respectively. The dark boxes, denoted "NaN", represent two parameters obtained from the literature for the male model, but estimated in the female model. These parameters were not varied in the analysis, but are represented in the matrix to keep the same parameter numbering as that presented in the female case above. Each index $j = \{1, 2, 3, \ldots, 50\}$ represents one of 50 parameters. Table C.12 shows a one-to-one correspondence between indices and parameters.

Table C.12: Ordered list of estimated parameters as presented in the sensitivity analysis results.

j	Parameter	j	Parameter	j	Parameter
1	δ_H	18	$\alpha^E_{H,\text{TG}\to\text{FFA–GLR}}$	35	$\lambda^G_{L,\text{GAP}\to\text{G6P}}$
2	δ_M	19	$\lambda^E_{M,\text{GLC}\to\text{G6P}}$	36	$\alpha^G_{L,\text{GAP}\to\text{G6P}}$
3	δ_{GI}	20	$\alpha^E_{M,\text{GLC}\to\text{G6P}}$	37	$\lambda^G_{L,\text{G6P}\to\text{GLC}}$
4	τ_Q	21	$\lambda^E_{M,\text{GLY}\to\text{G6P}}$	38	$\alpha^G_{L,\text{G6P}\to\text{GLC}}$
5	γ_M	22	$\alpha^E_{M,\text{GLY}\to\text{G6P}}$	39	$\lambda^G_{L,\text{GLY}\to\text{G6P}}$
6	h	23	$\lambda^E_{M,\text{PYR}\to\text{ALA}}$	40	$\alpha^G_{L,\text{GLY}\to\text{G6P}}$
7	k_1	24	$\alpha^E_{M,\text{PYR}\to\text{ALA}}$	41	$\lambda^G_{L,\text{ALA}\to\text{PYR}}$
8	k_2	25	$\lambda^E_{M,\text{FFA}\to\text{ACoA}}$	42	$\alpha^G_{L,\text{ALA}\to\text{PYR}}$
9	k_3	26	$\alpha^E_{M,\text{FFA–ACoA}}$	43	$\lambda^G_{A,\text{TG}\to\text{FFA–GLR}}$
10	k_4	27	$\lambda^E_{M,\text{TG}\to\text{FFA–GLR}}$	44	$\alpha^G_{A,\text{TG}\to\text{FFA–GLR}}$
11	k_5	28	$\alpha^E_{M,\text{TG}\to\text{FFA–GLR}}$	45	$\lambda^E_{A,\text{TG}\to\text{FFA–GLR}}$
12	D	29	$\lambda^G_{GI,\text{TG}\to\text{FFA–GLR}}$	46	$\alpha^E_{A,\text{TG}\to\text{FFA–GLR}}$
13	$\lambda^E_{H,\text{GLC}\to\text{G6P}}$	30	$\alpha^G_{GI,\text{TG}\to\text{FFA–GLR}}$	47	$\tau^\dagger_{Q_M}$
14	$\alpha^E_{H,\text{GLC}\to\text{G6P}}$	31	$\lambda^E_{GI,\text{TG}\to\text{FFA–GLR}}$	48	$V^\ddagger_{\text{max},M,\text{PYR}\to\text{LAC}}$
15	$\lambda^E_{H,\text{FFA}\to\text{ACoA}}$	32	$\alpha^E_{GI,\text{TG}\to\text{FFA–GLR}}$	49	$V^\ddagger_{\text{max},A,\text{TG}\to\text{FFA–GLR}}$
16	$\alpha^E_{H,\text{FFA–ACoA}}$	33	$\lambda^G_{L,\text{PYR}\to\text{GAP}}$	50	γ_H
17	$\lambda^E_{H,\text{TG}\to\text{FFA–GLR}}$	34	$\alpha^G_{L,\text{PYR}\to\text{GAP}}$		

† This parameter, specific to skeletal muscle, represents the time constant for blood flow regulation; see Eq (6.17) in the main text.
‡ Parameters estimated only in the female model.

C.5 Model equations

Table C.13: Dynamic mass balance equation in tissue/organ x

1. GLC	$\mathrm{V}_{x,\mathrm{GLC}}\frac{\mathrm{dC}_{x,\mathrm{GLC}}}{dt} = \phi_{x,\mathrm{G6P}\to\mathrm{GLC}} - \phi_{x,\mathrm{GLC}\to\mathrm{G6P}} + Q_x(\mathrm{C}_{a,\mathrm{GLC}} - \sigma_{x,\mathrm{GLC}}\mathrm{C}_{x,\mathrm{GLC}})$
2. PYR	$\mathrm{V}_{x,\mathrm{PYR}}\frac{\mathrm{dC}_{x,\mathrm{PYR}}}{dt} = \phi_{x,\mathrm{GAP}\to\mathrm{PYR}} + \phi_{x,\mathrm{LAC}\to\mathrm{PYR}} + \phi_{x,\mathrm{ALA}\to\mathrm{PYR}} - \phi_{x,\mathrm{PYR}\to\mathrm{GAP}} - \phi_{x,\mathrm{PYR}\to\mathrm{LAC}} - \phi_{x,\mathrm{PYR}\to\mathrm{ALA}} - \phi_{x,\mathrm{PYR}\to\mathrm{ACoA}} + Q_x(\mathrm{C}_{a,\mathrm{PYR}} - \sigma_{x,\mathrm{PYR}}\mathrm{C}_{x,\mathrm{PYR}})$
3. LAC	$\mathrm{V}_{x,\mathrm{LAC}}\frac{\mathrm{dC}_{x,\mathrm{LAC}}}{dt} = \phi_{x,\mathrm{PYR}\to\mathrm{LAC}} - \phi_{x,\mathrm{LAC}\to\mathrm{PYR}} + Q_x(\mathrm{C}_{a,\mathrm{LAC}} - \sigma_{x,\mathrm{LAC}}\mathrm{C}_{x,\mathrm{LAC}})$
4. ALA	$\mathrm{V}_{x,\mathrm{ALA}}\frac{\mathrm{dC}_{x,\mathrm{ALA}}}{dt} = \phi_{x,\mathrm{PYR}\to\mathrm{ALA}} - \phi_{x,\mathrm{ALA}\to\mathrm{PYR}} + Q_x(\mathrm{C}_{a,\mathrm{ALA}} - \sigma_{x,\mathrm{ALA}}\mathrm{C}_{x,\mathrm{ALA}})$
5. GLR	$\mathrm{V}_{x,\mathrm{GLR}}\frac{\mathrm{dC}_{x,\mathrm{GLR}}}{dt} = \phi_{x,\mathrm{TG}\to\mathrm{FFA—GLR}} - \phi_{x,\mathrm{GLR}\to\mathrm{GRP}} + Q_x(\mathrm{C}_{a,\mathrm{GLR}} - \sigma_{x,\mathrm{GLR}}\mathrm{C}_{x,\mathrm{GLR}})$
6. FFA	$\mathrm{V}_{x,\mathrm{FFA}}\frac{\mathrm{dC}_{x,\mathrm{FFA}}}{dt} = 3\phi_{x,\mathrm{TG}\to\mathrm{FFA—GLR}} + \frac{1}{8}\phi_{x,\mathrm{ACoA}\to\mathrm{FFA}} - \phi_{x,\mathrm{FFA—GRP}\to\mathrm{TG}} - \phi_{x,\mathrm{FFA}\to\mathrm{ACoA}} + Q_x(\mathrm{C}_{a,\mathrm{FFA}} - \sigma_{x,\mathrm{FFA}}\mathrm{C}_{x,\mathrm{FFA}})$
7. TG	$\mathrm{V}_{x,\mathrm{TG}}\frac{\mathrm{dC}_{x,\mathrm{TG}}}{dt} = \frac{1}{3}\phi_{x,\mathrm{FFA—GRP}\to\mathrm{TG}} - \phi_{x,\mathrm{TG}\to\mathrm{FFA—GLR}} + Q_x(\mathrm{C}_{a,\mathrm{TG}} - \sigma_{x,\mathrm{TG}}\mathrm{C}_{x,\mathrm{TG}})$
8. O_2	$\mathrm{V}_{x,\mathrm{O_2}}\frac{\mathrm{dC}_{x,\mathrm{O_2}}}{dt} = -\phi_{x,\mathrm{O_2}\to\mathrm{H_2O}} + Q_x(\mathrm{C}_{a,\mathrm{O_2}} - \sigma_{x,\mathrm{O_2}}\mathrm{C}_{x,\mathrm{O_2}})$
9. CO_2	$\mathrm{V}_{x,\mathrm{CO_2}}\frac{\mathrm{dC}_{x,\mathrm{CO_2}}}{dt} = \phi_{x,\mathrm{PYR}\to\mathrm{ACoA}} + 2\phi_{x,\mathrm{ACoA}\to\mathrm{CO_2}} + Q_x(\mathrm{C}_{a,\mathrm{CO_2}} - \sigma_{x,\mathrm{CO_2}}\mathrm{C}_{x,\mathrm{CO_2}})$
10. G6P	$\mathrm{V}_{x,\mathrm{G6P}}\frac{\mathrm{dC}_{x,\mathrm{G6P}}}{dt} = \phi_{x,\mathrm{GLC}\to\mathrm{G6P}} + \frac{1}{2}\phi_{x,\mathrm{GAP}\to\mathrm{G6P}} + \phi_{x,\mathrm{GLY}\to\mathrm{G6P}} - \phi_{x,\mathrm{G6P}\to\mathrm{GLC}} - \phi_{x,\mathrm{G6P}\to\mathrm{GAP}} - \phi_{x,\mathrm{G6P}\to\mathrm{GLY}}$
11. GLY	$\mathrm{V}_{x,\mathrm{GLY}}\frac{\mathrm{dC}_{x,\mathrm{GLY}}}{dt} = \phi_{x,\mathrm{G6P}\to\mathrm{GLY}} - \phi_{x,\mathrm{GLY}\to\mathrm{G6P}}$
12. GAP	$\mathrm{V}_{x,\mathrm{GAP}}\frac{\mathrm{dC}_{x,\mathrm{GAP}}}{dt} = 2\phi_{x,\mathrm{G6P}\to\mathrm{GAP}} + \phi_{x,\mathrm{PYR}\to\mathrm{GAP}} + \phi_{x,\mathrm{GRP}\to\mathrm{GAP}} - \phi_{x,\mathrm{GAP}\to\mathrm{G6P}} - \phi_{x,\mathrm{GAP}\to\mathrm{PYR}} - \phi_{x,\mathrm{GAP}\to\mathrm{GRP}}$
13. GRP	$\mathrm{V}_{x,\mathrm{GRP}}\frac{\mathrm{dC}_{x,\mathrm{GRP}}}{dt} = \phi_{x,\mathrm{GLR}\to\mathrm{GRP}} + \phi_{x,\mathrm{GAP}\to\mathrm{GRP}} - \phi_{x,\mathrm{GRP}\to\mathrm{GAP}} - \frac{1}{3}\phi_{x,\mathrm{FFA—GRP}\to\mathrm{TG}}$
14. ACoA	$\mathrm{V}_{x,\mathrm{ACoA}}\frac{\mathrm{dC}_{x,\mathrm{ACoA}}}{dt} = \phi_{x,\mathrm{PYR}\to\mathrm{ACoA}} + 8\phi_{x,\mathrm{FFA}\to\mathrm{ACoA}} - \phi_{x,\mathrm{ACoA}\to\mathrm{FFA}} - \phi_{x,\mathrm{ACoA}\to\mathrm{CO_2}}$
15. CoA	$\mathrm{V}_{x,\mathrm{CoA}}\frac{\mathrm{dC}_{x,\mathrm{CoA}}}{dt} = \phi_{x,\mathrm{ACoA}\to\mathrm{FFA}} + \phi_{x,\mathrm{ACoA}\to\mathrm{CO_2}} - \phi_{x,\mathrm{PYR}\to\mathrm{ACoA}} - 8\phi_{x,\mathrm{FFA}\to\mathrm{ACoA}}$
16. NAD^+	$\mathrm{V}_{x,\mathrm{NAD^+}}\frac{\mathrm{dC}_{x,\mathrm{NAD+}}}{dt} = \begin{array}{l}\phi_{x,\mathrm{PYR}\to\mathrm{GAP}} + \phi_{x,\mathrm{PYR}\to\mathrm{LAC}} + \phi_{x,\mathrm{GAP}\to\mathrm{GRP}} + \frac{14}{8}\phi_{x,\mathrm{ACoA}\to\mathrm{FFA}} + 2\phi_{x,\mathrm{O_2}\to\mathrm{H_2O}} \\ -\phi_{x,\mathrm{GAP}\to\mathrm{PYR}} - \phi_{x,\mathrm{LAC}\to\mathrm{PYR}} - \phi_{x,\mathrm{GRP}\to\mathrm{GAP}} - \phi_{x,\mathrm{PYR}\to\mathrm{ACoA}} - 14\phi_{x,\mathrm{FFA}\to\mathrm{ACoA}} - 4\phi_{x,\mathrm{ACoA}\to\mathrm{CO_2}}\end{array}$
17. NADH	$\mathrm{V}_{x,\mathrm{NADH}}\frac{\mathrm{dC}_{x,\mathrm{NADH}}}{dt} = \begin{array}{l}\phi_{x,\mathrm{GAP}\to\mathrm{PYR}} + \phi_{x,\mathrm{LAC}\to\mathrm{PYR}} + \phi_{x,\mathrm{GRP}\to\mathrm{GAP}} + \phi_{x,\mathrm{PYR}\to\mathrm{ACoA}} + 14\phi_{x,\mathrm{FFA}\to\mathrm{ACoA}} + 4\phi_{x,\mathrm{ACoA}\to\mathrm{CO_2}} \\ -\phi_{x,\mathrm{PYR}\to\mathrm{GAP}} - \phi_{x,\mathrm{PYR}\to\mathrm{LAC}} - \phi_{x,\mathrm{GAP}\to\mathrm{GRP}} - \frac{14}{8}\phi_{x,\mathrm{ACoA}\to\mathrm{FFA}} - 2\phi_{x,\mathrm{O_2}\to\mathrm{H_2O}}\end{array}$
18. ATP	$\mathrm{V}_{x,\mathrm{ATP}}\frac{\mathrm{dC}_{x,\mathrm{ATP}}}{dt} = \begin{array}{l}2\phi_{x,\mathrm{GAP}\to\mathrm{PYR}} + \phi_{x,\mathrm{ACoA}\to\mathrm{CO_2}} + 6\phi_{x,\mathrm{O_2}\to\mathrm{H_2O}} + \phi_{x,\mathrm{PCR}\to\mathrm{CR}} - \phi_{x,\mathrm{GLC}\to\mathrm{G6P}} - \phi_{x,\mathrm{G6P}\to\mathrm{GAP}} - 3\phi_{x,\mathrm{PYR}\to\mathrm{GAP}} \\ -\phi_{x,\mathrm{G6P}\to\mathrm{GLY}} - \phi_{x,\mathrm{GLR}\to\mathrm{GRP}} - 2\phi_{x,\mathrm{FFA}\to\mathrm{ACoA}} - \frac{7}{8}\phi_{x,\mathrm{ACoA}\to\mathrm{FFA}} - 2\phi_{x,\mathrm{FFA—GRP}\to\mathrm{TG}} - \phi_{x,\mathrm{CR}\to\mathrm{PCR}} - \phi_{x,\mathrm{ATP}\to\mathrm{ADP}}\end{array}$
19. ADP	$\mathrm{V}_{x,\mathrm{ADP}}\frac{\mathrm{dC}_{x,\mathrm{ADP}}}{dt} = \begin{array}{l}\phi_{x,\mathrm{GLC}\to\mathrm{G6P}} + \phi_{x,\mathrm{G6P}\to\mathrm{GAP}} + 3\phi_{x,\mathrm{PYR}\to\mathrm{GAP}} + \phi_{x,\mathrm{G6P}\to\mathrm{GLY}} + \phi_{x,\mathrm{GLR}\to\mathrm{GRP}} + 2\phi_{x,\mathrm{FFA}\to\mathrm{ACoA}} + \frac{7}{8}\phi_{x,\mathrm{ACoA}\to\mathrm{FFA}} \\ +2\phi_{x,\mathrm{FFA—GRP}\to\mathrm{TG}} + \phi_{x,\mathrm{CR}\to\mathrm{PCR}} + \phi_{x,\mathrm{ATP}\to\mathrm{ADP}} - 2\phi_{x,\mathrm{GAP}\to\mathrm{PYR}} - \phi_{x,\mathrm{ACoA}\to\mathrm{CO_2}} - 6\phi_{x,\mathrm{O_2}\to\mathrm{H_2O}} - \phi_{x,\mathrm{PCR}\to\mathrm{CR}}\end{array}$
20. Pi	$\mathrm{V}_{x,\mathrm{Pi}}\frac{\mathrm{dC}_{x,\mathrm{Pi}}}{dt} = \begin{array}{l}2\phi_{x,\mathrm{PYR}\to\mathrm{GAP}} + \frac{1}{2}\phi_{x,\mathrm{GAP}\to\mathrm{G6P}} + \phi_{x,\mathrm{G6P}\to\mathrm{GLC}} + 2\phi_{x,\mathrm{G6P}\to\mathrm{GLY}} + 2\phi_{x,\mathrm{FFA}\to\mathrm{ACoA}} + \frac{7}{8}\phi_{x,\mathrm{ACoA}\to\mathrm{FFA}} \\ +\frac{7}{3}\phi_{x,\mathrm{FFA—GRP}\to\mathrm{TG}} + \phi_{x,\mathrm{ATP}\to\mathrm{ADP}} - \phi_{x,\mathrm{GAP}\to\mathrm{PYR}} - \phi_{x,\mathrm{GLY}\to\mathrm{G6P}} - 6\phi_{x,\mathrm{O_2}\to\mathrm{H_2O}} - \phi_{x,\mathrm{ACoA}\to\mathrm{CO_2}}\end{array}$
21. PCR	$\mathrm{V}_{x,\mathrm{PCR}}\frac{\mathrm{dC}_{x,\mathrm{PCR}}}{dt} = \phi_{x,\mathrm{CR}\to\mathrm{PCR}} - \phi_{x,\mathrm{PCR}\to\mathrm{CR}}$
22. CR	$\mathrm{V}_{x,\mathrm{CR}}\frac{\mathrm{dC}_{x,\mathrm{CR}}}{dt} = \phi_{x,\mathrm{PCR}\to\mathrm{CR}} - \phi_{x,\mathrm{CR}\to\mathrm{PCR}}$

Organ/tissue x refers to brain, heart, skeletal muscle, GI tract, liver, adipose tissue, or "others"; $\mathrm{V}_{x,i} := V_{\mathrm{eff},x,i}$ is the effective volume of substrate i in tissue x. Since we assumed that each tissue is a spatially lumped tissue-capillary compartment, the distribution volume of substrate i differs from the physical tissue volume (V_x) [345]. If substrate i exists in blood and in tissue x, $\mathrm{V}_{\mathrm{eff},x,i}$ =0.93 V_x + $\sigma_{x,i}$(0.07 V_x); otherwise, if substrate i exists only in tissue x, $\mathrm{V}_{\mathrm{eff},x,i}$ =0.8 V_x (e.g., see Ref. [72] and the related references therein).

Table C.14: Metabolic reaction fluxes

1. Glycolysis I — GLC + ATP → G6P + ADP

$$\phi_{x,\mathrm{GLC}\to\mathrm{G6P}} = V_{x,\mathrm{GLC}\to\mathrm{G6P}} \left(\frac{\frac{\mathrm{C}_{x,\mathrm{GLC}}}{\mathrm{K}_{x,\mathrm{GLC}}}}{1 + \frac{\mathrm{C}_{x,\mathrm{GLC}}}{\mathrm{K}_{x,\mathrm{GLC}}}} \right) \left(\frac{\frac{\mathrm{C}_{x,\mathrm{ATP}}}{\mathrm{C}_{x,\mathrm{ADP}}}}{\mathrm{K}_{x,\frac{\mathrm{ATP}}{\mathrm{ADP}}} + \frac{\mathrm{C}_{x,\mathrm{ATP}}}{\mathrm{C}_{x,\mathrm{ADP}}}} \right)$$

2. Glycolysis II — G6P + ATP → 2 GAP + ADP

$$\phi_{x,\mathrm{G6P}\to\mathrm{GAP}} = V_{x,\mathrm{G6P}\to\mathrm{GAP}} \left(\frac{\frac{\mathrm{C}_{x,\mathrm{G6P}}}{\mathrm{K}_{x,\mathrm{G6P}}}}{1 + \frac{\mathrm{C}_{x,\mathrm{G6P}}}{\mathrm{K}_{x,\mathrm{G6P}}}} \right) \left(\frac{\left(\frac{\mathrm{C}_{x,\mathrm{ADP}}}{\mathrm{C}_{x,\mathrm{ATP}}}\right)^2}{\mathrm{K}^2_{x,\frac{\mathrm{ADP}}{\mathrm{ATP}}} + \left(\frac{\mathrm{C}_{x,\mathrm{ADP}}}{\mathrm{C}_{x,\mathrm{ATP}}}\right)^2} \right)$$

3. Glycolysis III — GAP + Pi + NAD^+ + 2 ADP → PYR + NADH + 2 ATP

$$\phi_{x,\mathrm{GAP}\to\mathrm{PYR}} = V_{x,\mathrm{GAP}\to\mathrm{PYR}} \left(\frac{\frac{\mathrm{C}_{x,\mathrm{GAP}}}{\mathrm{K}_{x,\mathrm{GAP}}} \frac{\mathrm{C}_{x,\mathrm{Pi}}}{\mathrm{K}_{x,\mathrm{Pi}}}}{1 + \frac{\mathrm{C}_{x,\mathrm{GAP}}}{\mathrm{K}_{x,\mathrm{GAP}}} + \frac{\mathrm{C}_{x,\mathrm{Pi}}}{\mathrm{K}_{x,\mathrm{Pi}}} + \frac{\mathrm{C}_{x,\mathrm{GAP}}}{\mathrm{K}_{x,\mathrm{GAP}}} \frac{\mathrm{C}_{x,\mathrm{Pi}}}{\mathrm{K}_{x,\mathrm{Pi}}}} \right) \left(\frac{\frac{\mathrm{C}_{x,\mathrm{NAD+}}}{\mathrm{C}_{x,\mathrm{NADH}}}}{\mathrm{K}_{x,\frac{\mathrm{NAD+}}{\mathrm{NADH}}} + \frac{\mathrm{C}_{x,\mathrm{NAD+}}}{\mathrm{C}_{x,\mathrm{NADH}}}} \right) \left(\frac{\frac{\mathrm{C}_{x,\mathrm{ADP}}}{\mathrm{C}_{x,\mathrm{ATP}}}}{\mathrm{K}_{x,\frac{\mathrm{ADP}}{\mathrm{ATP}}} + \frac{\mathrm{C}_{x,\mathrm{ADP}}}{\mathrm{C}_{x,\mathrm{ATP}}}} \right)$$

4. Gluconeogenesis I — PYR + 3 ATP + NADH → GAP + 3 ADP + NAD^+ + 2 Pi

$$\phi_{x,\mathrm{PYR}\to\mathrm{GAP}} = V_{x,\mathrm{PYR}\to\mathrm{GAP}} \left(\frac{\frac{\mathrm{C}_{x,\mathrm{PYR}}}{\mathrm{K}_{x,\mathrm{PYR}}}}{1 + \frac{\mathrm{C}_{x,\mathrm{PYR}}}{\mathrm{K}_{x,\mathrm{PYR}}}} \right) \left(\frac{\frac{\mathrm{C}_{x,\mathrm{NADH}}}{\mathrm{C}_{x,\mathrm{NAD+}}}}{\mathrm{K}_{x,\frac{\mathrm{NADH}}{\mathrm{NAD+}}} + \frac{\mathrm{C}_{x,\mathrm{NADH}}}{\mathrm{C}_{x,\mathrm{NAD+}}}} \right) \left(\frac{\frac{\mathrm{C}_{x,\mathrm{ATP}}}{\mathrm{C}_{x,\mathrm{ADP}}}}{\mathrm{K}_{x,\frac{\mathrm{ATP}}{\mathrm{ADP}}} + \frac{\mathrm{C}_{x,\mathrm{ATP}}}{\mathrm{C}_{x,\mathrm{ADP}}}} \right)$$

5. Gluconeogenesis II — 2 GAP → G6P + Pi

$$\phi_{x,\mathrm{GAP}\to\mathrm{G6P}} = V_{x,\mathrm{GAP}\to\mathrm{G6P}} \left(\frac{\frac{\mathrm{C}_{x,\mathrm{GAP}}}{\mathrm{K}_{x,\mathrm{GAP}}}}{1 + \frac{\mathrm{C}_{x,\mathrm{GAP}}}{\mathrm{K}_{x,\mathrm{GAP}}}} \right)$$

6. Gluconeogenesis III — G6P → GLC + Pi

$$\phi_{x,\mathrm{G6P}\to\mathrm{GLC}} = V_{x,\mathrm{G6P}\to\mathrm{GLC}} \left(\frac{\frac{\mathrm{C}_{x,\mathrm{G6P}}}{\mathrm{K}_{x,\mathrm{G6P}}}}{1 + \frac{\mathrm{C}_{x,\mathrm{G6P}}}{\mathrm{K}_{x,\mathrm{G6P}}}} \right)$$

7. Glycogenesis — G6P + ATP → GLY + ADP + 2 Pi

$$\phi_{x,\mathrm{G6P}\to\mathrm{GLY}} = V_{x,\mathrm{G6P}\to\mathrm{GLY}} \left(\frac{\frac{\mathrm{C}_{x,\mathrm{G6P}}}{\mathrm{K}_{x,\mathrm{G6P}}}}{1 + \frac{\mathrm{C}_{x,\mathrm{G6P}}}{\mathrm{K}_{x,\mathrm{G6P}}}} \right) \left(\frac{\frac{\mathrm{C}_{x,\mathrm{ATP}}}{\mathrm{C}_{x,\mathrm{ADP}}}}{\mathrm{K}_{x,\frac{\mathrm{ATP}}{\mathrm{ADP}}} + \frac{\mathrm{C}_{x,\mathrm{ATP}}}{\mathrm{C}_{x,\mathrm{ADP}}}} \right)$$

8. Glycogenolysis — GLY + Pi → G6P

$$\phi_{x,\mathrm{GLY}\to\mathrm{G6P}} = V_{x,\mathrm{GLY}\to\mathrm{G6P}} \left(\frac{\frac{\mathrm{C}_{x,\mathrm{GLY}}}{\mathrm{K}_{x,\mathrm{GLY}}} \frac{\mathrm{C}_{x,\mathrm{Pi}}}{\mathrm{K}_{x,\mathrm{Pi}}}}{1 + \frac{\mathrm{C}_{x,\mathrm{GLY}}}{\mathrm{K}_{x,\mathrm{GLY}}} + \frac{\mathrm{C}_{x,\mathrm{Pi}}}{\mathrm{K}_{x,\mathrm{Pi}}} + \frac{\mathrm{C}_{x,\mathrm{GLY}}}{\mathrm{K}_{x,\mathrm{GLY}}} \frac{\mathrm{C}_{x,\mathrm{Pi}}}{\mathrm{K}_{x,\mathrm{Pi}}}} \right) \left(\frac{\left(\frac{\mathrm{C}_{x,\mathrm{ADP}}}{\mathrm{C}_{x,\mathrm{ATP}}}\right)^2}{\mathrm{K}^2_{x,\frac{\mathrm{ADP}}{\mathrm{ATP}}} + \left(\frac{\mathrm{C}_{x,\mathrm{ADP}}}{\mathrm{C}_{x,\mathrm{ATP}}}\right)^2} \right)$$

9. Pyruvate Reduction — PYR + NADH → LAC + NAD^+

$$\phi_{x,\mathrm{PYR}\to\mathrm{LAC}} = V_{x,\mathrm{PYR}\to\mathrm{LAC}} \left(\frac{\frac{\mathrm{C}_{x,\mathrm{PYR}}}{\mathrm{K}_{x,\mathrm{PYR}}}}{1 + \frac{\mathrm{C}_{x,\mathrm{PYR}}}{\mathrm{K}_{x,\mathrm{PYR}}}} \right) \left(\frac{\frac{\mathrm{C}_{x,\mathrm{NADH}}}{\mathrm{C}_{x,\mathrm{NAD^+}}}}{\mathrm{K}_{x,\frac{\mathrm{NADH}}{\mathrm{NAD^+}}} + \frac{\mathrm{C}_{x,\mathrm{NADH}}}{\mathrm{C}_{x,\mathrm{NAD^+}}}} \right)$$

10. Lactate Oxidation $\mathrm{LAC} + \mathrm{NAD^+} \rightarrow \mathrm{PYR} + \mathrm{NADH}$

$$\phi_{x,\mathrm{LAC}\to\mathrm{PYR}} = V_{x,\mathrm{LAC}\to\mathrm{PYR}} \left(\frac{\frac{\mathrm{C}_{x,\mathrm{LAC}}}{\mathrm{K}_{x,\mathrm{LAC}}}}{1 + \frac{\mathrm{C}_{x,\mathrm{LAC}}}{\mathrm{K}_{x,\mathrm{LAC}}}} \right) \left(\frac{\frac{\mathrm{C}_{x,\mathrm{NAD^+}}}{\mathrm{C}_{x,\mathrm{NADH}}}}{\mathrm{K}_{x,\frac{\mathrm{NAD^+}}{\mathrm{NADH}}} + \frac{\mathrm{C}_{x,\mathrm{NAD^+}}}{\mathrm{C}_{x,\mathrm{NADH}}}} \right)$$

11. Glycerol Phosphorylation $\mathrm{GLR} + \mathrm{ATP} \rightarrow \mathrm{GRP} + \mathrm{ADP}$

$$\phi_{x,\mathrm{GLR}\to\mathrm{GRP}} = V_{x,\mathrm{GLR}\to\mathrm{GRP}} \left(\frac{\frac{\mathrm{C}_{x,\mathrm{GLR}}}{\mathrm{K}_{x,\mathrm{GLR}}}}{1 + \frac{\mathrm{C}_{x,\mathrm{GLR}}}{\mathrm{K}_{x,\mathrm{GLR}}}} \right) \left(\frac{\frac{\mathrm{C}_{x,\mathrm{ATP}}}{\mathrm{C}_{x,\mathrm{ADP}}}}{\mathrm{K}_{x,\frac{\mathrm{ATP}}{\mathrm{ADP}}} + \frac{\mathrm{C}_{x,\mathrm{ATP}}}{\mathrm{C}_{x,\mathrm{ADP}}}} \right)$$

12. GAP Reduction $\mathrm{GAP} + \mathrm{NADH} \rightarrow \mathrm{GRP} + \mathrm{NAD^+}$

$$\phi_{x,\mathrm{GAP}\to\mathrm{GRP}} = V_{x,\mathrm{GAP}\to\mathrm{GRP}} \left(\frac{\frac{\mathrm{C}_{x,\mathrm{GAP}}}{\mathrm{K}_{x,\mathrm{GAP}}}}{1 + \frac{\mathrm{C}_{x,\mathrm{GAP}}}{\mathrm{K}_{x,\mathrm{GAP}}}} \right) \left(\frac{\frac{\mathrm{C}_{x,\mathrm{NADH}}}{\mathrm{C}_{x,\mathrm{NAD^+}}}}{\mathrm{K}_{x,\frac{\mathrm{NADH}}{\mathrm{NAD^+}}} + \frac{\mathrm{C}_{x,\mathrm{NADH}}}{\mathrm{C}_{x,\mathrm{NAD^+}}}} \right)$$

13. GRP Oxidation $\mathrm{GRP} + \mathrm{NAD^+} \rightarrow \mathrm{GAP} + \mathrm{NADH}$

$$\phi_{x,\mathrm{GRP}\to\mathrm{GAP}} = V_{x,\mathrm{GRP}\to\mathrm{GAP}} \left(\frac{\frac{\mathrm{C}_{x,\mathrm{GRP}}}{\mathrm{K}_{x,\mathrm{GRP}}}}{1 + \frac{\mathrm{C}_{x,\mathrm{GRP}}}{\mathrm{K}_{x,\mathrm{GRP}}}} \right) \left(\frac{\frac{\mathrm{C}_{x,\mathrm{NAD^+}}}{\mathrm{C}_{x,\mathrm{NADH}}}}{\mathrm{K}_{x,\frac{\mathrm{NAD^+}}{\mathrm{NADH}}} + \frac{\mathrm{C}_{x,\mathrm{NAD^+}}}{\mathrm{C}_{x,\mathrm{NADH}}}} \right)$$

14. Alanine Formation $\mathrm{PYR} \rightarrow \mathrm{ALA}$

$$\phi_{x,\mathrm{PYR}\to\mathrm{ALA}} = V_{x,\mathrm{PYR}\to\mathrm{ALA}} \left(\frac{\frac{\mathrm{C}_{x,\mathrm{PYR}}}{\mathrm{K}_{x,\mathrm{PYR}}}}{1 + \frac{\mathrm{C}_{x,\mathrm{PYR}}}{\mathrm{K}_{x,\mathrm{PYR}}}} \right)$$

15. Alanine Utilization $\mathrm{ALA} \rightarrow \mathrm{PYR}$

$$\phi_{x,\mathrm{ALA}\to\mathrm{PYR}} = V_{x,\mathrm{ALA}\to\mathrm{PYR}} \left(\frac{\frac{\mathrm{C}_{x,\mathrm{ALA}}}{\mathrm{K}_{x,\mathrm{ALA}}}}{1 + \frac{\mathrm{C}_{x,\mathrm{ALA}}}{\mathrm{K}_{x,\mathrm{ALA}}}} \right)$$

16. Pyruvate Oxidation $\mathrm{PYR} + \mathrm{CoA} + \mathrm{NAD^+} \rightarrow \mathrm{ACoA} + \mathrm{NADH} + \mathrm{CO_2}$

$$\phi_{x,\mathrm{PYR}\to\mathrm{ACoA}} = V_{x,\mathrm{PYR}\to\mathrm{ACoA}} \left(\frac{\frac{\mathrm{C}_{x,\mathrm{PYR}}}{\mathrm{K}_{x,\mathrm{PYR}}} \frac{\mathrm{C}_{x,\mathrm{CoA}}}{\mathrm{K}_{x,\mathrm{CoA}}}}{1 + \frac{\mathrm{C}_{x,\mathrm{PYR}}}{\mathrm{K}_{x,\mathrm{PYR}}} + \frac{\mathrm{C}_{x,\mathrm{CoA}}}{\mathrm{K}_{x,\mathrm{CoA}}} + \frac{\mathrm{C}_{x,\mathrm{PYR}}}{\mathrm{K}_{x,\mathrm{PYR}}} \frac{\mathrm{C}_{x,\mathrm{CoA}}}{\mathrm{K}_{x,\mathrm{CoA}}}} \right) \left(\frac{\frac{\mathrm{C}_{x,\mathrm{NAD^+}}}{\mathrm{C}_{x,\mathrm{NADH}}}}{\mathrm{K}_{x,\frac{\mathrm{NAD^+}}{\mathrm{NADH}}} + \frac{\mathrm{C}_{x,\mathrm{NAD^+}}}{\mathrm{C}_{x,\mathrm{NADH}}}} \right)$$

17. Fatty Acid Oxidation $\mathrm{FFA} + 8\ \mathrm{CoA} + 2\ \mathrm{ATP} + 14\ \mathrm{NAD^+} \rightarrow 8\ \mathrm{ACoA} + 2\ \mathrm{ADP} + 2\ \mathrm{Pi} + 14\ \mathrm{NADH}$

$$\phi_{x,\mathrm{FFA}\to\mathrm{ACoA}} = V_{x,\mathrm{FFA}\to\mathrm{ACoA}} \left(\frac{\frac{\mathrm{C}_{x,\mathrm{FFA}}}{\mathrm{K}_{x,\mathrm{FFA}}} \frac{\mathrm{C}_{x,\mathrm{CoA}}}{\mathrm{K}_{x,\mathrm{CoA}}}}{1 + \frac{\mathrm{C}_{x,\mathrm{FFA}}}{\mathrm{K}_{x,\mathrm{FFA}}} + \frac{\mathrm{C}_{x,\mathrm{CoA}}}{\mathrm{K}_{x,\mathrm{CoA}}} + \frac{\mathrm{C}_{x,\mathrm{FFA}}}{\mathrm{K}_{x,\mathrm{FFA}}} \frac{\mathrm{C}_{x,\mathrm{CoA}}}{\mathrm{K}_{x,\mathrm{CoA}}}} \right) \left(\frac{\frac{\mathrm{C}_{x,\mathrm{NAD^+}}}{\mathrm{C}_{x,\mathrm{NADH}}}}{\mathrm{K}_{x,\frac{\mathrm{NAD^+}}{\mathrm{NADH}}} + \frac{\mathrm{C}_{x,\mathrm{NAD^+}}}{\mathrm{C}_{x,\mathrm{NADH}}}} \right)$$

18. Fatty Acid Synthesis $8\ \mathrm{ACoA} + 7\ \mathrm{ATP} + 14\ \mathrm{NADH} \rightarrow \mathrm{FFA} + 8\ \mathrm{CoA} + 7\ \mathrm{ADP} + 7\ \mathrm{Pi} + 14\ \mathrm{NAD^+}$

$$\phi_{x,\mathrm{ACoA}\rightarrow\mathrm{FFA}} = V_{x,\mathrm{ACoA}\rightarrow\mathrm{FFA}} \left(\frac{\frac{\mathrm{C}_{x,\mathrm{ACoA}}}{\mathrm{K}_{x,\mathrm{ACoA}}}}{1 + \frac{\mathrm{C}_{x,\mathrm{ACoA}}}{\mathrm{K}_{x,\mathrm{ACoA}}}} \right) \left(\frac{\frac{\mathrm{C}_{x,\mathrm{NADH}}}{\mathrm{C}_{x,\mathrm{NAD^+}}}}{\mathrm{K}_{x,\frac{\mathrm{NADH}}{\mathrm{NAD^+}}} + \frac{\mathrm{C}_{x,\mathrm{NADH}}}{\mathrm{C}_{x,\mathrm{NAD^+}}}} \right) \left(\frac{\frac{\mathrm{C}_{x,\mathrm{ATP}}}{\mathrm{C}_{x,\mathrm{ADP}}}}{\mathrm{K}_{x,\frac{\mathrm{ATP}}{\mathrm{ADP}}} + \frac{\mathrm{C}_{x,\mathrm{ATP}}}{\mathrm{C}_{x,\mathrm{ADP}}}} \right)$$

19. Lipolysis $\mathrm{TG} \rightarrow \mathrm{GLR} + 3\ \mathrm{FFA}$

$$\phi_{x,\mathrm{TG}\rightarrow\mathrm{FFA—GLR}} = V_{x,\mathrm{TG}\rightarrow\mathrm{FFA—GLR}} \left(\frac{\frac{\mathrm{C}_{x,\mathrm{TG}}}{\mathrm{K}_{x,\mathrm{TG}}}}{1 + \frac{\mathrm{C}_{x,\mathrm{TG}}}{\mathrm{K}_{x,\mathrm{TG}}}} \right)$$

20. Triglyceride Synthesis $\mathrm{GRP} + 3\ \mathrm{FFA} + 6\ \mathrm{ATP} \rightarrow \mathrm{TG} + 6\ \mathrm{ADP} + 7\ \mathrm{Pi}$

$$\phi_{x,\mathrm{FFA—GRP}\rightarrow\mathrm{TG}} = V_{x,\mathrm{FFA—GRP}\rightarrow\mathrm{TG}} \left(\frac{\frac{\mathrm{C}_{x,\mathrm{FFA}}}{\mathrm{K}_{x,\mathrm{FFA}}} \frac{\mathrm{C}_{x,\mathrm{GRP}}}{\mathrm{K}_{x,\mathrm{GRP}}}}{1 + \frac{\mathrm{C}_{x,\mathrm{FFA}}}{\mathrm{K}_{x,\mathrm{FFA}}} + \frac{\mathrm{C}_{x,\mathrm{GRP}}}{\mathrm{K}_{x,\mathrm{GRP}}} + \frac{\mathrm{C}_{x,\mathrm{FFA}}}{\mathrm{K}_{x,\mathrm{FFA}}} \frac{\mathrm{C}_{x,\mathrm{GRP}}}{\mathrm{K}_{x,\mathrm{GRP}}}} \right) \left(\frac{\frac{\mathrm{C}_{x,\mathrm{ATP}}}{\mathrm{C}_{x,\mathrm{ADP}}}}{\mathrm{K}_{x,\frac{\mathrm{ATP}}{\mathrm{ADP}}} + \frac{\mathrm{C}_{x,\mathrm{ATP}}}{\mathrm{C}_{x,\mathrm{ADP}}}} \right)$$

21. TCA Cycle $\mathrm{ACoA} + \mathrm{ADP} + \mathrm{Pi} + 4\ \mathrm{NAD^+} \rightarrow 2\ \mathrm{CO_2} + \mathrm{CoA} + \mathrm{ATP} + 4\ \mathrm{NADH}$

$$\phi_{x,\mathrm{ACoA}\rightarrow\mathrm{CO_2}} = V_{x,\mathrm{ACoA}\rightarrow\mathrm{CO_2}} \left(\frac{\frac{\mathrm{C}_{x,\mathrm{ACoA}}}{\mathrm{K}_{x,\mathrm{ACoA}}} \frac{\mathrm{C}_{x,\mathrm{Pi}}}{\mathrm{K}_{x,\mathrm{Pi}}}}{1 + \frac{\mathrm{C}_{x,\mathrm{ACoA}}}{\mathrm{K}_{x,\mathrm{ACoA}}} + \frac{\mathrm{C}_{x,\mathrm{Pi}}}{\mathrm{K}_{x,\mathrm{Pi}}} + \frac{\mathrm{C}_{x,\mathrm{ACoA}}}{\mathrm{K}_{x,\mathrm{ACoA}}} \frac{\mathrm{C}_{x,\mathrm{Pi}}}{\mathrm{K}_{x,\mathrm{Pi}}}} \right) \left(\frac{\frac{\mathrm{C}_{x,\mathrm{ADP}}}{\mathrm{C}_{x,\mathrm{ATP}}}}{\mathrm{K}_{x,\frac{\mathrm{ADP}}{\mathrm{ATP}}} + \frac{\mathrm{C}_{x,\mathrm{ADP}}}{\mathrm{C}_{x,\mathrm{ATP}}}} \right) \left(\frac{\frac{\mathrm{C}_{x,\mathrm{NAD^+}}}{\mathrm{C}_{x,\mathrm{NADH}}}}{\mathrm{K}_{x,\frac{\mathrm{NAD^+}}{\mathrm{NADH}}} + \frac{\mathrm{C}_{x,\mathrm{NAD^+}}}{\mathrm{C}_{x,\mathrm{NADH}}}} \right)$$

22. Oxidative Phosphorylation $\mathrm{O_2} + 6\ \mathrm{ADP} + 6\ \mathrm{Pi} + 2\ \mathrm{NADH} \rightarrow 2\ \mathrm{H_2O} + 6\ \mathrm{ATP} + 2\ \mathrm{NAD^+}$

$$\phi_{x,\mathrm{O_2}\rightarrow\mathrm{H_2O}} = V_{x,\mathrm{O_2}\rightarrow\mathrm{H_2O}} \left(\frac{\frac{\mathrm{C}_{x,\mathrm{O_2}}}{\mathrm{K}_{x,\mathrm{O_2}}} \frac{\mathrm{C}_{x,\mathrm{Pi}}}{\mathrm{K}_{x,\mathrm{Pi}}}}{1 + \frac{\mathrm{C}_{x,\mathrm{O_2}}}{\mathrm{K}_{x,\mathrm{O_2}}} + \frac{\mathrm{C}_{x,\mathrm{Pi}}}{\mathrm{K}_{x,\mathrm{Pi}}} + \frac{\mathrm{C}_{x,\mathrm{O_2}}}{\mathrm{K}_{x,\mathrm{O_2}}} \frac{\mathrm{C}_{x,\mathrm{Pi}}}{\mathrm{K}_{x,\mathrm{Pi}}}} \right) \left(\frac{\frac{\mathrm{C}_{x,\mathrm{ADP}}}{\mathrm{C}_{x,\mathrm{ATP}}}}{\mathrm{K}_{x,\frac{\mathrm{ADP}}{\mathrm{ATP}}} + \frac{\mathrm{C}_{x,\mathrm{ADP}}}{\mathrm{C}_{x,\mathrm{ATP}}}} \right) \left(\frac{\frac{\mathrm{C}_{x,\mathrm{NADH}}}{\mathrm{C}_{x,\mathrm{NAD^+}}}}{\mathrm{K}_{x,\frac{\mathrm{NADH}}{\mathrm{NAD^+}}} + \frac{\mathrm{C}_{x,\mathrm{NADH}}}{\mathrm{C}_{x,\mathrm{NAD^+}}}} \right)$$

23. Phosphocreatine Breakdown $\mathrm{PCR} + \mathrm{ADP} \rightarrow \mathrm{CR} + \mathrm{ATP}$

$$\phi_{x,\mathrm{PCR}\rightarrow\mathrm{CR}} = V_{x,\mathrm{PCR}\rightarrow\mathrm{CR}} \left(\frac{\frac{\mathrm{C}_{x,\mathrm{PCR}}}{\mathrm{K}_{x,\mathrm{PCR}}}}{1 + \frac{\mathrm{C}_{x,\mathrm{PCR}}}{\mathrm{K}_{x,\mathrm{PCR}}}} \right) \left(\frac{\frac{\mathrm{C}_{x,\mathrm{ADP}}}{\mathrm{C}_{x,\mathrm{ATP}}}}{\mathrm{K}_{x,\frac{\mathrm{ADP}}{\mathrm{ATP}}} + \frac{\mathrm{C}_{x,\mathrm{ADP}}}{\mathrm{C}_{x,\mathrm{ATP}}}} \right)$$

24. Phosphcreatine Synthesis $\mathrm{CR} + \mathrm{ATP} \rightarrow \mathrm{PCR} + \mathrm{ADP}$

$$\phi_{x,\mathrm{CR}\rightarrow\mathrm{PCR}} = V_{x,\mathrm{CR}\rightarrow\mathrm{PCR}} \left(\frac{\frac{\mathrm{C}_{x,\mathrm{CR}}}{\mathrm{K}_{x,\mathrm{CR}}}}{1 + \frac{\mathrm{C}_{x,\mathrm{CR}}}{\mathrm{K}_{x,\mathrm{CR}}}} \right) \left(\frac{\frac{\mathrm{C}_{x,\mathrm{ATP}}}{\mathrm{C}_{x,\mathrm{ADP}}}}{\mathrm{K}_{x,\frac{\mathrm{ATP}}{\mathrm{ADP}}} + \frac{\mathrm{C}_{x,\mathrm{ATP}}}{\mathrm{C}_{x,\mathrm{ADP}}}} \right)$$

25. ATP Hydrolysis $\mathrm{ATP} \rightarrow \mathrm{ADP} + \mathrm{Pi}$

$$\phi_{x,\mathrm{ATP}\rightarrow\mathrm{ADP}} = V_{x,\mathrm{ATP}\rightarrow\mathrm{ADP}} \left(\frac{\frac{\mathrm{C}_{x,\mathrm{ATP}}}{\mathrm{K}_{x,\mathrm{ATP}}}}{1 + \frac{\mathrm{C}_{x,\mathrm{ATP}}}{\mathrm{K}_{x,\mathrm{ATP}}}} \right)$$

C.6 Some key metabolic fluxes

- Net gluconeogenesis $= \frac{\phi_{x,\text{GAP}\rightarrow\text{G6P}}}{2} - \phi_{x,\text{G6P}\rightarrow\text{GAP}}$, where x is liver;
- Net glycogenolysis $= \phi_{x,\text{GLY}\rightarrow\text{G6P}} - \phi_{x,\text{G6P}\rightarrow\text{GLY}}$, where x is brain, heart, skeletal muscle, GI tract, liver, and adipose tissue;
- Lipolysis $= \phi_{x,\text{TG}\rightarrow\text{FFA–GLR}}$, where x is heart, skeletal muscle, GI tract, liver, and adipose tissue;
- Net TG breakdown $= \phi_{x,\text{TG}\rightarrow\text{FFA–GLR}} - \frac{\phi_{x,\text{FFA–GRP}\rightarrow\text{TG}}}{3}$,
- Summing the above fluxes for all relevant organs yields whole-body fluxes.

Appendix D

Appendix to Chapter 7

D.1 Mathematical model of metabolism

In this section we formulate a mathematical model describing human metabolism and the dynamics of metabolic flexibility. We model seven tissue compartments: brain, heart, liver, GI tract, skeletal muscle, adipose tissue, and "other tissues" (Figure 7.1). The latter includes the kidneys, upper extremity muscles, and remaining tissues. Each compartment is characterized by dynamic mass balance equations governing 25 cellular metabolic reactions involving 22 substrates (refer to Table D.1). All compartments are interconnected via blood circulation. This model represents an extension of our previously published whole-body model [3] that focused on fuel homeostasis during exercise without food intake. Our model accounts for the synthesis and transport of each substrate across compartments.

Our focus here is to investigate the temporal evolution of substrate concentrations following a single meal and short fast of less than 24 hours. A meal is defined as a combination of carbohydrates and fat. It is important to note that protein is not included in our modelling. The investigation involves two meal compositions: a high-carbohydrate meal, with 90% of caloric intake from carbohydrates and 10% from fat; and a high-fat meal, with an equal distribution of 50% caloric intake from carbohydrates and 50% from fat. Carbohydrate specifically refers to glucose, and fat refers to TG. Table 7.2 provides details on meal composition. We assume the usage of glucose and TG by all tissues and organs to be dependent on the amount of each substrate in the blood plasma. We construct the model one compartment at a time and start with the blood compartment as this acts as the main transport medium for substrates between the different organs and tissues of the body. We note that no synthesis of glucose or TG occurs in the circulation.

Table D.1: List of substrates and metabolic reactions

Substrates	**Reactions**
1. GLC: Glucose	1. Glycolysis I, $\phi_{\mathrm{GLC}\rightarrow\mathrm{G6P}}$
2. PYR: Pyruvate	2. Glycolysis II, $\phi_{\mathrm{G6P}\rightarrow\mathrm{GAP}}$
3. LAC: Lactate	3. Glycolysis III, $\phi_{\mathrm{GAP}\rightarrow\mathrm{PYR}}$
4. ALA: Alanine	4. Gluconeogenesis I, $\phi_{\mathrm{PYR}\rightarrow\mathrm{GAP}}$
5. GLR: Glycerol	5. Gluconeogenesis II, $\phi_{\mathrm{GAP}\rightarrow\mathrm{G6P}}$
6. FFA: Free fatty acids	6. Gluconeogenesis III, $\phi_{\mathrm{G6P}\rightarrow\mathrm{GLC}}$
7. TG: Triglycerides	7. Glycogenesis, $\phi_{\mathrm{G6P}\rightarrow\mathrm{GLY}}$
8. O_2: Oxygen	8. Glycogenolysis, $\phi_{\mathrm{GLY}\rightarrow\mathrm{G6P}}$
9. CO_2: Carbon dioxide	9. Pyruvate reduction, $\phi_{\mathrm{PYR}\rightarrow\mathrm{LAC}}$
10. G6P: Glucose-6-phosphate	10. Lactate oxidation, $\phi_{\mathrm{LAC}\rightarrow\mathrm{PYR}}$
11. GLY: Glycogen	11. Glycerol phosphorylation, $\phi_{\mathrm{GLR}\rightarrow\mathrm{GRP}}$
12. GAP: Glyceraldehyde-3-phosphate	12. GAP reduction, $\phi_{\mathrm{GAP}\rightarrow\mathrm{GRP}}$
13. GRP: Glycerol-3-phosphate	13. GRP oxidation, $\phi_{\mathrm{GRP}\rightarrow\mathrm{GAP}}$
14. ACoA: Acetyl coenzyme A	14. Alanine formation, $\phi_{\mathrm{PYR}\rightarrow\mathrm{ALA}}$
15. CoA: Coenzyme A	15. Alanine utilization, $\phi_{\mathrm{ALA}\rightarrow\mathrm{PYR}}$
16. NAD^+: Nicotinamide adenine dinucleotide[a]	16. Pyruvate oxidation, $\phi_{\mathrm{PYR}\rightarrow\mathrm{ACoA}}$
17. NADH: Nicotinamide adenine dinucleotide[b]	17. Fatty acids oxidation, $\phi_{\mathrm{FFA}\rightarrow\mathrm{ACoA}}$
18. ATP: Adenosine triphosphate	18. Fatty acids synthesis, $\phi_{\mathrm{ACoA}\rightarrow\mathrm{FFA}}$
19. ADP: Adenosine diphosphate	19. Lipolysis, $\phi_{\mathrm{TG}\rightarrow\mathrm{FFA\text{–}GLR}}$
20. Pi: Phosphate	20. Triglycerides synthesis, $\phi_{\mathrm{FFA\text{–}GRP}\rightarrow\mathrm{TG}}$
21. PCR: Phosphocreatine	21. TCA cycle, $\phi_{\mathrm{ACoA}\rightarrow\mathrm{CO_2}}$
22. CR: Creatine	22. Oxidative phosphorylation, $\phi_{\mathrm{O_2}\rightarrow\mathrm{H_2O}}$
	23. Phosphocreatine breakdown, $\phi_{\mathrm{PCR}\rightarrow\mathrm{CR}}$
	24. Phosphocreatine synthesis, $\phi_{\mathrm{CR}\rightarrow\mathrm{PCR}}$
	25. ATP hydrolysis, $\phi_{\mathrm{ATP}\rightarrow\mathrm{ADP}}$

[a] Oxidized
[b] Reduced

D.1.1 Blood compartment and dietary intake

The model simulates a meal by adding glucose and TG into the bloodstream. The model blood compartment serves as the primary conduit for substrate transport among the seven tissue compartments. Besides glucose and TG, the transport of the following substrates also occurs between blood and tissue: pyruvate, lactate, alanine, glycerol, free fatty acids, oxygen, and carbon dioxide. The alteration in the concentration of a substrate in the circu-

lation is governed by the cumulative transport fluxes among all organs and the circulation, and, in the case of glucose and TG, a source term. Consequently, the plasma concentration of a substrate i is modified as follows:

$$V_{\text{blood}} \frac{\mathrm{d}C_{a,i}}{\mathrm{d}t} = -\sum_{x} Q_x (C_{a,i} - \sigma_{x,i} C_{x,i}) - \mathrm{UR}_{O,i} + F_i^{\text{meal}}(t - t_{\text{meal}}). \tag{D.1}$$

Here, V_{blood} is the blood volume, Q_x is the blood flow to/from organ x, $C_{a,i}$ is the plasma concentration of substrate i, $C_{x,i}$ is the corresponding concentration of substrate i in organ x, and $\sigma_{x,i}$ is the partition coefficient of substrate i. These partition coefficients, unchanging, indicate the relative distribution of metabolites between blood and organs at rest. The expression $Q_x(C_{a,i} - \sigma_{x,i}C_{x,i})$ characterizes the net rate of substrate absorption into organ x, with the negative sign indicating transport out of the circulation. x represents brain, heart, skeletal muscle, GI tract, liver, and adipose tissue. The "other tissues" compartment includes the kidneys, upper extremity muscles, and remaining tissues, and lacks any metabolic reactions. It functions as a source or sink for the nine substrates exchanged between blood and tissues. In the case of other species found exclusively in tissues, the source or sink terms are nil. Let $\mathrm{UR}_{O,i}$ denote the source or sink term for substrate i in tissue O, which represents *other tissues*. A positive value indicates uptake of the corresponding substrate, while a negative value indicates release into the circulation. The source or sink values are set to maintain the overall mass balance of the whole-body model at rest. However, for substrates such as lactate and glycerol, which can be excreted by the kidneys when present in excess in the circulation, the source or sink terms are dynamic and can model excretion. When i represents lactate or glycerol,

$$\mathrm{UR}_{O,i} = \mathrm{UR}^0_{O,i} + \max\Big(0, Q_O\big(C_{a,i} - C^{\text{thresh}}_{a,i}\big)\Big), \tag{D.2}$$

where $\mathrm{UR}^0_{O,i}$ is the basal rate of uptake or release of substrate i from *other tissues*, Q_O is the blood flow to *other tissues*, $C_{a,i}$ is the blood concentration of substrate i, and $C^{\text{thresh}}_{a,i}$ is the corresponding excretion threshold. The kidney is both a lactate producer and consumer. For instance, in the absorptive state, kidneys act as recipients of the lactate shuttle, and when in excess, they serve as sites of net lactate disposal [463, 464]. Given that normal lactate levels are less than 2 mM [465], $C^{\text{thresh}}_{a,\text{LAC}}$ is set to 2 mM. According to Nelson et al. [466], plasma glycerol concentrations above 0.327 ± 0.190 mM are associated with urinary glycerol excretion. Thus, $C^{\text{thresh}}_{a,\text{GLR}}$ is set to 0.33 mM. For other substrates—glucose, pyruvate, alanine, TG, oxygen, and carbon dioxide, $\mathrm{UR}_{O,i} = \mathrm{UR}^0_{O,i}$.

We model the rate of appearance of glucose and TG in the blood using *modified* equa-

tions introduced by Pearson et al. [392]:

$$\mathrm{F}^{\mathrm{meal}}_{\mathrm{GLC}}(t - t_{\mathrm{meal}}) = \theta_{\mathrm{GLC}} \cdot \frac{t - t_{\mathrm{meal}}}{\tau^2_{\mathrm{GLC}}(\theta_{\mathrm{GLC}})} \exp\left\{ -\frac{(t - t_{\mathrm{meal}})^2}{2\tau^2_{\mathrm{GLC}}(\theta_{\mathrm{GLC}})} \right\}, \tag{D.3}$$

and

$$\mathrm{F}^{\mathrm{meal}}_{\mathrm{TG}}(t - t_{\mathrm{meal}}) = \theta_{\mathrm{TG}} \cdot \frac{t - t_{\mathrm{meal}}}{\tau^2_{\mathrm{TG}}(\theta_{\mathrm{TG}})} \exp\left\{ -\frac{\big((t - t_{\mathrm{meal}}) - 200\big)^2}{2\tau^2_{\mathrm{TG}}(\theta_{\mathrm{TG}})} \right\}, \tag{D.4}$$

where t and t_{meal} indicate time (in min), and t_{meal} specifically marks the beginning of a meal. According to Frayn [154], glucose peaks 30-60 mins after a meal, and TG peaks 3-4 hours after a meal. The term $(t - t_{\mathrm{meal}} - 200)$ models this delayed peak in TG appearance. For $i \neq$ GLC or TG, $F_i^{\mathrm{meal}} = 0$. The functions θ_{GLC} and θ_{TG} are the concentrations of exogenous glucose and TG, respectively, and determine the magnitude of substrate excursion entering the circulation. The functions $\tau_{\mathrm{GLC}}(\theta_{\mathrm{GLC}})$ and $\tau_{\mathrm{TG}}(\theta_{\mathrm{TG}})$ determine the timescale of substrate release into the blood. While Pearson et al. [392] defined τ_{GLC} and τ_{GLC} as constants, we define them as dynamic parameters. We model $\tau_{\mathrm{GLC}}(\theta_{\mathrm{GLC}})$ and $\tau_{\mathrm{TG}}(\theta_{\mathrm{TG}})$ as sigmoids, which depend on the size of the ingested meal, and lead to the desired peak times of release:

$$\tau_{\mathrm{GLC}}(\theta_{\mathrm{GLC}}) = M^0_{\mathrm{GLC}} + M^{\max}_{\mathrm{GLC}} \frac{\theta^2_{\mathrm{GLC}}}{K^2_{\mathrm{GLC}} + \theta^2_{\mathrm{GLC}}}, \tag{D.5}$$

and

$$\tau_{\mathrm{TG}}(\theta_{\mathrm{TG}}) = M^0_{\mathrm{TG}} + M^{\max}_{\mathrm{TG}} \frac{\theta^2_{\mathrm{TG}}}{K^2_{\mathrm{TG}} + \theta^2_{\mathrm{TG}}}, \tag{D.6}$$

where $M^0_{(\cdot)}$ (min) is fixed and represents the basal gastric emptying time for an exogenous substrate, $M^{\max}_{(\cdot)}$ (min) is the maximal gastric emptying time, and $K_{(\cdot)}$ (mmol) is the half-emptying threshold in the gut. Our modification leads to a more physiological representation of substrate release into the peripheral circulation following the intake of a mixed meal compared to the initial model presented in Ref. [392]. In all of the above equations, t, τ_{GLC}, and τ_{TG} are expressed in minutes. We set $M^0_{\mathrm{GLC}} = 30$, $M^{\max}_{\mathrm{GLC}} = 60$, $M^0_{\mathrm{TG}} = 60$, and $M^{\max}_{\mathrm{TG}} = 120$, in accordance with Ref. [154].

D.1.2 Pancreatic hormones

The pancreas has a dual role in regulating macronutrient absorption and metabolism. It secretes digestive enzymes (exocrine function) and pancreatic hormones (endocrine function) [154]. Acinar cells, also known as exocrine cells, produce pancreatic juices containing

digestive enzymes like amylase, pancreatic lipase, and trypsinogen. Pancreatic hormones, on the other hand, are released in an endocrine manner—directly into the bloodstream. Endocrine cells aggregate to form the islets of Langerhans, making up only 1–2% of the entire organ. These islets resemble small, island-like structures within the exocrine pancreatic tissue [467]. The endocrine pancreas is a key contributor to blood glucose regulation by producing the hormones insulin and glucagon. While glucagon increases blood glucose levels, insulin acts to decrease them. Specialized cells, namely the glucagon-producing α-cells (15–20% of total islet cells) and insulin-producing β-cells (65–80% of total cells), are responsible for synthesizing these hormones [467]. In this model, there is no distinct pancreatic compartment; instead, the release and elimination of hormones from the plasma are described through phenomenological functions that capture the established relationships between plasma glucose levels and hormone concentrations (Figure D.1).

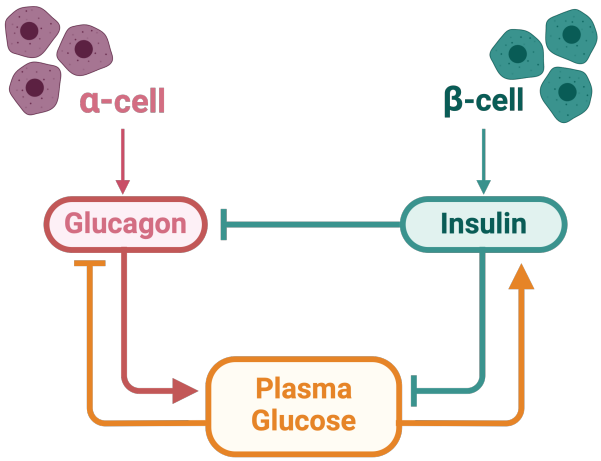

Figure D.1: Endocrine control of plasma glucose. Blunt arrows indicate inhibition, while pointed arrows indicate stimulation. Regarding the effects of insulin and glucagon on plasma glucose, arrows denote the signaling of glucose utilization (blunted arrows) or production (pointed arrows) by other organs. Created with BioRender.com.

Equations (D.7) and (D.8) below describe the dynamics of insulin and glucagon, respectively; together, they represent the pancreatic hormone responses.

$$\frac{\mathrm{d}C_I}{\mathrm{d}t} = k_I^0 + \psi(C_{a,\mathrm{GLC}}) \cdot V_{\max_I} \frac{C_{a,\mathrm{GLC}}^{n_1}}{K_{m_{\mathrm{GLC}}}^{n_1} + C_{a,\mathrm{GLC}}^{n_1}} - D \cdot C_I, \tag{D.7}$$

$$\frac{\mathrm{d}C_G}{\mathrm{d}t} = k_G^0 + \theta(C_{a,\mathrm{GLC}}) \cdot V_{\max_G} \frac{K_{i_{\mathrm{GLC}}}^{n_2}}{K_{i_{\mathrm{GLC}}}^{n_2} + C_{a,\mathrm{GLC}}^{n_2}} \cdot \frac{K_{i_I}^{n_3}}{K_{i_I}^{n_3} + C_I^{n_3}} - D \cdot C_G, \tag{D.8}$$

with

$$\psi(C_{a,\mathrm{GLC}}) = \begin{cases} 0 & C_{a,\mathrm{GLC}} < 2.5 \\ 1 - (C_{a,\mathrm{GLC}} - 7.5)^2/25 & 2.5 \leq C_{a,\mathrm{GLC}} \leq 7.5 \\ 1 & 7.5 < C_{a,\mathrm{GLC}} \end{cases} \tag{D.9}$$

and

$$\theta(C_{a,\mathrm{GLC}}) = \begin{cases} 1 & C_{a,\mathrm{GLC}} < 2.5 \\ 1 - (C_{a,\mathrm{GLC}} - 2.5)^2/25 & 2.5 \leq C_{a,\mathrm{GLC}} \leq 7.5 \\ 0 & 7.5 < C_{a,\mathrm{GLC}} \end{cases} \tag{D.10}$$

k_I^0 and k_G^0 represent the basal rates of insulin and glucagon secretion, respectively, while $V_{\mathrm{max,I}}$ and $V_{\mathrm{max,G}}$ represent the maximum rate coefficients. $K_{m,\mathrm{GLC}}$ is the glucose concentration at which half of $V_{\mathrm{max,I}}$ is achieved. Similarly, $K_{i,\mathrm{GLC}}$ and $K_{i,I}$ serve as inflection points for the glucose and insulin sigmoids, respectively. These values, known as inhibition constants, indicate the concentration required for half-maximum inhibition. The exponents n_1, n_2, and n_3 denote the slopes of the sigmoids, characterizing sensitivity of responses. D represents the disappearance rate of insulin and glucagon. The parameter values are sourced from literature or determined through fitting to experimental data (refer to Section D.2). Specifically, $K_{m,\mathrm{GLC}} = 7$ mM [154, 468], $K_{i,\mathrm{GLC}} = 20$ mM [469], $K_{i,I} = 90$ pM [470], $n_1 = 7$ [471], and $D = 0.1$ min^{-1} [472]. The remaining parameters—$k_I^0, k_G^0, V_{\mathrm{max,I}}, V_{\mathrm{max,G}}, n_2$, and n_3—are estimated from the available data [9, 12, 13].

These responses (Eqs (D.7) and (D.8)) are sigmoid functions that range between basal hormone secretion rates (k_I^0 and k_G^0) and maximal hormone secretion rates ($k_I^0 + V_{\mathrm{max,I}}$ and $k_G^0 + V_{\mathrm{max,G}}$). They monotonically increase with rising blood glucose levels for insulin (Eq (D.7)) and decrease for glucagon (Eq (D.8)). In terms of regulation, glucose stimulates insulin release while suppressing glucagon secretion [154]. Furthermore, recent work by Vergari et al. [470] indicates direct paracrine inhibition of glucagon secretion by insulin. The relationships between glucose and pancreatic hormones follow characteristic sigmoid dose–response curves [71, 154], which we modeled by a Michaelis-Menten-like hyperbolic functions. We assumed that the hormones degrade at a rate linearly proportional to their respective concentrations ($D \cdot C_I$ and $D \cdot C_G$). We introduced the terms $\theta(C_{a,\mathrm{GLC}})$ and $\psi(C_{a,\mathrm{GLC}})$ to capture the influence of glucose on maximum rate coefficients. Specifically, the $V_{\max}$ values for hormone secretion correlate with the prevailing glucose concentration [473]—$\psi(C_{a,\mathrm{GLC}})$ increases with glucose, while $\theta(C_{a,\mathrm{GLC}})$ decreases. Both are formulated to maintain a steady-state plasma glucose concentration of 5 mM [338].

D.1.3 Organ and tissue compartments

In the whole-body model, a spatially lumped capillary blood domain facilitates the exchange of nutrients and metabolic substrates with spatially lumped domains of tissue cells, each representing one of the modeled organs or tissues. Each organ compartment, except "other tissues", is characterized by a set of organ-specific metabolic reactions. Figure D.2 provides a comprehensive overview of all the metabolic pathways represented in our models, and Table D.2 delineates tissue-specific metabolic pathways.

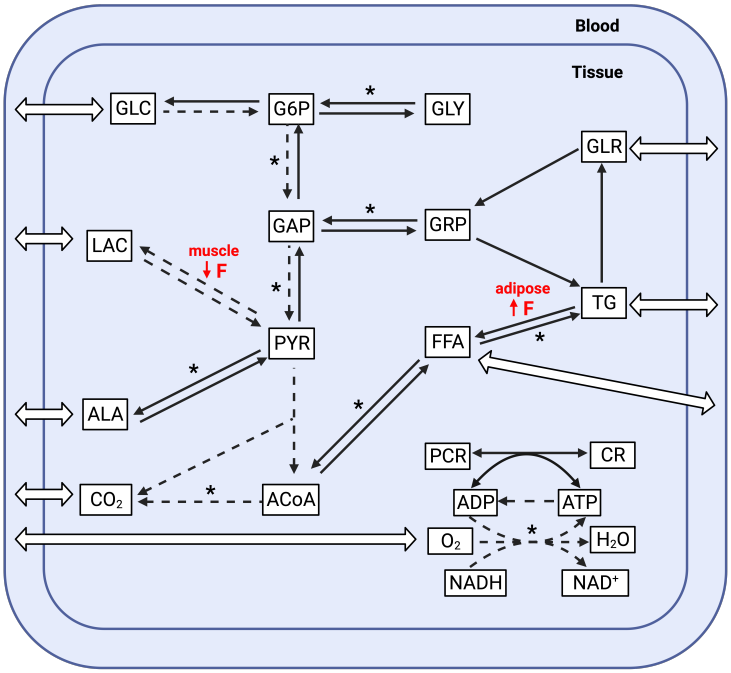

Figure D.2: Union map of all-organ metabolic pathways. 9 substrates are transported between blood and tissues (open arrows). Black arrows are tissue-specific pathways, whereas dashed arrows represent common pathways found in all tissues. Pathways marked with an asterisk (*) are composed of multiple reaction steps but grouped together as a single step in this model. Reaction rates in females that are significantly different from males at rest are marked by an arrow indicating the direction of change and the symbol F. Substrate abbreviations are listed in Table D.1. Figure reproduced from Abo et al. [3] with permission.

Table D.2: Map of tissue-specific metabolic pathways. A filled box means the existence of the corresponding pathway. In addition to the common pathways depicted in Fig. D.2, each tissue has its own different set of metabolic pathways. Table reproduced from Abo et al. [3] with permission.

Pathways	Brain	Heart	Skeletal muscle	GI tract	Liver	Adipose tissue
Gluconeogenesis I, II, III (PYR→GAP,GAP→G6P,G6P→GLC)					■	
Glycogenesis (G6P→GLY)	■	■	■		■	
Glycogenolysis (GLY→G6P)	■	■	■		■	
Fatty acid synthesis (ACoA→FFA)					■	
Fatty acid oxidation (FFA→ACoA)		■	■		■	■
Lipolysis (TG→FFA+GLR)		■	■	■	■	■
TG synthesis (FFA+GRP→TG)		■	■	■	■	■
Glycerol phosphorylation (GLR→GRP)		■	■		■	
GAP reduction (GAP→GRP)						■
GRP oxidation (GRP→GAP)					■	
Alanine breakdown (ALA→PYR)					■	
Alanine synthesis (PYR→ALA)			■			
PCR breakdown (PCR→CR)	■	■	■	■		
PCR synthesis (CR→PCR)	■	■	■	■		

The general form of the mass balance equation for chemical species i in tissue x is

$$V_x \frac{\mathrm{d}C_{x,i}}{\mathrm{d}t} = P_{x,i} - U_{x,i} + Q_x(C_{a,i} - \sigma_{x,i}C_{x,i}), \tag{D.11}$$

where V_x is a constant parameter representing the volume of tissue x. The terms $P_{x,i}$ and $U_{x,i}$ denote the production and utilization rates of substrate i in tissue x, respectively. Q_x is fixed and corresponds to the blood flow to tissue x, while $C_{a,i}$ and $C_{x,i}$ represent the arterial and tissue concentrations of substrate i respectively. The parameter $\sigma_{x,i}$ denotes the

partition coefficient of substrate i, which remains fixed and reflects the relative distribution of metabolites between blood and tissues at rest. The first two terms on the right side of Eq (D.11) express the net metabolic reaction rate of substrate i in tissue x. The third term, $Q_x(C_{a,i} - \sigma_{x,i}C_{x,i})$, is the net rate of absorption or release of substrate i in tissue x. It is worth noting that only 9 substrates (substrates 1 to 9 in Table D.1) are transported between blood and tissue.

In the absorptive period following a meal rich in carbohydrates or fats, hyperglycemia and/or hypertriglyceridemia may occur. Hyperglycemia is typically defined by blood glucose levels exceeding 6.1 mM [468], while hypertriglyceridemia is indicated by blood TG levels surpassing 2 mM [154]. Hyperglycemia plays a role in stimulating glucose uptake by splanchnic (liver and GI tract) and peripheral (mainly skeletal muscle) tissues. Liver cells are primarily equipped with the GLUT-2 glucose transporter, which does not respond to insulin. This implies that the rate and direction of glucose movement across the hepatocyte membrane depend on the relative concentrations of glucose inside and outside the cell. In skeletal muscle, glucose uptake is predominantly mediated by the insulin-sensitive glucose transporter, GLUT4. The conventional expectation is that hyperinsulinemia follows hyperglycemia, leading to the stimulation of glucose uptake. This occurs through an increase in the number of GLUT4 transporters at the cell membrane and enhanced disposal of glucose within the cell [154]. However, it is noteworthy that hyperglycemia, even in the absence of hyperinsulinemia, independently stimulates muscle glucose uptake [474]. To enhance the model's ability for maintaining glucose homeostasis under different metabolic conditions, we assume that glucose uptake into the liver and skeletal muscle is stimulated by hyperglycemia, regardless of whether it is coupled with hyperinsulinemia or not. In these organs, the partition coefficient for glucose, which modulates the organ's capacity for uptake or release of glucose, is a dynamic parameter

$$\sigma_{x,\mathrm{GLC}} = \sigma^0_{x,\mathrm{GLC}}\left(1 - \frac{1}{1+\exp\{-2(C_{a,\mathrm{GLC}} - 9)\}}\right), \quad C_{a,\mathrm{GLC}} > 6.1\mathrm{mM} \tag{D.12}$$

and $\sigma_{x,\mathrm{GLC}} = \sigma^0_{x,\mathrm{GLC}}$, otherwise. In this equation, x denotes the liver or skeletal muscle, and $\sigma^0_{x,\mathrm{GLC}}$ represents the partition coefficient under normal glucose levels. The slope of the sigmoid is set to 2 to simulate the rapid clearance of glucose during hyperglycemia, in line with expectations for healthy individuals [154, 468]. The inflection point of the sigmoid is chosen as 9 so that glucose levels above 6.1 mM start to elicit a response. Similarly, in the fed state, adipose tissue serves as the primary site for the uptake of dietary TG. Therefore, during postabsorptive hypertriglyceridemia, we assume that the influx of TG into adipose

tissue is modulated as follows:

$$\sigma_{x,\mathrm{TG}} = \sigma^0_{x,\mathrm{TG}} \left(1 - \frac{1}{1 + \exp\{-2(C_{a,\mathrm{TG}} - 4)\}} \right), \quad C_{a,\mathrm{TG}} > 2\mathrm{mM} \tag{D.13}$$

where x represents adipose tissue, and $\sigma^0_{x,\mathrm{TG}}$ denotes the partition coefficient under normal TG levels. In this case as well, the slope of the sigmoid is set to 2, and the inflection point is chosen so that TG levels above 2 mM initiate a response. For the remaining substrates (substrates 10 to 22 in Table D.1), which exist exclusively within tissues, the net metabolic rate is

$$V_x \frac{\mathrm{d}C_{x,i}}{\mathrm{d}t} = P_{x,i} - U_{x,i}. \tag{D.14}$$

Production and utilization rates encompass all contributing metabolic reactions, formulated as:

$$P_{x,i} - U_{x,i} = \sum_{k=1}^{m} \gamma_{s_k \to s_i} \phi_{x,s_k \to s_i} - \sum_{k=1}^{n} \gamma_{s_i \to s_k} \phi_{x,s_i \to s_k}. \tag{D.15}$$

Here, $\phi_{x,s_k \to s_i}$ denotes the rate at which substrate s_k is utilized to form substrate s_i in tissue x, and vice versa for $\phi_{x,s_i \to s_k}$. The constants $\gamma_{(\cdot)}$ represent the respective stoichiometric coefficients. m refers to the number of processes forming substrate i, while n is the number of processes consuming substrate i.

D.1.4 Basal metabolic reaction rate

Biochemical reactions *in vivo* are intricate metabolic processes that encompass multiple reaction steps. Our modelling approach follows a top-down systems perspective [66, 68, 72] and characterizes biochemical reactions as aggregate 'pseudo' processes by stoichiometrically combining several elementary reactions (Figure D.2). Many lumped reactions are considered irreversible, reflecting the tendency of corresponding regulatory enzymes *in vivo* to have large equilibrium constants favoring product formation [72]. As part of our modelling framework, reversible reactions, such as the one involving the enzyme lactate dehydrogenase (LDH) where lactate is synthesized from pyruvate and can also be converted back to pyruvate, are deconstructed into two irreversible reactions. Consequently, all lumped reactions are treated as specific instances of a general irreversible, uni-uni (or bi-bi when two reactants are involved) substrate to product enzymatic reaction. Each reaction also includes the metabolic controller pairs ATP:ADP and NADH:NAD^+, whose

ratios are known to regulate reaction fluxes [72].

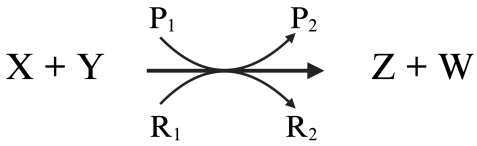

(D.16)

In this context, P_1 and P_2 denote ATP and ADP or vice versa, representing the phosphorylation state, while R_1 and R_2 stand for NADH and NAD^+ or vice versa, indicating the redox state.

Rates of utilization ($\phi_{x,s_i \to s_k}$) for any substrate s_i in tissue x vary based on the substrate concentration $C_{x,i}$, unless otherwise specified, as well as on the phosphorylation state (PS) and the redox state (RS). As a general reaction, reactants X and Y and products Z and W are considered. The corresponding reaction rate equation in tissue x is:

$$\begin{aligned}\phi_{x,X\text{–}Y\to Z\text{–}W} = V_{\max,x,X\text{–}Y\to Z\text{–}W} \left(\frac{\frac{C_X}{K_X} \cdot \frac{C_Y}{K_Y}}{1 + \frac{C_X}{K_X} + \frac{C_Y}{K_Y} + \frac{C_X}{K_X} \cdot \frac{C_Y}{K_Y}} \right) \\ \times \left(\frac{\mathrm{PS}^{\pm}}{\mu^{\pm} + \mathrm{PS}^{\pm}} \right) \left(\frac{\mathrm{RS}^{\pm}}{\nu^{\pm} + \mathrm{RS}^{\pm}} \right)\end{aligned} \tag{D.17}$$

where $V_{\max,x,X\text{–}Y\to Z\text{–}W}$, K_X, and K_Y represent phenomenological maximum rate coefficients and Michaelis parameters specific to the reaction process. C_X and C_Y denote the concentrations of substrate X and Y in tissue x. The phosphorylation states are $\mathrm{PS}^+ = C_{\mathrm{ATP}}/C_{\mathrm{ADP}}$ in the forward direction and $\mathrm{PS}^- = C_{\mathrm{ADP}}/C_{\mathrm{ATP}}$ in the opposite direction. Similarly, redox states are denoted as $\mathrm{RS}^+ = C_{\mathrm{NADH}}/C_{\mathrm{NAD^+}}$ and $\mathrm{RS}^- = C_{\mathrm{NAD^+}}/C_{\mathrm{NADH}}$. Parameters $\mu^{\pm}$ and $\nu^{\pm}$ are associated with the energy controller pairs.

It is noteworthy that AMP acts as a crucial allosteric regulator of glycogen phosphorylase for glycogenolysis (GLY→G6P) and phosphofructokinase-1 (PFK-1) for glycolysis II (G6P→GAP). Since AMP is not explicitly included in this model, AMP/ATP is approximated by $[ADP/ATP]^2$ in these reactions (see Table D.18). The maximum rate coefficients, Michaelis parameters, $\mu^{\pm}$ and $\nu^{\pm}$ values, along with in-tissue substrate concentrations, are sourced from Ref. [3] and the references therein.

D.1.5 Metabolic response to eating

Postprandial metabolism and nutrient storage. Following a mixed meal, glucose concentrations in the systemic circulation typically increase within less than 30 minutes.

However, it takes a longer interval, approximately 3-4 hours, to observe rises in blood fat levels [154]. The process of nutrient absorption is facilitated by a rapid increase in the insulin/glucagon ratio, which strongly influences postprandial metabolism [475, 476]. In healthy individuals, glucagon is suppressed after mixed meal or glucose ingestion, while insulin increases by at least an order of magnitude [9, 154, 477]. We thus simplified our approach by using insulin alone instead of the insulin-to-glucagon ratio as our metabolic signal from blood to tissues. Consequently, we define insulin-regulated enzyme activity factors, which are determined by plasma insulin concentration and vary for each organ:

$$\mathrm{B}_x = V^x_{\max_\beta} \frac{C_I^n}{\mathrm{K}^{x^n}_{m_\beta} + C_I^n}, \tag{D.18}$$

and

$$\Gamma_x = V^x_{\max_\gamma} \frac{C_I^k}{\mathrm{K}^{x^k}_{m_\gamma} + C_I^k}, \tag{D.19}$$

where activation by insulin is denoted by B_x and inhibition by insulin is denoted by Γ_x. B_x and Γ_x are functions of insulin that are independent of substrate i. The subscript x denotes the different organs and tissues. The parameters $V^x_{\max_\beta}$ and $V^x_{\max_\gamma}$ represent maximum rate coefficients, $\mathrm{K}^x_{m_\beta}$ and $\mathrm{K}^x_{m_\gamma}$ represent Michaelis parameters, n and k are hill coefficients modulating the strength of the response. For a given reaction, the maximum rate coefficient $V_{\max,x,i}$, characterizing the metabolic flux i in tissue x (see Eq D.17), is modulated by insulin activity factors as follows:

$$V_{\max,x,i} = V^0_{\max,x,i}\big(1 + \mathrm{B}_x - \Gamma_x\big). \tag{D.20}$$

$V^0_{\max,x,i}$ represents basal maximum rate coefficients (constants), while $V_{\max,x,i}$ represents dynamic maximum rate coefficients regulated by insulin, influencing metabolic rates via Eq (D.17). We note that for $V_{\max,x,i}$ to assume physiological values (> 0), $1 + \mathrm{B}_x > \Gamma_x$ with $\mathrm{B}_x, \Gamma_x \geq 0$. We also note that K_m values are chosen 'large enough' compared to (i.e., same order of magnitude as) postprandial insulin concentrations. As such, $\mathrm{B}_x \approx 0$ and $\Gamma_x \approx 0$ when insulin returns to basal pre-meal levels. Table D.3 lists the reactions modulated by insulin, along with the corresponding affected organs. Frayn [154] qualitatively described the enzymes and reactions affected by insulin. Consequently, we introduced insulin-regulated enzyme activity factors that modulate the production rates of the reactions outlined in Table D.3.

Postabsorptive metabolism and nutrient mobilization. The term "postabsorptive state" implies that all contents of the previous meal have been absorbed from the GI

Table D.3: Reactions affected by pancreatic hormones during the postprandial phase

Hormone	Effect	Reaction #	Reaction	Affected organs
Insulin	↑	1	Glycolysis I	H, M, G, L, A
	↑	2	Glycolysis II	H, M, G, L, A
	↑	3	Glycolysis III	H, M, G, L, A
	↑	7	Glycogenesis	H, M, L
	↑	16	Pyruvate oxidation	A, M, L
	↑	18	Fatty acids synthesis	L
	↑	20	TG synthesis	L, A
	↓	4	Gluconeogenesis I	L
	↓	5	Gluconeogenesis II	L
	↓	6	Gluconeogenesis III	L
	↓	8	Glycogenolysis	M, L
	↓	19	Lipolysis	G, A

Symbols H, M, G, L, A denote heart, skeletal muscle, GI tract, liver, and adipose tissue, respectively. (↑) signifies activation, while (↓) signifies inhibition. The qualitative effects of insulin on reaction rates are discussed in the works of Frayn [154] (chapters 5 and 7) and Kurata [66]. Additional information regarding the reactions and relevant metabolites can be found in Table D.1.

tract, and that not much time has passed, as signs of starvation would otherwise appear. In the postabsorptive state, the blood glucose concentration usually hovers slightly below 5 mM. The concentration of insulin in plasma returns to basal values, which can vary widely among individuals but is typically around 60 pM. The concentration of glucagon also returns to basal values, approximately 20–30 pM [154]. Since insulin and glucagon concentrations are of comparable magnitudes, we employ the well-known glucagon/insulin ratio (GIR) and define the GIR-regulated enzyme activity factors that are active during the postabsorptive phase. This ratio correlates with metabolic changes during the postabsorptive phase [475].

$$\mathrm{B}_x^{\mathrm{fat}} = V^x_{\max_{\beta,\mathrm{fat}}} \frac{\mathrm{GIR}^m}{\mathrm{K}^{x^m}_{m_{\beta,\mathrm{fat}}} + \mathrm{GIR}^m}, \tag{D.21}$$

and

$$\Gamma_x^{\text{fat}} = V^x_{\max_{\gamma,\text{fat}}} \frac{\text{GIR}^q}{\text{K}^{x^q}_{m_{\gamma,\text{fat}}} + \text{GIR}^q}, \tag{D.22}$$

where activation by GIR is modulated by B_x^{fat} and inhibition by GIR is modulated by Γ_x^{fat}. The subscript x denotes the different organs and tissues. The parameters $V^x_{\max_{\beta,\text{fat}}}$, $V^x_{\max_{\gamma,\text{fat}}}$, $\text{K}^x_{m_{\beta,\text{fat}}}$, $\text{K}^x_{m_{\gamma,\text{fat}}}$, and exponents m and q are defined as before (see Eqs (D.18)-(D.19)). For a given reaction, the maximum rate coefficient $V_{\max,x,i}$ is modulated by GIR-regulated enzyme activity factors as follows:

$$V_{\max,x,i} = V^0_{\max,x,i}\big(1 + \text{B}_x^{\text{fat}} - \Gamma_x^{\text{fat}}\big). \tag{D.23}$$

Here too, $V_{\max,x,i}$ assumes physiological values (> 0) when $1+\text{B}_x^{\text{fat}} > \Gamma_x^{\text{fat}}$ with $\text{B}_x^{\text{fat}}, \Gamma_x^{\text{fat}} \geq 0$. We note that $\text{B}_x^{\text{fat}} \approx 0$ and $\Gamma_x^{\text{fat}} \approx 0$ during the postprandial phase because GIR ≈ 0, i.e., $C_I \gg C_G$. Table D.4 contains the reactions that are affected by insulin and glucagon, as well as which organ is affected.

Notably, skeletal muscle and cardiac cells lack glucagon receptors [347], but reduced insulin levels can signal metabolic pathways in these organs during the postabsorptive phase [478]. Thus, during the postabsorptive phase, the heart and skeletal muscle solely respond to an insulin signal:

$$\text{B}^{\text{fat}}_{\{M,H\}} = \rho(C_{a,\text{GLC}}) \cdot V^{\{M,H\}}_{\max_{\beta,\text{fat}}} \frac{C_I^m}{\text{K}^{\{M,H\}^m}_{m_{\beta,\text{fat}}} + C_I^m}, \tag{D.24}$$

and

$$\Gamma^{\text{fat}}_{\{M,H\}} = \rho(C_{a,\text{GLC}}) \cdot V^{\{M,H\}}_{\max_{\gamma,\text{fat}}} \frac{C_I^q}{\text{K}^{\{M,H\}^q}_{m_{\gamma,\text{fat}}} + C_I^q}, \tag{D.25}$$

where

$$\rho(C_{a,\text{GLC}}) = 1 - \frac{1}{1 + \exp\{-4(C_{a,\text{GLC}} - 4.4)\}}. \tag{D.26}$$

The logistic sigmoid function, denoted as $\rho(C_{a,\text{GLC}})$, serves as a switch governing the activation and deactivation of postabsorptive insulin-regulated enzyme activity factors in skeletal muscle and heart. It is based on blood glucose levels. The threshold defining the shift from normoglycemia to hypoglycemia is established at 4.4 mM, as specified by Berger and Zdzieblo [468]. This value is utilized to determine the initiation of the postabsorptive phase in these organs. It is noteworthy that $\rho(C_{a,\text{GLC}})$ approaches 0 during the postprandial phase when $C_{a,\text{GLC}} > 4.4$ mM, and so is only activated during the postabsorptive phase.

The slope, set to -4, ensures a rapid shift from activation ($\rho(C_{a,\mathrm{GLC}}) \approx 1$) to deactivation ($\rho(C_{a,\mathrm{GLC}}) \approx 0$) even with slight deviations of $C_{a,\mathrm{GLC}}$ above 4.4 mM. This modelling decision is influenced by the observation that skeletal myocytes can directly sense extracellular glucose concentrations, activating a signaling pathway for hormone-independent metabolic activation. This glucose sensing pathway acts in concert with insulin to enhance muscle glucose utilization, contributing to the maintenance of systemic glucose homeostasis [475, 479]. Table D.4 lists the reactions in skeletal muscle and heart that are affected by insulin during the postabsorptive phase.

Table D.4: Reactions affected by pancreatic hormones during the postabsorptive phase

Hormone	Effect	Reaction #	Reaction	Affected organs
Insulin	↑	8	Glycogenolysis	M
	↑	14	Alanine formation	M
	↑	16	Pyruvate oxidation	M
	↑	17	Fatty acids oxidation	H, M
	↓	7	Glycogenesis	M
Glucagon	↑	4	Gluconeogenesis I	L
	↑	5	Gluconeogenesis II	L
	↑	6	Gluconeogenesis III	L
	↑	8	Glycogenolysis	L
	↑	10	Lactate oxidation	L
	↑	15	Alanine utilization	L
	↑	16	Pyruvate oxidation	L
	↑	17	Fatty acids oxidation	L
	↓	7	Glycogenesis	L
	↓	9	Pyruvate reduction	L

Symbols H, M, L, denote heart, skeletal muscle, and liver, respectively. (↑) signifies activation, while (↓) signifies inhibition. The qualitative effects of insulin and glucagon on reaction rates are discussed in the works of Frayn [154] (chapters 5 and 7), Sandoval and D'Alessio [389], Adeva-Andany et al. [480], and Kurata [66]. Additional information regarding the reactions and relevant metabolites can be found in Table D.1.

D.1.6 Virtual subjects

We consider lean, healthy male and female subjects. Table D.5 provides details regarding physical attributes, including tissue weights and basal blood flows.

Male: 70 Kg body weight, aged between 20 and 35 years. Regarding body composition, skeletal muscle constitutes 40% of the total body weight, and adipose tissue accounts for 16%. In the initial conditions for each simulation, the subject is in a state of overnight fast (8-12 h), with a cardiac output of 5.5 l/min and a resting RQ of 0.8.

Female: 58 Kg body weight, aged between 20 and 35 years. Regarding body composition, skeletal muscle constitutes 30% of the total body weight, and adipose tissue accounts for 29.5%. In the initial conditions for each simulation, the subject is in a state of overnight fast (8-12 h), with a cardiac output of 5 l/min and a resting RQ of 0.8.

D.2 Parameter estimation

While the qualitative effects of insulin and glucagon are known (Tables D.3-D.4), the specific parameters governing insulin- and glucagon-induced metabolic regulation remain less established. We conducted parameter estimations based on experimental data [9, 10, 12, 13] and reference ranges from literature sources (Table D.6). The parameter values for simulating the metabolism of a healthy adult (either male or female) in an overnight fasted condition are detailed in our prior work [3] and are also accessible in Tables D.8–D.16. Parameters associated with metabolic changes in response to feeding and subsequent fasting, as outlined in Table 7.1, were estimated using *fmincon*, a gradient-based constrained optimization algorithm commonly known as *constrained nonlinear optimization* or *nonlinear programming*. This algorithm was applied to minimize the difference between model-predicted concentrations and concentration data over 6 to 10 hours following various mixed meals.

Let p_0 denote the initial guess set for model parameters. For parameters associated with in-tissue regulation by insulin and glucagon (Eqs (D.18)–(D.25)), the maximum rate coefficients ($V^x_{\max}$) for enzyme activity factors are fixed at 1. The Michaelis constants (K^x_m) are set to the midpoint of the reference range obtained from the literature, while the hill coefficients (n^x) are set to 1. Concerning the dynamics of plasma insulin and glucagon (Eqs (D.7)–(D.8)), the maximum rate coefficients ($V_{\max_I}$, $V_{\max_G}$), basal secretion rates

Table D.5: Physical characteristics

	Male		Female		References
Tissue/Organ	Weight (Kg)	Volume (L)†	Weight (Kg)	Volume (L)†	
Brain	1.40	1.35	1.20	1.15	[70, 331, 332]
Heart	0.331	0.315	0.253	0.241	[70, 331, 333]
Skeletal muscle	22.4[a]	21.33	13.6[a]	12.95	[70, 331, 333]
GI tract	2.0	1.89	2.0	1.89	[68, 70, 333]
Liver	1.80	1.67	1.40	1.30	[70, 331, 334]
Adipose tissue	11.0[b]	11.9	17.1[c]	18.5	[68, 70, 331, 333]
Others[d]	31.069	29.59	22.447	21.38	[335]
Whole-body	70.0	68.045	58.0	57.411	[70, 331]
Blood flow (l/min)[e]					
Brain	0.75		0.75		
Heart	0.25		0.25		
Skeletal muscle	0.9		0.9		
GI tract	1.1		1.1		
Liver	1.50		1.35		[336]
Adipose tissue	0.36		0.36		
Others[d]	1.74		1.39		
Whole-body	5.5		5.0		[70, 337]

[a] Skeletal muscles, excluding upper extremities which account for 18-20% of total weight. Male total: 28 Kg; female total: 17 Kg.
[b] Based on 16% body fat content.
[c] Based on 29.5% body fat content.
[d] Values for "Others" are chosen to balance whole-body values.
[e] Unless otherwise noted, regional blood flows are assumed to be the same between sexes. Values are reproduced from Ref. [3].
† Organ volumes are calculated by dividing each tissue weight by its density: brain (1.04 Kg/L)[332], heart and skeletal muscle (1.05 Kg/L)[333], GI tract (1.06 Kg/L)[333], liver (1.08 Kg/L)[334], adipose tissue (0.923 Kg/L)[333]. Assuming that *others* include only nonfat tissues, a tissue density of 1.05 Kg/L is used [335]. The total volume of the body is calculated by adding the volumes of all compartments.

(k_I^0, k_G^0), and hill coefficients (n_2, n_3) are uniformly set to 1. Regarding dietary influx (Eqs (D.5)–(D.6)), the half-emptying gut thresholds for glucose (K_{GLC}) and TG (K_{TG}) are fixed at half the values of the average daily intake of macronutrients, as outlined in the literature. Reference ranges are elaborated in Table D.6.

We then established a set of lower (lb) and upper (ub) bounds for the free variables in p_0, ensuring that the solution remains within the range lb $\leq p_0 \leq$ ub. Hill coefficients are confined to the range of 1 to 4, unless specific evidence suggests otherwise, given that cooperative binding and allosteric enzymatic processes seldom produce Hill coefficients exceeding 4 [481]. All half-maximum constants (K_m^x, K_{GLC}, and K_{TG}) have lb = min(range)/2 and ub = max(range) $\times$ 2. We opted not to strictly adhere to experimental ranges to accommodate variability between experiments and acknowledge that many reactions are modeled as 'pseudo' processes through stoichiometric combinations of several elementary reactions (Figure D.2). Maximum rate coefficients ($\mathrm{V}_{\mathrm{max}}^x$, $\mathrm{V}_{\mathrm{max}_I}$, $\mathrm{V}_{\mathrm{max}_G}$) are restricted between 0 and 100 when modelling the activation of a reaction and between 0 and 1 when modelling the inhibition of a reaction. The latter constraint arises from the equation form for inhibition (see Eqs D.20 and D.23). Model equations are solved using *ode15s* (MATLAB 2021a), a variable-step, variable-order solver ranging from orders 1 to 5. This solver is an implicit integration algorithm designed for stiff systems.

For a given substrate (or hormone) s, consider the weighted residuals:

$$\epsilon_s^2 = \sum_{i=1}^{N_s} \frac{\left(y_{s,i} - \hat{y}_{s,i}(\boldsymbol{\theta})\right)^2}{\sigma_{s,i}^2}, \tag{D.27}$$

where $y_{s,i}$ represents the measured data point i for substrate (or hormone) s, $\sigma_{s,i}$ denotes the corresponding experimental standard error, N_s signifies the total number of data points for substrate s, and $\hat{y}_{s,i}(\boldsymbol{\theta})$ is the predicted value given the set of parameters $\boldsymbol{\theta}$. Consequently, we aim to minimize a problem specified by

$$\min_{\boldsymbol{\theta}} f(\boldsymbol{\theta}) = \sum_{s \in S} \epsilon_s^2 \quad \text{subject to lb} \leq \boldsymbol{\theta} \leq \text{ub} \tag{D.28}$$

Set $S = \{$insulin, glucagon, GLC, LAC, TG, FFA, GLR, $\mathrm{GLY_M}$, $\mathrm{GLY_L}\}$ specifically for the male model. The subscripts M and L correspond to skeletal muscle and liver, respectively. Substrate abbreviations are outlined in Table D.1. The data represent plasma concentrations of hormones and substrates and are detailed in Table D.7. We utilized time series data reflecting dynamic concentrations following single meals of various compositions spanning 6 to 10 hours post food intake. All datasets were concurrently employed for parameter estimation. A comprehensive list of estimated parameters is provided in Table D.6.

Table D.6: Estimated model parameters

Organ	Parameters	Range
Insulin	$k_I^0 = 1.8$	— pM/min
	$\mathrm{V}_{\mathrm{max}_I} = 62$	— pM/min
	$\mathrm{K}_{m_{\mathrm{GLC}}} = 7$	7–20 mM [154, 468]
	$n_1 = 7$	4.6–8.4 [471]
Glucagon	$k_G^0 = 0.5$	— pM/min
	$\mathrm{V}_{\mathrm{max}_G} = 5.4$	— pM/min
	$\mathrm{K}_{i_{\mathrm{GLC}}} = 20$	4–20 mM [469]
	$\mathrm{K}_{i_I} = 90$	$\sim$ 100 pM [470]
	$n_2 = 4$	unitless
	$n_3 = 4$	unitless
Heart	$\mathrm{V}^{\mathrm{H}}_{\mathrm{max}_\beta} = 2$	— mmol/min
	$\mathrm{K}^{\mathrm{H}}_{m_\beta} = 350$	348-720 mM [482]
	$n_1^{\mathrm{H}} = 4$	unitless
	$\mathrm{V}^{\mathrm{H}}_{\mathrm{max}_{\beta,\mathrm{fat}}} = 8$	— mmol/min
	$\mathrm{K}^{\mathrm{H}}_{m_{\beta,\mathrm{fat}}} = 9$	6-70 mM [483, 484]
	$n_2^{\mathrm{H}} = 2$	unitless
Muscle	$\mathrm{V}^{\mathrm{M}}_{\mathrm{max}_\beta} = 18$	— mmol/min
	$\mathrm{K}^{\mathrm{M}}_{m_\beta} = 250$	348-720 mM [482]
	$n^{\mathrm{M}} = 2$	unitless
	$\mathrm{V}^{\mathrm{M}}_{\mathrm{max}_{\beta 2}} = 1.8$	— mmol/min
	$\mathrm{K}^{\mathrm{M}}_{m_{\beta 2}} = 250$	348-720 mM [482]
	$\mathrm{V}^{\mathrm{M}}_{\mathrm{max}_\gamma} = 1$	— mmol/min
	$\mathrm{K}^{\mathrm{M}}_{m_\gamma} = 120$	348-720 mM [482]
	$\mathrm{V}^{\mathrm{M}}_{\mathrm{max}_{\beta,\mathrm{fat}}} = 2$	— mmol/min
	$\mathrm{K}^{\mathrm{M}}_{m_{\beta,\mathrm{fat}}} = 12$	6-70 mM [483, 484]
	$\mathrm{V}^{\mathrm{M}}_{\mathrm{max}_{\beta,\mathrm{fat2}}} = 10$	— mmol/min
	$\mathrm{K}^{\mathrm{M}}_{m_{\beta,\mathrm{fat2}}} = 15$	6-70 mM [483, 484]
	$\mathrm{V}^{\mathrm{M}}_{\mathrm{max}_{\gamma,\mathrm{fat}}} = 1$	— mmol/min
	$\mathrm{K}^{\mathrm{M}}_{m_{\gamma,\mathrm{fat}}} = 10$	6-70 mM [483, 484]

Organ	Parameters	Range
Adipose	$\mathrm{V}^{\mathrm{A}}_{\mathrm{max}_\beta} = 5$	— mmol/min
	$\mathrm{K}^{\mathrm{A}}_{m_\beta} = 400$	348-720 mM [482]
	$n_1^{\mathrm{A}} = 3$	unitless
	$\mathrm{V}^{\mathrm{A}}_{\mathrm{max}_{\beta 2}} = 17$	— mmol/min
	$\mathrm{K}^{\mathrm{A}}_{m_{\beta 2}} = 80^{\mathrm{a}}$	348-720 mM [482]
	$n_2^{\mathrm{A}} = 2$	unitless
	$\mathrm{V}^{\mathrm{A}}_{\mathrm{max}_\gamma} = 1$	— mmol/min
	$\mathrm{K}^{\mathrm{A}}_{m_\gamma} = 130$	42-160 mM [482, 483]
	$n_3^{\mathrm{A}} = 4$	unitless
GI Tract	$\mathrm{V}^{\mathrm{G}}_{\mathrm{max}_\beta} = 2$	— mmol/min
	$\mathrm{K}^{\mathrm{G}}_{m_\beta} = 480$	348-720 mM [482]
	$n^{\mathrm{G}} = 4$	unitless
	$\mathrm{V}^{\mathrm{G}}_{\mathrm{max}_\gamma} = 1$	— mmol/min
	$\mathrm{K}^{\mathrm{G}}_{m_\gamma} = 280$	42-160 mM [482, 483]
Liver	$\mathrm{V}^{\mathrm{L}}_{\mathrm{max}_\beta} = 22$	— mmol/min
	$\mathrm{K}^{\mathrm{L}}_{m_\beta} = 350$	348-720 mM [482]
	$n^{\mathrm{L}} = 2$	unitless
	$\mathrm{V}^{\mathrm{L}}_{\mathrm{max}_{\beta 2}} = 38$	— mmol/min
	$\mathrm{K}^{\mathrm{L}}_{m_{\beta 2}} = 350$	348-720 mM [482]
	$\mathrm{V}^{\mathrm{L}}_{\mathrm{max}_{\beta 3}} = 2.2$	— mmol/min
	$\mathrm{K}^{\mathrm{L}}_{m_{\beta 3}} = 350$	348-720 mM [482]
	$\mathrm{V}^{\mathrm{L}}_{\mathrm{max}_\gamma} = 1$	— mmol/min
	$\mathrm{K}^{\mathrm{L}}_{m_\gamma} = 90$	120-300 mM [482]
	$\mathrm{V}^{\mathrm{L}}_{\mathrm{max}_{\beta,\mathrm{fat}}} = 2$	— mmol/min
	$\mathrm{K}^{\mathrm{L}}_{m_{\beta,\mathrm{fat}}} = 1^{\mathrm{b}}$	0.4–6 [10, 482, 484]
	$\mathrm{V}^{\mathrm{L}}_{\mathrm{max}_{\beta,\mathrm{fat2}}} = 10$	— mmol/min
	$\mathrm{K}^{\mathrm{M}}_{m_{\beta,\mathrm{fat2}}} = 0.6^{\mathrm{b}}$	0.4–6 [10, 482, 484]
	$\mathrm{V}^{\mathrm{L}}_{\mathrm{max}_{\gamma,\mathrm{fat}}} = 1$	— mmol/min
	$\mathrm{K}^{\mathrm{L}}_{m_{\gamma,\mathrm{fat}}} = 2^{\mathrm{b}}$	0.4–6 [10, 482, 484]
Dietary	$K_G{}^{\mathrm{c}}$	0-1667 mmol [154]
influx	$K_T{}^{\mathrm{d}}$	0-117 mmol [154]

[a] This value was manually curated to reproduce experimental data.
[b] These values are dimensionless, representing the Michaelis constants for GIR-regulated enzyme activity factors, where GIR itself is dimensionless, denoting the ratio of glucagon to insulin. The estimated range of values is derived from experimental data. Resting glucagon concentrations typically fall between 27 and 36.5 pM [10]. Considering the reference range for insulin (6-70 pM) [482, 484], the broadest interval for GIR is $[27/70, 36.5/6]$.
[c] The average daily intake of carbohydrates is $\sim$ 300g. The molecular mass of glucose is 0.18 mmol/g [154]. Assuming that all ingested carbohydrates are digestible and eventually converted to glucose, we derived the upper bound by converting g to mmol.
[d] The average daily intake of fat is $\sim$ 100g. The molecular mass of fat is 0.85 mmol/g [154]. Assuming that all ingested fats, in the form of neutral fats or triglycerides, we derived the upper bound by converting g to mmol.

Table D.7: Experimental data used for parameter estimation and model validation

Experiment	Subjects		Meal		Observables		
	Sex	Age	CHO	Fat	Substrates	# points	Time frame
Frayn et al. [9]	5M/3F	29–64	96g	33g	GLC	9	0–360 mins
					LAC	9	
					FFA	9	
					INS	9	
Coppack et al. [13]	3M/4F	30–35	96g	33g	LAC	9	0–360 mins
					GLR	9	
					TG	9	
Taylor et al. [12]	4M/4F	23–27	289g	45g	GLY_M	10	0–420 mins
Taylor et al. [10]	6M/2F	18–40	139g	17g	GLY_L	9	0–560 mins
Taylor et al. [10][a]	6M/2F	18–40	139g	17g	GLC	17/22[b]	0–600 mins
					INS		
Hansen et al. [11][a]	10M	21–27	58g	27.7g	GLC	15	0–600 mins
					INS		

Sex is male (M) or female (F); Age is in years; CHO, carbohydrates. INS: insulin; GLC: glucose, LAC: lactate, GLR: glycerol; FFA: free fatty acids; TG: triglycerides; GLY, glycogen. The subscripts M and L denote skeletal muscle and liver, respectively. Meal uptake occurs at $t = 0$.
[a] Data employed for validating the male model, while all other datasets were utilized in the process of parameter estimation.
[b] 17 data points for insulin and 22 data points for glucose.

D.3 Model parameters

Table D.8: Physical characteristics

	Male		Female	
Organ/Tissue	Blood flow (l/min)	Weight (Kg)	Blood flow (l/min)	Weight (Kg)
Brain	0.75[455]	1.4[70, 331]	0.75	1.2[70, 331]
Heart	0.25	0.331[70, 331]	0.25	0.253[70, 331]
Skeletal muscle	0.9[456, 457]	22.4†[70, 331]	0.9	13.6†[70, 331]
GI tract	1.1	2.0[68, 70]	1.1	2.0[68, 70]
Liver	0.4[70, 331]	1.8[70, 331]	0.25[70, 331]	1.4[70, 331]
Adipose tissue	0.36[458]	11*[68, 70, 331]	0.36	17.1**[70, 331]
Others	1.74	31.069	1.39	22.447
Whole body	5.5[337]	70[68, 70, 331]	5.0[70]	58[70, 331]

Subjects are in overnight fasted conditions. Values for "Others" are chosen to balance whole-body values. † Skeletal muscles, excluding upper extremities which account for 18-20% of total weight. Male total: 28 kg; female total: 17 kg. $*$ Based on 16% body fat content. $**$ Based on 29% body fat content. References are given in brackets. Where experimental data is lacking, female values are assumed to be the same as male values.

Organ volumes are calculated by dividing each tissue weight by its density: brain (1.04 Kg/L)[332], heart and skeletal muscle (1.05 Kg/L)[333], GI tract (1.06 Kg/L)[333], liver (1.08 Kg/L)[334], adipose tissue (0.923 Kg/L)[333]. Assuming that *others* include only nonfat tissues, a tissue density of 1.05 Kg/L is used [335]. The total volume of the body is calculated by adding the volumes of all compartments. Tissue volumes are reported in the main article text.

Table D.9: Substrate and hormone concentrations in blood

	Male	Female
Substrate	Arterial concentration (mM)	Arterial concentration (mM)
GLC	5.0	4.91[14]
PYR	0.068	—
LAC	0.7	—
ALA	0.192	—
GLR	0.07	—
FFA	0.66	0.76[14]
TG	0.99	0.93[15]
O_2	8.0	—
CO_2	21.7	—
Hormone	Plasma concentration (pM)	Plasma concentration (pM)
C_I	45	60
C_G	27	39 [8]

Values at rest for healthy subjects after an overnight fast. Male values are taken from Ref. [68] and references therein. C_I and C_G denote concentrations of insulin and glucagon, respectively. (—) Same values for male and female models. In brackets are references for significantly different values in females compared to males.

Table D.10: Substrate concentrations in each organ/tissue (mM)

Substrate	Brain	Heart	Skeletal muscle	GI tract	Liver	Adipose Tissue
GLC	1.12	1.0	0.48	1.0	8.0	2.54
PYR	0.15	0.2	0.048	0.2	0.37	0.37
LAC	1.45	3.88	1.44	3.88	0.82	0.82
ALA	0	0	1.3	0	0.23	0
GLR	0	0.015	0.064	0.015	0.07	0.22
FFA	0	0.021	0.53	0.021	0.57	0.57
TG	0	3.12	**14.8/18.94**†	450	2.93	**990***
O_2	0.027	0.96	0.49	0.49	0.027	0.027
CO_2	15.43	20.0	15.43	15.43	15.43	15.43
G6P	0.16	0.17	0.24	0.17	0.2	0.2
GLY	2.0	33.0	**95.0***	33.0	**417***	0
GAP	0.15	0.01	0.08	0.01	0.11	0.11
GRP	0	0.29	0.15	0.29	0.24	0.24
ACoA	0.0068**	0.0012	0.0022	0.0012	0.035	0.035
CoA	0.06	0.012	0.018	0.012	0.14	0.14
NAD^+	0.064	0.40	0.45	0.4	0.45	0.45
NADH	0.026	0.045	0.05	0.045	0.05	0.05
ATP	2.45	3.4	6.15	3.4	2.74	2.74
ADP	0.54	0.02	0.02	0.02	1.22	1.22
Pi	2.4	1.66	2.70	1.66	4.6	4.6
PCR	4.6	8.3	20.1	8.3	0	0
CR	5.6	3.5	10.45	3.5	0	0

Values at rest after an overnight fast taken from Ref. [68] and references therein. When two values are listed, they correspond to male/female, otherwise there is no sex difference in substrate concentrations. $*$ For most substrates (excluding null concentrations), sex differences in tissue weights, hence tissue volumes, lead to sex differences in substrate content in each tissue. For example, absolute GLY content is higher in male liver and skeletal muscle, and absolute TG content is higher in female adipose tissue. In addition, women have a higher concentration of intramyocellular lipid (IMCL), despite having a smaller tissue volume. † Women have a 28% higher area density compared to men. IMCL area density (%)= # IMCL/area×mean IMCL size×100% [321]. This result is directly proportional to the lipid concentration per unit volume (mM). $**$ Data from Ref. [459].

Table D.11: Resting values of O_2 consumption and CO_2 production

Organ/Tissue	$\dot{V}O_2$ (ml/min)	$\dot{V}CO_2$ (ml/min)
Brain	51.07	51.07
Heart	26.80	20.61
Skeletal muscle	41.04	32.01
GI tract	10.21	10.21
Liver	62.72	43.72
Adipose tissue	10.08	7.17
Others	48.08	35.21
Whole body	250	200

Subjects are at rest after an overnight fast. Whole-body respiratory quotient (RQ) at rest is 0.8 in female and male models. RQ= $\dot{V}CO_2/\dot{V}O_2$, where $\dot{V}O_2$ and $\dot{V}CO_2$ are oxygen consumption and carbon dioxide production rates. Values for "Others" are chosen to balance whole-body values. Data are taken from Ref. [68] for male. We assumed RQ values are the same at rest in females and males according to Ref. [16].

Table D.12: Organ/tissue metabolic fluxes, $\phi_{X\to Y}$(mmol/min) and reaction maximal velocities, $V_{X\to Y}$ (mmol/min)

	Brain		Heart		Skeletal muscle		GI tract		Liver		Adipose tissue	
Fluxes	$\phi_{X\to Y}$	$V^0_{X\to Y}$	$\phi_{X\to Y}$	$V^0_{X\to Y}$	$\phi_{X\to Y}$	$V^0_{X\to Y}$	$\phi_{X\to Y}$	$V^0_{X\to Y}$	$\phi_{X\to Y}$	$V^0_{X\to Y}$	$\phi_{X\to Y}$	$V^0_{X\to Y}$
$\phi_{GLC\to G6P}$	0.38	0.79	0.04	0.088	0.165	0.398	0.076	0.167	0.17	0.765	0.038	0.079
$\phi_{G6P\to GAP}$	0.38	1.52	0.04	0.16	0.165	0.66	0.076	0.304	0.17	0.68	0.038	0.152
$\phi_{GAP\to PYR}$	0.76	12.16	0.08	1.28	0.33	5.28	0.152	2.432	0.34	5.44	0.056	0.896
$\phi_{PYR\to GAP}$	0	0	0	0	0	0	0	0	0.93	7.44	0	0
$\phi_{GAP\to G6P}$	0	0	0	0	0	0	0	0	1.04	2.08	0	0
$\phi_{G6P\to GLC}$	0	0	0	0	0	0	0	0	0.9	1.8	0	0
$\phi_{G6P\to GLY}$	0.003	0.012	0.04	0.16	0.125	0.5	0	0	0.1	0.4	0	0
$\phi_{GLY\to G6P}$	0.003	0.024	0.04	0.32	0.125	1.0	0	0	0.48	3.84	0	0
$\phi_{PYR\to LAC}$	0.7	2.8	0.088	0.352	1.0/**0.85**†	14.85/**12.62**†	0.2	0.8	0.21	0.84	0.036	0.144
$\phi_{LAC\to PYR}$	0.7	2.8	0.128	0.512	0.488*	12.51	0.2	0.8	0.48	1.92	0.01	0.04
$\phi_{GLR\to GRP}$	0	0	0.004	0.016	0.127	0.508	0	0	0.144	0.576	0	0
$\phi_{GAP\to GRP}$	0	0	0	0	0	0	0	0	0	0	0.02	0.08
$\phi_{GRP\to GAP}$	0	0	0	0	0	0	0	0	0.111	0.444	0	0
$\phi_{PYR\to ALA}$	0	0	0	0	0.04	0.08	0	0	0	0	0	0
$\phi_{ALA\to PYR}$	0	0	0	0	0	0	0	0	0.32	0.64	0	0
$\phi_{PYR\to ACoA}$	0.76	6.08	0.12	0.96	0.292*	2.745	0.152	1.216	0.0013*	0.01*	0.03	0.24
$\phi_{FFA\to ACoA}$	0	0	0.035	0.28	0.088*	0.701	0	0	0.136	1.088	0.02*	0.16
$\phi_{ACoA\to FFA}$	0	0	0	0	0	0	0	0	0.112	0.896	0	0
$\phi_{TG\to FFA—GLR}$	0	0	0.004	0.008	0.13	0.26	0.04	0.08	0.004	0.008	0.095*/**0.114**†	0.19/**0.228**†
$\phi_{FFA—GRP\to TG}$	0	0	0.012	0.096	0.381	3.048	0	0	0.1	0.8	0.06	0.48
$\phi_{ACoA\to CO_2}$	0.76	12.16	0.4	6.4	0.623	9.968	0.152	2.432	0.976	15.62	0.08	1.28
$\phi_{O_2\to H_2O}$	2.28	18.71	1.165	9.327	1.832	14.68	0.456	3.653	2.702	22.18	0.25	2.05
$\phi_{PCR\to CR}$	1.86	7.44	2.0	8.0	20.0	80.0	2.0	8.0	0	0	0	0
$\phi_{CR\to PCR}$	1.86	7.44	2.0	8.0	20.0	80.0	2.0	8.0	0	0	0	0
$\phi_{ATP\to ADP}$	15.20	30.4	7.33	14.66	10.82	21.64	3.04	6.08	13.92	27.84	2.74	5.47

Values at rest after an overnight fast taken from Ref. [68]. When two values are listed, they correspond to male/female, otherwise we assumed no sex difference. $*$ Assumed fluxes under resting conditions. † Estimated female values based on experimental data as presented in Abo et al. [3].

Table D.13: Distinctive Michaelis-Menten parameters

Fluxes	K_M	Brain	Heart	Skeletal muscle	GI tract	Liver	Adipose tissue
$\phi_{GLC \to G6P}$	K_{GLC}	0.05	0.1	0.1	0.1	10.0	0.1
$\phi_{PYR \to LAC\dagger}$	K_{PYR}			0.6			
$\phi_{LAC \to PYR}$	K_{LAC}			17.0			
$\phi_{PYR \to ACoA}$	K_{PYR}			0.065			
$\phi_{O_2 \to H_2O}$	K_{O_2}	0.7	0.7	0.7	0.7	0.7	0.7

Values taken from Ref. [68] and references therein. All values are in mM, except for K_{O_2} values which are in μM. † Specifically for this flux, ν^+ or $K_{\frac{NADH}{NAD^+}} = 0.011$ mM. We assumed no sex difference.

Table D.14: Blood-tissue transport rates (mmol/min) in each tissue/organ

Organ/Tissue	GLC	PYR	LAC	ALA	GLR	FFA	TG
Brain	0.380	0	0	0	0	0	0
Heart	0.040	0	0.040	0	0	0.035	0
Skeletal muscle	0.165	0.005/0.003	-0.112/-0.095	-0.040	-0.003	0.046	0.003
GI tract	0.076	0	0	0	-0.040	-0.120	0.006
Liver	-0.731	0	0.270	0.320	0.140	0.210	-0.029
Adipose tissue	0.038	0	0.056	0	-0.097	-0.211	0.02
Others	0.062	-0.005/-0.003	-0.142/-0.271	-0.280	0	0.040	0
Sum	0.03	0	0	0	0	0	0

Values at rest after an overnight fast taken from Ref. [68] and references therein. These values correspond to the term $Q_x(C_a - \sigma_{x,i}C_{x,i})$ in Eq (A1) in the main article text. Positive values represent substrate uptake into tissue/organs, while negative values represent substrate release into the circulation. Values in "others" are chosen to yield a zero balance at rest. The net sum of 0.03 for glucose indicates that organs consume glucose for energy even when at rest, i.e., blood glucose levels gradually decrease following an overnight fast. When two values are listed, they correspond to male/female, otherwise we assumed no sex difference.

Table D.15: Blood-tissue transport partition coefficients (dimensionless)

Substrate	Brain	Heart	Skeletal muscle	GI tract	Liver	Adipose tissue
Male						
GLC	4.0119	4.84	10.0347	4.931	0.6796	1.9269
PYR	0.4533	0.34	1.3009	0.34	0.1838	0.1838
LAC	0.4828	0.1392	0.5725	0.1804	0.6341	1.0434
ALA	0	0	0.1819	0	-0.10	0
GLR	0	4.6667	1.1458	7.0909	0.0481	1.5429
FFA	0	24.762	1.1488	36.623	1.0526	2.1861
TG	0	0.3173	0.06667	2.187e-3	0.3430	
O_2	183.704	3.3483	12.1723	15.481	215.90	249.976
CO_2	1.6034	1.269	1.5092	1.4332	1.5104	1.4640
Female						
GLC	3.9315	4.75	9.8472	4.841	0.6744	1.8915
PYR	—	—	1.3530	—	—	—
LAC	—	—	0.5596	—	0.6098	—
ALA	0	0	—	0	-0.1958	0
GLR	0	—	—	—	—	—
FFA	0	29.524	1.3375	41.385	1.2164	2.3616
TG	0	0.2981	0.0489	2.0545e-3	0.3232	8.8328e-4
O_2	—	—	—	—	206.97	—
CO_2	—	—	—	—	1.5219	1.4560

A value of zero indicates no substrate uptake or release. (—) Same values for male and female models.

Table D.16: Parameters identified directly from data and/or the literature

Parameter	Value	Equation
$C_{a,\mathrm{LAC}}^{\mathrm{thresh}}$	2 mM [465]	A2
$C_{a,\mathrm{GLR}}^{\mathrm{thresh}}$	0.33 mM [466]	A2
M_G^0	30 min [154]	A5
$M_G^{\max}$	60 min [154]	A5
M_T^0	60 min [154]	A6
$M_T^{\max}$	120 min [154]	A6
D	0.1 min^{-1} [472]	A7, A8

D.4 Sensitivity analysis

We conducted a local, one-at-a-time, sensitivity analysis of the male and female models. Our parameters of interest are fat mass and muscle mass. Local sensitivity analysis involves systematically perturbing each parameter around its nominal value and observing the resulting changes in the model predictions. This results in an approximation of the first-order partial derivative of the model output with respect to the perturbed parameter [462]. Aside from being numerically efficient, sensitivity coefficients obtained from local deterministic sensitivity analysis have the advantage of being intuitive in their interpretation, regardless of the method used.

For each parameter p_j, we calculated relative sensitivities using a forward difference approximation:

$$S_{ij}(t) \approx \frac{p_j}{y_i(p_j, t)} \cdot \frac{y_i(p_j + \Delta p_j, t) - y_i(p_j, t)}{\Delta p_j}, \tag{D.29}$$

where S_{ij} is the first-order local sensitivity coefficient of parameter p_j on model output y_i at time t. We used Δp_j of 5% either up or down. At baseline, the male model has body weight of 70 Kg, with 40% muscle mass and 16% fat mass. The female model has body weight of 58 Kg, with 30% muscle mass and 29.5% fat mass. Our model output of interest are metabolic fluxes in the liver and adipose tissue. Specifically, glycolysis, gluconeogenesis, glycogenesis, and glycogenolysis in the liver, and adipose tissue lipolysis. Results are shown in Figures D.3, D.4, and D.5.

We presented a comprehensive analysis of the findings in the main text and recapitulate the key points here. In general, the magnitude of sensitivity coefficients increases with the duration of fasting, indicating that variations in body composition influence model predictions during the postabsorptive phase, more so than during the absorptive phase.This implies that sex-related differences resulting from body composition variations become more pronounced in our model during fasting than immediately after a meal, aligning with our observations in the main text. In the early postabsorptive phase (9 hours post-meal), liver-related fluxes (gluconeogenesis, glycolysis, glycogenolysis, and glycogenesis) exhibit higher sensitivity to variations in fat and muscle mass in both male and female models. However, in the late postabsorptive phase (24 hours after a meal), adipose tissue lipolysis emerges as the most sensitive flux to changes in body composition. This result underscores an inherent metabolic transition from glucose metabolism, involving the breakdown of glycogen by the liver to produce glucose, to fat metabolism, where adipose tissue undergoes lipolysis, releasing stored lipids as FFA into the circulation for other organs to utilize as fuel. For both high-carbohydrate and high-fat meals, sensitivities are comparable within either the male or female model. Across sexes, the female model demonstrates a higher

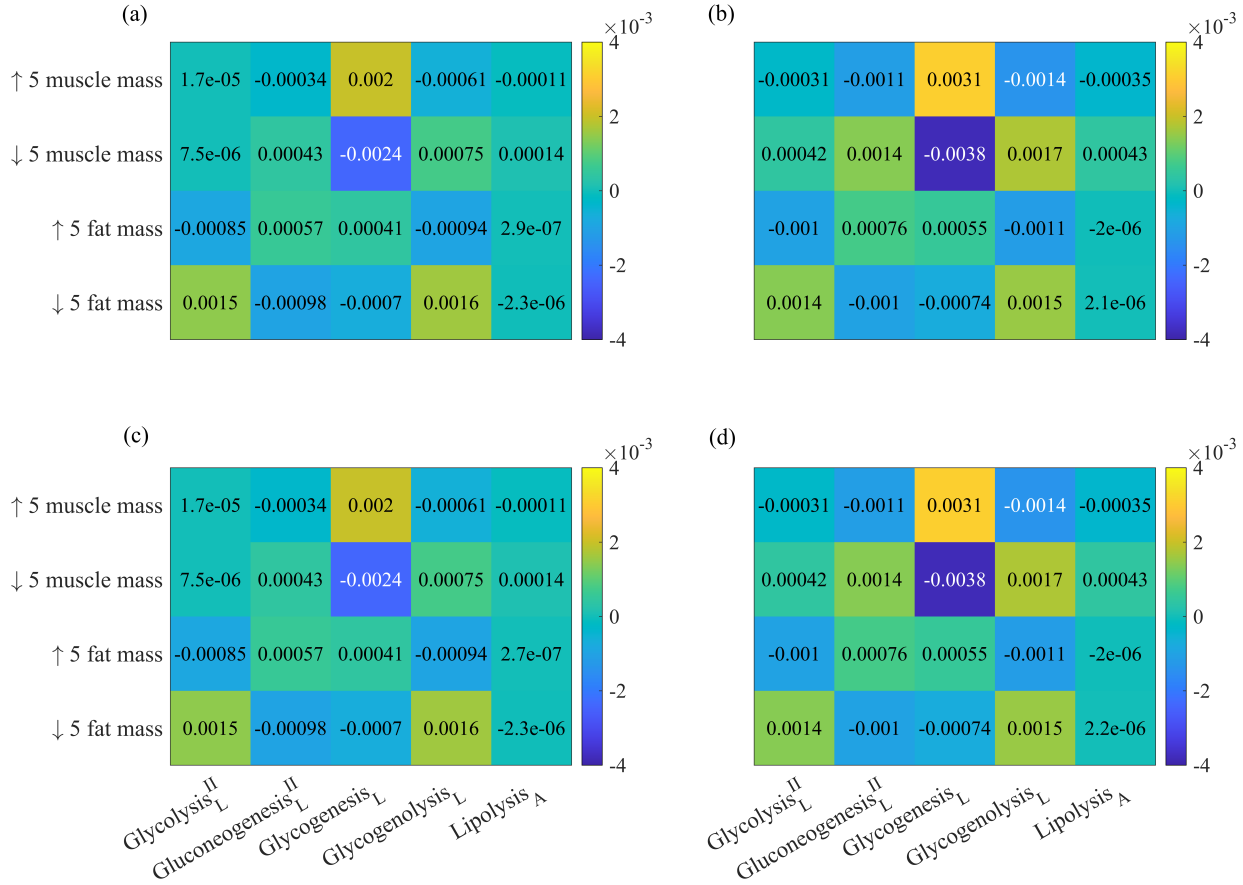

Figure D.3: Results of local sensitivity analysis at 3 hours post-meal. (a) Male model and HiC; (b) female model and HiC; (c) male model and HiF; (d) Female model and HiF. HiC, high-carbohydrate meal; HiF, high-fat meal. Glycolysis II, $\phi_{\text{G6P}\to\text{GAP}}$; gluconeogenesis II, $\phi_{\text{GAP}\to\text{G6P}}$; glycogenesis, $\phi_{\text{G6P}\to\text{GLY}}$; glycogenolysis, $\phi_{\text{GLY}\to\text{G6P}}$, lipolysis, $\phi_{\text{TG}\to\text{FFA–GLR}}$.

sensitivity overall to variations in body composition compared to the male model, although these differences are marginal.

Overall, the sensitivity coefficients exhibit small magnitudes across both the absorptive and postabsorptive phases (Figures D.3–D.5). This suggests that model predictions are robust to variations in body composition (within the range we explored). The observed sex differences are likely attributed to effective mechanistic and rate differences between the sexes. The outcomes of this sensitivity analysis, coupled with our calibration approach,

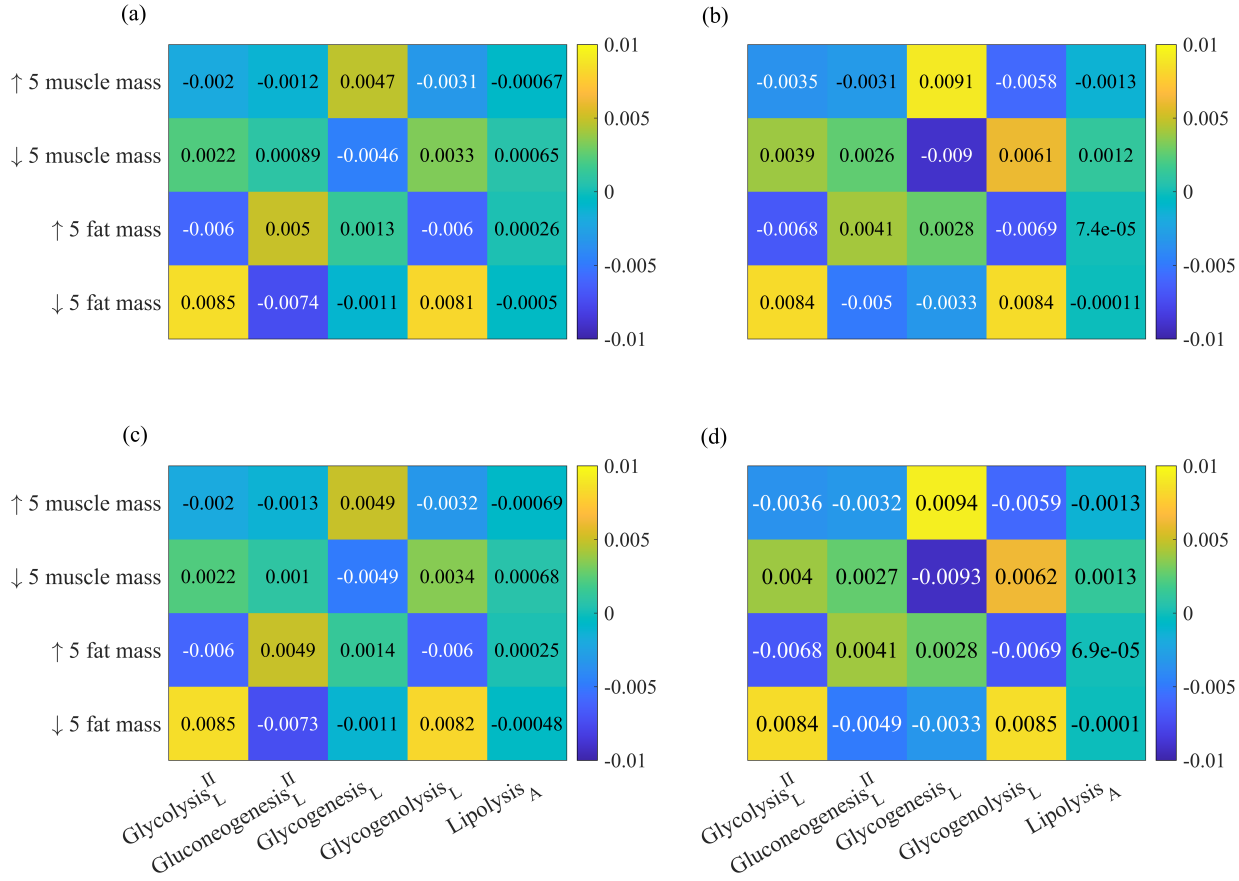

Figure D.4: Results of local sensitivity analysis at 9 hours post-meal. (a) Male model and HiC; (b) female model and HiC; (c) male model and HiF; (d) Female model and HiF. HiC, high-carbohydrate meal; HiF, high-fat meal. Glycolysis II, $\phi_{\text{G6P}\rightarrow\text{GAP}}$; gluconeogenesis II, $\phi_{\text{GAP}\rightarrow\text{G6P}}$; glycogenesis, $\phi_{\text{G6P}\rightarrow\text{GLY}}$; glycogenolysis, $\phi_{\text{GLY}\rightarrow\text{G6P}}$, lipolysis, $\phi_{\text{TG}\rightarrow\text{FFA–GLR}}$.

show that key model output variables are robust to variations in body composition.

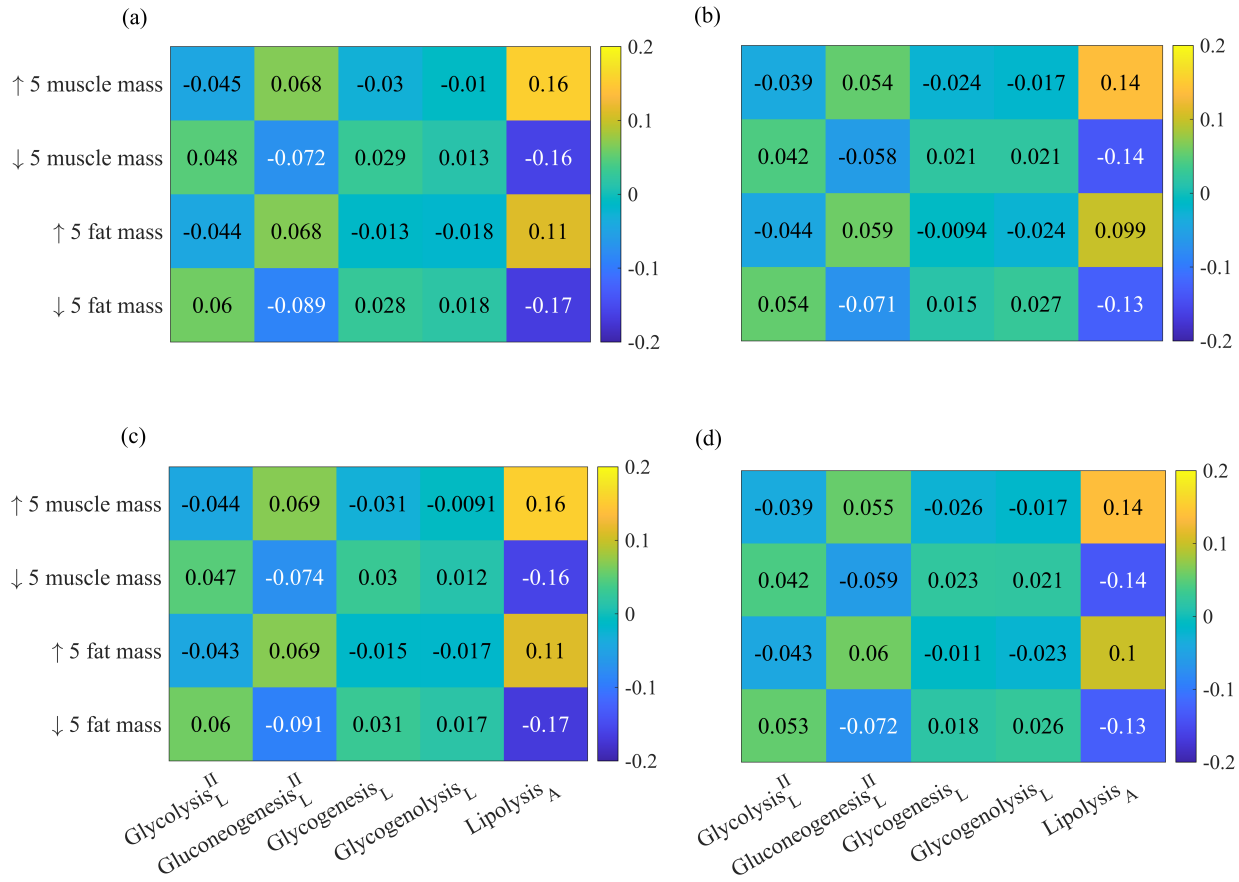

Figure D.5: Results of local sensitivity analysis at 24 hours post-meal. (a) Male model and HiC; (b) female model and HiC; (c) male model and HiF; (d) Female model and HiF. HiC, high-carbohydrate meal; HiF, high-fat meal. Glycolysis II, $\phi_{\text{G6P}\to\text{GAP}}$; gluconeogenesis II, $\phi_{\text{GAP}\to\text{G6P}}$; glycogenesis, $\phi_{\text{G6P}\to\text{GLY}}$; glycogenolysis, $\phi_{\text{GLY}\to\text{G6P}}$, lipolysis, $\phi_{\text{TG}\to\text{FFA–GLR}}$.

D.5 Model equations

Table D.17: Dynamic mass balance equation in tissue/organ x

1. GLC	$\mathrm{V}_x \frac{\mathrm{dC}_{x,\mathrm{GLC}}}{\mathrm{d}t} = \phi_{x,\mathrm{G6P}\to\mathrm{GLC}} - \phi_{x,\mathrm{GLC}\to\mathrm{G6P}} + Q_x(\mathrm{C}_{a,\mathrm{GLC}} - \sigma_{x,\mathrm{GLC}}\mathrm{C}_{x,\mathrm{GLC}})$
2. PYR	$\mathrm{V}_x \frac{\mathrm{dC}_{x,\mathrm{PYR}}}{\mathrm{d}t} = \phi_{x,\mathrm{GAP}\to\mathrm{PYR}} + \phi_{x,\mathrm{LAC}\to\mathrm{PYR}} + \phi_{x,\mathrm{ALA}\to\mathrm{PYR}} - \phi_{x,\mathrm{PYR}\to\mathrm{GAP}} - \phi_{x,\mathrm{PYR}\to\mathrm{LAC}} - \phi_{x,\mathrm{PYR}\to\mathrm{ALA}} - \phi_{x,\mathrm{PYR}\to\mathrm{ACoA}} + Q_x(\mathrm{C}_{a,\mathrm{PYR}} - \sigma_{x,\mathrm{PYR}}\mathrm{C}_{x,\mathrm{PYR}})$
3. LAC	$\mathrm{V}_x \frac{\mathrm{dC}_{x,\mathrm{LAC}}}{\mathrm{d}t} = \phi_{x,\mathrm{PYR}\to\mathrm{LAC}} - \phi_{x,\mathrm{LAC}\to\mathrm{PYR}} + Q_x(\mathrm{C}_{a,\mathrm{LAC}} - \sigma_{x,\mathrm{LAC}}\mathrm{C}_{x,\mathrm{LAC}})$
4. ALA	$\mathrm{V}_x \frac{\mathrm{dC}_{x,\mathrm{ALA}}}{\mathrm{d}t} = \phi_{x,\mathrm{PYR}\to\mathrm{ALA}} - \phi_{x,\mathrm{ALA}\to\mathrm{PYR}} + Q_x(\mathrm{C}_{a,\mathrm{ALA}} - \sigma_{x,\mathrm{ALA}}\mathrm{C}_{x,\mathrm{ALA}})$
5. GLR	$\mathrm{V}_x \frac{\mathrm{dC}_{x,\mathrm{GLR}}}{\mathrm{d}t} = \phi_{x,\mathrm{TG}\to\mathrm{FFA—GLR}} - \phi_{x,\mathrm{GLR}\to\mathrm{GRP}} + Q_x(\mathrm{C}_{a,\mathrm{GLR}} - \sigma_{x,\mathrm{GLR}}\mathrm{C}_{x,\mathrm{GLR}})$
6. FFA	$\mathrm{V}_x \frac{\mathrm{dC}_{x,\mathrm{FFA}}}{\mathrm{d}t} = 3\phi_{x,\mathrm{TG}\to\mathrm{FFA—GLR}} + \frac{1}{8}\phi_{x,\mathrm{ACoA}\to\mathrm{FFA}} - \phi_{x,\mathrm{FFA—GRP}\to\mathrm{TG}} - \phi_{x,\mathrm{FFA}\to\mathrm{ACoA}} + Q_x(\mathrm{C}_{a,\mathrm{FFA}} - \sigma_{x,\mathrm{FFA}}\mathrm{C}_{x,\mathrm{FFA}})$
7. TG	$\mathrm{V}_x \frac{\mathrm{dC}_{x,\mathrm{TG}}}{\mathrm{d}t} = \frac{1}{3}\phi_{x,\mathrm{FFA—GRP}\to\mathrm{TG}} - \phi_{x,\mathrm{TG}\to\mathrm{FFA—GLR}} + Q_x(\mathrm{C}_{a,\mathrm{TG}} - \sigma_{x,\mathrm{TG}}\mathrm{C}_{x,\mathrm{TG}})$
8. O_2	$\mathrm{V}_x \frac{\mathrm{dC}_{x,\mathrm{O_2}}}{\mathrm{d}t} = -\phi_{x,\mathrm{O_2}\to\mathrm{H_2O}} + Q_x(\mathrm{C}_{a,\mathrm{O_2}} - \sigma_{x,\mathrm{O_2}}\mathrm{C}_{x,\mathrm{O_2}})$
9. CO_2	$\mathrm{V}_x \frac{\mathrm{dC}_{x,\mathrm{CO_2}}}{\mathrm{d}t} = \phi_{x,\mathrm{PYR}\to\mathrm{ACoA}} + 2\phi_{x,\mathrm{ACoA}\to\mathrm{CO_2}} + Q_x(\mathrm{C}_{a,\mathrm{CO_2}} - \sigma_{x,\mathrm{CO_2}}\mathrm{C}_{x,\mathrm{CO_2}})$
10. G6P	$\mathrm{V}_x \frac{\mathrm{dC}_{x,\mathrm{G6P}}}{\mathrm{d}t} = \phi_{x,\mathrm{GLC}\to\mathrm{G6P}} + \frac{1}{2}\phi_{x,\mathrm{GAP}\to\mathrm{G6P}} + \phi_{x,\mathrm{GLY}\to\mathrm{G6P}} - \phi_{x,\mathrm{G6P}\to\mathrm{GLC}} - \phi_{x,\mathrm{G6P}\to\mathrm{GAP}} - \phi_{x,\mathrm{G6P}\to\mathrm{GLY}}$
11. GLY	$\mathrm{V}_x \frac{\mathrm{dC}_{x,\mathrm{GLY}}}{\mathrm{d}t} = \phi_{x,\mathrm{G6P}\to\mathrm{GLY}} - \phi_{x,\mathrm{GLY}\to\mathrm{G6P}}$
12. GAP	$\mathrm{V}_x \frac{\mathrm{dC}_{x,\mathrm{GAP}}}{\mathrm{d}t} = 2\phi_{x,\mathrm{G6P}\to\mathrm{GAP}} + \phi_{x,\mathrm{PYR}\to\mathrm{GAP}} + \phi_{x,\mathrm{GRP}\to\mathrm{GAP}} - \phi_{x,\mathrm{GAP}\to\mathrm{G6P}} - \phi_{x,\mathrm{GAP}\to\mathrm{PYR}} - \phi_{x,\mathrm{GAP}\to\mathrm{GRP}}$
13. GRP	$\mathrm{V}_x \frac{\mathrm{dC}_{x,\mathrm{GRP}}}{\mathrm{d}t} = \phi_{x,\mathrm{GLR}\to\mathrm{GRP}} + \phi_{x,\mathrm{GAP}\to\mathrm{GRP}} - \phi_{x,\mathrm{GRP}\to\mathrm{GAP}} - \frac{1}{3}\phi_{x,\mathrm{FFA—GRP}\to\mathrm{TG}}$
14. ACoA	$\mathrm{V}_x \frac{\mathrm{dC}_{x,\mathrm{ACoA}}}{\mathrm{d}t} = \phi_{x,\mathrm{PYR}\to\mathrm{ACoA}} + 8\phi_{x,\mathrm{FFA}\to\mathrm{ACoA}} - \phi_{x,\mathrm{ACoA}\to\mathrm{FFA}} - \phi_{x,\mathrm{ACoA}\to\mathrm{CO_2}}$
15. CoA	$\mathrm{V}_x \frac{\mathrm{dC}_{x,\mathrm{CoA}}}{\mathrm{d}t} = \phi_{x,\mathrm{ACoA}\to\mathrm{FFA}} + \phi_{x,\mathrm{ACoA}\to\mathrm{CO_2}} - \phi_{x,\mathrm{PYR}\to\mathrm{ACoA}} - 8\phi_{x,\mathrm{FFA}\to\mathrm{ACoA}}$
16. NAD^+	$\mathrm{V}_x \frac{\mathrm{dC}_{x,\mathrm{NAD^+}}}{\mathrm{d}t} = \begin{array}{l}\phi_{x,\mathrm{PYR}\to\mathrm{GAP}} + \phi_{x,\mathrm{PYR}\to\mathrm{LAC}} + \phi_{x,\mathrm{GAP}\to\mathrm{GRP}} + \frac{14}{8}\phi_{x,\mathrm{ACoA}\to\mathrm{FFA}} + 2\phi_{x,\mathrm{O_2}\to\mathrm{H_2O}} \\ -\phi_{x,\mathrm{GAP}\to\mathrm{PYR}} - \phi_{x,\mathrm{LAC}\to\mathrm{PYR}} - \phi_{x,\mathrm{GRP}\to\mathrm{GAP}} - \phi_{x,\mathrm{PYR}\to\mathrm{ACoA}} - 14\phi_{x,\mathrm{FFA}\to\mathrm{ACoA}} - 4\phi_{x,\mathrm{ACoA}\to\mathrm{CO_2}}\end{array}$
17. NADH	$\mathrm{V}_x \frac{\mathrm{dC}_{x,\mathrm{NADH}}}{\mathrm{d}t} = \begin{array}{l}\phi_{x,\mathrm{GAP}\to\mathrm{PYR}} + \phi_{x,\mathrm{LAC}\to\mathrm{PYR}} + \phi_{x,\mathrm{GRP}\to\mathrm{GAP}} + \phi_{x,\mathrm{PYR}\to\mathrm{ACoA}} + 14\phi_{x,\mathrm{FFA}\to\mathrm{ACoA}} + 4\phi_{x,\mathrm{ACoA}\to\mathrm{CO_2}} \\ -\phi_{x,\mathrm{PYR}\to\mathrm{GAP}} - \phi_{x,\mathrm{PYR}\to\mathrm{LAC}} - \phi_{x,\mathrm{GAP}\to\mathrm{GRP}} - \frac{14}{8}\phi_{x,\mathrm{ACoA}\to\mathrm{FFA}} - 2\phi_{x,\mathrm{O_2}\to\mathrm{H_2O}}\end{array}$
18. ATP	$\mathrm{V}_x \frac{\mathrm{dC}_{x,\mathrm{ATP}}}{\mathrm{d}t} = \begin{array}{l}2\phi_{x,\mathrm{GAP}\to\mathrm{PYR}} + \phi_{x,\mathrm{ACoA}\to\mathrm{CO_2}} + 6\phi_{x,\mathrm{O_2}\to\mathrm{H_2O}} + \phi_{x,\mathrm{PCR}\to\mathrm{CR}} - \phi_{x,\mathrm{GLC}\to\mathrm{G6P}} - \phi_{x,\mathrm{G6P}\to\mathrm{GAP}} - 3\phi_{x,\mathrm{PYR}\to\mathrm{GAP}} \\ -\phi_{x,\mathrm{G6P}\to\mathrm{GLY}} - \phi_{x,\mathrm{GLR}\to\mathrm{GRP}} - 2\phi_{x,\mathrm{FFA}\to\mathrm{ACoA}} - \frac{7}{8}\phi_{x,\mathrm{ACoA}\to\mathrm{FFA}} - 2\phi_{x,\mathrm{FFA—GRP}\to\mathrm{TG}} - \phi_{x,\mathrm{CR}\to\mathrm{PCR}} - \phi_{x,\mathrm{ATP}\to\mathrm{ADP}}\end{array}$
19. ADP	$\mathrm{V}_x \frac{\mathrm{dC}_{x,\mathrm{ADP}}}{\mathrm{d}t} = \begin{array}{l}\phi_{x,\mathrm{GLC}\to\mathrm{G6P}} + \phi_{x,\mathrm{G6P}\to\mathrm{GAP}} + 3\phi_{x,\mathrm{PYR}\to\mathrm{GAP}} + \phi_{x,\mathrm{G6P}\to\mathrm{GLY}} + \phi_{x,\mathrm{GLR}\to\mathrm{GRP}} + 2\phi_{x,\mathrm{FFA}\to\mathrm{ACoA}} + \frac{7}{8}\phi_{x,\mathrm{ACoA}\to\mathrm{FFA}} \\ +2\phi_{x,\mathrm{FFA—GRP}\to\mathrm{TG}} + \phi_{x,\mathrm{CR}\to\mathrm{PCR}} + \phi_{x,\mathrm{ATP}\to\mathrm{ADP}} - 2\phi_{x,\mathrm{GAP}\to\mathrm{PYR}} - \phi_{x,\mathrm{ACoA}\to\mathrm{CO_2}} - 6\phi_{x,\mathrm{O_2}\to\mathrm{H_2O}} - \phi_{x,\mathrm{PCR}\to\mathrm{CR}}\end{array}$
20. Pi	$\mathrm{V}_x \frac{\mathrm{dC}_{x,\mathrm{Pi}}}{\mathrm{d}t} = \begin{array}{l}2\phi_{x,\mathrm{PYR}\to\mathrm{GAP}} + \frac{1}{2}\phi_{x,\mathrm{GAP}\to\mathrm{G6P}} + \phi_{x,\mathrm{G6P}\to\mathrm{GLC}} + 2\phi_{x,\mathrm{G6P}\to\mathrm{GLY}} + 2\phi_{x,\mathrm{FFA}\to\mathrm{ACoA}} + \frac{7}{8}\phi_{x,\mathrm{ACoA}\to\mathrm{FFA}} \\ +\frac{7}{3}\phi_{x,\mathrm{FFA—GRP}\to\mathrm{TG}} + \phi_{x,\mathrm{ATP}\to\mathrm{ADP}} - \phi_{x,\mathrm{GAP}\to\mathrm{PYR}} - \phi_{x,\mathrm{GLY}\to\mathrm{G6P}} - 6\phi_{x,\mathrm{O_2}\to\mathrm{H_2O}} - \phi_{x,\mathrm{ACoA}\to\mathrm{CO_2}}\end{array}$
21. PCR	$\mathrm{V}_x \frac{\mathrm{dC}_{x,\mathrm{PCR}}}{\mathrm{d}t} = \phi_{x,\mathrm{CR}\to\mathrm{PCR}} - \phi_{x,\mathrm{PCR}\to\mathrm{CR}}$
22. CR	$\mathrm{V}_x \frac{\mathrm{dC}_{x,\mathrm{CR}}}{\mathrm{d}t} = \phi_{x,\mathrm{PCR}\to\mathrm{CR}} - \phi_{x,\mathrm{CR}\to\mathrm{PCR}}$

Organ/tissue x refers to brain, heart, skeletal muscle, GI tract, liver, adipose tissue, or "others"; V_x is a constant parameter and represents the volume of substrate of organ or tissue x. Table D.18 details the metabolic fluxes, $\phi_{x,(\cdot)}$.

Table D.18: Metabolic reaction fluxes

1. Glycolysis I — GLC + ATP → G6P + ADP

$$\phi_{x,\mathrm{GLC}\to\mathrm{G6P}} = V_{x,\mathrm{GLC}\to\mathrm{G6P}} \left(\frac{\frac{\mathrm{C}_{x,\mathrm{GLC}}}{\mathrm{K}_{x,\mathrm{GLC}}}}{1 + \frac{\mathrm{C}_{x,\mathrm{GLC}}}{\mathrm{K}_{x,\mathrm{GLC}}}} \right) \left(\frac{\frac{\mathrm{C}_{x,\mathrm{ATP}}}{\mathrm{C}_{x,\mathrm{ADP}}}}{\mathrm{K}_{x,\frac{\mathrm{ATP}}{\mathrm{ADP}}} + \frac{\mathrm{C}_{x,\mathrm{ATP}}}{\mathrm{C}_{x,\mathrm{ADP}}}} \right)$$

2. Glycolysis II — G6P + ATP → 2 GAP + ADP

$$\phi_{x,\mathrm{G6P}\to\mathrm{GAP}} = V_{x,\mathrm{G6P}\to\mathrm{GAP}} \left(\frac{\frac{\mathrm{C}_{x,\mathrm{G6P}}}{\mathrm{K}_{x,\mathrm{G6P}}}}{1 + \frac{\mathrm{C}_{x,\mathrm{G6P}}}{\mathrm{K}_{x,\mathrm{G6P}}}} \right) \left(\frac{\left(\frac{\mathrm{C}_{x,\mathrm{ADP}}}{\mathrm{C}_{x,\mathrm{ATP}}}\right)^2}{\mathrm{K}^2_{x,\frac{\mathrm{ADP}}{\mathrm{ATP}}} + \left(\frac{\mathrm{C}_{x,\mathrm{ADP}}}{\mathrm{C}_{x,\mathrm{ATP}}}\right)^2} \right)$$

3. Glycolysis III — GAP + Pi + NAD^+ + 2 ADP → PYR + NADH + 2 ATP

$$\phi_{x,\mathrm{GAP}\to\mathrm{PYR}} = V_{x,\mathrm{GAP}\to\mathrm{PYR}} \left(\frac{\frac{\mathrm{C}_{x,\mathrm{GAP}}}{\mathrm{K}_{x,\mathrm{GAP}}} \frac{\mathrm{C}_{x,\mathrm{Pi}}}{\mathrm{K}_{x,\mathrm{Pi}}}}{1 + \frac{\mathrm{C}_{x,\mathrm{GAP}}}{\mathrm{K}_{x,\mathrm{GAP}}} + \frac{\mathrm{C}_{x,\mathrm{Pi}}}{\mathrm{K}_{x,\mathrm{Pi}}} + \frac{\mathrm{C}_{x,\mathrm{GAP}}}{\mathrm{K}_{x,\mathrm{GAP}}} \frac{\mathrm{C}_{x,\mathrm{Pi}}}{\mathrm{K}_{x,\mathrm{Pi}}}} \right) \left(\frac{\frac{\mathrm{C}_{x,\mathrm{NAD+}}}{\mathrm{C}_{x,\mathrm{NADH}}}}{\mathrm{K}_{x,\frac{\mathrm{NAD+}}{\mathrm{NADH}}} + \frac{\mathrm{C}_{x,\mathrm{NAD+}}}{\mathrm{C}_{x,\mathrm{NADH}}}} \right) \left(\frac{\frac{\mathrm{C}_{x,\mathrm{ADP}}}{\mathrm{C}_{x,\mathrm{ATP}}}}{\mathrm{K}_{x,\frac{\mathrm{ADP}}{\mathrm{ATP}}} + \frac{\mathrm{C}_{x,\mathrm{ADP}}}{\mathrm{C}_{x,\mathrm{ATP}}}} \right)$$

4. Gluconeogenesis I — PYR + 3 ATP + NADH → GAP + 3 ADP + NAD^+ + 2 Pi

$$\phi_{x,\mathrm{PYR}\to\mathrm{GAP}} = V_{x,\mathrm{PYR}\to\mathrm{GAP}} \left(\frac{\frac{\mathrm{C}_{x,\mathrm{PYR}}}{\mathrm{K}_{x,\mathrm{PYR}}}}{1 + \frac{\mathrm{C}_{x,\mathrm{PYR}}}{\mathrm{K}_{x,\mathrm{PYR}}}} \right) \left(\frac{\frac{\mathrm{C}_{x,\mathrm{NADH}}}{\mathrm{C}_{x,\mathrm{NAD+}}}}{\mathrm{K}_{x,\frac{\mathrm{NADH}}{\mathrm{NAD+}}} + \frac{\mathrm{C}_{x,\mathrm{NADH}}}{\mathrm{C}_{x,\mathrm{NAD+}}}} \right) \left(\frac{\frac{\mathrm{C}_{x,\mathrm{ATP}}}{\mathrm{C}_{x,\mathrm{ADP}}}}{\mathrm{K}_{x,\frac{\mathrm{ATP}}{\mathrm{ADP}}} + \frac{\mathrm{C}_{x,\mathrm{ATP}}}{\mathrm{C}_{x,\mathrm{ADP}}}} \right)$$

5. Gluconeogenesis II — 2 GAP → G6P + Pi

$$\phi_{x,\mathrm{GAP}\to\mathrm{G6P}} = V_{x,\mathrm{GAP}\to\mathrm{G6P}} \left(\frac{\frac{\mathrm{C}_{x,\mathrm{GAP}}}{\mathrm{K}_{x,\mathrm{GAP}}}}{1 + \frac{\mathrm{C}_{x,\mathrm{GAP}}}{\mathrm{K}_{x,\mathrm{GAP}}}} \right)$$

6. Gluconeogenesis III — G6P → GLC + Pi

$$\phi_{x,\mathrm{G6P}\to\mathrm{GLC}} = V_{x,\mathrm{G6P}\to\mathrm{GLC}} \left(\frac{\frac{\mathrm{C}_{x,\mathrm{G6P}}}{\mathrm{K}_{x,\mathrm{G6P}}}}{1 + \frac{\mathrm{C}_{x,\mathrm{G6P}}}{\mathrm{K}_{x,\mathrm{G6P}}}} \right)$$

7. Glycogenesis — G6P + ATP → GLY + ADP + 2 Pi

$$\phi_{x,\mathrm{G6P}\to\mathrm{GLY}} = V_{x,\mathrm{G6P}\to\mathrm{GLY}} \left(\frac{\frac{\mathrm{C}_{x,\mathrm{G6P}}}{\mathrm{K}_{x,\mathrm{G6P}}}}{1 + \frac{\mathrm{C}_{x,\mathrm{G6P}}}{\mathrm{K}_{x,\mathrm{G6P}}}} \right) \left(\frac{\frac{\mathrm{C}_{x,\mathrm{ATP}}}{\mathrm{C}_{x,\mathrm{ADP}}}}{\mathrm{K}_{x,\frac{\mathrm{ATP}}{\mathrm{ADP}}} + \frac{\mathrm{C}_{x,\mathrm{ATP}}}{\mathrm{C}_{x,\mathrm{ADP}}}} \right)$$

8. Glycogenolysis — GLY + Pi → G6P

$$\phi_{x,\mathrm{GLY}\to\mathrm{G6P}} = V_{x,\mathrm{GLY}\to\mathrm{G6P}} \left(\frac{\frac{\mathrm{C}_{x,\mathrm{GLY}}}{\mathrm{K}_{x,\mathrm{GLY}}} \frac{\mathrm{C}_{x,\mathrm{Pi}}}{\mathrm{K}_{x,\mathrm{Pi}}}}{1 + \frac{\mathrm{C}_{x,\mathrm{GLY}}}{\mathrm{K}_{x,\mathrm{GLY}}} + \frac{\mathrm{C}_{x,\mathrm{Pi}}}{\mathrm{K}_{x,\mathrm{Pi}}} + \frac{\mathrm{C}_{x,\mathrm{GLY}}}{\mathrm{K}_{x,\mathrm{GLY}}} \frac{\mathrm{C}_{x,\mathrm{Pi}}}{\mathrm{K}_{x,\mathrm{Pi}}}} \right) \left(\frac{\left(\frac{\mathrm{C}_{x,\mathrm{ADP}}}{\mathrm{C}_{x,\mathrm{ATP}}}\right)^2}{\mathrm{K}^2_{x,\frac{\mathrm{ADP}}{\mathrm{ATP}}} + \left(\frac{\mathrm{C}_{x,\mathrm{ADP}}}{\mathrm{C}_{x,\mathrm{ATP}}}\right)^2} \right)$$

9. Pyruvate Reduction — PYR + NADH → LAC + NAD^+

$$\phi_{x,\mathrm{PYR}\to\mathrm{LAC}} = V_{x,\mathrm{PYR}\to\mathrm{LAC}} \left(\frac{\frac{\mathrm{C}_{x,\mathrm{PYR}}}{\mathrm{K}_{x,\mathrm{PYR}}}}{1 + \frac{\mathrm{C}_{x,\mathrm{PYR}}}{\mathrm{K}_{x,\mathrm{PYR}}}} \right) \left(\frac{\frac{\mathrm{C}_{x,\mathrm{NADH}}}{\mathrm{C}_{x,\mathrm{NAD^+}}}}{\mathrm{K}_{x,\frac{\mathrm{NADH}}{\mathrm{NAD^+}}} + \frac{\mathrm{C}_{x,\mathrm{NADH}}}{\mathrm{C}_{x,\mathrm{NAD^+}}}} \right)$$

10. Lactate Oxidation $\mathrm{LAC} + \mathrm{NAD^+} \rightarrow \mathrm{PYR} + \mathrm{NADH}$

$$\phi_{x,\mathrm{LAC}\to\mathrm{PYR}} = V_{x,\mathrm{LAC}\to\mathrm{PYR}} \left(\frac{\frac{\mathrm{C}_{x,\mathrm{LAC}}}{\mathrm{K}_{x,\mathrm{LAC}}}}{1 + \frac{\mathrm{C}_{x,\mathrm{LAC}}}{\mathrm{K}_{x,\mathrm{LAC}}}} \right) \left(\frac{\frac{\mathrm{C}_{x,\mathrm{NAD^+}}}{\mathrm{C}_{x,\mathrm{NADH}}}}{\mathrm{K}_{x,\frac{\mathrm{NAD^+}}{\mathrm{NADH}}} + \frac{\mathrm{C}_{x,\mathrm{NAD^+}}}{\mathrm{C}_{x,\mathrm{NADH}}}} \right)$$

11. Glycerol Phosphorylation $\mathrm{GLR} + \mathrm{ATP} \rightarrow \mathrm{GRP} + \mathrm{ADP}$

$$\phi_{x,\mathrm{GLR}\to\mathrm{GRP}} = V_{x,\mathrm{GLR}\to\mathrm{GRP}} \left(\frac{\frac{\mathrm{C}_{x,\mathrm{GLR}}}{\mathrm{K}_{x,\mathrm{GLR}}}}{1 + \frac{\mathrm{C}_{x,\mathrm{GLR}}}{\mathrm{K}_{x,\mathrm{GLR}}}} \right) \left(\frac{\frac{\mathrm{C}_{x,\mathrm{ATP}}}{\mathrm{C}_{x,\mathrm{ADP}}}}{\mathrm{K}_{x,\frac{\mathrm{ATP}}{\mathrm{ADP}}} + \frac{\mathrm{C}_{x,\mathrm{ATP}}}{\mathrm{C}_{x,\mathrm{ADP}}}} \right)$$

12. GAP Reduction $\mathrm{GAP} + \mathrm{NADH} \rightarrow \mathrm{GRP} + \mathrm{NAD^+}$

$$\phi_{x,\mathrm{GAP}\to\mathrm{GRP}} = V_{x,\mathrm{GAP}\to\mathrm{GRP}} \left(\frac{\frac{\mathrm{C}_{x,\mathrm{GAP}}}{\mathrm{K}_{x,\mathrm{GAP}}}}{1 + \frac{\mathrm{C}_{x,\mathrm{GAP}}}{\mathrm{K}_{x,\mathrm{GAP}}}} \right) \left(\frac{\frac{\mathrm{C}_{x,\mathrm{NADH}}}{\mathrm{C}_{x,\mathrm{NAD^+}}}}{\mathrm{K}_{x,\frac{\mathrm{NADH}}{\mathrm{NAD^+}}} + \frac{\mathrm{C}_{x,\mathrm{NADH}}}{\mathrm{C}_{x,\mathrm{NAD^+}}}} \right)$$

13. GRP Oxidation $\mathrm{GRP} + \mathrm{NAD^+} \rightarrow \mathrm{GAP} + \mathrm{NADH}$

$$\phi_{x,\mathrm{GRP}\to\mathrm{GAP}} = V_{x,\mathrm{GRP}\to\mathrm{GAP}} \left(\frac{\frac{\mathrm{C}_{x,\mathrm{GRP}}}{\mathrm{K}_{x,\mathrm{GRP}}}}{1 + \frac{\mathrm{C}_{x,\mathrm{GRP}}}{\mathrm{K}_{x,\mathrm{GRP}}}} \right) \left(\frac{\frac{\mathrm{C}_{x,\mathrm{NAD^+}}}{\mathrm{C}_{x,\mathrm{NADH}}}}{\mathrm{K}_{x,\frac{\mathrm{NAD^+}}{\mathrm{NADH}}} + \frac{\mathrm{C}_{x,\mathrm{NAD^+}}}{\mathrm{C}_{x,\mathrm{NADH}}}} \right)$$

14. Alanine Formation $\mathrm{PYR} \rightarrow \mathrm{ALA}$

$$\phi_{x,\mathrm{PYR}\to\mathrm{ALA}} = V_{x,\mathrm{PYR}\to\mathrm{ALA}} \left(\frac{\frac{\mathrm{C}_{x,\mathrm{PYR}}}{\mathrm{K}_{x,\mathrm{PYR}}}}{1 + \frac{\mathrm{C}_{x,\mathrm{PYR}}}{\mathrm{K}_{x,\mathrm{PYR}}}} \right)$$

15. Alanine Utilization $\mathrm{ALA} \rightarrow \mathrm{PYR}$

$$\phi_{x,\mathrm{ALA}\to\mathrm{PYR}} = V_{x,\mathrm{ALA}\to\mathrm{PYR}} \left(\frac{\frac{\mathrm{C}_{x,\mathrm{ALA}}}{\mathrm{K}_{x,\mathrm{ALA}}}}{1 + \frac{\mathrm{C}_{x,\mathrm{ALA}}}{\mathrm{K}_{x,\mathrm{ALA}}}} \right)$$

16. Pyruvate Oxidation $\mathrm{PYR} + \mathrm{CoA} + \mathrm{NAD^+} \rightarrow \mathrm{ACoA} + \mathrm{NADH} + \mathrm{CO_2}$

$$\phi_{x,\mathrm{PYR}\to\mathrm{ACoA}} = V_{x,\mathrm{PYR}\to\mathrm{ACoA}} \left(\frac{\frac{\mathrm{C}_{x,\mathrm{PYR}}}{\mathrm{K}_{x,\mathrm{PYR}}} \frac{\mathrm{C}_{x,\mathrm{CoA}}}{\mathrm{K}_{x,\mathrm{CoA}}}}{1 + \frac{\mathrm{C}_{x,\mathrm{PYR}}}{\mathrm{K}_{x,\mathrm{PYR}}} + \frac{\mathrm{C}_{x,\mathrm{CoA}}}{\mathrm{K}_{x,\mathrm{CoA}}} + \frac{\mathrm{C}_{x,\mathrm{PYR}}}{\mathrm{K}_{x,\mathrm{PYR}}} \frac{\mathrm{C}_{x,\mathrm{CoA}}}{\mathrm{K}_{x,\mathrm{CoA}}}} \right) \left(\frac{\frac{\mathrm{C}_{x,\mathrm{NAD^+}}}{\mathrm{C}_{x,\mathrm{NADH}}}}{\mathrm{K}_{x,\frac{\mathrm{NAD^+}}{\mathrm{NADH}}} + \frac{\mathrm{C}_{x,\mathrm{NAD^+}}}{\mathrm{C}_{x,\mathrm{NADH}}}} \right)$$

17. Fatty Acid Oxidation $\mathrm{FFA} + 8\ \mathrm{CoA} + 2\ \mathrm{ATP} + 14\ \mathrm{NAD^+} \rightarrow 8\ \mathrm{ACoA} + 2\ \mathrm{ADP} + 2\ \mathrm{Pi} + 14\ \mathrm{NADH}$

$$\phi_{x,\mathrm{FFA}\to\mathrm{ACoA}} = V_{x,\mathrm{FFA}\to\mathrm{ACoA}} \left(\frac{\frac{\mathrm{C}_{x,\mathrm{FFA}}}{\mathrm{K}_{x,\mathrm{FFA}}} \frac{\mathrm{C}_{x,\mathrm{CoA}}}{\mathrm{K}_{x,\mathrm{CoA}}}}{1 + \frac{\mathrm{C}_{x,\mathrm{FFA}}}{\mathrm{K}_{x,\mathrm{FFA}}} + \frac{\mathrm{C}_{x,\mathrm{CoA}}}{\mathrm{K}_{x,\mathrm{CoA}}} + \frac{\mathrm{C}_{x,\mathrm{FFA}}}{\mathrm{K}_{x,\mathrm{FFA}}} \frac{\mathrm{C}_{x,\mathrm{CoA}}}{\mathrm{K}_{x,\mathrm{CoA}}}} \right) \left(\frac{\frac{\mathrm{C}_{x,\mathrm{NAD^+}}}{\mathrm{C}_{x,\mathrm{NADH}}}}{\mathrm{K}_{x,\frac{\mathrm{NAD^+}}{\mathrm{NADH}}} + \frac{\mathrm{C}_{x,\mathrm{NAD^+}}}{\mathrm{C}_{x,\mathrm{NADH}}}} \right)$$

18. Fatty Acid Synthesis $8\ \mathrm{ACoA} + 7\ \mathrm{ATP} + 14\ \mathrm{NADH} \rightarrow \mathrm{FFA} + 8\ \mathrm{CoA} + 7\ \mathrm{ADP} + 7\ \mathrm{Pi} + 14\ \mathrm{NAD^+}$

$$\phi_{x,\mathrm{ACoA}\rightarrow\mathrm{FFA}} = V_{x,\mathrm{ACoA}\rightarrow\mathrm{FFA}} \left(\frac{\frac{\mathrm{C}_{x,\mathrm{ACoA}}}{\mathrm{K}_{x,\mathrm{ACoA}}}}{1 + \frac{\mathrm{C}_{x,\mathrm{ACoA}}}{\mathrm{K}_{x,\mathrm{ACoA}}}} \right) \left(\frac{\frac{\mathrm{C}_{x,\mathrm{NADH}}}{\mathrm{C}_{x,\mathrm{NAD^+}}}}{\mathrm{K}_{x,\frac{\mathrm{NADH}}{\mathrm{NAD^+}}} + \frac{\mathrm{C}_{x,\mathrm{NADH}}}{\mathrm{C}_{x,\mathrm{NAD^+}}}} \right) \left(\frac{\frac{\mathrm{C}_{x,\mathrm{ATP}}}{\mathrm{C}_{x,\mathrm{ADP}}}}{\mathrm{K}_{x,\frac{\mathrm{ATP}}{\mathrm{ADP}}} + \frac{\mathrm{C}_{x,\mathrm{ATP}}}{\mathrm{C}_{x,\mathrm{ADP}}}} \right)$$

19. Lipolysis $\mathrm{TG} \rightarrow \mathrm{GLR} + 3\ \mathrm{FFA}$

$$\phi_{x,\mathrm{TG}\rightarrow\mathrm{FFA—GLR}} = V_{x,\mathrm{TG}\rightarrow\mathrm{FFA—GLR}} \left(\frac{\frac{\mathrm{C}_{x,\mathrm{TG}}}{\mathrm{K}_{x,\mathrm{TG}}}}{1 + \frac{\mathrm{C}_{x,\mathrm{TG}}}{\mathrm{K}_{x,\mathrm{TG}}}} \right)$$

20. Triglyceride Synthesis $\mathrm{GRP} + 3\ \mathrm{FFA} + 6\ \mathrm{ATP} \rightarrow \mathrm{TG} + 6\ \mathrm{ADP} + 7\ \mathrm{Pi}$

$$\phi_{x,\mathrm{FFA—GRP}\rightarrow\mathrm{TG}} = V_{x,\mathrm{FFA—GRP}\rightarrow\mathrm{TG}} \left(\frac{\frac{\mathrm{C}_{x,\mathrm{FFA}}}{\mathrm{K}_{x,\mathrm{FFA}}} \frac{\mathrm{C}_{x,\mathrm{GRP}}}{\mathrm{K}_{x,\mathrm{GRP}}}}{1 + \frac{\mathrm{C}_{x,\mathrm{FFA}}}{\mathrm{K}_{x,\mathrm{FFA}}} + \frac{\mathrm{C}_{x,\mathrm{GRP}}}{\mathrm{K}_{x,\mathrm{GRP}}} + \frac{\mathrm{C}_{x,\mathrm{FFA}}}{\mathrm{K}_{x,\mathrm{FFA}}} \frac{\mathrm{C}_{x,\mathrm{GRP}}}{\mathrm{K}_{x,\mathrm{GRP}}}} \right) \left(\frac{\frac{\mathrm{C}_{x,\mathrm{ATP}}}{\mathrm{C}_{x,\mathrm{ADP}}}}{\mathrm{K}_{x,\frac{\mathrm{ATP}}{\mathrm{ADP}}} + \frac{\mathrm{C}_{x,\mathrm{ATP}}}{\mathrm{C}_{x,\mathrm{ADP}}}} \right)$$

21. TCA Cycle $\mathrm{ACoA} + \mathrm{ADP} + \mathrm{Pi} + 4\ \mathrm{NAD^+} \rightarrow 2\ \mathrm{CO_2} + \mathrm{CoA} + \mathrm{ATP} + 4\ \mathrm{NADH}$

$$\phi_{x,\mathrm{ACoA}\rightarrow\mathrm{CO_2}} = V_{x,\mathrm{ACoA}\rightarrow\mathrm{CO_2}} \left(\frac{\frac{\mathrm{C}_{x,\mathrm{ACoA}}}{\mathrm{K}_{x,\mathrm{ACoA}}} \frac{\mathrm{C}_{x,\mathrm{Pi}}}{\mathrm{K}_{x,\mathrm{Pi}}}}{1 + \frac{\mathrm{C}_{x,\mathrm{ACoA}}}{\mathrm{K}_{x,\mathrm{ACoA}}} + \frac{\mathrm{C}_{x,\mathrm{Pi}}}{\mathrm{K}_{x,\mathrm{Pi}}} + \frac{\mathrm{C}_{x,\mathrm{ACoA}}}{\mathrm{K}_{x,\mathrm{ACoA}}} \frac{\mathrm{C}_{x,\mathrm{Pi}}}{\mathrm{K}_{x,\mathrm{Pi}}}} \right) \left(\frac{\frac{\mathrm{C}_{x,\mathrm{ADP}}}{\mathrm{C}_{x,\mathrm{ATP}}}}{\mathrm{K}_{x,\frac{\mathrm{ADP}}{\mathrm{ATP}}} + \frac{\mathrm{C}_{x,\mathrm{ADP}}}{\mathrm{C}_{x,\mathrm{ATP}}}} \right) \left(\frac{\frac{\mathrm{C}_{x,\mathrm{NAD^+}}}{\mathrm{C}_{x,\mathrm{NADH}}}}{\mathrm{K}_{x,\frac{\mathrm{NAD^+}}{\mathrm{NADH}}} + \frac{\mathrm{C}_{x,\mathrm{NAD^+}}}{\mathrm{C}_{x,\mathrm{NADH}}}} \right)$$

22. Oxidative Phosphorylation $\mathrm{O_2} + 6\ \mathrm{ADP} + 6\ \mathrm{Pi} + 2\ \mathrm{NADH} \rightarrow 2\ \mathrm{H_2O} + 6\ \mathrm{ATP} + 2\ \mathrm{NAD^+}$

$$\phi_{x,\mathrm{O_2}\rightarrow\mathrm{H_2O}} = V_{x,\mathrm{O_2}\rightarrow\mathrm{H_2O}} \left(\frac{\frac{\mathrm{C}_{x,\mathrm{O_2}}}{\mathrm{K}_{x,\mathrm{O_2}}} \frac{\mathrm{C}_{x,\mathrm{Pi}}}{\mathrm{K}_{x,\mathrm{Pi}}}}{1 + \frac{\mathrm{C}_{x,\mathrm{O_2}}}{\mathrm{K}_{x,\mathrm{O_2}}} + \frac{\mathrm{C}_{x,\mathrm{Pi}}}{\mathrm{K}_{x,\mathrm{Pi}}} + \frac{\mathrm{C}_{x,\mathrm{O_2}}}{\mathrm{K}_{x,\mathrm{O_2}}} \frac{\mathrm{C}_{x,\mathrm{Pi}}}{\mathrm{K}_{x,\mathrm{Pi}}}} \right) \left(\frac{\frac{\mathrm{C}_{x,\mathrm{ADP}}}{\mathrm{C}_{x,\mathrm{ATP}}}}{\mathrm{K}_{x,\frac{\mathrm{ADP}}{\mathrm{ATP}}} + \frac{\mathrm{C}_{x,\mathrm{ADP}}}{\mathrm{C}_{x,\mathrm{ATP}}}} \right) \left(\frac{\frac{\mathrm{C}_{x,\mathrm{NADH}}}{\mathrm{C}_{x,\mathrm{NAD^+}}}}{\mathrm{K}_{x,\frac{\mathrm{NADH}}{\mathrm{NAD^+}}} + \frac{\mathrm{C}_{x,\mathrm{NADH}}}{\mathrm{C}_{x,\mathrm{NAD^+}}}} \right)$$

23. Phosphocreatine Breakdown $\mathrm{PCR} + \mathrm{ADP} \rightarrow \mathrm{CR} + \mathrm{ATP}$

$$\phi_{x,\mathrm{PCR}\rightarrow\mathrm{CR}} = V_{x,\mathrm{PCR}\rightarrow\mathrm{CR}} \left(\frac{\frac{\mathrm{C}_{x,\mathrm{PCR}}}{\mathrm{K}_{x,\mathrm{PCR}}}}{1 + \frac{\mathrm{C}_{x,\mathrm{PCR}}}{\mathrm{K}_{x,\mathrm{PCR}}}} \right) \left(\frac{\frac{\mathrm{C}_{x,\mathrm{ADP}}}{\mathrm{C}_{x,\mathrm{ATP}}}}{\mathrm{K}_{x,\frac{\mathrm{ADP}}{\mathrm{ATP}}} + \frac{\mathrm{C}_{x,\mathrm{ADP}}}{\mathrm{C}_{x,\mathrm{ATP}}}} \right)$$

24. Phosphcreatine Synthesis $\mathrm{CR} + \mathrm{ATP} \rightarrow \mathrm{PCR} + \mathrm{ADP}$

$$\phi_{x,\mathrm{CR}\rightarrow\mathrm{PCR}} = V_{x,\mathrm{CR}\rightarrow\mathrm{PCR}} \left(\frac{\frac{\mathrm{C}_{x,\mathrm{CR}}}{\mathrm{K}_{x,\mathrm{CR}}}}{1 + \frac{\mathrm{C}_{x,\mathrm{CR}}}{\mathrm{K}_{x,\mathrm{CR}}}} \right) \left(\frac{\frac{\mathrm{C}_{x,\mathrm{ATP}}}{\mathrm{C}_{x,\mathrm{ADP}}}}{\mathrm{K}_{x,\frac{\mathrm{ATP}}{\mathrm{ADP}}} + \frac{\mathrm{C}_{x,\mathrm{ATP}}}{\mathrm{C}_{x,\mathrm{ADP}}}} \right)$$

25. ATP Hydrolysis $\mathrm{ATP} \rightarrow \mathrm{ADP} + \mathrm{Pi}$

$$\phi_{x,\mathrm{ATP}\rightarrow\mathrm{ADP}} = V_{x,\mathrm{ATP}\rightarrow\mathrm{ADP}} \left(\frac{\frac{\mathrm{C}_{x,\mathrm{ATP}}}{\mathrm{K}_{x,\mathrm{ATP}}}}{1 + \frac{\mathrm{C}_{x,\mathrm{ATP}}}{\mathrm{K}_{x,\mathrm{ATP}}}} \right)$$

D.6 Key metabolic fluxes

- Gluconeogenesis $= \phi_{x,\mathrm{GAP}\rightarrow\mathrm{G6P}}$, where x is liver;
- Glycolysis $\phi_{x,\mathrm{G6P}\rightarrow\mathrm{GAP}}$, where x is brain, heart, skeletal muscle, GI tract, liver, and

adipose tissue;

- Net hepatic gluconeogenesis $= \frac{\phi_{x,\text{GAP}\rightarrow\text{G6P}}}{2} - \phi_{x,\text{G6P}\rightarrow\text{GAP}}$, where x is liver;
- Glycogenesis $= \phi_{x,\text{G6P}\rightarrow\text{GLY}}$, where x is brain, heart, skeletal muscle, and liver;
- Glycogenolysis $= \phi_{x,\text{GLY}\rightarrow\text{G6P}}$, where x is brain, heart, skeletal muscle, and liver;
- Net glycogenolysis $= \phi_{x,\text{GLY}\rightarrow\text{G6P}} - \phi_{x,\text{G6P}\rightarrow\text{GLY}}$, where x is brain, heart, skeletal muscle, and liver;
- Lipolysis $= \phi_{x,\text{TG}\rightarrow\text{FFA–GLR}}$, where x is heart, skeletal muscle, GI tract, liver, and adipose tissue;
- TG synthesis $= \phi_{x,\text{FFA–GRP}\rightarrow\text{TG}}$, where x is heart, skeletal muscle, GI tract, liver, and adipose tissue;
- Net TG breakdown $= \phi_{x,\text{TG}\rightarrow\text{FFA–GLR}} - \frac{\phi_{x,\text{FFA–GRP}\rightarrow\text{TG}}}{3}$, where x is heart, skeletal muscle, GI tract, liver, and adipose tissue;
- Summing the above fluxes for all relevant organs yields whole-body fluxes.